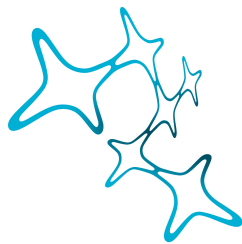


AMALIA BRAUN

DIRECTION SELECTIVITY OF
MOTION SENSITIVE
T5 NEURONS IN
DROSOPHILA



Graduate School of
Systemic Neurosciences

LMU Munich

Dissertation der Graduate School of Systemic Neurosciences der
Ludwig-Maximilians-Universität München

26th of April, 2024

Amalia Braun

Direction selectivity of motion sensitive T5 neurons in Drosophila

Dissertation der Graduate School of Systemic Neurosciences der
Ludwig-Maximilians-Universität München.

E-MAIL:

amalia.braun@bi.mpg.de

26th of April, 2024

First reviewer and supervisor
Prof. Dr. Alexander Borst
Max Planck Institute for Biological Intelligence

Second reviewer
Prof. Dr. Laura Busse
Ludwig Maximilians University

Date of submission
26th of April, 2024

Date of Defense
12th of December, 2024

SUMMARY

Neural circuits provide the basis for all computations in the brain. Understanding how information is processed within these circuits is a fundamental goal in neuroscience research. Studying neural circuits with a relatively small number of neurons has provided important insight into the brain's computational properties. The motion vision circuit of the fruit fly, *Drosophila melanogaster*, is one of such commonly studied neural networks. The ability to detect visual motion is vital for all sighted animals to navigate in the environment, escape predators and detect conspecifics. Already more than half a century ago, the first algorithmic models described the computation of motion direction from visual signals. An essential aspect in this model of motion detection is the enhancement of signals moving in the preferred direction (preferred-direction enhancement) and the suppression of signals moving in the opposite or null direction (null-direction suppression), both crucial for accurate motion perception. Many studies have advanced our understanding of how the computation of visual motion is implemented at the neural and biophysical level in *Drosophila*. The discovery of T4 and T5 cells, the first direction-selective neurons in the motion vision circuit, followed by the characterisation of their input elements, was an important milestone. At the beginning of my doctoral studies, the computational and biophysical mechanisms of how the T4 and T5 neurons become direction selective was still elusive.

The goal of my doctoral research was to understand how motion is computed in the OFF motion vision pathway at the level of T5 neurons in *Drosophila melanogaster*. As described in my first publication, I discovered how null-direction suppression is realised in the *Drosophila* OFF motion vision pathway ([Manuscript 1](#); [Braun et al., 2023](#)). A pivotal finding emerged from connectomic analysis, uncovering a columnar microcircuit among certain input neurons to T5. Using two-photon calcium imaging in combination with thermogenetics, optogenetics, apoptotic methods, and pharmacology, I demonstrated how disynaptic inhibition shapes the tuning of OFF motion detectors in *Drosophila*, directly linked to the identified columnar microcircuit. Additionally, the CT1 cell was pinpointed as the input neuron crucial for null-direction suppression at the T5 neuron level, marking a significant advancement in our understanding of visual OFF motion detection. In the course of studying connectivity of the OFF motion vision pathway and its downstream circuits, I contributed to the first full connectome of the adult fly brain, a worldwide collaborative effort led to a complete neural wiring diagram of an adult fly brain ([Manuscript 2](#); [Dorkenwald et al., 2024](#)). Moreover, this connectome provides systematic and hierarchical annotations of ~130,000 neurons, which covers neuronal classes, cell types and developmental units. ([Manuscript 3](#); [Schlegel et al., 2024](#)). Finally, I was involved in the catalogue of neuronal cell types and

wiring diagrams for the visual system of *Drosophila* (**Manuscript 4**; Matsliah et al., 2024).

Taken together, the manuscripts contained in this thesis advance the knowledge of motion detection in the OFF pathway as well as the synaptic connectivity of a whole adult fly brain.

CONTENTS

i	Introduction	1
1	Processing of sensory information in the brain	1
2	Models of motion vision	3
2.1	Hassenstein-Reichardt detector	3
2.2	Barlow-Levick detector	4
2.3	Three-arm detector	5
3	Tools in circuit neuroscience	8
3.1	<i>Drosophila melanogaster</i> as a model organism	8
3.2	Genetic techniques	8
3.2.1	Expression systems	8
3.2.2	Effector genes	10
3.3	Physiological techniques	14
3.3.1	Two-photon calcium imaging	14
3.3.2	Whole-cell patch clamp recording	15
3.4	Electron microscopy	15
4	Visual motion processing in <i>Drosophila</i>	18
4.1	The retina and optic lobe	18
4.2	Two parallel neural circuits of motion vision	19
4.2.1	T5 cells and the OFF pathway	23
4.2.2	T4 cells and the ON pathway	24
5	Goal of this thesis	25
ii	Publications	27
1	Manuscript 1: Disynaptic inhibition shapes tuning of OFF-motion detectors in <i>Drosophila</i>	27
2	Manuscript 2: Neuronal wiring diagram of an adult brain	51
3	Manuscript 3: Whole-brain annotation and multi-connectome cell typing quantifies circuit stereotype in <i>Drosophila</i>	87
4	Manuscript 4: Neuronal parts list and wiring diagram for a visual system	129
iii	Discussion	171
1	Connectomes	171
2	From motion information to behaviour	174
2.1	Downstream circuits of T4 and T5 neurons	174
3	Comparing vertebrate and invertebrate visual systems	177
4	Comparing T4 ON neurons and T5 OFF neurons in <i>Drosophila</i>	180
4.1	Multiplicative disinhibition in the preferred direction of T4 neurons	182
4.2	Potential biophysical mechanism for preferred direction-enhancement in T5 neurons	182
5	Outlook	185
	Bibliography	187

LIST OF FIGURES

Figure 1	Hassenstein-Reichardt detector	4
Figure 2	Barlow-Levick detector	5
Figure 3	Three-arm detector	7
Figure 4	Illustration of the Gal4-UAS system in <i>Drosophila</i>	9
Figure 5	Illustration of two optogenetic channels	13
Figure 6	Volume electron microscopy methods	17
Figure 7	Optic lobe of <i>Drosophila</i>	18
Figure 8	Neural elements of ON and OFF motion vision detection	20
Figure 9	Direction-selective T5 neurons	22
Figure 10	Directional tuning of T5c	181

I | INTRODUCTION

1 PROCESSING OF SENSORY INFORMATION IN THE BRAIN

Information processing in the brain is a complex and multi-layered process that involves the transformation of sensory inputs into electrical signals of neurons, the processing and integration of such signals with other external or internal signals, and finally the control of behavioural output by concerted activation of specific sets of muscles. The sensory systems are fundamental mechanisms that equip animals with the ability to gather and process information from their surroundings. Through these systems, organisms can detect various physical properties such as light, sound, and odour, which are essential for navigating through the environment, identifying resources, interacting socially and avoiding danger. Early processing stages of sensory systems extract certain stimulus features and represent them in parallel for further use in guiding behaviour (Laughlin, 1981; Heng et al., 2020). Transduction is the critical process through which sensory receptors convert physical stimuli into electrical signals and differs across sensory modalities: in vision for example, photons activate light sensitive rhodopsins, while in olfaction, odour molecules bind to specialised receptors. The electrical signals within neurons consist of ion currents and membrane potentials. The information encoded in these electrical signals is then transmitted to downstream neurons via electrical or chemical synapses. Through biophysical mechanisms within and between neurons, electrical signals are processed and computed to interpret sensory information. Sensory stimuli are rich in information regarding their identity (the type of stimulus), timing (the occurrence), intensity (the magnitude), and location (the origin) (Fechner, 1860). The aspect of timing is encoded as neurons become active in response to the presence or absence of a stimulus. Often specific neurons respond to stimulus onset and offset. Stimulus intensity may provide a good example of understanding a part of the neural code: in general, as stimulus intensity increases, so does the neuronal response amplitude (Adrian and Zotterman, 1926; Joesch et al., 2008). An example of this can be observed in the olfactory receptor neurons of female *Drosophila*. The closer a male is to a female (increase of stimulus intensity), the stronger the response of their olfactory receptor neurons becomes (Taisz et al., 2023). Stimulus identity and location are different from timing and intensity, due to the unique characteristics of each sensory system. For instance, the sense of smell is highly adept at distinguishing between different types of odours. This is achieved through the use of a diverse array of receptor proteins with different ligand-binding specificity and combinatorial neural code (Buck and Axel, 1991; Malnic et al., 1999). However, the physical

properties of olfactory stimuli makes olfaction suboptimal for fast and precise stimulus localisation. The localisation of an olfactory source is determined by computational analysis of intensity and temporal differences received at spatially separated antennae. This requires precise calculations to determine not only the intensity differences but also the time-of-arrival differences between the two locations, enabling the system to locate the source.

The visual system, on the other hand, benefits from a geometric receptor layout that inherently maps the visual field in egocentric coordinates, which are centred on the observer's perspective. This layout facilitates the rapid and accurate encoding of stimulus location at the sensory level. However, for a comprehensive understanding of the visual environment in allocentric terms, which are independent of the observer's current position and orientation, additional variables must be considered. These include the orientation of the eyes, the position of the head as well as movement of the observer or environment, among others. Such considerations are crucial for converting the egocentric data collected by the visual receptors into a more globally relevant allocentric map. It is thought that the visual streams responsible for processing information about identity and location are processed separately in the brains of mammals and also flies, leading to the naming of the neural circuits as the what and where pathways (Goodale and Milner, 1992; Taisz et al., 2023). The computations required to extract identity or location seem specific to the feature, arguing for separate streams during processing steps.

In summary, the sensory systems translate complex sensory stimuli into neural signals. Neural circuits extract and integrate relevant information from these neuronal signals to guide behaviour. The computations necessary often occur in a single cell, integrating a multitude of different inputs into a single output. It is therefore crucial to choose a well-defined but tractable circuit to investigate such computations. This doctoral thesis examines one such neural circuit—motion vision in *Drosophila melanogaster*, which is particularly suitable for understanding how brains process sensory information. Focusing on the neural circuits of motion detection offers a window into the broader understanding of brain functionality and information processing.

2 MODELS OF MOTION VISION

Motion vision refers to the ability of an organism to perceive and interpret movement within its environment through its visual system. This process involves detecting changes in the position of objects relative to the observer or the movement of the observer relative to the environment. Motion detection is crucial for behaviours like navigation, detection of potential mating partners or predator avoidance (Gabbiani et al., 1999; Masseck et al., 2010; Borst, 2014; Mauss et al., 2017b; Oteiza et al., 2017). Organisms rely on neural computations to behave appropriately to moving stimuli.

Already more than a century ago one of the first conceptualisations of how motion is detected by the visual system was proposed. The physiologist Sigmund Exner published a theory and a neuronal model for motion perception in 1894. Exner envisioned that when a visual stimulus moves across the retina, the signal it produces spreads symmetrically in opposite directions. He postulated that when two neighbouring points on the retina are stimulated sequentially due to motion, the neural responses would result in a summation of signals to perceive motion. In contrast, if neighbouring points on the retina were stimulated simultaneously, the summation of these signals would not convey the sense of motion, due to the missing temporal aspects in motion (Figure 1A; Exner, 1894). From his conceptualisation of the differential combination of signals, Exner inferred that elementary detectors would have a directional selectivity to motion. His foundational work laid the groundwork for later, more detailed models of motion perception.

2.1 Hassenstein-Reichardt detector

Inspired by behavioural observations of tethered beetles (*Chlorophanus viridis*) walking on a spherical y-maze, Hassenstein and Reichardt built upon Exner's theory about half a century later (Von Hassenstein and Reichardt, 1956; Reichardt, 1961). In this behavioural experiment the walking insect had to turn left- or rightwards while being presented with vertical black and white stripes rotating around it. Hassenstein and Reichardt observed that the beetle would turn in the same direction as the stripe motion (Von Hassenstein and Reichardt, 1956). Turning in the same direction as the rotation of the environment is called optomotor response, enabling animals to adjust their course in response to changes in their surroundings. In order to understand the computation underlying the ability to sense the direction of visual motion, Hassenstein and Reichardt proposed a correlation-type motion detector (Von Hassenstein and Reichardt, 1956).

The Hassenstein-Reichardt detector contains two neighbouring, spatially offset input channels (photoreceptors) that receive local light signals (see Figure 1B). One of the channels (A) delays the received signal, whereas there is no temporal delay on the other channel (B). One step further (C), the signal from the delayed channel is multiplied with the signal from the non-delayed channel. If a visual signal moves from left to right, channels A and B will be activated sequentially, with a delay that depends on the

velocity of motion. Due to the combination of the spatial offset between A and B and the temporal delay introduced in channel A, both signals coincide at C, where they interact in a non-linear fashion. This nonlinearity is often modelled as a multiplication. Motion in the preferred direction (PD), in this case left-to-right, will lead to a signal in C (Figure 1B) that is stronger than the linear sum of $A+B$. However, if motion occurs in the opposite direction, signals from B and A will not coincide at C, leading to a smaller response amplitude at C (null direction, ND; Figure 1B). This mechanism results in a detector that is sensitive to one direction of motion by enhancing motion signals in their preferred direction (preferred-direction enhancement). By pairing two detectors in a mirror symmetrical way and subtracting the output of both multiplication subunits, responses are positive for motion in the preferred direction and negative for motion in the null direction (Von Hassenstein and Reichardt, 1956).

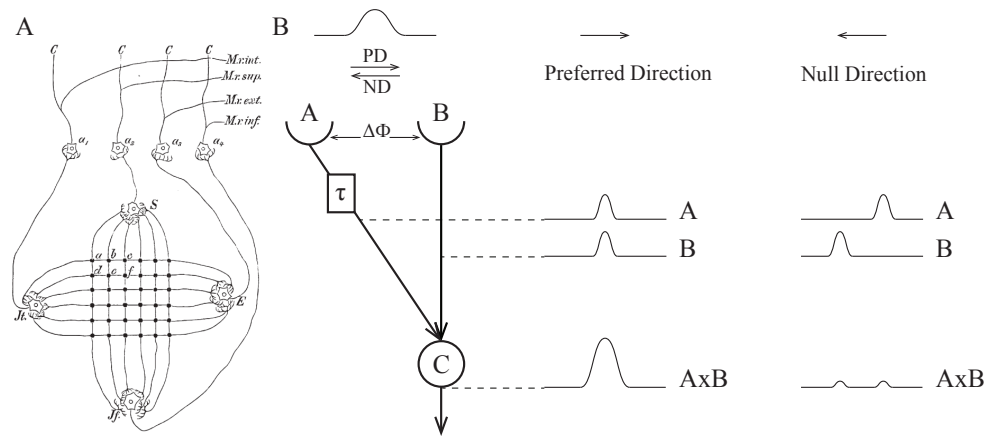


Figure 1: Hassenstein-Reichardt detector: (A) Exner's early concept of a motion detection circuit (Exner, 1894). (B) The correlation-type motion detector comprises two neighbouring, spatially offset ($\Delta\Phi$) input channels that receive light signals. One of the channels A delays the received signal (τ) while there is no temporal delay on the other channel B. One step further C, the signal from the delayed channel is multiplied with the signal from the non-delayed channel. When the input signal moves in the preferred direction, the temporal separation of the signals in both channels, due to $\Delta\Phi$, is compensated in the left arm by a factor of τ . This adjustment ensures that inputs from both arms coincide, leading to an enhanced output after the multiplication. When the input signal moves in the null direction, the delay is increased by τ and results in two separated small responses after the multiplication.

2.2 Barlow-Levick detector

About a decade later, Barlow and Levick proposed a similar mechanism to describe the responses of direction-selective ganglion cells in the retina of rabbits (Barlow and Levick, 1965). Like the Hassenstein-Reichardt detector, this detector consists of two spatially separated input channels of which one is direct and one delayed (see Figure 2). Instead of a multiplication of the

two inputs, the Barlow-Levick detector divides the two input signals. If both input signals, one direct and excitatory, the other delayed and inhibitory, coincide at the non-linear stage C, minimal output is produced (see Figure 2). This is the case when visual stimulation is presented in the null direction. In contrast, if visual stimulation occurs in the preferred direction, the excitatory (A) and inhibitory (B) inputs do not coincide at the non-linear stage C resulting in a response signal (see Figure 2). The Barlow-Levick detector is sensitive to one direction of motion by suppressing signals evoked by motion in their null direction (null-direction suppression; Barlow and Levick, 1965).

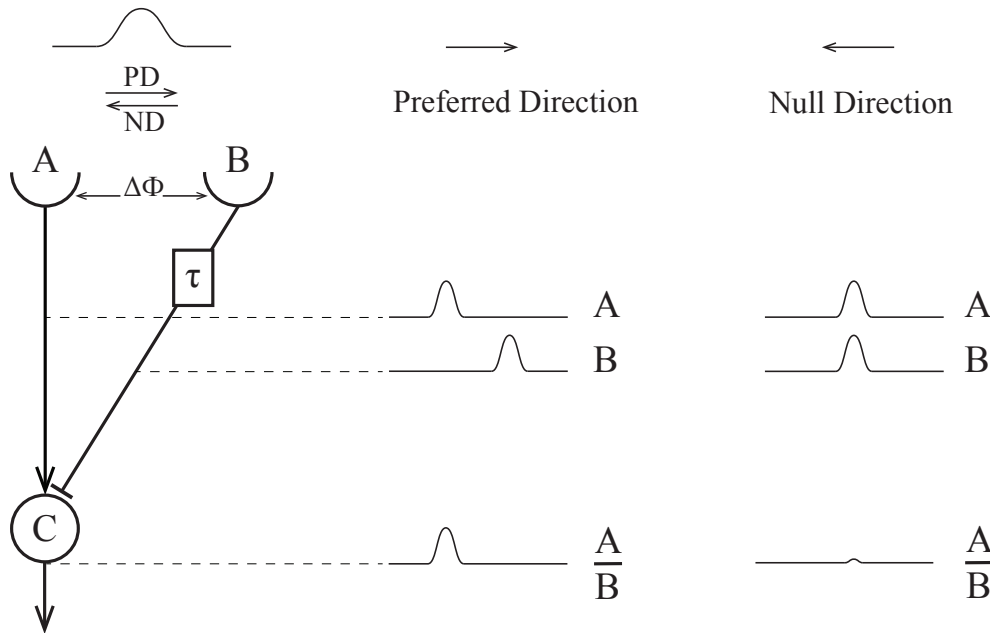


Figure 2: Barlow-Levick detector: The correlation-type motion detector comprises two neighbouring, spatially offset ($\Delta\Phi$) input channels that receive light signals. There is no temporal delay on the channel (A), while channel B delays the received signal (τ). One step further (C), the signal from the non-delayed channel is divided by the signal from the delayed channel. When the input signal moves in the preferred direction, the delay is increased by τ and results in a stronger response after the division. When the input signal moves in the null direction, the temporal separation of the signals in both channels, due to $\Delta\Phi$, is compensated in the right arm by a factor of τ . This adjustment ensures that inputs from both arms coincide, leading to a decreased output after the division.

2.3 Three-arm detector

For a long time, the algorithmic models described above were regarded as the two competing models in describing direction selectivity in neurons. However, more recently in *Drosophila melanogaster* evidence for both mechanisms was found (Haag et al., 2016). Combining the elements of both the Hassenstein-Reichardt and the Barlow-Levick detectors produces a stronger and more precise directional signal to visual motion, that

corresponds to functional signals (Arenz et al., 2017; Haag et al., 2016). This three-arm detector integrates features of both: it enhances preferred direction while suppressing null-direction signals, all within a single three-armed structure (see Figure 3). In detail, channel B processes the received signal without any delay, whereas channels A and C introduce a delay (τ) to the signal. At the next stage (D), the signal from channel B, is combined with the signal from the delayed channel A through multiplication and then divided by the signal from the delayed channel C. When the input signal moves in the preferred direction, the delay (τ) compensates for the temporal difference between the signals in channels A and B, ensuring that their inputs align. For channel C, the delay is lengthened by τ , enhancing the response after multiplication and division at stage D. Conversely, when the input signal moves in the null direction, the temporal gap between the signals in channels B and C is compensated in the right arm by a delay (τ). The delay applied to the multiplicative input from channel A is extended by τ , resulting in a diminished response after the multiplication and division at stage D.

In *Drosophila* this integration of three arms is anatomically supported by the observation that revealed a tripartite structure in the dendrites of direction-selective neurons (Takemura et al., 2017; Shinomiya et al., 2019). To investigate the neural circuits that form the basis of these detector models, neuroscientists make use of a wide range of techniques. These methods allow detailed exploration of the brain's complex networks.

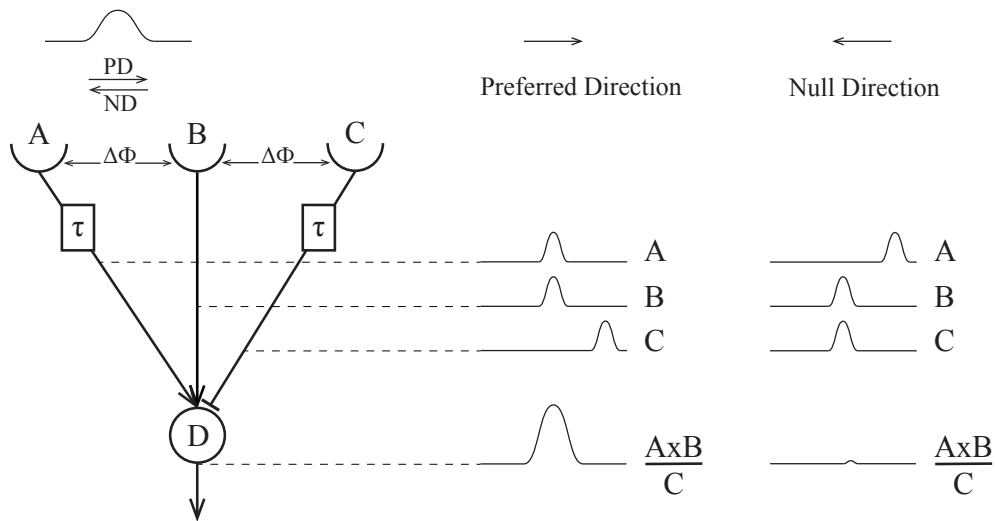


Figure 3: Three-arm detector: This three-arm detector integrates features of both Hassenstein-Reichardt and Barlow-Levick detectors: it enhances preferred direction while suppressing null direction signals, all within a single three-armed structure. There is no temporal delay on the channel (B), while channel A and C delay (τ) the received signal. One step further (D), the signal from the non-delayed channel B is multiplied with the delayed A channel and divided by the signal from the delayed C channel. When the input signal moves in the preferred direction, the temporal separation of the signals in both channels, due to the spatial differences of inputs $\Delta\Phi$, is compensated in the left arm by a delay (τ). This adjustment ensures that inputs from A and B arms coincide. For the divisive input C, the delay is increased by τ . This results in a stronger response after multiplication and division (D). When the input signal moves in the null direction, the temporal separation of the signals in channel B and C, due to $\Delta\Phi$, is compensated in the right arm by a delay (τ). For the multiplicative input A, the delay is increased by τ . This results in a weaker response after multiplication and division (D).

3 TOOLS IN CIRCUIT NEUROSCIENCE

Progress in science often relies on the development of new techniques. Neuroscience, for example, has been revolutionised by the invention of the patch-clamp technique (Neher and Sakmann, 1976) giving access to the minute current that flows through a single membrane channel, or by two-photon microscopy (Denk et al., 1990) allowing to stimulate fluorescence in a defined voxel of space deep inside a piece of nervous tissue. In addition to such 'physical' techniques, the invention of genetic techniques has an equal share in the progress made in neuroscience in the past decades. This is where the fruit fly *Drosophila melanogaster* comes into play.

3.1 *Drosophila melanogaster* as a model organism

In fundamental neuroscience many tools have been developed for *Drosophila melanogaster*, commonly known as the fruit fly. It has been studied since the early 20th century. Since Thomas Morgan began studying the principles of heredity in 1910 (Morgan, 1910), the fruit fly has the richest genetic toolkit among other common model organisms in neuroscience such as mice, *C. elegans*, and zebrafish.

The fruit fly is a common model organism in many fields, for instance developmental biology, genetics and neuroscience. It has several benefits as a model organism. Its rapid life cycle of about 10 days from egg to adult makes it possible to study several generations in a short period of time. Breeding and husbandry of fruit flies in a laboratory is relatively cheap and easy; they can live in tubes containing yeast food at an ambient temperature of around 25°C. A healthy female fly lays several hundred eggs in its lifetime. *Drosophila* shares a surprising amount of genetic similarity with humans, making it a popular model organism for fundamental studies on human diseases (Ugur et al., 2016; Mirzoyan et al., 2019).

The brain of a fruit fly is simple and contains only ~200,000 neurons (Raji and Potter, 2021), compared to mice with ~70 million neurons (Reardon, 2017) or humans with ~85 billion neurons (Herculano-Houzel, 2009). Despite its simplicity, the fly is able to see, smell, hear, learn and perform many complex and social behaviours like navigation and mating. Due to *Drosophila's* well understood genetics, it is relatively easy to manipulate their genes. This is beneficial to access and study specific neurons in the brain. In the subsequent paragraphs, I introduce some of the most relevant tools and techniques in the field of *Drosophila* neuroscience.

3.2 Genetic techniques

3.2.1 Expression systems

A challenge in circuit neuroscience is to reproducibly gain access to the same, identifiable neurons to probe their function across individuals. This challenge has been handled in the fruit fly using binary expression

systems. These are powerful tools that allow cell type specific targeting of any genetically encodable tool of interest. The main principle of a binary expression system are the two separate components, one defining where the expression occurs and the other what is expressed. One advantage of this is that these two components can be combined arbitrarily. To be able to do that, a large library of fly lines was generated and constantly grows, as more tools and cell types are discovered. This is crucial to understand the function of specific neurons.

Such binary expression systems like the Gal4-UAS system (Figure 4; Brand and Perrimon, 1993; Venken et al., 2011) consist of two components following the *what* and *where* principle. The Gal4-UAS system involves the reporter line using the UAS (upstream-activation-sequence) promoter, which determines what (which effector protein) is expressed. This can be combined with a driver line, relying on the yeast transcription factor Gal4, which determines where expression occurs (Brand and Perrimon, 1993). Crossing a driver and target fly line carrying Gal4 or UAS constructs respectively, result in progeny expressing both Gal4 and UAS. The tissue-specific Gal4 protein binds to the UAS sequence allowing the expression of the gene of interest in a cell type specific manner (Figure 4). Importantly, two orthogonal binary expression systems, LexA/LexAop (Lai and Lee, 2006) and the Q system (Potter et al., 2010), are commonly combined with GAL4-UAS to drive multiple reporters with independent expression patterns.

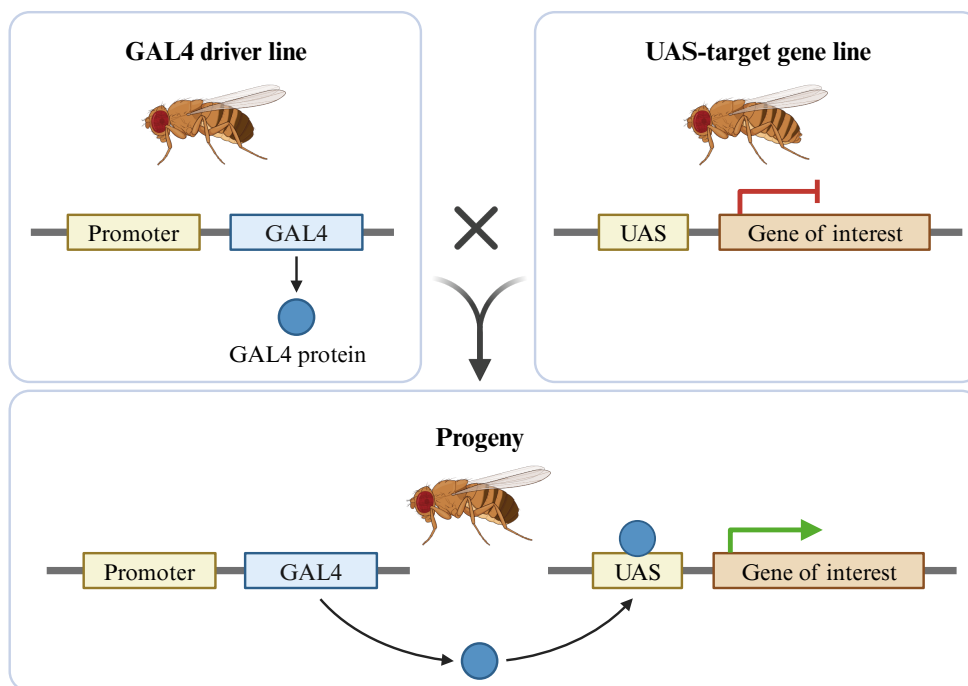


Figure 4: Illustration of the Gal4-UAS system in *Drosophila*: A driver line (Gal4) and an effector line (UAS) are crossed (top). The progeny expresses both GAL4 and UAS. The tissue-specific Gal4 protein binds to the UAS sequence allowing the expression of the gene of interest in a cell type specific manner (bottom) (Brand and Perrimon, 1993). Created with BioRender.com.

These drivers often label a group of neurons rather than individual neurons. To refine this and target single neurons or a more specific subset of neurons, an intersectional strategy can further specify the neuronal labelling pattern. Using a split version of the GAL4 transcription factor in which the activation domain (AD) and the DNA-binding domain (DBD) are controlled by distinct enhancers, one can create a combined driver line, where the reporter is only expressed in cells where both the AD and DBD components are present (Luan et al., 2006; Pfeiffer et al., 2010).

3.2.2 Effector genes

Effector genes can have diverse functions and effects. Commonly used in neuroscience are effector genes that manipulate neural activity in circuits or visualise the morphology or functional properties.

Loss of function

When manipulating neural activity we have to distinguish between decreasing or increasing activity. To assess whether a specific neuron type is involved in a circuit function or a behaviour, silencing of its activity is an insightful approach. There are several different tools to remove specific neurons from a circuit.

The most extreme intervention is to express apoptosis related genes like reaper or hid which can be used to permanently eliminate specific cell types (White et al., 1994; Zhou et al., 1997). However, this approach still carries the risk of causing unintended damage in non targeted regions. The absence of a cell type might influence the development of the brain and circuit connectivity.

Instead of ablating neurons, neural activity can be suppressed by expressing inwardly rectifying potassium channels Kir2.1 that hyperpolarizes these cells (Baines et al., 2001). These neurons can not transfer signals to downstream partners. Another way to silence a neuron would be to express the Tetanus neurotoxin (TNT) light chain, to block synaptic transmission in specific neurons. TNT cleaves neural synaptobrevin which is necessary for synaptic vesicle release (Sweeney et al., 1995). While these three neuronal silencing tools are highly effective, they lack reversibility and temporal specificity, meaning they cannot be easily controlled or limited to a specific time period. It can be beneficial to selectively silence neurons only during specific time periods to for example avoid long term effects. The expression of the transgene *shibire^{ts}* blocks the synaptic transmission with a different mechanism. *Shibire^{ts}* is a temperature-sensitive mutated allele of the dynamin gene in *Drosophila* (Kitamoto, 2001). Dynamin is a GTPase that is essential for synaptic vesicle recycling, hence important for chemical synaptic transmission. Below ~29°C, the re-uptake of vesicles by dynamin from the synaptic cleft is not affected. When the temperature of the flies' environment is raised to above 29°C, the fusion of vesicles with

the presynaptic membrane is halted within minutes causing a disrupted re-uptake of neurotransmitters. This leads to a depletion of vesicles and disrupts chemical transmission. Lowering the temperature again releases the block effect. Therefore, the same fly can be used for both control and silencing experiments. However, it is important to note that both behaviour and cellular physiology is temperature dependent which makes more control experiments necessary.

The transgenic expression of light-sensitive transmembrane ion channels (e.g. channelrhodopsin) or ion pumps (e.g. halorhodopsin), derived from microorganisms, have revolutionised the field of neuroscience (Boyden et al., 2005). Channel specific wavelengths of light either open or close the channel in response to light, allowing or preventing channel specific ions to pass the cell membrane. This results in a change in membrane currents and either depolarizes (channelrhodopsin) or hyperpolarizes (halorhodopsin) the neuron. Since the first demonstration of channelrhodopsin's ability to activate hippocampal neurons with millisecond precision (Boyden et al., 2005), the number of optogenetic tools has grown fast.

The expression of an archaeal light-activated chloride pump halorhodopsin from *Natronomonas pharaonis* (NpHR) can hyperpolarize and inhibit targeted neurons from firing action potentials when exposed to yellow light (~570 nm) (Zhang et al., 2007). This discovery had a major impact on the development of the early optogenetic silencing tools. Many of the early optogenetic silencing tools relied on modified forms of halorhodopsin (NpHR), including the enhanced NpHR (eNpHR) (Gradinaru et al., 2008). Alternatives to chloride pumps are proton pumps, that hyperpolarize a neuron by pumping protons out of the cell, and light-gated anion channels (ACRs), including GtACR1 and GtACR2 (Govorunova et al., 2015). These anion channels derived from the algae species *Guillardia theta* exhibit a robust chloride ion influx triggered by light. GtACR1 and GtACR2 are very light sensitive, efficiently cause membrane hyperpolarization, and have fast kinetics. They differ in their peak sensitivity: GtACR1 has its peak at ~515 nm (green light; Figure 5A), whereas GtACR2 has its peak at ~470 nm (blue light). As mentioned before, blue light interferes with the visual system of *Drosophila*. Yet, GtACR1 has been demonstrated to induce fast and reversible silencing of neurons within the visual system of *Drosophila melanogaster* without interfering with visual processing (Mauss et al., 2017a). A key aspect of this technique is the variability in the wavelengths of light required to activate different channels. The wavelengths, and therefore the choice of the optogenetic tool, must be carefully selected not to interfere with other light sensitive systems and ensure the specificity and accuracy of the experimental manipulation. On the other hand, multiple optogenetic tools can be used simultaneously, provided their activation spectra do not overlap.

Beyond the tools that manipulate neural activity, the ability to selectively interfere with the function of individual genes in a cell type-specific manner offers a variety of opportunities for understanding neural computations. The UAS-Gal4 system (Figure 4) can be used to knock down expression of any gene in a cell type specific way using RNA interference (RNAi). The

transgene encodes a small strand of RNA that is complementary to the mRNA of the gene of interest. Molecular cascades cause degradation of the mRNA of a targeted gene, thus the protein of interest is not translated (Dietzl et al., 2007; Perkins et al., 2015). One significant limitation of this tool is the potential for unintended developmental effects of unspecific gene targeting. Adequate controls are necessary to avoid a misinterpretation of the results.

Gain of function

As mentioned above, when manipulating neurons we have to distinguish between decreasing or increasing neural activity. Artificially activating specific groups of neurons can aid in determining whether certain circuit components are sufficient for specific functions. In the next paragraph I will introduce some of the tools that increase neural activity and therefore activate neurons.

Heat-sensitive cation channel TrpA₁ reversibly opens at a temperature above 26°C, thus causing a strong depolarization in the targeted neurons (Rosenzweig et al., 2005; Hamada et al., 2008). This tool is beneficial to activate neurons in a controlled and reversible manner. However the temporal resolution is not extremely precise and happens rather on the level of seconds than milliseconds.

Enhanced temporal control of the cation channel P₂X₂ enables to evoke strong depolarization, and therefore increase neural activity (Lima and Miesenböck, 2005). Initially, P₂X₂ was developed as an optogenetic tool activated by binding light-released adenosine triphosphate (ATP). The limitation of this tool is that it requires a local injection of caged ATP. Caged ATP is inactive until it gets activated by light and then can activate the cation channel P₂X₂. Injecting caged ATP into a specific area of the brain adds complexity and less precision to the experimental procedure, especially compared to other optogenetic tools that can be activated more directly by light.

Optogenetic tools can produce either an excitatory or inhibitory impact on the neuron, depending on the ion specificity of the protein. Channelrhodopsin-2 (ChR2) is such a genetically encodable light-gated ion channel. It was initially isolated in *Chlamydomonas reinhardtii*, a green alga (Nagel et al., 2003). It functions as a non-selective cation channel with a peak sensitivity of ~470 nm (blue light). Influx of positively charged ions leads to a depolarization of the targeted neuron, enabling the initiation of an action potential, thereby activating the neuron. The blue light that activates ChR2 coincides with the peak activation wavelength of Rhodopsin 1 in *Drosophila*, a protein crucial for their visual system. Hence, optogenetic stimulation with blue light interferes with the visual system of *Drosophila* and can lead to unwanted artefacts. Therefore, red-shifted optogenetic tools like ReaChR (~540 nm; Lin et al., 2013; Inagaki et al., 2014) and CsChrimson (~570 nm; Figure 5B; Klapoetke et al., 2014) are more suitable for *Drosophila* vision research. The red light not only minimises visual interference but

it also allows deeper tissue penetration, even through the cuticle of the fly head.

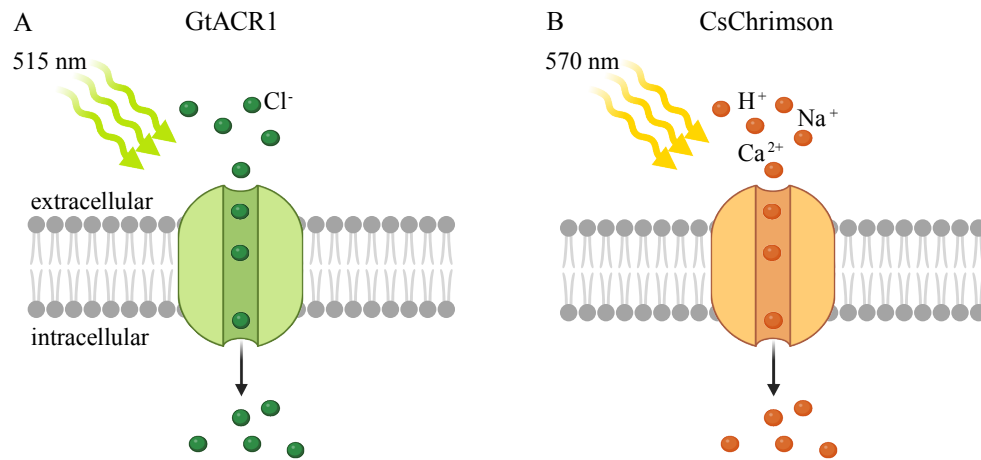


Figure 5: Illustration of two optogenetic channels: (A) Anion channel (GtACR₁) opens at a wavelength of ~515 nm and causes a cell to hyperpolarize. (B) Cation channel (CsChrimson) opens at a wavelength of ~570 nm and causes a cell to depolarize. Created with BioRender.com.

GFP visualisation

To visualise neurons of interest, with the UAS-Gal4 system (Figure 4) it is possible to express structural markers. The commonly used tool is the jellyfish-derived green fluorescent protein (GFP) (Chalfie et al., 1994). Its structure allows it to fluoresce when exposed to blue light (excitation wavelength: 488 nm). GFP can be expressed as a cytosolic or membrane-bound fluorescent protein in targeted cells. This tool enables scientists to transgenically label single cells in vivo, ex vivo and in fixed tissues. Nowadays, there are numerous genetically modified variations of fluorescent proteins with different wavelength properties. The improvements in genetic protein engineering and fluorescence microscopy allows strong and clear expression and high-resolution images to study for example the anatomical properties of cells.

Activity reporter

Fluorescent proteins have been further modified to act as functional reporters of neuronal activity. Genetically encoded calcium indicators (GECIs), designed to fluoresce in presence of calcium ions, are used as a proxy for neuronal activity. The concept of calcium as a proxy for neural activity is based on the increase in calcium concentration inside a neuron when it depolarizes. More specifically, the concentration of Ca²⁺ is low when the cell is at rest. Depolarization triggers the opening of voltage-gated ion channels, allowing an influx of Ca²⁺ ions into the cell (Hille, 1991). Among these sensors, GCaMP sensors are the most

commonly used. They are a fusion of the fluorescent protein GFP and the calcium-binding protein calmodulin (Nakai et al., 2001). Over the years, numerous enhancements have been made to GCaMP, resulting in significant improvements of sensor kinetics, sensitivity, brightness and signal-to-noise ratio (Chen et al., 2013; Dana et al., 2019; Zhang et al., 2023). Until recently, GCaMP's capabilities were primarily limited to detecting neuron depolarization. The latest version, GCaMP8, has been demonstrated to also be able to report hyperpolarization in visual neurons of *Drosophila* (Zhang et al., 2023), in line with previous electrophysiological characterisations of these neurons (Juusola et al., 2016). Calcium indicators can only detect membrane voltage changes that lead to a significant change in calcium concentration, thereby only being an indirect reporter of the neuron's membrane voltage.

This problem can be overcome using indicators that directly report membrane voltage changes. In the last few years, a number of genetically encoded voltage indicators (GEVIs) have been developed (Xu et al., 2017; Lin and Schnitzer, 2016; Knöpfel and Song, 2019). GEVIs change their level of fluorescence in response to changes in membrane potential. Voltage imaging, compared to calcium imaging, is capable of detecting fast spikes and subthreshold dynamics. Nevertheless, voltage indicators are challenged by a lower signal-to-noise ratio and faster photobleaching (Lin and Schnitzer, 2016). However, ongoing research is continually enhancing the performance of voltage indicators (Abdelfattah et al., 2019; Li et al., 2020a), making it a promising tool for neuroscientists in the recent past and near future (Ammer et al., 2023; Mishra et al., 2023).

3.3 Physiological techniques

Using the genetic tools mentioned previously, researchers can investigate specific cells of interest by expressing fluorescent indicators. In the following section I will briefly describe two techniques that are commonly used in the field to study the physiology of neurons.

3.3.1 Two-photon calcium imaging

In vivo two-photon microscopy in combination with the expression of for example GCaMP in neurons is a powerful technique that enables researchers to visualise and record neural activity in live tissues. Two-photon microscopy (Denk et al., 1990) relies on a femtosecond-pulsed laser (at ~920 nm infrared light) to stimulate the fluorescence protein of GCaMP. Two coinciding photons are required to overcome the excitation threshold to excite the fluorophore. The energy required to excite the fluorophore of GCaMP from its ground state to a higher energy state is only achieved when absorbing two photons simultaneously instead of one photon. Importantly, unlike in traditional fluorescence microscopy, two-photon excitation is limited to a very small focal point. This reduces photodamage outside the area of interest and minimises photobleaching of the fluorophore, making it possible to image neurons for extended periods. Photomultiplier tubes

are essential for detecting faint fluorescent levels. The high sensitivity of photomultiplier tubes allows for precise detection of the weak signals. This enables researchers to employ lower laser intensity, reducing photobleaching and tissue damage. Infrared light has a longer wavelength compared to visible light, which allows it to penetrate deeper into tissue. The wavelength of infrared light used by the laser is outside of the visual range of the photoreceptors of *Drosophila*. This ensures that the laser light used for two-photon calcium imaging does not interfere with the fly's visual perception. It allows researchers to study neurons in the visual system of *Drosophila* without disturbing behaviour and visual perception. Overall, two-photon imaging is a versatile technique to investigate neural activity in the brain of *Drosophila* and other organisms.

3.3.2 Whole-cell patch clamp recording

Electrophysiological whole-cell patch clamp recordings (Neher and Sakmann, 1976) allow to directly measure the electrical properties of a single cell in vivo with high temporal resolution. A glass micropipette, containing an electrolyte solution and a thin electrode, is positioned against the cell membrane to create a seal. Breaking the membrane within this sealed area enables the mixing of the pipette's solution with the cell's cytosol. With voltage-clamp recordings (Cole and Moore, 1960; Hodgkin and Huxley, 1952), the characterisation of ion flow across a cell's membrane is possible. The membrane potential is controlled by an amplifier while measuring the electrical current. In current-clamp, the changes in membrane potential of a cell is recorded as a result of changes in ion channel activity. Comprehensive instructions for conducting whole-cell patch-clamp recordings in the visual system of *Drosophila* are available in Joesch et al. (2008); Mauss and Borst (2016); Groschner et al. (2022). Two primary limitations of whole-cell patch clamp recordings are the small size of the soma and the anatomical accessibility of the neurons. However, successful recordings have been achieved across different areas of the fly brain (Wilson et al., 2004; Murthy et al., 2008; Joesch et al., 2008; Fenk et al., 2021). Recent advancements also allow for the possibility of recording from smaller neurons, with soma sizes as small as three μm , indicating significant progress in the field (Gruntman et al., 2018, 2019; Groschner et al., 2022).

3.4 Electron microscopy

In circuit neuroscience the anatomical structure, location and connection of neurons is important information to find neurons of interest and their function.

Santiago Ramón y Cajal studied neural anatomy already in the late 19th century. He applied Camillo Golgi's silver staining method and light microscopy to various brain structures to draw individual neurons, resulting in the accepted theory of modern neuroscience – the neuron doctrine. Using these methods, anatomical knowledge of the neural structure of the fly's brain was gained by systematic drawings of *Calliphora* (Cajal and Sánchez,

1915; Strausfeld, 1976) and of *Drosophila* (Fischbach and Dittrich, 1989). Until today these resources are very valuable in the field. Modern techniques shine light into more detailed anatomical analysis and connectivity of neurons.

To understand the function of neuronal circuits it is beneficial to have a comprehensive map of neuronal connections in a brain, a so-called wiring diagram. Currently, electron microscopy (EM) (Knoll and Ruska, 1932) is the only method that achieves sufficient resolution to create a neuron level wiring diagram, or connectome.

There are two main methods to acquire volume EM datasets, differing in size, resolution and completeness. Here I briefly introduce two modern volume EM methods: (1) transmission electron microscopy (TEM) and (2) Scanning electron microscopy (SEM).

(1) Transmission electron microscopy (TEM) relies on capturing images from electrons that pass through a sample. For this the sample needs to be cut in slices of only a few nanometers. After incubating the tissue in heavy metals to label cell membranes, in serial section TEM (ssTEM; Figure 6A; Harris et al., 2006), individual thin slices are cut with a diamond knife and transferred to a support grid. In the transmission electron microscope, electrons are accelerated and targeted to the sample slice. Electrons that pass through the slice are further guided through electromagnetic lenses to bring the electrons into focus and form an image on a phosphor layer to acquire an image with a digital camera. Electrons that hit heavy metal located in the cell membranes are scattered and do not end up on the phosphor layer, making these parts of the image darker. In the complex post-acquisition phase, the images are assembled into an aligned and coherent volume.

(2) Scanning electron microscopy (SEM), on the other hand, relies on collecting electrons that back-scatter from the surface of a sample with an electron detector positioned above the sample. As for TEM, first the tissue is stained with heavy metals to enhance the electron contrast at the membranes. One example of SEM is the method named focused ion beam scanning electron microscopy (FIB-SEM; Figure 6B) (Knott et al., 2008; Heymann et al., 2006). Here, the tissue is cut into blocks. Due to the focused ion beam scanning over the surface, a very thin surface layer is milled off with every image until the sample is entirely scanned. Alternatively, a SEM method named serial block-face SEM (SBEM; Figure 6C) (Denk and Horstmann, 2004) removes very thin surface layers by mechanically cutting off tissue slices with a diamond knife after each scan.

Unlike ssTEM, with FIB-SEM and SBEM the imaged sections are lost due to the milling or cutting and can not be imaged again. Currently, FIB-SEM offers the highest z-resolution of up to 5 nm (Knott et al., 2008). SBEM and ssTEM, using diamond knives to cut serial sections, offer a z-resolution of 20-30 nm and 40-50 nm, respectively (Briggman et al., 2011; Harris et al., 2006).

After recording and digitally aligning the data, all EM approaches face the challenge to reconstruct, proofread and annotate neurons and synapses. Manual tracing of neuron morphology and annotating synapses is very labour intensive and time consuming. This approach was partly replaced

by automated segmentation of neurons and automated synapse detection (Scheffer et al., 2020; Dorkenwald et al., 2021; Heinrich et al., 2018; Buhmann et al., 2021).

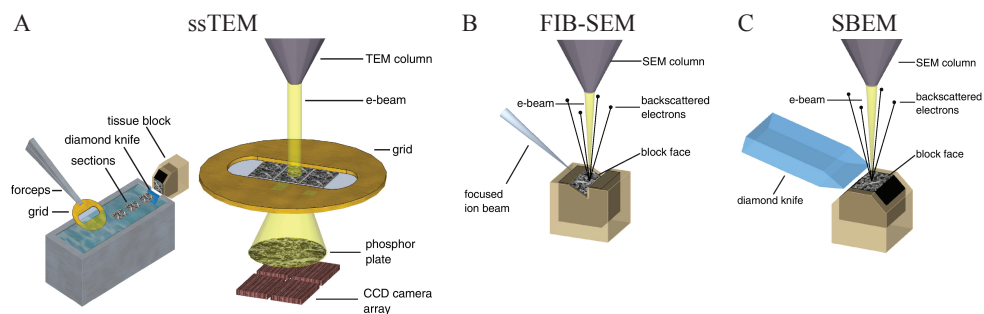


Figure 6: Volume electron microscopy methods: (A) Serial section transmission electron microscopy (ssTEM). (B) Focused ion beam scanning electron microscopy (FIB-SEM). (C) serial block-face scanning electron microscopy. Images adapted from Briggman and Bock (2012) with permission.

Following pioneering studies by Sydney Brenner’s lab mapping all neurons and synaptic connections in the worm, *C. elegans* (White et al., 1986), monumental efforts have been made by the *Drosophila* research field to create a comprehensive connectome of the fruit fly brain, identifying all cell types and their synaptic connectivity. Parts of fly brains have been reconstructed from EM datasets, which provided important insights into neural circuits and their functions. For example, these reconstructions have shed light on how the brain generates social behaviours (Schretter et al., 2020; Deutsch et al., 2020) or memory-related behaviours (Li et al., 2020a). Beside others, the wiring diagram of the visual system (Shinomiya et al., 2015; Takemura et al., 2017; Shinomiya et al., 2019) and olfactory system (Li et al., 2020a; Bates et al., 2020; Schlegel et al., 2021) have been mapped and related to functions.

All of these morphological, physiological and genetic techniques described above are crucial for today’s fundamental research in circuit neuroscience. *Drosophila melanogaster* as a model organism enables researchers to gain detailed insight into how neural circuits in a brain process information.

4 VISUAL MOTION PROCESSING IN *DROSOPHILA*

The study of visual information processing has greatly benefited from flies as a model organism. Extensive research on their visual system, by using neurogenetic techniques, anatomical analysis, physiological and behavioural approaches, has provided a deep understanding of their visual capabilities.

4.1 The retina and optic lobe

The brain of the fruit fly consists of a central brain and two optic lobes, one on each side (Figure 7B). The brain has a size of roughly 0.5 mm in diameter (Peng et al., 2011) —comparable to a poppy seed— and contains about 200,000 neurons (Raji and Potter, 2021). These neurons endow the fly with capabilities such as vision, olfaction, audition, learning, as well as many complex and social behaviours. A large number of neurons are visual neurons located in the optic lobes. Below the retina, each optic lobe is composed of four neuropils: the lamina, the medulla, the lobula and the lobula plate (Figure 7C). Together, each optic lobe contains ~38,500 single neurons across 226 neuron types (Dorkenwald et al., 2024; Matsliah et al., 2024), highlighting the complexity of the fly’s visual system. In comparison, the mouse retina contains ~330,000 single neurons across 138 neuron types (Li et al., 2024).

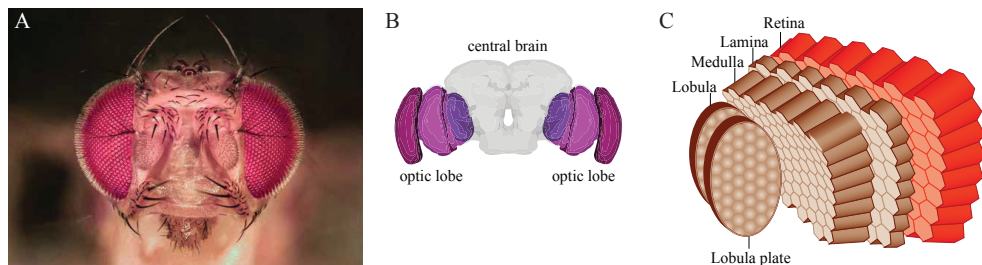


Figure 7: Optic lobe of *Drosophila*: (A) Head of *Drosophila melanogaster* (Image by Florian Richter). (B) Anatomical representation of the fly’s brain. The neuropils of the optic lobes are shown in purple colours, the central brain in grey. Adapted from codex.com (Flywire). (C) Schematic of the neuropils in the optic lobe highlighting their columnar structure (adapted from Borst (2014) with permission).

As is common for insects, *Drosophila* has compound eyes, composed of numerous small units known as facets or ommatidia. An adult fruit fly’s eye typically consists of around 800 ommatidia (Figure 7A). The visual axes of neighbouring ommatidia diverge, with an average interommatidial angle of roughly 5° (Götz, 1964). Each ommatidium can be thought of as an isolated miniature light sensor, equipped with a lens and eight photoreceptors each (R1-R8). These photoreceptors convert incoming photons of light

into electrical signals through a process called phototransduction. The photoreceptor cells are sensitive to light due to a protein called rhodopsin. When a photon hits the photoreceptor, it activates rhodopsin, triggering a cascade of molecular events that lead to the generation of an electrical signal. The presence of different types of rhodopsin enables the detection of various wavelengths of light. Photoreceptors R1 to R6 are specialised to detect changes in light intensity in the UV (~370 nm) and blue light (~475 nm) region of the spectrum (Salcedo et al., 1999; Sharkey et al., 2020), and are key players in the fly's ability to perceive motion. Photoreceptors R7 and R8 each exhibit two distinct spectral subtypes, known as pale and yellow. R7 is sensitive to UV light with its absorption maximum at ~345 nm (R7-pale) and ~375 nm (R7-yellow) (Feiler et al., 1992). R8 is sensitive to blue and green light with its absorption maximum at ~437 nm (R8-pale) and ~508 nm (R8-yellow) (Salcedo et al., 1999). R7 and R8 contribute predominantly to colour vision (Heisenberg and Buchner, 1977; Yamaguchi et al., 2008, 2010) as well as to the motion pathway (Wardill et al., 2012; Longden et al., 2023). Within the fly brain, further processing of visual motion information occurs in the optic lobes. The lamina, medulla, lobula and lobula plate are organised in a highly structured columnar and retinotopic manner. Each ommatidia is represented as a column in these neuropils, with neighbouring columns receiving input from neighbouring ommatidia in the eye. Consequently, in alignment with the number of ommatidia in a fly's eye, each columnar neuron type in the lamina, medulla and lobula that is involved in the motion vision circuit is replicated ~800 times.

4.2 Two parallel neural circuits of motion vision

As briefly described above, photoreceptors are the first cells in the eye that receive light and convert the energy of the light to an electrical signal by a phototransduction cascade. The electrical signal generated by photoreceptors in each ommatidium in response to a photon is transmitted onto lamina monopolar cells via histamine (Hardie, 1989). There are five different lamina monopolar cell types that project from the lamina to different layers in the medulla (Figure 8A; Meinertzhagen and O'Neil, 1991). All neuropils are structured in layers, orthogonal to the columnar structure. Analogous to the mammalian retina (Dowling, 1987), the processing of light increments and light decrements is separated in two parallel pathways: The ON pathway, which primarily receives input from glutamatergic L1 neurons, and the OFF pathway, which primarily receives input from cholinergic L2 neurons (Joesch et al., 2010), respectively. The L-cell types that project from the lamina to the medulla connect photoreceptors with medulla/transmedulla neurons. The medulla contains more than 60 different cell types (Fischbach and Dittrich, 1989). Here, mostly medulla intrinsic (Mi) and transmedullary (Tm) neurons relay information to T4 and T5 neurons. T4 and T5 neurons are the first direction-selective neurons in the ON and OFF motion vision circuit, respectively (Maisak et al., 2013). EM studies described the presynaptic partners of T4 and T5 neurons (Takemura et al., 2013; Shinomiya et al., 2014, 2015, 2019; Takemura et al., 2017).

A single T₄ neuron of the ON pathway receives columnar input at its dendrite from Mi₉, Mi₁, Tm₃, Mi₄, C₃ and CT₁ (complex tangential neuron 1) neurons. The dendrites of T₄ neurons are located in layer 10 of the medulla (Figure 8A). A single T₅ neuron of the OFF pathway receives columnar input at its dendrite from Tm₉, Tm₁, Tm₂, Tm₄, and CT₁ neurons. Unlike T₄, T₅ dendrites are located in layer one of the lobula (Figure 8A). These input neurons are characterised with a variety of temporal and spatial receptive fields with low-pass or band-pass characteristics. Importantly all are non-direction-selective neurons (Behnia et al., 2014; Meier et al., 2014; Strother et al., 2014; Ammer et al., 2015; Fisher et al., 2015; Serbe et al., 2016; Yang et al., 2016; Arenz et al., 2017; Drews et al., 2020; Meier and Borst, 2019).

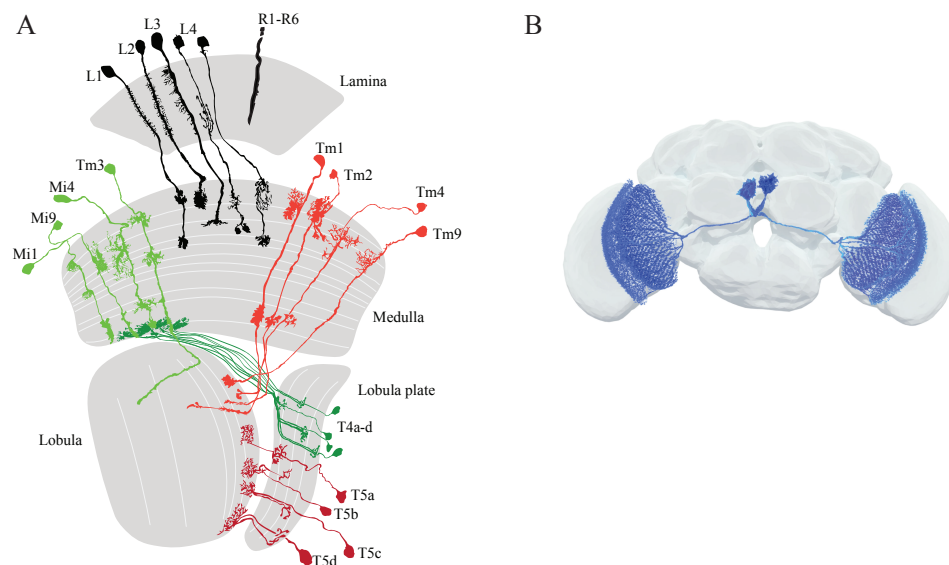


Figure 8: Neural elements of ON and OFF motion vision detection: Schematic of the optic lobe including the morphology of the neural elements of the ON (green) and OFF (red) motion vision pathway. (A) Each cell type is displayed only once for simplicity but every cell type exists in each of the ~800 columns. Image adapted from Fischbach and Dittrich (1989) with permission. Note that CT₁ terminals are missing in this representation. (B) Morphology of both large-field amacrine cells CT₁ – one on each hemisphere. The some of each CT₁ neurons is located on the contralateral side. The single terminals of these highly compartmentalized neurons span the medulla layer M₁₀ and the lobula layer L₁ in each column (CT₁ Image rendering by Amy Sterling - FlyWire).

Despite the fact that inhibiting L₁ and L₂ neurons reduces behavioural responses to moving stimuli (Rister et al., 2007), these neurons are not the exclusive inputs to the motion vision pathway. The L₃ neuron, which is cholinergic and responds to dark moving edges, provides input to the OFF pathway via transmedullary neuron Tm₉ (Silies et al., 2013; Fisher et al., 2015), as well as to the ON pathway via medulla intrinsic neurons Mi₁ and Mi₉ (Takemura et al., 2017). The cholinergic L₄ neuron, also responds to dark moving edges and provides input to the OFF pathway via Tm₂ (Meier et al., 2014; Takemura et al., 2011; Tuthill et al., 2013). Although the

functional role of L5 in the motion vision pathway is not well understood (Tuthill et al., 2013; Strother et al., 2018), EM reconstructions indicate that L5 is presynaptic to Mi4 in the ON pathway (Takemura et al., 2013).

T4 and T5 neurons are the elementary motion detectors in *Drosophila*. T4 and T5 represent the first stage of direction-selective responses within the ON and OFF motion vision circuit, respectively. Both T4 and T5 cells are divided into four subtypes (a-d), each selective for one of the four cardinal directions (upward, downward, front-to-back, back-to-front, Figure 9A; Maisak et al., 2013). The dendritic morphology of the four subtypes are slightly different. The dendrites of each subtype are pointing in one of the four cardinal directions against their preferred direction (Takemura et al., 2017; Shinomiya et al., 2019). As an example, T4c/T5c dendritic branches face downwards from its branching point, having its preferred direction to upward motion. Each subtype exists ~800 times per optic lobe which means that there are in total about 6400 single T4 and T5 dendrites spread out over the medulla (T4) and lobula (T5) of the optic lobe.

The dendrites of all T4 and T5 neurons span over multiple columns and receive input from different columnar neurons at distinct areas of their dendrites (more detail in section 4.2.1 and 4.2.2). Each dendrite can be segmented into three adjacent areas according to intrinsic coordinates: the distal tip, the central area, and the proximal area (Figure 9C-D). Supported by these anatomical observations (Takemura et al., 2017; Shinomiya et al., 2019), the recently proposed three-arm model (section 2.3) likewise suggests that T4 and T5 receives its input from three neighbouring areas (Figure 9B). That model results in a stronger and more precise directional signal in response to visual motion (Arenz et al., 2017; Haag et al., 2016; Leong et al., 2016). Functional studies that involved blocking synaptic input neurons to T4 or T5 dendrites also suggest three input elements (Ammer et al., 2015; Serbe et al., 2016).

The axon terminals of each of the four T4/T5 subtypes project to a specific layer in the lobula plate (Figure 8A; Fischbach and Dittrich, 1989). This neuropil is structured in four layers. Layer 1 receives input from T4/T5 a-subtype neurons that respond to front-to-back motion, layer 2 receives input from T4/T5 b-subtype neurons that respond to back-to-front motion, layer 3 receives input from T4/T5 c-subtype neurons that respond to upward motion and layer 4 receives input from T4/T5 d-subtype neurons that respond to downward motion (Figure 9A; Maisak et al., 2013). T4 and T5 neurons project to lobula plate tangential cells via cholinergic synapses (Schnell et al., 2012; Mauss et al., 2014). These tangential cells integrate ON and OFF signals in large receptive fields (Joesch et al., 2010; Schnell et al., 2012) in a fully-opponent direction-selective fashion i.e. they depolarize in response to their preferred direction and hyperpolarize in response to their null direction (Joesch et al., 2008). The direction selectivity of tangential cells mostly results from the integration of local motion information from T4 and T5 neurons to gain global motion information (Schnell et al., 2012; Mauss et al., 2014; Barnhart et al., 2018). Blocking the synaptic output of T4/T5

cells results in non-responsive lobula plate tangential cells and reduced behavioural reactions to moving visual stimuli (Schnell et al., 2012; Maisak et al., 2013; Bahl et al., 2013; Schilling and Borst, 2015). Silencing synaptic transmission of OFF pathway Tm cells, upstream of T5, reduces responses of tangential cells specifically to OFF motion as well (Serbe et al., 2016). Lobula plate tangential cells are the principal output neurons from the lobula plate and relay wide-field motion information to areas in the central brain, to neck motor neurons and descending neurons (Borst and Haag, 2002; Haag et al., 2007; Wertz et al., 2008, 2012; Suver et al., 2016).

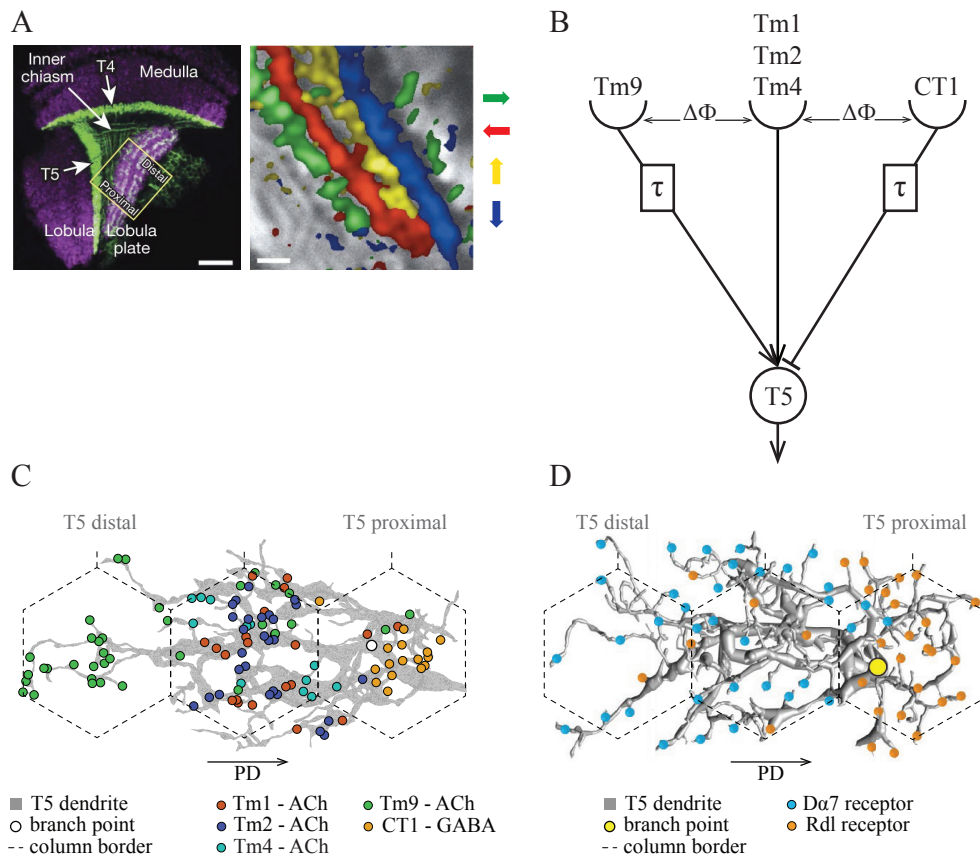


Figure 9: Direction-selective T5 neurons: (A) The dendrites of T4 neurons (ON pathway) are located in the medulla, while the dendrites of T5 neurons (OFF pathway) are located in the lobula (left). T4 and T5 neurons are divided into four specialized subtypes, each being selective for one of the cardinal directions (right). Image from Maisak et al. (2013) with permission. (B) Three-arm detector architecture representing the three input columns of a T5 neuron. (C) From electron microscopy studies, the synaptic input distribution on a single T5 dendrite (grey). Each coloured circle represents a synaptic connection from Tm9, Tm1, Tm2, Tm4 and CT1 input neurons. Columnar borders are indicated by grey dashed lines. Image adapted from Braun et al. (2023) (open access, CC BY 4.0 DEED) (D) Receptor distribution on a single T5 dendrite (grey). CT1 GABAergic inputs to T5 dendrites are made onto Rdl receptors (right). Tm1, Tm2 and Tm4 cholinergic inputs to T5 dendrites are made onto $D\alpha 7$ receptors (middle). For Tm9 inputs it is not shown which receptors are located on the distal side of T5 dendrites (left). Image adapted from Fendl et al. (2020) (open access, CC BY 4.0 DEED).

4.2.1 T5 cells and the OFF pathway

An essential neuropil in the OFF pathway is the lobula. Here, the T5 neurons form their dendrites (Figure 8A). T5 neurons are the elementary motion detectors for brightness decrements in the fly. They represent the first stage of direction-selective responses within the OFF pathway. Every single dendrite receives input from approximately seven columns. Using EM reconstructions and synapse visualisation made the distribution of synaptic inputs along T5 dendrites visible (Figure 9C; Shinomiya et al., 2019). At the distal tip of the T5 dendrite (the preferred-direction side: the side of the dendrite where motion in the preferred direction first reaches the dendrite) the majority of synaptic connections are formed by presynaptic Tm9 neurons. In the central region of T5 dendrites, synaptic connections predominantly involve Tm1, Tm2 and Tm4 neurons. On the proximal side (the null-direction side) of T5 dendrites, the majority of presynaptic connections are formed by CT1 (Figure 9C). This spatial arrangement between a single T5 neuron and all its columnar input neurons is consistent for all T5 neurons.

Importantly, all Tm input neurons to T5 have been described as cholinergic, directionally unselective and responsive to only OFF visual stimuli (Meier et al., 2014; Strother et al., 2014; Behnia et al., 2014; Serbe et al., 2016; Arenz et al., 2017). The response kinetics of Tm input neurons vary and provide a variety of temporal filters, ranging from fast, transient Tm2 and Tm4 neurons over intermediate Tm1 neurons to slow and sustained Tm9 neurons (Serbe et al., 2016).

Prior to the electron microscopy analysis conducted by Shinomiya et al. (2019), the CT1 neuron had been overlooked and was not considered essential for motion processing in *Drosophila* (Figure 8B). Functional calcium imaging experiments and compartmental modelling revealed that this special large-field amacrine cell is highly compartmentalised (Meier and Borst, 2019). A single CT1 cell acts as hundreds of parallel functional units that are electrically isolated. Moreover, this intriguing neuron is responsive to ON stimuli within the medulla and to OFF stimuli within the lobula (Meier and Borst, 2019), a characteristic that corresponds with its unique morphology (Figure 8B). CT1 terminals in the columns of the medulla make connections with T4 neurons, integrating it into the ON pathway as an ON cell. Similarly, its terminals in the columns of the lobula connect with T5 neurons, positioning it as an OFF cell within the OFF pathway. Notably, the CT1 neuron provides GABAergic inhibitory input (Takemura et al., 2017), standing out as the primary columnar inhibitory input to T5 among the cholinergic Tm inputs.

As mentioned above, T5 inputs are spatially segregated along its dendrite, leading to a spatial segregation of chemical synapses and receptors between T5 and its presynaptic partners. Utilising fluorescent tagging of receptor proteins in single neurons (FlpTag) and UAS-transgenes expressing GFP-tagged neurotransmitter receptors (Fendl et al., 2020), researchers identified the chloride channel Rdl (Resistant to dieldrin) as the receptor for T5's GABAergic inhibitory CT1 input (Figure 9D; Fendl et al., 2020). At the dendrite's centre, cholinergic inputs from Tm1, Tm2 and Tm4

target the excitatory $D\alpha 7$ receptors (Fendl et al., 2020). However, the receptor corresponding to the cholinergic Tm9 input remains unresolved, with $D\alpha 7$ shown to be located less at the distal side (Figure 9D; Fendl et al., 2020). There are ten ionotropic, nicotinic Acetylcholine receptors and three metabotropic, muscarinic Acetylcholine receptors described in *Drosophila*. According to previous RNA sequencing studies, T5 neurons express nearly every Acetylcholine receptor subunit (Pankova and Borst, 2016; Davis et al., 2020; Hörmann et al., 2020). There is ongoing discussion in the field regarding whether metabotropic Acetylcholine receptors might be located at the distal side of T5 dendrites (Fendl et al., 2020). Until today this awaits further investigations.

4.2.2 T4 cells and the ON pathway

An essential neuropil in the ON pathway is the medulla. Here the T4 neurons form their dendrites (Figure 8A). T4 neurons are the elementary motion detectors for brightness increments in the fly. They represent the first stage of direction-selective responses along the ON pathway.

T4 neurons serve a role in the ON pathway that is analogous to the function of T5 neurons in the OFF pathway. As for T5, there have been EM studies that reveal the distribution of the synaptic inputs along T4 dendrites (Takemura et al., 2017; Shinomiya et al., 2019). At the distal tip of the T4 dendrite (the preferred-direction side) the majority of synaptic connections are formed by a glutamatergic Mi9 neuron with the postsynaptic glutamate-gated Cl^- channel $GluCl\alpha$ as the receptor at the T4 dendrite (Fendl et al., 2020). Hence, Mi9 is inhibitory onto T4 (Cully et al., 1996; Liu and Wilson, 2013). In the central region of T4 dendrites, Mi3 and Tm3 neurons make cholinergic inputs onto excitatory $D\alpha 7$ receptors at T4. On the proximal side (the null-direction side) of T4 dendrites, the majority of presynaptic connections are formed by GABAergic Mi4, CT1 and C3 neurons, where the chloride channel Rdl resides.

In contrast to the OFF pathway where all T5 input neurons are OFF neurons, in the ON pathway not all input neurons are ON neurons. The Mi9 neuron as an exception responds to dark edges within the ON pathway (Arenz et al., 2017).

In summary, the ON- and OFF pathways serve as parallel mechanisms for decoding similar types of information. While the general architecture of T4 and T5 dendrites within these pathways is similar, the nature of their input features and receptor types diverge. This implies that the underlying computations at the dendritic level are likely different.

5 GOAL OF THIS THESIS

In the past, motion vision has been extensively explored through various approaches, including developmental, molecular, computational, functional and structural research. As I started my doctoral work, the wiring diagram of the motion vision circuit in the optic lobe had been mapped (Shinomiya et al., 2015; Takemura et al., 2017; Shinomiya et al., 2019). Functional two-photon calcium imaging studies had discovered the direction-selective properties of T4 and T5 neurons (Maisak et al., 2013; Haag et al., 2017) as well as the properties of their non-direction-selective inputs (Behnia et al., 2014; Meier et al., 2014; Strother et al., 2014; Ammer et al., 2015; Fisher et al., 2015; Serbe et al., 2016; Yang et al., 2016; Arenz et al., 2017; Drews et al., 2020; Meier and Borst, 2019). The pressing question of how the first direction-selective neurons – T4 and T5 – become direction selective was poorly understood at the beginning of my doctoral research. In the course of my dissertation research, I aimed to deepen the understanding by investigating how motion is computed in the OFF motion vision pathway, specifically at the level of T5 neurons in *Drosophila melanogaster*.

In my first publication, I discovered an important circuit mechanism underlying the direction selectivity of T5 neurons. I describe how null-direction suppression is realised in the OFF motion vision pathway in *Drosophila* (Manuscript 1; Braun et al., 2023). A pivotal finding emerged from connectomics analysis, uncovering a columnar microcircuit among certain input neurons to T5. Using two-photon calcium imaging in combination with thermogenetics, optogenetics, apoptotic methods, and pharmacology, we demonstrated how disynaptic inhibition shapes the tuning of OFF motion detectors in *Drosophila*, directly linked to the identified columnar microcircuit. Additionally, we pinpointed CT1 as the specific input neuron crucial for null-direction suppression at the T5 neuron level, marking a significant advancement in our understanding of OFF motion vision detection.

In the course of studying connectivity of the OFF motion vision pathway and its downstream circuits, I contributed to the first full connectome of the adult fly brain. Previously, only specific regions of fly brains had been mapped using electron microscopy datasets, which already provided important insights into neural circuits and their functions. However, these segmented datasets made it impossible to analyse the circuits connecting various regions of the fly brain. A worldwide collaborative effort led to a complete neural wiring diagram of an adult fly brain (Manuscript 2; Dorkenwald et al., 2024). This milestone in *Drosophila* connectomics allows researchers to study neural circuits throughout the entire brain, rather than being limited to isolated regions. Moreover, this connectome provides systematic and hierarchical annotations of ~130,000 neurons, which covers neuronal classes, cell types and developmental units. Such extensive documentation enables any researchers to navigate through this dataset to find circuit systems and neurons of interest (Manuscript 3; Schlegel et al., 2024). Finally, I was involved in the catalogue of neuronal cell types and wiring diagrams for the visual system of *Drosophila* (Manuscript 4; Matsliah et al., 2024).

II

PUBLICATIONS

1 MANUSCRIPT 1: DISYNAPTIC INHIBITION SHAPES TUNING OF OFF-MOTION DETECTORS IN *DROSOPHILA*

Summary

The circuitry underlying the detection of visual motion in *Drosophila melanogaster* is one of the best studied networks in neuroscience. Lately, electron microscopy reconstructions, algorithmic models, and functional studies have proposed a common motif for the cellular circuitry of an elementary motion detector based on both supralinear enhancement for preferred direction and sublinear suppression for null-direction motion. In T5 cells, however, all columnar input neurons (Tm1, Tm2, Tm4, and Tm9) are excitatory. So, how is null-direction suppression realized there? Using two-photon calcium imaging in combination with thermogenetics, optogenetics, apoptotics, and pharmacology, we discovered that it is via CT1, the GABAergic large-field amacrine cell, where the different processes have previously been shown to act in an electrically isolated way. Within each column, CT1 receives excitatory input from Tm9 and Tm1 and provides the sign-inverted, now inhibitory input signal onto T5. Ablating CT1 or knocking down GABA-receptor subunit Rdl significantly broadened the directional tuning of T5 cells. It thus appears that the signal of Tm1 and Tm9 is used both as an excitatory input for preferred direction enhancement and, through a sign inversion within the Tm1/Tm9-CT1 microcircuit, as an inhibitory input for null-direction suppression.

Authors

Amalia Braun^{1,2}, Alexander Borst¹, Matthias Meier¹

¹ Max Planck Institute for Biological Intelligence, Martinsried, Germany.

² Graduate School of Systemic Neurosciences, LMU Munich, Germany.

This article is published in *Current Biology*; [Braun et al. \(2023\)](#).

Contributions

A. Braun, A. Borst, and M. Meier conceived the study and designed the experiments. **A. Braun** reconstructed, identified and together with M. Meier analyzed the connectivity of EM neurons. A. Borst performed the modeling experiment. **A. Braun**, and M. Meier performed and evaluated calcium imaging experiments, confocal imaging, and wrote the manuscript with the help of all authors.

Disynaptic inhibition shapes tuning of OFF-motion detectors in *Drosophila*

Highlights

- A columnar microcircuit improves directional tuning of T5 neurons
- Tm1 and Tm9 neurons provide indirect inhibitory input to T5 via CT1
- CT1 inhibits T5 via GABA-receptor subunit *Rdl*

Authors

Amalia Braun, Alexander Borst,
Matthias Meier

Correspondence

amalia.braun@bi.mpg.de (A.B.),
matthias.meier@bi.mpg.de (M.M.)

In brief

How is null-direction suppression realized in the *Drosophila* OFF-motion pathway? Braun et al. demonstrate that disynaptic inhibition within a columnar microcircuit through Tm1, Tm9, and CT1 mediates null-direction suppression. They identify GABA-receptor subunit *Rdl* as an important player in this operation. Algorithmic modeling underlines the results.



Braun et al., 2023, Current Biology 33, 2260–2269
June 5, 2023 © 2023 The Authors. Published by Elsevier Inc.
<https://doi.org/10.1016/j.cub.2023.05.007>



Article

Disynaptic inhibition shapes tuning of OFF-motion detectors in *Drosophila*

Amalia Braun,^{1,*} Alexander Borst,¹ and Matthias Meier^{1,2,*}

¹Max Planck Institute for Biological Intelligence, Department of Circuits – Computation – Models, Am Klopferspitz 18, 82152 Martinsried, Germany

²Lead contact

*Correspondence: amalia.braun@bi.mpg.de (A.B.), matthias.meier@bi.mpg.de (M.M.)

<https://doi.org/10.1016/j.cub.2023.05.007>

SUMMARY

The circuitry underlying the detection of visual motion in *Drosophila melanogaster* is one of the best studied networks in neuroscience. Lately, electron microscopy reconstructions, algorithmic models, and functional studies have proposed a common motif for the cellular circuitry of an elementary motion detector based on both supralinear enhancement for preferred direction and sublinear suppression for null-direction motion. In T5 cells, however, all columnar input neurons (Tm1, Tm2, Tm4, and Tm9) are excitatory. So, how is null-direction suppression realized there? Using two-photon calcium imaging in combination with thermogenetics, optogenetics, apoptotics, and pharmacology, we discovered that it is via CT1, the GABAergic large-field amacrine cell, where the different processes have previously been shown to act in an electrically isolated way. Within each column, CT1 receives excitatory input from Tm9 and Tm1 and provides the sign-inverted, now inhibitory input signal onto T5. Ablating CT1 or knocking down GABA-receptor subunit *Rdl* significantly broadened the directional tuning of T5 cells. It thus appears that the signal of Tm1 and Tm9 is used both as an excitatory input for preferred direction enhancement and, through a sign inversion within the Tm1/Tm9-CT1 microcircuit, as an inhibitory input for null-direction suppression.

INTRODUCTION

One major function of sensory neural systems is to relay information about the environment to higher processing stages in the brain, enabling organisms to interact with their surroundings. Efficient filtering is indispensable to make sense of the plethora of incoming signals.¹ In the vertebrate retina, for instance, a variety of parallel-processing units, retinal ganglion cells, represent diverse cues of the visual scenery like color, contrast, velocity, or the direction of moving objects.^{2,3} This requires extensive computation within only a few synapses.

The visual system of fruit flies has evolved to perform precise computations with few neurons, resulting in highly adaptive behavior.⁴ The detection of visual motion in *Drosophila* has turned out to be an excellent test bed for scientists investigating neural processing and understanding the implementation of algorithmic models (reviewed in Borst et al.⁵).

The compound eye of fruit flies consists of approximately 750 facets also called ommatidia that tile the entire visual space and give rise to a retinotopic map of the environment. The area of the fly brain that is dedicated to the detection of visual signals, the optic lobe and consists of the lamina, the medulla, the lobula, and the lobula plate. Each of these neuropils comprises repetitive units called columns and reflects the spatial layout of the faceted eye in a retinotopic map. Within the visual processing stream, T4 and T5 cells are the first neurons to respond to visual motion in a directionally selective way. T4 cells extend their dendrites in the most proximal layer of the medulla and respond to moving bright edges (ON pathway). T5 cell dendrites receive

their input in the most proximal layer of the lobula and are responsive to moving dark edges (OFF pathway). The dendrites of both T4 and T5 cells span several columns, thus receiving input from neighboring locations in space. Each neuron can be classified by the direction of visual motion it is most excitable to—referred to as its preferred direction (PD), while showing little response when stimulated in the opposite direction (null direction [ND]). Within each column, there exist four subtypes of T4 and T5 neurons that are tuned to the four cardinal directions (front-to-back, back-to-front, upward, and downward).⁶ According to their PD, the axon terminals of T4 and T5 cells are located within one of the four layers of the lobula plate.

The identification of these local motion detectors, combined with the advent of modern transgenics and connectomics, has substantially deepened our understanding of the circuitry over the past decade.^{5–11} Two algorithmic models have proven valuable in describing the computation of direction selectivity: (1) the Hassenstein-Reichardt correlator where signals from two spatially offset locations are multiplied after exhibiting differential temporal filtering, resulting in PD enhancement¹²; and (2) the Barlow-Levick detector where a divisive nonlinearity combines a direct and a delayed line, suppressing ND motion.¹³ At the level of motion-sensitive T4 and T5 cells in the fly optic lobe, both mechanisms have been demonstrated experimentally (Figure 1A).^{14–18} The identity, morphology, and—to some extent—physiology of the key players in this computation have been described,^{19–26} proposing a circuit arrangement suitable for the implementation of an elementary motion detector.



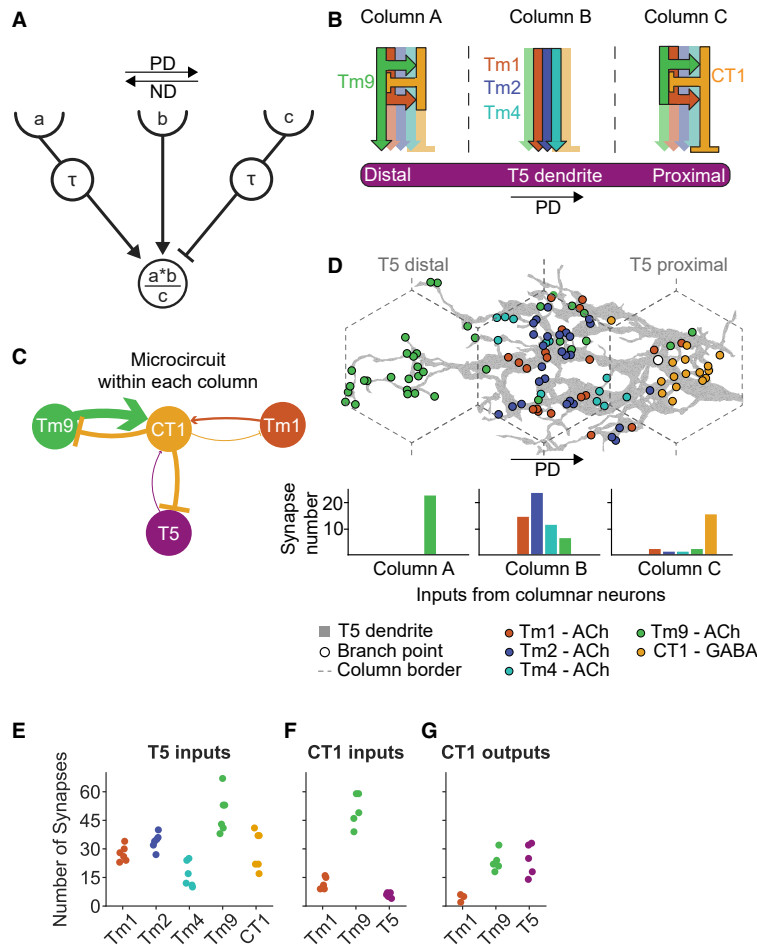


Figure 1. Structural and synaptic organization of the T5 pathway

(A) Three-arm circuit model architecture for motion detection in *Drosophila* representing the three input columns of a T5 neuron comprising of a multiplicative interaction between a delayed (τ) excitatory (a), a direct excitatory line (b), and a divisive interaction between the direct and a delayed inhibitory input (c).

(B) Schematic diagram of the five major inputs onto the T5 dendrite in three neighboring columns based on their synapse distribution. Within each input column (dashed line) the connections between neurons are indicated through arrows. Each column contains the same set of columnar neurons. Lighter arrows indicate columnar input neurons that exist in each column but do not form a strong synaptic connection at that side of the T5 neuron.

(C) Schematic representation of the interconnections between Tm1, Tm9, T5, and CT1 within each column. The width of the arrows indicates the number of synapses.

(D) Synaptic input distribution on a single EM reconstructed T5 dendrite (gray) (*flywire.ai*). This example dendrite is tuned to motion from left to right and spans three neighboring columns along the axis of its preferred direction (PD). Tm9 synapses (green) are located on the distal (PD) side, Tm1 (red), Tm2 (blue), and Tm4 (cyan) synapses are located at the center, and CT1 at the proximal side (ND) of the T5 dendrite. Columnar borders are indicated by gray dashed lines. The bar charts quantify the number of synapses between T5 and its columnar input neurons in each of the three neighboring columns.

(E–G) Quantification of synaptic connectivity between T5 and its major inputs traced in Flywire. Results are depicted for each neuron ($n_{T5} = 6$, $n_{CT1} = 5$). (E) Sum of all synapses of the five major input neurons to the T5 dendrite. (F) Maximum number of synapses for all reconstructed CT1 inputs. (G) Maximum number for all CT1 output synapses. See also Figure S1.

Recently, electrophysiological investigations have unraveled the mechanism behind the computation of direction selectivity in T4 dendrites. Here, several neurons provide inhibitory input for ND suppression,²⁴ while release from glutamatergic inhibition enhances the cholinergic excitation for motion along the PD, further sharpening the directional tuning of T4 cells.²⁷ However, the functional mechanism the fly brain uses to transform spatiotemporal information about light intensity into direction-selective signals in the T5 counterpart remains to be discovered. The neural pathway selective for brightness decrements has been attributed to T5 cells and their upstream synaptic partners unicolunar Tm1, Tm2, Tm4, Tm9, and multicolumnar CT1 (Figure 1B).^{6,28} The neurotransmitter profile of these neurons suggests excitatory roles for all cholinergic Tm cells and proposes an inhibitory function for GABAergic CT1 (Figure 1B).^{11,29–31} In contrast to the columnar Tm cells, multicompartmental large-field CT1 exhibits a peculiar morphology with electrically isolated terminals³² acting as post- and presynaptic sites simultaneously. Within each column, CT1 receives its major input from one Tm9 and one Tm1 neuron and makes output synapses on the T5 dendrite (Figure S1). Intriguingly, all of CT1s

synaptic connections seem to be reciprocal. This results in a columnar microcircuit with reciprocal connections between Tm1, Tm9, and CT1 as an “input stage” and CT1 and T5 as the output of the subnetwork (Figure 1C). However, no functional data are available to date on the CT1 circuit and its role in motion processing.

In this study, we combine thermogenetic, optogenetic, apoptotic as well as pharmacologic techniques to investigate the neural network underlying the computation of directional signals in the *Drosophila* OFF-motion pathway.

RESULTS

Network architecture based on EM connectivity analysis

Recently, a complete volume of a full adult fly brain (FAB) was recorded using electron microscopy (EM)³³ and made publicly available for reconstruction (*flywire.ai*).³⁴ This development has enabled researchers to verify and reproduce previously published data, as well as discover unknown synaptic connections, without the need to generate a separate dataset. Within the FAB dataset we reconstructed six T5 neurons and analyzed all their

presynaptic partners (Figures 1D and 1E). We reproduced previous findings that columnar elements Tm9, Tm2, Tm1, and Tm4 constitute the majority of T5 inputs, in addition to multicompartmental CT1 (Figure 1E).^{11,30} Figure 1D depicts an EM reconstruction of an example T5 dendrite (gray) tuned to motion from left to right that spans three neighboring columns along the axis of its PD. The spatial distribution of input synapses on the T5 dendrite illustrates how closely the anatomical distribution matches the proposed circuit layout—i.e., with Tm9 neurons providing input on the preferred (distal) arm; Tm1, Tm2, and Tm4 in the center; and CT1 on the null (proximal) side of the T5 dendrite.

We next focused our analysis on the CT1 subcircuit. Considering isolated CT1 terminals in the lobula as separate units, we found that they receive most of their inputs from Tm9 and, to a lesser extent, from Tm1 and T5 cells (Figure 1F).¹¹ Interestingly, all connections turned out to be reciprocal—i.e., CT1 is also presynaptic to Tm9, Tm1, and T5 (Figure 1G). The number of individual cells connected to CT1 in one column differs between cell types. While CT1 interacts with exactly one Tm1 and one Tm9 cell per column, it contacts multiple T5 cells with a high variability in synapse counts (Figures S1D and S1E). This is due to the multicolumnar anatomy of T5 dendrites and the fact that each column contains four T5 subtypes tuned to each of the four cardinal directions.

Cholinergic inputs determine the preferred direction response of OFF elementary motion detectors

Previous studies have already investigated the role of Tm inputs to various stimuli and at different readout stages.^{15,20,23,25,26} In order to make assumptions about their specific roles for the computation of direction selectivity of T5, however, it is indispensable to probe their contribution under consistent, functionally relevant stimulus conditions at the level of T5 neurons. Electrophysiological characterizations of T5 responses have indicated that both preferred and ND motion result in depolarizations.³⁵ Since depolarizing responses can also be resolved by genetically encoded calcium indicators, we decided to investigate T5 activity via recording calcium levels under a two-photon microscope.

To test whether a lack of input signals from each of the four major cholinergic elements (Tm1, Tm2, Tm4, and Tm9) affects T5 responses, we stimulated flies expressing the calcium indicator GCaMP6m in layer three T4 and T5 (T4/T5c) cells with dark edges moving in their preferred (up) and ND (down) (Figure 2A). In a first set of experiments, we suppressed the outputs of individual Tm cell types using the thermogenetic silencer *shibire^{ts}*³⁶ (see Table S1 for genotypes). We found that silencing the putatively excitatory inputs generally affected T5 responses recorded in the lobula to stimuli moving in their PD. ND signals were mildly, but significantly reduced for Tm1 and Tm4 cell blocks (Figures 2B and 2C). Moreover, observed effects differed in amplitude between Tm cells in line with their synaptic contribution to T5, with Tm9 and Tm2 having the strongest effect on T5 PD responses followed by Tm4. Silencing Tm1 had no effect (Figures 2B and 2C) on T5 PD responses. Qualitatively similar results had already been described using the lobula plate tangential cells one synapse downstream as a readout.²³

There are two experimental disadvantages of using *shibire^{ts}* in our setup: first the lack of temporal precision over the thermogenetic activation, creating the possibility of introducing long term effects or compensatory mechanisms; and second, the

necessity for control and test experiments with flies of different genotypes (see STAR Methods). In order to overcome these shortcomings, we established a new protocol that allowed us to exploit the temporal precision of optogenetics. We chose to hyperpolarize Tm cells using the optogenetic tool *GtACR1*^{37,38} (see Figure S2 for expression patterns). This setup gave us the ability to acutely alter the output of presynaptic elements of T5 by activating the light-gated, hyperpolarizing ion channel *GtACR1* during visual stimulation, while recording the activity of direction-selective T5 cells in the lobula plate (Figures 2E and 2F). We titrated the two-photon laser, the optogenetic activation light, and the visual stimulus to minimize undesired activation of *GtACR1* in control conditions and simultaneously maximize visual responses and Tm cell hyperpolarization (see STAR Methods for details). We excluded visual artifacts by delivering optogenetic light pulses to control flies not expressing *GtACR1* (Figure S2E). Using this temporally precise method, we found that hyperpolarizing Tm9 or Tm2 most strongly reduced T5 responses to PD motion followed by Tm4. Hyperpolarizing Tm1 had no effect on T5 responses (Figures 2E and 2F). T5 responses to ND motion remained unaltered when we hyperpolarized any of the presynaptic Tm neurons, except Tm9 where we observed a small, yet significant decrease in response amplitude. Taken together, we could confirm the previous *shibire^{ts}* results using acute optogenetic hyperpolarization of individual Tm cell types, further strengthening our confidence in these findings.

We conclude that cholinergic Tm neurons shape the tuning of T5 PD responses to moving dark edges while the suppression of ND responses must be mediated through another channel.

Functional connectivity analysis reveals disynaptic mechanism for null-direction suppression

Suppressing the output of presynaptic elements is one way to learn about their functional relevance in a neural circuit. Another way to gain insight is the activation of individual elements. From the intricate circuitry indicated by connectomics, we hypothesized two effects on T5 responses when activating selected Tm neurons: an increase in T5 responses through the direct connection (Tm2/Tm4) and decreased T5 calcium responses mediated through the Tm9/Tm1-CT1 route (Figure 1B).

In order to test our hypotheses, we expressed the light-gated, depolarizing ion channel *Chrimson*³⁹ in individual Tm cell types while recording T5c calcium responses in the lobula plate to visual stimuli. Our experimental protocol consisted of the delivery of the optogenetic light stimulus one second prior to the beginning of the visual stimulation (Figure 2D). This way we could resolve the effect of Tm cell output on T5 with and without visual stimulation.

Depolarizing the direct-input neuron Tm2 resulted in an immediate increase in calcium levels in T5 cells prior to visual stimulation (Figure 3A). The amplitude of the visual response, however, remained similar to control conditions. Activation of the input neuron Tm4 had no effect on T5 calcium levels. This was unexpected given the effect of Tm4 silencing evident in Figure 2. Activating Tm1 and Tm9 resulted in a more complex pattern of T5 calcium levels (Figure 3A). There was no observable effect on T5 calcium traces prior to visual stimulation. This could be due to two reasons: First, we cannot resolve a decrease in baseline fluorescence caused by a potentially hyperpolarizing input through the Tm1/Tm9-CT1 microcircuit; or

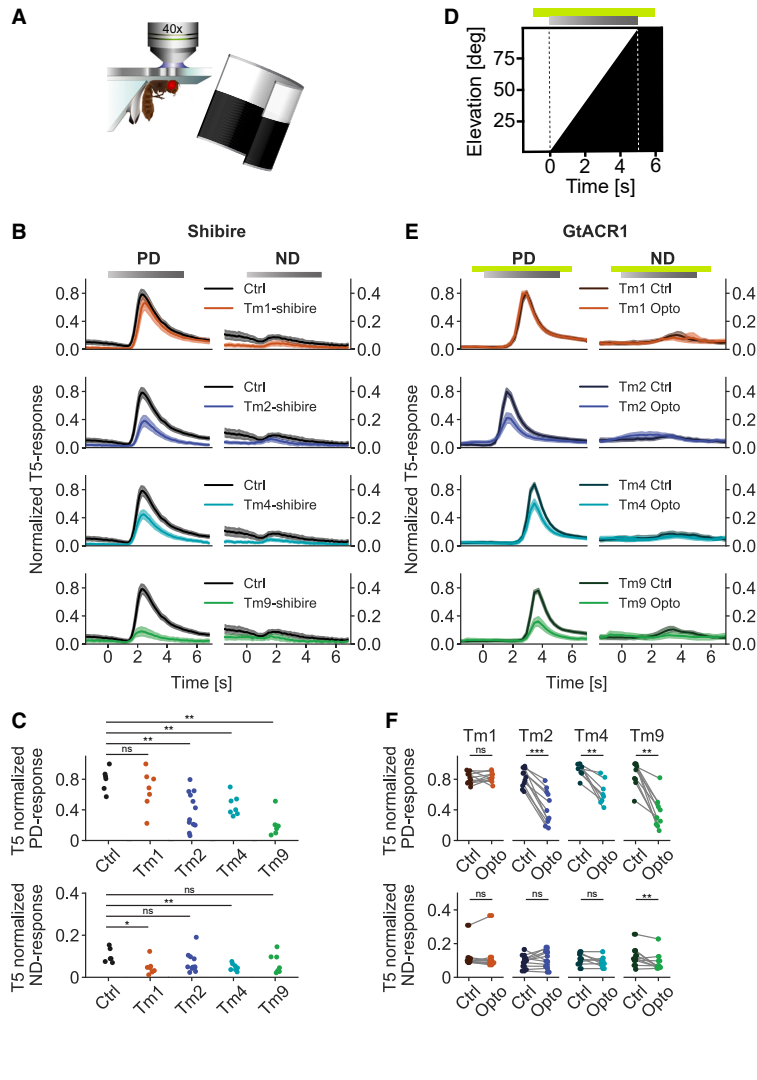


Figure 2. Functional relevance of the cholinergic input elements to the T5 motion detector

(A) Experimental setup for *in vivo* two-photon imaging.

(B) Response aligned T5c calcium traces (normalized to the maximum for each T5c dendrite) while presenting the fly with a dark edge moving in the preferred (PD) and null direction (ND) at 30°/s. The cholinergic inputs to T5 neurons (Tm1, Tm2, Tm4, and Tm9) were blocked using temperature sensitive mutation of Dynamin (*shibre^{ts}*). Black traces represent T5c responses in genetic control flies ($n_{ctrl} = 6$). The colored traces represent T5c responses after the synaptic output of the respective neuron type has been blocked using *shibre^{ts}* ($n_{Tm1} = 7$, $n_{Tm2} = 12$, $n_{Tm4} = 7$, and $n_{Tm9} = 7$). The timing of the visual stimulus is shown in (D) and by the bar on top. Results are depicted as mean values \pm SEM.

(C) Quantification of T5c normalized peak responses in preferred and null direction (data from B). Each point represents the maximal response of a single fly (see STAR Methods for details).

(D) X-t plot (spatial elevation as a function of time) of a dark edge moving upward on the arena (starting at 0 s, ending at 5 s). Timing and duration of the optogenetic stimulation is represented by the green bar. The optogenetic stimulus starts 1 s before (−1 s) and ends 1 s after the visual stimulus (6 s).

(E) Same as (C), but the light-gated, hyperpolarizing ion channel *GtACR1* was expressed in Tm neurons and activated by locally constraint, dim light impulse (565 nm, 1.07 μ W/mm²) through the objective. Light traces depict the normalized calcium activity of T5c neurons when the respective input neuron type has been optogenetically hyperpolarized. Dark traces represent T5c responses of the optogenetic control within the same fly (optogenetic light off). The timing of the visual and optogenetic stimulus is shown in (D) and by the bars on top. Results are depicted as mean values \pm SEM ($n_{Tm1} = 10$, $n_{Tm2} = 11$, $n_{Tm4} = 8$, $n_{Tm9} = 10$).

(F) Quantification of T5c normalized peak responses in preferred and null direction (data from E). Each point represents the maximal response of a single fly. Corresponding responses in one fly are connected by a gray line. $p \leq 0.05$ *; $p \leq 0.01$ **; $p \leq 0.001$ ***. See also Figure S2.

second, excitation via the direct input of Tm1 and Tm9 on the T5 dendrite is canceled by a putatively shunting synapse between CT1 and T5.

Further scrutinizing the T5 visual responses, we found that optogenetically depolarizing either Tm1 or Tm9 cells led to a reduction of PD responses in T5 while leaving ND responses unaltered (Figures 3A and 3B). Whereas this result may seem counterintuitive due to the putative excitatory nature of Tm1 and Tm9, it can readily be explained by considering the Tm1/Tm9-CT1 subcircuit. Optogenetically depolarizing either Tm1 or Tm9 leads to the activation of CT1, which provides an inhibitory signal onto T5. This disynaptic shunting inhibition then reduces the response of T5 cells to visual motion.

To further characterize the Tm1/Tm9-CT1 microcircuit, we investigated the functional connectivity between Tm1/Tm9 and CT1 by recording calcium signals in CT1 while driving

activity in either presynaptic neuron with *Chrimson*. When depolarizing Tm1 or Tm9 we observed a clear, sustained increase in CT1 calcium levels (Figure 3C), confirming their connectivity. Interestingly, the amplitude of T5 responses is higher when activating Tm1 compared with Tm9, although CT1 receives more synaptic input from Tm9. This could be due to reciprocal signaling between CT1 and its synaptic partners (see Figures 1D and 1G).

Overall, these data provide evidence that the reduction in T5 responses to PD stimulation upon activation of Tm1 or Tm9 shown in Figure 3A result from disynaptic inhibition through CT1.

Since previous transcriptomic and immunohistochemical studies have shown that CT1 most likely uses GABA as its major neurotransmitter,^{40–42} we next sought to remove GABAergic inhibition from the T5 circuitry. To this end we applied GABA_A-

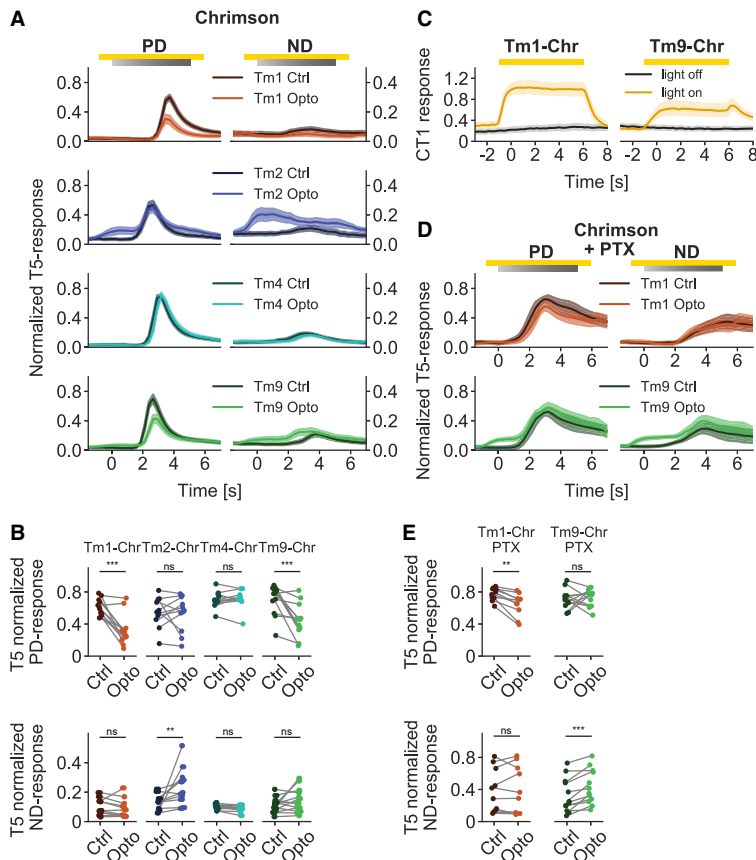


Figure 3. Functional connectivity analysis through optogenetics and pharmacology

(A) Response aligned T5c calcium traces (normalized to the maximum for each T5c dendrite) while presenting the fly with a dark edge moving in the preferred (PD) and null direction (ND) at 30°/s. The cholinergic inputs to T5 neurons (Tm1, Tm2, Tm4, Tm9) were activated using light-gated, depolarizing ion channel *Chrimson*. Dark traces represent T5c responses during optogenetic control trials (no light) and light traces show optogenetic activation (light on, 593 nm, 1.07 $\mu\text{W}/\text{mm}^2$). ($n_{\text{Tm1}} = 12$, $n_{\text{Tm2}} = 11$, $n_{\text{Tm4}} = 11$, $n_{\text{Tm9}} = 13$). The timing of the visual and optogenetic stimulus is shown in 2D and by the bars on top. Results are depicted as mean values \pm SEM. (B) Quantification of T5c normalized peak responses in preferred and null direction (data from A). Each point represents the maximal response of a single fly. Corresponding responses in one fly are connected by a gray line. (C) Fluorescence change ($\Delta F/F$) of CT1 terminals in the lobula upon optogenetic activation of Tm1 (left) and Tm9 (right) through *Chrimson*. No visual stimulus was presented to the flies (black screen). The timing of the optogenetic stimulus is indicated by the bar on top. Error shades indicate \pm SEM. $n_{\text{Tm1}} = 10$, $n_{\text{Tm9}} = 10$. (D) Same as (A) for Tm1 and Tm9 *Chrimson* activation after bath-application of GABA_AR antagonist picrotoxin (PTX) for 10 min. The timing of the visual and optogenetic stimulus is shown in (D) and by the bars on top. $n_{\text{Tm1}} = 10$, $n_{\text{Tm9}} = 12$. (E) Quantification (as in B) in preferred and null direction of PTX experiments (data from D). $p \leq 0.05$ *; $p \leq 0.01$ **; $p \leq 0.001$ ***. See also Figure S2.

receptor antagonist picrotoxin (PTX) to the extracellular solution. While this procedure likely blocks GABAergic transmission throughout the whole optic lobes, which also leads to changes in neural signaling outside of the T5 circuit, we could still see a number of specific effects that helped us to better understand this network.

First, as expected,²² we observed a clear increase in T5 responses in ND under control conditions. This indicates that ND suppression is most likely mediated through GABAergic inhibition. Second, when bath applying PTX, activation of Tm9 alone—without visual stimulation—led to an increase of calcium levels in T5 (Figure 3D), which was not observed when no PTX was applied (Figure 3A). This further corroborates the hypothesis that CT1 provides shunting inhibition onto the T5 dendrite that masks the excitatory signal of Tm9 in the experiments in Figure 3A. Interestingly, the activation of Tm1 cells alone does not result in increased T5 responses under PTX application.

A third observation is that, in the presence of PTX, the reduction in response amplitude in PD disappeared when Tm9 was activated and was reduced when Tm1 was activated (Figures 3D and 3E). This provides further evidence for the hypothesis that inhibition at the level of T5 dendrites is provided through the Tm1/Tm9-CT1 microcircuit.

Taken together, optogenetic activation combined with calcium imaging confirms the functional connectivity of the T5 network suggesting a disynaptic mechanism for ND suppression.

Null-direction suppression is mediated through CT1 via GABA-receptor subunit *Rdl*

In a further set of experiments, we set out to provide direct evidence for the role of CT1 in the computation of direction selectivity in the *Drosophila* OFF pathway. In contrast to columnar Tm neurons, CT1 exhibits a unique anatomy where one compartmentalized neuron acts as many hundred independent subunits.³² It is probably due to this distinct morphology that any attempt to use classic thermo- or optogenetic tools as in previous experiments (see Figures 2 and 3) had failed to produce a functional phenotype. Therefore, we genetically expressed apoptotic genes *hid* and *reaper*⁴³ to ablate both CT1 neurons in individual flies (Figure 4A) and to test the calcium responses of T5c cells to visual stimuli.

When stimulating flies with dark edges moving upward, i.e., along their PD, ablating CT1 did not have any effect on T5c responses. However, when presented with ND stimuli, CT1-*hid/rpr* flies exhibited a significant increase in T5 calcium responses compared with control flies (Figure 4B). Testing the responses to dark edges moving in 11 different directions in these flies revealed

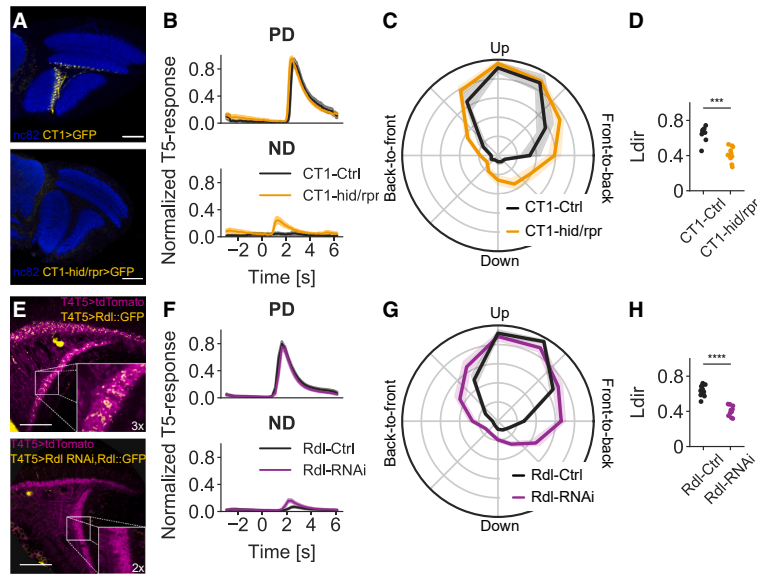


Figure 4. The specific role of CT1 in the directional tuning of T5

(A) Confocal fluorescent images of the neuropils in the optic lobe in horizontal view (blue). Top: example image of a CT1-Gal4 UAS-GFP expressing fly (yellow). Bottom: example image of a CT1-Gal4 UAS-*hid/rpr*, UAS-GFP expressing fly where no GFP signal was detectable. Scale bars: 20 μ m.

(B) Response aligned T5c calcium traces (normalized to the maximum for each T5c dendrite) while presenting the fly with a dark edge moving in the preferred (PD) and null direction (ND) at 30°/s. Black traces represent signals from control flies; yellow traces represent signals from control flies; yellow traces represent flies where CT1 cells were ablated using UAS-*hid/rpr* ($n_{ctrl} = 8$, $n_{CT1-hid/rpr} = 9$). Error shades indicate \pm SEM.

(C) Polar plot of the directional tuning of T5c calcium responses in Gal4-CT1, UAS-*hid/rpr* flies to dark edges moving in 11 different directions. Each datapoint represents the maximum T5c response to either direction of visual motion, normalized to the maximum per fly. Color code as in (B).

(D) Width of the directional tuning curves indicated by directional index L_{dir} (see STAR Methods) for Gal4-CT1, UAS-*hid/rpr* flies. Each datapoint represents the L_{dir} value of a unique fly. Color code as in (B).

(E) Fluorescent images of T4/T5-lexA, lexAop-GCaMP6m in horizontal view (magenta). Top: example image of *Rdl* receptor expression (yellow). Inset: 3-fold magnification. Bottom: example image of *Rdl* receptor expression using UAS-*Rdl*-RNAi in T4/T5 neurons where no *Rdl* GFP signal was detectable. Inset: 2-fold magnification. Scale bars: 20 μ m.

(F) As in (B) but magenta traces represent T5c calcium responses in T4T5-Gal4, UAS-*Rdl*-RNAi flies. $n_{ctrl} = 13$, $n_{Rdl-RNAi} = 10$.

(G) Directional tuning curves as in (C) for T4/T5-Gal4, UAS-*Rdl*-RNAi flies. Color code as in (F).

(H) Directional tuning indicated by L_{dir} , as in (D) for T4/T5-Gal4, UAS-*Rdl*-RNAi flies. Color code as in (F). $p \leq 0.05$ *; $p \leq 0.01$ **; $p \leq 0.001$ ***; $p \leq 0.0001$ ****. See also Figure S3.

that removing CT1 from the circuit led to a broader tuning curve (Figure 4C) and, thus, decreased the direction selectivity of T5c cells (Figure 4D). This effect was not observed in T4 cell responses to ON edges (Figure S3). These data provide strong evidence that CT1 indeed plays a crucial role in ND suppression in the T5 pathway.

Since CT1 is the only known GABAergic input neuron to T5, ablating CT1 should lead to similar results as removing the respective GABA receptor from T5. Transcriptomic analysis of T5 neurons has indicated the presence of GABA-receptor subunit *Rdl*.^{40,42,44} We therefore knocked down the *Rdl* receptor in T4 and T5 neurons using RNAi^{45,46} (Figure 4E) and tested their directional tuning. We found that the directional tuning curve of T5 was broader than in control flies (Figures 4F–4H), strongly resembling the results of the CT1 ablation experiments (Figures 4B–4D). This broadening of the tuning curve is reflected in a significant reduction of direction selectivity of T5c cells in *Rdl*-RNAi flies compared with controls (Figure 4H).

Taken together, these data highlight the role of CT1 in providing an inhibitory signal for null-suppression that shapes T5 direction selectivity and pinpoint GABA-receptor subunit *Rdl* as a key player in its computation.

Functional compatibility of CT1 signals with current model hypothesis

One prerequisite common to all current models for elementary motion detection is the differential temporal filtering of the inputs (Figure 1A), consisting of at least one direct and two

temporally delayed signal streams. In the past, several studies have recorded response properties of columnar elements and compared their temporal characteristics with predictions from modeling efforts.^{9,15,23,47} It has, however, also become apparent that cellular responses can vary based on stimulus characteristics like local and global contrasts.^{25,26,48} To allow conclusions about the physiological fit of CT1 signals as the delayed, inhibitory signal to the T5 cell, we needed to assess its response characteristics. It is important to do so using consistent and functionally relevant motion stimuli³² (as in Figures 2, 3, and 4). We found that CT1 exhibits slow, sustained calcium responses to moving dark edges—as expected given its major input Tm9 (Figure 5A), compared with fast, transient responses in Tm2.^{9,20,23} These data not only confirm the functional role of CT1 in ND suppression but also demonstrate that its temporal response properties make it an ideal candidate to act as the slow, inhibitory signal for ND suppression in T5 cells.

Algorithmic modeling underlines the importance of CT1 for T5 directional tuning

As a final effort in the characterization of ND suppression in the *Drosophila* OFF pathway, we performed model simulations. Since at present there is no biophysical insight into how PD enhancement is implemented on the T5 dendrite, we used a classic algorithmic model that combines a Hassenstein-Reichardt type detector for PD enhancement i.e., a multiplication and a Barlow-Levick type model for ND suppression i.e., a

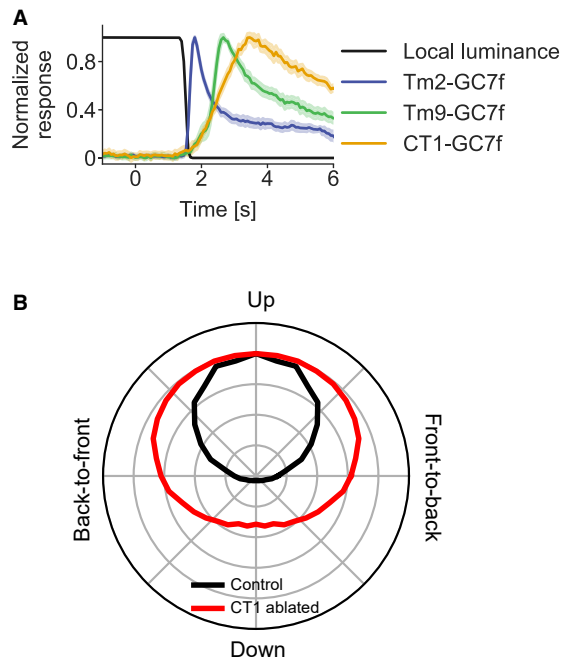


Figure 5. Temporal properties of T5 inputs and directional tuning map of model simulation

(A) Normalized two-photon calcium activity of Tm2 (blue), Tm9 (green), and CT1 (yellow) terminals in the lobula as a function of time in response to dark edges. Traces are aligned to the response onset. The black trace depicts the change in local luminance in a 7° wide window. $n_{Tm2} = 11$, $n_{Tm9} = 12$, $n_{CT1} = 10$. Error shades indicate \pm SEM.

(B) Directional tuning map of an algorithmic model (see Figure 1A) stimulated with moving dark edges in different direction. Three input signals (a, b, c) are high-pass filtered to simulate lamina inputs ($\tau_{HP} = 250$ ms). The low-pass time constants for inputs a and c were $\tau_{LP} = 200$ ms. Black trace, control condition; red trace, simulated CT1 ablation (c = 0).

division (Figure 1A).¹⁵ In short, we considered three inputs (a, b, c) to a local motion detector. The three inputs were each offset in space corresponding to the preferred, central, and null sides of the T5 dendrite (see Figure 1). Furthermore, they were subject to differential temporal filtering, in accordance with functional data known about the columnar input elements to T5 (see STAR Methods for details). The algorithmic operation carried out by the detector then is $\frac{a \times b}{c + DC}$; the DC value is necessary to avoid division by 0. We tested the model by presenting it with moving dark edges in different directions to obtain a directional tuning map like those in Figures 4C and 4G. Under simulated control conditions we could readily reproduce the tuning curves in T5 cells (Figure 5B, black trace). We next modified the model to resemble the experiments where CT1 was ablated or *Rdl* receptor subunits were knocked down by removing input c. Here, we could observe a substantial broadening of the tuning curve (Figure 5B, red trace). While the amplitude of the model ND response was larger than the experimentally measured calcium response to ND after ablation of CT1, the effect qualitatively resembled the results observed in the experiments.

DISCUSSION

In this study we investigated the functional role of the major constituents of the *Drosophila* OFF-motion pathway. We first confirmed the synaptic contribution of the presynaptic elements to T5 cells using an independent, publicly available EM dataset. We then demonstrated their role in the computation of local motion detection using thermogenetic and optogenetic silencing, activation and pharmacology. Finally, we unraveled a disynaptic mechanism for ND suppression through Tm9/Tm1 and CT1 via inhibitory GABA-receptor subunit *Rdl*. This work represents a major advancement toward understanding motion processing in the OFF pathway by addressing the longstanding question of how inhibition in the lobula can be achieved through exclusively cholinergic inputs from the medulla. The results represent a striking example of efficient coding where a neural network leverages a single signal for multiple purposes.

Disynaptic mechanism in the CT1 microcircuit

Balance between excitation and inhibition is essential for the maintenance of neuronal function in general. Particularly in the vertebrate cortex, examples of disynaptic inhibition can be found, where complex networks consisting of feedforward and feedback inhibition regulate brain states and ensure normal brain function.^{49–51} Additionally, disynaptic inhibitory motifs have been described in larval *Drosophila* premotor neurons.⁵² The CT1 microcircuit represents a particular example for such a computation. Tm9 and Tm1 signals are relayed directly onto T5 dendrites via cholinergic receptors. In parallel, they are sign-inverted through CT1 and used as an inhibitory signal for ND suppression (Figures 1A and 1B). Another intriguing detail about the Tm1/Tm9-CT1 microcircuit is the reciprocity of all its connections. Our activation experiments in Figure 3 showed that CT1 terminals are activated through the synaptic inputs from Tm1 and Tm9. The PTX experiments in Figure 3 provided evidence that direct Tm9 input on T5 is suppressed by CT1 activity. This could be either within the subcircuit through reciprocal connections or through the shunting effect of CT1 on T5 dendrites. Future experiments can help to shine light onto the intricate interplay between these four cell types.

Differences between ON- and OFF-motion detection

Across phyla, the detection of visual motion is organized separately for brightness increments and decrements.^{53–55} There is a number of studies that have looked at this split from different perspectives. There are for instance advantages in terms of efficiency in neural coding⁵⁶ but also differences in the image statistics of natural scenes that are reflected in differences in tuning properties of ON and OFF detectors.⁵⁷ It is also very interesting to look at the different circuit solutions for seemingly similar problems that have been created through the course of evolution. ND suppression in the *Drosophila* ON pathway, is likely implemented through columnar, inhibitory Mi4 cells^{11,27} while in the OFF pathway there is a seemingly complicated detour through a morphologically peculiar CT1 cell that inverts the sign of Tm1 and Tm9 signals. In principle there are two possible concepts that could explain the dissimilarities. On the one hand, adaptation to different environmental conditions like

the visual scenery could have led to the emergence of different wiring solutions that have proven to be most robust for the specific requirements. On the other hand, the divergence between the two channels could be due to modular evolution, where different components evolve independently before being integrated into a larger context, combined with constraints in development. In this case the differences of the circuits would not be due to different functional requirements, but rather because they were the most feasible solutions given the specific developmental constraints.

Biophysical mechanism for the computation of direction selectivity in T5

Recently, a biophysical mechanism for PD enhancement in T4 was discovered.²⁷ Here, an increase of T4 input resistance induced by disinhibition from Mi9 amplifies the response to the excitatory Mi1 signal, resembling a multiplicative operation. In T5, however, there are no inhibitory neurons on the preferred side of the T5 dendrite. Hence, we expect a different mechanism at work for multiplication. Transcriptomic analyses have described the presence of both nicotinic and metabotropic acetylcholine receptors on T5.^{40,42} In principle two mechanisms are conceivable to implement an enhancing nonlinearity; First, a multiplicative operation at the level of the postsynaptic membrane potential could result from an interaction of ionotropic and metabotropic receptors via second messenger cascades. As a second possibility, the supralinearity could be implemented by an activation threshold of a calcium channel that requires the simultaneous input from two presynaptic neurons (reviewed by London and Häusser¹). Further anatomical and electrophysiological investigation will help to elucidate the mechanism for PD enhancement.

ND suppression, on the other hand, has long been the more puzzling part in understanding OFF-motion detection due to the lack of inhibitory input from columnar elements.³⁵ With the experiments described above, we provide evidence that CT1 plays an important part in ND suppression. We could further propose a biophysical mechanism through GABA-receptor subunit *Rdl* that provides an inhibitory signal necessary for ND suppression in T5 cells.

The differences in effect amplitude that we observed in our model simulations (Figure 5) compared with the physiological data (Figure 4) could in theory hint at an additional, hitherto undiscovered mechanism that would shape ND suppression in parallel to the disynaptic inhibition via CT1. The anatomical layout of the input elements on the T5 dendrite, however, makes this possibility unlikely. It would rather be conceivable that, in the case of CT1-*hid/rpr*, not only the inhibitory input of CT1 on T5 is ablated but also the feedback connections of CT1 on Tm1 and Tm9. This mismatch in balance between excitation and inhibition, in combination with compensatory mechanisms that might be in place due to the absence of CT1 inputs could lead to unforeseen effects on the tuning of T5 cells. Compensatory mechanisms might also play a role in the *Rdl*-RNAi experiments. It would be very interesting to see how the acute inactivation of CT1 terminals in the lobula would alter the tuning curve of T5 neurons. The development of new, improved genetic tools will hopefully enable us to perform such experiments in the future and help to answer that question.

STAR★METHODS

Detailed methods are provided in the online version of this paper and include the following:

- KEY RESOURCES TABLE
- RESOURCE AVAILABILITY
 - Lead contact
 - Materials availability
 - Data and code availability
- EXPERIMENTAL MODEL AND SUBJECT DETAILS
 - Fly husbandry
- METHOD DETAILS
 - Generation of fly lines
 - Immunohistochemistry
 - Confocal microscopy
 - Two-photon-microscopy
 - Visual stimulation
 - Thermogenetics
 - Optogenetics
 - Pharmacology
 - Neuron tracing in FAFB
 - Model simulations
- QUANTIFICATION AND STATISTICAL ANALYSIS
 - Calcium imaging
 - Statistical analysis

SUPPLEMENTAL INFORMATION

Supplemental information can be found online at <https://doi.org/10.1016/j.cub.2023.05.007>.

ACKNOWLEDGMENTS

We are grateful to Aljoscha Leonhardt for carefully reading the manuscript; and Jonatan Mais for discussions. We thank the Princeton FlyWire team and members of the Murthy and Seung labs for development and maintenance of FlyWire (supported by BRAIN Initiative grant MH117815 to Murthy and Seung). We also acknowledge members of the Princeton FlyWire team and the FlyWire consortium for neuron proofreading. Zairene Lenizo contributed to neuron tracing. We thank the Janelia Research Campus for sharing the enhancer-Gal4 construct. Flies obtained from the Bloomington Drosophila Stock Center (NIH P40OD018537) were used in this study. We would further like to thank Jesús Pujol-Martí for providing stainings and Jesús Pujol-Martí and Tabea Schilling for flies.

A. Braun is a member of the Graduate School of Systemic Neurosciences (GSN) Munich. This work was funded by the Max Planck Society.

AUTHOR CONTRIBUTIONS

A. Braun, A. Borst, and M.M. conceived the study and designed the experiments. A. Braun reconstructed, identified and together with M.M. analyzed the connectivity of EM neurons. A. Borst performed the modeling experiment. A. Braun, and M.M. performed and evaluated calcium imaging experiments, confocal imaging, and wrote the manuscript with the help of all authors.

DECLARATION OF INTERESTS

The authors declare no competing interests.

INCLUSION AND DIVERSITY

We support inclusive, diverse, and equitable conduct of research.

Received: January 10, 2023
Revised: April 2, 2023
Accepted: May 3, 2023
Published: May 25, 2023

REFERENCES

- London, M., and Häusser, M. (2005). Dendritic computation. *Annu. Rev. Neurosci.* 28, 503–532. <https://doi.org/10.1146/annurev.neuro.28.061604.135703>.
- Werblin, F.S., and Dowling, J.E. (1969). Organization of the retina of the mud-puppy, *Necturus maculosus*. II. Intracellular recording. *J. Neurophysiol.* 32, 339–355. <https://doi.org/10.1152/jn.1969.32.3.339>.
- Baden, T., Berens, P., Franke, K., Román Rosón, M., Bethge, M., and Euler, T. (2016). The functional diversity of retinal ganglion cells in the mouse. *Nature* 529, 345–350. <https://doi.org/10.1038/nature16468>.
- Muijres, F.T., Elzinga, M.J., Iwasaki, N.A., and Dickinson, M.H. (2015). Body saccades of *Drosophila* consist of stereotyped banked turns. *J. Exp. Biol.* 218, 864–875. <https://doi.org/10.1242/jeb.114280>.
- Borst, A., Haag, J., and Mauss, A.S. (2020). How fly neurons compute the direction of visual motion. *J. Comp. Physiol. A Neuroethol. Sens. Neural Behav. Physiol.* 206, 109–124. <https://doi.org/10.1007/s00359-019-01375-9>.
- Maisak, M.S., Haag, J., Ammer, G., Serbe, E., Meier, M., Leonhardt, A., Schilling, T., Bahl, A., Rubin, G.M., Nern, A., et al. (2013). A directional tuning map of *Drosophila* elementary motion detectors. *Nature* 500, 212–218. <https://doi.org/10.1038/nature12320>.
- Jenett, A., Rubin, G.M., Ngo, T.T.B., Shepherd, D., Murphy, C., Dionne, H., Pfeiffer, B.D., Cavallaro, A., Hall, D., Jeter, J., et al. (2012). A GAL4-driver line resource for *Drosophila* neurobiology. *Cell Rep.* 2, 991–1001. <https://doi.org/10.1016/j.celrep.2012.09.011>.
- Takemura, S.Y., Bharioke, A., Lu, Z., Nern, A., Vitaladevuni, S., Rivlin, P.K., Katz, W.T., Olbris, D.J., Plaza, S.M., Winston, P., et al. (2013). A visual motion detection circuit suggested by *Drosophila* connectomics. *Nature* 500, 175–181. <https://doi.org/10.1038/nature12450>.
- Behnia, R., Clark, D.A., Carter, A.G., Clandinin, T.R., and Desplan, C. (2014). Processing properties of ON and OFF pathways for *Drosophila* motion detection. *Nature* 512, 427–430. <https://doi.org/10.1038/nature13427>.
- Strother, J.A., Nern, A., and Reiser, M.B. (2014). Direct observation of ON and OFF pathways in the *Drosophila* visual system. *Curr. Biol.* 24, 976–983. <https://doi.org/10.1016/j.cub.2014.03.017>.
- Shinomiya, K., Huang, G., Lu, Z., Parag, T., Xu, C.S., Aniceto, R., Ansari, N., Cheatham, N., Lauchie, S., Neace, E., et al. (2019). Comparisons between the ON- and OFF-edge motion pathways in the *Drosophila* brain. *eLife* 8, <https://doi.org/10.7554/eLife.40025>.
- Von Hassenstein, B., and Reichardt, W. (1956). Systemtheoretische analyse der Zeit-, Reihenfolgen- und Vorzeichenbewertung bei der Bewegungsperzeption des Rüsselkäfers *Chlorophanus*. *Zeitschrift für Naturforschung B* 11, 513–524. <https://doi.org/10.1515/znb-1956-9-1004>.
- Barlow, H.B., and Levick, W.R. (1965). The mechanism of directionally selective units in rabbit's retina. *J. Physiol.* 178, 477–504. <https://doi.org/10.1113/jphysiol.1965.sp007638>.
- Haag, J., Arenz, A., Serbe, E., Gabbiani, F., and Borst, A. (2016). Complementary mechanisms create direction selectivity in the fly. *eLife* 5, <https://doi.org/10.7554/eLife.17421.001>.
- Arenz, A., Drews, M.S., Richter, F.G., Ammer, G., and Borst, A. (2017). The temporal tuning of the *Drosophila* Motion detectors is determined by the dynamics of their input elements. *Curr. Biol.* 27, 929–944. <https://doi.org/10.1016/j.cub.2017.01.051>.
- Leong, J.C.S., Esch, J.J., Poole, B., Ganguli, S., and Clandinin, T.R. (2016). Direction selectivity in *Drosophila* emerges from preferred-direction enhancement and null-direction suppression. *J. Neurosci.* 36, 8078–8092. <https://doi.org/10.1523/JNEUROSCI.1272-16.2016>.
- Borst, A. (2018). A biophysical mechanism for preferred direction enhancement in fly motion vision. *PLoS Comput. Biol.* 14, e1006240. <https://doi.org/10.1371/journal.pcbi.1006240>.
- Zavatone-Veth, J.A., Badwan, B.A., and Clark, D.A. (2020). A minimal synaptic model for direction selective neurons in *Drosophila*. *J. Vis.* 20, 2. <https://doi.org/10.1167/JOV.20.2.2>.
- Fischbach, K.-F., and Dittrich, A.P.M. (1989). The optic lobe of *Drosophila melanogaster*. I. A golgi analysis of wild-type structure. *Cell Tissue Res.* 258, 441–475. <https://doi.org/10.1007/BF00218858>.
- Meier, M., Serbe, E., Maisak, M.S., Haag, J., Dickson, B.J., and Borst, A. (2014). Neural circuit components of the *Drosophila* OFF motion vision pathway. *Curr. Biol.* <https://doi.org/10.1016/j.cub.2014.01.006>.
- Ammer, G., Leonhardt, A., Bahl, A., Dickson, B.J., and Borst, A. (2015). Functional specialization of neural input elements to the *Drosophila* ON motion detector. *Curr. Biol.* 25, 2247–2253. <https://doi.org/10.1016/j.cub.2015.07.014>.
- Fisher, Y.E., Silies, M., and Clandinin, T.R.; Clandinin Correspondence (2015). Orientation selectivity sharpens motion detection in *Drosophila*. *Neuron* 88, 390–402. <https://doi.org/10.1016/j.neuron.2015.09.033>.
- Serbe, E., Meier, M., Leonhardt, A., and Borst, A. (2016). Comprehensive characterization of the major presynaptic elements to the *Drosophila* OFF motion detector. *Neuron* 89, 829–841. <https://doi.org/10.1016/j.neuron.2016.01.006>.
- Gruntman, E., Romani, S., and Reiser, M.B. (2018). Simple integration of fast excitation and offset, delayed inhibition computes directional selectivity in *Drosophila*. *Nat. Neurosci.* 21, 250–257. <https://doi.org/10.1038/s41593-017-0046-4>.
- Kohn, J.R., Portes, J.P., Christenson, M.P., Abbott, L.F., and Behnia, R. (2021). Flexible filtering by neural inputs supports motion computation across states and stimuli. *Curr. Biol.* 31, 5249–5260.e5. <https://doi.org/10.1016/j.cub.2021.09.061>.
- Ramos-Traslosheros, G., and Silies, M. (2021). The physiological basis for contrast opponency in motion computation in *Drosophila*. *Nat. Commun.* 12, 4987. <https://doi.org/10.1038/s41467-021-24986-w>.
- Groschner, L.N., Malis, J.G., Zuidinga, B., and Borst, A. (2022). A biophysical account of multiplication by a single neuron. *Nature* 603, 119–123. <https://doi.org/10.1038/s41586-022-04428-3>.
- Joesch, M., Schnell, B., Raghu, S.V., Reiff, D.F., and Borst, A. (2010). ON and OFF pathways in *Drosophila* motion vision. *Nature* 468, 300–304. <https://doi.org/10.1038/nature09545>.
- Raghu, S.V., and Borst, A. (2011). Candidate glutamatergic neurons in the visual system of *Drosophila*. *PLoS One* 6, e19472. <https://doi.org/10.1371/JOURNAL.PONE.0019472>.
- Shinomiya, K., Karuppudurai, T., Lin, T.Y., Lu, Z., Lee, C.H., and Meinertzhagen, I.A. (2014). Candidate neural substrates for off-edge motion detection in *Drosophila*. *Curr. Biol.* 24, 1062–1070. <https://doi.org/10.1016/j.cub.2014.03.051>.
- Eckstein, N., Bates, A.S., Du, M., Hartenstein, V., Jefferis, G.S.X.E., and Funke, J. (2020). Neurotransmitter classification from electron microscopy images at synaptic sites in *Drosophila*. Preprint at bioRxiv. <https://doi.org/10.1101/2020.06.12.148775>.
- Meier, M., and Borst, A. (2019). Extreme compartmentalization in a *Drosophila* amacrine cell. *Curr. Biol.* 29, 1545–1550.e2. <https://doi.org/10.1016/j.cub.2019.03.070>.
- Zheng, Z., Lauritzen, J.S., Perlman, E., Robinson, C.G., Nichols, M., Milkie, D., Torrens, O., Price, J., Fisher, C.B., Sharifi, N., et al. (2018). A complete electron microscopy volume of the brain of adult *Drosophila melanogaster*. *Cell* 174, 730–743.e22. <https://doi.org/10.1016/j.cell.2018.06.019>.
- Dorkenwald, S., McKellar, C.E., Macrina, T., Kemnitz, N., Lee, K., Lu, R., Wu, J., Popovych, S., Mitchell, E., Nehoran, B., et al. (2022). FlyWire: online community for whole-brain connectomics. *Nat. Methods* 19, 119–128. <https://doi.org/10.1038/s41592-021-01330-0>.
- Gruntman, E., Romani, S., and Reiser, M.B. (2019). The computation of directional selectivity in the *Drosophila* OFF motion pathway. *eLife* 8, <https://doi.org/10.7554/eLife.50706>.

36. Kitamoto, T. (2001). Conditional modification of behavior in *Drosophila* by targeted expression of a temperature-sensitive *shibire* allele in defined neurons. *J. Neurobiol.* 47, 81–92. <https://doi.org/10.1002/neu.1018>.
37. Govorunova, E.G., Sineshchekov, O.A., Janz, R., Liu, X., and Spudich, J.L. (2015). NEUROSCIENCE. Natural light-gated anion channels: A family of microbial rhodopsins for advanced optogenetics. *Science* 349, 647–650. <https://doi.org/10.1126/science.aaa7484>.
38. Mauss, A.S., Busch, C., and Borst, A. (2017). Optogenetic neuronal silencing in *drosophila* during visual processing. *Sci. Rep.* 7, 13823. <https://doi.org/10.1038/s41598-017-14076-7>.
39. Klapoetke, N.C., Murata, Y., Kim, S.S., Pulver, S.R., Birdsey-Benson, A., Cho, Y.K., Morimoto, T.K., Chuong, A.S., Carpenter, E.J., Tian, Z., et al. (2014). Independent optical excitation of distinct neural populations. *Nat. Methods* 11, 338–346. <https://doi.org/10.1038/nmeth.2836>.
40. Kurmangaliyev, Y.Z., Yoo, J., Locascio, S.A., and Zipursky, S.L. (2019). Modular transcriptional programs separately define axon and dendrite connectivity. *eLife* 8, <https://doi.org/10.7554/eLife.50822>.
41. Fendl, S., Vieira, R.M., and Borst, A. (2020). Conditional protein tagging methods reveal highly specific subcellular distribution of ion channels in motion-sensing neurons. *eLife* 9, 1–48. <https://doi.org/10.7554/eLife.62953>.
42. Hörmann, N., Schilling, T., Ali, A.H., Serbe, E., Mayer, C., Borst, A., and Pujol-Marti, J. (2020). A combinatorial code of transcription factors specifies subtypes of visual motion-sensing neurons in *Drosophila* dev186296. *Development* 147, /266871/AM/A-COMBINATORIAL-CODE-OF-TRANSCRIPTION-FACTORS. <https://doi.org/10.1242/DEV.186296>.
43. Grether, M.E., Abrams, J.M., Agapite, J., White, K., and Steller, H. (1995). The head involution defective gene of *Drosophila melanogaster* functions in programmed cell death. *Genes Dev.* 9, 1694–1708. <https://doi.org/10.1101/gad.9.14.1694>.
44. Ffrench-Constant, R.H., Mortlock, D.P., Shaffer, C.D., MacIntyre, R.J., and Roush, R.T. (1991). Molecular cloning and transformation of cyclodiene resistance in *Drosophila*: an invertebrate γ -aminobutyric acid subtype A receptor locus. *Proc. Natl. Acad. Sci. USA* 88, 7209–7213. <https://doi.org/10.1073/pnas.88.16.7209>.
45. Fire, A., Xu, S., Montgomery, M.K., Kostas, S.A., Driver, S.E., and Mello, C.C. (1998). Potent and specific genetic interference by double-stranded RNA in *Caenorhabditis elegans*. *Nature* 391, 806–811. <https://doi.org/10.1038/35888>.
46. Dietzl, G., Chen, D., Schnorrer, F., Su, K.C., Barinova, Y., Fellner, M., Gasser, B., Kinsey, K., Oettel, S., Scheiblaue, S., et al. (2007). A genome-wide transgenic RNAi library for conditional gene inactivation in *Drosophila*. *Nature* 448, 151–156. <https://doi.org/10.1038/nature05954>.
47. Yang, H.H.H., St-Pierre, F., Sun, X., Ding, X., Lin, M.Z.Z., and Clandinin, T.R.R. (2016). Subcellular imaging of voltage and calcium signals reveals neural processing in vivo. *Cell* 166, 245–257. <https://doi.org/10.1016/j.cell.2016.05.031>.
48. Drews, M.S., Leonhardt, A., Pirogova, N., Richter, F.G., Schuetzenberger, A., Braun, L., Serbe, E., and Borst, A. (2020). Dynamic signal compression for robust motion vision in flies. *Curr. Biol.* 30, 209–221.e8. <https://doi.org/10.1016/j.cub.2019.10.035>.
49. Troyer, T.W., Krukowski, A.E., Priebe, N.J., and Miller, K.D. (1998). Contrast-invariant orientation tuning in cat visual cortex: thalamocortical input tuning and correlation-based intracortical connectivity. *J. Neurosci.* 18, 5908–5927. <https://doi.org/10.1523/JNEUROSCI.18-15-05908.1998>.
50. Monier, C., Chavane, F., Baudot, P., Graham, L.J., and Frégnac, Y. (2003). Orientation and direction selectivity of synaptic inputs in visual cortical neurons: A diversity of combinations produces spike tuning. *Neuron* 37, 663–680. [https://doi.org/10.1016/S0896-6273\(03\)00064-3](https://doi.org/10.1016/S0896-6273(03)00064-3).
51. Silberberg, G., and Markram, H. (2007). Disynaptic inhibition between neocortical pyramidal cells mediated by Martinotti cells. *Neuron* 53, 735–746. <https://doi.org/10.1016/j.neuron.2007.02.012>.
52. Carreira-Rosario, A., Zarin, A.A., Clark, M.Q., Manning, L., Fetter, R.D., Cardona, A., and Doe, C.Q. (2018). MDN brain descending neurons coordinately activate backward and inhibit forward locomotion. *eLife* 7, <https://doi.org/10.7554/eLife.38554>.
53. Segev, R., Puchalla, J., and Berry, M.J. (2006). Functional organization of ganglion cells in the salamander retina. *J. Neurophysiol.* 95, 2277–2292. <https://doi.org/10.1152/JN.00928.2005>.
54. Ghosh, K.K., Bujan, S., Haverkamp, S., Feigenspan, A., and Wässle, H. (2004). Types of bipolar cells in the mouse retina. *J. Comp. Neurol.* 469, 70–82. <https://doi.org/10.1002/CNE.10985>.
55. Hashimoto, T., Katai, S., Saito, Y., Kobayashi, F., and Goto, T. (2013). ON and OFF channels in human retinal ganglion cells. *J. Physiol.* 591, 327–337. <https://doi.org/10.1113/JPHYSIOL.2012.243683>.
56. Gjorgjieva, J., Sompolinsky, H., and Meister, M. (2014). Benefits of pathway splitting in sensory coding. *J. Neurosci.* 34, 12127–12144. <https://doi.org/10.1523/JNEUROSCI.1032-14.2014>.
57. Leonhardt, A., Ammer, G., Meier, M., Serbe, E., Bahl, A., and Borst, A. (2016). Asymmetry of *Drosophila* ON and OFF motion detectors enhances real-world velocity estimation. *Nat. Neurosci.* 19, 706–715. <https://doi.org/10.1038/nn.4262>.
58. Takemura, S.Y., Nern, A., Chklovskii, D.B., Scheffer, L.K., Rubin, G.M., and Meinertzhagen, I.A. (2017). The comprehensive connectome of a neural substrate for 'ON' motion detection in *Drosophila*. *eLife* 6, <https://doi.org/10.7554/eLife.24394>.
59. Pfeiffer, B.D., Truman, J.W., and Rubin, G.M. (2012). Using translational enhancers to increase transgene expression in *Drosophila*. *Proc. Natl. Acad. Sci. USA* 109, 6626–6631. <https://doi.org/10.1073/pnas.1204520109>.
60. Buhmann, J., Sheridan, A., Malin-Mayor, C., Schlegel, P., Gerhard, S., Kazimiers, T., Krause, R., Nguyen, T.M., Heinrich, L., Lee, W.A., et al. (2021). Automatic detection of synaptic partners in a whole-brain *Drosophila* electron microscopy data set. *Methods* 18, 771–774. <https://doi.org/10.1038/s41592-021-01183-7>.
61. Heinrich, L., Funke, J., Pape, C., Nunez-Iglesias, J., and Saalfeld, S. (2018). Synaptic cleft segmentation in non-isotropic volume electron microscopy of the complete *Drosophila* Brain. In *Lecture Notes in Computer Science* (including subseries Lecture Notes in Artificial Intelligence and Lecture Notes in Bioinformatics), (Springer Verlag), pp. 317–325. https://doi.org/10.1007/978-3-030-00934-2_36.



STAR★METHODS

KEY RESOURCES TABLE

REAGENT or RESOURCE	SOURCE	IDENTIFIER
Antibodies		
Anti-nc82 mouse monoclonal antibody	DSHB	RRID: AB_2314866
Living Colors DsRed Rabbit Polyclonal	Clontech	Clontech: 632496
Chicken-anti-GFP polyclonal	Rockland	Rockland: 600901215
Goat anti-mouse-Atto-647N	Rockland	Rockland: 610156121
Goat anti-rabbit-Alexa-568	Invitrogen	Cat# A-11011; RRID: AB_2535730
Goat-anti-chicken Alexa488	Invitrogen	RRID: AB_2534096
GFP booster Atto-647N	ChromoTek	RRID: AB_2629215
Chemicals, Peptides, and Recombinant Proteins		
Picrotoxin	TCI	Cat# C0375
Deposited Data		
Raw and Analyzed Data	This paper	https://doi.org/10.17617/3.QE3MFT
Experimental Models: Organisms/Strains		
Canton S (Wildtype)	BDSC	RRID: BDSC_64349
w-; R41G07-p65.AD; R74G01-GAL4-DBD (Tm1split/SS00796)	BDSC	RRID: BDSC_86810
w-; R28D05-p65.AD; R82F12-Gal4.DBD (Tm2split)	BDSC	RRID: BDSC_86811
w-; R53C02-p65.AD; R60H04-GAL4.DBD (Tm4split)	BDSC	RRID: BDSC_86801
w-; R24C08-p65.AD; R70B08-GAL4.DBD (Tm9split)	BDSC	RRID: BDSC_86797
w-; +; VT12282-Gal4 (Tm2)	Serbe et al., 2016 ²³	N/A
w-; +; R35H01-Gal4 (Tm4)	Serbe et al., 2016 ²³	N/A
w-; +; VT65303-Gal4 (Tm9)	Serbe et al., 2016 ²³	N/A
l., 201665303-Gal4 (Tm9)-GAL4.D	Takemura et al. ⁵⁸	N/A
w-; +; VT50384-lexA (T4/T5)	Barry Dickson	Haag and Arenz ¹⁴
w-; VT041034-lexAGAD; + (Tm1)	JRC/Aljoscha Nern	N/A
w-; GMR24C08-lexA; + (Tm9)	BDSC	RRID: BDSC_62012
w-; pJFRC7-20XUAS-GtACR1-EYFP; +	Mauss et al. ³⁸	N/A
w-; 20XUAS-CsChrimson.mCherry; +	BDSC	RRID: BDSC_82181
w-; +; 13XLexAop2-IVS-CsChrimson.tdTomato	BDSC	RRID: BDSC_82183
w-; +; 13XLexAop-IVS-GCaMP6m	BDSC	RRID: BDSC_44277
w-; 20XUAS-IVS-jGCaMP7f; +	BDSC	RRID: BDSC_80906
w-; +; 20XUAS-IVS-jGCaMP7f	BDSC	RRID: BDSC_79031
w+; R39H12-Gal4; + (T4/T5)	This paper	N/A
w-; 10XUAS-mCD8GFP; +	BDSC	RRID: BDSC_79626
w-; 20XUAS-Rdl.GFP; +	BDSC	RRID: BDSC_92150
w-; +; 10XUAS-IVS-myr::tdTomato	BDSC	RRID: BDSC_32221
w-; +; UAS-Rdl RNAi8-10	BDSC	RRID: BDSC_89903
Yw UAS-rpr, UAS-Hid; +; +	Barry Dickson	N/A
rry Dickson-03NAi8-105)+6mmson.tdTo	Pfeiffer et al. ⁵⁹	N/A

RESOURCE AVAILABILITY

Lead contact

matthias.meier@bi.mpg.de

Materials availability

Newly generated fly line is available from the [lead contact](#) upon request.

Data and code availability

Data and code for analysis and modeling are publicly available at the at the Edmond Open Research Data Repository of the Max Planck Society: <https://doi.org/10.17617/3.QE3MFT>.

EXPERIMENTAL MODEL AND SUBJECT DETAILS

Fly husbandry

All flies (*Drosophila melanogaster*) were raised on standard cornmeal agar medium at 60% humidity, 25°C, 12h light/ 12h dark cycle. For optogenetic experiments we fed the flies for two days with a 1mM all-trans retinal (ATR) yeast paste by covering the agar medium. These vials were wrapped in aluminum foil to circumvent photo instability of ATR. For all experiments we used 2-3 days old female flies. See [Table S1](#) for genotypes.

METHOD DETAILS

Generation of fly lines

For generating the R39H12-Gal4 line on the second chromosome, the P{R39H12-GAL4} plasmid (Janelia Research Campus) was injected into the su(Hw)attP5 landing site strain BL#34765 for PhiC31 integrase-mediated transgenesis.

Injections were performed by BestGene (<https://www.thebestgene.com/>).

Immunohistochemistry

Fly brains were dissected in a phosphate-buffered saline (PBS) and fixed in 4% PFA (in PBS with 0.1% Triton X) for 25 minutes at room temperature. Brains were washed 5 five times in PBT (PBS with 0.3% Triton X) and blocked overnight in 10% normal goat serum (NGS) in PBT. Subsequently, the brains were incubated with the primary antibody solution (antibody with 5% NGS in PBT) for 48 hours at 4°C. Further the brains were washed 5 times in PBT and incubated with the secondary antibody solution for 48 hours at 4°C. Again, the brains were washed in PBT overnight at 4°C, washed in PBS and then mounted in Vectashield medium (VectorLabs).

Primary antibody: mouse-anti-nc82 (1:20), DsRed rabbit polyclonal (1:400), chicken-anti-GFP polyclonal (1:400)

Secondary antibody: goat-anti-mouse Atto647N (1:400), goat-anti-rabbit Alexa568 (1:400), goat-anti-chicken Alexa488 (1:400)

Nano-GFP-booster dilutions: GFP booster Atto647N (1:400)

Confocal microscopy

Images were acquired on a Leica Stellaris 5 confocal microscope with a 63x glycerol-immersion objective (Leica, 11506353) at a resolution of 1024x1024 pixels. Images were processed using Fiji (v2.3).

Two-photon-microscopy

For functional calcium imaging a custom-built two-photon laser scanning microscope was used as previously described.⁶ Briefly, flies were anesthetized on ice and with thorax and legs glued to a Plexiglas holder with bees' wax. The head was bent down to expose the posterior side of the head. The head was inserted into a fitting opening in aluminum foil that was clamped in a recording chamber. After adding external saline, a small window on the left side of the flies' head was cut open. Muscles, adipose tissue and trachea were removed mechanically.

Images were usually recorded at a resolution of 64 x 64 pixels and a frame rate of 15 Hz. Optogenetic experiments were recorded with 128 x 128 pixels and a frame rate of 3.8 Hz. Data acquisition was performed in Matlab R2013b (MathWorks) using ScanImage 3.8 software (Vidrio Technologies, LLC).

Visual stimulation

Visual stimuli were presented on a custom-built projector-based arena.¹⁵ Two micro-projectors (TI DLP Lightcrafter 3000) project onto the back of a cylindrical screen. The projectors were restricted to emit light between 500 nm to 600 nm wavelength which allowed a refresh rate of 180Hz and a maximum luminance of 276 ± 48 cd/m². The arena covered 180° in azimuth and 105° in elevation of the fly's visual field.

For optogenetic experiments ([Figures 2](#) and [3](#)) we presented full screen OFF edges at low luminance of 32 cd/m² in both preferred (upwards) and null direction (downwards) moving at a velocity of 30°/s. Experiments for the directional tuning of T5 neurons ([Figures 4](#) and [S3](#)) we presented full field edges traveling in 12 directions at 50°/s. OFF edges had an edge luminance of 11 cd/m² and a background luminance of 216 cd/m². To test for the neuron's temporal properties ([Figure 5](#)), we presented OFF edges at 11 cd/m² on a background of 108 cd/m². Stimuli were shown at 50°/s. Experiments where no visual stimulation was involved the arena was turned off. Each stimulus was repeated three to five times and all protocols were randomized for each recording.

Thermogenetics

We expressed *shibire*^{ts} in Tm neurons using the Gal4-UAS system and heat-shocked the flies in a 37°C warm water bath for 60 minutes to irreversibly induce *shibire*^{ts} (see Meier et al.²⁰ and Pfeiffer et al.⁵⁹). The blocking experiments under the

two-photon microscope were obtained within two hours after a 60 min heat-shock application. Control flies (*w+*; *+/+*; *+VT50384-lexA,13XlexAop2-IVS-GCaMP6m*) for thermogenetic experiments did not express *shibire^{ts}* but were subject to the same heat-shock protocol to ensure that the high temperature treatment does not influence the response properties of T5 or the dynamics of the calcium indicator.

Optogenetics

Optogenetic illumination was performed using an epifluorescence light path of the microscope through a 40x water immersion objective. To control the light intensity the neutral density filter D-2.0 Mounted Absorptive Neutral (NE30A, Thorlabs) was used. Further the shutter was closed to its minimum to only shine light onto a small area of the flies' brain. The optogenetic *GtACR1* stimulation was performed at a wavelength of 565 ± 24 nm and a light intensity of $1.07 \mu\text{W}/\text{mm}^2$; 565/24 BrightLine HC (F37-565, AHF). The optogenetic *Chrimson* stimulation was performed at a wavelength of 593 ± 33 nm; 593/33 BrightLine HC (F47-597, AHF). We titrated the two-photon laser, the optogenetic activation light, and the visual stimulus in order to minimize undesired activation of *GtACR1* in control conditions and simultaneously maximize visual responses and Tm cell hyperpolarization. The automated onset/offset of the optogenetic light was programmed to one second before and after the visual stimulation (also see Figure 2D). To prevent activation of *GtACR1* and *Chrimson* through the two-photon laser, we restricted the imaging regions to the lobula plate where no overlap with Tm neurons exists. Control conditions (Ctrl) for optogenetic experiments were measured in the same flies but with no optogenetic stimulation and therefore only visual stimulation (Figures 2E, 2F, and 3). Further we performed a control for the presented light (Figures S2E and S2F), both with a wavelength of 565 nm and 593 nm to verify that the flies do not visually detect the optogenetic light from above. For these controls only T4T5c-*lexA, lexAopGCaMP6m* was expressed and neither *GtACR1* nor *Chrimson*.

Pharmacology

Picrotoxin (PTX, TCI) 50mM stock in DMSO was diluted in external saline and added directly with a pipette to the prepared fly. The final concentration was 2.5 mM. To allow for diffusion the recording was started 10 min after adding PTX to the fly and lasted not longer than 15 min after.

Neuron tracing in FAFB

We used a serial section transmission electron microscopy volume to reconstruct the morphology and connectivity of neurons of interest in a female fly brain volume (FAFB³³). Within the FlyWire proofreading environment, flywire.ai,³⁴ we used an automated segmentation as well as a synapse prediction of the FAFB dataset.^{60,61} Only pre-/ postsynaptic partners with at least two synapses were included in analysis. The T5 neurons and CT1 terminals for analysis were selected randomly across the optic lobe of the right side of the EM dataset.

List of T5 segment IDs in FlyWire and x, y, z coordinates: 720575940613383422 (79550, 73404, 6782), 720575940627301058 (85877, 76643, 6560), 720575940637143741 (79022, 70680, 6873), 720575940633628256 (82427, 72067, 6817), 720575940642903918 (77918, 69988, 6859), 720575940628186363 (81595, 72851, 6763).

List of CT1 lobula terminal segment IDs in FlyWire and x, y, z coordinates: 720575940623101191 (92308, 78633, 5224), 720575940627267580 (88666, 75710, 5276), 720575940613586188 (92429, 73291, 5710), 720575940624936841 (92022, 73054, 5683), 720575940623100935 (91967, 77718, 5236).

Tm1 FlyWire ID and x, y, z coordinates: 720575940605875902 (73020, 92652, 4226)

Tm9 FlyWire ID and x, y, z coordinates: 720575940648906617 (71294, 89907, 4089)

Model simulations

The algorithmic model consists of three input lines (a, b, c) that are offset by five degrees (corresponding to the offset between ommatidia in the *Drosophila* retina). All inputs are high pass filtered with a time constant τ_{HP} of 250 ms to simulate the physiological cellular inputs (through lamina neuron L2). In addition, inputs a and c are lowpass filtered with a time constant τ_{LP} of 200 ms. To avoid divisions by 0 we introduced a DC component in the denominator of $DC=0.2$. The algorithmic operation is the following:

$$\frac{a * b}{c + DC}$$

To simulate preferred direction enhancement (Hassenstein-Reichardt type model), inputs a and b are multiplied. Null direction suppression (Barlow-Levick type detector) is modeled by division through input c. For the simulated CT1 ablation we set c to zero, i.e., considered only the Hassenstein-Reichardt detector ($a*b/DC$). We simulated OFF edge input onto the detector. To obtain the tuning curves depicted in Figure 5B, the detector was rotated in steps of 10 degrees resulting in 36 directions of stimulation.

QUANTIFICATION AND STATISTICAL ANALYSIS

Calcium imaging

All calcium imaging data were analyzed as described in¹⁵ with custom written software in Python 2.7. Vertical and horizontal translations were used to automatically register images.



Regions of interest (ROIs) were drawn manually. For each ROI the signal was spatially averaged to create a $\Delta F/F$ time trace. Signals were normalized to the maximum response per fly except if stated otherwise. To prevent “smearing” of the calcium traces due to different locations of the receptive fields of individual neurons, the response of individual neurons of one type were temporally aligned based on the cross-correlation maximum between the time derivative of $\Delta F/F$ of each neuron and the previous aligned neurons (Except [Figure 3C](#)). Error shades represent \pm standard error of the means (SEM) over flies. Quantifications ([Figures 2 and 3](#)) represent the peak PD-response per fly averaged over trials.

The Directional turning ([Figure 4](#), L_{dir}) was calculated as the magnitude of the resultant vector divided by the sum of the individual vectors' magnitudes:

$$L_{dir} = \frac{\left| \sum_{\varphi} v(\varphi) \right|}{\sum_{\varphi} |v(\varphi)|}$$

Statistical analysis

Statistical analyses were performed in GraphPad Prism 9. For all optogenetic experiments we performed a Wilcoxon matched-pairs signed rank test. All other datasets were analyzed by the Mann-Whitney test. P-value ≤ 0.05 *; p-value ≤ 0.01 **; p-value ≤ 0.001 ***; p-value ≤ 0.0001 ****. More details on the statistical analysis are provided in [Table S2](#).

Current Biology, Volume 33

Supplemental Information

**Disynaptic inhibition shapes tuning
of OFF-motion detectors in *Drosophila***

Amalia Braun, Alexander Borst, and Matthias Meier

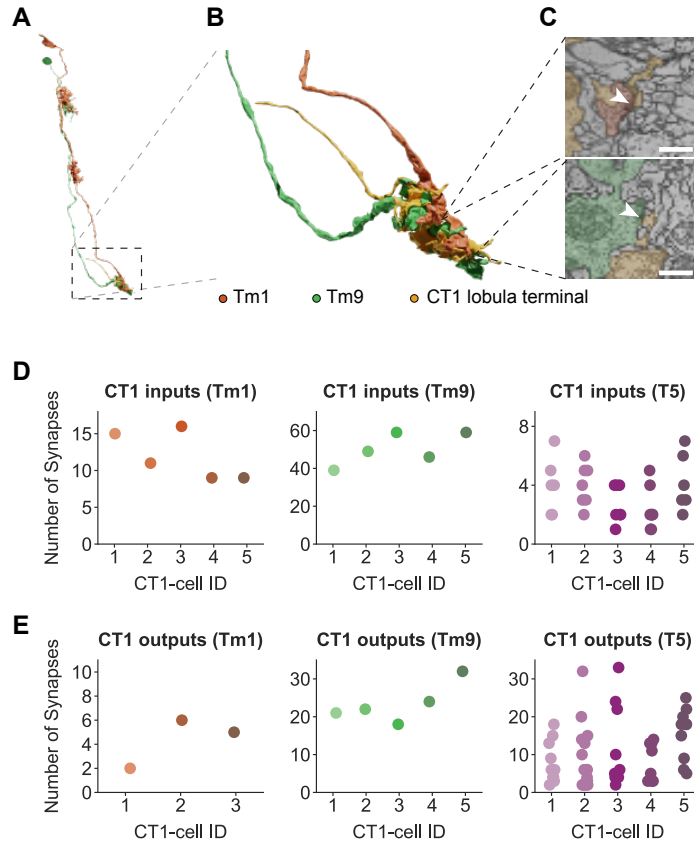


Figure S1. Connectomic analysis, related to Figure 1

(A) 3D EM reconstructions of the Tm1/Tm9 – CT1 microcircuit in a single column (data from flywire.ai). **(B)** Zoom in of A to the terminals of the microcircuit in the lobula. **(C)** Example synapses (Tm1 – CT1 (top)) and (Tm9 – CT1 (bottom)) are shown in the EM (inset) with the arrow pointing at the T-bar. Scalebar corresponds to 500 nm. **(D)** Number of input synapses for five representative CT1 terminals in the lobula. Each CT1 terminal only forms synapses with one Tm1 and one Tm9 cell of the same column and connects to many T5 cells with a variable number of synapses. **(E)** Same as A for the output neurons of CT1 lobula terminals.

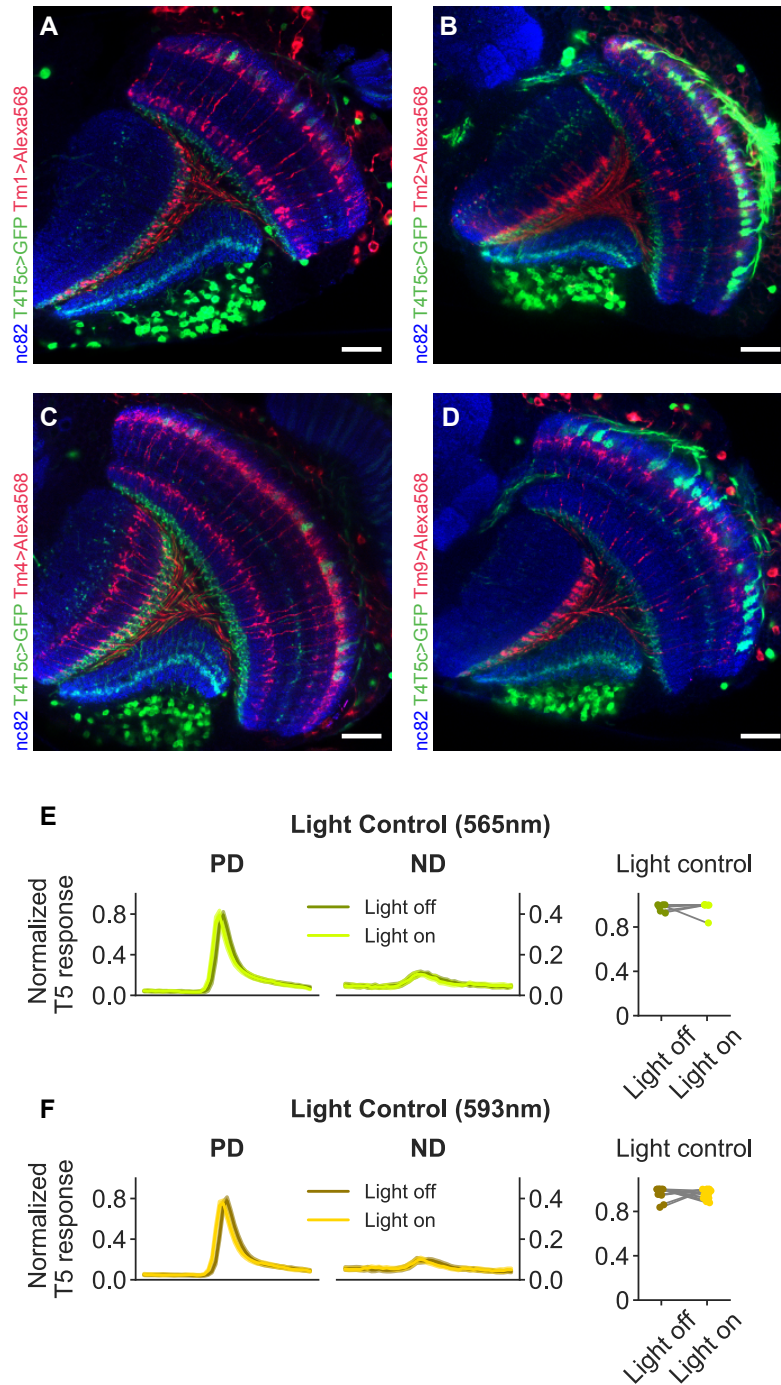


Figure S2. Expression patterns of T4c/T5c and Tm neurons - T5c control calcium traces, related to Figure 2, 3 (A – D) Confocal cross section through the optic lobe of a fly. Blue: Neuropils of the optic lobe (medulla, lobula, lobula plate). Green: Expression pattern of LexAop-GFP under the control of T4c/T5c-lexA driver line. Red: Expression pattern of Gal4 lines for Tm neurons used for optogenetic experiments. (A) Tm1; (B) Tm2; (C) Tm4; (D) Tm9. Scalebar corresponds to 20 μ m. (E) Response aligned T5c control calcium traces (normalized to the maximum for each T5c dendrite), where no light-gated, hyperpolarizing ion channel GtACR1 was expressed in Tm neurons, while presenting the fly with a dark edge moving in the preferred (PD) and null direction (ND) at 30°/s. To control for the optogenetic light a locally constraint, a dim light impulse (565 nm, 1.07 μ W/mm²) was presented through the objective onto the optic lobe. Light traces depict the normalized calcium activity of T5c neurons when the optogenetic light was on. Dark traces represent T5c responses of the optogenetic control within the same fly (optogenetic light off). The timing of the visual and optogenetic stimulus is shown in 2D. Results are depicted as mean values \pm SEM (n = 6). (F) Same control experiment as in E but for the wavelength of 593 nm (n = 13). This wavelength was use for all Chrimson experiments in Figure 3.

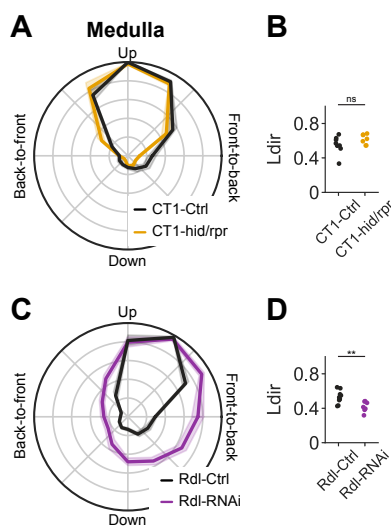


Figure S3. Directional tuning of T4c calcium responses, related to Figure 4

(A) Polar plot of the directional tuning of T4c calcium responses in Gal4-CT1, UAS-hid/rpr flies to bright edges moving in 11 different directions. Each datapoint represents the maximum T4c response to either direction of visual motion, normalized to the maximum per fly. **(B)** Width of the directional tuning curves indicated by directional index L_{dir} (see STAR methods for details) for Gal4-CT1, UAS-hid/rpr flies. Each datapoint represents the L_{dir} value of a unique fly. Color code as in A. $n_{ctrl} = 8$, $n_{CT1-hid/rpr} = 9$. **(C)** As in A. But magenta traces represent T4c calcium responses in T4T5-Gal4, UAS-Rdl-RNAi flies. **(D)** Directional tuning indices L_{dir} as in B for T4/T5-Gal4, UAS-Rdl-RNAi flies. $n_{ctrl} = 13$, $n_{Rdl-RNAi} = 10$. P-value ≤ 0.05 * ; p-value ≤ 0.01 ** ; p-value ≤ 0.001 ***.

Figure	Short Name	Genotype
Figure 2B	Tm1-shibire T4T5c GCaMP6m	w+; R41G07-p65.AD/pJFRC100-20XUAS-TTS-Shibire-ts1; R74G01-Gal4.DBD/VT50384-lexA,13XlexAop2-IVS-GCaMP6m
	Tm2-shibire T4T5c GCaMP6m	w+; +/pJFRC100-20XUAS-TTS-Shibire-ts1; VT12282-Gal4/VT50384-lexA,13XlexAop2-IVS-GCaMP6m
	Tm4-shibire T4T5c GCaMP6m	w+; +/pJFRC100-20XUAS-TTS-Shibire-ts1; R35H01-Gal4/VT50384-lexA,13XlexAop2-IVS-GCaMP6m
	Tm9-shibire T4T5c GCaMP6m	w+; +/pJFRC100-20XUAS-TTS-Shibire-ts1; VT65303-Gal4/VT50384-lexA,13XlexAop2-IVS-GCaMP6m
	Control (Ctrl) T4T5c GCaMP6m	w+; +/+; +/VT50384-lexA,13XlexAop2-IVS-GCaMP6m
Figure 2E	Tm1-GtACR1 T4T5c GCaMP6m	w+; R41G07-p65.AD/pJFRC7-20XUAS-GtACR1-EYFP; R74G01-Gal4.DBD/VT50384-lexA,13XlexAop2-IVS-GCaMP6m
	Tm2-GtACR1 T4T5c GCaMP6m	w+; R28D05-p65.AD/pJFRC7-20XUAS-GtACR1-EYFP; R82F12-Gal4.DBD/VT50384-lexA,13XlexAop2-IVS-GCaMP6m
	Tm4-GtACR1 T4T5c GCaMP6m	w+; R53C02-p65.AD/pJFRC7-20XUAS-GtACR1-EYFP; R60H04-Gal4.DBD/VT50384-lexA,13XlexAop2-IVS-GCaMP6m
	Tm9-GtACR1 T4T5c GCaMP6m	w+; R24C08-p65.AD/pJFRC7-20XUAS-GtACR1-EYFP; R70B08-Gal4.DBD/VT50384-lexA,13XlexAop2-IVS-GCaMP6m
Figure 3A/3D	Tm1-Chrimson T4T5c GCaMP6m	w+; R41G07-p65.AD/20XUAS-CsChrimson.mCherry; R74G01-Gal4.DBD/VT50384-lexA,13XlexAop2-IVS-GCaMP6m
Figure 3A	Tm2- Chrimson T4T5c GCaMP6m	w+; R28D05-p65.AD/20XUAS-CsChrimson.mCherry; R82F12-Gal4.DBD/VT50384-lexA,13XlexAop2-IVS-GCaMP6m
Figure 3A	Tm4- Chrimson T4T5c GCaMP6m	w+; R53C02-p65.AD/20XUAS-CsChrimson.mCherry; R60H04-Gal4.DBD/VT50384-lexA,13XlexAop2-IVS-GCaMP6m
Figure 3A/3D	Tm9- Chrimson T4T5c GCaMP6m	w+; R24C08-p65.AD/20XUAS-CsChrimson.mCherry; R70B08-Ga;4.DBD/VT50384-lexA,13XlexAop2-IVS-GCaMP6m
Figure 3C	Tm1-Chrimson CT1 GCaMP7f	w+; VT041034-LexAGAD/R65E11-AD, 20XUAS-IVS-jGCaMP7f; 13XLexAop2-IVS-CsChrimson.tdTomato/R20C09-DBD, 20XUAS-IVS-jGCaMP7f
	Tm9-Chrimson CT1 GCaMP7f	w+; GMR24C08-lexA/R65E11-AD, 20XUAS-IVS-jGCaMP7f; 13XLexAop2-IVS-CsChrimson.tdTomato/R20C09-DBD, 20XUAS-IVS-jGCaMP7f
Figure 4A top	Control CT1	w+; R65E11-AD/10XUAS-mCD8GFP; R20C09-DBD/+
Figure 4A bottom	CT1-hid/rpr	yw UAS-rpr, UAS-hid; R65E11-AD/10XUAS-mCD8GFP; R20C09-DBD/+

Figure 4B/4C/4D	Control (Ctrl) T4T5c GCaMP6m	w+; +/+; +/VT50384-lexA,13XlexAop2-IVS-GCaMP6m
	CT1-hid/rpr T4T5c GCaMP6m	yw UAS-rpr, UAS-hid; R65E11-AD/+; R20C09-DBD/VT50384-lexA,13XlexAop2-IVS-GCaMP6m
Figure 4E top	Rdl-GFP (T4T5)	w+; 20XUAS-Rdl.GFP/R39H12-Gal4; +/10XUAS-IVS-myr::tdTomato
Figure 4E bottom	Rdl RNAi-GFP (T4T5)	w+; 20XUAS-Rdl.GFP/R39H12-Gal4; UAS-Rdl RNAi8-10/10XUAS-IVS-myr::tdTomato
Figure 4F/4G/4H	Control (Ctrl) T4T5c GCaMP6m	w+; +/+; +/VT50384-lexA,13XlexAop2-IVS-GCaMP6m
	T4T5 Rdl-RNAi T4T5c GCaMP6m	w+; R39H12-Gal4/R39H12-Gal4; UAS-Rdl RNAi8-10/VT50384-lexA,13XlexAop2-IVS-GCaMP6m
Figure 5	Tm2 GCaMP7f	w+; R28D05-p65.AD/20XUAS-IVS-jGCaMP7f; R82F12-Gal4.DBD/20XUAS-IVS-jGCaMP7f
	Tm9 GCaMP7f	w+; R24C08-p65.AD/20XUAS-IVS-jGCaMP7f; R70B08-Gal4.DBD/20XUAS-IVS-jGCaMP7f
	CT1 GCaMP7f	w+; +/R65E11-AD, 20XUAS-IVS-jGCaMP7f; +/R20C09-DBD, 20XUAS-IVS-jGCaMP7f
Figure S2A	Tm1>Alexa568, T4T5c>GFP	w+; R41G07-p65.AD/20XUAS-CsChrimson.mCherry; R74G01-Gal4.DBD/VT50384-lexA,13XlexAop2-IVS-GCaMP6m
Figure S2B	Tm2>Alexa568, T4T5c>GFP	w+; R28D05-p65.AD/20XUAS-CsChrimson.mCherry; R82F12-Gal4.DBD/VT50384-lexA,13XlexAop2-IVS-GCaMP6m
Figure S2C	Tm4>Alexa568, T4T5c>GFP	w+; R53C02-p65.AD/20XUAS-CsChrimson.mCherry; R60H04-Gal4.DBD/VT50384-lexA,13XlexAop2-IVS-GCaMP6m
Figure S2D	Tm9>Alexa568, T4T5c>GFP	w+; R24C08-p65.AD/20XUAS-CsChrimson.mCherry; R70B08-Gal4.DBD/VT50384-lexA,13XlexAop2-IVS-GCaMP6m
Figure S2E/S2F	Control (Ctrl) T4T5c GCaMP6m	w+; +/+; +/VT50384-lexA,13XlexAop2-IVS-GCaMP6m
Figure S3A/S3B	Control (Ctrl) T4T5c GCaMP6m	w+; +/+; +/VT50384-lexA,13XlexAop2-IVS-GCaMP6m
	CT1-hid/rpr T4T5c GCaMP6m	yw UAS-rpr, UAS-hid; R65E11-AD/+; R20C09-DBD/VT50384-lexA,13XlexAop2-IVS-GCaMP6m
Figure S3C/S3D	Control (Ctrl) T4T5c GCaMP6m	w+; +/+; +/VT50384-lexA,13XlexAop2-IVS-GCaMP6m
	T4T5 Rdl-RNAi T4T5c GCaMP6m	w+; R39H12-Gal4/R39H12-Gal4; UAS-Rdl RNAi8-10/VT50384-lexA,13XlexAop2-IVS-GCaMP6m

Table S1. List of all experimental genotypes, related to STAR Methods

Figure	Comparing	Statistical test	p-value	
Figure 2C	Ctrl - Tm1 PD (shibire)	Mann-Whitney U test	0.3112	ns
	Ctrl - Tm2 PD (shibire)	Mann-Whitney U test	0.002	**
	Ctrl - Tm4 PD (shibire)	Mann-Whitney U test	0.0047	**
	Ctrl - Tm9 PD (shibire)	Mann-Whitney U test	0.0012	**
	Ctrl - Tm1 ND (shibire)	Mann-Whitney U test	0.035	*
	Ctrl - Tm2 ND (shibire)	Mann-Whitney U test	0.0831	ns
	Ctrl - Tm4 ND (shibire)	Mann-Whitney U test	0.0047	**
	Ctrl - Tm9 ND (shibire)	Mann-Whitney U test	0.2949	ns
	Figure 2F	Ctrl - Tm1 PD (GtACR1)	Wilcoxon matched-pairs signed rank test	0.4922
Ctrl - Tm2 PD (GtACR1)		Wilcoxon matched-pairs signed rank test	0.001	***
Ctrl - Tm4 PD (GtACR1)		Wilcoxon matched-pairs signed rank test	0.0078	**
Ctrl - Tm9 PD (GtACR1)		Wilcoxon matched-pairs signed rank test	0.002	**
Ctrl - Tm1 ND (GtACR1)		Wilcoxon matched-pairs signed rank test	0.2754	ns
Ctrl - Tm2 ND (GtACR1)		Wilcoxon matched-pairs signed rank test	0.5195	ns
Ctrl - Tm4 ND (GtACR1)		Wilcoxon matched-pairs signed rank test	0.0781	ns
Ctrl - Tm9 ND (GtACR1)		Wilcoxon matched-pairs signed rank test	0.002	**
Figure 3B		Ctrl - Tm1 PD (Chrimson)	Wilcoxon matched-pairs signed rank test	0.001
	Ctrl - Tm2 PD (Chrimson)	Wilcoxon matched-pairs signed rank test	0.8984	ns
	Ctrl - Tm4 PD (Chrimson)	Wilcoxon matched-pairs signed rank test	0.8311	ns
	Ctrl - Tm9 PD (Chrimson)	Wilcoxon matched-pairs signed rank test	0.0007	***
	Ctrl - Tm1 ND (Chrimson)	Wilcoxon matched-pairs signed rank test	0.1099	ns
	Ctrl - Tm2 ND (Chrimson)	Wilcoxon matched-pairs signed rank test	0.0049	**
	Ctrl - Tm4 ND (Chrimson)	Wilcoxon matched-pairs signed rank test	0.2061	ns
	Ctrl - Tm9 ND (Chrimson)	Wilcoxon matched-pairs signed rank test	0.2163	ns
	Figure 3E	Ctrl - Tm1 PD (Chrimson) PTX	Wilcoxon matched-pairs signed rank test	0.002
Ctrl - Tm9 PD (Chrimson) PTX		Wilcoxon matched-pairs signed rank test	0.9097	ns
Ctrl - Tm1 ND (Chrimson) PTX		Wilcoxon matched-pairs signed rank test	0.9219	ns
Ctrl - Tm9 ND (Chrimson) PTX		Wilcoxon matched-pairs signed rank test	0.0005	***
Figure 4D	CT1Ctrl - CT1- <i>hid/rpr</i>	Mann-Whitney U test	0.0005	***
Figure 4H	Rdl Ctrl – Rdl-RNAi	Mann-Whitney U test	<0.0001	****
Figure S3B	CT1Ctrl - CT1- <i>hid/rpr</i> (T4)	Mann-Whitney U test	0.152	ns
Figure S3D	Rdl Ctrl – Rdl-RNAi (T4)	Mann-Whitney U test	0.0031	**

Table S2. Statistical analysis, related to STAR Methods

2 MANUSCRIPT 2: NEURONAL WIRING DIAGRAM OF AN ADULT BRAIN

Summary

Connections between neurons can be mapped by acquiring and analysing electron microscopic brain images. In recent years, this approach has been applied to chunks of brains to reconstruct local connectivity maps that are highly informative, but nevertheless inadequate for understanding brain function more globally. Here we present a neuronal wiring diagram of a whole brain containing 5×10^7 chemical synapses between 139,255 neurons reconstructed from an adult female *Drosophila melanogaster*. The resource also incorporates annotations of cell classes and types, nerves, hemilineages and predictions of neurotransmitter identities. Data products are available for download, programmatic access and interactive browsing and have been made interoperable with other fly data resources. We derive a projectome—a map of projections between regions—from the connectome and report on tracing of synaptic pathways and the analysis of information flow from inputs (sensory and ascending neurons) to outputs (motor, endocrine and descending neurons) across both hemispheres and between the central brain and the optic lobes. Tracing from a subset of photoreceptors to descending motor pathways illustrates how structure can uncover putative circuit mechanisms underlying sensorimotor behaviours. The technologies and open ecosystem reported here set the stage for future large-scale connectome projects in other species.

Authors

Sven Dorkenwald, Arie Matsliah, Amy R Sterling, Philipp Schlegel, Szi-chieh Yu, Claire E. McKellar, Albert Lin, Marta Costa, Katharina Eichler, Yijie Yin, Will Silversmith, Casey Schneider-Mizell, Chris S. Jordan, Derrick Brittain, Akhilesh Halageri, Kai Kuehner, Oluwaseun Ogedengbe, Ryan Morey, Jay Gager, Krzysztof Kruk, Eric Perlman, Runzhe Yang, David Deutsch, Doug Bland, Marissa Sorek, Ran Lu, Thomas Macrina, Kisuk Lee, J. Alexander Bae, Shang Mu, Barak Nehoran, Eric Mitchell, Sergiy Popovych, Jingpeng Wu, Zhen Jia, Manuel Castro, Nico Kemnitz, Dodam Ih, Alexander Shakeel Bates, Nils Eckstein, Jan Funke, Forrest Collman, Davi D. Bock, Gregory S.X.E. Jefferis, H. Sebastian Seung, Mala Murthy & The **FlyWire Consortium**

This article is published in *Nature*; [Dorkenwald et al. \(2024\)](#).

Contributions

Members of the **FlyWire Consortium** contributed proofreading and annotations. S.G. provided [braincircuits.io](#). T.M. and N.K. realigned the dataset with methods developed by E.M., B.N. and T.M. and infrastructure developed by S.P. and Z.J. J.A.B. and S.M. wrote code for masking defects and misalignments. K.L. trained the convolutional net for

boundary detection, using ground-truth data realigned by D.I. J.W. used the convolutional net to generate an affinity map that was segmented by R.L. N.K., M.A.C., O.O., A.H., C.S.J., K. Kuehner and A.R.S. adapted and improved Neuroglancer for proofreading and annotations. J.G., K. Kruk, A.M., S.D. F.C. and C.S.-M. created interactive analysis and annotation tools for the community. A.M. created Codex with help from A.R.S., S.D., K. Kuehner and R.M. A.R.S. and A.M. created the website. A.R.S., C.E.M. and M.S. onboarded community members and tested new proofreaders. A.R.S., M.S., C.S.J. and C.E.M. designed tutorials. C.E.M., A.R.S. and M.S. provided community support. S.D., F.C., C.S.-M., C.S.J., A.H., D. Brittain and W.S. built and maintained CAVE for FlyWire and managed user access. S.D., P.S., A.M. and E.P. curated the data and made it available for download. E.P. and D.D.B. provided a coordinate mapping service. A.S.B., N.E., G.S.X.E.J. and J.F. provided neurotransmitter information. S.-c.Y., C.E.M., M.C., K.E., Y.Y. and P.S. trained and managed proofreaders. S.D., S.-c.Y., P.S. and G.S.X.E.J. led the targeted proofreading effort. S.D., P.S., A.M., A.C. and K. Kuehner maintained the proofreading management platforms. S.D. evaluated the proofreading accuracy. S.D., A.L., H.S.S., D.D. and R.Y. analysed the data. S.D., D. Bland and S.-c.Y. annotated and analysed the ocellar circuit. S.D., H.S.S., M.M., A.L., P.S. and A.R.S. wrote the manuscript with feedback from A.S.B., W.H., G.S.X.E.J. and contributions from all authors. H.S.S., M.M., G.S.X.E.J. and D.D.B. sponsored large-scale proofreading. G.S.X.E.J. and D.D.B. led the Cambridge effort. M.M. and H.S.S. led the overall effort.

FlyWire Consortium

Doug Bland, Krzysztof Kruk, Zairene Lenizo, Alexander Shakeel Bates, Nseraf, Austin T. Burke, Katharina Eichler, Nashra Hadjerol, Kyle Patrick Willie, Ryan Willie, Yijie Yin, John Anthony Ocho, Sven Dorkenwald, Joshua Bañez, Arti Yadav, Shirleyjoy Serona, Rey Adrian Candilada, Dustin Garner, Philipp Schlegel, Jet Ivan Dolorosa, Ariel Dagohoy, Remer Tancontian, Mendell Lopez, Regine Salem, Griffin Badalamente, annkri (Anne Kristiansen), Kendrick Joules Vinson, Nelsie Panes, Laia Serratos Capdevila, Anjali Pandey, Darrel Jay Akiatan, Ben Silverman, Dharini Sapkal, Shaina Mae Monungolh, Jay Gager, Varun Sane, Miguel Albero, AzureJay (Jaime Skelton), Márcia dos Santos, David Deutsch, Zeba Vohra, Kaiyu Wang, Emil Kind, Chitra Nair, Dhvani Patel, Imaan F. M. Tamimi, Michelle Darapan Pantujan, James Hebditch, Alexandre Javier, Rashmita Rana, Bhargavi Parmar, Merlin Moore, Mark Lloyd Pielago, Allien Mae Gogo, Markus William Pleijzier, Mark Larson, Joseph Hsu, Thomas Stocks, Jacquilyn Laude, Itisha Joshi, Chereb Martinez, Dhara Kakadiya, John David Asis, **Amalia Braun**, Clyde Angelo Lim, Alvin Josh Mandahay, Marchan Manaytay, Marina Gkantia, Kaushik Parmar, Quinn Vanderbeck, Claire E.McKellar, Philip Lenard Ampo, Daril Bautista, Irene Salgarella, Christopher Dunne, John Clyde Saguimpa, Eva Munnelly, Chan Hyuk Kang, Jansen Seguido, Jinmook Kim, Gizem Sancer, Lucia Kmecova, Christa Baker, Jenna Joroff, Steven Calle, Cathy Pilapil, Yashvi Patel, Olivia Sato, Siqi Fang, Paul Brooks, Mai Bui, JousterL (Matthew Lichtenberger), edmark tamboboy, Katie Molloy, Alexis E Santana-Cruz, Janice Salocot, Celia David, Kfay,

Seongbong Yu, Arzoo Diwan, Farzaan Salman, Szi-chieh Yu, Monika Pate7, TR77, Sarah Morejohn, Sebastian Molina-Obando, Sanna Koskela, Tansy Yang, bl4ckscor (Daniel Lehmann), Sangeeta Sisodiya, Selden Koolman, Philip K. Shiu, Sky Cho, Brian Reicher, Marlon Blanquart, Marissa Sorek, Lucy Houghton, Hyungjun Choi, Matt Collie, Joanna Eckhardt, Benjamin Gorko, Li Guo, Zhihao Zheng, Alisa Poh, Marina Lin, István Taisz, Wes Murfin, Álvaro Sanz Díez, Peter Gibb, Nils Reinhard, Nidhi Patel, Sandeep Kumar, Minsik Yun, Megan Wang, Devon Jones, Lucas Encarnacion-Rivera, Annalena Oswald, Akanksha Jadia, Leonie Walter, Nik Drummond, Ibrahim Tastekin, Xin Zhong, Yuta Mabuchi, Fernando J Figueroa Santiago, Urja Verma, Nick Byrne, Edda Kunze, Thomas Crahan, Hewhoamareismyself (Ryan Margossian), Haein Kim, Iliyan Georgiev, Fabianna Szorenyi, Benjamin Bargeron, Tomke Stuermer, Damian Demarest, Atsuko Adachi, Burak Gü7, Andrearwen, Robert Turnbull, a5hmr, Andrea Sandoval, Diego A. Pacheco, Haley Croke, Alexander Thomson, Jonas Chojetzki, Connor Laughland, Suchetana B. Dutta, Paula Guiomar Alarcón de Antón, Binglin Huang, Patricia Pujols, Isabel Haber, Amanda González-Segarra, Albert Lin, Daniel T. Choe, Veronika Lukyanova, Marta Costa, Maria Ioannidou, Zequan Liu, Tatsuo Okubo, Miriam A. Flynn, Gianna Vitelli, Meghan Laturney, Feng Li, Shuo Cao, Carolina Manyari-Diaz, Hyunsoo Yim, Anh Duc Le, Kate Maier, Seungyun Yu, Yeonju Nam, Mavil, Nino Mancini, Eleni Samara, Amanda Abusaif, Audrey Francis, Jesse Gayk, Sommer S. Huntress, Raquel Barajas, Mindy Kim, Xinyue Cui, Amy R Sterling, Anna Li, Gabriella R. Sterne, Lena Lörsch, Keehyun Park, Alan Mathew, TaewanKim, Guan-ting Wu, Serene Dhawan, Margarida Brotas, Cheng-hao Zhang, Shanice Bailey, Alexander Del Toro, Arie Matsliah, Kisuk Lee, Thomas Macrina, Casey Schneider-Mizell, Mert Erginkaya, Sergiy Popovych, Oluwaseun Ogedengbe, Runzhe Yang, Akhilesh Halageri, Will Silversmith, Stephan Gerhard, Andrew Champion, Nils Eckstein, Dodam Ih, Nico Kemnitz, Manuel Castro, Zhen Jia, Jingpeng Wu, Eric Mitchell, Barak Nehoran, Shang Mu, J. Alexander Bae, Ran Lu, Eric Perlman, Ryan Morey, Kai Kuehner, Derrick Brittain, Chris S. Jordan, David J. Anderson, Rudy Behnia, Salil S. Biday5, Davi D. Bock, Alexander Borst, Eugenia Chiapp3, Forrest Collman, Kenneth J. Colodner, Andrew Dacks, Barry Dickson, Jan Funke, Denise Garcia, Stefanie Hampel, Volker Hartenstein, Bassem Hassan, Charlotte Helfrich-Forster, Wolf Huetteroth, Gregory S.X.E. Jefferis, Jinseop Kim, Sung Soo Kim, Young-Joon Kim, Wei-Chung Lee, Gerit A. Linneweber, Gaby Maimon, Richard Mann, Mala Murthy, Michael Pankratz, Lucia Prieto-Godino, Jenny Read, Michael Reiser, Katie von Reyn, Carlos Ribeiro, Kristin Scott, Andrew M. Seeds, Mareike Selcho, H. Sebastian Seung, Marion Silies, Julie Simpson, Mathias F. Wernet, Rachel I. Wilson, Fred W. Wolf, Zepeng Yao, Nilay Yapici, Meet Zandawala

My contribution to this publication in detail

For this publication I contributed with a number of 1104 annotations and 3125 proofreading edits to complete the connectome of an adult fly brain.

Neuronal wiring diagram of an adult brain

<https://doi.org/10.1038/s41586-024-07558-y>

Received: 11 July 2023

Accepted: 10 May 2024

Published online: 2 October 2024

Open access

 Check for updates

Sven Dorkenwald^{1,2}, Arie Matsliah¹, Amy R. Sterling^{1,3}, Philipp Schlegel^{4,5}, Szi-chieh Yu¹, Claire E. McKellar¹, Albert Lin^{1,6}, Marta Costa⁵, Katharina Eichler⁵, Yijie Yin⁵, Will Silversmith¹, Casey Schneider-Mizell⁷, Chris S. Jordan¹, Derrick Brittain⁷, Akhilesh Halageri¹, Kai Kuehner¹, Oluwaseun Ogedengbe¹, Ryan Morey¹, Jay Gager¹, Krzysztof Kruk³, Eric Perlman⁸, Runzhe Yang^{1,2}, David Deutsch^{1,9}, Doug Bland¹, Marissa Sorek^{1,3}, Ran Lu¹, Thomas Macrina^{1,2}, Kisuk Lee^{1,10}, J. Alexander Bae^{1,11}, Shang Mu¹, Barak Nehoran^{1,2}, Eric Mitchell¹, Sergiy Popovych^{1,2}, Jingpeng Wu¹, Zhen Jia¹, Manuel A. Castro¹, Nico Kemnitz¹, Dodam Ih¹, Alexander Shakeel Bates^{4,12,13}, Nils Eckstein¹⁴, Jan Funke¹⁴, Forrest Collman⁷, Davi D. Bock¹⁵, Gregory S. X. E. Jefferis^{4,5}, H. Sebastian Seung^{1,2,23}, Mala Murthy^{1,2,23} & The FlyWire Consortium*

Connections between neurons can be mapped by acquiring and analysing electron microscopic brain images. In recent years, this approach has been applied to chunks of brains to reconstruct local connectivity maps that are highly informative^{1–6}, but nevertheless inadequate for understanding brain function more globally. Here we present a neuronal wiring diagram of a whole brain containing 5×10^7 chemical synapses⁷ between 139,255 neurons reconstructed from an adult female *Drosophila melanogaster*^{8,9}. The resource also incorporates annotations of cell classes and types, nerves, hemilineages and predictions of neurotransmitter identities^{10–12}. Data products are available for download, programmatic access and interactive browsing and have been made interoperable with other fly data resources. We derive a projectome—a map of projections between regions—from the connectome and report on tracing of synaptic pathways and the analysis of information flow from inputs (sensory and ascending neurons) to outputs (motor, endocrine and descending neurons) across both hemispheres and between the central brain and the optic lobes. Tracing from a subset of photoreceptors to descending motor pathways illustrates how structure can uncover putative circuit mechanisms underlying sensorimotor behaviours. The technologies and open ecosystem reported here set the stage for future large-scale connectome projects in other species.

Although rudimentary nervous systems existed in more ancient animals, brains evolved around half a billion years ago¹³, and are essential for the generation of sophisticated behaviours. It is widely accepted that dividing a brain into regions is helpful for understanding brain function, but questions remain on the utility of finer-grain information about connectivity. In fact, efforts to construct wiring diagrams at the level of neurons and synapses have been controversial^{14,15}. Scepticism has flourished largely owing to a lack of technologies that could reconstruct such wiring diagrams^{16,17}, so obtaining such diagrams has remained hypothetical. The situation began to change in the 2000s owing to the efforts of a small community of researchers. Here we present a neuronal wiring diagram of a whole adult brain and, here and in the accompanying studies, we analyse its connectivity to highlight the utility of this endeavour.

Although small, the brain of *D. melanogaster* contains 10^5 neurons and 10^8 synapses that enable a fly to see, smell, hear, walk and fly. Flies engage in dynamic social interactions¹⁸, navigate over distances¹⁹ and

form long-term memories²⁰. Portions of fly brains have been reconstructed from electron microscopy images, which have sufficient resolution to reveal the fine branches of neurons and the synapses that connect them. The resulting wiring diagrams of neural circuits have provided crucial insights into how the brain generates social^{21,22}, memory-related²³ or navigation²⁴ behaviours. Wiring diagrams of other fly brain regions have been mapped and related to visual², auditory²⁵ and olfactory^{23,26} functions. The circuit organization revealed by these wiring diagrams show similarities to mammalian brains^{27,28}.

These wiring diagrams and many others from mammals^{4–6} have been derived from pieces of brain. However, recordings of *Drosophila* neural activity have revealed nearly brain-wide encoding of sensory²⁹ and motor³⁰ variables. These studies and others in vertebrates highlight that understanding how the brain processes sensory information or drives behaviour will require understanding global information flow at the scale of the entire brain.

¹Princeton Neuroscience Institute, Princeton University, Princeton, NJ, USA. ²Computer Science Department, Princeton University, Princeton, NJ, USA. ³Eyewire, Boston, MA, USA. ⁴Neurobiology Division, MRC Laboratory of Molecular Biology, Cambridge, UK. ⁵*Drosophila* Connectomics Group, Department of Zoology, University of Cambridge, Cambridge, UK. ⁶Center for the Physics of Biological Function, Princeton University, Princeton, NJ, USA. ⁷Allen Institute for Brain Science, Seattle, WA, USA. ⁸Yikes LLC, Baltimore, MD, USA. ⁹Department of Neurobiology, University of Haifa, Haifa, Israel. ¹⁰Brain and Cognitive Sciences Department, Massachusetts Institute of Technology, Cambridge, MA, USA. ¹¹Electrical and Computer Engineering Department, Princeton University, Princeton, NJ, USA. ¹²Harvard Medical School, Boston, MA, USA. ¹³Centre for Neural Circuits and Behaviour, The University of Oxford, Oxford, UK. ¹⁴Janelia Research Campus, Howard Hughes Medical Institute, Ashburn, VA, USA. ¹⁵Department of Neurological Sciences, Larner College of Medicine, University of Vermont, Burlington, VT, USA. *A full list of members and their affiliations appears in the Supplementary Information. A list of authors and their affiliations appears at the end of the paper. ✉e-mail: sseung@princeton.edu; mmurthy@princeton.edu

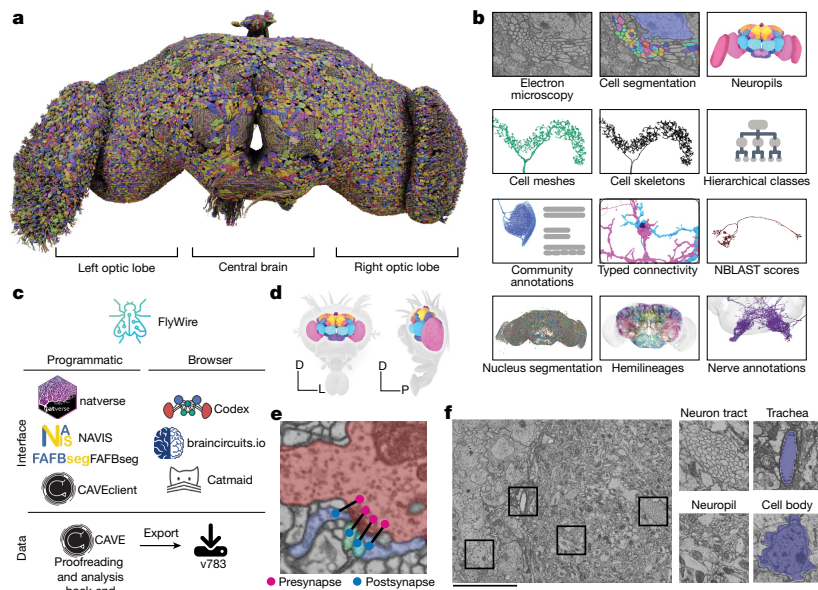


Fig. 1 | A connectomic reconstruction of a whole fly brain. a, All neuron morphologies reconstructed with FlyWire. All neurons in the central brain and both optic lobes were segmented and proofread. Note that image and dataset are mirror inverted relative to the native fly brain. **b**, An overview of many of the FlyWire resources that are being made available. FlyWire leverages existing resources for electron microscopy imagery by Zheng et al.⁹, synapse predictions by Buhmann et al.⁷ and Heinrich et al.¹¹⁸, and neurotransmitter predictions by Eckstein et al.¹⁰. Annotations of the FlyWire brain dataset such as hemilineages, nerves and hierarchical classes are established in the accompanying paper¹². **c**, FlyWire uses CAVE³⁰ for proofreading, data management and analysis back

end. The data can be accessed programmatically through CAVEclient, navis, fafbseg and natverse¹¹⁹, and through the browser in Codex, Catmaid Spaces and braincircuits.io. Static exports of the data are also available. **d**, The *Drosophila* brain can be divided into spatially defined regions based on neuropils⁸⁰ (Extended Data Fig. 1). Neuropils for the lamina are not shown. D, dorsal; L, lateral; P, posterior. **e**, Synaptic boutons in the fly brain are often polyadic such that there are multiple postsynaptic partners per presynaptic bouton. Each link between a pre- and a postsynaptic location is a synapse. **f**, Neuron tracts, trachea, neuropil and cell bodies can be readily identified from the electron microscopy data acquired by Zheng et al.⁹. Scale bar, 10 μ m.

Until now, the closest antecedent to a wiring diagram of the whole brain has been the reconstruction of a fly ‘hemibrain’¹, a pioneering resource that has already become indispensable to *Drosophila* researchers. It is estimated to contain around 20,000 neurons that are ‘uncropped’—that is, minimally truncated by the borders of the imaged volume, and 14 million synapses between them. Our reconstruction of an entire adult brain contains 139,255 neurons (Fig. 1a and Supplementary Video 1) and 54.5 million synapses between these neurons. To aid exploration and analysis, this connectome has been densely annotated by the FlyWire Consortium. In our companion paper, Schlegel et al.¹² provide a curated brain-wide hierarchy of annotations including more than 8,400 distinct cell types, completing the description of this resource (and should therefore preferably be cited alongside this paper; https://codex.flywire.ai/about_flywire). These and many other data products (Fig. 1b and Supplementary Fig. 1) are available for download, programmatic access and interactive browsing and have been made interoperable with other fly data resources through a growing ecosystem of software tools (Fig. 1c). The primary portal to the data is the FlyWire Connectome Data Explorer (Codex; <https://codex.flywire.ai/>), which makes the information visualizable and queryable.

The wiring diagram from our whole-brain reconstruction is sufficiently complete to be designated a ‘connectome’ (defined in Discussion). It represents substantial progress over neuronal reconstructions of *Caenorhabditis elegans*^{31,32} (300 neurons, 10^4 synapses) and the 1st instar larva of *Drosophila*³³ (3,000 neurons, 5×10^5 synapses). Our connectome advances beyond the hemibrain in several ways. For example, it includes the suboesophageal zone (SEZ) of the central brain, which is important for diverse functions such as gustation and mechanosensation^{34,35}, and contains many of the processes of neurons that descend from the brain to the ventral nerve cord to drive motor

behaviours. Additionally, it includes annotations for descending and ascending neurons³⁶ for many sexually dimorphic neurons (analysed by Deutsch et al. (manuscript in preparation); available at <https://codex.flywire.ai/>) and an entire optic lobe¹¹. Our reconstruction of both optic lobes goes far beyond existing maps of columnar visual circuitry. Connections between the optic lobes and central brain are included, as explored by refs. 37,38. Also included are neurons that extend into the brain through the nerves and neck connective, which are essential for tracing sensorimotor pathways, as illustrated here and in the accompanying studies^{11,12,34,36–45}.

Our reconstruction utilized image acquisition and analysis techniques that are distinct from those used for the hemibrain (Methods and Discussion). However, we have built directly on the hemibrain in an important way. Schlegel et al.¹² used the cell types proposed for the hemibrain as a starting point for cell typing neurons in the central brain in FlyWire. This approach was enabled by a growing ecosystem of software tools serving interoperability between different fly data sources (Fig. 1c). Additional annotations in the SEZ and optic lobes, which are largely absent from the hemibrain, were contributed by *Drosophila* research groups in the FlyWire Consortium as well as citizen scientists, and are described in more detail here and in the accompanying papers. Synapse predictions⁷ and estimates of neurotransmitter identities¹⁰ were also contributed by the community.

After matching, Schlegel et al.¹² also compared our wiring diagram with the hemibrain where they overlap and showed that cell-type counts and strong connections were largely in agreement. This means that the combined effects of natural variability across individuals and ‘noise’ due to imperfect reconstruction tend to be modest, so our wiring diagram of a single brain should be useful for studying any wild-type *Drosophila melanogaster* individual. However, there are known differences

between the brains of male and female flies⁴⁶. In addition, principal neurons of the mushroom body, a brain structure required for olfactory learning and memory, show high variability⁴². Some mushroom body connectivity patterns have even been found to be near random⁴⁷, although deviations from randomness have since been identified⁴⁸. In short, *Drosophila* wiring diagrams are useful because of their stereotypy, yet also open the door to studies of connectome variation.

In addition to describing the FlyWire brain resource, this Article also presents analyses that illustrate how the data products can be used. Additional whole-brain network analyses are provided by Lin et al.⁴⁹ and Pospisil et al.³⁹. From the connectome, we derive a projectome, a reduced map of projections between 78 fly brain regions known as neuropils (Fig. 1d, Extended Data Fig. 1 and Supplementary Video 2). We trace synaptic pathways and analyse information flow from the inputs to the outputs of the brain, across both hemispheres, and between the central brain and the optic lobes. In particular, the organization of excitation and inhibition in pathways from photoreceptors in the ocelli to descending motor neurons immediately suggests hypotheses about circuit mechanisms of behaviour.

Reconstruction of a whole fly brain

Images of an entire adult female fly brain (Fig. 1e,f) were previously acquired by serial section transmission electron microscopy and released into the public domain by Zheng et al.⁹. We previously realigned the electron microscopy images, automatically segmented all neurons in the images, created a computational system that allows interactive proofreading of the segmentation⁵⁰, and assembled an online community⁸ (FlyWire). During the initial phase, much of the proofreading was done by a distributed community of *Drosophila* research groups in the FlyWire Consortium, and focused on neurons of interest to these groups. During the later phase, the remaining neurons were mainly proofread by centralized teams at Princeton and Cambridge, with contributions from citizen scientists worldwide. The recruitment and training of proofreaders and their workflows are described in the Methods.

Chemical synapses were automatically detected in the images as pairs of presynapse–postsynapse locations⁷. The whole brain contains 0.0175 mm³ of neuropil volume and around 130 million synapses. This equates to 7.4 synapses per μm^3 , a much higher density than that of mammalian cortex^{51,52} (less than 1 synapse per μm^3). The central brain and left and right optic lobes (including the lamina) contain 0.0103, 0.0036 and 0.0036 mm³ of neuropil volume, respectively, with synapse counts in approximately the same proportion. Synapses were combined with proofread neurons using the Connectome Annotation Versioning Engine⁵⁰ (CAVE) to yield the connectome.

We next assessed completeness and accuracy of proofreading. We had already shown that FlyWire proofreading can yield accurate results⁸ through comparison with light microscopic reconstructions of neurons that are known to be highly stereotyped across individual flies. A second method is to subject reconstructed neurons to an additional round of proofreading, which was previously shown to yield few changes⁸. Because proofreading workflows and personnel have changed over time, and accuracy can vary across brain regions, we repeated this evaluation by subjecting 826 neurons from the central brain to a further round of proofreading. Relative to this additional round, our proofread dataset achieved an average F_1 score of 99.2% by volume (Extended Data Fig. 2a,b).

By quantifying how many of the automatically detected synapses are attached to proofread segments, as opposed to being isolated in tiny ‘orphan’ segments, we can estimate completeness of the proofreading. We found high attachment rates of presynapses (approximately 122 million presynapses (93.7%) attached), whereas attachment rates of postsynapses were lower (approximately 58.1 million postsynapses (44.7%) attached) owing to less proofreading and reattachment of twigs, which

contain most of the postsynapses⁸ (Extended Data Fig. 2c,d). Attachment rates were generally in agreement between the two hemispheres of FlyWire and with the hemibrain (Extended Data Fig. 2e–g) and varied by neuropil (Supplementary Fig. 2). As with the hemibrain¹, false negative synapses are the dominant type of error but false positives also exist. For this reason, analyses using the connectome should consider thresholding to remove spurious connections. Thresholds should be adjusted to the individual analyses. For the analyses presented below (and connections indicated at <https://codex.flywire.ai>), we use a threshold of five synapses to determine a connection between two neurons. The accompanying paper by Matsliah et al.¹¹ found a threshold of two synapses appropriate for analysing connections in the optic lobes. Assuming that such errors are statistically independent, accuracy is expected to be high for detection of connections involving multiple synapses^{12,53}.

We estimate that FlyWire’s brain reconstruction took around 33 person-years of manual proofreading. The reconstruction remains open for proofreading and annotations, and new versions of the resource will be released in future (the analysis presented here is from version 783). This enables correction of remaining errors as they are discovered and further rounds of validation to be performed.

Intrinsic neurons of the brain

A brain is defined as a structure of the nervous system that is co-localized with the sense organs in the head of an animal. Often left implicit in the definition is the idea of centralization—that most central nervous system (CNS) neurons are located in the brain. The idea involves a subtlety arising from the fact that neurons are spatially extended objects. If all of the synapses of a neuron are wholly contained in the brain, we say that the neuron is intrinsic to the brain. This contrasts with a neuron that straddles the brain and other CNS regions. The fraction of intrinsic neurons can be interpreted as the degree to which the CNS is centralized in the brain.

Of the 139,255 proofread neurons in FlyWire (Supplementary Video 1), 118,501 are intrinsic to the brain (Fig. 2a–c), which is defined as the central brain and optic lobes (Fig. 1a). Intrinsic neurons of the brain make up three-quarters of the adult fly nervous system^{54–56} and amount to 85% of brain neurons. Their predominance means that the brain communicates primarily with itself, and only secondarily with the outside world (Fig. 2b).

For comparison, intrinsic neurons of the larval fly brain make up one-quarter to one-third of its nervous system³³. Intrinsic neurons of the *C. elegans* brain make up 8–15% of its nervous system (Methods).

Afferent and efferent neurons

Brain neurons that are not intrinsic can be divided into two categories, depending on the locations of their cell bodies. For afferent (sensory and ascending) neurons, the cell body is outside the brain, whereas for efferent (descending, motor and endocrine) neurons, the cell body is contained in the brain. It is generally accurate to think of an afferent neuron as a brain input, and an efferent neuron as a brain output. The relation to information flow is actually more subtle, however, as most fly neurites carry a mixture of presynapses and postsynapses on both dendrites and axons^{10,33,53}.

Our companion paper¹² exhaustively identifies all afferent and efferent neurons contained in cross sections of nerves and the neck connective running between the brain and ventral nerve cord (VNC) (Fig. 2d). Almost 95% of these neurons were in the neck connective, antennal nerve and maxillary–labial nerve. Although afferents are truncated in our reconstruction, Schlegel et al.¹² and other community members^{35,57} were able to determine the sensory organs corresponding to the 5,375 non-visual sensory neurons (Fig. 2e,f) on the basis of morphology and nerve assignments. Non-visual sensory neurons enter

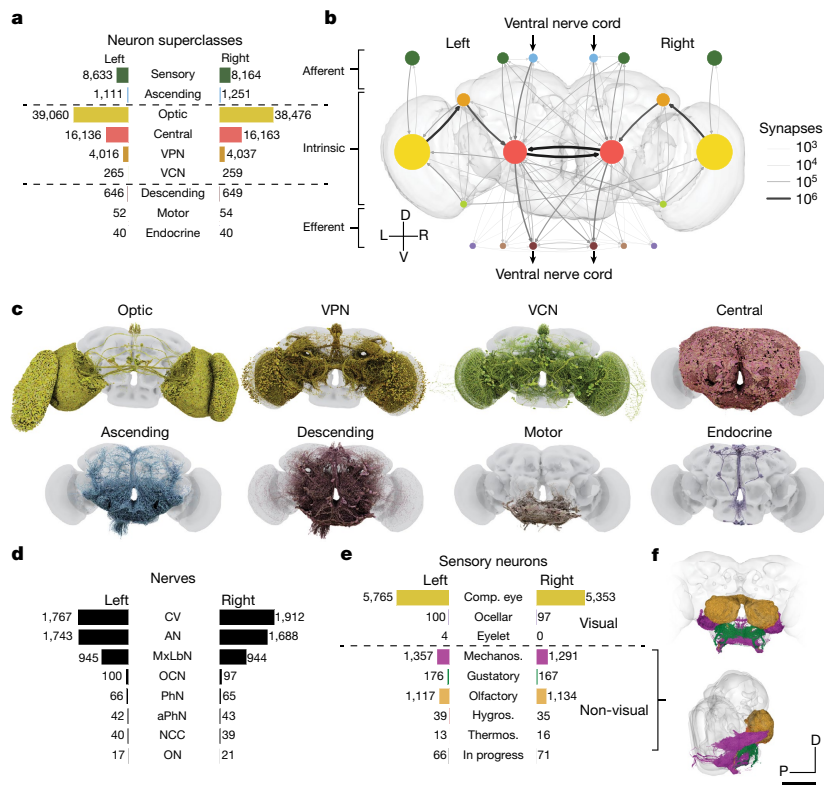


Fig. 2 | Neuron categories. **a**, We grouped neurons in the fly brain by ‘flow’: intrinsic, afferent or efferent. Each flow class is further divided into ‘superclasses’ on the basis of location and function. Neuron annotations are described in more detail in our companion paper¹². 201 neurons were not assigned to a hemisphere and are thus omitted from this panel. **b**, Using these neuron annotations, we created an aggregated synapse graph between the superclasses in the fly brain. D, dorsal; L, left; R, right; V, ventral. **c**, Renderings of all neurons in each superclass. **d**, There are eight nerves into each hemisphere in addition to the ocellar nerve and the cervical connective nerve. All neurons traversing the nerves have been

reconstructed and accounted for. AN, antennal nerve; aPhN, accessory pharyngeal nerve; CV, cervical (neck) connective nerve; MxLbN, maxillary-labial nerve; NCC, nervii corpora cardiaca; OCN, ocellar nerve; ON, occipital nerve; PhN, pharyngeal nerve. **e**, Sensory neurons can be subdivided by the sensory modality that they respond to. Almost all sensory neurons have been typed by modality. The counts for the medial ocelli were omitted and are shown in Fig. 7b. Comp. eye, compound eye; hygros., hygrosensory; mechanos., mechanosensory; thermos., thermosensory. **f**, Renderings of all non-visual sensory neurons. Scale bar, 100 μ m.

the brain through nerves (Fig. 2d) that mostly terminate in the antennal lobe or the SEZ (we define the SEZ as containing the following neuropils: saddle (SAD), gnathal ganglia (GNG), antennal mechanosensory and motor centre (AMMC) and prow (PRW) (neuropils definitions are provided in Extended Data Fig. 1))⁵⁸. The antennal lobe is the first relay centre for processing of olfactory information, and many of the olfactory receptor neuron (ORN) inputs to the antennal lobe were also reconstructed in the hemibrain. The SEZ receives more diverse inputs, including the projections of both mechanoreceptor and gustatory receptor neurons—these projections were not contained in the hemibrain. The nerves contained few efferent neurons, among which were head motor neurons ($n = 106$) or endocrine neurons ($n = 80$) (Fig. 2a–c). Many efferent neurons have branches in the SEZ, including most of the 106 motor neurons.

Visual afferents are by far the most numerous type of sensory input, and enter the brain directly rather than through nerves. There are photoreceptor axons projecting from the compound eyes ($n = 11,118$), ocelli ($n = 273$) and eyelets ($n = 8$, of which 4 have been identified).

The neurons traversing the neck connective were grouped into 1,303 efferent (descending) and 2,362 afferent (ascending) neurons (Fig. 2a–c). Cell-type annotations for many of these neurons are available³⁶, facilitating a matching of reconstructions from two separate electron microscopy datasets of a VNC^{54–56,59} and enabling circuits

spanning the whole CNS (brain and VNC) to be at least schematically mapped.

Optic lobes and central brain

Of the 118,501 intrinsic neurons, 32,388 are fully contained in the central brain and 77,536 are fully contained in the optic lobes and ocellar ganglia (this number excludes the photoreceptors, which are sensory afferent neurons). The domination of the count by visual areas reflects the nature of *Drosophila* as a highly visual animal.

The optic lobes and ocellar ganglia also contain 8,053 neurons—the visual projection neurons¹² (VPNs)—that project into the central brain. We provide a more detailed analysis of connections in the ocellar ganglion in Fig. 7. Many VPNs are columnar types that tile the visual field. VPNs target specific neuropils (for example, anterior optic tubercle (AOTU), posterior lateral protocerebrum (PLP) and posterior ventrolateral protocerebrum (PVLP)) or optic glomeruli^{60,61} in the central brain. The influence of VPNs can be very strong; 892 central neurons receive more than half their synapses from VPNs.

The hemibrain already characterized several VPN types along with their outputs in the central brain¹. Our whole-brain reconstruction reveals many other aspects of VPN connectivity, such as their inputs in the medulla, lobula and lobula plate⁶². In addition to feedforward

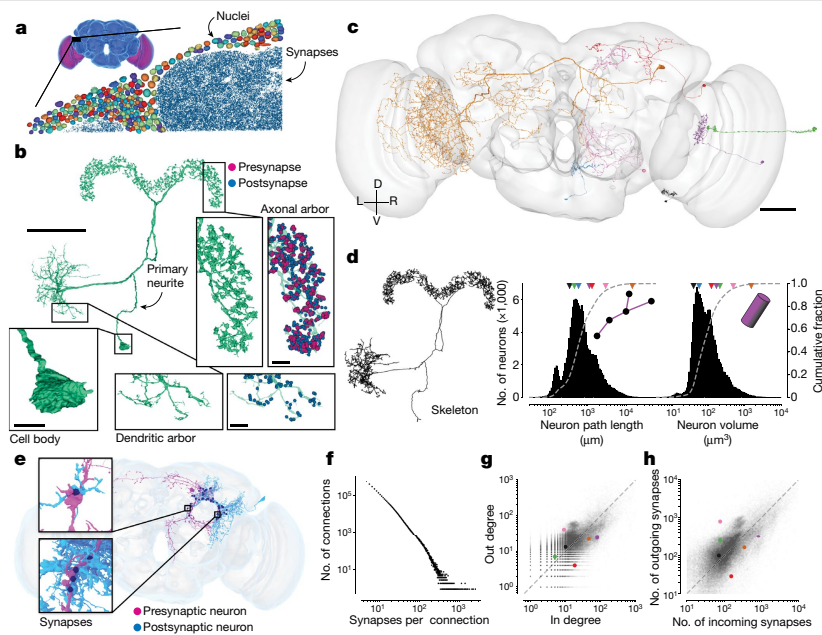


Fig. 3 | Neuron and connection sizes. **a**, The synapse-rich (synapses shown in blue) neuropil is surrounded by a layer of nuclei (random colours) located at the outside of the brain as well as between the optic lobes (purple) and the central brain (blue). **b**, An LPsP (lateral accessory lobe–posterior slope–protocerebral bridge)³ neuron can be divided into morphologically distinct regions. Synapses (purple and blue) are found on the neuronal twigs and only rarely on the backbone. **c**, We selected seven diverse neurons as a reference for **d–h**. **d**, The morphology of a neuron can be reduced to a skeleton (left) from which the path length can be measured. The histograms show the distribution of path length (middle) and volume (right; the sum of all internal voxels) for all neurons. The triangles on top of the distributions indicate the measurements of the neurons in **c**.

e, Connections in the fly brain are usually multisynaptic, as in this example of neurons connecting with 71 synapses. **f**, The number of connections with a given number of synapses. **g**, In degree and out degree of intrinsic neurons in the fly brain are linearly correlated ($R = 0.76$). The dashed line is the unity line. Coloured dots indicate measurements of the neurons in **c**. **h**, The number of synapses per neuron varies between neurons by more than one order of magnitude and the number of incoming and outgoing synapses is linearly correlated ($R = 0.81$). Only intrinsic neurons were included in this plot. The dashed line is the unity line. Coloured dots indicate measurements of the neurons in **c**. Scale bars: 50 μm , **b** (main image) and **c**; 10 μm , **b** (expanded views).

targeting of central neurons, VPNs make 20% of their synapses onto other VPNs and 21% onto optic lobe neurons. Ganguly et al.³⁸ and Garner et al.³⁷ further investigated the visual projections to the central complex and the mushroom body.

There are 524 neurons that project from the central brain to the optic lobes. We call these visual centrifugal neurons⁶¹ (VCNs). They are distinct from previously defined types of VCNs that are fully contained in the optic lobe and their functions are mostly unknown. VCNs are 15 times less numerous than VPNs. Nevertheless, half of all optic lobe neurons receive five or more synapses from VCNs, showing that much early visual processing incorporates feedback from the central brain. Centrifugal inputs to the retina are found in many vertebrate species, including humans⁶³.

Many VCNs arborize broadly in the optic lobe, appearing to cover the entire visual field. Some VCNs, however, cover only a subset of columns within a portion of the visual field. A few optic lobe neurons receive as many as 50% of their synapses from VCNs. These belong to the class of peptidergic neurons involved in circadian rhythms⁴⁰. Tm5c is a columnar type (necessary for the preference of *Drosophila* for UV over visible light⁶⁴), with more than 10% of its inputs coming from VCNs.

Neuron superclasses

The neuron classes introduced above are organized into a hierarchy, as explained in our companion paper¹². The three ‘flow’ classes (afferent, intrinsic and efferent) are divided into the nine superclasses (Fig. 2a). A simplified representation of the connectome as a graph in which nodes are superclasses is shown in Fig. 2b. Node sizes reflect neuron number

and link widths indicate connection number. This is the first of several simplified representations of the connectome that we introduce here.

Neurons and glia

A basic property of the fly brain is that cell bodies are spatially segregated from neurites. Cell bodies reside near the surface (‘rind’) of the brain (Fig. 3a), surrounding a synapse-rich interior that comprises mainly of entangled neurons and glia, fibre bundles or tracts, and tubules of the tracheal system (Fig. 1f and Supplementary Fig. 3a).

A typical non-sensory *Drosophila* neuron is unipolar and consists of a primary neurite (also known as cell body fibre) that leaves the cell body (soma), enters the neuropil, and branches into secondary and higher-order neurites (Fig. 3b). Secondary neurites can sometimes be classified as axons if presynapses clearly dominate, or as dendrites if postsynapses clearly dominate^{10,33,53}. Such an axon–dendrite distinction was made, for example, when defining VPNs and VCNs above.

However, in general, a mixture of presynapses and postsynapses is found on all non-primary neurites^{10,33,53,65} (Fig. 3b). In addition, the soma of insect neurons is separated from the main processes (Fig. 3b). Given this structure, the concept that signals pass from dendrites to soma to axon, which is often a good approximation for mammalian neurons, does not apply for non-sensory neurons in the fly.

Neurons vary greatly in size and shape (Fig. 3c). We computed skeletons for all reconstructed neurons (Fig. 3d) to measure neuronal path lengths. The median path length of an intrinsic neuronal arbor was 685 μm (Fig. 3d). It has been argued that branched arbors are optimal for achieving a high degree of connectivity with other neurons⁶⁶.

Neurons with short path lengths are interesting exceptions, and can be found in both the optic lobes and central brain. Path length and volume of intrinsic neurons both varied over two orders of magnitude (Fig. 3d; path length percentiles: 0.1%, 0.138 mm; 99.9%, 19.15 mm; volume percentiles: 0.1%, $16 \mu\text{m}^3$; 99.9%, $3,001 \mu\text{m}^3$). The whole brain contains approximately 122 million attached presynapses with a total neuronal path length of around 149 m, an average of 0.82 presynapses per micrometre of path length.

Sizes vary significantly between different cell superclasses (Extended Data Figs. 3a–f and 4). Optic lobe neurons are on average much shorter than central brain neurons (0.69 mm versus 2.13 mm on average) and take up a smaller volume (0.0069 mm^3 versus 0.0086 mm^3 total neuronal volume), which is why the optic lobes dominate the brain by neuron number but not by volume or synapse count. Visual centrifugal neurons are among the largest in the brain, and are larger on average than VPns (4.92 mm versus 1.56 mm path length on average). We measured much shorter path lengths and volumes for afferent neurons because only part of their axonal arbors is contained within the brain (Extended Data Fig. 3b,e), whereas arbors of efferent, motor and descending neurons which also have some of their arbor outside the brain, were among the largest we measured (Extended Data Fig. 3c,f).

A small fraction of brain volume is made up of glial cells, which are categorized into six types⁶⁷. We estimated that 13% of the cell bodies in the electron microscopy dataset are non-neuronal or glial. Only a few astrocyte-like glia have been proofread (Supplementary Fig. 3b). Sheet-like fragments of ensheathing glia are readily found near fibre bundles in the automated reconstruction. Further proofreading of glia could be prioritized in the future if there is community demand.

Synapses and connections

Our connectome includes only chemical synapses; the identification of electrical synapses awaits a future electron microscopy dataset with higher resolution (Discussion). Therefore, we use the term ‘synapse’ to mean chemical synapse. A *Drosophila* synapse is generally polyadic, meaning that a single presynapse communicates with multiple target postsynapses (Fig. 1e). In FlyWire, a polyadic synapse is represented as multiple synapses, each of which is a pair of presynaptic and postsynaptic locations⁷. Polyadic synapses are common in other invertebrate species, such as *C. elegans*, and exist in some mammalian brain structures (for example, retina).

We define a connection from neuron A to neuron B as the set of synapses from A to B. A connection typically contains multiple synapses, and the number of synapses can be large (Fig. 3e,f). Connections with fewer than 10 synapses are typical, but a single connection can comprise more than 100 synapses ($n = 15,837$) or even more than 1,000 synapses ($n = 27$). The strongest connection that we identified was from a VCN (LT39) onto a wide-field lobula neuron (mALC2), and contained more than 2,400 synapses.

Setting a threshold of at least five synapses for determining a strong connection is likely to be adequate for avoiding false positives in the dataset while not missing connections (Methods). We observed 2,700,513 such connections between 134,181 identified neurons. There are several reasons to focus on strong connections. First, a connection with many synapses is expected to be strong in a physiological sense, other things being equal⁶⁸. Second, strong connections are more reproducible across individuals¹². Third, higher accuracy (both precision and recall) of automatic detection is expected for strong connections, assuming that errors are statistically independent^{1,53}.

One of the most basic properties of a node in any network is its degree, the number of nodes to which it is linked to. To characterize the degree distribution in the *Drosophila* connectome, we focused on intrinsic neurons because unlike afferent and efferent neurons, they do not suffer from undercounting of connections owing to truncation.

For any neuron, in degree is defined as its number of presynaptic partners (input neurons), and out degree is defined as its number of postsynaptic partners (output neurons). The median in degree and out degree of intrinsic neurons are 11 and 13 (Fig. 3g), respectively, with the restriction mentioned above to connections involving five or more synapses. These median values do not appear to be substantially different from the median in degree and out degree of 10 and 19, respectively, for neurons in the *C. elegans* hermaphrodite, considering that it contains several hundred times fewer neurons than *Drosophila*.

The neuron in the *Drosophila* brain with maximum degree is a visual GABAergic (γ -aminobutyric acid-producing) interneuron (CT1), with 6,399 postsynaptic partners and 5,080 presynaptic partners (CT1 in the left hemisphere). Most neuropils of the *Drosophila* brain contain one or a few large GABAergic neurons private to that neuropil, with high in degree and out degree (see Lin et al.⁴⁹ for further analysis on connectivity motifs); these neurons are considered to be important for local feedback gain control⁶⁹. The *Drosophila* brain contains neurons with much higher degree than—for example—the *C. elegans* hermaphrodite³² for which the neuron with maximum degree is a command interneuron (AVAL) with 110 postsynaptic partners and 64 presynaptic partners.

The number of synapses established by a neuron is correlated with its total neurite path length ($R = 0.80$ (presynapse), $R = 0.89$ (postsynapse); Extended Data Fig. 3g). Presynapse and postsynapse counts are similarly correlated per neuron ($R = 0.81$; Fig. 3h). We tested whether large neurons tend to use their many synapses to create stronger connections with individual neurons versus more connections with many different neurons. The total number of synapses established by a neuron was much better correlated with its in and out degrees ($R = 0.93$ and $R = 0.94$, respectively) than its average connection strength ($R = 0.25$ and $R = 0.3$, respectively; Extended Data Fig. 3h,i). This indicates that on average, neurons scale their number of target neurons much more than the strength of an individual connection. It remains to be tested whether the additional target neurons are from the same type or from different cell types.

Connections and neurons are not necessarily the functional units of neural computation. For certain large fly neurons, the arbors are composed of multiple compartments that function somewhat independently⁷⁰. These subcellular compartments, rather than whole cells, should perhaps be regarded as nodes of the connectome. In this case, CT1 would be replaced by many nodes with lower degrees, and the connection from LT39 to mALC2 would be replaced by many connections with fewer synapses between compartments of these neurons. A connectome of neuronal compartments can in principle be studied using our resource, which includes the location of every synapse.

Neurotransmitter identity

A statistical prediction of the small molecule neurotransmitter (GABA (γ -aminobutyric acid), glutamate, acetylcholine, serotonin, dopamine and octopamine) secreted by each neuron is available. A number of validations suggest that the predictions are highly accurate in aggregate¹⁰, but for any given synapse the prediction could be wrong. We assume that every neuron secretes a single small molecule neurotransmitter and combine the predictions for all outgoing synapses to an estimate that we assign to all outgoing synapses of a neuron—that is, we provisionally assume that neurons obey Dale’s law, although it is known that co-transmission does occur in the fly brain⁷¹.

GABAergic neurons had higher degrees on average than glutamatergic and cholinergic neurons (median in- and out degrees of intrinsic neurons: GABA, 14 incoming and 16 outgoing partners; glutamate, 11 incoming and 13 outgoing partners; acetylcholine, 10 incoming and 13 outgoing partners; Extended Data Fig. 3j). Across all neuron categories, we found that GABAergic neurons were on average longer than glutamatergic and cholinergic neurons (median length of intrinsic

Article

neurons: GABA, 0.88 mm; glutamate, 0.85 mm; acetylcholine, 0.63 mm; Extended Data Fig. 3k).

As a rule, we assume that cholinergic neurons are excitatory and GABAergic and glutamatergic neurons are inhibitory^{72,73}. Lin et al.⁴⁹ identified all GABAergic and glutamatergic neurons that are bidirectionally coupled with large numbers of cholinergic neurons. This reciprocal inhibitory–excitatory motif is widespread throughout the fly brain.

From connectome to projectome

For mammals, tracer injection studies have mapped the axonal projections between brain regions of mouse^{74,75} and macaque⁷⁶. In the fly, large numbers of light microscopy reconstructions of single neurons have been aggregated to map projections between brain regions^{77,78}. Such maps have been called projectomes⁷⁹ or mesoscale connectomes¹⁴. In such techniques, the sampling of axons is difficult to control, and therefore accurate quantification of projection strength is challenging.

Here we computed a projectome from a synapse-level connectome (Fig. 4a and Extended Data Fig. 5). The interior of the fly brain has been subdivided into hierarchical neuropil regions⁸⁰ (Fig. 1 and Extended Data Fig. 1). Our fly projectome is defined as a map of projections between these neuropil regions. Because cell bodies are spatially separated from neuropils, a fly neuron cannot typically be assigned to a single brain region. This is unlike the situation for a mammalian neuron, which is conventionally assigned to the region containing its cell body. A typical fly neuron belongs to multiple neuropils.

The projectome is a neuropil–neuropil matrix, and is computed as follows. Each intrinsic neuron contributes to the projections between neuropils where it has presynaptic and postsynaptic sites. We weighted neuron projections by the product of the respective number of synapses and normalized the result for every neuron such that the neuropil–neuropil matrix sums to the total number of intrinsic neurons. Each column corresponds to all the neurons projecting to a neuropil and each row corresponds to all neurons projecting out of it (Fig. 4b). Each square then represents the summed fractional weight of all neurons projecting between two neuropils (Fig. 4c,d). We added afferent and efferent neurons to the matrix by calculating the sum of the weighted neuron projections per superclass to and from all neuropils, respectively.

Whereas each neuropil is connected to many others, most neurons have synaptic sites in only a few neuropils (Fig. 4e). The largest weights in the projectome tend to be internal to individual neuropils, such as within the medulla or within the fan-shaped body⁴⁹. The largest inter-neuropil projections overall are lobula to medulla, whereas within the central brain the largest inter-neuropil projections are mushroom body, medial lobe to mushroom body, calyx.

We repeated this process to construct projectomes for each fast neurotransmitter type (Extended Data Fig. 5). Some neuropil–neuropil connections exist strongly for one neurotransmitter but not others. For example, the neuropils making up the central complex (fan-shaped body, ellipsoid body, protocerebral bridge and noduli) and the mushroom body (calyx, pedunculus, vertical lobe and medial lobe) are largely linked by excitatory connections.

We observed a strong symmetry between projections in the left and right hemisphere as well as with the central neuropils located on the midline (Extended Data Fig. 6a,b); this highlights the strong similarity between the two sides of the brain. We observed that contralateral projections (projections from one side of the brain to the other) were generally weaker than projections to the same or ipsilateral neuropil (Extended Data Fig. 6c). The strongest contralateral projections are between left and right superior protocerebrum, followed by left and right anterior ventrolateral protocerebrum. Of note, projection weights were not strongly correlated to inter-neuropil distance. Although the strongest projections are often between nearby neuropils, there are

also many nearby neuropils that do not share strong connections (Extended Data Fig. 6d).

The SEZ (Fig. 4f) is the ventral portion of the central brain, and has been shown to contribute to a variety of behaviours⁵⁸. It is almost entirely unrepresented in the hemibrain reconstruction¹, and is only partially reconstructed in the larval brain³³. The five neuropils in the SEZ (left and right AMMC, GNG, SAD and PRW; Fig. 4f; breakdown by neuropil in Supplementary Figs. 4 and 5) amount to 17.8% of central brain neuropil volume (0.0018 mm³ out of 0.0103 mm³); they contain afferents mostly from non-visual sensory neurons (mechanosensory and taste) and ascending neurons, as well as a large number of efferents (motor, endocrine and descending neurons; descending neurons receive on average 52% of their inputs in one of the five SEZ neuropils). The SEZ is thus important for information flow to and from the brain. Judging from the projectome (Fig. 4a), the SEZ neuropils interact with almost all parts of the brain. Notable exceptions are the central complex (ellipsoid body, fan-shaped body, protocerebral bridge and noduli) and the mushroom body, suggesting less crosstalk between those circuits and neurons in the SEZ (explored in more detail in Fig. 6; see also Pospisil et al.³⁹).

Hemispheric organization

Our reconstruction includes both left and right brain hemispheres. This is important for tracing sensorimotor pathways that cross from one side to the other, and more generally for understanding interactions between the two hemispheres. The projectome (Fig. 4a) reveals that most projections are ipsilateral or between neuropils on the same side of the brain.

The low fraction of non-ipsilateral neurons is primarily due to their scarceness in the optic lobes. Only 139 neurons (0.2%) in the optic lobes cross hemispheres and cross the central brain without making synapses there (Supplementary Fig. 6)—these neurons are considered to be ‘fully contained’ in the optic lobes because our definition depends only on synapse locations. These neurons mediate direct interactions between the two optic lobes, and their rarity suggests that these interactions represent a smaller fraction of the computations that occur within the optic lobes. Integration of information from both eyes may rely more on the abundant crossing connections between the central brain targets (AOTU, PLP and PVLV) of VPNS.

A higher proportion (40%) of central brain neurons are non-ipsilateral, largely owing to central neuropils, similar to those of the central complex and SEZ. To classify non-ipsilateral neurons, we began by examining the spatial distributions of their postsynapses (inputs). We divided the neuropils into three categories. Left and right categories included the neuropils that come in mirror-symmetric pairs. Centre included the seven remaining neuropils that are located on the midline. For each neuron, we computed the proportions of its postsynapses in left, right and centre neuropils (Extended Data Fig. 7). Each neuron was assigned to the dominant category, and near-ties were rare. The exceptions are symmetric neurons with cell bodies at the midline of the brain (Supplementary Fig. 7, $n = 89$).

Next, we explored how many neurons of left and right categories have presynapses (outputs) in the other hemisphere. Similar to the analysis of the 1st instar larval connectome³³, we found that neurons projecting to the other hemisphere can be grouped into bilateral neurons, those with outputs in both hemispheres, and contralateral neurons, which almost exclusively had presynapses in the other hemisphere (Fig. 4g–i). Notably, a much larger fraction of VCNs projected to the contralateral hemisphere than VPNS, and both VCNs and neurons of the central brain contain a large fraction of bilateral neurons (Fig. 4h). As stated above, this analysis again revealed the dominance of ipsilateral connections in the brain. Whereas mixing between the hemispheres is more rare, mixing between sensory modalities within a hemisphere is common (Fig. 6).

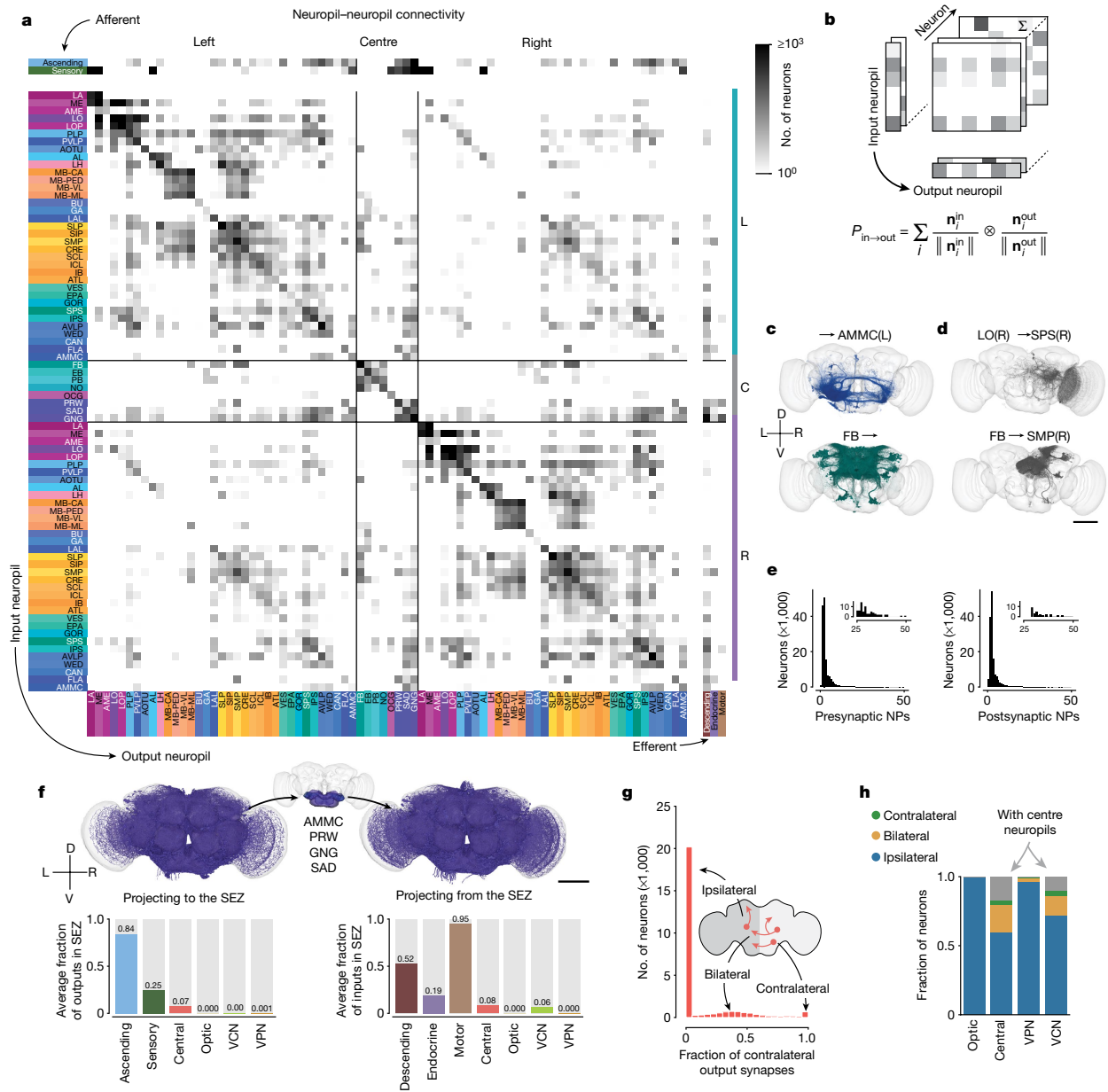


Fig. 4 | Neuropil projections and analysis of crossing neurons. **a**, Whole-brain neuropil–neuropil connectivity matrix. The main matrix was generated from intrinsic neurons, and afferent and efferent neuron classes are shown on the side. Incoming synapses onto afferent neurons and outgoing synapses from efferent neurons were not considered for this matrix. See Extended Data Fig. 5 for neurotransmitter-specific matrices. Neuropils are defined in Extended Data Fig. 1. C, centre neuropils; L, left neuropils; R, right neuropils. **b**, Cartoon describing the generation of the matrix in **a**. The connectivity of each neuron is mapped onto synaptic projections between different neuropils. n_j^{out} and n_j^{in} are vectors of numbers of synapses for each neuropil and neuron. **c, d**, Examples from the matrix in **a** with each render corresponding to one row or column in

the matrix (**c**) and examples from the matrix with each render corresponding to one square in the matrix (**d**). **e**, Most neurons have pre- and postsynaptic locations in fewer than four neuropils. Insets show a closer view of the long tail of the distribution. NPs, neuropils. **f**, Renderings (subset of 3,000 each) and input and output fractions of neurons projecting to and from the SEZ. The SEZ is composed roughly of five neuropils (the AMMC has left and right homologues). Average input and output fractions were computed by summing the row and column values of the SEZ neuropils in the superclass-specific projection matrices. **g**, Fraction of contralateral synapses for each central brain neuron. **h**, Fraction of ipsilateral, bilateral and contralateral neurons projecting to and from the centre neuropils per superclass. Scale bars, 100 μ m.

Many types of fly neurons are known to exhibit striking stereotypy across individuals, as well as across both hemispheres of the same individual. Schlegel et al.¹² show quantitatively using FlyWire brain and hemibrain data that these two types of stereotypy are similar in degree.

Optic lobes, columns and beyond

So far we have mentioned neurons that connect the optic lobes with each other, or with the central brain. The intricate circuitry within each

Article

optic lobe is also included in the FlyWire brain connectome. Matsliah et al.¹¹ analysed and typed all neurons intrinsic to the right optic lobe. Photoreceptor axons terminate in the lamina and medulla, neuropils of the optic lobes (Fig. 5a,b). Each eye contains approximately 800 ommatidia that map to columns in the lamina that are arranged in a hexagonal lattice (Fig. 5c). This structure repeats in subsequent neuropils from lamina to medulla to lobula to lobula plate. The neuropils have been finely subdivided into layers that are perpendicular to the columns⁸¹. The 2D visual field is mapped onto each layer and any given cell type tends to synapse in some subset of the layers. Cell types vary greatly in size, with uni-columnar cell types being the smallest; (for example, Mi4); at the other extreme are large cells that span almost all columns (for example, Dm17); in between the extremes are many multi-columnar cell types (for example, Dm12) (Fig. 5c).

Mi4 is a true 'tiling' type—that is, its arbors cover the visual field with little or no overlap, and have similar size and shape (Fig. 5c). Dm12 arbors overlap with each other, but the spatial arrangement is still regular. These and other distal medullary cell types were previously characterized by multicolour light microscopy⁸². Our electron microscopy reconstructions reveal even more detailed information about the spatial patterning of these types (for example, co-fasciculation of neurites of neighbouring Dm12 cells; Fig. 5c). More importantly, the FlyWire reconstruction encompasses all multi-columnar cell types, including those outside the medulla. Judging from the many examples we have studied throughout the optic lobe, it seems that regular coverage of the visual field without gaps is a defining criterion for most cell types, similar to mammalian retina⁸³. There are, however, exceptional cell types that cover the visual field in an irregular manner. For example, there are exactly two LPi4 cells per optic lobe⁸⁴. The shapes of each pair are complementary, as if they were created by cutting the visual field into two pieces with a jigsaw (Fig. 5d); this tiling was not evident when reconstructing only a portion of an optic lobe⁸⁴.

Much of the existing research on wide-field visual motion processing has relied on the simplifying idea that the computations are mostly in columnar circuits, and the columnar outputs are finally integrated by large tangential cells in the lobula plate. This research has been aided by wiring diagrams containing connections between cells in the same column or neighbouring columns². In previous studies, an absence of information across columns has necessitated treating each column as identical in simulations of the optic lobe⁸⁵. The FlyWire brain connectome contains not only the columnar neurons, but also all neurons that extend across columns (Fig. 5c). These neurons are both excitatory and inhibitory, and can support interactions between even distant columns. This opens the possibility of a much richer understanding of optic lobe computations and is further explored by Christenson et al.⁴¹ in investigating hue selectivity.

Analysis of information flow

Although afferent and efferent neurons make up a numerically small proportion of the brain (estimated 13.9% and 1.1%, respectively), they are important because they connect the brain to the outside world. Examining connections of these neurons is useful when attempting to predict the functions of intrinsic neurons from the connectome. For example, one might try to identify the shortest path in the connectome from an afferent (input) neuron that leads to a given intrinsic neuron. The sensory modality of the afferent neuron could provide a clue regarding the function of the intrinsic neuron. This approach, although intuitive, ignores connection strengths and multiplicities of parallel pathways. We therefore use a probabilistic model to estimate information flow in the connectome²⁶, starting from a set of seed neurons (Fig. 6a and Methods).

The likelihood of a neuron being traversed increases with the fraction of inputs from already traversed neurons up to an input fraction of 30%, after which traversal is guaranteed (Fig. 6a). We ran the traversal

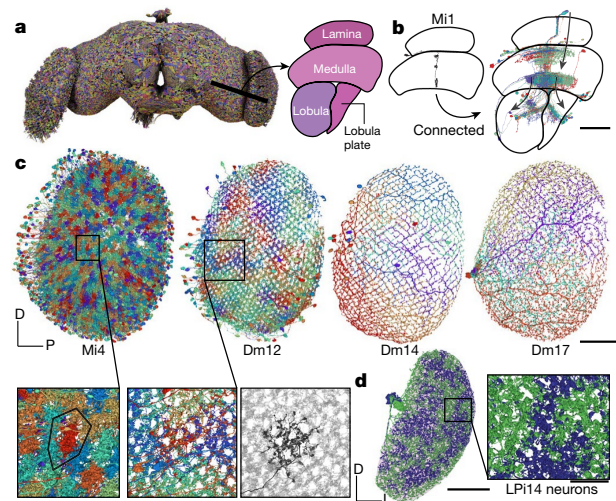


Fig. 5 | Optic lobes. **a**, Rendering of a subset of the neurons in the fly brain. A cut through the optic lobe is highlighted and neuropils are annotated. **b**, A single Mi1 neuron (left) and all neurons that share a connection with the single Mi1 neuron (at least five synapses) (right). Three large neurons (CT1, OA-AL2b2 and Dm17) were excluded for the visualization. **c**, Top, Mi4, Dm12, Dm14 and Dm17 neurons in the right optic lobe, as annotated by Matsliah et al.¹¹. Bottom, expanded views of the outlined regions in Mi4 and Dm12 show the local structure. For Dm12, the right image shows a single neuron in black and all other Dm12 neurons are in background. **d**, The two LPi4 neurons in the right lobula plate (neuropil shown in background). Scale bars: 50 μm , **b** and **c**, **d** (main image); 10 μm , **c**, **d** (expanded views).

model for every subset of afferent neurons as seeds ($n = 12$ input modalities to the central brain (Fig. 2e and Supplementary Fig. 8; full list in Methods)). We then measured the flow distance from these starting neurons to all intrinsic and efferent neurons of the central brain. For instance, the neurons reached early from gustatory neurons (Fig. 6b) match second-order projection neurons identified by Snell et al.⁸⁶ using *trans*-Tango.

To visualize information flow for neurons with inputs in the central brain in a common space, we treated the traversal distances starting from each seed population as a neuron embedding and built a uniform manifold approximation and projection (UMAP) from all of these embeddings (Fig. 6c). Within the map, we found that neurons of the same cell class (for example, two groups of Kenyon cells, all mushroom body output neurons, all antennal lobe local neurons and all central complex neurons) cluster, indicating that cell types can in part be defined by their proximity to different input neurons. Next, we displayed traversal order on top of the UMAP plot to compare traversal orders starting from different modalities (Fig. 6c,d). We find that almost every neuron in the central brain can be reached by starting from any modality—this 'small world' property of the network is covered in more detail by Lin et al.⁴⁹ Comparing orders revealed that almost all neurons in the central brain are reached early starting from some modality, with the exception of neurons in the central complex (Fig. 6c,d and Extended Data Fig. 9), highlighting that the central complex is dominated by internal computations²⁴. Kenyon cells were contained in two clusters—one of which is targeted very early from olfactory receptor neurons and the other is targeted early by VPNs⁸⁷.

We then ranked all neurons by their traversal distance from each set of starting neurons and normalized the order to percentiles. For instance, a neuron at the 20th percentile had a lower rank than 80% of neurons. This enabled us to determine how early information from each afferent modality reached various targets, including the descending neurons,

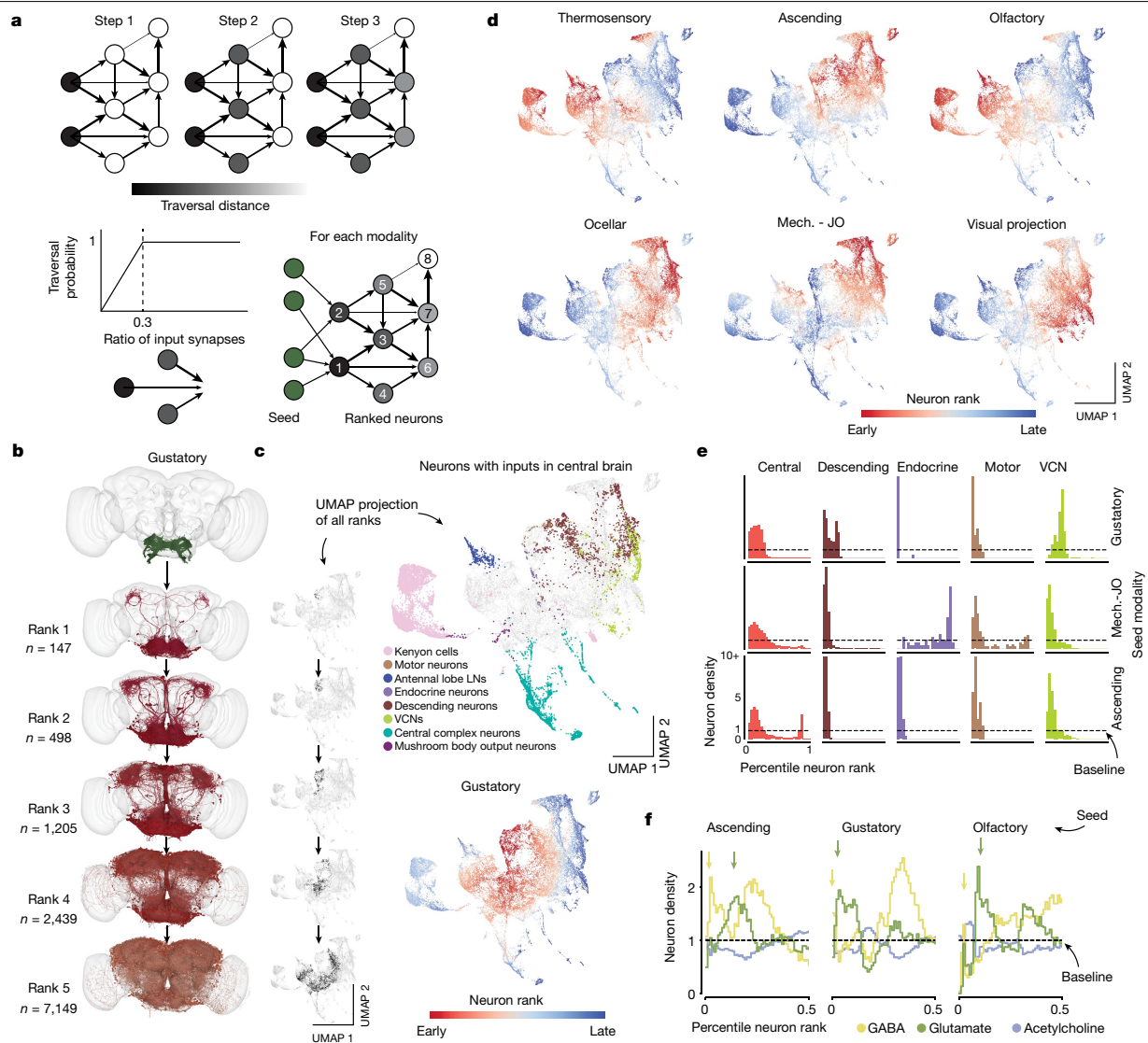


Fig. 6 | Information flow through the *Drosophila* central brain. **a**, We applied an information flow model for connectomes²⁸ to the connectome of the central brain neurons. Neurons are traversed probabilistically according to the ratio of incoming synapses from neurons that are in the traversed set. The information flow calculations were seeded with the afferent classes of neurons (including the sensory categories). **b**, We rounded the traversal distances to assign neurons to layers. For gustatory neurons, we show a subset of the neurons (up to 1,000) that are reached in each layer. Neurons are coloured according to the traversal distance in **c**. **c**, UMAP analysis of the matrix of traversal distances, resulting in a 2D representation of each neuron in the central brain. Neurons from the same class co-locate (see also Extended Data Fig. 9). The small UMAP plots aligned with layers in **b** show where the neurons for each rank from the gustatory

neurons fall within the distribution (black dots). Bottom, we coloured neurons in the UMAP plot by the rank order in which they are reached from gustatory seed neurons. Red neurons are reached earlier than blue neurons. LN, local neuron. **d**, As in **c**, bottom, for multiple seed neuron sets (see Extended Data Fig. 8c for the complete set). Mech.-JO, mechanosensory–Johnston’s organ. **e**, For each sensory modality, we used the traversal distances to establish a neuron ranking. Graphs show the distributions of neurons of each superclass within the specific rankings for each sensory modality (see Extended Data Fig. 8a for the complete set). **f**, Neurons were assigned to neurotransmitter types. Graphs show their distribution within the traversal rankings similar to **d**. Arrows highlight the sequence of GABA–glutamate peaks found for almost all sensory modalities (see Extended Data Fig. 8b for the complete set).

endocrine neurons, motor neurons and VCNs (Fig. 6e and Extended Data Fig. 8a). Endocrine neurons are closest to the gustatory sensory neurons, whereas motor and descending neurons were reached early for mechanosensory and visual afferents (Extended Data Fig. 8a).

We next tested whether the afferent cell classes target inhibitory neurons early or late. We found that putative inhibitory neurons (neurons predicted to express GABA and glutamate) were overrepresented in the set of early neurons (Fig. 6f). Surprisingly, we identified a sequence of

GABAergic and glutamatergic peaks in the sequence of targeted neurons that was replicated for almost all afferent modalities (Extended Data Fig. 8b).

Our information flow analysis provides a compressed representation of the connectome, but currently ignores signs of connections (neurotransmitter identity) and the biophysics of neurons and synapses, and therefore terms such as ‘early’ and ‘late’ should not be interpreted as true latencies to sensory stimulation. Shiu et al.³⁴ and Pospisil et al.³⁹

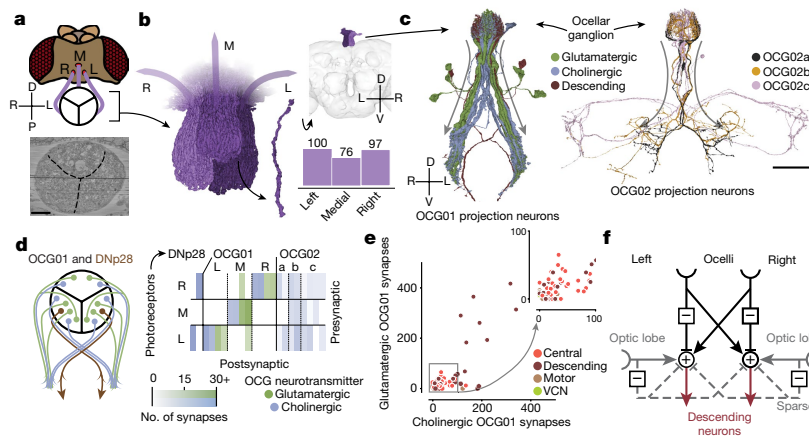


Fig. 7 | Ocellar circuits and their integration with VPNs. **a**, Overview of the three ocelli (left (L), medial (M) and right (R)) positioned on the top of the head. Photoreceptors from each ocellus project to a specific subregion of the ocellar ganglion which are separated by glia (marked with black lines on the electron micrograph (bottom)). Left and right are flipped in accordance with the orientation of the dataset (Methods). **b**, Renderings of the axons of the photoreceptors (left) and their counts (bottom right). Top right, location of the ocellar ganglion relative to the brain. **c**, Renderings of OCG01, OCG02 and

DNp28 neurons with arbors. ‘Information flow’ from presynapses and postsynapses is indicated by arrows along the arbors. **d**, Connectivity matrix of connections between photoreceptors and ocellar projection neurons, including two descending neurons (DNp28). **e**, Comparison of number of glutamatergic and cholinergic synapses from ocellar projection neurons from the lateral eyes onto downstream neurons coloured by superclass ($R = 0.78, P < 10^{-26}$). **f**, Summary of the observed connectivity between ocellar projection neurons, VPNs and descending neurons. Scale bars, 100 μm .

use the connectome to model *Drosophila* brain dynamics and include connection weights (number of synapses) and putative connection signs (excitatory or inhibitory).

Cell types and other annotations

Neurons in *Drosophila* are considered to be identifiable across hemispheres and individuals, enabling cell-type classification of all neurons in FlyWire’s brain dataset. Such classification is useful for generating testable hypotheses about circuit function from the connectome. FlyWire community members, many of whom are experts in diverse regions of the fly brain, have shared 133,700 annotations of 114,209 neurons (Supplementary Fig. 9), including comprehensive cell typing in the optic lobe¹¹, the majority of sexually dimorphic neurons and sensory neurons³⁵, as well as a diversity of cell types throughout the brain, including the SEZ (Fig. 2f). Each neuron in FlyWire is also given a unique identifier on the basis of the neuropil through which it receives and sends most of its information. Curation of these annotations continues, and we invite further community efforts to identify cell types, which can be contributed through Codex (<https://codex.flywire.ai>).

In addition, matching between cell types identified in the hemibrain¹ and both hemispheres of FlyWire’s brain dataset provides additional annotations for neurons contained in both datasets. Our companion paper¹² provides annotations for more than 8,400 unique cell types via such matching. All cell annotations can be queried in Codex. Some of these have already been mentioned, such as the ‘flow’ annotations of intrinsic versus afferent versus efferent, superclass annotations (Fig. 2), connectivity tags (such as rich club, broadcaster or highly reciprocal)⁴², neurotransmitter predictions¹⁰ and left–right annotations for cell body location⁸⁸, in addition to lineages or groups of neurons derived from a single neuroblast.

Ocellar circuit, from inputs to outputs

The completeness of the FlyWire brain connectome enables tracing complete pathways from sensory inputs to motor outputs. We demonstrate this capability by examining circuits that emanate from the

ocellar ganglion and leveraging cell-type information. In addition to the large compound eyes, flying insects have smaller visual sensory organs⁸⁹, including the three ocelli on the dorsal surface of the head cuticle (Fig. 7a). The ocelli project a blurry image of light-level changes in the UV and blue region of the spectrum^{90,91} and are thought to be useful for flight control and orientation relative to the horizon⁹². Notably, although the role of the ocelli has been hypothesized (for example, light-level differences between the eyes when the fly is shifted off axis should quickly drive righting motions of the head, wings and body to stabilize gaze and re-orient the body), little is known about the circuitry downstream of this sensory organ that would mediate this function.

We find that photoreceptor axons ($n = 273$) from the three ocelli innervate three distinct regions of the ocellar ganglion separated by glial sheets (Fig. 7a,b). The ocellar ganglion additionally contains 63 neurons that we categorized into four broad groups (Fig. 7c and Extended Data Fig. 10a): local neurons ($n = 16$), 2 types of interneurons, divided on the basis of their arborizations and caliber (OCG01 ($n = 12$), OCG02 ($n = 8$)), descending neurons (DNp28, $n = 2$), and centrifugal or feedback neurons ($n = 25$). Ocellar local neurons are small and connect sparsely with photoreceptors from all ocelli.

Twelve OCG01 interneurons and two descending neurons (DNp28, one per lateral ocellus) represent the main pathway from the ocellar ganglion to the central brain. DNp28 projects to the intermediate, haltere, wing and neck tectula of the ventral nerve cord^{55,93}. In each ocellus, half of the OCG01s were inferred to express glutamate (likely inhibitory), and the other half were inferred to express acetylcholine (likely excitatory). There are four OCG01s per ocellus (Fig. 7d). OCG01s tile the ocellar ganglion, indicating that their receptive fields tile the visual fields of the ocelli (Extended Data Fig. 10b,c). OCG02 axons are much thinner than OCG01 axons, and likely transmit signals more slowly. Two OCG02 subgroups (a and b) innervate similar neuropils to the OCG01s (inferior posterior slope (IPS) and superior posterior slope (SPS)), and OCG02c neurons target the PLP, a brain region that also receives input from VPNs from the compound eyes⁶⁰.

Neurons downstream from OCG01s in the IPS, SPS and GNG receive inhibitory input from the ipsilateral ocellus and excitatory input from the contralateral ocellus (Fig. 7d, left), and the amount of synaptic input from each ocellus is tightly correlated (Fig. 7e, $R = 0.78$,

$P < 10^{-26}$)—this balance is likely to be a key ingredient in how signals are integrated (the descending circuits are activated by a signal difference between the eyes). We found that 15 different descending neurons each receive more than 200 synapses from the OCG01 neurons. For example, 2 descending neurons in each hemisphere received more than 30% of their synaptic inputs in the brain from ocellar projection neurons: DNp20/DNOVS1 (left: 57%, right: 44%) and DNp22/DNOVS2 (left: 36%, right: 33%). DNOVS1 and other descending neurons with strong input from OCG01s generally also receive strong input from ipsilateral VPNS (neurons that connect the optic lobe to the central brain) (Extended Data Fig. 10d). For example, DNOVS1 is known to be activated by rotational optic flow fields across the compound eye, and projects to the neck motor system^{94,95}. A handful of glutamatergic (putative inhibitory) VPNS also sparsely innervate descending neurons in both hemispheres. As the ocelli transmit mainly information about light levels, the dense integration with motion direction signals from the compound eyes was not previously appreciated, but should aid in precision adjustments of head and body movements for gaze stabilization and flight control⁹⁶.

There is also extensive feedback from the brain directly to the ocellar ganglion via 25 ocellar centrifugal neurons (OCC). We found striking targeting specificity of two OCC subgroups (OCC01a and OCC01b, predicted to be cholinergic) which synapse onto all OCG01 and DNp28 neurons with strong connections compared with their overall synaptic budget (Extended Data Fig. 10e). The OCC01s receive input in a wide range of neuropils, notably the SEZ, as well as IPS and SPS, the same neuropils that receive inputs from the OCG projection neurons (Extended Data Fig. 10f). The role of the OCCs in gating visual information and potentially driving the OCGs in the absence of photoreceptor activity remains to be determined.

On the basis of our analysis of connectivity, we hypothesize how the pathways from the ocelli to descending neurons function (Fig. 7f). As in a Braitenberg vehicle for phototaxis⁹⁷, excitation and inhibition are organized so that the head and body of the fly should roll around the anteroposterior axis to orient the ocelli towards light. In this compact example, the whole-brain connectome, which extends from brain inputs to outputs, uncovers new pathways and facilitates the generation of testable hypotheses for circuit mechanisms of sensorimotor behaviour.

Discussion

Connectome analysis

We use the term ‘connectome’ to mean a neuronal wiring diagram of an entire nervous system, or at least an entire brain⁹⁸. This is in keeping with the intent of the original definition¹⁴, which emphasized comprehensiveness. Similarly, the term ‘genome’ refers to the entire DNA sequence of an organism, or at least the entirety of genes. Our neuronal wiring diagram of a whole fly brain arguably crosses the threshold for being called a connectome, although it would be reasonable to insist that a connectome should include the ventral nerve cord as well as the brain. Either way, the comprehensiveness of our wiring diagram has significant benefits for brain research and enables many kinds of studies that were not previously possible using wiring diagrams of portions of the fly brain. The optic lobes and the SEZ are two prominent regions that are mostly absent from the hemibrain. Both sides of the brain are now included, which enables the tracing of pathways that cross the midline. Owing to the presence of afferent and efferent neurons, pathways can be traced from sensory inputs to intrinsic neurons and brain outputs (motor, endocrine and descending neurons). This was done in a global manner to analyse the neuropil projectome, by using the information flow model, and more specifically to uncover the structure and hypothesize a circuit mechanism for behaviours supported by the ocelli. A set of companion studies provides additional global analyses of the connectome and studies of specific families of pathways^{11,12,34,36–45}.

For the first time, one can now compare entire connectomes of different species, starting with *D. melanogaster* and *C. elegans*, as touched on here and explored in more depth by Lin et al.⁴⁹. It also enables comparison of connectomes of the same species at different developmental stages³³. Although FlyWire is currently the only adult fly connectome, it can be compared with the hemibrain reconstruction in regions where they overlap to detect wiring differences between adults of the same species and to validate and extend cell-type definitions¹².

Finally, the connectome now enables brain simulations—partial connectomes of the early visual system of the fly³ had already inspired simulations of visual processing⁸⁵. This effort has now been extended to leverage the full connectome^{34,39} and to—for example—predict taste responses of neurons³⁴. These simulations assume that that physiological connection strength is proportional to anatomical synapse count, either globally³⁴, or for synapses sharing the same presynaptic and postsynaptic cell types⁸⁵, and have inferred connection signs (excitatory versus inhibitory) from neurotransmitter identity as predicted from electron microscopy images¹⁰ or from transcriptomics⁹⁹. Ongoing discoveries regarding the biophysics of fly neurons will guide efforts to make simulations more realistic. For example, inhibition can be shunting rather than subtractive in some fly neurons¹⁰⁰, and the conductance of an inhibitory synapse can be ten times higher than that of an excitatory synapse¹⁰¹. Whereas the simulations mentioned above were based on point neuron models, future simulations could utilize multicompartmental neuron models constructed using the synapse locations and reconstructed neuronal morphologies provided by FlyWire, as well as emerging data about ion channels and receptors from transcriptomics and proteomics.

Electron microscopy data acquisition and reconstruction

The hemibrain¹ was reconstructed from $8 \times 8 \times 8 \text{ nm}^3$ images acquired by focused ion beam scanning electron microscopy^{102–104} (FIB-SEM), a form of block face electron microscopy^{105,106}. By contrast, FlyWire’s reconstruction is based on a full adult fly brain (FAFB) dataset⁹ of $4 \times 4 \times 40 \text{ nm}^3$ images acquired by serial section transmission electron microscopy (ssTEM). Initially, the lower z resolution and higher prevalence of artefacts made alignment and reconstruction of ssTEM datasets challenging. These were cited by the hemibrain effort to justify the use of FIB-SEM despite its higher cost, slower speed and complex operation requiring many 20- μm slabs to be imaged individually and then stitched together¹. Computational advances have now closed this gap¹⁰⁷ and FAFB images were accurately aligned with a new approach that leverages convolutional nets¹⁰⁸. The hemibrain images were automatically segmented using flood-filling convolutional nets¹⁰⁹, whereas FlyWire used the older, less computationally expensive approach of boundary-detecting convolutional nets^{110,111}. Overall, from acquisition to reconstruction to analysis to dissemination, the technology stack used by FlyWire is distinct from that used for the hemibrain. A notable overlap is the use of neuroglancer¹¹² for browser-based 3D visualization.

FlyWire’s whole-brain automated segmentation was proofread with an estimated 33 person-years of effort (Methods), whereas hemibrain proofreading required 50 person-years for a part of the brain¹. Notably, the accuracy of our proofread wiring diagram is similar to that of the hemibrain (Extended Data Fig. 2 and Supplementary Fig. 3). For both FIB-SEM and ssTEM, incomplete attachment of twigs to backbones is currently the main factor that limits the accuracy of reconstructing synaptic connectivity, and in both cases synaptic connectivity is limited to chemical synapses. Higher resolution might enable the reconstruction of electrical synapses, which are included in the *C. elegans* connectome^{31,32}.

Limitations of our reconstruction

We showed that the attachment rates of twigs is sufficient to facilitate detection of nearly all large connections⁸ (those with more than nine synapses). Nonetheless, the observed synapse counts underrepresent

Article

the actual number of synapses and some connections with few synapses remain undetected. Substantial improvements in twig attachment are unobtainable with further proofreading, as increasing the postsynaptic attachment rate from 44.7% to 50% would require further proofreading of more than 700,000 fragments. Therefore, increases in twig attachments will rely on improvements in image acquisition, image alignment and automated reconstruction. Although proofreading was largely carried out in a neuropil-agnostic manner, attachment rates differ between neuropils (Supplementary Fig. 2) owing to differences in the number of synapses on twigs and backbones and how challenging a neuropil was to reconstruct. Although these effects are largely symmetric, the optic lobe was affected by a one-sided artefact. The left lamina was partially severed from the medulla in the left hemisphere (Fig. 1a), reducing the reconstruction accuracy for some of the lamina neurons on one side (Supplementary Fig. 2).

The automated synapse detection currently used by FlyWire was performed by Buhmann et al.⁷ in an independent effort. By combining the FlyWire brain reconstruction with these synapses, the resulting connectome inherits the limitations from both. In the case of the synapse detection, users should be aware that the ground truth was limited to a few neuropils. As a result, synapse detection performance is lower for some cell types, and we are aware that sensory neurons are particularly affected. FlyWire's reconstruction is compatible with any synapse prediction method and improved synapse prediction will be made available in the future.

Imaging larger

Imaging a larger volume would open up other interesting opportunities. Reconstructing and proofreading a full CNS would enable the mapping of all pathways linking the brain and VNC. In the meantime, it is already possible to establish correspondences between FlyWire and FANC³⁶, a reconstruction of a VNC from another female fly^{54,59}. The first *C. elegans* connectome was obtained similarly as a mosaic drawn from multiple worms³¹. Imaging an entire fly, both CNS and body, would enable the addition of sensory organs and muscles to the reconstruction. This also has precedent in the *C. elegans* connectome³², which includes neuromuscular junctions, the *Platynereis dumerilii* larva¹¹³, and the 1st instar *Drosophila* larva for which a whole-animal electron microscopy dataset was recently published¹¹⁴.

Technologies developed for FlyWire have already been applied to millimetre-scale chunks of mammalian brain^{4,5}, which are more than 50 times larger in volume than a fly brain. The US National Institutes of Health has begun a transformative project to reconstruct a whole mouse brain from an exabyte of electron microscopy images¹¹⁵ and a report from the Wellcome trust recently examined the road to a whole mouse brain connectome¹¹⁶.

Openness

The 1996 Bermuda Principles mandated daily release of Human Genome Project sequences into the public domain¹¹⁷. We believe that openness is also important for large-scale connectomics projects, particularly because these projects are expensive, require coordinated effort and take several years to complete—sharing connectomes only after proofreading and annotation are completed prevents scientific discovery that can occur while the connectome is being completed. Shortly after its inception in 2019, FlyWire has been open to any *Drosophila* researcher, and set forth clear principles for coordination of scientific effort that prioritized attribution through keeping track of edits to and annotations of the dataset. Hundreds of scientists and proofreaders from more than 50 laboratories joined FlyWire with more than 200 of them contributing more than 100 edits (Supplementary Table 1) and 86 contributing ten or more annotations (Supplementary Table 2). As a result of openness, there are multiple studies that used completed portions of FlyWire's brain connectome as proofreading proceeded (Supplementary Table 3). Openness has also enabled FlyWire to move

faster by incorporating data sources from the community. The electron microscopy data on which FlyWire's brain connectome is built was shared in 2018 by Bock and colleagues⁹. The synapse data was published by Buhmann et al.⁷, neurotransmitter labels were published by Eckstein et al.¹⁰, numerous annotations were contributed by Schlegel et al.¹², neck connective neuron annotations were contributed by Stürner et al.³⁶, optic lobe annotations were contributed by Matsliah et al.¹¹ and so far, more than 90,000 cell annotations have been shared by the community. Many cells have received multiple annotations from these sources, and discrepancies will continue to be adjudicated by the community, a process that has improved accuracy in cell-type classification. Overall, we anticipate that similar approaches based on an open ecosystem will enable connectomics to scale more efficiently, economically and equitably.

Online content

Any methods, additional references, Nature Portfolio reporting summaries, source data, extended data, supplementary information, acknowledgements, peer review information; details of author contributions and competing interests; and statements of data and code availability are available at <https://doi.org/10.1038/s41586-024-07558-y>.

1. Scheffer, L. K. et al. A connectome and analysis of the adult *Drosophila* central brain. *eLife* **9**, e57443 (2020).
2. Takemura, S.-Y. et al. A visual motion detection circuit suggested by *Drosophila* connectomics. *Nature* **500**, 175–181 (2013).
3. Takemura, S., Nern, A., Chklovskii, D. B. & Scheffer, L. K. The comprehensive connectome of a neural substrate for 'ON' motion detection in *Drosophila*. *eLife* **6**, e24394 (2017).
4. MICrONS Consortium. Functional connectomics spanning multiple areas of mouse visual cortex. Preprint at bioRxiv <https://doi.org/10.1101/2021.07.28.454025> (2021).
5. Shapson-Coe, A. et al. A petavoxel fragment of human cerebral cortex reconstructed at nanoscale resolution. *Science* **384**, eadk4858 (2024).
6. Loomba, S. et al. Connectomic comparison of mouse and human cortex. *Science* **377**, eabo0924 (2022).
7. Buhmann, J. et al. Automatic detection of synaptic partners in a whole-brain *Drosophila* electron microscopy data set. *Nat. Methods* **18**, 771–774 (2021).
8. Dorkenwald, S. et al. FlyWire: online community for whole-brain connectomics. *Nat. Methods* **19**, 119–128 (2022).
9. Zheng, Z. et al. A complete electron microscopy volume of the brain of adult *Drosophila melanogaster*. *Cell* **174**, 730–743.e22 (2018).
10. Eckstein, N. et al. Neurotransmitter classification from electron microscopy images at synaptic sites in *Drosophila melanogaster*. *Cell* **187**, 2574–2594.e23 (2024).
11. Matsliah, A. et al. Neuronal parts list and wiring diagram for a visual system. *Nature* <https://doi.org/10.1038/s41586-024-07981-1> (2024).
12. Schlegel, P. et al. Whole-brain annotation and multi-connectome cell typing of *Drosophila*. *Nature* <https://doi.org/10.1038/s41586-024-07686-5> (2024).
13. Ma, X., Hou, X., Edgecombe, G. D. & Strausfeld, N. J. Complex brain and optic lobes in an early Cambrian arthropod. *Nature* **490**, 258–261 (2012).
14. Sporns, O., Tononi, G. & Kötter, R. The human connectome: a structural description of the human brain. *PLoS Comput. Biol.* **1**, e42 (2005).
15. Costandi, M. Anti-connectome-ism. *The Guardian* (21 September 2012).
16. Lichtman, J. W. & Denk, W. The big and the small: challenges of imaging the brain's circuits. *Science* **334**, 618–623 (2011).
17. Briggman, K. L. & Bock, D. D. Volume electron microscopy for neuronal circuit reconstruction. *Curr. Opin. Neurobiol.* **22**, 154–161 (2012).
18. Coen, P. et al. Dynamic sensory cues shape song structure in *Drosophila*. *Nature* **507**, 233–237 (2014).
19. Fisher, Y. E. Flexible navigational computations in the *Drosophila* central complex. *Curr. Opin. Neurobiol.* **73**, 102514 (2022).
20. Cognigni, P., Felsenberg, J. & Waddell, S. Do the right thing: neural network mechanisms of memory formation, expression and update in *Drosophila*. *Curr. Opin. Neurobiol.* **49**, 51–58 (2018).
21. Schretter, C. E. et al. Cell types and neuronal circuitry underlying female aggression in *Drosophila*. *eLife* **9**, e58942 (2020).
22. Deutsch, D. et al. The neural basis for a persistent internal state in *Drosophila* females. *eLife* **9**, e59502 (2020).
23. Li, F. et al. The connectome of the adult *Drosophila* mushroom body provides insights into function. *eLife* **9**, e62576 (2020).
24. Hulse, B. K. et al. A connectome of the *Drosophila* central complex reveals network motifs suitable for flexible navigation and context-dependent action selection. *eLife* **10**, e66039 (2021).
25. Baker, C. A. et al. Neural network organization for courtship-song feature detection in *Drosophila*. *Curr. Biol.* **32**, 3317–3333.e7 (2022).
26. Schlegel, P., Bates, A. S., Stürner, T. & Jagannathan, S. R. Information flow, cell types and stereotypy in a full olfactory connectome. *eLife* **10**, e66018 (2021).
27. Borst, A. & Helmstaedter, M. Common circuit design in fly and mammalian motion vision. *Nat. Neurosci.* **18**, 1067–1076 (2015).

28. Farris, S. M. Are mushroom bodies cerebellum-like structures? *Arthropod Struct. Dev.* **40**, 368–379 (2011).
29. Pacheco, D. A., Thiberge, S. Y., Pnevmatikakis, E. & Murthy, M. Auditory activity is diverse and widespread throughout the central brain of *Drosophila*. *Nat. Neurosci.* **24**, 93–104 (2021).
30. Brezovec, B. E. et al. Mapping the neural dynamics of locomotion across the *Drosophila* brain. *Curr. Biol.* **34**, 710–726.e4 (2024).
31. White, J. G., Southgate, E., Thomson, J. N. & Brenner, S. The structure of the nervous system of the nematode *Caenorhabditis elegans*. *Philos. Trans. R. Soc. Lond. B* **314**, 1–340 (1986).
32. Cook, S. J. et al. Whole-animal connectomes of both *Caenorhabditis elegans* sexes. *Nature* **571**, 63–71 (2019).
33. Winding, M. et al. The connectome of an insect brain. *Science* **379**, eadd9330 (2023).
34. Shiu, P. K. et al. A *Drosophila* computational brain model reveals sensorimotor processing. *Nature* <https://doi.org/10.1038/s41586-024-07763-9> (2024).
35. Eichler, K. et al. Somatotopic organization among parallel sensory pathways that promote a grooming sequence in *Drosophila*. *eLife* **12**, RP87602 (2024).
36. Stürner, T. et al. Comparative connectomics of the descending and ascending neurons of the *Drosophila* nervous system: stereotypy and sexual dimorphism. Preprint at *bioRxiv* <https://doi.org/10.1101/2024.06.04.596633> (2024).
37. Garner, D. et al. Connectome reconstruction predicts visual features used for navigation. *Nature* <https://doi.org/10.1038/s41586-024-07967-z> (2024).
38. Ganguly, I., Heckman, E. L., Litwin-Kumar, A., Clowney, E. J. & Behnia, R. Diversity of visual inputs to Kenyon cells of the *Drosophila* mushroom body. *Nat. Commun.* **15**, 5698 (2024).
39. Pospisil, D. A. et al. The fly connectome reveals a path to the effectome. *Nature* <https://doi.org/10.1038/s41586-024-07982-0> (2024).
40. Reinhard, N., Fukuda, A., Manoli, G., Derksen, E. & Saito, A. Synaptic and peptidergic connectomes of the *Drosophila* circadian clock. Preprint at *bioRxiv* <https://doi.org/10.1101/2023.09.11.557222> (2023).
41. Christenson, M. P. et al. Hue selectivity from recurrent circuitry in *Drosophila*. *Nat. Neurosci.* **27**, 1137–1147 (2024).
42. Lin, A. et al. Network statistics of the whole-brain connectome of *Drosophila*. *Nature* <https://doi.org/10.1038/s41586-024-07968-y> (2024).
43. Sapkal, N. et al. Neural circuit mechanisms underlying context-specific halting in *Drosophila*. *Nature* <https://doi.org/10.1038/s41586-024-07854-7> (2024).
44. Seung, H. S. Predicting visual function by interpreting a neuronal wiring diagram. *Nature* <https://doi.org/10.1038/s41586-024-07953-5> (2024).
45. Cornean, J. et al. Heterogeneity of synaptic connectivity in the fly visual system. *Nat. Commun.* **15**, 1570 (2024).
46. Cachero, S., Ostrovsky, A. D., Jai, Y. Y. & Dickson, B. J. Sexual dimorphism in the fly brain. *Curr. Biol.* **20**, 1589–1601 (2010).
47. Murthy, M., Fiete, I. & Laurent, G. Testing odor response stereotypy in the *Drosophila* mushroom body. *Neuron* **59**, 1009–1023 (2008).
48. Zheng, Z. et al. Structured sampling of olfactory input by the fly mushroom body. *Curr. Biol.* **32**, 3334–3349.e6 (2022).
49. Lin, A. et al. Network statistics of the whole-brain connectome of *Drosophila*. Preprint at *bioRxiv* <https://doi.org/10.1101/2023.07.29.551086> (2023).
50. Dorkenwald, S. et al. CAVE: Connectome Annotation Versioning Engine. Preprint at *bioRxiv* <https://doi.org/10.1101/2023.07.26.550598> (2023).
51. Schüz, A. & Palm, G. Density of neurons and synapses in the cerebral cortex of the mouse. *J. Comp. Neurol.* **286**, 442–455 (1989).
52. Dorkenwald, S. et al. Automated synaptic connectivity inference for volume electron microscopy. *Nat. Methods* **14**, 435–442 (2017).
53. Schneider-Mizell, C. M. et al. Quantitative neuroanatomy for connectomics in *Drosophila*. *eLife* **5**, e12059 (2016).
54. Phelps, J. S. et al. Reconstruction of motor control circuits in adult *Drosophila* using automated transmission electron microscopy. *Cell* **184**, 759–774.e18 (2021).
55. Takemura, S.-Y. et al. A connectome of the male *Drosophila* ventral nerve cord. *eLife* **13**, RP97769 (2024).
56. Marin, E. C. et al. Systematic annotation of a complete adult male *Drosophila* nerve cord connectome reveals principles of functional organisation. Preprint at *bioRxiv* <https://doi.org/10.1101/2023.06.05.543407> (2023).
57. Kim, H. et al. Wiring patterns from auditory sensory neurons to the escape and song-relay pathways in fruit flies. *J. Comp. Neurol.* **528**, 2068–2098 (2020).
58. Sterne, G. R., Otsuna, H., Dickson, B. J. & Scott, K. Classification and genetic targeting of cell types in the primary taste and premotor center of the adult *Drosophila* brain. *eLife* **10**, e71679 (2021).
59. Azevedo, A. et al. Connectomic reconstruction of a female *Drosophila* ventral nerve cord. *Nature* **631**, 360–368 (2024).
60. Wu, M. et al. Visual projection neurons in the *Drosophila* lobula link feature detection to distinct behavioral programs. *eLife* **5**, e21022 (2016).
61. Otsuna, H. & Ito, K. Systematic analysis of the visual projection neurons of *Drosophila melanogaster*. I. Lobula-specific pathways. *J. Comp. Neurol.* **497**, 928–958 (2006).
62. Zhao, A. et al. A comprehensive neuroanatomical survey of the *Drosophila* lobula plate tangential neurons with predictions for their optic flow sensitivity. Preprint at *bioRxiv* <https://doi.org/10.1101/2023.10.16.562634> (2023).
63. Répérant, J. et al. The centrifugal visual system of vertebrates: a comparative analysis of its functional anatomical organization. *Brain Res. Rev.* **52**, 1–57 (2006).
64. Karupudurai, T. et al. A hard-wired glutamatergic circuit pools and relays UV signals to mediate spectral preference in *Drosophila*. *Neuron* **81**, 603–615 (2014).
65. Meinertzhagen, I. A. Of what use is connectomics? A personal perspective on the *Drosophila* connectome. *J. Exp. Biol.* **221**, jeb164954 (2018).
66. Chklovskii, D. B. Synaptic connectivity and neuronal morphology: two sides of the same coin. *Neuron* **43**, 609–617 (2004).
67. Kremer, M. C., Jung, C., Batelli, S., Rubin, G. M. & Gaul, U. The glia of the adult *Drosophila* nervous system. *Glia* **65**, 606–638 (2017).
68. Ohyama, T. et al. A multilevel multimodal circuit enhances action selection in *Drosophila*. *Nature* **520**, 633–639 (2015).
69. Hong, E. J. & Wilson, R. I. Simultaneous encoding of odors by channels with diverse sensitivity to inhibition. *Neuron* **85**, 573–589 (2015).
70. Meier, M. & Borst, A. Extreme compartmentalization in a *Drosophila* amacrine cell. *Curr. Biol.* **29**, 1545–1550.e2 (2019).
71. Croset, V., Treiber, C. D. & Waddell, S. Cellular diversity in the *Drosophila* midbrain revealed by single-cell transcriptomics. *eLife* **7**, e34550 (2018).
72. Molina-Obando, S. et al. ON selectivity in the *Drosophila* visual system is a multisynaptic process involving both glutamatergic and GABAergic inhibition. *eLife* **8**, e49373 (2019).
73. Liu, W. W. & Wilson, R. I. Glutamate is an inhibitory neurotransmitter in the *Drosophila* olfactory system. *Proc. Natl Acad. Sci. USA* **110**, 10294–10299 (2013).
74. Zingg, B. et al. Neural networks of the mouse neocortex. *Cell* **156**, 1096–1111 (2014).
75. Oh, S. W. et al. A mesoscale connectome of the mouse brain. *Nature* **508**, 207–214 (2014).
76. Markov, N. T. et al. A weighted and directed interareal connectivity matrix for macaque cerebral cortex. *Cereb. Cortex* **24**, 17–36 (2014).
77. Meissner, G. W. et al. A searchable image resource of *Drosophila* GAL4 driver expression patterns with single neuron resolution. *eLife* **12**, e80660 (2023).
78. Chiang, A.-S. et al. Three-dimensional reconstruction of brain-wide wiring networks in *Drosophila* at single-cell resolution. *Curr. Biol.* **21**, 1–11 (2011).
79. Kasthuri, N. & Lichtman, J. W. The rise of the 'projectome'. *Nat. Methods* **4**, 307–308 (2007).
80. Ito, K. et al. A systematic nomenclature for the insect brain. *Neuron* **81**, 755–765 (2014).
81. Fischbach, K.-F. & Dittrich, A. P. M. The optic lobe of *Drosophila melanogaster*. I. A Golgi analysis of wild-type structure. *Cell Tissue Res.* **258**, 441–475 (1989).
82. Nern, A., Pfeiffer, B. D. & Rubin, G. M. Optimized tools for multicolor stochastic labeling reveal diverse stereotyped cell arrangements in the fly visual system. *Proc. Natl Acad. Sci. USA* **112**, E2967–E2976 (2015).
83. Bae, J. A. et al. Digital museum of retinal ganglion cells with dense anatomy and physiology. *Cell* **173**, 1293–1306.e19 (2018).
84. Shinomiya, K., Nern, A., Meinertzhagen, I. A., Plaza, S. M. & Reiser, M. B. Neuronal circuits integrating visual motion information in *Drosophila melanogaster*. *Curr. Biol.* **32**, 3529–3544.e2 (2022).
85. Lappalainen, J. K. et al. Connectome-constrained networks predict neural activity across the fly visual system. *Nature* <https://doi.org/10.1038/s41586-024-07939-3> (2024).
86. Snell, N. J. et al. Complex representation of taste quality by second-order gustatory neurons in *Drosophila*. *Curr. Biol.* **32**, 3758–3772.e4 (2022).
87. Vogt, K. et al. Direct neural pathways convey distinct visual information to *Drosophila* mushroom bodies. *eLife* **5**, e14009 (2016).
88. Mu, S. et al. 3D reconstruction of cell nuclei in a full *Drosophila* brain. Preprint at *bioRxiv* <https://doi.org/10.1101/2021.11.04.467197> (2021).
89. Hofbauer, A. & Buchner, E. Does *Drosophila* have seven eyes? *Naturwissenschaften* **76**, 335–336 (1989).
90. Hu, K. G., Reichert, H. & Stark, W. S. Electrophysiological characterization of *Drosophila* ocelli. *J. Comp. Physiol.* **126**, 15–24 (1978).
91. Stark, W. S., Sapp, R. & Carlson, S. D. Ultrastructure of the ocellar visual system in normal and mutant *Drosophila melanogaster*. *J. Neurogenet.* **5**, 127–153 (1989).
92. Stange, G., Stowe, S., Chahl, J. S. & Massaro, A. Anisotropic imaging in the dragonfly median ocellus: a matched filter for horizon detection. *J. Comp. Physiol. A* **188**, 455–467 (2002).
93. Cheong, H. S. J. et al. Transforming descending input into behavior: the organization of premotor circuits in the *Drosophila* male adult nerve cord connectome. Preprint at *bioRxiv* <https://doi.org/10.1101/2023.06.07.543976> (2023).
94. Suver, M. P., Huda, A., Iwasaki, N., Safarik, S. & Dickinson, M. H. An array of descending visual interneurons encoding self-motion in *Drosophila*. *J. Neurosci.* **36**, 11768–11780 (2016).
95. Haag, J., Wertz, A. & Borst, A. Integration of lobula plate output signals by DNOV51, an identified premotor descending neuron. *J. Neurogenet.* **27**, 1992–2000 (2007).
96. Kim, A. J., Fenk, L. M., Lyu, C. & Maimon, G. Quantitative predictions orchestrate visual signaling in *Drosophila*. *Cell* **168**, 280–294.e12 (2017).
97. Braitenberg, V. *Vehicles: Experiments in Synthetic Psychology* (MIT Press, 1984).
98. Seung, H. S. *Connectome: How the Brain's Wiring Makes Us Who We Are* (Houghton Mifflin Harcourt, 2012).
99. Davis, F. P. et al. A genetic, genomic, and computational resource for exploring neural circuit function. *eLife* **9**, e50901 (2020).
100. Groschner, L. N., Malis, J. G., Zuidinga, B. & Borst, A. A biophysical account of multiplication by a single neuron. *Nature* **603**, 119–123 (2022).
101. Ammer, G. et al. Multilevel visual motion opponency in *Drosophila*. *Nat. Neurosci.* **26**, 1894–1905 (2023).
102. Knott, G., Marchman, H., Wall, D. & Lich, B. Serial section scanning electron microscopy of adult brain tissue using focused ion beam milling. *J. Neurosci.* **28**, 2959–2964 (2008).
103. Xu, C. S. et al. Enhanced FIB-SEM systems for large-volume 3D imaging. *eLife* **6**, e25916 (2017).
104. Hayworth, K. J. et al. Gas cluster ion beam SEM for imaging of large tissue samples with 10 nm isotropic resolution. *Nat. Methods* **17**, 68–71 (2020).
105. Denk, W. & Horstmann, H. Serial block-face scanning electron microscopy to reconstruct three-dimensional tissue nanostructure. *PLoS Biol.* **2**, e329 (2004).
106. Leighton, S. B. SEM images of block faces, cut by a miniature microtome within the SEM - a technical note. *Scan. Electron Microsc.* **1981**, 73–76 (1981).
107. Macrina, T. et al. Petascale neural circuit reconstruction: automated methods. Preprint at *bioRxiv* <https://doi.org/10.1101/2021.08.04.455162> (2021).
108. Popovych, S. et al. Petascale pipeline for precise alignment of images from serial section electron microscopy. *Nat. Commun.* **15**, 289 (2024).
109. Januszewski, M. et al. High-precision automated reconstruction of neurons with flood-filling networks. *Nat. Methods* **15**, 605–610 (2018).

110. Jain, V. et al. Supervised learning of image restoration with convolutional networks. In *Proc. 2007 IEEE 11th International Conference on Computer Vision* 636–643 (IEEE, 2007).

111. Turaga, S. C. et al. Convolutional networks can learn to generate affinity graphs for image segmentation. *Neural Comput.* **22**, 511–538 (2010).

112. Maitin-Shepard, J. *Neuroglancer*. <https://github.com/google/neuroglancer> (2020).

113. Veraszto, C. et al. Whole-animal connectome and cell-type complement of the three-segmented *Platynereis dumerilii* larva. Preprint at *bioRxiv* <https://doi.org/10.1101/2020.08.21.260984> (2020).

114. Schoofs, A. et al. Serotonergic reinforcement of a complete swallowing circuit. Preprint at *bioRxiv* <https://doi.org/10.1101/2023.05.26.542464> (2023).

115. Ngai, J. BRAIN 2.0: transforming neuroscience. *Cell* **185**, 4–8 (2022).

116. Jefferis, G., Collinson, L., Bosch, C., Costa, M. & Schlegel, P. *Scaling up Connectomics: the road to a whole mouse brain connectome* (Wellcome, 2023).

117. Collins, F. S., Morgan, M. & Patrinos, A. The Human Genome Project: lessons from large-scale biology. *Science* **300**, 286–290 (2003).

118. Heinrich, L., Funke, J., Pape, C., Nunez-Iglesias, J. & Saalfeld, S. Synaptic cleft segmentation in non-isotropic volume electron microscopy of the complete *Drosophila* brain. In *Medical Image Computing and Computer Assisted Intervention – MICCAI 2018* (eds Frangi, A. F. et al.) 317–325 (Springer, 2018).

119. Bates, A. S. et al. The natterse: a versatile toolbox for combining and analysing neuroanatomical data. *eLife* **9**, e53350 (2020).

Publisher's note Springer Nature remains neutral with regard to jurisdictional claims in published maps and institutional affiliations.



Open Access This article is licensed under a Creative Commons Attribution 4.0 International License, which permits use, sharing, adaptation, distribution and reproduction in any medium or format, as long as you give appropriate credit to the original author(s) and the source, provide a link to the Creative Commons licence, and indicate if changes were made. The images or other third party material in this article are included in the article's Creative Commons licence, unless indicated otherwise in a credit line to the material. If material is not included in the article's Creative Commons licence and your intended use is not permitted by statutory regulation or exceeds the permitted use, you will need to obtain permission directly from the copyright holder. To view a copy of this licence, visit <http://creativecommons.org/licenses/by/4.0/>.

© The Author(s) 2024

The FlyWire Consortium

Krzysztof Kruk³, Doug Bland¹, Zairene Lenizo¹⁶, Austin T. Burke¹, Kyle Patrick Willie¹, Alexander Shakeel Bates^{4,5,12,13}, Nikitas Serafetinidis³, Nashra Hadjerol¹⁶, Ryan Willie¹, Katharina Eichler⁵, Ben Silverman¹, John Anthony Ocho¹⁶, Joshua Bañez¹⁶, Yijie Yin⁵, Rey Adrian Candilada¹⁶, Sven Dorkenwald¹², Jay Gager¹, Anne Kristiansen³, Nelsie Panes¹⁶, Arti Yadav¹⁷, Remer Tancontian¹⁶, Shirleyjoy Serona¹⁶, Jet Ivan Dolorosa¹⁶, Kendrick Jules Vinson¹⁶, Dustin Garner¹⁶, Regine Salem¹⁶, Ariel Dagohoy¹⁶, Philipp Schlegel¹⁵, Jaime Skelton³, Mendell Lopez¹⁶, Laia Serratos Capdevila⁵, Griffin Badalamente⁵, Thomas Stocks⁵, Anjali Pandey¹⁷, Darrel Jay Akiatan¹⁶, James Hebditch¹, Celia David¹, Dharini Sapkal¹⁷, Shaina Mae Monungolh¹⁶, Varun Sane⁵, Mark Lloyd Pielago¹⁶, Miguel Albero¹⁶, Jacquilyn Laude¹⁶, Márcia dos Santos⁵, David Deutsch¹⁹, Zeba Vohra¹⁷, Kaiyu Wang¹⁴, Allien Mae Gogo¹⁶, Emil Kind¹⁹, Alvin Josh Mandahay¹⁶, Chereb Martinez¹⁶, John David Asis¹⁶, Chitra Nair¹⁷, Dhvani Patel¹⁷, Marchan Manaytay¹⁶, Imaan F. M. Tamim¹⁵, Clyde Angelo Lim¹⁶, Philip Lenard Ampo¹⁶, Michelle Darapan Pantujan¹⁶, Alexandre Javier⁵, Daril Bautista¹⁶, Rashmita Rana¹⁷, Jansen Seguido¹⁶, Bhargavi Parmar¹⁷, John Clyde Saguimpa¹⁶, Merlin Moore¹, Markus William Pleijzier⁴, Mark Larson²⁰, Joseph Hsu⁵, Itisha Joshi¹⁷, Dhara Kakadiya¹⁷, Amalia Braun¹, Cathy Pilapil¹⁶, Marina Gkantia⁵, Kaushik Parmar¹⁷, Quinn Vanderbeck¹², Claire E. McKellar¹, Irene Salgarella³, Christopher Dunne⁵, Eva Munnelly⁵, Chan Hyuk Kang²², Lena Lörsch²³, Jinmook Lee²², Lucia Kmevcova²⁴, Gizem Sancer²⁵, Christa Baker¹, Szi-chieh Yu¹, Jenna Joroff¹², Steven Calle²⁴, Yashvi Patel¹⁷, Olivia Sato²⁰, Siqi Fang⁵, Janice Salocot¹⁶, Farzaan Salman²⁶, Sebastian Molina-Obando²³, Paul Brooks⁵, Mai Bui²⁷, Matthew Lichtenberger³, Edward Tamboboy¹⁶, Katie Molloy²⁰,

Alexis E. Santana-Cruz²⁴, Anthony Hernandez³, Seongbong Yu²², Marissa Sorek¹³, Arzoo Diwan¹⁷, Monika Patel¹⁷, Travis R. Aiken³, Sarah Morejohn¹, Sanna Koskela¹⁴, Tansy Yang¹⁴, Daniel Lehmann³, Jonas Chojetzki²³, Sangeeta Sisodiya¹⁷, Selden Koolman¹, Philip K. Shiu²⁸, Sky Cho²⁷, Annika Bast²³, Brian Reicher²⁰, Marlon Blaquart⁵, Lucy Houghton¹⁸, Hyunjung Choi²², Maria Ioannidou²³, Matt Collie²⁰, Joanna Eckhardt¹, Benjamin Gorko¹⁸, Li Guo¹⁸, Zhihao Zheng¹, Alisa Poh²⁹, Marina Lin²⁷, István Taisz², Wes Murfin³⁰, Álvaro Sanz Díez³¹, Nils Reinhard³², Peter Gibb¹², Nidhi Patel¹⁷, Sandeep Kumar¹, Minsik Yun³³, Megan Wang¹, Devon Jones¹, Lucas Encarnacion-Rivera³⁴, Annalena Oswald²³, Akanksha Jadia¹⁷, Mert Erginkaya²⁵, Nik Drummond⁵, Leonie Walter³⁹, Ibrahim Tastekin³⁵, Xin Zhong¹⁹, Yuta Mabuchi³⁶, Fernando J. Figueroa Santiago²⁴, Urja Verma¹⁷, Nick Byrne²⁰, Edda Kunze¹⁹, Thomas Crahan¹⁸, Ryan Margossian³, Haein Kim³⁶, Iliyan Georgiev², Fabianna Szorenyi²⁴, Atsuko Adachi³¹, Benjamin Barger³⁷, Tomke Stürner⁴⁵, Damian Demarest³⁶, Burak Gür²³, Andrea N. Becker³, Robert Turnbull¹⁵, Miriam A. Flynn¹⁴, Andrea Sandoval²⁸, Anthony Moreno-Sanchez³⁹, Diego A. Pacheco¹², Eleni Samara²¹, Haley Croke³⁹, Alexander Thomson¹⁴, Connor Laughland¹⁴, Suchetana B. Dutta¹⁹, Paula Guiomar Alarcón de Antón¹⁹, Binglin Huang¹⁶, Patricia Pujols²⁴, Isabel Haber²⁰, Amanda González-Segarra²⁸, Albert Lin¹⁴, Daniel T. Choe¹⁰, Veronika Lukyanova⁴¹, Marta Costa⁵, Nino Mancini³⁷, Zequan Liu¹², Tatsuo Okubo¹², Jinseong Kim²², Gianna Vitelli³⁷, Meghan Laturney²⁸, Feng Li¹⁴, Shuo Cao⁴³, Carolina Manyari-Diaz³⁷, Hyunsoo Yim⁴⁰, Anh Duc Le³⁹, Kate Maier³⁷, Seungyun Yu²², Yeonju Nam²², Daniel Bába³, Amanda Abusaif²⁸, Audrey Francis¹⁴, Jesse Gayk¹⁷, Sommer S. Huntress⁴⁵, Raquel Barajas³⁵, Mindy Kim²⁰, Xinyue Cui³⁶, Amy R. Sterling¹³, Gabriella R. Sterne²⁶, Anna Li¹², Keehyun Park²², Georgia Dempsey², Alan Mathew³⁷, Jinseong Kim²², Taewon Kim²², Guan-ting Wu⁴⁶, Serene Dhawan¹⁷, Margarida Brotas³⁵, Cheng-hao Zhang⁴⁶, Shanice Bailey⁵, Alexander Del Toro²⁸, Arie Matsliah¹, Kisuk Lee¹¹⁰, Thomas Macrina¹², Casey Schneider-Mizell¹⁷, Sergiy Popovych¹², Oluwaseun Ogedengbe¹, Runzhe Yang¹, Akhilesh Halageri¹, Will Silversmith¹, Stephan Gerhard⁴⁵, Andrew Champion⁴⁵, Nils Eckstein¹⁴, Dodam Ih¹, Nico Kemnitz¹, Manuel A. Castro¹, Zhen Jia¹, Jingpeng Wu¹, Eric Mitchell¹, Barak Nehoran¹², Shang Mu¹, J. Alexander Bae¹¹¹, Ran Lu¹, Eric Perlman⁵, Ryan Morey¹, Kai Kuehner¹, Derrick Brittain¹, Chris S. Jordan¹, David J. Anderson¹³, Rudy Behnia³¹, Salil S. Bidaye³⁷, Davi D. Bock¹⁵, Alexander Borst²¹, Eugenia Chiappe³⁵, Forrest Collman⁷, Kenneth J. Colodner⁴⁵, Andrew Dacks²⁶, Barry Dickson¹⁴, Jan Funke¹⁴, Denise Garcia³⁹, Stefanie Hampel²⁴, Volker Hartenstein⁴⁹, Bassem Hassan¹⁹, Charlotte Helfrich-Forster³², Wolf Hueteroth⁵⁰, Gregory S. X. E. Jefferis⁴⁵, Jinseop Kim²², Sung Soo Kim¹⁶, Young-Joon Kim³³, Jae Young Kwon²², Wei-Chung Lee¹², Gerit A. Linneweber¹⁹, Gaby Maimon¹⁴, Richard Mann³, Mala Murthy¹, Alexander Noselli⁵¹, Michael Pankratz²⁹, Lucia Prieto-Godino⁴⁷, Jenny Read⁴¹, Michael Reiser¹⁴, Katie von Reyn²⁹, Carlos Ribeiro³⁵, Kristin Scott²⁹, Andrew M. Seeds²⁴, Mareike Selcho⁵⁰, H. Sebastian Seung¹², Marion Silies²³, Julie Simpson¹⁸, Scott Waddell⁵², Mathias F. Wernet¹⁹, Rachel I. Wilson¹², Fred W. Wolf⁵³, Zepeng Yao⁵⁴, Nilay Yapici³⁶ & Meet Zandawala³²

¹⁶SixEleven, Davao City, Philippines. ¹⁷ariadne.ai, Buchrain, Switzerland. ¹⁸University of California, Santa Barbara, CA, USA. ¹⁹Freie Universität Berlin, Berlin, Germany. ²⁰Harvard, Boston, MA, USA. ²¹Department Circuits-Computation-Models, Max Planck Institute for Biological Intelligence, Planegg, Germany. ²²Sungkyunkwan University, Seoul, South Korea. ²³Johannes-Gutenberg University Mainz, Mainz, Germany. ²⁴Institute of Neurobiology, University of Puerto Rico Medical Sciences Campus, San Juan, Puerto Rico. ²⁵Department of Neuroscience, Yale University, New Haven, CT, USA. ²⁶Department of Biology, West Virginia University, Morgantown, WV, USA. ²⁷Program in Neuroscience and Behavior, Mount Holyoke College, South Hadley, MA, USA. ²⁸University of California, Berkeley, CA, USA. ²⁹University of Queensland, Brisbane, Queensland, Australia. ³⁰Independent researcher, Fort Collins, CO, USA. ³¹Zuckerman Institute, Columbia University, New York, NY, USA. ³²Julius-Maximilians-Universität Würzburg, Würzburg, Germany. ³³Gwangju Institute of Science and Technology, Gwangju, South Korea. ³⁴Stanford University School of Medicine, Stanford, CA, USA. ³⁵Champalimad Foundation, Lisbon, Portugal. ³⁶Cornell University, Ithaca, NY, USA. ³⁷Max Planck Florida Institute for Neuroscience, Jupiter, FL, USA. ³⁸University of Bonn, Bonn, Germany. ³⁹Drexel, Philadelphia, PA, USA. ⁴⁰Seoul National University, Seoul, South Korea. ⁴¹Newcastle University, Newcastle, UK. ⁴²RWTH Aachen University, Aachen, Germany. ⁴³Caltech, Pasadena, CA, USA. ⁴⁴Rockefeller University, New York, NY, USA. ⁴⁵Mount Holyoke College, South Hadley, MA, USA. ⁴⁶National Hualien Senior High School, Hualien, Taiwan. ⁴⁷The Francis Crick Institute, London, UK. ⁴⁸Aware, Zurich, Switzerland. ⁴⁹University of California, Los Angeles, CA, USA. ⁵⁰Institute of Biology, Leipzig University, Leipzig, Germany. ⁵¹Université Côte d'Azur, CNRS, Inserm, iBV, Nice, France. ⁵²University of Oxford, Oxford, UK. ⁵³University of California, Merced, CA, USA. ⁵⁴University of Florida, Gainesville, FL, USA.

Methods

Specimen, alignment and segmentation

Multiple brains of 7-day-old (iso) w1118 × (iso) Canton-S/G1 adult female flies were screened by Zheng et al.⁹ and one was picked for electron microscopy imaging. Zheng et al.⁹ published the original electron microscopy stack (FAFB14) which we previously realigned⁸ (FAFB14.1) using a neural network trained to predict pairwise displacement fields^{108,120}. We produced transformations between the FAFB14 and FAFB14.1 which are accessible via *natverse*, *navis* and *flybrains*. We automatically segmented all cells in the dataset⁸ using a neuronal boundary-detecting neural network¹²¹ and mean affinity agglomeration^{107,122}.

Neuropils

Meshes for individual neuropils were based on work by Ito et al.⁸⁰. More specifically, we took meshes previously generated from a full brain segmentation of the JFRC2 template brain which are also used by the Virtual Fly Brain project (see also <https://natverse.org/nat.flybrains/reference/JFRC2NP.surf.html>). These meshes were moved from JFRC2 into FlyWire (FAFB14.1) space through a series of non-rigid transforms. In addition, we also generated two neuropil meshes for the laminae and for the ocellar ganglion. For these, the FlyWire synapse cloud was voxelized with 2 μm isotropic resolution, meshed using the marching cube algorithm using Python and manually post-processed in Blender 3d.

We calculated a volume for each neuropil using its mesh. In the aggregated volumes presented in the paper we assigned the lamina, medulla, accessory medulla, lobula and lobula plate to the optic lobe. The remaining neuropils but the ocellar ganglion were assigned to the central brain.

Neuropil synapse assignments

We assigned synapses to neuropils based on their presynaptic location. We used *ncollpyde* (<https://pypi.org/project/ncollpyde/>) to calculate whether the location was within a neuropil mesh and assigned the synapse accordingly. Some synapses remained unassigned after this step because the neuropils only resemble rough outlines of the underlying data. We then assigned all remaining synapses to the closest neuropil if the synapse was within 10 μm from it. The remaining synapses were left unassigned.

Correction of left–right inversion

Our reconstruction used the FAFB electron microscopy dataset⁹. A number of consortium members (A. Bates, P. Kandimalla and S. Noselli) alerted us that the FAFB imagery seemed to be left–right inverted based on the cell types innervating the asymmetric body¹²³. Eventually a left–right inversion during FAFB imaging was confirmed. All side annotations in figures, in *Codex* and elsewhere are based on the true biological side. For technical reasons, we were unable to invert the underlying FAFB image data and therefore continue to show images and reconstructions in the same orientation as in Zheng et al.⁹, although we now know that in such frontal views the fly's left is on the viewer's left. For full details of this issue including approaches to display FAFB and other brain data with the correct chirality, please see the companion paper¹².

Proofreading system

FlyWire uses CAVE⁵⁰ for hosting the proofreadable segmentation and all of its annotations. CAVE's proofreading system is the *PyChunkedGraph* which has been described in detail elsewhere^{8,124}.

Proofreading annotations

Any user in FlyWire was able to mark a cell as complete, indicating that a cell was good for analysis. However, such annotations did not prevent future proofreading of a cell as commonly smaller branches were added later on. We created an annotation table for these completion markings. Each completion marking was defined by a point in space

and the cell segment that overlapped with this point at any given time during proofreading was associated with the annotation. We created a webservice allowing users to submit completion markings for any cell. For convenience, we added an interface to this surface directly into Neuroglancer such that users can submit completion information for cells right after proofreading (Supplementary Fig. 10). When users submitted completion annotations we also recorded the current state of the cell. We encouraged users to submit new completion markings for a cell that they edited to indicate that edits were intentional. Recording the status of a cell at submission enabled us to calculate volumetric changes to a cell through further proofreading and flag cells for review if they received substantial changes without new completion markings.

Onboarding proofreaders

Proofreaders came from several distinct labour pools: community members, citizen scientists from Eyewire (Flyers), and professional proofreading teams at Princeton and Cambridge. Proofreaders at Princeton consisted of staff at Princeton University and at SixEleven. Similarly, proofreading at Cambridge was performed by staff at Cambridge University and Ariadne. All proofreaders completed the built-in interactive tutorial and were directed to self-guided proofreading training. For practice and learning purposes, the Sandbox, a complete replica of the FlyWire data, allowed new users to freely make edits and explore without affecting the actual 'Production' dataset. When ready, an onboarding coordinator tested the new proofreader before giving access to the Production dataset⁸. Later onboarding called for users to send demonstration Sandbox edits that were reviewed by the onboarding coordinator. A new class of view-only users was introduced in early 2023, allowing researchers early data access for analysis purposes. All early access users attended a live onboarding session in Zoom prior to being granted edit or view access.

Training the professional proofreading team

The professional proofreading team received additional proofreading training. Correct proofreading relies on a diverse array of 2D and 3D visual cues. Proofreaders learned about 3D morphology, resulting from false merger or false split without knowing what types of cells they are. Proofreaders studied various types of ultrastructures as the ultrastructures provide valuable 2D cues and serve as reliable guides for accurate tracing. Before professional proofreaders were admitted into Production, each of them practiced on average >200 cells in a testing dataset where additional feedback was given. In this dataset, we determined the accuracy of test cells by comparing them to ground-truth reconstructions. To improve proofreading quality, peer learning was highly encouraged.

Recruitment of citizen scientists

The top 100 players from Eyewire, a gamified electron microscopy reconstruction platform that crowdsources reconstructions in mouse retina and zebrafish hindbrain¹²⁵, received an invitation to beta test proofreading in FlyWire. A new set of user onboarding and training materials were created for citizen scientists, including: a blog, forum and public Google docs. We created bite-sized introduction videos, a comprehensive FlyWire 101 resource, as well as an Optic Lobe Cell Guide to aid users in understanding the unique morphology of flies. A virtual Citizen Science Symposium introduced players to the project, after which the self-dubbed 'Flyers' began creating their own resources, such as a new comprehensive visual guide to cell types, conducting literature reviews, and even developing helpful FlyWire plugins. As of publication, FlyWire has 12 add-on apps ranging from a batch processor to cell naming helper (<https://blog.flywire.ai/2022/08/11/flywire-addons/>).

Proofreading strategy to complete the connectome

As previously described⁸, proofreading of the connectome was focused on the microtubule-rich 'backbones' of neurons. Microtubule-free

Article

'twigs' were only added if discovered incidentally or sought out specifically by members of the community. After proofreading, users marked neuronal segments as 'complete' indicating that neurons were ready for analysis but further changes remained possible. While *Drosophila* neuroscientist members of the FlyWire community generally contributed proofreading for their neurons of interest, the bulk of the segments was proofread by professional proofreaders in the following way. First, we proofread all segments with an automatically detected nucleus in the central brain⁸⁸ by extending it as much as possible and removing all false mergers (pieces of other neurons or glia attached). Second, we proofread the remaining segments in descending order of their synapse count (pre+post) up to a predefined size threshold of 100 synapses. Third, we proofread remaining segments if they had at least one connection containing at least 15 synapses.

Quality assurance

To assess quality, a group of expert centralized proofreaders conducted a review of 3,106 segments in the central brain. These specific neurons were chosen based on certain criteria such as significant change since being marked complete and small overall volume. An additional 826 random neurons were included in the review pool as well. Proofreaders were unaware which neurons were added for quality measurement and which ones because they were flagged by a metric. We compared the 826 neurons before and after the review and found that the initial reconstruction scored an average F1-Score of 99.2% by volume (Extended Data Fig. 2a,b). F1-Score is defined as the harmonic mean of recall (R) and precision (P) with precision defined as the ratio of true positives (TP) among positively classified elements (TP + FP (false positives)) and recall defined as the ratio of TPs among all true elements (TP + FN (false negatives)).

$$P = \frac{TP}{TP + FP}$$
$$R = \frac{TP}{TP + FN}$$
$$F1 = \frac{2 \times P \times R}{P + R}$$

Quantification of proofreading effort

Any quantification of the total proofreading time that was required to create the FlyWire resource is a rough estimate because of the distributed nature of the community, the interlacing of analysis and proofreading and the variability in how proofreading was performed. The second public release, version 783, required 3,013,513 edits. We measured proofreading times during early proofreading rounds that included proofreading of whole cells in the central brain. We collected timings and number of edits for 29,135 independent proofreading tasks after removing outliers with more than 500 edits. From these data, we were able to calculate an average time per edit. However, we observed that proofreading times per edit were much higher for proofreading tasks that required few edits (<5). That meant that our measurements were not representative for the second round of proofreading which went over all segments with >100 synapses. These usually required 1–5 edits. We adjusted for that by computing estimates for proofreading speeds of both rounds by limiting the calculations to a subset of the timed tasks: (round 1) The average time per edit in our proofreading time dataset, (round 2) the average time of tasks with 1–5 edits. We averaged these times for an overall proofreading time because the number of tasks in each category were similar. The result was an average time of 79 s per edit which adds up to an estimate of 33.1 person-years assuming a 2,000 h work year.

Attachment rates

We adopted the attachment rate (also referred to as 'completion rate') calculations from the hemibrain¹. Every presynaptic and postsynaptic location was assigned to a segment. Using the neuropil assignments,

we then calculated the fraction of presynapses that were assigned to segments marked as proofread for each neuropil and analogous for postsynaptic locations.

Comparison with the hemibrain

We retrieved the latest completion rates and synapse numbers for the hemibrain from neuprint (v1.2.1). In some cases, neuropil comparisons were not directly possible because of redefined regions in the hemibrain dataset. We excluded these regions from the comparison.

Crowdsourced annotation

The large FlyWire community and diversity of expertise enabled us to crowdsourcing the identification of neurons. There is no limit to the number of annotations a neuron can receive. A standardized format is encouraged but not required. One user might first report that a neuron is a descending interneuron, whereas another might add that it is the giant fibre descending neuron, and yet another might add all its synonyms and citations from the literature. Contributors' names are visible so they can be consulted if there is disagreement. The disadvantage to this approach is that there is no single precise name for every neuron, but the advantage is a richness of information and dialogue. The annotations are not meant to be a finished, static list, but rather a continually growing, living data source. These annotations were solicited from the FlyWire community through town halls, email announcements, interest groups in the FlyWire forum, online instructions, and by personal contact from the community manager. Citizen scientists also contributed annotations, after receiving training on particular cell types by experts.

Neuron categorizations

Neuron categorization, sensory modality annotations and nerve assignments are described in detail in our companion paper¹². In brief, neurons were assigned to one of three 'flow' classes: afferent (to the brain), intrinsic (within the brain) and efferent (out of the brain). Intrinsic neurons had their entire arbor within the FlyWire brain dataset. This included cells that projected to and from the SEZ. Next, each flow class was divided into superclasses in the following way. afferent: sensory, ascending. intrinsic: central, optic, visual projection (from the optic lobes to the central brain), visual centrifugal (from the central brain to the optic lobes). efferent: endocrine, descending, motor.

Quantification of intrinsic neurons

We define whether a neuron is 'intrinsic' to a region on the basis of its synapse locations, rather than its arbor. In other words, the neurites of an intrinsic neuron are allowed to exit the region, provided that they do not make synapses after leaving. Information about *C. elegans* synapse locations was obtained from the diagrams in White et al.³¹.

The 'brain' of *C. elegans* can be defined as the neuropil extending from the ring-shaped structure around the pharynx to the excretory pore. (We follow the authors who call this region the nerve ring plus the anterior portion of the ventral nerve cord, though some authors refer to the combined structure as the nerve ring.) Nine neurons (RIR, RIV, RMDD, RMD and RMDV) are intrinsic to the nerve ring itself. An additional 26 neurons (AIA, AIB, AIM, AIN, AIY, AIZ, RIA, RIB, RIC, RIH, RIM, RIS, RMF and RMH) are intrinsic to the combined structure, for a total of 35 intrinsic neurons in the brain.

It should be understood that this estimate has 'error bars' because of definitional ambiguities. Ten motor neurons (RMH, RMF and RMD) could arguably be removed from the list, as it is unclear whether motor neurons qualify as intrinsic neurons. Or the brain could be enlarged by moving the posterior border further behind the excretory pore, which would add 10 neurons (RIF, RIG, RMG, ADE and ADA). To make these ambiguities explicit, we estimate 35 ± 10 intrinsic neurons. Of the 302 CNS neurons, 180 make synapses in the brain¹²⁶. Therefore, neurons intrinsic to the brain make up about 15 to 25% of brain neurons, and 8 to 15% of CNS neurons.

Skeletonization and path length calculation

We generated skeletons for all neurons marked as proofread using skeletor (<https://github.com/navis-org/skeletor>), which implements multiple skeletonization algorithms such as TEASAR²²⁷. In brief, neuron meshes from the exported segmentation (LOD 1) were downloaded and skeletonized using the wavefront method in skeletor. These raw skeletons were then further processed (for example, to remove false twigs and heal breaks) and produce downsampled versions using navis¹²⁸ (<https://github.com/navis-org/navis>). A modified version of this skeletonization pipeline is implemented in fabseg (<https://github.com/navis-org/fabseg-py>).

Quantifying cell volume and surface area

We calculated cell volumes and surface areas using CAVE's L2Cache⁵⁰. Volumes were computed by counting all voxels within a cell segment and multiplying the count by the voxel resolution. Area calculations were more complicated and were performed by overlap through shifts in voxel space. We shifted the binarized segment in each dimension individually and extracted the overlap of false and true voxels. For each dimension, we counted the extracted voxels and multiplied the count by the voxel resolution of the given dimensions. Finally, we added up per dimension area estimates. This measurement will overestimate area slightly but smoothed measurements are ill-defined and were too compute intensive.

Synaptic connections

We imported the automatically predicted synapses from Buhmann et al.⁷, which we combined with the synapse segmentations by Heinrich et al.¹¹⁸ to assign scores to all synapses to improve precision. Buhmann et al. introduced a machine learning model to predict for each voxel whether it is part of a postsynaptic site. For voxels classified as postsynaptic a vector to the presynaptic site is predicted which is then used to create synaptic connections. Hence, synaptic partners predicted by Buhmann et al. are represented by a connector between a postsynaptic and a presynaptic location without further annotation about the size of the synapse. Heinrich et al. on the other hand segmented the synaptic clefts. Buhmann et al. suggested using the probability maps from Heinrich et al. to improve performance by locating the highest probability score along their predicted connectors (called score in the next paragraph).

The synapse classifier by Buhmann et al. was trained on ground truth from the CREMI challenge (<https://cremi.org>). The three CREMI datasets contain three $5 \times 5 \times 5 \mu\text{m}$ cubes from the calyx in FAFB14 with 1,965 synapses. While the classifier from Buhmann et al. was trained and validated on only this dataset, they evaluated its performance on multiple regions (calyx, lateral horn, ellipsoid body and protocerebral bridge). It should be noted that performance varies by region.

The dataset published by Buhmann et al. contained ~244 million synapses. We removed synapses from the imported list if they fulfilled any of the following criteria: (1) either the pre- or postsynaptic location remained unassigned to a segment (proofread or unproofread); (2) It had a score ≤ 50 . Additionally, we removed duplicate synapse annotations between the same pre- and postsynaptic partners, defined as those within a distance of 100 nm from another synapse annotation according to their presynaptic coordinate. After filtering, we were left with ~130 million synapses.

Eckstein et al.¹⁰ created a machine learning model to predict neurotransmitter identities for all synapses from Buhmann et al. based on the electron microscopy imagery alone. Each synapse was assigned a probability for one of six neurotransmitters: acetylcholine, glutamate, GABA, serotonin, dopamine and octopamine. They used neurotransmitter identities published for individual neuronal cell types and built a dataset with 3,025 neurons with known transmitter type assuming

Dale's law applies. Eckstein et al. reported a per-synapse accuracy of 87% and a per neuron (majority vote) accuracy of 94%.

The methods described in this section used the FAFB14 version of the electron microscopy stack. We applied a transformation to all synapses to map them into the FlyWire FAFB14.1 space. The vector field for the transformation had a resolution of $64 \times 64 \times 40 \text{ nm}$.

Connection threshold

For all the analyses presented in this paper, save for synapse distributions, we employed a consistent threshold of >4 . Our decision to use a synapse threshold on connections was due partly to the fact that synapses in the FlyWire's brain dataset were not manually proofread. For these analyses, many of which demonstrate the high interconnectivity of the fly brain, we chose a conservative threshold to ensure that considered connections are real. Use of a threshold is also in keeping with previous work analysing wiring diagrams in *Drosophila*⁷. Thus, we are probably undercounting the number of true connections. The distribution of synapse counts (Fig. 3f) does not display any bimodality that could be used to set the threshold. Therefore, the choice of 5 synapses per connection is a reasonable but arbitrary one. By analysing the network properties of the FlyWire brain connectome, Lin et al. found that statistical properties of the whole-brain network, such as reciprocity and clustering coefficient, are robust to our choice of threshold⁴⁹. The FlyWire data are available without an imposed threshold, so users can choose their own appropriate threshold for their specific use case.

Neuropil projectome construction

Under the simplifying assumptions that information flow through the neuron can be approximated by the fraction of synapses in a given region, and that inputs and outputs can be treated independently, we can construct a matrix representing the projections of a single neuron between neuropils. The fractional inputs of a given neuron are a $1 \times N$ vector containing the fraction of incoming synapses the neuron has in each of the N neuropils, and the fractional outputs are a similar vector containing the fraction of outgoing synapses in each of the N neuropils. We multiply these vectors against each other to generate the $N \times N$ matrix of the neuron's fractional weights. Summing these matrices across all intrinsic neurons produces a matrix of neuropil-to-neuropil connectivity (Fig. 4a). In this projectome, all neurons contribute an equal total weight of one.

Dominant input side

We assigned neuropils to the left and right hemispheres or the centre if the neuropil has no homologue. We then counted how many postsynapses each neuron had in each of these three regions and assigned it to the one with the largest count.

Contralateral and bilateral neuron analysis

For each neuron, we calculated the fraction of presynapses in the left and right hemisphere. The hemisphere opposite its dominant input side was named the contralateral hemisphere. We excluded neurons that had either most of their presynapses or most of their postsynapses in the centre region.

Rank analysis and information flow

We used the information flow algorithm implemented by Schlegel et al.^{26,128} (<https://github.com/navis-org/navis>) to calculate a rank for each neuron starting with a set of seed neurons. The algorithm traverses the synapse graph of neurons probabilistically. The likelihood of a neuron being added to the traversed set increased linearly with the fraction of synapses it receives from already traversed neurons up to 30% and was guaranteed above this threshold. We repeated the rank calculation for all sets of afferent neurons as seed as well as the whole set of sensory neurons. The groups we used are: olfactory receptor neurons, gustatory receptor neurons, mechanosensory Johnston's organ neurons, head and neck bristle mechanosensory neurons, mechanosensory taste

Article

peg neurons, thermosensory neurons, hyrosensory neurons, VPNS, visual photoreceptors, ocellar photoreceptors and ascending neurons.

Additionally, we created input seeds by combining all listed modalities, all sensory modalities, and all listed modalities with visual sensory groups excluded.

For each modality we performed 10,000 runs, which were averaged. We then ordered the neurons according to their rank and assigned them a percentile based on their location in the order. To compute a reduced dimensionality, we treated the vector of all ranks (one for each modality) as neuron embedding and calculated two dimensional embeddings using UMAP¹²⁹ with the following parameters: $n_components=2$, $min_dist=0.35$, $metric = "cosine"$, $n_neighbors=50$, $learning_rate = .1$, $n_epochs=1000$.

Reporting summary

Further information on research design is available in the Nature Portfolio Reporting Summary linked to this article.

Data availability

All data have been made publicly available. Codex (<https://codex.flywire.ai/>), braincircuits.io and Catmaid spaces (<https://fafb-flywire.catmaid.org/>) facilitate non-programmatic access. Most of the data can be directly download from codex (<https://codex.flywire.ai/api/download>). All data, including the volumetric data and meshes, can be programmatically accessed through CAVE and cloudvolume. We provide tutorials for programmatic access at <https://github.com/seung-lab/FlyConnectome>. Data dumps of the connectivity data (<https://doi.org/10.5281/zenodo.10676866>) and flow calculations (<https://doi.org/10.5281/zenodo.12588557>) are made available on zenodo for download.

Code availability

FlyWire uses CAVE for hosting of its proofreading and analysis platform for which all code is publicly available at <https://github.com/CAVEconnectome>. The code for Codex is available at <https://github.com/murthylab/codex>.

- Mitchell, E., Keselj, S., Popovych, S., Buniatyán, D. & Seung, H. S. Siamese encoding and alignment by multiscale learning with self-supervision. Preprint at <https://doi.org/10.48550/arXiv.1904.02643> (2019).
- Lee, K., Zung, J., Li, P., Jain, V. & Seung, H. S. Superhuman accuracy on the SNEM3D Connectomics Challenge. Preprint at <https://doi.org/10.48550/arXiv.1706.00120> (2017).
- Lu, R., Zlateski, A. & Seung, H. S. Large-scale image segmentation based on distributed clustering algorithms. Preprint at <https://doi.org/10.48550/arXiv.2106.10795> (2021).
- Lapraz, F. et al. Asymmetric activity of NetrinB controls laterality of the *Drosophila* brain. *Nat. Commun.* **14**, 1052 (2023).
- Dorkenwald, S. et al. Binary and analog variation of synapses between cortical pyramidal neurons. *eLife* **11**, e76120 (2022).
- Kim, J. S. et al. Space-time wiring specificity supports direction selectivity in the retina. *Nature* **509**, 331–336 (2014).
- Brittin, C. A., Cook, S. J., Hall, D. H., Emmons, S. W. & Cohen, N. A multi-scale brain map derived from whole-brain volumetric reconstructions. *Nature* **591**, 105–110 (2021).
- Sato, M., Bitter, I., Bender, M. A., Kaufman, A. E. & Nakajima, M. TEASAR: tree-structure extraction algorithm for accurate and robust skeletons. In *Proc. 8th Pacific Conference on Computer Graphics and Applications* (eds Barsky, B. A. et al.) (IEEE, 2000); <https://doi.org/10.1109/PCCGA.2000.883951>.

- Schlegel, P. et al. navis-org/navis: version 1.5.0. *Zenodo* <https://doi.org/10.5281/ZENODO.8191725> (2023).
- McInnes, L., Healy, J. & Melville, J. UMAP: uniform manifold approximation and projection for dimension reduction. Preprint at <https://doi.org/10.48550/arXiv.1802.03426> (2018).

Acknowledgements The authors thank J. Wiggins, G. McGrath and D. Barlieb for computer system administration; M. Hussein for project administration; J. Maitin-Shepard for Neuroglancer; P. N. Gomez for help with GPU-cluster deployment; the management at SixEleven and Ariadne for coordination and proofreader management; and T. Sloan for creating the whole-brain renderings and videos. We thank O. Hobert, S. Cook and S. Emmons for contributing their expertise on *C. elegans*. M.M. and H.S.S. acknowledge support from the National Institutes of Health (NIH) BRAIN Initiative RF1 MH117815, RF1 MH129268 and U24 NS126935, from the Princeton Neuroscience Institute, as well as assistance from Google and Amazon. D.D.B. was supported by NIH NIMH BRAIN Initiative grant 1RF1MH120679-01 and a Neuronex2 award (NSF 2014862). G.S.X.E.J. and D.D.B. were supported by a Wellcome Trust Collaborative Award (203261/Z/16/Z). G.S.X.E.J. was supported by Wellcome Trust Collaborative Award 220343/Z/20/Z and a Neuronex2 award (MRC MC_EX_MR/TO46279/1), and received core support from the MRC (MC-U105188491). A.L. was supported by the NSF through the Center for the Physics of Biological Function (PHY-1734030). I. Tastekin was supported with a Marie Skłodowska-Curie postdoctoral fellowship (H2020-WF-01-2018-867459 to Ibrahim Tastekin) and by the Portuguese Research Council (Grant PTDC/MED-NEU/4001/2021). A.S. and S.H. were supported by National Institute Of Neurological Disorders And Stroke of the National Institutes of Health under Award Number RFNS121911. D. Brittain, C.S.-M. and F.C. thank the Allen Institute for Brain Science founder, P. G. Allen, for his vision, encouragement and support. This work was also supported by the Intelligence Advanced Research Projects Activity via Department of Interior/Interior Business Center contract no. D16PC0005 to H.S.S. The US Government is authorized to reproduce and distribute reprints for Governmental purposes notwithstanding any copyright annotation thereon. The views and conclusions contained herein are those of the authors and should not be interpreted as necessarily representing the official policies or endorsements, either expressed or implied, of Intelligence Advanced Research Projects Activity, Department of Interior/Interior Business Center or the US Government.

Author contributions Members of the FlyWire Consortium contributed proofreading and annotations (Supplementary Tables 1 and 2). S.G. provided braincircuits.io. T.M. and N.K. realigned the dataset with methods developed by E.M., B.N. and T.M. and infrastructure developed by S.P. and Z.J. J.A.B. and S.M. wrote code for masking defects and misalignments. K.L. trained the convolutional net for boundary detection, using ground-truth data realigned by D.I. J.W. used the convolutional net to generate an affinity map that was segmented by R.L. N.K., M.A.C., O.O., A.H., C.S.J., K. Kuehner and A.R.S. adapted and improved Neuroglancer for proofreading and annotations. J.G., K. Kruk, A.M., S.D. F.C. and C.S.-M. created interactive analysis and annotation tools for the community. A.M. created Codex with help from A.R.S., S.D., K. Kuehner and R.M. A.R.S. and A.M. created the website. A.R.S., C.E.M. and M.S. onboarded community members and tested new proofreaders. A.R.S., M.S., C.S.J. and C.E.M. designed tutorials. C.E.M., A.R.S. and M.S. provided community support. S.D., F.C., C.S.-M., C.S.J., A.H., D. Brittain and W.S. built and maintained CAVE for FlyWire and managed user access. S.D., P.S., A.M. and E.P. curated the data and made it available for download. E.P. and D.D.B. provided a coordinate mapping service. A.S.B., N.E., G.S.X.E.J. and J.F. provided neurotransmitter information. S.-c.Y., C.E.M., M.C., K.E., Y.Y. and P.S. trained and managed proofreaders. S.D., S.-c.Y., P.S. and G.S.X.E.J. led the targeted proofreading effort. S.D., P.S., A.M., A.C. and K. Kuehner maintained the proofreading management platforms. S.D. evaluated the proofreading accuracy. S.D., A.L., H.S.S., D.D. and R.Y. analysed the data. S.D., D. Bland and S.-c.Y. annotated and analysed the ocellar circuit. S.D., H.S.S., M.M., A.L., P.S. and A.R.S. wrote the manuscript with feedback from A.S.B., W.H., G.S.X.E.J. and contributions from all authors. H.S.S., M.M., G.S.X.E.J. and D.D.B. sponsored large-scale proofreading. G.S.X.E.J. and D.D.B. led the Cambridge effort. M.M. and H.S.S. led the overall effort.

Competing interests T.M., K.L., S.P., D.I., N.K. and H.S.S. declare financial interests in Zetta AI.

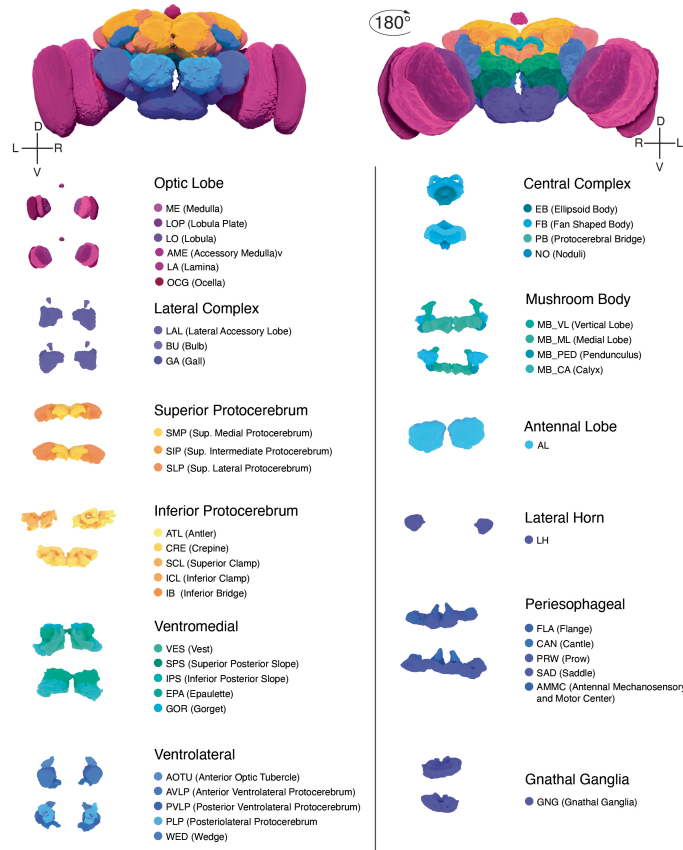
Additional information

Supplementary information The online version contains supplementary material available at <https://doi.org/10.1038/s41586-024-07558-y>.

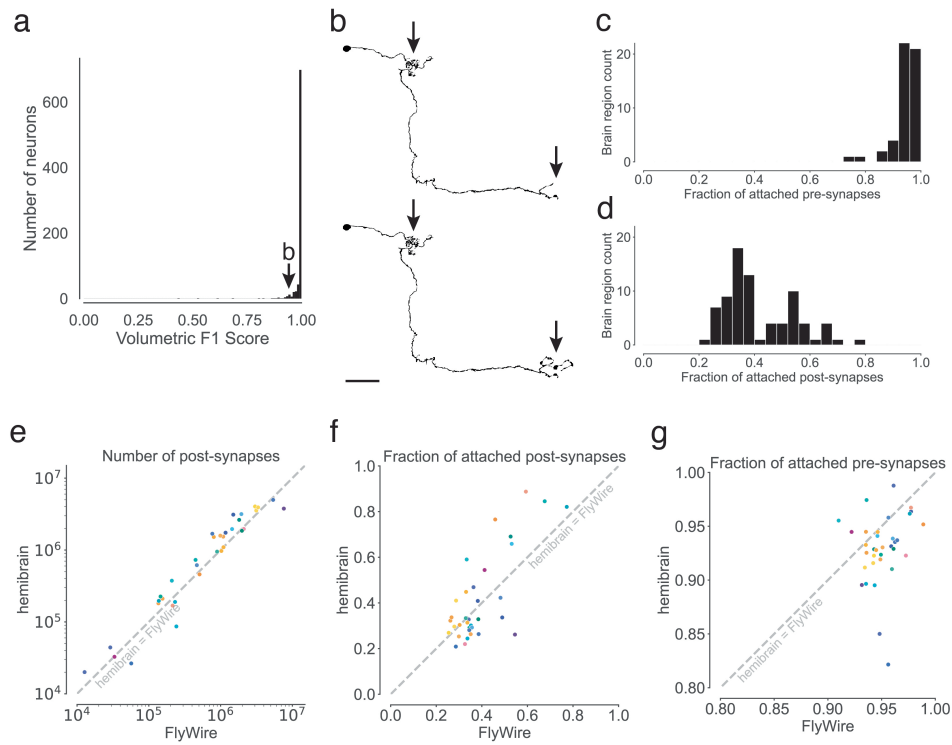
Correspondence and requests for materials should be addressed to H. Sebastian Seung or Mala Murthy.

Peer review information *Nature* thanks Srinivas Turaga and the other, anonymous, reviewer(s) for their contribution to the peer review of this work. Peer review reports are available.

Reprints and permissions information is available at <http://www.nature.com/reprints>.

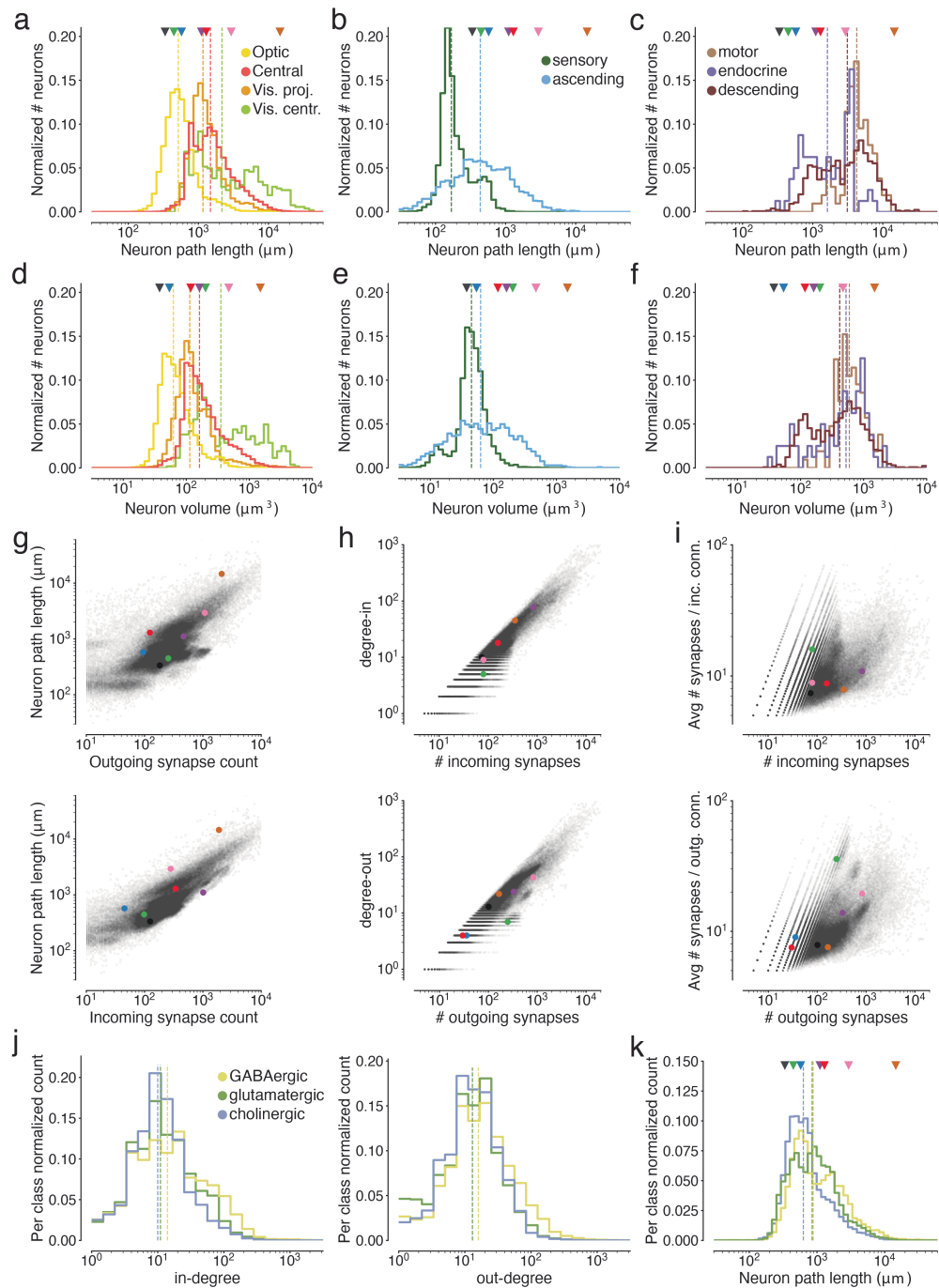


Extended Data Fig. 1 | Neuropils of the fly brain.



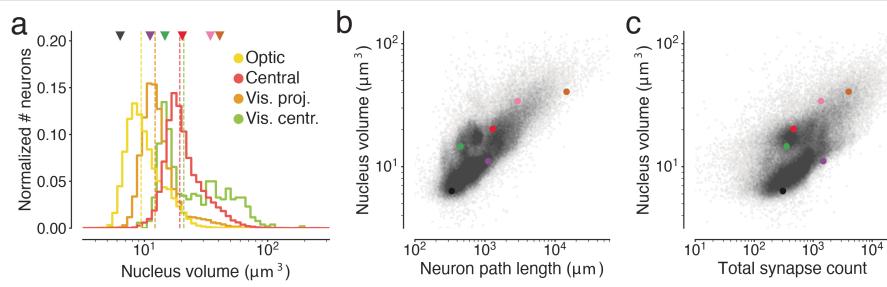
Extended Data Fig. 2 | Completeness and accuracy of FlyWire's reconstruction. (a) shows the result of our evaluation of proofread segments in the central brain. Experts attempted further proofreading of 826 neurons. We computed volumetric overlaps between the original and the final segment to calculate precision, recall, and F1 Scores. (b) Examples (top: before, bottom: after) of the changes made during further proofreading for a neuron scoring an F1-Score of 0.936. Arrows highlight locations that changed. (c,d) For each neuropil, we quantified what fraction of the synapses within it are pre- and postsynaptically

attached to a proofread segment. (c) displays the distribution for presynaptic attachment and (d) the distribution for postsynaptic attachment. (e, f, g) Comparisons between FlyWire's reconstruction and the hemibrain were made for overlapping neuropils. Dots represent neuropils and are colored according to Extended Data Fig. 1. (e) Comparison of the number of automatically detected synapses. The axes are log-transformed. (f) Comparison of post-synaptic completion rates and (g) pre-synaptic completion rate. The axes are truncated.

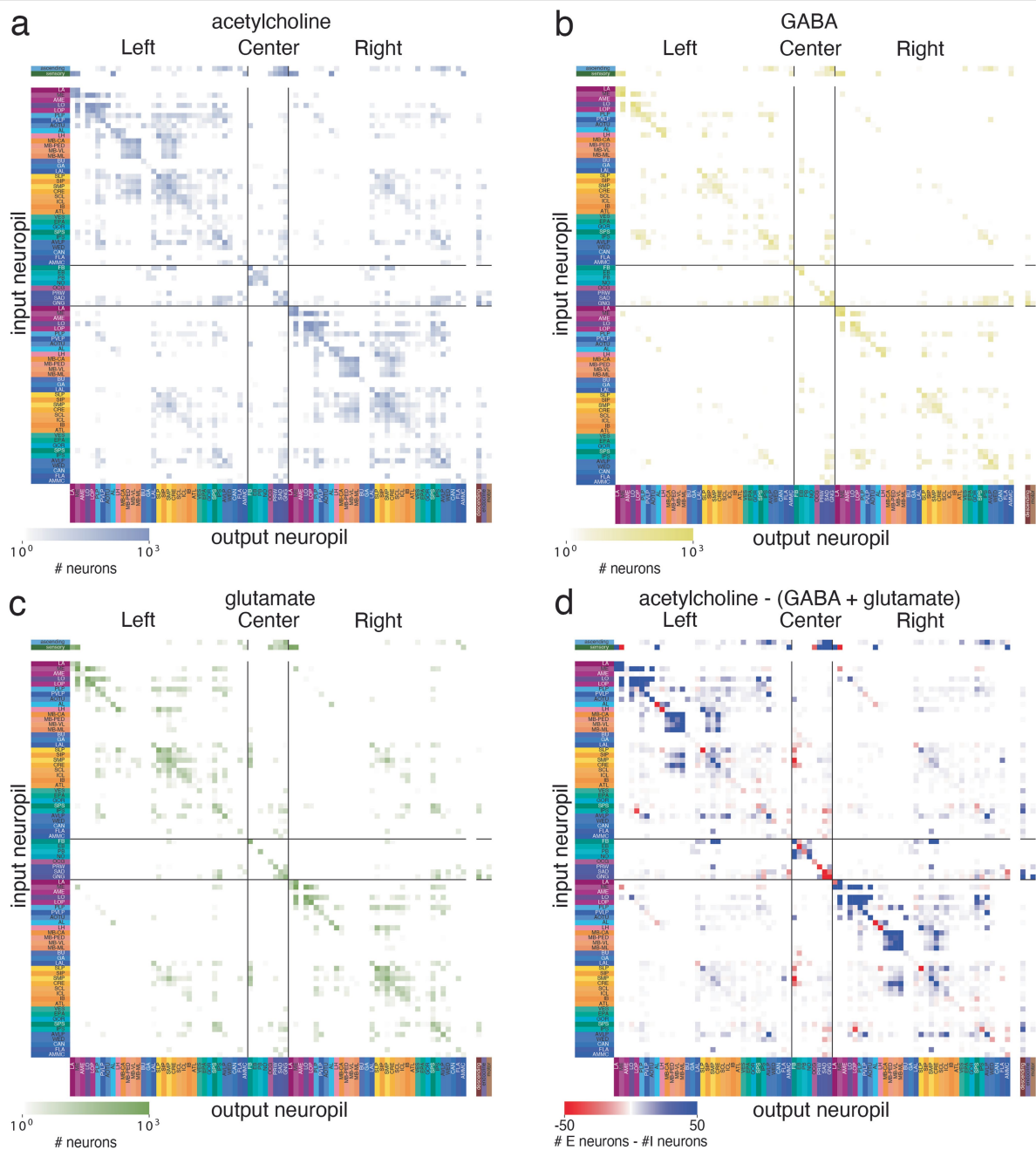


Extended Data Fig. 3 | Measurements of neuron size. Colored markers refer to neurons in Fig. 3b. Vertical dashed lines are medians. (a) Neuron path lengths of intrinsic neurons, (b) afferent neurons, and (c) efferent neurons by super-class. (d) Volumes of intrinsic neurons, (e) afferent neurons, and (f) efferent neurons by super-class. (g) Comparisons of path lengths and number of incoming and outgoing synapses. (h) For intrinsic neurons, comparisons of the in- and out-

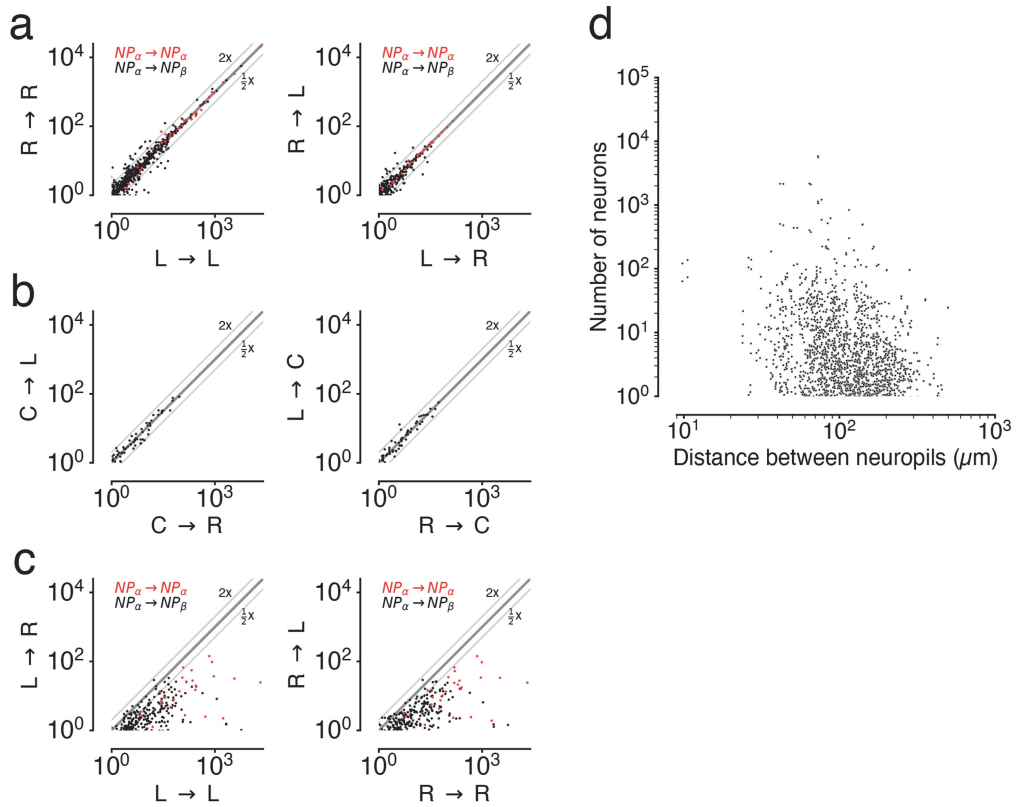
degrees with the number of incoming and outgoing synapses. Every dot is a neuron. (i) Comparison of average connection strengths (synapses per connection) with the number of synapses. Every dot is a neuron. (j) In- and out-degree distributions by neurotransmitter type. (k) Neuron path lengths by neurotransmitter type.



Extended Data Fig. 4 | Measurements of neuron size. Colored markers refer to neurons in Fig. 3b. Vertical dashed lines are medians. (a) Nucleus volume of intrinsic neurons, (b) Comparisons of nucleus volume and path length for intrinsic neurons and (c) nucleus volume and total synapse count.

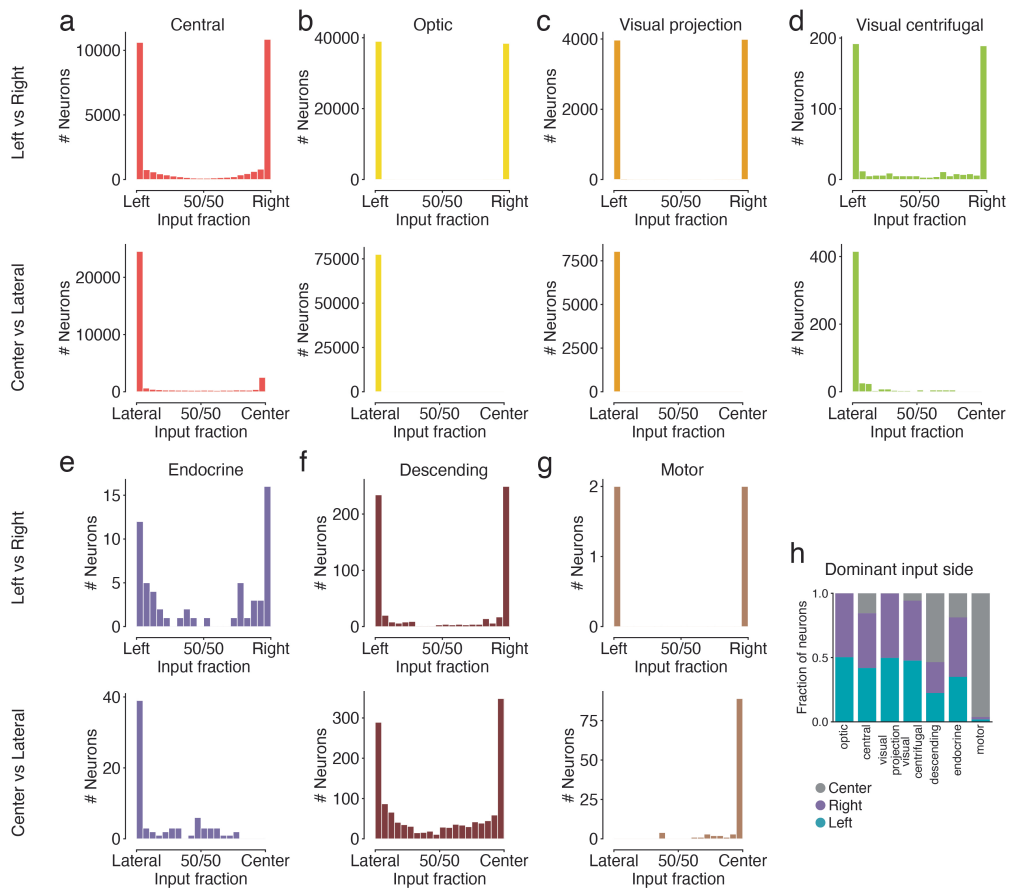


Extended Data Fig. 5 | Neuropil-neuropil projection maps. (a) Projection maps produced as in Fig. 4a limited to connections from cholinergic, (b) GABAergic, and (c) glutamatergic neurons. (d) The difference between the putative excitatory (acetylcholine) and the putative inhibitory (GABA, glutamate) projection maps.



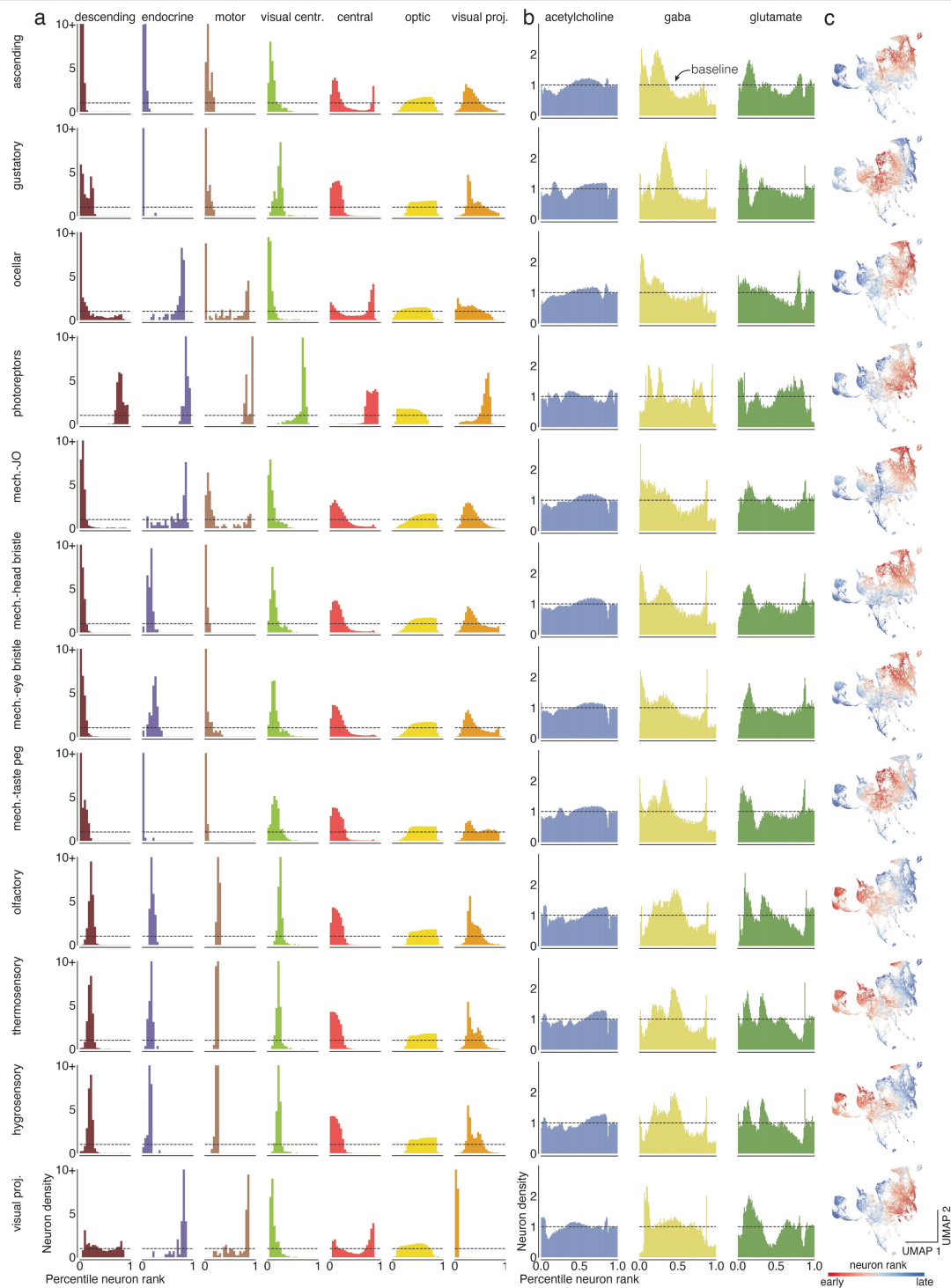
Extended Data Fig. 6 | Neuropil-neuropil projections compared between hemispheres. Each dot is a neuropil-neuropil projection in one hemisphere and the axes show the fractional weights as calculated in Fig. 4a,b. Red dots are comparisons between the same neuropils in different hemispheres (e.g. AMMC(L) → VLP(L) vs AMMC(R) → VLP(R)). (a) Comparison of projections between neuropils in both hemispheres and between hemispheres.

(b) Comparisons of projections with the center neuropils. (c) Comparisons of projections between ipsilateral and contralateral neuropil projections. (d) Comparisons of the distances between neuropil centroids with the fractional neuron weights. Connections within neuropils were excluded and neuropil pairs connected with <1 fractional neuron weight are not shown.



Extended Data Fig. 7 | Input side analysis. We assigned postsynaptic locations to either the center region or the left or right hemisphere. (a-g) For each superclass, (top plot). The lower plot shows the fraction of synapses in the center vs

the lateral regions for all neurons. (h) Each neuron was assigned to the side where it received most of its inputs.



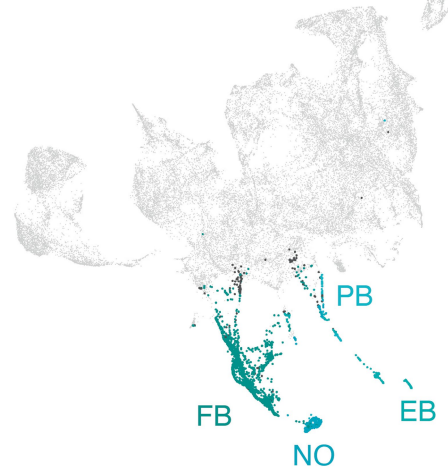
Extended Data Fig. 8 | Percentile ranks for every modality. (a) For each sensory modality (rows) we used the traversal distances to establish a neuron ranking. Each panel shows the distributions of neurons of each super-class within the sensory modality specific rankings. (b) Same as in (a) for the fast

neurotransmitters. (c) Neurons in the central brain shown in the UMAP plot are colored by the rank order in which they are reached from a given seed neuron set. Red neurons are reached earlier than blue neurons.

a

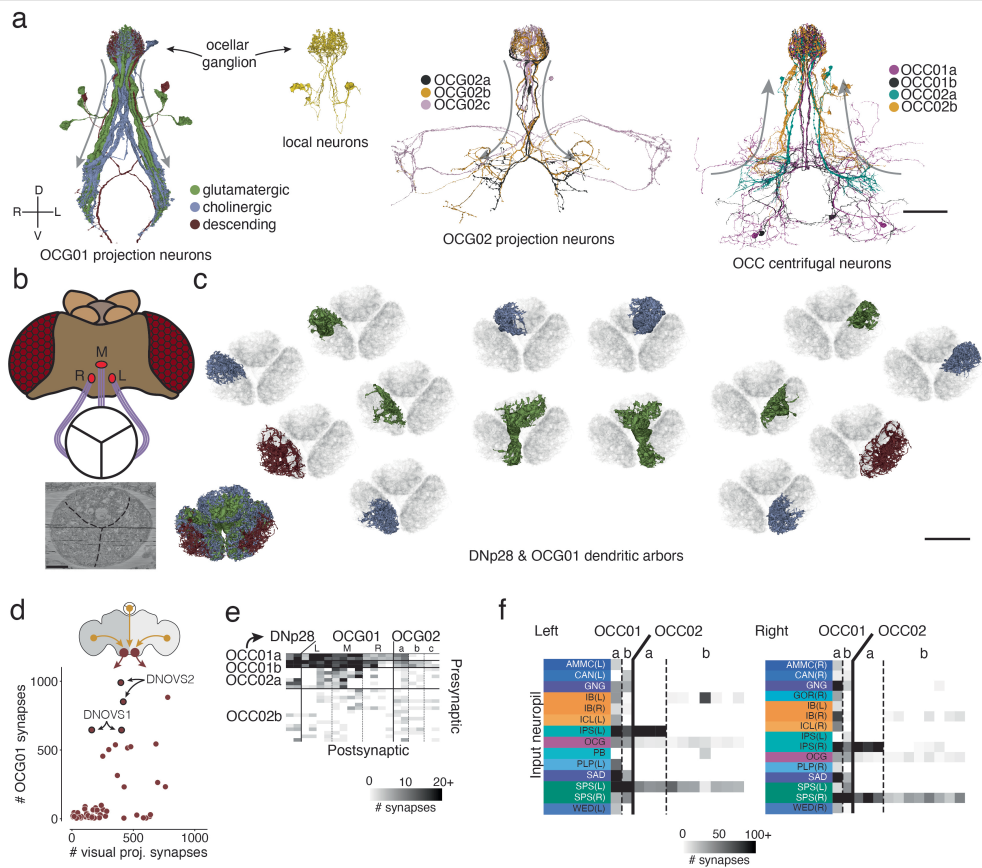


b



Extended Data Fig. 9 | Rank-based UMAP projection and neuropils. (a) Every neuron in the central brain was assigned to the neuropil where it received the most synapses. Every dot is then colored by the assigned neuropil (see Extended

Data Fig. 1 for neuropil colormap). (b) Same as in a but limited to the central complex neurons. Neurons in the central complex with an assigned neuropil other than the ones shown are colored black.



Extended Data Fig. 10 | Ocellar circuit. (a) Renderings of all neurons (excluding the photoreceptors) with arbors in the ocellar ganglion. “Information flow” from pre- and postsynapses is indicated by arrows along the arbors. (b) Overview of the three ocelli (left, medial, right) which are positioned on the top of the head. Photoreceptors from each ocellus project to a specific subregion of the ocellar ganglion which are separated by glia (marked with black lines on the EM). (c) Top view of the dendritic arbors within the ocellar ganglion of each DNp28

(brown) and OCG01 (blue: cholinergic, green: glutamatergic). The render on the lower shows all 12 OCG01s and 2 DNp28s. Each other render shows one neuron in color and all others in the background in gray for reference. (d) Comparison of number of synapses from OCG01 neurons and visual projection neurons onto descending neurons. (e) Connectivity matrix for connections between ocellar centrifugal neurons and ocellar projection neurons. (f) Inputs to ocellar centrifugal neurons by neuropil. Scale bars: 100 μ m (a), 20 μ m (c).

Reporting Summary

Nature Portfolio wishes to improve the reproducibility of the work that we publish. This form provides structure for consistency and transparency in reporting. For further information on Nature Portfolio policies, see our [Editorial Policies](#) and the [Editorial Policy Checklist](#).

Statistics

For all statistical analyses, confirm that the following items are present in the figure legend, table legend, main text, or Methods section.

- | | |
|-------------------------------------|---|
| n/a | Confirmed |
| <input type="checkbox"/> | <input checked="" type="checkbox"/> The exact sample size (n) for each experimental group/condition, given as a discrete number and unit of measurement |
| <input checked="" type="checkbox"/> | <input type="checkbox"/> A statement on whether measurements were taken from distinct samples or whether the same sample was measured repeatedly |
| <input type="checkbox"/> | <input type="checkbox"/> The statistical test(s) used AND whether they are one- or two-sided
<i>Only common tests should be described solely by name; describe more complex techniques in the Methods section.</i> |
| <input checked="" type="checkbox"/> | <input type="checkbox"/> A description of all covariates tested |
| <input checked="" type="checkbox"/> | <input type="checkbox"/> A description of any assumptions or corrections, such as tests of normality and adjustment for multiple comparisons |
| <input checked="" type="checkbox"/> | <input type="checkbox"/> A full description of the statistical parameters including central tendency (e.g. means) or other basic estimates (e.g. regression coefficient) AND variation (e.g. standard deviation) or associated estimates of uncertainty (e.g. confidence intervals) |
| <input checked="" type="checkbox"/> | <input type="checkbox"/> For null hypothesis testing, the test statistic (e.g. F , t , r) with confidence intervals, effect sizes, degrees of freedom and P value noted
<i>Give P values as exact values whenever suitable.</i> |
| <input checked="" type="checkbox"/> | <input type="checkbox"/> For Bayesian analysis, information on the choice of priors and Markov chain Monte Carlo settings |
| <input checked="" type="checkbox"/> | <input type="checkbox"/> For hierarchical and complex designs, identification of the appropriate level for tests and full reporting of outcomes |
| <input type="checkbox"/> | <input checked="" type="checkbox"/> Estimates of effect sizes (e.g. Cohen's d , Pearson's r), indicating how they were calculated |

Our web collection on [statistics for biologists](#) contains articles on many of the points above.

Software and code

Policy information about [availability of computer code](#)

Data collection

Data analysis

For manuscripts utilizing custom algorithms or software that are central to the research but not yet described in published literature, software must be made available to editors and reviewers. We strongly encourage code deposition in a community repository (e.g. GitHub). See the Nature Portfolio [guidelines for submitting code & software](#) for further information.

Data

Policy information about [availability of data](#)

All manuscripts must include a [data availability statement](#). This statement should provide the following information, where applicable:

- Accession codes, unique identifiers, or web links for publicly available datasets
- A description of any restrictions on data availability
- For clinical datasets or third party data, please ensure that the statement adheres to our [policy](#)

All data is made publicly available. Codex (codex.flywire.ai), braincircuits.io, and Catmaid spaces (fafb-flywire.catmaid.org) facilitate non-programmatic access. Most of the data can be directly download from codex (codex.flywire.ai/api/download). All data, including the volumetric data and meshes, can be programmatically accessed through CAVE and cloudvolume. We provide tutorials for programmatic access here: <https://github.com/seung-lab/FlyConnectome>

Research involving human participants, their data, or biological material

Policy information about studies with [human participants or human data](#). See also policy information about [sex, gender \(identity/presentation\), and sexual orientation](#) and [race, ethnicity and racism](#).

Reporting on sex and gender	Use the terms <i>sex</i> (biological attribute) and <i>gender</i> (shaped by social and cultural circumstances) carefully in order to avoid confusing both terms. Indicate if findings apply to only one sex or gender; describe whether sex and gender were considered in study design; whether sex and/or gender was determined based on self-reporting or assigned and methods used. Provide in the source data disaggregated sex and gender data, where this information has been collected, and if consent has been obtained for sharing of individual-level data; provide overall numbers in this Reporting Summary. Please state if this information has not been collected. Report sex- and gender-based analyses where performed, justify reasons for lack of sex- and gender-based analysis.
Reporting on race, ethnicity, or other socially relevant groupings	Please specify the socially constructed or socially relevant categorization variable(s) used in your manuscript and explain why they were used. Please note that such variables should not be used as proxies for other socially constructed/relevant variables (for example, race or ethnicity should not be used as a proxy for socioeconomic status). Provide clear definitions of the relevant terms used, how they were provided (by the participants/respondents, the researchers, or third parties), and the method(s) used to classify people into the different categories (e.g. self-report, census or administrative data, social media data, etc.) Please provide details about how you controlled for confounding variables in your analyses.
Population characteristics	Describe the covariate-relevant population characteristics of the human research participants (e.g. age, genotypic information, past and current diagnosis and treatment categories). If you filled out the behavioural & social sciences study design questions and have nothing to add here, write "See above."
Recruitment	Describe how participants were recruited. Outline any potential self-selection bias or other biases that may be present and how these are likely to impact results.
Ethics oversight	Identify the organization(s) that approved the study protocol.

Note that full information on the approval of the study protocol must also be provided in the manuscript.

Field-specific reporting

Please select the one below that is the best fit for your research. If you are not sure, read the appropriate sections before making your selection.

Life sciences Behavioural & social sciences Ecological, evolutionary & environmental sciences

For a reference copy of the document with all sections, see [nature.com/documents/nr-reporting-summary-flat.pdf](https://www.nature.com/documents/nr-reporting-summary-flat.pdf)

Life sciences study design

All studies must disclose on these points even when the disclosure is negative.

Sample size	This manuscript is based on one image dataset from one fly brain
Data exclusions	No data was excluded
Replication	We did not replicate this study on other animals
Randomization	N/A
Blinding	N/A

Reporting for specific materials, systems and methods

We require information from authors about some types of materials, experimental systems and methods used in many studies. Here, indicate whether each material, system or method listed is relevant to your study. If you are not sure if a list item applies to your research, read the appropriate section before selecting a response.

Materials & experimental systems

n/a	Involvement
<input checked="" type="checkbox"/>	<input type="checkbox"/> Antibodies
<input checked="" type="checkbox"/>	<input type="checkbox"/> Eukaryotic cell lines
<input checked="" type="checkbox"/>	<input type="checkbox"/> Palaeontology and archaeology
<input type="checkbox"/>	<input checked="" type="checkbox"/> Animals and other organisms
<input checked="" type="checkbox"/>	<input type="checkbox"/> Clinical data
<input checked="" type="checkbox"/>	<input type="checkbox"/> Dual use research of concern
<input checked="" type="checkbox"/>	<input type="checkbox"/> Plants

Methods

n/a	Involvement
<input checked="" type="checkbox"/>	<input type="checkbox"/> ChIP-seq
<input checked="" type="checkbox"/>	<input type="checkbox"/> Flow cytometry
<input checked="" type="checkbox"/>	<input type="checkbox"/> MRI-based neuroimaging

Animals and other research organisms

Policy information about [studies involving animals](#); [ARRIVE guidelines](#) recommended for reporting animal research, and [Sex and Gender in Research](#)

Laboratory animals	7-day-old [iso] w1118 x [iso] Canton-S G1 adult female flies
Wild animals	N/A
Reporting on sex	Female
Field-collected samples	N/A
Ethics oversight	N/A. Sample was collected by prior study

Note that full information on the approval of the study protocol must also be provided in the manuscript.

Plants

Seed stocks	<i>Report on the source of all seed stocks or other plant material used. If applicable, state the seed stock centre and catalogue number. If plant specimens were collected from the field, describe the collection location, date and sampling procedures.</i>
Novel plant genotypes	<i>Describe the methods by which all novel plant genotypes were produced. This includes those generated by transgenic approaches, gene editing, chemical/radiation-based mutagenesis and hybridization. For transgenic lines, describe the transformation method, the number of independent lines analyzed and the generation upon which experiments were performed. For gene-edited lines, describe the editor used, the endogenous sequence targeted for editing, the targeting guide RNA sequence (if applicable) and how the editor was applied.</i>
Authentication	<i>Describe any authentication procedures for each seed stock used or novel genotype generated. Describe any experiments used to assess the effect of a mutation and, where applicable, how potential secondary effects (e.g. second site T-DNA insertions, mosaicism, off-target gene editing) were examined.</i>

3 MANUSCRIPT 3: WHOLE-BRAIN ANNOTATION AND MULTI-CONNECTOME CELL TYPING QUANTIFIES CIRCUIT STEREOTYPE IN *DROSOPHILA*

Summary

The fruit fly *Drosophila melanogaster* has emerged as a key model organism in neuroscience, in large part due to the concentration of collaboratively generated molecular, genetic and digital resources available for it. Here we complement the approximately 140,000 neuron FlyWire whole-brain connectome with a systematic and hierarchical annotation of neuronal classes, cell types and developmental units (hemilineages). Of 8,453 annotated cell types, 3,643 were previously proposed in the partial hemibrain connectome, and 4,581 are new types, mostly from brain regions outside the hemibrain subvolume. Although nearly all hemibrain neurons could be matched morphologically in FlyWire, about one-third of cell types proposed for the hemibrain could not be reliably reidentified. We therefore propose a new definition of cell type as groups of cells that are each quantitatively more similar to cells in a different brain than to any other cell in the same brain, and we validate this definition through joint analysis of FlyWire and hemibrain connectomes. Further analysis defined simple heuristics for the reliability of connections between brains, revealed broad stereotypy and occasional variability in neuron count and connectivity, and provided evidence for functional homeostasis in the mushroom body through adjustments of the absolute amount of excitatory input while maintaining the excitation/inhibition ratio. Our work defines a consensus cell type atlas for the fly brain and provides both an intellectual framework and open-source toolchain for brain-scale comparative connectomics.

Authors

Philipp Schlegel, Yijie Yin, Alexander S. Bates, Sven Dorckenwald, Katharina Eichler, Paul Brooks, Daniel S. Han, Marina Gkantia, Marcia dos Santos, Eva J. Munnely, Griffin Badalamente, Laia Serratosa Capdevila, Varun A. Sane, Markus W. Pleijzier, Imaan F.M. Tamimi, Christopher R. Dunne, Irene Salgarella, Alexandre Javier, Siqi Fang, Eric Perlman, Tom Kazimiers, Sridhar R. Jagannathan, Arie Matsliah, Amy R. Sterling, Szi-chieh Yu, Claire E. McKellar, **FlyWire Consortium**, Marta Costa, H. Sebastian Seung, Mala Murthy, Volker Hartenstein, Davi D. Bock & Gregory S.X.E. Jefferis

This article is published in *Nature*; [Schlegel et al. \(2024\)](#).

Contributions

FlyWire Consortium, contribution as in Manuscript 2

Whole-brain annotation and multi-connectome cell typing of *Drosophila*

<https://doi.org/10.1038/s41586-024-07686-5>

Received: 14 July 2023

Accepted: 6 June 2024

Published online: 2 October 2024

Open access

 Check for updates

Philipp Schlegel^{1,2}, Yijie Yin², Alexander S. Bates^{1,3,4}, Sven Dorkenwald^{5,6}, Katharina Eichler², Paul Brooks², Daniel S. Han^{1,7}, Marina Gkantia², Marcia dos Santos², Eva J. Munnelly², Griffin Badalamente², Laia Serratos Capdevila², Varun A. Sane², Alexandra M. C. Fragniere², Ladann Kiassat², Markus W. Pleijzier¹, Tomke Stürner^{1,2}, Imaan F. M. Tamimi², Christopher R. Dunne², Irene Salgarella², Alexandre Javier², Siqi Fang², Eric Perlman⁸, Tom Kazimiers⁹, Sridhar R. Jagannathan², Arie Matsliah⁶, Amy R. Sterling^{6,10}, Szi-chieh Yu⁶, Claire E. McKellar⁶, FlyWire Consortium^{*,**}, Marta Costa², H. Sebastian Seung^{5,6}, Mala Murthy⁶, Volker Hartenstein¹¹, Davi D. Bock^{12,13} & Gregory S. X. E. Jefferis^{1,2,13}

The fruit fly *Drosophila melanogaster* has emerged as a key model organism in neuroscience, in large part due to the concentration of collaboratively generated molecular, genetic and digital resources available for it. Here we complement the approximately 140,000 neuron FlyWire whole-brain connectome¹ with a systematic and hierarchical annotation of neuronal classes, cell types and developmental units (hemilineages). Of 8,453 annotated cell types, 3,643 were previously proposed in the partial hemibrain connectome², and 4,581 are new types, mostly from brain regions outside the hemibrain subvolume. Although nearly all hemibrain neurons could be matched morphologically in FlyWire, about one-third of cell types proposed for the hemibrain could not be reliably reidentified. We therefore propose a new definition of cell type as groups of cells that are each quantitatively more similar to cells in a different brain than to any other cell in the same brain, and we validate this definition through joint analysis of FlyWire and hemibrain connectomes. Further analysis defined simple heuristics for the reliability of connections between brains, revealed broad stereotypy and occasional variability in neuron count and connectivity, and provided evidence for functional homeostasis in the mushroom body through adjustments of the absolute amount of excitatory input while maintaining the excitation/inhibition ratio. Our work defines a consensus cell type atlas for the fly brain and provides both an intellectual framework and open-source toolchain for brain-scale comparative connectomics.

The adult fruit fly represents the current frontier for whole-brain connectomics. With 139,255 neurons, the newly completed full adult female brain (FAFB) connectome is intermediate in log scale between the first connectome of *Caenorhabditis elegans* (302 neurons^{3,4}) and the mouse (10⁸ neurons), a desirable but currently intractable target⁵. The availability of a complete adult fly brain connectome now allows brain-spanning circuits to be mapped and linked to circuit dynamics and behaviour as has long been possible for the nematode and more recently the *Drosophila* larva (3,016 neurons)⁶. However, the adult fly has richer behaviour, including complex motor control while walking or in flight⁷, courtship behaviour⁸, involved decision making⁹, flexible associative memory^{10,11}, spatial learning¹² and complex^{13,14} multisensory^{15,16} navigation.

The FlyWire brain connectome reported in our companion paper¹ is by some margin the largest and most complex yet obtained. The

full connectome, derived from the approximately 100 teravoxel FAFB whole-brain electron microscopy (EM) volume¹⁷, can be represented as a graph with 139,255 nodes and around 15.1 million weighted edges. Here we formulate and answer key questions that are essential to interpreting connectomes at this scale regarding (1) how we know which edges are important; (2) how we can simplify the connectome graph to aid automated or human analysis; and (3) the extent to which this connectome is a snapshot of a single brain or representative of this species as a whole (or have we collected a ‘snowflake’?). These questions are inextricably linked with connectome annotation and cell type identification^{18,19} within and across datasets.

At the most basic level, navigating this connectome would be extremely challenging without a comprehensive system of annotations, which we now provide. Our annotations represent an indexed

¹Neurobiology Division, MRC Laboratory of Molecular Biology, Cambridge, UK. ²*Drosophila* Connectomics Group, Department of Zoology, University of Cambridge, Cambridge, UK. ³Department of Neurobiology and Howard Hughes Medical Institute, Harvard Medical School, Boston, MA, USA. ⁴Centre for Neural Circuits and Behaviour, University of Oxford, Oxford, UK. ⁵Computer Science Department, Princeton University, Princeton, NJ, USA. ⁶Princeton Neuroscience Institute, Princeton University, Princeton, NJ, USA. ⁷School of Mathematics and Statistics, University of New South Wales, Sydney, New South Wales, Australia. ⁸Yikes, Baltimore, MD, USA. ⁹kazmos, Dresden, Germany. ¹⁰Eyewire, Boston, MA, USA. ¹¹Molecular, Cell and Developmental Biology, University of California Los Angeles, Los Angeles, CA, USA. ¹²Department of Neurological Sciences, Larner College of Medicine, University of Vermont, Burlington, VT, USA. ¹³A list of authors and their affiliations appears at the end of the paper. ¹⁴A full list of members and their affiliations appears in the Supplementary Information. ¹⁵e-mail: dbock@uvm.edu; jefferis@mrc-lmb.cam.ac.uk

Article

and hierarchical human-readable parts list^{18,20}, enabling biologists to explore their systems and neurons of interest. Connectome annotation is also crucial to ensuring data quality as it inevitably reveals segmentation errors that must be corrected. Furthermore, there is a rich history in *Drosophila* of probing the circuit basis of a wide range of innate and learned behaviours as well as their developmental genetic origins; realizing the full potential of this dataset is only possible by cross-identifying cell types within the connectome with those characterized in the published and in-progress literature. This paper reports this key component of the connectome together with the open source tools (Table 1) and resources that we have generated. As the annotation and proofreading of the connectome are inextricably linked, the companion paper¹ and this paper will preferably be co-cited as they jointly describe the FlyWire resource.

Comparison with cell types proposed using the partial hemibrain connectome² confirmed that the majority of fly cell types is highly stereotyped, and defined simple rules for which connections within a connectome are reliable and therefore more likely to be functional. However, this comparison also revealed unexpected variability in some cell types and demonstrated that many cell types originally reported in the hemibrain could not be reliably reidentified. This discovery necessitated the development and application of a new robust approach for defining cell types jointly across connectomics datasets. Overall, this effort lays the foundation both for deep interrogation of current and anticipated fly connectomes from normal individuals, but also future studies of sexual dimorphism, experience-dependent plasticity, development and disease at the whole-brain scale.

Hierarchical annotation of a connectome

Annotations defining different kinds of neurons are key to exploring and interpreting any connectome; but, with the FlyWire connectome—which we report jointly with the companion paper¹—now exceeding the 100,000 neuron mark, they are also both of increased significance and more challenging to generate. We defined a comprehensive, systematic and hierarchical set of annotations based on the anatomical organization of the brain (Fig. 1 and Supplementary Videos 1 and 2), as well as the developmental origin and coarse morphology of neurons (Fig. 2). Building on these as well as validating cell types identified from pre-existing datasets, we then defined a set of consensus terminal cell types intended to capture the finest level of organization that is reproducible across brains (Fig. 3).

We first collected and curated basic metadata for every neuron in the dataset including soma position and side, and entry or exit nerve for afferent and efferent neurons, respectively (Fig. 1). Our group also predicted neurotransmitter identity for all neurons as reported elsewhere²¹. We then defined a hierarchy of four levels: flow > superclass > class > cell type, which provide salient labels at different granularities (Fig. 1a, Supplementary Table 1 and Extended Data Fig. 2).

The first two levels, flow and superclass, were densely annotated: every neuron is either afferent, efferent or intrinsic to the brain (flow) and falls into one of the nine superclasses: sensory (periphery to brain), motor (brain to periphery), endocrine (brain to corpora allata/cardiac), ascending (ventral nerve cord (VNC) to brain), descending (brain to VNC), visual projection (optic lobes to central brain), visual centrifugal (central brain to optic lobes), or intrinsic to the optic lobes or the central brain (Fig. 1b and Supplementary Table 2). Mapping to the <https://virtualflybrain.org/> (ref. 22) database enables cross-referencing of neurons and types with other publications (Methods). Note that due to an inversion of the left–right axis during the original acquisition of the FAFB dataset¹⁷, identified during preparation of this work (Extended Data Fig. 1; see the ‘FAFB laterality’ section of the Methods), frontal figures in this work and the FlyWire connectome¹ have the fly’s left on the viewer’s left, and the fly’s right on the viewer’s right, that

Table 1 | Software tools used

Name	GitHub repository	Description
navis	navis-org/navis	Analysis (for example, NBLAST) and visualization of neuron morphologies in Python.
navis-flybrains	navis-org/navis-flybrains	Transform data between brain templates (including hemibrain and FAFB) in Python.
fafbseg-py	flyconnectome/fafbseg-py	Query and work with auto-segmented FAFB data (including FlyWire) in Python.
cocoa	flyconnectome/cocoa	Analysis suite for comparative connectomics in Python.
neuprint-python	connectome-neuprint/neuprint-python	Query data from neuPrint, developed by Stuart Berg (Janelia Research Campus).
fafbseg	natverse/fafbseg	Support for working with FlyWire segmentation, meshes and annotations in R.
neupintr	natverse/neupintr	Support for working with neuPrint databases including the hemibrain connectome in R.
coconat coconatfly	natverse/coconat natverse/coconatfly	Analysis suite for comparative connectomics in R.
Pyroglancer	SridharJagannathan/pyroglancer	Pythonic interface to neuroglancer for displaying neuronal data.

is, the opposite of the usual convention. However, all side labels are biologically correct.

The class field contains pre-existing neurobiological groupings from the literature (for example, for central complex neurons; Supplementary Table 3) and is sparsely annotated (43%) for the central brain, in large part because past research has favoured some brain areas over others. In the optic lobes, 99% of neurons have a generic class based on their neuropil innervation. Finally, 98% of all central brain neurons were given a terminal cell type, a majority of which could be linked to at least one report in the literature (Fig. 1c). Our annotations for the optic lobes include cell types for 92% of neurons in both left and right optic lobes. A separate report²³ will describe comprehensive typing of all neurons intrinsic to the optic lobes. In total, we collected over 870,000 annotations for all 139,255 neurons; all are available for download and through neuroglancer scenes (Methods and Extended Data Fig. 11). A total of 32,388 (23%) neurons are intrinsic to the central brain and 77,536 (54%) neurons are intrinsic to the optic lobes. The optic lobes and the central brain are connected through 8,053 visual projection and 524 visual centrifugal neurons. The central brain receives afferent input through 5,512 sensory and 2,362 ascending neurons. Efferent output is realized through 1,303 descending, 80 endocrine and 106 motor neurons.

We find marked stereotypy in the number of central brain intrinsic neurons—for example, between the left and the right hemisphere, they differ by only 27 (0.1%) neurons. For superclasses with less consistency in left versus right counts, such as the ascending neurons (140, 11%), the discrepancies are typically due to ambiguity in the sidedness (Fig. 1d and Methods).

Combining the dense superclass annotation for all neurons with the connectome¹ gives a birds-eye view of the input/output connectivity of the central brain (Fig. 1f): 55% of the central brain’s synaptic input comes from the optic system; 25% from the VNC through ascending neurons; and only 18% from peripheral sensory neurons. This is surprising as sensory neurons are almost as numerous as visual projection neurons (Fig. 1d,e); individual visual projection neurons therefore provide about 2.5 times more synapses, underscoring the value of this information stream. Input neurons make about two synapses onto central brain neurons for every one synapse onto output

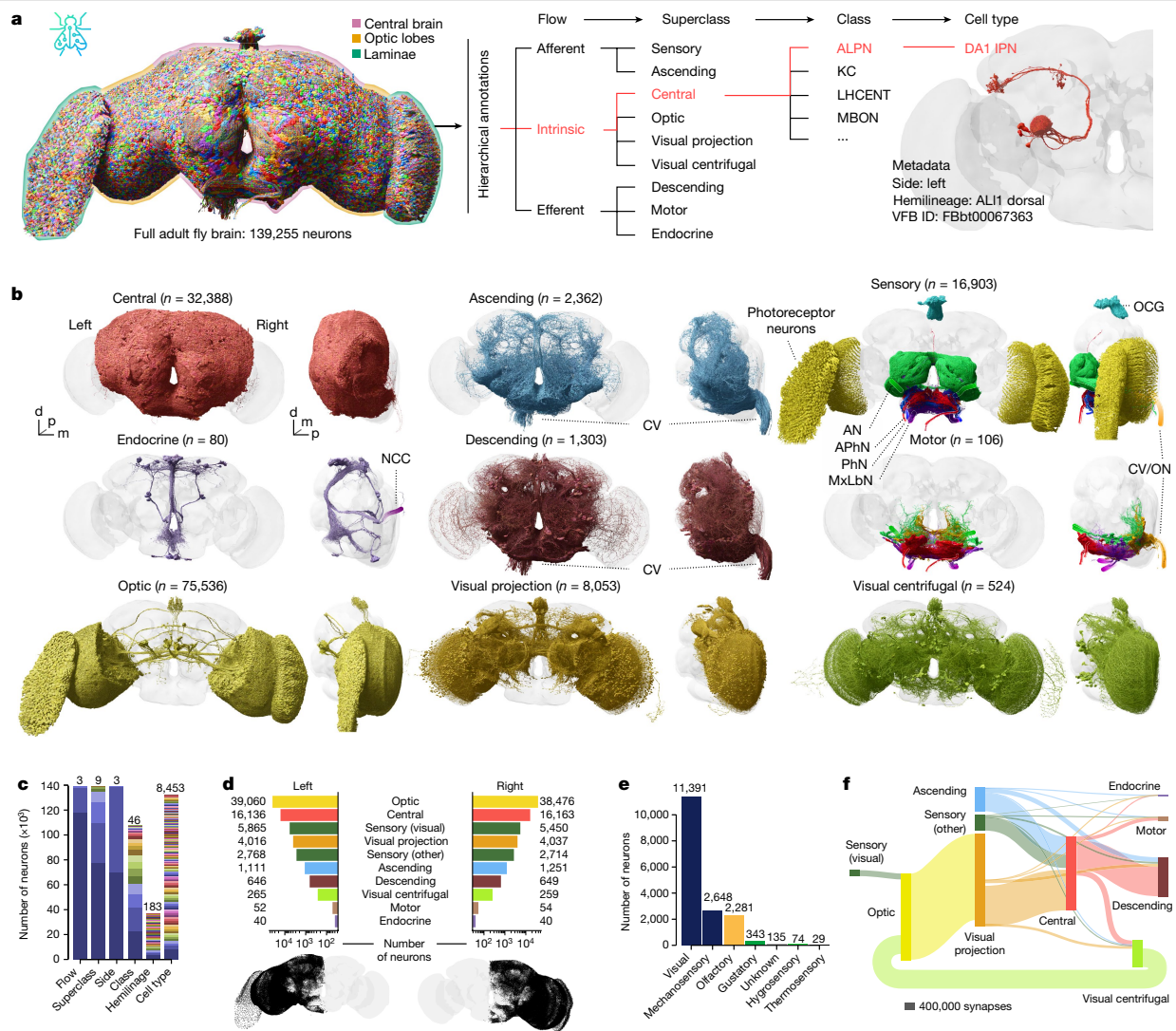


Fig. 1 | Hierarchical annotation schema for a whole-brain connectome. **a**, Hierarchical annotation schema for the FlyWire dataset (see the companion paper¹). Annotations for example cell type DA1 IPN (right) are highlighted in red. **b**, Renderings of neurons for each superclass. AN, antennal nerve; APHN, accessory pharyngeal nerve; CV, cervical connective; d, dorsal; m, medial; MxLbN, maxillary-labial nerve; NCC, corpora cardiaca nerves; OCG, ocellar ganglion; ON, occipital nerves; PhN, pharyngeal nerve; p, posterior.

c, Annotation counts per field. Each colour within a bar represents discrete values; the numbers above bars count the discrete values. **d**, Left versus right neuron counts per superclass. Bottom, the left and right soma locations, respectively. **e**, Breakdown of sensory neuron counts into modalities. **f**, Flow chart of superclass-level, feed-forward (afferent to intrinsic to efferent) connectivity.

neurons. Most output synapses target the VNC through descending neurons (75%); the rest provide centrifugal feedback onto the optic system (15%), motor neuron output (9%) and endocrine output to the periphery (1%).

A full atlas of neuronal lineages

Our top-level annotations (flow, superclass, class) provide a systematic but relatively coarse grouping of neurons compared with >5,000 terminal cell types expected from previous work on the hemibrain². We therefore developed an intermediate level of annotation based on hemilineages—this provides a powerful bridge between the developmental origin and molecular specification of neurons and their place within circuits in the connectome (Fig. 2a).

Central brain neurons and a minority of visual projection neurons are generated by around 120 identified neuroblasts per hemisphere. Each of these stem cells is defined by a unique transcriptional code and generates a stereotyped lineage in a precise birth order by asymmetric division^{24–27} (Fig. 2b). Each neuroblast typically produces two hemilineages^{28,29} that differ markedly in neuronal morphology and can express different neurotransmitters from one another, but neurons in each hemilineage usually express a single fast-acting transmitter^{21,30}. Hemilineages therefore represent a natural functional as well as developmental grouping by which to study the nervous system. Within a hemilineage, neurons form processes that extend together in one cohesive bundle (the hemilineage tract) that enters, traverses and interconnects neuropil compartments in a stereotypical pattern (Fig. 2c). Comparing these features between EM and previous light-level

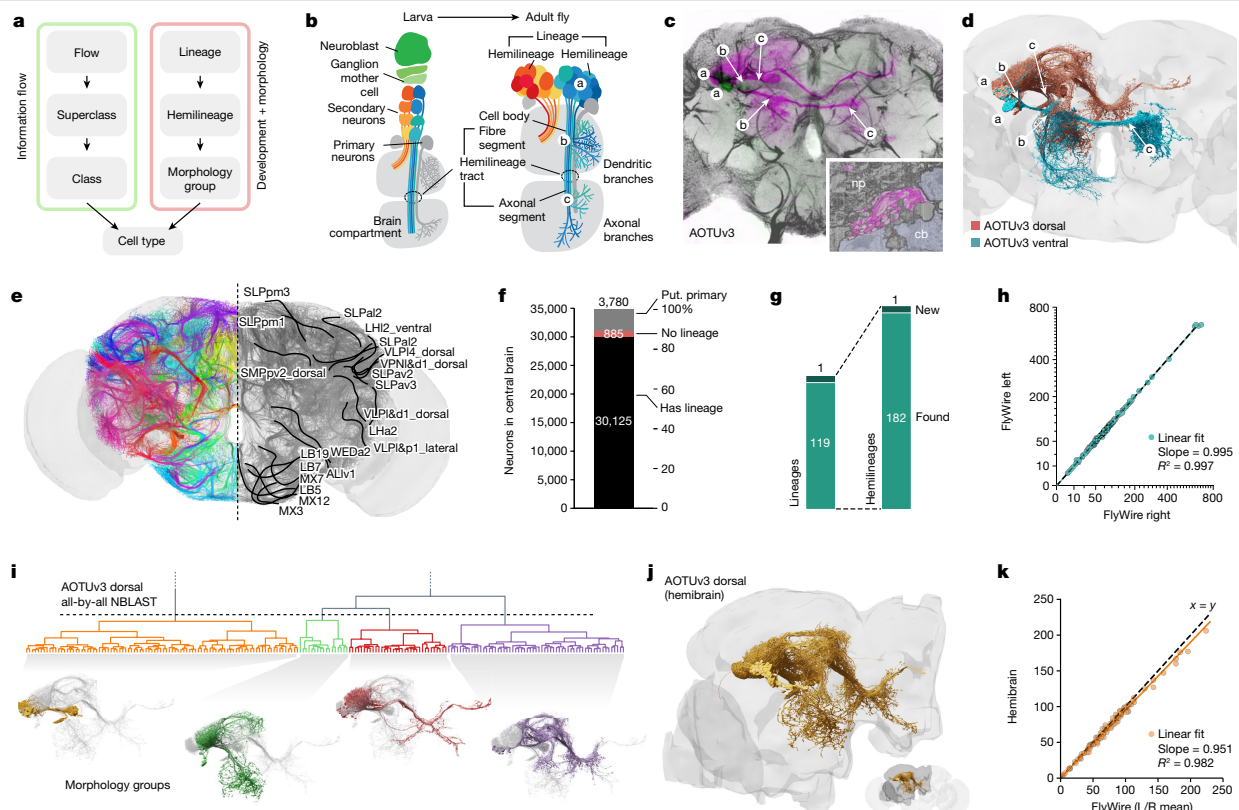


Fig. 2 | Annotation of developmental units. **a**, Illustration of the two complementary sets of annotations. **b**, Developmental organization of neuroblast hemilineages. **c**, Light-level image of an example AOTUv3 lineage clone; the lower case letters link canonical features of each hemilineage to the cartoon in **b**. Inset: cell body fibre tract in the EM. cb, cell body; np, neuropil. **d**, AOTUv3 neurons in FlyWire split into its two hemilineages. **e**, Cell body fibre bundles from all identified hemilineages, partially annotated on the right. **f**, The number of central brain neurons with an identified lineage; annotation of

(putative (put.) primary neurons is based on literature or expert assessment of morphology. **g**, The number of identified unique (hemi)lineages. **h**, Left versus right number of neurons contained in each hemilineage. **i**, Example morphological clustering of the AOTUv3 dorsal hemilineage reveals four distinct subgroups. **j**, Neurons belonging to the AOTUv3 dorsal hemilineage identified in the hemibrain connectome. **k**, FlyWire versus hemibrain number of neurons for cross-identified hemilineages.

data^{31–34} enabled us to compile the first definitive atlas of all hemilineages in the central brain (Fig. 2c–e and Methods).

In total, we successfully identified 120 neuroblast lineages in FlyWire comprising 183 hemilineages for 88% (30,233 total) of central brain neurons (Fig. 2e,f and Extended Data Fig. 3). The unassigned neurons are likely primary neurons born during embryonic development, which account for 10% of neurons in the adult brain^{35,36}. We tentatively designated 3,779 (11%) as primary neurons either based on specific identification in the literature²⁷ or expert assessment of diagnostic morphological features such as larger cell bodies and broader projections. A further 797 neurons (2%) did not co-fasciculate with any hemilineage tracts, even though their morphology suggested that they are later-born secondary neurons³⁷. This developmental atlas is comprehensive as, after reviewing discrepancies between previous studies (Methods), we identified all 119 expected lineages plus one new lineage.

The number of neurons per hemilineage can vary widely (Fig. 2h)—for example, counting both hemispheres, FLAa1 contains just 30 neurons whereas MBp4 (which makes the numerous Kenyon cells that are required for memory storage) has 1,335. However, in general, the number of neurons per hemilineage is between 60 and 282 (10th to 90th percentile, respectively). Nevertheless, the numbers of neurons within each hemilineage were highly reliable, differing only by 3% ($\pm 4\%$)

between the left and right hemispheres (Fig. 2h). This is consistent with the near-equality of neurons per hemisphere noted in Fig. 1, and indicates great precision in the developmental programs controlling neuron number. We also identified neurons belonging to 125 hemilineages in the hemibrain dataset (Fig. 2j), a connectome comprising approximately half of a female fly brain² (Fig. 3a). The number of neurons per hemilineage strongly correlates across brains ($R^2 = 0.98$), with FlyWire hemilineages containing on average around 5% more neurons (Fig. 2k).

Although hemilineages typically contain functionally and morphologically related neurons, subgroups can be observed³⁷. We further divided each hemilineage into distinct morphology groups, each innervating similar brain regions and taking similar internal tracts, using NBLAST morphological clustering³⁸ (Fig. 2i, Methods, Extended Data Fig. 3, Supplementary Files 3 and 4 and Supplementary Video 3). This generated a total of 528 groupings that are consistent across hemispheres and provide an additional layer of annotations between the hemilineage and cell type levels.

Validating cell types across brains

We next sought to compare FlyWire against the hemibrain connectome²; this contains most of one central brain hemisphere and parts

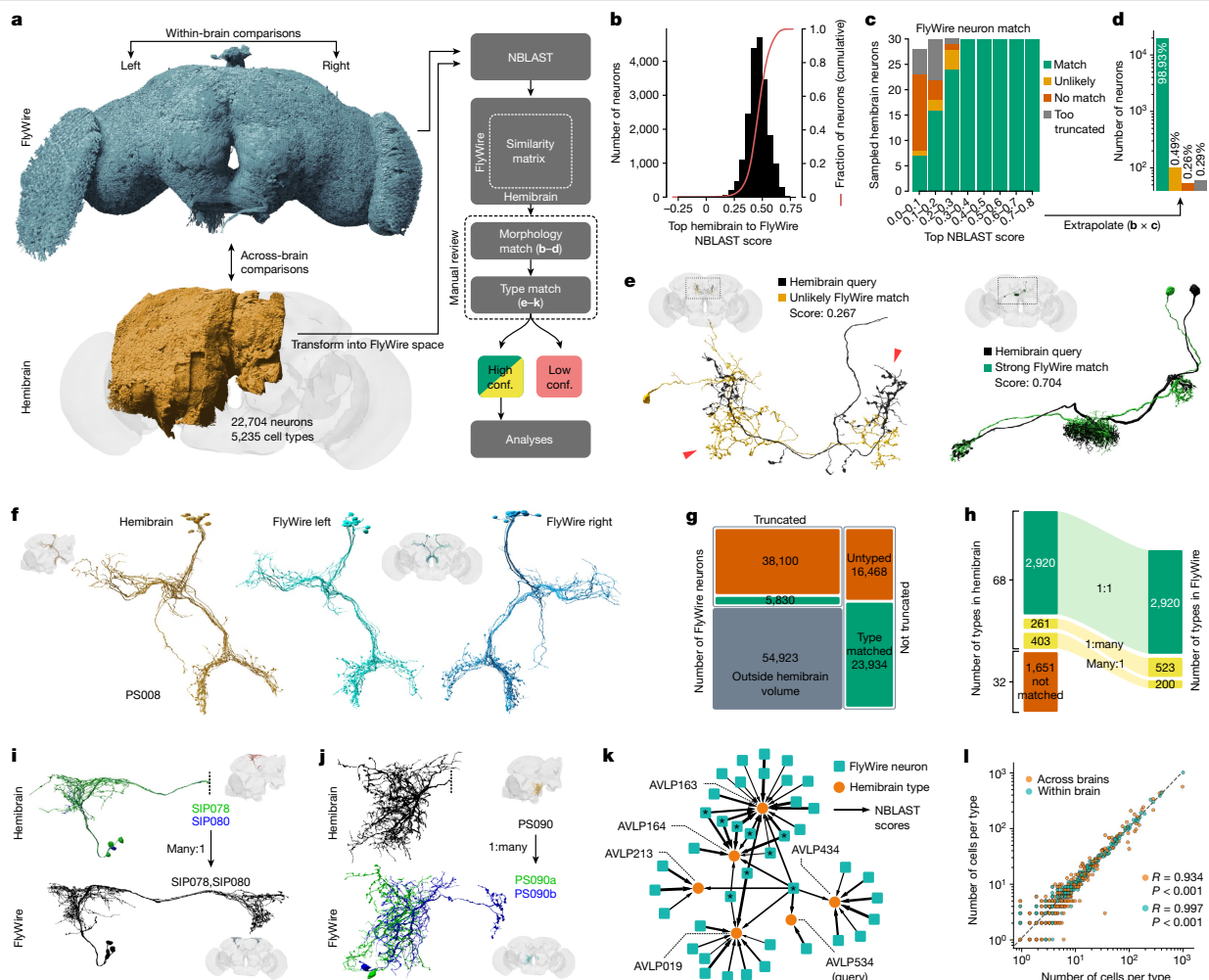


Fig. 3 | Across-brain stereotypy. **a**, Schematic of the pipeline for matching neurons between FlyWire and the Janelia hemibrain connectomes. Conf., confidence. **b**, The distribution of top hemibrain to FlyWire NBLAST scores. **c**, Manual review for a sample of top NBLAST hits. **d**, The extrapolated number of hemibrain neurons with matches in FlyWire. **e**, Example for unlikely (left) and strong (right) morphology match. **f**, Example of a high-confidence cell type (PS008) that is unambiguously identifiable across all three hemispheres. **g**, Counts of FlyWire neurons that were assigned a hemibrain type. **h**, The number of hemibrain cell types that were successfully identified and the

resulting number of FlyWire cell types. **i, j**, Examples for many:1 (**i**) and 1:many (**j**) hemibrain type matches. The dotted vertical lines indicate truncation of the hemibrain neurons. **k**, Graph representation of top NBLAST hits between FlyWire neurons and hemibrain types. This subgraph contains nodes within a radius of three edges from the query cell type (AVLP534). Neurons matching multiple cell types (asterisks) must be manually resolved, which is not always possible. **l**, The number of cells per cross-matched cell type within a brain (FlyWire left versus right) and across brains (FlyWire versus hemibrain).

of the optic lobe. The hemibrain was previously densely cell typed by a combination of two automated procedures followed by extensive manual review^{2,39–41}: NBLAST morphology clustering initially yielded 5,235 morphology types; multiple rounds of CBLAST connectivity clustering split some types, generating 640 connectivity types for a final total of 5,620 types. We have reidentified just 14% of connectivity types and therefore use the 5,235 morphology types as a baseline for comparison. Although 389 (7%) of the hemibrain cell types were previously established in the literature and recorded in the <https://virtualflybrain.org/database>²², principally through analysis of genetic driver lines¹⁹, the great majority (90%) were newly proposed using the hemibrain, that is, derived from a single hemisphere of a single animal. This was reasonable given the pioneering nature of the hemibrain reconstruction, but the availability of the FlyWire connectome now allows for a more stringent re-examination.

We approach this by considering each cell type in the hemibrain as a prediction: if we can reidentify a distinct group of cells with the same properties in both hemispheres of the FlyWire dataset, then we conclude that a proposed hemibrain cell type has been tested and validated. To perform this validation, we first used non-rigid three-dimensional (3D) registration to map meshes and skeletons of all hemibrain neurons into FlyWire space, enabling direct co-visualization of both datasets and a range of automated analyses. We then used NBLAST³⁸ to calculate morphological similarity scores between all hemibrain neurons and the approximately 84,000 FlyWire neurons with arbours at least partially contained within the hemibrain volume (Fig. 3a,b and Extended Data Fig. 4a–c). We manually reviewed the top five NBLAST hits for a random sample of individual neuron-to-neuron matches and found that high NBLAST scores typically indicate a good morphological match (Fig. 3c). Extrapolating from this sample, we expect 99% of hemibrain

neurons to have a morphologically very similar neuron in FlyWire (Fig. 3d).

We next attempted to map hemibrain cell types onto FlyWire neurons. Candidate type matches were manually reviewed by co-visualization and only those with high confidence were accepted (Fig. 3f–h and Methods). Crucially, this initial morphological matching process generated a large corpus of shared cell type labels between datasets; with these in place, we developed an across-dataset connectivity clustering method that enabled us to investigate and resolve difficult cases (see the ‘hemibrain cell type matching with connectivity’ section of the Methods).

The majority of hemibrain cell types (56%; 2,920 out of 5,235 types) were unambiguously found in the FlyWire dataset (Fig. 3f). A further 664 (13%) hemibrain types were mapped but had to be either merged (many:1) or further split (1:many) (Fig. 3h). In total, 7% of proposed hemibrain types were combined to define new ‘composite’ types (for example, SIP078, SIP080) because the hemibrain split could not be recapitulated when examining neurons from both FlyWire and the hemibrain (Fig. 3i and Extended Data Fig. 4e–g). This is not too surprising as the hemibrain philosophy was explicitly to err on the side of splitting in cases of uncertainty². We found that 5% of proposed hemibrain types needed to be split, for example, because truncation of neurons in the hemibrain removed a key defining feature (Fig. 3j). Together these revisions mean that the 3,584 reidentified hemibrain cell types map onto 3,643 consensus cell types (Fig. 3h). All revisions were confirmed by across-dataset connectivity clustering.

Notably, 1,651 (32%) hemibrain cell types could not be reidentified in FlyWire. Ambiguities due to hemibrain truncation can partially explain this: we were much more successful at matching neurons that were not truncated in the hemibrain (Fig. 3g). However, this appears not to be the main explanation. Especially in cases of multiple, very similar, ‘adjacent’ hemibrain types, we often encountered ‘chains’ of ambiguity that made assigning types difficult (Fig. 3k). Further investigation (Fig. 6) suggests that the majority of these unmatched hemibrain types are not exactly replicable across animals. Instead, we show that multi-connectome analysis can generate validated cell types that are robust to interindividual variation.

In conclusion, we validated 3,643 high-confidence consensus cell type labels for 43,737 neurons from three different hemispheres and two different brains (Fig. 3g). Collectively these cross-matched neurons cover 46.5% of central brain edges (comprising 49% of synapses) in the FlyWire graph. This body of high-confidence cross-identified neurons enables both within-brain (FlyWire left versus right hemisphere) and across-brain (FlyWire versus hemibrain) comparisons.

Cell types are highly stereotyped

Using the consensus cell type labels, we found that the numbers of cells per type across the three hemispheres are closely correlated (Fig. 3l). About one in six cell types shows a difference in numbers between the left and right hemisphere and one in three across brains (FlyWire versus hemibrain). The mean difference in the number of cells per type is small though: 0.3 (± 1.8) within brains and 0.8 (± 10) across brains. Importantly, cell types with fewer neurons per type are less variable (Extended Data Fig. 4i, j). At the extreme, ‘singleton’ cell types account for 59% of all types in our sample; they often appear to be embryonic-born, or early secondary neurons, and only very rarely comprise more than one neuron—only 3% of neurons that are singletons in both FlyWire hemispheres have more than 1 member in the hemibrain. By contrast, more numerous cell types are also more likely to vary in number both within but even more so across brains (Extended Data Fig. 4i, j).

Synapse counts were also largely consistent within cell types, both within and across brains. To enable a fair comparison, the FlyWire synapse cloud was restricted to the smaller hemibrain volume. Although this does not correct for other potential confounds such as differences

in the synaptic completion rates or synapse detection, pre- and post-synapse counts per cell type were highly correlated, both within brains (Pearson $R = 0.99$; $P < 0.001$) and across brains (Pearson $R = 0.92$ and 0.76 for pre- and post-synapses, respectively; $P < 0.001$; Fig. 4a, b and Extended Data Fig. 4k, l). This is an important quality control and pre-requisite for subsequent connectivity comparisons.

The fly brain is mostly left–right symmetric, but inspection of the FlyWire dataset revealed a small number of asymmetries. For example, LC6 and LC9 visual projection neurons form a large axon bundle that follows the normal path in the right hemisphere⁴² but, in the left hemisphere, it loops over (that is, medial) the mushroom body peduncle; nevertheless, the axons still find their correct targets as previously reported⁴³. We annotated other examples of this ranging from small additional/missing branches to misguided neurite bundles and found that only 0.4% of central brain neurons exhibit such biological oddities (Extended Data Fig. 5).

Interpreting connectomes

Brain wiring develops through a complex and probabilistic developmental process^{44,45}. To interpret the connectome, it is vital to obtain a basic understanding of how variable that biological process is. This is complicated by the fact that the connectome we observe is shaped not just by biological variability but also by technical noise, for example, from segmentation issues, synapse detection errors and synaptic completion rates (the fraction of synapses attached to proofread neurons) (Fig. 4a). Here we use the consensus cell types to assess which connections are reliably observed across three hemispheres of connectome data. We use the term ‘edge’ to describe the set of connections between two cell types, and its ‘weight’ as the number of unitary synapses (no threshold, that is, ≥ 1 synapses) forming that connection.

Weights of individual edges are highly correlated within (Pearson $R = 0.97$, $P < 0.001$) and across (Pearson $R = 0.8$, $P < 0.001$) brains (Fig. 4c and Extended Data Fig. 6a). Consistent with this, cell types exhibit highly similar connectivity within as well as across brains (Fig. 4d and Extended Data Fig. 6b, c). While the connectivity (cosine) similarity across brains is lower than within brains ($P < 0.001$), the effect size is small (0.045 ± 0.096) and is at least in part due to the aforementioned truncation in the hemibrain.

We next examined, for a given edge between two cell types in one hemisphere, the odds of finding the same connection in another hemisphere or brain. Examination of 572,980 edges present in at least one of the three brain hemispheres showed that 53% of the edges observed in the hemibrain were also found in FlyWire. This fraction is slightly higher when comparing between the two FlyWire hemispheres: left to right: 61%; right to left: 59% (Fig. 4e). Weaker edges were less likely to be consistent: an edge consisting of a single synapse in the hemibrain has a 42% chance to be also present in a single FlyWire hemisphere, and only a 16% chance to be seen in both hemispheres of FlyWire (Fig. 4f). By contrast, any edge of more than ten synapses in any hemisphere can be reproducibly ($>90\%$ of the time, rounded) found in the other two hemispheres. Although only 16% of all edges meet this threshold, they comprise around 79% of all synapses (Fig. 4g and Extended Data Fig. 6e). We also analysed normalized edge weights expressed as the fraction of the input onto each downstream neuron; this accounts for the small difference in synaptic completion rate between FlyWire and the hemibrain. With this treatment, the distributions are almost identical for within and across brain comparisons (Fig. 4g (compare the left and right panels)); edges constituting $\geq 0.9\%$ of the target cell type’s total inputs have a greater than 90% chance of persisting (Fig. 4g (right)). Around 7% of edges, collectively containing over half (54%) of all synapses, meet this threshold.

We observed that the fraction of edges persisting across datasets plateaued as the edge weight increased. Using a level of 99% edge persistence, we can define a second principled heuristic: edges greater than

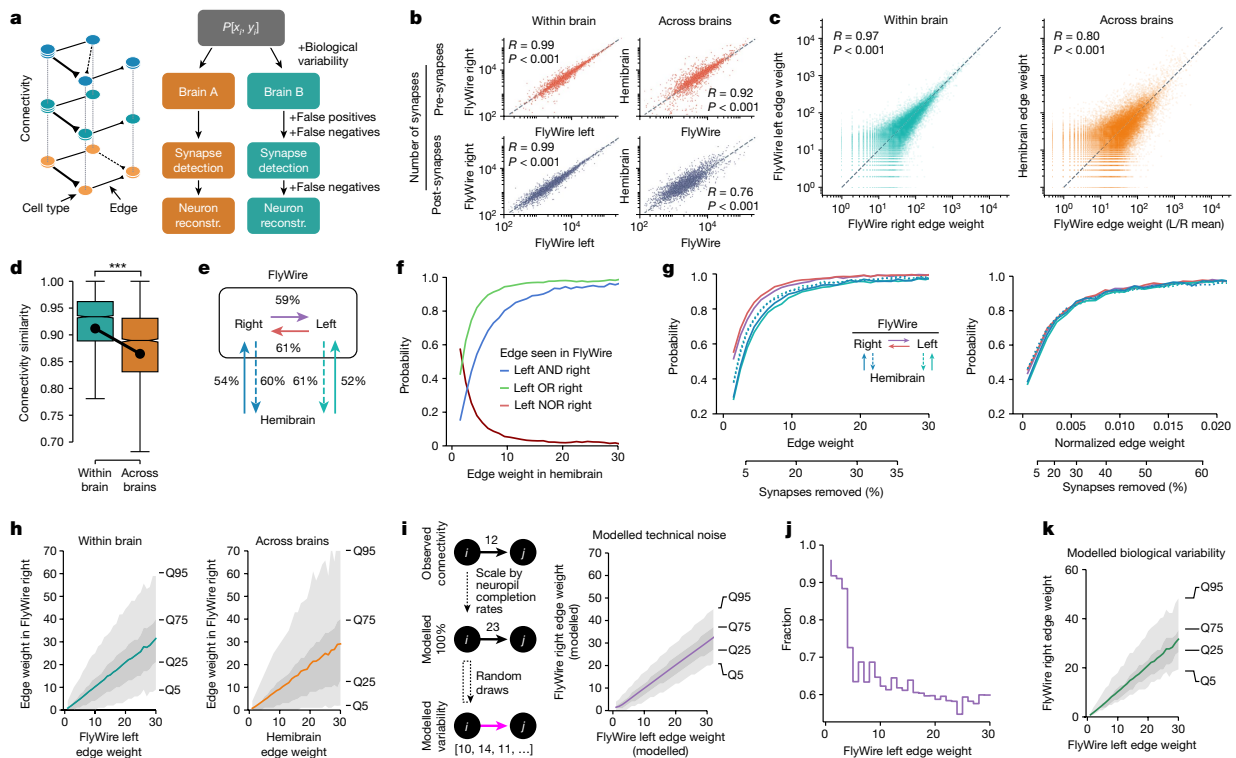


Fig. 4 | Connectivity stereotypy. **a**, Connectivity comparisons and potential sources of variability. Reconst., reconstruction. **b**, The number of pre- and post-synapses per cross-matched cell type. **c, d**, Edge weights (**c**) and cosine connectivity similarity (**d**) between cross-matched cell types. The whiskers represent 1.5× the interquartile range. **e**, The percentage of edges in one hemisphere that can be found in another hemisphere. **f**, The probability that an edge present in the hemibrain is found in one, both or neither of the hemispheres in FlyWire. A plot with normalized edge weights is shown in Extended Data Fig. 6d. **g**, The probability that an edge is found within and across brains as a function of total (left) and normalized (right) edge weight. The second x axis shows the percentage of synapses below a given weight. **h**, Correlation of across-edge (left) and within-edge (right) edge weights.

2.6% edge weight (or 31 synapses) can be considered to be strong. Note that these statistics defined across the whole connectome can have exceptions in individual neurons. For example, descending neuron DNp42 receives 34 synapses from PLP146 in FlyWire right, but none on the left or hemibrain; this may well be an example of developmental noise (that is, bona fide biological variability, rather than technical noise).

So far, we have examined only the binary question of whether an edge exists or not. However, the conservation of edge weight is also highly relevant for interpreting connectomes. We next considered, given that an edge is present in two or more hemispheres, the odds that it will have a similar weight. Edge weights within and across brains are highly correlated (Fig. 4c), a 30-synapse edge in the hemibrain, for example, will on average consist of 29 synapses in FlyWire, despite differences in synaptic detection and completion rates for these two datasets imaged with different EM modalities¹. The variance of edge weights is considerable though: 25% of all 30-synapse hemibrain edges will consist of fewer than 13 synapses in FlyWire, and 5% will consist of only 1–2 synapses. Consistency is greater when looking within FlyWire: a 30-synapse edge on the left will, on average, consist of 31 synapses on the right. Still, 25% of all 30-synapse edges on the left will consist of 21 synapses or less on the right, and 5% of only 1–8 synapses (Fig. 4h).

The envelopes represent quantiles. **i**, Model for the impact of technical noise (synaptic completion rate, synapse detection) on synaptic weight from cell types i to j . The raw weight from the connectome for each individual edge is scaled up by the computed completion rate for all neurons within the relevant neuropil; random draws of the same fraction of those edges then allow an estimate of technical noise. **j**, Observed variability explainable by technical noise as fraction of FlyWire left–right edge pairs that fall within the 5–95% quantiles for the modelled technical noise. **k**, Modelled biological variability (observed variability – technical noise). R (**b** and **c**) is the Pearson correlation coefficient. For **d**, statistical analysis was performed using unpaired t -tests; $***P < 0.001$.

To assess how much of this edge weight variability is biological and how much is technical, we modelled the impact of technical noise on a fictive ground truth connectome (Fig. 4i and Methods). This model was randomly subsampled according to postsynaptic completion rate (in the mushroom body calyx, for example, there is a 6% difference between the left and right hemisphere of FlyWire; Extended Data Fig. 6f), and synapses were randomly added and deleted according to the false-positive and false-negative rates reported for the synapse detection⁴⁶. Repeated application of this procedure generated a distribution of edge weights between each cell type pair expected due to technical noise alone. On average, 65% of the observed variability of edge weight between hemispheres fell within the range expected due to technical noise; this fraction approached 100% for weaker synapses (Fig. 4j). For example, cell type LHAV3g2 targets LHAV3g2 with 30 synapses on the left but only 23 on the right of FlyWire, which is within the 5–95% quantiles expected due to technical noise alone. Overall, this analysis shows that observed variability (Fig. 4h (left)) is greater than can be accounted for by technical noise, establishing a lower bound for likely biological variability (Fig. 4k), and suggests another simple heuristic: differences in edge weights of 30% or less may be entirely due to technical noise and should not be overinterpreted.

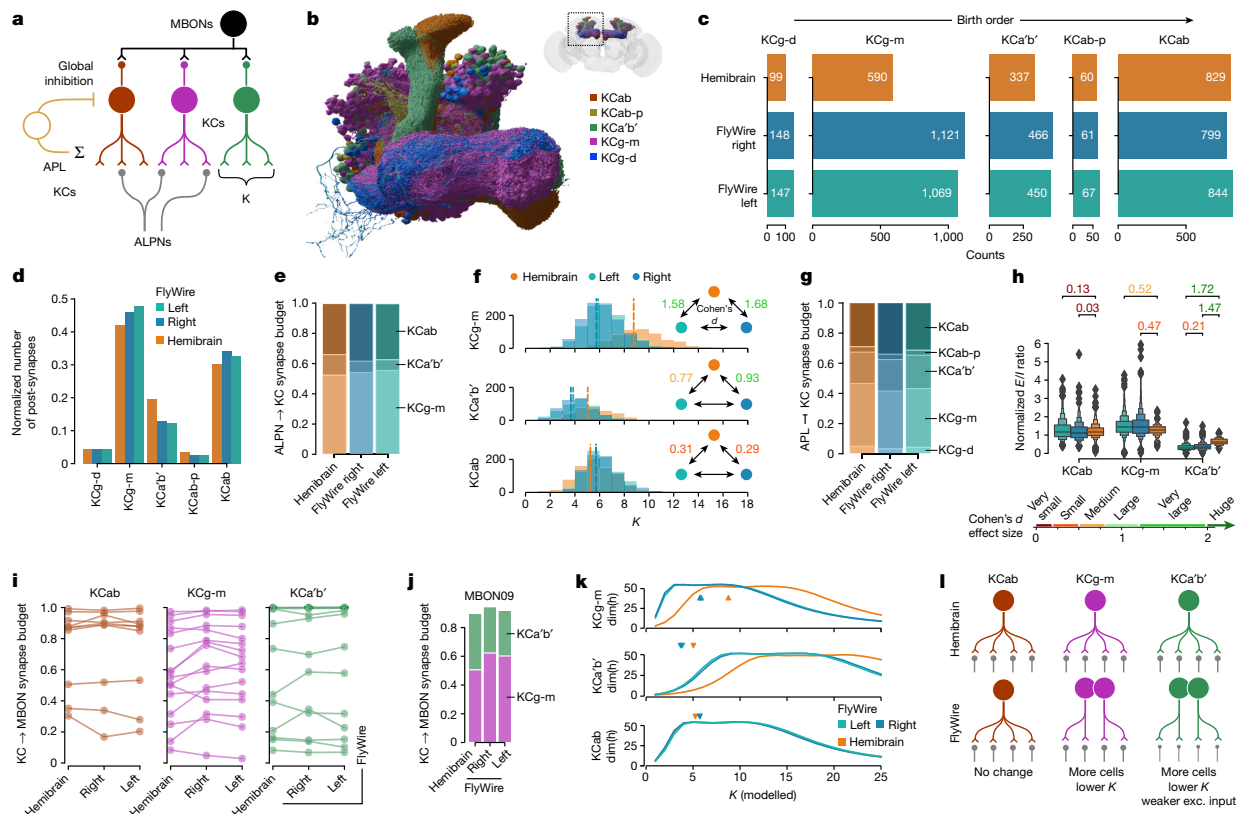


Fig. 5 | Variability in the mushroom body. **a**, Schematic of mushroom body circuits. *K* refers to the number of ALPN types that a KC samples from. Neuron types not shown are as follows: DANs, DPM and OANs. **b**, Rendering of KC types. **c**, Per-type KC counts across the three hemispheres. **d**, KC post-synapse counts, normalized to total KC post-synapses in each dataset. **e**, The fraction of ALPN to KC budget spent on individual KC types. **f**, The number of ALPN types a KC receives input from *K*. The dotted vertical lines represent the mean. **g**, The fraction of APL to KC budget spent on individual KC types. **h**, The normalized

excitation/inhibition ratio for KCs. An explanation of enhanced box plots is provided in the Methods. **i**, The fraction of MBON input budget coming from KCs. Each line represents an MBON type. **j**, MBON09 as an example for KC to MBON connectivity. All MBONs are shown in Extended Data Fig. 7. **k**, Dimensionality (*dim(h)*) as function of a modelled *K*. The arrowheads mark observed mean *K* values. **l**, Summarizing schematic. Exc., excitatory. For **f** and **h**, Cohen's *d* effect size values are shown for pairwise comparisons where $P \leq 0.01$; Welch's tests (**f**) and Kolmogorov–Smirnov tests (**h**) were applied.

Variability in the mushroom body

The comprehensive annotation of cell types in the FlyWire dataset revealed that the number of Kenyon cells (KCs), the intrinsic neurons of the mushroom body, is 30% larger per hemisphere than in the hemibrain (2,597 KCs in FlyWire right; 2,580 in FlyWire left; and 1,917 in hemibrain), well above the average variation in cell counts ($5 \pm 12\%$). While these KC counts are within the previously reported range⁴⁷, the difference presents an opportunity to investigate how connectomes accommodate perturbations in cell count. The mushroom body contains five principal cell classes: KCs, mushroom body output neurons (MBONs), modulatory neurons (dopaminergic neurons (DANs) and octopaminergic neurons (OANs)), the dorsal paired medial (DPM) and anterior paired lateral neuron (APL) giant interneurons⁴⁸ (Fig. 5a). KCs further divide into five main cell types on the basis of which parts of the mushroom body they innervate: KCab, KCab-p, KCg-m, KCa'b' and KCg-d (Fig. 5b). Of those, KCab, KCa'b' and KCg-m are the primary recipients of largely random^{39,49} (but see ref. 50) olfactory input through around 130 antennal lobe projection neurons (ALPNs) comprising 58 canonical types^{39,40}. Global activity in the mushroom body is regulated through an inhibitory feedback loop mediated by APL, a single large GABAergic neuron⁵¹. Analogous to the mammalian cerebellum, KCs transform the dense overlapping odour responses of the early olfactory

system into sparse non-overlapping representations that enable the animal to discriminate between individual odours during associative learning^{52,53}. The difference in cell counts is not evenly distributed across all KC types: KCg-m (and to a lesser extent KCg-d and KCa'b') are almost twice as numerous in FlyWire versus hemibrain while KCab and KCab-p are present in similar numbers (Fig. 5c). Protein starvation during the larval stage can induce specific increases in KCg-m number⁵⁴, suggesting that environmental variations in food resources may have contributed to this difference.

To examine how this affects the mushroom body circuitry, we opted to compare the fraction of the input or output synaptic budget across different KCs, as this is well matched to our question and naturally handles a range of technical noise issues that seemed particularly prominent in the mushroom body completion rate (Methods and Extended Data Fig. 7a). We found that, despite the large difference in KCg-m cell counts between FlyWire and hemibrain, this cell type consistently makes and receives 32% and 45% of all KC pre-synapses and post-synapses, respectively (Fig. 5d and Extended Data Fig. 7e). This suggested that individual FlyWire KCg-m neurons receive fewer inputs and make fewer outputs than their hemibrain counterparts. The share of ALPN outputs allocated to KCg-m is around 55% across all hemispheres (Fig. 5e), and the average ALPN to KCg-m connection is comparable in strength across hemispheres (Extended Data Fig. 7f); however, each

KCg-m neuron receives input from a much smaller number of ALPN types in FlyWire than in the hemibrain (5.74, 5.89 and 8.76 for FlyWire left, right and hemibrain, respectively; Fig. 5f). FlyWire KCg-m neurons therefore receive inputs with the same strength but from fewer ALPNs.

This pattern holds for other KCg-m synaptic partners as well. Similar to the excitatory ALPNs, the share of APL outputs allocated to KCg-m neurons is essentially constant across hemispheres (Fig. 5g). Thus, each individual KCg-m neuron receives proportionally less inhibition from the APL, as well as less excitation, maintaining a similar excitation/inhibition ratio (Fig. 5h). Furthermore, as a population, KCg-m neurons contribute similar amounts of input to MBONs (Fig. 5i,j and Extended Data Fig. 7h).

Past theoretical work has shown that the number (K) of discrete odour channels (that is, ALPN types) providing input to each KC has an optimal value for maximizing dimensionality of KC activity and, therefore, discriminability of olfactory input^{52,53}. The smaller value for K observed for KCg-m neurons in the FlyWire connectome (Fig. 5g) raises the question of how dimensionality varies with K for each of the KC types. Using the neural network rate model described previously⁵², we calculated dimensionality as a function of K for each of the KC types, using the observed KC counts, ALPN to KC connectivity and global inhibition from the APL. This analysis revealed that optimal values for K are lower for KCg-m neurons in FlyWire than in the hemibrain (Fig. 5k), consistent with the observed values.

Taken together, these results demonstrate that, for KCg-m neurons, the brain compensates for a developmental perturbation by changing a single parameter: the number of odour channels each KC samples from. By contrast, KCa'b' cells, which are also more numerous in FlyWire than in the hemibrain, appear to use a hybrid strategy of reduced K combined with a reduction in ALPN to KCa'b' connection strength (Extended Data Fig. 7f). These findings contradict earlier studies in which a global increase in KC numbers through genetic manipulation triggered an increase in ALPN axon boutons (indicating a compensatory increase in excitatory drive to KCs) and a modest increase in KC claws (suggesting an increase rather than decrease in K)^{55,56}. This may be due to the differences in the nature and timing of the perturbation in KC cell number, and the KC types affected.

Toward multiconnectome cell typing

As the first dense, large-scale connectome of a fly brain, the hemibrain dataset proposed over 5,000 previously unknown cell types in addition to confirming around 400 previously reported types recorded in the <http://virtualflybrain.org/database>²². As this defines a de facto standard cell typing for large parts of the fly brain, our initial work plan was simply to reidentify hemibrain cell types in FlyWire, providing a critical resource for the fly neuroscience community. While this was successful for 68% of hemibrain cell types (Fig. 3), 32% could not be validated. Given the great stereotypy generally exhibited by the fly nervous system, this result is both surprising and interesting.

We can imagine two basic categories of explanation. First, that through ever closer inspection, we may successfully reidentify these missing cell types. Second, that these definitions, mostly based on a single brain hemisphere, might not be robust to variation across individuals. Distinguishing between these two explanations is not at all straightforward. We began by applying across-dataset connectivity clustering to large groups of unmatched hemibrain and FlyWire neurons. We observed that most remaining hemibrain types showed complex clustering patterns, which both separated neurons from the same proposed cell type and recombined neurons of different proposed hemibrain types.

While it is always more difficult to prove a negative result, these observations strongly suggest that the majority of the remaining 1,696 hemibrain types are not robust to interindividual variation. We

therefore developed a definition of cell type that uses interanimal variability: a cell type is a group of neurons that are each more similar to a group of neurons in another brain than to any other neuron in the same brain. This definition can be used with different similarity metrics but, for connectomics data, a similarity measure incorporating morphology and/or connectivity is most useful. Our algorithmic implementation of this definition operates on the co-clustering dendrogram by finding the smallest possible clusters that satisfy two criteria (Fig. 6a): (1) each cluster must contain neurons from all three hemispheres (hemibrain, FlyWire right and FlyWire left); (2) within each cluster, the number of neurons from each hemisphere must be approximately equal.

Determining how to cut a dendrogram generated by data clustering is a widespread challenge in data science for which there is no single satisfactory solution. A key advantage of the cell type definition that we propose is that it provides very strong guidance about how to assign neurons to clusters. This follows naturally from the fact that connectome data provide us with all neurons in each dataset, rather than a random subsample. This advantage of completeness is familiar from analogous problems such as the ability to identify orthologous genes when whole genomes are available⁵⁷.

Analysis of the hemibrain cell type AOTU063 provides a relatively straightforward example of our approach (Fig. 6b and Extended Data Fig. 10). Morphology-based clustering generates a single group, comprising all six AOTU063 neurons from each of the three hemispheres. However, clustering based on connectivity reveals two discrete groups, with equal numbers of neurons from each hemisphere, suggesting that this type should be split further. Here, algorithmic analysis across multiple connectomes reveals consistent connectivity differences between subsets of AOTU063 neurons.

To test whether this approach is applicable to more challenging sets of neurons, we set aside the hemibrain types and performed a complete retying of neurons in the central complex (Fig. 6c), a centre for navigation in the insect brain that has been subject to detailed connectome analysis⁴¹. We selected two large groups of neurons innervating the fan-shaped body (FB) that show a key difference in organization. The first group, FC1–3 (357 neurons in total), consists of columnar cell types that tile the FB innervating adjacent non-overlapping columns. The second group, FB1–9 (897 neurons in total), contains tangential neurons where neurons of the same cell type are precisely co-located in space⁴¹ (Fig. 6d). Standard NBLAST similarity assumes that neurons of the same cell type overlap closely in space; although this is true for most central brain types, it does not hold for repeated columnar neurons such as those in the optic lobe or these FC neurons of the FB. We therefore used a connectivity-only distance metric co-clustering across the three hemispheres. This resulted in seven FC clusters satisfying the above criteria (Fig. 6e,f). Five of these cross-brain types have a one-to-one correspondence with hemibrain types, while two are merges of multiple hemibrain types; only a small number of neurons are recombined across types (Fig. 6g). For the second group, FB1–9, a combined morphology and connectivity embedding was used. Co-clustering across the three hemispheres generated 114 cell types compared to 146 cell types in the hemibrain (Fig. 6h and Extended Data Fig. 8). In total, 44% of these types correspond one-to-one to a hemibrain cell type; 11% are splits (1:many), 12% are merges (many:1) and 33% are recombinations (many:many) of hemibrain cell types. The 67% (44 + 11 + 12) success rate of this de novo approach in identifying hemibrain cell types is slightly higher than the 61% achieved in our directed work in Fig. 3; it is consistent with the notion that further effort could still identify some unmatched hemibrain types, but that the majority will probably require retying.

All of the preceding efforts have focused on cell typing neurons contained within both FlyWire and the hemibrain. We next examined the extensive regions of the brain covered only by FlyWire and not by hemibrain. Based on the lessons learned from the joint analysis of

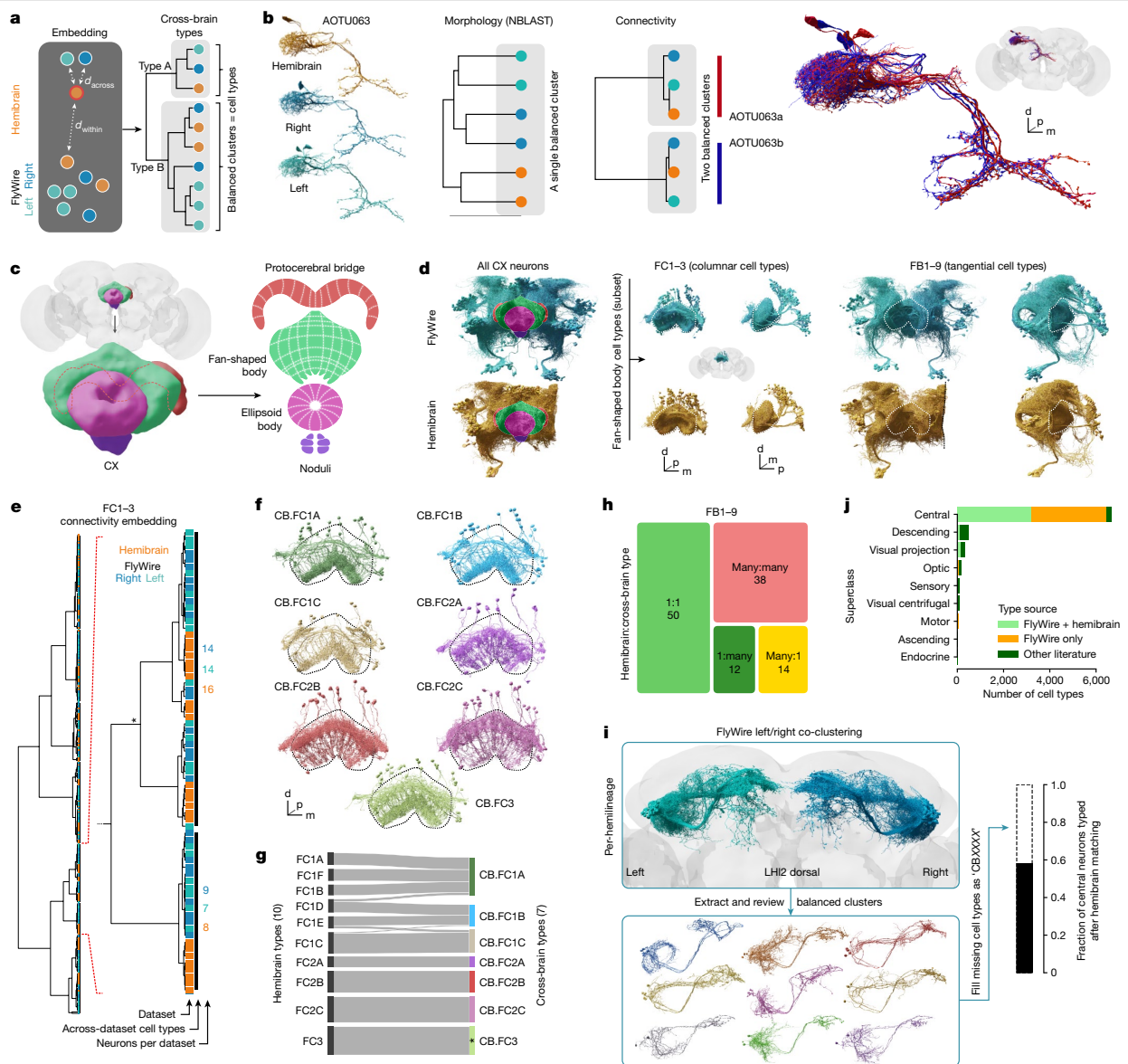


Fig. 6 | Across-brain cell typing. **a**, Cell type is defined as a group of neurons that are each more similar to a group in another brain than to any neurons in the same brain. We expect cell type clusters to be balanced, that is, contain neurons from all three hemispheres in approximately even numbers. **b**, Example of a hemibrain cell type (AOTU063) that is morphologically homogeneous but has two cross-brain consistent connectivity types and can therefore be split. **c**, Main neuropils making up the central complex (CX). **d**, Overview of all CX cells (left) and two subsets of fan-shaped body (FB, dotted outlines) cell types: FC1–3 and FB1–9 (right). **e**, Hierarchical clustering from connectivity embedding for FC1–3 cells. A magnification of cross-brain cell type clusters is

shown. The asterisk marks a cluster that was manually adjusted. **f**, Renderings of FC1–3 across-brain types; the FB is outlined. The tiling of FC1–3 neurons can be discerned. **g**, Comparison of FC1–3 hemibrain and cross-brain cell types. The colours correspond to those in **f**. **h**, Mappings between hemibrain and cross-brain cell types for FB1–9. A detailed flow chart is provided in Extended Data Fig. 8. **i**, The pipeline for generating types for neurons without a hemibrain cell type. Hemilineage LHI2 dorsal is shown as an example. The box plot shows the fraction of FlyWire neurons with a hemibrain-derived cell type. **j**, Cell type source broken down by super class.

hemibrain and FlyWire, we ran a co-clustering of neurons from the two hemispheres of FlyWire to fill in missing cell types (Fig. 6i,j and Extended Data Fig. 9). This combined both morphology and connectivity measures, was carried out separately for each hemilineage and produced 3,200 new central brain cell types for a total of 8,453 including the optic lobes. We further compared double-hemisphere (FlyWire left/right) and triple-hemisphere analysis (FlyWire + hemibrain) for 25 cross-identified lineages that are not truncated in the hemibrain. This

comparison found that 70% of these new types survive addition of a third hemisphere with minor edits (1:many, many:1). That percentage increases to 84% if we exclude cases in which just one neuron changes clusters (Extended Data Fig. 9).

In summary, cell typing based on joint analysis of multiple connectomes proved capable of recapitulating many cell types identified in the hemibrain dataset, while also defining new candidate cell types that are consistent both within and across datasets. Further validation

of the new types proposed by this approach will depend on additional *Drosophila* connectomes, which are forthcoming. We predict that cell types defined in this manner will be substantially more robust than cell types defined from a single connectome alone.

Discussion

Here we generated human-readable annotations for all neurons in the fly brain at various levels of granularity: superclass, cell class, hemilineage, morphology group and cell type. These annotations provide salient groupings that have already been proven to be useful not only in our own analyses, but also in many of those in our companion paper¹ as well as other publications in the FlyWire paper package introduced there, and to researchers now using the online platforms Codex (<https://codex.flywire.ai>) and FAFB-FlyWire CATMAID spaces (<https://fafb-flywire.catmaid.org>). Hemilineage annotations also provide a key starting point to link the molecular basis of the development of the central brain to the wiring revealed by the connectome; such work has already begun in the more repetitive circuits of the optic lobe⁵⁸.

The cell type atlas that we provide of 8,453 cell types, covering 96.4% of all neurons in the brain, is to our knowledge the largest ever proposed (the hemibrain had 5,235) and, crucially, by some margin the largest ever validated collection of cell types¹⁹. In *C. elegans*, the 118 cell types inferred from the original connectome have been clearly supported by analysis of subsequent connectomes and molecular data^{3,59,60}. In a few cases in mammals, it has been possible to produce catalogues of order 100 cell types that have been validated by multimodal data, for example, in the retina or motor cortex^{20,61}. Although large scale molecular atlases in the mouse produce highly informative hierarchies of up to 5,000 clusters^{62–64}, they do not yet try to define terminal cell types—the finest unit that is robust across individuals—with precision. Here we tested over 5,000 predicted cell types, resulting in 3,884 validated cell types using three hemispheres of connectome data. Informed by this, we use the FlyWire dataset to propose an additional 3,685 cell types.

Lessons for cell typing

Our experience of cell typing the FlyWire dataset together with our earlier participation in the hemibrain cell typing effort leads us to draw a number of lessons. First, we think that it is helpful to frame cell types generated in one dataset as predictions or hypotheses that can be tested either through additional connectome data or data from other modalities. Related to this, although the two hemispheres of the same brain can be treated as two largely independent datasets, we do see evidence that variability can be correlated across hemispheres (Fig. 4). We therefore recommend the use of three or more hemispheres to define and validate new cell types both because of increased statistical confidence and because across-brain comparisons are a strong test of cell type robustness. Third, there is no free lunch in the classic lumping versus splitting debate. The hemibrain cell typing effort preferred to split rather than lump cell types, reasoning that over-splitting could easily be remedied by merging cell types at a later date². Although this approach seemed reasonable at the time, it appears to have led to cell types being recombined: when using a single dataset, even domain experts may find it very hard to distinguish conserved differences between cell types from interindividual noise. Moreover, although some recent studies have argued that cell types are better defined by connectivity than morphology, we find that there is a place for both. For de novo cell typing of future connectomes, we recommend an initial morphology-only matching to assign obvious matches; these shared cell type labels can then be used to define connection similarity across datasets. This then allows extraction of balanced clusters from combined morphology and connectivity co-clustering that can be used to assign or refine existing cell types.

Related to this, we find that across-dataset connection similarity is an extremely powerful way to identify cell types. However,

connectivity-based typing is typically used iteratively and especially when used within a single dataset this may lead to selection of idiosyncratic features. Moreover, neurons can connect similarly but come from a different developmental lineage, or express a different neurotransmitter, precluding them from sharing a cell type. Combining these two points, we would summarize that matching by morphology appears to be both more robust and sometimes less precise, whereas connectivity matching is a powerful tool that must be wielded with care.

In conclusion, connectome data are particularly suitable for cell typing: they are inherently multimodal (by providing morphology and connectivity), while the ability to see all cells within a brain (completeness) is uniquely powerful. Our multiconnectome typing approach (Fig. 6) provides a robust and efficient way to use such data; cell types that have passed the rigorous test of across-connectome consistency are very unlikely to be revised (permanence). We suspect that connectome data will become the gold standard for cell typing. Linking molecular and connectomics cell types will therefore be key. One promising new approach is exemplified by the prediction of neurotransmitter identity directly from EM images²¹ but many others will be necessary.

Finally, we address the three questions introduced in the introduction.

Can we simplify the connectome graph?

Cell typing reduces the complexity of the connectome graph. This has important implications for analysis, modelling, experimental work and developmental biology. For example, we can reduce the 131,811 typed nodes in the raw connectome graph into a cell type graph with 8,453 nodes; the number of edges is similarly reduced. This should significantly aid human reasoning about the connectome. It will also make numerous network analyses possible as well as substantially reduce the degrees of freedom in brain scale modelling^{65,66}. It is important to note that, while collapsing multiple cells for a given cell type into a single node is often desirable, other use cases such as modelling studies may still need to retain each individual cell. However, if key parameters are determined on a per cell type basis, then the complexity of the resultant model can be much reduced. A recent study⁶⁵ optimized and analysed a highly successful model of large parts of the fly visual system with just 734 free parameters by using connectomic cell types.

For *Drosophila* experimentalists using the connectome, cell typing identifies groups of cells that probably form functional units. Most of these are linked though <http://virtualflybrain.org/> to the published literature and in many cases to molecular reagents. Others will be more easily identified for targeted labelling and manipulation after typing. Finally, cell typing effectively compresses the connectome, reducing the bits required to store and specify the graph. For a fly-sized connectome, this is no longer that important for computational analysis, but it may be important for brain development. Some⁶⁷ have argued that evolution has selected highly structured brain connectivity enabling animals to learn very rapidly, but that these wiring diagrams are far too complex to be specified explicitly in the genome; rather, they must be compressed through a 'genomic bottleneck', which may itself have been a crucial part of evolving robust and efficient nervous systems. If we accept this argument, lossy compression based on aggregating nodes with similar cell type labels, approximately specifying strong edges and largely ignoring weak edges would reduce the storage requirements by orders of magnitude and could be a specific implementation of this bottleneck.

Which edges are important?

The question of which of the 15.1 million edges in the connectome to pay attention to is critical for its interpretation. Intuitively, we assume that the more synapses that connect two neurons, the more important that connection must be. There is some very limited evidence in support of this assumption correlating anatomical and functional connectivity^{68,69} (compare in mammals⁷⁰). In lieu of physiological data, we postulate that edges that are critical to brain function should be

Article

consistently found across brains. By comparing connections between cell types identified in three hemispheres, we find that edges stronger than ten synapses or $\geq 0.9\%$ of the target's inputs have a greater than 90% chance to be preserved (Fig. 4f). This provides a simple heuristic for determining which edges are likely to be functionally relevant. It is also highly consistent with findings from the larval connectome, in which left–right asymmetries in connectivity vanish after removing edges weaker than $< 1.25\%$ (ref. 71). However, note that edges falling below the threshold might still significantly contribute to the brain's function.

We further address an issue that has received little attention (but see ref. 72): the impact of technical factors (such as segmentation, proofreading, synapse detection) and biological variability on the final connectome and how to compensate for it. In our hands, a model of technical noise could explain up to 30% difference in edge weights. While this model was made specifically for the two hemispheres of FlyWire, it highlights the general point that a firm understanding of all sources of variability will be vital for the young field of comparative connectomics to distinguish real and artificial differences.

Have we collected a snowflake?

The field of connectomics has long been criticized for unavoidably low $n^{73,74}$, raising the question of whether the brain of a single specimen is representative for all. For insects, there is a large body of evidence for morphological and functional stereotypy, although this information is available for only a minority of neurons and much less is known about stereotyped connectivity^{19,75,76}. For vertebrate brains, the situation is less clear again; it is generally assumed that subcortical regions will be more stereotyped, but cortex also has conserved canonical microcircuits⁷⁷ and recent evidence has shown that some cortical elements can be genetically and functionally stereotyped⁷⁸. Given how critical stereotypy is for connectomics, it is important to check whether that premise actually still holds true at the synaptic resolution.

For the fly connectome, the answer to our question is actually both more nuanced and more interesting than we initially imagined. Based on conservation of edges between FlyWire and hemibrain hemispheres, over 50% of the connectome graph is a snowflake. Of course, these non-reproducible edges are mostly weak. Our criterion for strong (highly reliable) edges applies to between 7–16% of edges but 50–70% of synapses.

We previously showed that the early olfactory system of the fly is highly stereotyped in both neuronal number and connectivity⁴⁰. That study used the same EM datasets—FAFB and the hemibrain—but was limited in scope as only manual reconstruction in FAFB was then available. We now analyse brain-wide data from two brains (FlyWire and the hemibrain) and three hemispheres to address this question and find a high degree of stereotypy at every level: neuron counts are highly consistent between brains, as are connections above a certain weight. However, when examining so many neurons in a brain, we can see that cell counts are very different for some neurons; furthermore, neurons occasionally do something unexpected (take a different route or make an extra branch on one side of the brain). In fact, we hypothesize that such stochastic differences are unnoticed variability present in most brains; this is reminiscent of the observation that most humans carry multiple significant genetic mutations. We did observe one example of a substantial biological difference that was consistent across hemispheres but not brains: the number of the KCg-m neurons in the mushroom bodies is almost twice as numerous in FlyWire than in the hemibrain. Notably, we found evidence that the brain compensates for this perturbation by modifying connectivity (Fig. 5).

In conclusion, we have not collected a snowflake. The core FlyWire connectome is highly conserved and the accompanying annotations will be broadly useful across all studies of *D. melanogaster*. However, our analyses show the importance of calibrating our understanding of

biological (and technical) variability—as has recently been done across animals in *C. elegans*⁶⁰ and across hemispheres in larval *Drosophila*^{71,79}. This will be crucial when using future connectomes to identify true biological differences, for example, in sexually dimorphic circuits or changes due to learning.

Online content

Any methods, additional references, Nature Portfolio reporting summaries, source data, extended data, supplementary information, acknowledgements, peer review information; details of author contributions and competing interests; and statements of data and code availability are available at <https://doi.org/10.1038/s41586-024-07686-5>.

1. Dorkenwald, S. et al. Neuronal wiring diagram of an adult brain. *Nature* <https://doi.org/10.1038/s41586-024-07558-y> (2024).
2. Scheffer, L. K. et al. A connectome and analysis of the adult central brain. *eLife* **9**, e57443 (2020).
3. White, J. G., Southgate, E., Thomson, J. N. & Brenner, S. The structure of the nervous system of the nematode *Caenorhabditis elegans*. *Philos. Trans. R. Soc. Lond. B* **314**, 1–340 (1986).
4. Varshney, L. R., Chen, B. L., Paniagua, E., Hall, D. H. & Chklovskii, D. B. Structural properties of the *Caenorhabditis elegans* neuronal network. *PLoS Comput. Biol.* **7**, e1001066 (2011).
5. Abbott, L. F. et al. The mind of a mouse. *Cell* **182**, 1372–1376 (2020).
6. Winding, M. et al. The connectome of an insect brain. *Science* **379**, eadd9330 (2023).
7. Bidaye, S. S., Machacek, C., Wu, Y. & Dickson, B. J. Neuronal control of *Drosophila* walking direction. *Science* **344**, 97–101 (2014).
8. von Philipsborn, A. C. et al. Neuronal control of *Drosophila* courtship song. *Neuron* **69**, 509–522 (2011).
9. Vijayan, V. et al. An internal expectation guides *Drosophila* egg-laying decisions. *Sci. Adv.* **8**, eabn3852 (2022).
10. Aso, Y. et al. Mushroom body output neurons encode valence and guide memory-based action selection in *Drosophila*. *eLife* **3**, e04580 (2014).
11. Séjourné, J. et al. Mushroom body efferent neurons responsible for aversive olfactory memory retrieval in *Drosophila*. *Nat. Neurosci.* **14**, 903–910 (2011).
12. Neuser, K., Triphan, T., Mronz, M., Poeck, B. & Strauss, R. Analysis of a spatial orientation memory in *Drosophila*. *Nature* **453**, 1244–1247 (2008).
13. Seelig, J. D. & Jayaraman, V. Neural dynamics for landmark orientation and angular path integration. *Nature* **521**, 186–191 (2015).
14. Giraldo, Y. M. et al. Sun navigation requires compass neurons in *Drosophila*. *Curr. Biol.* **28**, 2845–2852.e4 (2018).
15. Duistermars, B. J. & Frye, M. A. Crossmodal visual input for odor tracking during fly flight. *Curr. Biol.* **18**, 270–275 (2008).
16. Okubo, T. S., Patella, P., D'Alessandro, I. & Wilson, R. I. A neural network for wind-guided compass navigation. *Neuron* **107**, 924–940 (2020).
17. Zheng, Z. et al. A complete electron microscopy volume of the brain of adult *Drosophila melanogaster*. *Cell* **174**, 730–743 (2018).
18. Zeng, H. & Sanes, J. R. Neuronal cell-type classification: challenges, opportunities and the path forward. *Nat. Rev. Neurosci.* **18**, 530–546 (2017).
19. Bates, A. S., Janssens, J., Jefferis, G. S. & Aerts, S. Neuronal cell types in the fly: single-cell anatomy meets single-cell genomics. *Curr. Opin. Neurobiol.* **56**, 125–134 (2019).
20. Sanes, J. R. & Masland, R. H. The types of retinal ganglion cells: current status and implications for neuronal classification. *Annu. Rev. Neurosci.* **38**, 221–246 (2015).
21. Eckstein, N. et al. Neurotransmitter classification from electron microscopy images at synaptic sites in *Drosophila melanogaster*. *Cell* **187**, 2574–2594 (2024).
22. Court, R. et al. Virtual fly brain—an interactive atlas of the *Drosophila* nervous system. *Front. Physiol.* **14**, 1076533 (2023).
23. Matsliah, A. et al. Neuronal parts list and wiring diagram for a visual system. *Nature* <https://doi.org/10.1038/s41586-024-07981-1> (2024).
24. Younossi-Hartenstein, A., Nassif, C., Green, P. & Hartenstein, V. Early neurogenesis of the *Drosophila* brain. *J. Comp. Neurol.* **370**, 313–329 (1996).
25. Broadus, J. et al. New neuroblast markers and the origin of the aCC/pCC neurons in the *Drosophila* central nervous system. *Mech. Dev.* **53**, 393–402 (1995).
26. Urbach, R. & Technau, G. M. Molecular markers for identified neuroblasts in the developing brain of *Drosophila*. *Development* **130**, 3621–3637 (2003).
27. Yu, H.-H. et al. A complete developmental sequence of a *Drosophila* neuronal lineage as revealed by twin-spot MARCM. *PLoS Biol.* **8**, e1000461 (2010).
28. Jiang, Y. & Reichert, H. Programmed cell death in type II neuroblast lineages is required for central complex development in the *Drosophila* brain. *Neural Dev.* **7**, 3 (2012).
29. Kumar, A., Bello, B. & Reichert, H. Lineage-specific cell death in postembryonic brain development of *Drosophila*. *Development* **136**, 3433–3442 (2009).
30. Lacin, H. et al. Neurotransmitter identity is acquired in a lineage-restricted manner in the *Drosophila* CNS. *eLife* **8**, e43701 (2019).
31. Lovick, J. K. et al. Postembryonic lineages of the *Drosophila* brain: I. Development of the lineage-associated fiber tracts. *Dev. Biol.* **384**, 228–257 (2013).
32. Wong, D. C. et al. Postembryonic lineages of the *Drosophila* brain: II. Identification of lineage projection patterns based on MARCM clones. *Dev. Biol.* **384**, 258–289 (2013).
33. Ito, M., Masuda, N., Shinomiya, K., Endo, K. & Ito, K. Systematic analysis of neural projections reveals clonal composition of the *Drosophila* brain. *Curr. Biol.* **23**, 644–655 (2013).

34. Yu, H.-H. et al. Clonal development and organization of the adult *Drosophila* central brain. *Curr. Biol.* **23**, 633–643 (2013).
35. Veveryts, L. & Allan, D. W. Subtype-specific neuronal remodeling during *Drosophila* metamorphosis. *Fly* **7**, 78–86 (2013).
36. Marin, E. C., Watts, R. J., Tanaka, N. K., Ito, K. & Luo, L. Developmentally programmed remodeling of the *Drosophila* olfactory circuit. *Development* **132**, 725–737 (2005).
37. Lee, Y.-J. et al. Conservation and divergence of related neuronal lineages in the *Drosophila* central brain. *eLife* **9**, e53518 (2020).
38. Costa, M., Manton, J. D., Ostrovsky, A. D., Prohaska, S. & Jefferis, G. S. X. E. NBLAST: rapid, sensitive comparison of neuronal structure and construction of neuron family databases. *Neuron* **91**, 293–311 (2016).
39. Li, F. et al. The connectome of the adult *Drosophila* mushroom body provides insights into function. *eLife* **9**, e62576 (2020).
40. Schlegel, P. et al. Information flow, cell types and stereotypy in a full olfactory connectome. *eLife* **10**, e66018 (2021).
41. Hulse, B. K. et al. A connectome of the central complex reveals network motifs suitable for flexible navigation and context-dependent action selection. *eLife* **10**, e66039 (2021).
42. Wu, M. et al. Visual projection neurons in the *Drosophila* lobula link feature detection to distinct behavioral programs. *eLife* **5**, e21022 (2016).
43. Morimoto, M. M. et al. Spatial readout of visual looming in the central brain of *Drosophila*. *eLife* <https://doi.org/10.7554/eLife.57685> (2020).
44. Andriatsilavo, M. et al. Probabilistic axon targeting dynamics lead to individualized brain wiring. Preprint at *bioRxiv* <https://doi.org/10.1101/2022.08.26.505432> (2022).
45. Hiesinger, P. R. & Hassan, B. A. The evolution of variability and robustness in neural development. *Trends Neurosci.* **41**, 577–586 (2018).
46. Buhmann, J. et al. Automatic detection of synaptic partners in a whole-brain *Drosophila* electron microscopy data set. *Nat. Methods* **18**, 771–774 (2021).
47. Aso, Y. et al. The mushroom body of adult *Drosophila* characterized by GAL4 drivers. *J. Neurogenet.* **23**, 156–172 (2009).
48. Tanaka, N. K., Tanimoto, H. & Ito, K. Neuronal assemblies of the *Drosophila* mushroom body. *J. Comp. Neurol.* **508**, 711–755 (2008).
49. Caron, S. J. C., Ruta, V., Abbott, L. F. & Axel, R. Random convergence of olfactory inputs in the *Drosophila* mushroom body. *Nature* **497**, 113–117 (2013).
50. Zheng, Z. et al. Structured sampling of olfactory input by the fly mushroom body. *Curr. Biol.* **32**, 3334–3349 (2022).
51. Liu, X. & Davis, R. L. The GABAergic anterior paired lateral neuron suppresses and is suppressed by olfactory learning. *Nat. Neurosci.* **12**, 53–59 (2009).
52. Litwin-Kumar, A., Harris, K. D., Axel, R., Sompolinsky, H. & Abbott, L. F. Optimal degrees of synaptic connectivity. *Neuron* **93**, 1153–1164 (2017).
53. Stevens, C. F. What the fly's nose tells the fly's brain. *Proc. Natl Acad. Sci. USA* **112**, 9460–9465 (2015).
54. Lin, S. et al. Extremes of lineage plasticity in the *Drosophila* brain. *Curr. Biol.* **23**, 1908–1913 (2013).
55. Elkahlah, N. A., Rogow, J. A., Ahmed, M. & Clowney, E. J. Presynaptic developmental plasticity allows robust sparse wiring of the mushroom body. *eLife* **9**, e52278 (2020).
56. Ahmed, M. et al. Hacking brain development to test models of sensory coding. Preprint at *bioRxiv* <https://doi.org/10.1101/2023.01.25.525425> (2023).
57. Tatusov, R. L., Koonin, E. V. & Lipman, D. J. A genomic perspective on protein families. *Science* **278**, 631–637 (1997).
58. Yoo, J. et al. Brain wiring determinants uncovered by integrating connectomes and transcriptomes. *Curr. Biol.* **33**, 3998–4005 (2023).
59. Hobert, O., Glenwinkel, L. & White, J. Revisiting neuronal cell type classification in *Caenorhabditis elegans*. *Curr. Biol.* **26**, R1197–R1203 (2016).
60. Witvliet, D. et al. Connectomes across development reveal principles of brain maturation. *Nature* **596**, 257–261 (2021).
61. BRAIN Initiative Cell Census Network (BICCN). A multimodal cell census and atlas of the mammalian primary motor cortex. *Nature* **598**, 86–102 (2021).
62. Yao, Z. et al. A high-resolution transcriptomic and spatial atlas of cell types in the whole mouse brain. *Nature* <https://doi.org/10.1038/s41586-023-06808-9> (2023).
63. Zhang, M. et al. A molecularly defined and spatially resolved cell atlas of the whole mouse brain. *Nature* <https://doi.org/10.1101/2023.03.06.531348> (2023).
64. Langlieb, J. et al. The cell type composition of the adult mouse brain revealed by single cell and spatial genomics. Preprint at *bioRxiv* <https://doi.org/10.1101/2023.03.06.531307> (2023).
65. Lappalainen, J. K. et al. Connectome-constrained deep mechanistic networks predict neural responses across the fly visual system at single-neuron resolution. Preprint at *bioRxiv* <https://doi.org/10.1101/2023.03.11.532232> (2023).
66. Shiu, P. K. et al. A *Drosophila* computational brain model reveals sensorimotor processing. *Nature* <https://doi.org/10.1038/s41586-024-07763-9> (2024).
67. Zador, A. M. A critique of pure learning and what artificial neural networks can learn from animal brains. *Nat. Commun.* **10**, 3770 (2019).
68. Ohyama, T. et al. A multilevel multimodal circuit enhances action selection in *Drosophila*. *Nature* **520**, 633–639 (2015).
69. Lillvis, J. L. et al. Rapid reconstruction of neural circuits using tissue expansion and light sheet microscopy. *eLife* **11**, e81248 (2022).
70. Holler, S., Köstinger, G., Martin, K. A. C., Schuhknecht, G. F. P. & Stratford, K. J. Structure and function of a neocortical synapse. *Nature* **591**, 111–116 (2021).
71. Pedigo, B. D. et al. Generative network modeling reveals quantitative definitions of bilateral symmetry exhibited by a whole insect brain connectome. *eLife* **12**, e83739 (2023).
72. Priebe, C. E., Vogelstein, J. & Bock, D. Optimizing the quantity/quality trade-off in connectome inference. *Commun. Stat. Theory Methods* **42**, 3455–3462 (2013).
73. Lichtman, J. W. & Sanes, J. R. Ome sweet ome: what can the genome tell us about the connectome? *Curr. Opin. Neurobiol.* **18**, 346–353 (2008).
74. Bargmann, C. I. & Marder, E. From the connectome to brain function. *Nat. Methods* **10**, 483–490 (2013).
75. Vogelstein, J. T. et al. Discovery of brainwide neural-behavioral maps via multiscale unsupervised structure learning. *Science* **344**, 386–392 (2014).
76. Manning, L. et al. A resource for manipulating gene expression and analyzing cis-regulatory modules in the *Drosophila* CNS. *Cell Rep.* **2**, 1002–1013 (2012).
77. Douglas, R. J. & Martin, K. A. C. Mapping the matrix: the ways of neocortex. *Neuron* **56**, 226–238 (2007).
78. Economo, M. N. et al. Distinct descending motor cortex pathways and their roles in movement. *Nature* **563**, 79–84 (2018).
79. Schneider-Mizell, C. M. et al. Quantitative neuroanatomy for connectomics in *Drosophila*. *eLife* **5**, e12059 (2016).

Publisher's note Springer Nature remains neutral with regard to jurisdictional claims in published maps and institutional affiliations.



Open Access This article is licensed under a Creative Commons Attribution 4.0 International License, which permits use, sharing, adaptation, distribution and reproduction in any medium or format, as long as you give appropriate credit to the original author(s) and the source, provide a link to the Creative Commons licence, and indicate if changes were made. The images or other third party material in this article are included in the article's Creative Commons licence, unless indicated otherwise in a credit line to the material. If material is not included in the article's Creative Commons licence and your intended use is not permitted by statutory regulation or exceeds the permitted use, you will need to obtain permission directly from the copyright holder. To view a copy of this licence, visit <http://creativecommons.org/licenses/by/4.0/>.

© The Author(s) 2024

FlyWire Consortium

Krzysztof Kruk¹⁰, Doug Bland⁶, Zairene Lenizo¹³, Austin T. Burke⁶, Kyle Patrick Willie⁶, Alexander S. Bates^{1,3,4}, Nikitas Serafetinidis¹⁰, Nashra Hadjerol¹³, Ryan Willie⁶, Katharina Eichler², Ben Silverman⁶, John Anthony Ocho¹³, Joshua Bañez¹³, Yijie Yin², Rey Adrian Candilada¹³, Sven Dorkenwald⁵⁶, Jay Gager⁶, Anne Kristiansen¹⁰, Nelsie Panes¹³, Arti Yadav¹³, Remer Tancontian¹³, Shirleyjoy Serona¹³, Jet Ivan Dolorosa¹³, Kendrick Jules Vinson¹³, Dustin Garner¹⁶, Regine Salem¹³, Ariel Dagohoy¹³, Philipp Schlegel¹², Jaime Skelton¹⁰, Mendell Lopez²⁵, Laia Serratosa Capdevila², Griffin Badalamente², Thomas Stocks¹⁰, Anjali Pandey¹⁵, Darrel Jay Akiatan¹³, James Hebditch⁶, Celia David⁶, Dharini Sapkal¹⁰, Shaina Mae Monungoth¹³, Varun Sane², Mark Lloyd Pielago¹³, Miguel Albero¹³, Jacquilyn Laude¹³, Márcia dos Santos², David Deutsch^{6,7}, Zeba Vohra², Kaiyu Wang¹⁰, Allien Mae Gogo¹³, Emil Kind¹³, Alvin Josh Mandahay¹³, Chereb Martinez¹³, John David Asis¹³, Chitra Nair¹⁵, Dhvani Patel¹⁵, Marchan Manaytay¹³, Imaan F. M. Tamimi², Clyde Angelo Lim¹³, Philip Lenard Ampo¹³, Michelle Darapan Pantujan¹³, Alexandre Javier², Daril Bautista¹³, Rashmita Rana¹⁵, Jansen Seguido¹³, Bhargavi Parmar¹⁵, John Clyde Saguimua¹³, Mertlin Moore², Markus W. Plejzler², Mark Larson²⁰, Joseph Hsu², Itisha Joshi¹⁵, Dhara Kakadiya¹⁵, Amalia Braun²³, Cathy Pilapit¹³, Marina Gkantia², Kaushik Parmar¹⁵, Quinn Vanderberck¹⁴, Claire E. McKellar⁶, Irene Salgarella², Christopher Dunne², Eva Munnelly², Chan Hyuk Kang²², Lena Lörsch²³, Jinmook Lee²², Lucia Kmeceva²⁴, Gizem Sancer²⁵, Christa Baker⁶, Szi-chieh Yu⁶, Jenna Joroff⁴, Steven Calle²⁴, Yashvi Patel¹⁵, Olivia Sato²⁰, Siqi Fang², Janice Salocot¹³, Farzaan Salman²⁰, Sebastian Molina-Obando²³, Paul Brooks², Mai Bui²⁷, Matthew Lichtenberger¹⁰, Edmark Tamboboy¹³, Katie Molloy²⁰, Alexis E. Santana-Cruz²⁴, Anthony Hernandez¹⁰, Seongbong Yu²², Marissa Sokel^{6,10}, Arzoo Diwan¹⁵, Monika Patel¹⁵, Travis R. Aiken¹⁰, Sarah Morejohn⁶, Sanna Koskela¹⁸, Tansy Yang¹⁸, Daniel Lehmann¹⁰, Jonas Chojetzki²³, Sangeeta Sisodiya¹⁵, Selden Koolman⁶, Philip K. Shiu²⁸, Sky Cho²⁷, Annika Bast²³, Brian Reicher²⁰, Marlon Blanquart², Lucy Houghton²⁵, Hyungjun Choi²², Maria Ioannidou²³, Matt Collier²⁰, Joanna Eckhardt⁶, Benjamin Gorko¹⁶, Li Guo¹⁸, Zhihao Zheng⁶, Alisa Poh²⁹, Marina Lin²⁷, István Taisz², Wes Murfin³⁰, Álvaro Sanz Díez³¹, Nils Reinhard³², Peter Gibb¹⁴, Nidhi Patern¹⁵, Sandeep Kumar⁶, Minsik Yun³³, Megan Wang⁶, Devon Jones⁶, Lucas Encarnación-Rivera²⁴, Annalena Oswald²³, Akanksha Jadia¹⁵, Mert Erginkaya²⁵, Nik Drummond², Leonie Walter¹⁹, Ibrahim Tastekin³⁵, Xin Zhong¹⁹, Yuta Mabuchi³⁶, Fernando J. Yigueora Santiago²⁴, Urja Verma¹⁵, Nick Byrne²⁰, Edda Kunze⁶, Thomas Crahan¹⁶, Ryan Margossian¹⁰, Haein Kim³⁶, Iliyan Georgiev¹⁰, Fabianna Szorenyi²⁴, Atsuko Adachi³¹, Benjamin Bergeron³⁷, Tomke Stürner¹², Damian Demarest³⁸, Burak Gür²³, Andrea N. Becker¹⁰, Robert Turnbull², Ashley Morren¹⁰, Andrea Sandoval²⁰, Anthony Moreno-Sanchez³⁹, Diego A. Pacheco¹⁴, Eleni Samara²¹, Haley Croke³⁹, Alexander Thomson¹⁰, Connor Laughland¹⁸, Suchetana B. Dutta³⁰, Paula Guiomar Alarcón de Antón¹⁹, Binglin Huang¹⁶, Patricia Pujols²⁴, Isabel Haber²⁰, Amanda González-Segarra²⁸, Albert Lin^{6,40}, Daniel T. Choe⁴¹, Veronika Lukyanova⁴², Marta Costa², Nino Mancini³⁷, Zequan Liu⁴³, Tatsuo Okubo¹⁴, Miriam A. Flynn¹⁸, Gianna Vitelli³⁷, Meghan Laturney²⁸, Feng Li¹⁸, Shuo Cao⁴⁴, Carolina Manyari-Díaz³⁷, Hyunsoo Yim⁴¹, Anh Duc Le³⁹, Kate Maier³⁷, Seungyun Yu²², Yeonju Nam²², Daniel Bába¹⁰, Amanda Abusai²⁸, Audrey Francis¹⁵, Jesse Gayk¹⁵, Sommer S. Huntress⁴⁶, Raquel Barajas³⁵, Mindy Kim²⁰, Xinyue Cui³⁶, Amy R. Sterling^{6,10}, Gabriella R. Sterne²⁸, Anna Li¹⁴, Keehyun Park²², Georgia Dimpsey², Alan Mathew², Jinseong Kim²², Taewan Kim²², Guan-ting Wu⁴⁷, Serene Dhawan¹⁹, Margarida Brotas³⁵, Cheng-hao Zhang³⁵, Shanice Bailey², Alexander Del Toro²⁸, Arie Matsliah⁶, Kisuk Lee^{6,49}, Thomas Macrina^{5,6}, Casey Schneider-Mizell⁵⁰, Sergiy Popovych^{5,6}, Oluwaseun Ogedengbe⁶, Runzhe Yang⁶, Akhilesh Halageri⁶, Will Silversmith⁵, Stephan Gerhard⁴⁹, Andrew Champion¹², Nils Eckstein¹⁸, Dodam Ih⁶, Nico Kernitz², Manuel Castro⁶, Zhen Jia⁶, Jingpeng Wu⁶, Eric Mitchell⁶, Barak Nehoran^{5,6}, Shang Mu⁶, J. Alexander Bae^{6,52}, Ran Lu⁶, Eric Perlman⁶, Ryan Morey⁶, Kai Kuehner⁶, Derrick Brittain⁵⁰, Chris S. Jordan⁶, David J. Anderson¹⁴, Rudy Behnia³¹, Salil S. Bidaye³⁷, Davi D. Bock¹², Alexander Borst²¹, Eugenia Chiappe³⁸, Forrest Collman⁵⁰, Kenneth J. Colodner⁴⁸, Andrew Dacks²⁶, Barry Dickson¹⁸, Jan Funke¹⁸, Denise Garcia³⁹, Stefanie Hampel²⁴, Volker Hartenstein¹¹.

Article

Bassem Hassan¹⁹, Charlotte Helfrich-Forster³², Wolf Huetteroth⁵³, Gregory S. X. E. Jefferis¹², Jinseop Kim²², Sung Soo Kim¹⁶, Young-Joon Kim³³, Jae Young Kwon²², Wei-Chung Lee¹⁴, Gerit A. Linneweber¹⁹, Gaby Maimon⁴⁵, Richard Mann³¹, Mala Murthy⁶, Stéphane Noselli⁵⁴, Michael Pankratz³⁶, Lucia Prieto-Godino¹⁸, Jenny Read⁴², Michael Reiser¹⁸, Katie von Reyn³⁹, Carlos Ribeiro³⁵, Kristin Scott²⁸, Andrew M. Seeds²⁴, Mareike Selcho⁵³, H. Sebastian Seung^{5,6}, Marion Sillies²³, Julie Simpson¹⁶, Scott Waddell⁵⁵, Mathias F. Wernet¹⁹, Rachel I. Wilson¹⁴, Fred W. Wolf⁵⁶, Zepeng Yao⁵⁷, Nilay Yapici³⁶ & Meet Zandawala³²

¹³SixEleven, Davao City, Philippines. ¹⁴Harvard Medical School, Boston, MA, USA. ¹⁵ariadne.ai, Buchrain, Switzerland. ¹⁶University of California, Santa Barbara, Santa Barbara, CA, USA.

¹⁷Department of Neurobiology, University of Haifa, Haifa, Israel. ¹⁸Janelia Research Campus, Howard Hughes Medical Institute, Ashburn, VA, USA. ¹⁹Freie Universität Berlin, Berlin, Germany. ²⁰Harvard, Boston, MA, USA. ²¹Department Circuits-Computation-Models, Max Planck Institute for Biological Intelligence, Planegg, Germany. ²²Sungkyunkwan University, Seoul, South Korea. ²³Johannes-Gutenberg University Mainz, Mainz, Germany. ²⁴Institute of Neurobiology, University of Puerto Rico Medical Sciences Campus, San Juan, Puerto Rico.

²⁵Department of Neuroscience, Yale University, New Haven, CT, USA. ²⁶Department of Biology, West Virginia University, Morgantown, WV, USA. ²⁷Program in Neuroscience and

Behavior, Mount Holyoke College, South Hadley, MA, USA. ²⁸University of California, Berkeley, Berkeley, CA, USA. ²⁹University of Queensland, Brisbane, Queensland, Australia.

³⁰Independent consultant, Fort Collins, CO, USA. ³¹Zuckerman Institute, Columbia University, New York, NY, USA. ³²Julius-Maximilians-Universität Würzburg, Würzburg, Germany.

³³Gwangju Institute of Science and Technology, Gwangju, South Korea. ³⁴Stanford University School of Medicine, Stanford, CA, USA. ³⁵Champalimaud Foundation, Lisbon, Portugal.

³⁶Cornell University, Ithaca, NY, USA. ³⁷Max Planck Florida Institute for Neuroscience, Jupiter, FL, USA. ³⁸University of Bonn, Bonn, Germany. ³⁹Drexel, Philadelphia, PA, USA. ⁴⁰Center for the Physics of Biological Function, Princeton University, Princeton, NJ, USA.

⁴¹Seoul National University, Seoul, South Korea. ⁴²Newcastle University, Newcastle, UK. ⁴³RWTH Aachen University, Aachen, Germany. ⁴⁴Caltech, Pasadena, CA, USA. ⁴⁵Rockefeller University, New York, NY, USA.

⁴⁶Mount Holyoke College, South Hadley, MA, USA. ⁴⁷National Hualien Senior High School, Hualien, Taiwan. ⁴⁸The Francis Crick Institute, London, UK. ⁴⁹Brain & Cognitive Sciences Department, Massachusetts Institute of Technology, Cambridge, MA, USA.

⁵⁰Allen Institute for Brain Science, Seattle, WA, USA. ⁵¹Aware, Zurich, Switzerland. ⁵²Electrical and Computer Engineering Department, Princeton University, Princeton, NJ, USA.

⁵³Institute of Biology, Leipzig University, Leipzig, Germany. ⁵⁴Université Côte d'Azur, CNRS, Inserm, iBV, Nice, France. ⁵⁵University of Oxford, Oxford, UK. ⁵⁶University of California, Merced, Merced, CA, USA. ⁵⁷University of Florida, Gainesville, FL, USA.

Methods

Annotations

Base annotations. At the time of writing, the general FlyWire annotation system operates in a read-only mode in which users can add additional annotations for a neuron but cannot edit or delete existing annotations. Furthermore, the annotations consist of a single free-form text field bound to a spatial location. This enabled many FlyWire users (including our own group) to contribute a wide range of community annotations, which are reported in our companion paper⁴ but are not considered in this study. As it became apparent that a complete connectome could be obtained, we found that this approach was not a good fit for our goal of obtaining a structured, systematic and canonical set of annotations for each neuron with extensive manual curation. We therefore set up a web database (seatable; <https://seatable.io/>) that allowed records for each neuron to be edited and corrected over time; columns with specific acceptable values were added as necessary.

Each neuron was defined by a single point location (also known as a root point) and its associated PyChunkedGraph supervoxel. Root IDs were updated every 30 min by a Python script based on the *fabfseg* package (Table 1) to account for any edits. The canonical point for the neuron was either a location on a large-calibre neurite within the main arbour of the neuron, a location on the cell body fibre close to where it entered the neuropil or a position within the nucleus as defined by the nucleus segmentation table⁸⁰. The former was preferred as segmentation errors in the cell body fibre tracts regularly resulted in the wrong soma being attached to a given neuronal arbour. These soma swap errors persisted late into proofreading and, when fixed, resulted in annotation information being attached to the wrong neuron until this in turn was fixed.

We also note that our annotations include a number of non-neuronal cells/objects such as glia cells, trachea and extracellular matrix that others might find useful (superclass *not_a_neuron*; listed in Supplementary Data 2).

Soma position and side. Besides the canonical root point, the soma position was recorded for all neurons with a cell body. This was either based on curating entries in the nucleus segmentation table (removing duplicates or positions outside the nucleus) or on selecting a location, especially when the cell body fibre was truncated and no soma could be identified in the dataset. These soma locations were critical for a number of analyses and also allowed a consistent side to be defined for each neuron. This was initialized by mapping all soma positions to the symmetric JRC2018F template and then using a cutting plane at the midline perpendicular to the mediolateral (*x*) axis to define left and right. However, all soma positions within 20 μm of the midline plane were then manually reviewed. The goal was to define a consistent logical soma side based on examination of the cell body fibre tracts entering the brain; this ultimately ensured that cell types present, for example, in one copy per brain hemisphere, were always annotated so that one neuron was identified as the left and the other the right. In a small number of cases, for example, for the bilaterally symmetric octopaminergic ventral unpaired medial neurons, we assigned side as 'central'.

For sensory neurons, side refers to whether they enter the brain through the left or the right nerve. In a small number of cases we could not unambiguously identify the nerve entry side and assigned side as 'na'.

Biological outliers and sample artefacts. Throughout our proofreading, matching and cell typing efforts, we recorded cases of neurons that we considered to be biological outliers or showed signs of sample preparation and/or imaging artefacts.

Biological outliers range from small additional/missing branches to entire misguided neurite tracks, and were typically assessed within

the context of a given cell type and best possible contralateral matches within FlyWire and/or the hemibrain. When biological outliers were suspected, careful proofreading was undertaken to avoid erroneous merges or splits of neuron segmentation.

Sample artefacts come in two flavours:

(1) A small number of neurons exhibit a dark, almost black cytosol, which caused issues in the segmentation as well as synapse detection. This effect is often restricted to the neurons' axons. We consider these sample artefacts because it is not always consistent within cell types. For example, the cytosol in the axons of DM3 adPN is dark on the left and normal light on the right. Because the dark cytosol leads to worse synapse detection, probably due to lower contrast between the cytosol and synaptic densities, we typically excluded neurons (or neuron types) with sample artefacts from connectivity analyses. Anecdotally, this appears to happen at a much higher frequency in sensory neurons compared with in brain-intrinsic neurons.

(2) Some neurons are missing large arbours (for example, a whole axon or dendrite) because a main neurite suddenly ends and cannot be traced any further. This typically happens in commissures where many neurites co-fasciculate to cross the brain's midline. In some but not all cases, we were able to bridge those gaps and find the missing branch through left-right matching. Where neurons remained incomplete, we marked them as outliers.

Whether a neuron represents a biological outlier or exhibits sample preparation/segmentation artefacts is recorded in the status column of our annotations as 'outlier_bio' and 'outlier_seg', respectively. Note that these annotations are probably less comprehensive for the optic lobes than for the central brain. Examples plus quantification are presented in Extended Data Fig. 5.

Hierarchical annotations. Hierarchical annotations include flow, superclass, class (plus a subclass field in certain cases) and cell type. The flow and superclass were generally assigned based on an initial semi-automated approach followed by extensive and iterative manual curation. See Supplementary Table 3 for definitions and the sections below for details on certain superclasses.

Based on the superclasses we define two useful groupings which are used throughout the main text:

Central brain neurons consist of all neurons with their somata in the central brain defined by the five superclasses: central, descending, visual centrifugal, motor and endocrine.

Central brain associated neurons further include superclasses: visual projection neurons (VPNs), ascending neurons and sensory neurons (but omit sensory neurons with cell class: visual).

Cell classes in the central brain represent salient groupings/terms that have been previously used in the literature (examples are provided in Supplementary Table 3). For sensory neurons, the class indicates their modality (where known). For optic-lobe-intrinsic neurons cell class indicates their neuropil innervation: for example, cell class 'ME' are medulla local neurons, 'LA>ME' are neurons projecting from the lamina to the medulla and 'ME>LO.LOP' are neurons projecting from the medulla to both lobula and lobula plate.

Hemilineage annotations. Central nervous system lineages were initially mapped for the third instar larval brain, where, for each lineage, the neuroblast of origin and its progeny are directly visible⁸¹⁻⁸⁴. Genetic tools that allow stochastic clonal analysis⁸⁵ have enabled researchers to visualize individual lineages as GFP-marked 'clones'. Clones reveal the stereotyped morphological footprint of a lineage, its overall 'projection envelope'³², as well as the cohesive fibre bundles—hemilineage-associated tracts (HATs)—formed by neurons belonging to it. Using these characteristics, lineages could be also identified in the embryo and early larva^{86,87}, as well as in pupae and adults^{31-34,37,88}. HATs can be readily identified in the EM image data, and we used them, in

Article

conjunction with clonal projection envelopes, to identify hemilineages in the EM dataset through a combination of the following methods:

(1) Visual comparison of HATs formed by reconstructed neurons in the EM, and the light microscopy map reconstructed from anti-Neuroglian-labelled brains^{31,33,34}. In cross-section, tracts typically appear as clusters of 50–100 tightly packed, rounded contours of uniform diameter (~200 nm), surrounded by neuronal cell bodies (when sectioned in the cortex) or irregularly shaped terminal neurite branches and synapses (when sectioned in the neuropil area; Fig. 2c). The point of entry and trajectory of a HAT in the neuropil is characteristic for a hemilineage.

(2) Matching branching pattern of reconstructed neurons with the projection envelope of clones: as expected from the light microscopy map based on anti-Neuroglian-labelled brains³¹, the majority of hemilineage tracts visible in the EM dataset occur in pairs or small groups (3–5). Within these groups, individual tracts are often lined by fibres of larger (and more variable) diameter, as shown in Fig. 2c. However, the boundary between closely adjacent hemilineage tracts is often difficult to draw based on the EM image alone. In these cases, visual inspection and quantitative comparison of the reconstructed neurons belonging to a hemilineage tract with the projection envelope of the corresponding clone, which can be projected into the EM dataset through Pyroglancer (Table 1), assists in properly assigning neurons to their hemilineages.

(3) Identifying homologous HATs across three different hemispheres (left and right of FlyWire, hemibrain): by comparison of morphology (NBLAST³⁸), as well as connectivity (assuming that homologous neurons share synaptic partners), we were able to assign the large majority of neurons to specific HATs that matched in all three hemispheres.

In the existing literature, two systems for hemilineage nomenclature are used: Ito/Lee^{33,34} and Hartenstein^{31,32}. Although these systems overlap in large parts, some lineages have been described in only one but not the other nomenclature. In the main text, we provide (hemi) lineages according to the Ito/Lee nomenclature for simplicity. Below and in the Supplementary Information, we also provide both names as Ito/Lee/Hartenstein, and the mapping between the two nomenclatures is provided in Supplementary Data 3. From previous literature, we expected a total of around 119 lineages in the central brain, including the gnathal ganglia (GNG)^{31–34,84}. Indeed, we were able to identify all 119 lineages based on light-level clones and tracts, as well as the HATs in FlyWire. Moreover, we found one lineage, LHp3/CP5, which could not be matched to any clone. Thus, together, we have identified 120 lineages.

By comprehensively inspecting the hemilineage tracts originally in CATMAID and then in FlyWire, we can now reconcile previous reports. Specifically, new to refs. 33,34 (Ito/Lee nomenclature) are: CRE11/DALv3, LHp3/CP5, DILP/DILP, LALa1/BAIp2, SMPpm1/DPMm2 and VLP15/BLVa3_or_4—we gave these neurons lineage names according to the naming scheme in refs. 33,34. New to ref. 31 (Hartenstein nomenclature) are: SLPa5/BLAd5, SLPav3/BLVa2a, LHI3/BLVa2b, SLPpl3/BLVa2c, PBp1/CM6, SLPpl2/CP6, SMPpd2/DPLc6, PSp1/DPMI2 and LHp3/CP5—we named these units according to the Hartenstein nomenclature naming scheme. We did not take the following clones from ref. 33 into account for the total count of lineages/hemilineages, because they originate in the optic lobe and their neuroblast of origin has not been clearly demonstrated in the larva: VPnd2, VPnd3, VPnd4, VPnp2, VPnp3, VPnp4, VPnv1, VPnv2 and VPnv3.

Notably, although light-level clones from refs. 33,34 match very well the great majority of the time, sometimes clones with the same name only match partially. For example, the AOTUv1_ventral/DALcm2_ventral hemilineage seems to be missing in the AOTUv1/DALcm2 clone in the Ito collection³³. There appears to be a similar situation for the DM4/CM4, EBa1/DALv2 and LHI3/BLVa2b lineages. When there is a conflict, we have preferred clones as described in ref. 34.

For calculating the total number of hemilineages, to keep the inclusion criteria consistent with the lineages, we included the type

II lineages (DL1-2/CP2-3, DM1-6/DPMm1, DPMpm1, DPMpm2, CM4, CM1, CM3) by counting the number of cell body fibre tracts, acknowledging that they may or may not be hemilineages. Neuroblasts of type II lineages, instead of generating ganglion mother cells that each divide once, amplify their number, generating multiple intermediate progenitors that in turn continue dividing like neuroblasts^{28,89,90}. It has not been established how the tracts visible in type II clones (and included in Extended Data Fig. 3 and Supplementary Data 3 and 4) relate to the (large number of) type II hemilineages.

There are also 3 type I lineages (VPN1&d1/BLA12, VLP12/BLAv2 and VLPp&II/DPLpv) with more than two tracts in the clone; we included these additional tracts in the hemilineages provided in the text. Without taking these type I and type II tracts into account, we identified 141 hemilineages.

A minority of neurons in the central brain could not reliably be assigned to a lineage. These mainly include the (putative) primary neurons (3,780). Primary neurons, born in the embryo and already differentiated in the larva, form small tracts with which the secondary neurons become closely associated⁹¹. In the adult brain, morphological criteria that unambiguously differentiate between primary and secondary neurons have not yet been established. In cases in which experimental evidence exists²⁷, primary neurons have significantly larger cell bodies and cell body fibres. Loosely taking these criteria into account we surmise that a fraction of primary neurons forms part of the HATs defined as described above. However, aside from the HATs, we see multiple small bundles, typically close to but not contiguous with the HATs, which we assume to consist of primary neurons. Overall, these small bundles contained 3,780 neurons, designated as primary or putative primary neurons.

Hemilineage annotations in hemibrain. Hemilineage annotations in hemibrain were generated using the hemilineage annotations in FlyWire as the ground truth. For each hemilineage, we first obtained potential hemibrain matches to FlyWire neurons using a combination of NBLAST³⁸ scores and cell body fibre/cell type annotations. We then clustered neurons in all three hemispheres (FlyWire left, FlyWire right, hemibrain potential candidates) by morphology, and went through the clusters, to make sure that the hemilineage annotations correspond across brains at the finest level possible. To ensure that no neurons within a hemilineage were missed, we examined the cell body fibre bundles of each hemilineage in the hemibrain at the EM level. To further guarantee the completeness of hemilineage annotations, we inventoried all right hemisphere neurons in hemibrain with a cell type annotation, to ensure all neurons with a type annotation were assigned a hemilineage annotation where possible.

Morphological groups. Within a hemilineage, subgroups of neurons often share distinctive morphological characteristics. These morphological groups were identified for all hemilineages as follows. Neurons from FlyWire and hemibrain were transformed into the same hemisphere and pairwise NBLAST scores were generated for all neurons within a hemilineage. Intrahemilineage NBLAST scores were then clustered using HDBSCAN⁹², an adaptive algorithm that does not require a uniform threshold across all clusters, and that does not assume spherical distribution of data points in a cluster, compared to other clustering algorithms such as *k*-means clustering.

To test the robustness of the morphological groups, we reran the above analysis across one, two or three hemispheres. This treatment sometimes gave slightly different results. However, some groups of neurons consistently co-clustered across the different hemispheres; we termed these 'persistent clusters'. Early-born neurons, which are often morphologically unique, frequently failed to participate in persistent clusters, and were omitted from further analysis. We linked these persistent clusters across hemispheres using two- and three-hemisphere clustering; for example, when clustering FlyWire left and FlyWire right together for hemilineage AOTUv3_dorsal, the TuBu neurons from both the left and right hemispheres would fall into one cluster, which we termed a

morphological group. Morphological groups are therefore defined by consistent across-hemisphere clustering. When neurons of a given hemilineage were sufficiently contained by the hemibrain volume, all three hemispheres (two from FlyWire and one from hemibrain) were used; otherwise, the two hemispheres from FlyWire were used. As we prioritized consistency across 1, 2 and 3 hemisphere clustering, a minority of neurons with a hemilineage annotation do not have a morphological group. For example, if neuron type A clusters with type B in one-hemisphere clustering, but clusters with type C (and not B) in two-hemisphere clustering, then type A will not have a morphological group annotation.

After generating the morphological groups, we cross-checked these annotations against existing cross-identified hemibrain types and (FlyWire only) cell types. In a minority of cases, neurons of one hemibrain/cell type were annotated with multiple morphological groups. This occasionally reflected errors in assigning types, which were corrected; and others where individual neurons from a type were singled out due to additional branches/reconstruction issues. We therefore manually corrected some morphological group annotations to make them correspond maximally with the hemibrain/cell type annotations.

Overall, we divide hemilineages in each hemisphere into 528 morphological groups, with hemilineages typically having 1–6 morphological groups (10/90 quantile) and with each morphological group containing 2–52 neurons in each hemisphere (10/90 quantile).

Cell typing

Using methods described in detail in the sections below, we defined cell types for 96.4% of all neurons in the brain—98% and 92% for the central brain and optic lobes, respectively. The remaining 3.6% of neurons were largely (1) optic lobe local neurons for which we could not find a prior in existing literature or (2) neurons without clear contralateral pairings, including a number of neurons on the midline.

About 21% of our cell type annotations are principally derived from the hemibrain cell type matching effort (see the section below). The remainder was generated either by comparing to existing literature (for example, in case of optic lobe cell types or sensory neurons) and/or by finding left/right balanced clusters through a combination of NBLAST and connectivity clustering (Fig. 6 and Extended Data Figs. 8 and 9). New types were given a simple numerical cross-brain identifier (for example, CB0001) or, in the case of ascending neurons (ANs)/descending neurons (DNs), a more descriptive identifier (see the section below) as a provisional cell type label. A flow chart summary is provided in Extended Data Fig. 12.

For provenance, we provide two columns of cell types in our Supplementary Data:

hemibrain_type always refers to one or more hemibrain cell types; in rare occasions where a matched hemibrain neuron did not have a type, we recorded body IDs instead.

cell_type contains types that are either not derived from the hemibrain or that represent refinements (for example, a split or retyping) of hemibrain types.

Neurons can have both a cell_type and a hemibrain_type entry, in which case, the cell_type represents a refinement or correction and should take precedence. This generates the reported total count of 8,453 terminal cell types and includes 3,643 hemibrain-derived cell types (Fig. 3h (right side of the flow chart)) and 4,581 proposals for new types. New types consist of 3,504 CBXXXX types, 65 new visual centrifugal neuron types ('c' prefix, for example, cL08), 173 new VPN types ('e' suffix, for example, LTe07), 602 new AN types ('AN_' or 'SA_' prefix, for example, AN_SMP_1) and 237 new DN types ('e' suffix, for example, DNge094). The remaining 229 types are cell types known from other literature, for example, columnar cell types of the optic lobes.

Hemibrain cell type matching. We first used NBLAST³⁸ to match FlyWire neurons to hemibrain cell types (see 'Morphological comparisons' section). From the NBLAST scores, we extracted, for each

FlyWire neuron, a list of potential cell type hits using all hits in the 90th percentile. Individual FlyWire neurons were co-visualized with their potential hits in neuroglancer (see the 'Data availability' and 'Code availability' sections) and the correct hit (if found) was recorded. In difficult cases, we would also inspect the subtree of the NBLAST dendrograms containing the neurons in questions to include local cluster structure in the decision making (Extended Data Fig. 4e). In cases in which two or more hemibrain cell types could not be cleanly delineated in FlyWire (that is, there were no corresponding separable clusters) we recorded composite (many:1) type matches (Fig. 3i and Extended Data Figs. 4g and 12).

When a matched type was either missing large parts of its arbour due to truncation in the hemibrain or the comparison with the FlyWire matches suggested closer inspection was required, we used cross-brain connectivity comparisons (see the section below) to decide whether to adjust (split or merge) the type. A merge of two or more hemibrain types was recorded as, for example, SIP078.SIP080, while a split would be recorded as PS090a and PS090b (that is, with a lower-case letter as a suffix). In rare cases in which we were able to find a match for an untyped hemibrain neuron, we would record the hemibrain body ID as hemibrain type and assign a CBXXXX identifier as cell type.

Finally, the hemibrain introduced the concept of morphology types and 'connectivity types'². The latter represent refinements of the former and differ only in their connectivity. For example, morphology type SAD051 splits into two connectivity types: SAD051_a and SAD051_b, for which the {letter} indicates that these are connectivity types. Throughout our FlyWire↔hemibrain matching efforts we found connectivity types hard to reproduce and our default approach was to match only up to the morphology type. In some cases, for example, antennal lobe local neuron types like ILN2P_a and ILN2P_b, we were able to find the corresponding neurons in FlyWire.

Note that, in numerous cases that we reviewed but remain unmatched, we encountered what we call ambiguous 'daisy-chains': imagine four fairly similar cell types, A, B, C and D. Often these adjacent cell types represent a spectrum of morphologies where A is similar to B, B is similar to C and C is similar to D. The problem now is in unambiguously telling A from B, B from C and C from D. But, at the same time, A and D (on the opposite ends of the spectrum) are so dissimilar that we would not expect to assign them the same cell type (Fig. 3k and Extended Data Fig. 4h). These kinds of graded or continuous variation have been observed in a number of locations in the mammalian nervous system and represent one of the classic complications of cell typing¹⁸. Absent other compelling information that can clearly separate these groups, the only reasonable option would seem to be to lump them together. As this would erase numerous proposed hemibrain cell types, the de facto standard for the fly brain, we have been conservative about making these changes pending analysis of additional connectome data².

Hemibrain cell type matching with connectivity. In our hemibrain type matching efforts, about 12% of cell types could not be matched 1:1. In these cases, we used cross-dataset connectivity clustering (for example, to confirm the split of a hemibrain type or a merger of multiple cell types). To generate distances, we first produced separate adjacency matrices for each of the three hemispheres (FlyWire left, right and hemibrain). In these matrices, each row is a query neuron and each column is an up- or downstream cell type; the values are the connection weights (that is, number of synapses). We then combine the three matrices along the first axis (rows) and retain only the cell types (columns) that have been cross-identified in all hemispheres. From the resulting observation vector, we calculate a pairwise cosine distance. It is important to note that this connectivity clustering depends absolutely on the existence of a corpus of shared labels between the two datasets—without such shared labels, which were initially defined by

Article

morphological matching as described above, connectivity matching cannot function.

This pipeline is implemented in the `coconatfly` package (Table 1), which provides a streamlined interface to carry out such clustering. For example the following command can be used to see if the types given to a selection of neurons in the Lateral Accessory Lobe (LAL) are robust: `cf_cosine_plot(cf_ids('/type:LALO(08|09|10|42)', datasets=c("flywire", "hemibrain")))`.

An optional interactive mode allows for efficient exploration within a web browser. For further details and examples, see <https://natverse.org/coconatfly/>.

Defining robust cross-brain cell types. In Fig. 6, we used two kinds of distance metrics—one calculated from connectivity alone (used for FC1–3; Fig. 6e–g) and a second combining morphology + connectivity (used for FBI–9; Fig. 6h and Extended Data Fig. 8b–f) to help define robust cross-brain cell types. The connectivity distance is as described in the ‘Hemibrain cell type matching with connectivity’ section above). We note that the central complex retyping used FlyWire connectivity from the 630 release. The combined morphology + connectivity distances were generated by taking the sum of the connectivity and NBLAST distances. Connectivity-only works well in the case of cell types that do not overlap in space but instead tile a neuropil. For cell types that are expected to overlap in space, we find that adding NBLAST distances is a useful constraint to avoid mixing of otherwise clearly different types. From the distances, we generated a dendrogram representation using the Ward algorithm and then extracted the smallest possible clusters that satisfy two criteria: (1) each cluster must contain neurons from all three hemispheres (hemibrain, FlyWire right and FlyWire left); (2) within each cluster, the number of neurons from each hemisphere must be approximately equal.

We call such clusters ‘balanced’. The resulting groups were then manually reviewed.

Defining new provisional cell types. After the hemibrain type matching effort, around 40% of central brain neurons remained untyped. This included both neurons mostly or entirely outside the hemibrain volume (for example, from the GNG) but also neurons for which the potential hemibrain type matches were too ambiguous. To provide provisional cell types for these neurons, we ran the same cell typing pipeline described in the ‘Defining robust cross-brain cell types’ section above on the two hemispheres of FlyWire alone. In brief, we produced a morphology + connectivity co-clustering for each individual hemilineage (neurons without a hemilineage such as putative primary neurons were clustered separately) and extracted ‘balanced’ clusters, which were manually reviewed (Fig. 6i,j and Extended Data Fig. 9). Reviewed clusters were then used to add new or refine existing cell and hemibrain types:

- Clusters consisting entirely of previously untyped neurons were given a provisional CBXXXX cell type.
- Clusters containing a mix of hemibrain-typed and untyped neurons typically meant that, after further investigation, the untyped neurons were given the same hemibrain type.
- Hemibrain types split across multiple clusters were double checked (for example, by running a triple-hemisphere connectivity clustering), which often led to a split of the hemibrain type; for example, SMP408 was split into SMP408a–d.
- In rare cases, clusters contained a mix of two or more hemibrain types; these were double checked and the hemibrain types corrected (for example, by merging two or more hemibrain types, or by removing hemibrain type labels).

To validate a subset of the new, provisional cell types, we re-ran the clustering using three hemispheres (FlyWire + hemibrain) on 25 cross-identified hemilineages that are not truncated in the hemibrain

(Extended Data Fig. 9). The procedure was otherwise the same as for the double-clustering.

Optic lobe cell typing. We provide cell type annotations for >92% of neurons in both optic lobes. The vast majority of these types are based on previous literature^{42,93–99}. We started the typing effort by annotating well-known large tangential cells (for example, Am1 or LPi12), VPNs (for example, LT1s) as well as photoreceptor neurons. From there, we followed two general strategies, sometimes in combination: (1) for neurons with known connectivity fingerprints, we specifically hunted upstream or downstream of neurons of interest (for example, looking for T4a neurons upstream of LPi12). (2) We ran connectivity clustering as described above on both optic lobes combined. Clusters were manually reviewed and matched against literature. This was done iteratively; with each round adding new or refining existing cell types to inform the next round of clustering. Clusters that we could not confidently match against a previously described cell type were assigned a provisional (CBXXXX) type.

This effort was carried out independently of other FlyWire optic lobe intrinsic neuron typing, including ref. 23; the sole exception was the Mi1 cell type, which was initially based on annotations reported previously¹⁰⁰ and then reviewed. For this reason ref. 100 should be cited for the Mi1 annotations. Note that our typing focuses on previously reported cell types rather than defining new ones, but covers both optic lobes to enable accurate typing of visual project neurons (by defining their key inputs). For the 38,461 neurons of the right optic lobe (for which a comparison is possible), we report 156 cell types for 35,567 neurons compared with 229 cell types for 37,345 neurons in ref. 23.

VPNs and VCNs. Similar to cell typing in the central brain, a significant proportion of VPN (61%) and visual centrifugal neuron (VCN) (60%) types are derived from the hemibrain (see the ‘Hemibrain cell type matching’ section). These annotations are listed in the hemibrain_type column in the Supplementary Data.

To assign cell types to the remaining neurons and in some cases also to refine existing hemibrain types, we ran a double-hemisphere (FlyWire left–right) co-clustering. For VCNs, this was done as part of the per-hemilineage morphology-connectivity clustering described in the ‘Defining new provisional cell types’ section above. For VPNs of which the dendrites typically tile the optic neuropils, we generated and reviewed a separate connectivity-only clustering on all VPNs together. Groups extracted from this clustering were also cross-referenced with new literature from parallel typing efforts^{100,101} and those new cell type names were preferred for the convenience of the research community. In cases in which literature references could not be found, systematic names were generated de novo using the schemata below.

For VPNs the nomenclature follows the format [neuropil][C/T][e][XX], where neuropil refers to regions innervated by VPN dendrites; C/T denotes columnar versus tangential organization; e indicates identification through EM; and XX represents a zero padded two digit number.

For example: ‘MTe47’ for ‘medulla-tangential 47’.

For VCNs, the nomenclature follows the format [c][neuropil][XX], where c denotes centrifugal; neuropil refers to regions innervated by VCN axons; and XX represents a zero padded two digit number.

For example, ‘cM12’ for ‘centrifugal medulla-targeting 12’.

Note that new names were also given to non-canonical, generic hemibrain types, such as IB006. All new names are recorded in the cell_type column in the Supplementary Data.

The majority of VPNs (99.6%) and VCNs (98.3%) were assigned to specific types. Only 29 VPNs and 9 VCNs could not be confidently assigned a cell type and were therefore left untyped.

Sensory and motor neurons. We identified all non-visual sensory and motor neurons entering/exiting the brain through the antennal, eye, occipital and labial nerves by screening all axon profiles in a given nerve.

Sensory neurons were further cross-referenced to existing literature to assign modalities (through the class field) and, where applicable, a cell type. Previous studies have identified almost all head mechanosensory bristle and taste peg mechanosensory neurons¹⁰² in the left hemisphere (at the time of publication: right hemisphere). Gustatory sensory neurons were previously identified in ref. 103 and Johnston's organ neurons in refs. 104,105 in a version of the FAFB that used manual reconstruction (<https://fafb.catmaid.virtualflybrain.org>). Those neurons were identified in the FlyWire instance by transformation and overlay onto FlyWire space as described previously¹⁰².

Johnston's organ neurons in the right hemisphere were characterized based on innervation of the major AMMC zones (A, B, C, D, E and F), but not further classified into subzone innervation as shown previously¹⁰⁴. Other sensory neurons (mechanosensory bristle neurons, taste peg mechanosensory neurons and gustatory sensory neurons) in the right hemisphere were identified through NBLAST-based matching of their mirrored morphology to the left hemisphere and expert review. Olfactory, thermosensory and hygrosensory neurons of the antennal lobes were identified through their connectivity to cognate uniglomerular projection neurons and NBLAST-based matching to previously identified hemibrain neurons^{40,106}.

Visual sensory neurons (R1–6, R7–8 and ocellar photoreceptor neurons) were identified by manually screening neurons with pre-synapse in either the lamina, the medulla and/or the ocellar ganglia⁹³.

ANs and DNs. We seeded all profiles in a cross-section in the ventral posterior GNG through the cervical connective to identify all neurons entering and exiting the brain at the neck. We identified all DNs based on the following criteria: (1) soma located within the brain dataset; and (2) main axon branch leaving the brain through the cervical connective.

We next classified the DNs based on their soma location according to a previous report¹⁰⁷. In brief, the soma of DNa, DNb, DNc and DNd is located in the anterior half (a, anterior dorsal; b, anterior ventral; c, in the pars intercerebralis; d, outside cell cluster on the surface) and DNp in the posterior half of the central brain. DNg somas are located in the GNG.

To identify DNs described in ref. 107 in the EM dataset, we transformed the volume renderings of DN GAL4 lines into FlyWire space. Displaying EM and LM neurons in the same space enabled accurate matching of closely morphologically related neurons. For DNs without available volume renderings, we identified candidate EM matches by eye, transformed them into JRC2018U space and overlaid them onto the GAL4 or Split GAL4 line stacks (named in ref. 107 for that type) in Fiji for verification. Using these methods, we identified all but two (DNd01 and DNg25) in FAFB/FlyWire and annotated their cell type with the published nomenclature. All other unmatched DNs received a systematic cell type consisting of their soma location, an 'e' for EM type and a three digit number (for example, DNae001). A detailed account and analysis of DNs has been published¹⁰⁸ separately.

ANs were identified based on the following criteria: (1) no soma in the brain; and (2) main branch entering through the neck connective (note that some ANs make a dendrite after entry through the neck connective and then an axon).

To distinguish sensory ascending (SA) neurons from ANs, we analysed SA neuron morphology in the male VNC dataset MANC^{109,110}. First, we identified which longitudinal tract they travel to ascend to the brain¹¹¹ and then found GAL4 lines matching their VNC morphology. We next identified putative matching axons in the brain dataset by morphology and tract membership. A detailed description of this process and the lines used has been published separately¹⁰⁸.

FAFB laterality

In the fly brain, the asymmetric body is reproducibly around 4 times larger on the right hemisphere than on the left^{112–114}, except in rare cases

of situs inversus^{114,115}. However, completion of the FlyWire whole-brain connectome and associated cell typing showed the asymmetric body to be larger on the apparent left side of the brain rather than the right, suggesting an inversion of the left–right axis during initial acquisition of EM images comprising the FAFB dataset¹⁷. This hypothesis was confirmed by comparing of FAFB sample grids imaged using differential interference contrast microscopy to low-magnification views of corresponding EM image mosaics using CATMAID or neuroglancer. Grids were chosen with particularly obvious staining and sample preparation artefacts visible both in the differential interference contrast and low-magnification EM images (Extended Data Fig. 1), confirming that a left–right axis inversion had taken place during image acquisition.

Owing to the extensive post-processing of the FAFB dataset and derived datasets (for example, transformation fields, image mosaicing and stack registrations to produce aligned volumes, segmentation supervoxels, proofread neuron segmentations, skeletons, meshes and myriad 3D visualizations), which had been undertaken at the time at which this error was discovered, we deemed it impractical to correct this error at the raw data level. Instead, we break a convention of presentation: usually, frontal views of the fly brain place the fly's right on the viewer's left. Instead, in this paper, frontal views of the fly brain place the fly's right on the viewer's right—similar to the view one has of oneself while looking in a mirror. This maintains consistency with past publications. However, note that all labels of left and right in the figures in this paper, our companion papers, the supplemental annotations and associated digital repositories (for example, <https://codex.flywire.ai>, FAFB/FlyWire CATMAID) have been corrected to reflect the error during data acquisition. In these resources, a neuron labelled as being on the left is indeed on the left of the fly's brain.

For consistency with visualizations and datasets obeying the standard convention (fly's right on viewer's left), FlyWire data can be mirrored. To facilitate this, we provide tools to digitally mirror FAFB-FlyWire data using the Python flybrains (<https://github.com/navis-org/navis-flybrains>) or natverse nat.jrcbrains (<https://github.com/natverse/nat.jrcbrains>) packages (Extended Data Fig. 1c), through the `navis.mirror_brain()` and `nat.jrcbrains::mirror_fafb()` function calls, respectively. See the `fabseg-py` documentation for a tutorial on mirroring.

We also provide a neuroglancer scene in which both FlyWire and hemibrain data are displayed in the correct orientation: <https://tinyurl.com/flywirehflip783>. In this scene, a frontal view has both FAFB and hemibrain RHS to the left of the screen, obeying the standard convention. The scene displays the SA1 and SA2 neurons, which target the right asymmetric body for both FlyWire and the hemibrain, confirming that the RHS for both datasets has been superimposed (compare with Extended Data Fig. 1a).

Morphological comparisons

Throughout our analyses, NBLAST³⁸ was used to generate morphological similarity scores between neurons—for example, for matching neurons between the FlyWire and the hemibrain datasets, or for the morphological clustering of the hemilineages. In brief, NBLAST treats neurons as point clouds with associated tangent vectors describing directionality, so called dotprops. For a given query→target neuron pair, we perform a *k*-nearest neighbours search between the two point clouds and score each nearest-neighbour pair by their distance and the dot product of their vector. These are then summed up to compute the final query→target NBLAST score. It is important to note that direction of the NBLAST matters, that is, NBLASTing neurons A→B≠B→A. Unless otherwise noted, we use the minimum between the forward and reverse NBLAST scores.

The NBLAST algorithm is implemented in both `navis` and the `natverse` (Table 1). However, we modified the `navis` implementation for more efficient parallel computation in order to scale to pools of more than 100,000 neurons. For example, the all-by-all NBLAST matrix for the

Article

full 139,000 FlyWire neurons alone occupies over 500 GB of memory (32 bit floats). Most of the large NBLASTs were run on a single cluster node with 112 CPUs and 1 TB RAM provided by the MRC LMB Scientific Computing group, and took between 1 and 2 days (wall time) to complete.

Below, we provide recipes for the different NBLAST analyses used in this paper:

FlyWire all-by-all NBLAST. For this NBLAST, we first generated skeletons using the L2 cache. In brief, underlying the FlyWire segmentation is an octree data structure where level 0 represents supervoxels, which are then agglomerated over higher levels¹¹⁶. The second layer (L2) in this octree represents neurons as chunks of roughly $4 \times 4 \times 10 \mu\text{m}$ in size, which is sufficiently detailed for NBLAST. The L2 cache holds precomputed information for each L2 chunk, including a representative $x/y/z$ coordinate in space. We used the $x/y/z$ coordinates and connectivity between chunks to generate skeletons for all FlyWire neurons (implemented in *fabseg*; Table 1). Skeletons were then pruned to remove side branches smaller than $5 \mu\text{m}$. From those skeletons, we generated the dotprops for NBLAST using *navis*.

Before the NBLAST, we additionally transformed dotprops to the same side by mirroring those from neurons with side right onto the left. The NBLAST was then run only in forward direction (query→target) but, because the resulting matrix was symmetrical, we could generate minimum NBLAST scores using the transposed matrix: $\min(A + A^T)$.

This NBLAST was used to find left–right neuron pairs, define (hemi) lineages and run the morphology group clustering.

FlyWire—hemibrain NBLAST. For FlyWire, we re-used the dotprops generated for the all-by-all NBLAST (see the previous section). To account for the truncation of neurons in the hemibrain volume, we removed points that fell outside the hemibrain bounding box.

For the hemibrain, we downloaded skeletons for all neurons from *neuPrint* (<https://neuprint.janelia.org>) using *neuprint-python* and *navis* (Table 1). In addition to the approximately 23,000 typed neurons, we also included all untyped neurons (often just fragments) for a total of 98,000 skeletons. These skeletons were pruned to remove twigs smaller than $5 \mu\text{m}$ and then transformed from hemibrain into FlyWire (FAB14.1) space using a combination of non-rigid transforms^{116,117} (implemented through *navis*, *navis-flybrain* and *fabseg*; Table 1). Once in FlyWire space, they were resampled to 0.5 nodes per μm of cable to approximately match the resolution of the FlyWire L2 skeletons, and then turned into dotprops. The NBLAST was then run both in forward (FlyWire to hemibrain) and reverse (hemibrain to FlyWire) direction and the minimum between both were used.

This NBLAST allowed us to match FlyWire left against the hemibrain neurons. To also allow matching FlyWire right against the hemibrain, we performed a second run after mirroring the FlyWire dotprops to the opposite side.

In Fig. 3c,d, we manually reviewed NBLAST matches. For this, we sorted hemibrain neurons based on their highest NBLAST score to a FlyWire neuron into bins with a width of 0.1. From each bin, we picked 30 random hemibrain neurons (except for bin 0–0.1 which contained only 27 neurons in total) and scored their top five FlyWire matches as to whether a plausible match was among them. In total, this sample contained 237 neurons.

Cross-brain co-clustering. The pipeline for the morphology-based across brain co-clustering used in Fig. 6 and Extended Data Fig. 9 was essentially the same as for the FlyWire–hemibrain NBLAST with two exceptions: (1) we used high-resolution FlyWire skeletons instead of the coarser L2 skeletons (see below); and (2) both FlyWire and hemibrain skeletons were resampled to 1 node per μm before generating dotprops.

High-resolution skeletonization

In addition to the coarse L2 skeletons, we also generated high-resolution skeletons that were, for example, used to calculate the total length of neuronal cable reported in our companion paper¹ (149.2 m). In brief, we downloaded neuron meshes (LOD 1) from the flat 783 segmentation (available at [gs://flywire_v141_m783](https://flywire_v141_m783)) and skeletonized them using the wavefront method implemented in *skeletor* (<https://github.com/navis-org/skeletor>). Skeletons were then rerooted to their soma (if applicable), smoothed (by removing small artifactual bristles on the backbone), healed (segmentation issues can cause breaks in the meshes) and slightly downsampled. A modified version of this pipeline is implemented in *fabseg*. Skeletons are available for download (see the ‘Data availability’ and ‘Code availability’ sections).

Connectivity normalization

Throughout this paper, the basic measure of connection strength is the number of unitary synapses between two or more neurons⁷⁹; connections between adult fly neurons can reach thousands of such unitary synapses². Previous work in larval *Drosophila* has indicated that synaptic counts approximate contact area¹⁸, which is most commonly used in mammalian species when a high-resolution measure of anatomical connection strength is required. Connectomics studies also routinely use connection strength normalized to the target cell’s total inputs^{71,79}. For example, if neurons i and j are connected by 10 synapses and neuron j receives 200 inputs in total, the normalized connection weight i to j would be 5%. A previous study¹¹⁹ showed that while absolute number of synapses for a given connection changes drastically over the course of larval stages, the proportional (that is, normalized) input to the downstream neuron remains relatively constant¹¹⁹. Importantly, we have some evidence (Fig. 4g) that normalized connection weights are robust against technical noise (differences in reconstruction status, synapse detection). Note that, for analyses of mushroom body circuits, we use an approach based on the fraction of the input or output synaptic budget associated with different KC cell types; this differs slightly from the above definition and will be detailed in a separate section below.

Connectivity stereotypy analyses

For analyses on connectivity stereotypy (Fig. 4 and Extended Data Fig. 6) we excluded a number of cell types:

- KCs, due to the high variability in numbers and synapse densities in the mushroom body lobes between FlyWire and the hemibrain (Fig. 5 and Extended Data Fig. 7).
- Cell types that exist only on the left but not the right hemisphere of the hemibrain because our comparison was principally against the right hemisphere.
- Antennal lobe receptor neurons, because truncation/fragmentation in the hemibrain causes some ambiguity with respect to their side annotation.
- Cell types with members that have been marked as being affected by sample or imaging artefacts (that is, status ‘outlier_seg’).
- VPns, as they are heavily truncated in the hemibrain.

Among the remaining types, we used only the 1:1 and 1:many but not the many:1 matches. Taken together, we used 2,954 (hemibrain) types for the connectivity stereotypy analyses.

Availability through CATMAID Spaces

To increase the accessibility and reach of the annotated FlyWire connectome, meshes of proofread FlyWire neurons and synapses were skeletonized and imported into CATMAID, a widely used web-based tool for collaborative tracing, annotation and analysis of large-scale neuronal anatomy datasets^{79,120} (<https://catmaid.org>; Extended Data Fig. 10). Spatial annotations like skeletons are modelled using PostGIS

data types, a PostgreSQL extension that is popular in the geographic information system community. This enables us to reuse many existing tools to work with large spatial datasets, for example, indexes, spatial queries and mesh representation.

A publicly available version of the FlyWire CATMAID project is available online (<https://fafb-flywire.catmaid.org>). This project uses a new extension, called CATMAID Spaces (<https://catmaid.org/en/latest/spaces.html>), which allows users to create and administer their own tracing and annotation environments on top of publicly available neuronal image volumes and connectomic datasets. Moreover, users can now login through the public authentication service ORCID (<https://www.orcid.org>), so that everyone can log-in on public CATMAID projects. Users can also now create personal copies (Spaces) of public projects. The user then becomes an administrator, and can invite other users, along with the management of their permissions in this new project. Invitations are managed through project tokens, which the administrator can generate and send to invitees for access to the project. Both CATMAID platforms can talk to each other and it is possible to load data from the dedicated FAFB-FlyWire server in the more general Spaces environment.

Metadata annotations for each neuron (root id, cell type, hemilineage, neurotransmitter) were imported for FlyWire project release 783. Skeletons for all 139,255 proofread neurons were generated from the volumetric meshes (see the 'High-resolution skeletonization' section) and imported into CATMAID, resulting in 726,831,877 treenodes. To reduce the import time, skeletons were imported into CATMAID directly as database inserts through SQL, rather than through public RESTful APIs. FlyWire root IDs are available as metadata for each neuron, facilitating interchange with related resources such as FlyWire Codex¹. Synapses attached to reconstructed neurons were imported as CATMAID connector objects and attached to neuron skeletons by doing a PostgreSQL query to find the nearest node on each of the partner skeletons. Connector objects were linked to postsynaptic partners only if the downstream neuron was in the proofread data release (180,016,288 connections from the 130,054,535 synapses with at least one partner in the proofread set).

Synapse counts

Insect synapses are polyadic, that is, each presynaptic site can be associated with multiple postsynaptic sites. In contrast to the *Janelia* hemibrain dataset, the synapse predictions used in FlyWire do not have a concept of a unitary presynaptic site associated with a T-bar⁴⁶. Thus, pre-synapse counts used in this paper do not represent the number of presynaptic sites but rather the number of outgoing connections.

In *Drosophila* connectomes, reported counts of the inputs (post-synapses) onto a given neuron are typically lower than the true number. This is because fine-calibre dendritic fragments frequently cannot be joined onto the rest of the neuron, instead remaining as free-floating fragments in the dataset.

Technical noise model

To model the impact of technical noise such as proofreading status and synapse detection on connectivity, we first generated a fictive '100%' ground-truth connectivity. We took the connectivity between cell-typed left FlyWire neurons and scaled each edge weight (the number of synapses) by the postsynaptic completion rates in the respective neuropil. For example, all edge weights in the left mushroom body calyx (CA), which has a postsynaptic completion rate of 52.5%, were scaled by a factor of $100/52.5 = 1.9$.

In the second step, we simulated the proofreading process by randomly drawing (without replacement) individual synaptic connections from the fictive ground-truth until reaching a target completion rate. We further simulate the impact of false positives and false negatives by randomly adding and removing synapses to/from the draw according to

the precision (0.72) and recall (0.77) rates reported previously⁴⁶. In each round, we made two draws: (1) A draw using the original per-neuropil postsynaptic completion rates; and (2) a draw where we flip the completion rates for left and right neuropils, that is, use the left CA completion rate for the right CA and vice versa.

In each of the 500 rounds that we ran, we drew two weights for each edge. Both stem from the same fictive 100% ground-truth connectivity but have been drawn according to the differences in left versus right hemisphere completion rates. Combining these values, we calculated the mean difference and quantiles as function of the weight for the FlyWire left (that is, the draw that was not flipped) (Fig. 4i). We focussed this analysis on edge weights between 1 and 30 synapses because the frequency of edges stronger than that is comparatively low, leaving gaps in the data.

KC analyses

Connection weight normalization and synaptic budget analysis.

When normalizing connection weights, we typically convert them to the percentage of total input onto a given target cell (or cell type). However, in the case of the mushroom body, the situation is complicated by what we think is a technical bias in the synapse detection methods used for the two connectomes that causes certain kinds of unusual connections to be very different in frequency between the two datasets. We find that the total number of post-synapses as well as the post-synapse density in the mushroom body lobes are more than doubled in the hemibrain compared with in FlyWire (Extended Data Fig. 7b,c). This appears to be explained by certain connections (especially KC to KC connections, which are predominantly arranged with an unusual rosette configuration along axons and of which the functional significance is poorly understood¹²¹) being much more prevalent in the hemibrain than in FlyWire (Extended Data Fig. 7d). Some other neurons, including the APL giant interneuron, also make about twice as many synapses onto KCs in the hemibrain compared with in FlyWire (Extended Data Fig. 7a). As a consequence of this large number of inputs onto KC axons in the hemibrain, input percentages from all other cells are reduced in comparison with FlyWire.

To avoid this bias, and because our main goal in the KC analysis was to compare different populations of KCs, we instead expressed connectivity as a fraction of the total synaptic budget for upstream or downstream cell types. For example, we examined the fraction of the APL output that is spent on each of the different KC types. Similarly, we quantified connectivity for individual KCs as a fraction of the budget for the whole KC population.

Calculating K from observed connectivity.

Calculation of K , that is, the number of unique odour channels that each KC receives input from, was principally based on their synaptic connectivity. For this, we looked at their inputs from uniglomerular ALPNs and examined from how many of the 58 antennal lobe glomeruli does a KC receive input from. K as reported in Fig. 6 is based on non-thresholded connectivity. Filtering out weak connections does lower K but, importantly, our observations (for example, that KCg-m cells have a lower K in FlyWire than in the hemibrain) are stable across thresholds (Extended Data Fig. 7g).

KC model. A simple rate model of neural networks¹²² was used to generate the theoretical predictions of K , the number of ALPN inputs that each KC receives (Fig. 5k). KC activity is modelled by

$$\mathbf{h} = \mathbf{W} \cdot \mathbf{r}_{\text{PN}}$$

where \mathbf{h} is a vector of length M representing KC activity, \mathbf{W} is an $M \times N$ matrix representing the synaptic weights between the KCs and PNs, \mathbf{r}_{PN} is a vector of length N representing PN activity. The number of KCs and ALPNs is denoted by M and N , respectively. In this model, the PN

Article

activity is assumed to have zero mean, $\bar{\mathbf{r}}_{PN} = \mathbf{0}$, and be uncorrelated, $\overline{\mathbf{r}_{PN} \cdot \mathbf{r}_{PN}} = \mathbf{I}_N$. Here, \mathbf{I}_N is an $N \times N$ identity matrix and $\bar{\mathbf{r}}_{PN}$ denotes the average taken over independent realizations of \mathbf{r}_{PN} . Then, the ij th element of the covariance matrix of \mathbf{h} is

$$[\mathbf{C}]_{ij} = \overline{[\mathbf{h}]_i [\mathbf{h}]_j} = \sum_{k=0}^N [\mathbf{W}]_{ik} [\mathbf{W}]_{jk}.$$

More detailed calculations can be found in a previous report¹²². Randomized and homogeneous weights were used to populate \mathbf{W} , such that each row in \mathbf{W} has K elements that are $1 - \alpha$ and $N - K$ elements that are $-\alpha$. The parameter α represents a homogeneous inhibition corresponding to the biological, global inhibition by APL. The value inhibition was set to be $\alpha = A/M$, where $A = 100$ is an arbitrary constant and M is the number of KCs in each of the three datasets. The primary quantity of interest is the dimension of the KC activities defined by¹²²:

$$\dim(\mathbf{h}) = \frac{\text{Tr}[\mathbf{C}]^2}{\text{Tr}[\mathbf{C}^2]}$$

and how it changes with respect to K , the number of input connections. In other words, what are the numbers of input connections K onto individual KCs that maximize the dimensionality of their responses, \mathbf{h} , given M KCs, N ALPNs and a global inhibition α ?

From Fig. 5k, the theoretical values of K that maximize $\dim(\mathbf{h})$ in this simple model demonstrate the consistent shift towards lower values of K found in the FlyWire left and FlyWire right datasets when compared with the hemibrain.

The limitations of the model are as follows:

- (1) The values in the connectivity matrix \mathbf{W} take only two discrete values, either 0 and 1 or $1 - \alpha$ and α . In a way, this helps when calculating analytical results for the dimensionality of the KC activities. However, it is unrealistic as the connectomics data give the number of synaptic connections between the ALPNs and the KCs.
- (2) The global inhibition provided by APL to all of the mixing layer neurons is assumed to take a single value for all neurons. In reality, the level of inhibition would be different depending on the number of synapses between APL and the mixing layer neurons.
- (3) It is unclear whether the simple linear rate model presented in the original paper represents the behaviour of the biological neural circuit well. Furthermore, it remains unproven that the ALPN-KC neural circuit is attempting to maximize the dimensionality of the KC activities, albeit the theory is biologically well motivated (but see refs. 49,50).
- (4) The number of input connections to each mixing layer neuron is kept at a constant K for all neurons. It is definitely a simplification that can be corrected by introducing a distribution $P(K)$ but this requires further detailed modelling.

Statistical analyses

Unless otherwise stated, statistical analyses (such as Pearson R or cosine distance) were performed using the implementations in the `scipy`¹²³ Python package. To determine statistical significance, we used either t -tests for normally distributed samples, or Kolmogorov–Smirnov tests otherwise.

Cohen's d ¹²⁴ was calculated as follows:

$$d = \frac{\bar{x}_1 - \bar{x}_2}{s}$$

where pooled s.d. s is defined as:

$$s = \sqrt{\frac{(n_1 - 1)s_1^2 + (n_2 - 1)s_2^2}{n_1 + n_2 - 2}}$$

where the variance for one of the groups is defined as:

$$s_1^2 = \frac{1}{n_1 - 1} \sum_{i=1}^{n_1} (x_{1,i} - \bar{x}_1)^2$$

and similar for the other group.

Enhanced box plots—also called letter-value plots¹²⁵—in Fig. 5h and Extended Data Fig. 7f are a variation of box plots better suited to represent large samples. They replace the whiskers with a variable number of letter values where the number of letters is based on the uncertainty associated with each estimate, and therefore on the number of observations. The ‘fattest’ letters are the (approximate) 25th and 75th quantiles, respectively, the second fattest letters the (approximate) 12.5th and 87.5th quantiles and so on. Note that the width of the letters is not related to the underlying data.

Mapping to the VirtualFlyBrain database

The VirtualFlyBrain (VFB) database²² curates and extracts information from all publications relating to *Drosophila* neurobiology, especially neuroanatomy. The majority of published neuron reconstructions, including those from the hemibrain, can be examined in the VFB. Each individual neuron (that is, one neuron from one brain) has a persistent ID (of the form VFB_XXXXXXX). Where cell types have been defined, they have an ontology ID (for example, FBbt_00047573, the ID for the DNa02 DN cell type). Importantly, VFB cross-references neuronal cell types across publications even if different terms were used. It also identifies driver lines to label many neurons. In this paper, we generate an initial mapping providing FBbt IDs for the closest and fine-grained ontology term that already exists in their database. For example, a FlyWire neuron with a confirmed hemibrain cell type will receive a FBbt ID that maps to that exact cell type, while a DN that has been given a new cell type might only map to the coarser term ‘adult descending neuron’. Work is already underway with the VFB to assign both ontology IDs (FBbt) to all FlyWire cell types as well as persistent VFB_ids to all individual FlyWire neurons.

Reporting summary

Further information on research design is available in the Nature Portfolio Reporting Summary linked to this article.

Data availability

Data artefacts from this paper are available at GitHub (https://github.com/flyconnectome/flywire_annotations). This includes neuron annotations and other metadata; high-quality skeletons for all proofread FlyWire neurons; NBLAST scores for FlyWire versus hemibrain; all-by-all NBLAST scores for FlyWire. The repository may be periodically updated to improve annotations, but older versions will always remain available through GitHub's versioning system. Moreover, neuron annotations and other metadata are also provided in the Supplementary Information. NBLAST scores and skeletons have been deposited in a Zenodo repository (<https://doi.org/10.5281/zenodo.10877326>)¹²⁶. Connectivity data (for example, synapses table and edge list) are available (<https://doi.org/10.5281/zenodo.10676866>)¹²⁷. We provide a neuroglancer scene preconfigured for display and query of our annotations alongside the FlyWire neuron meshes and segmentation at <http://tinyurl.com/flywire783>. Users can add the annotations to arbitrary neuroglancer scenes themselves by adding a data subsource (Extended Data Fig. 11). There are two options: (1) “precomputed://https://flyem.mrc-lmb.cam.ac.uk/flyconnectome/ann/flytable-info-783” containing super class, cell type and side labels; (2) “precomputed://https://flyem.mrc-lmb.cam.ac.uk/flyconnectome/ann/flytable-info-783-all” additionally contains hemi-lineage information. We also provide programmatic access to the annotations through our `fafseg` R and Python packages (examples are provided in Table 1 and the online documentation). Annotations

have also been shared with Codex (<https://codex.flywire.ai/>), the connectome annotation versioning engine (CAVE), which can be queried through the CAVEclient (<https://github.com/seung-lab/CAVEclient>) and the FAFB-FlyWire CATMAID spaces (<https://fafb-flywire.catmaid.org>). At the time of writing, access to Codex and CAVE requires signing up using a Google account. To aid a number of analyses, hemibrain neuron meshes were mapped into FlyWire (FAFB14.1) space. These can be co-visualized with FlyWire neurons within neuroglancer (<https://tinyurl.com/flywire783>; this scene also includes a second copy of the hemibrain data (layer “hemibrain_meshes_mirr”), which have been non-rigidly mapped onto the opposite side of FAFB).

Code availability

Analyses were performed using open-source packages using both the R natverse¹²⁸ and Python navis infrastructures (a summary including links is provided in Table 1). The fabfseg R and Python packages have extensive functionality dedicated to working with FlyWire data, including querying annotations, fetching connectivity and working with the segmentation. Unless otherwise stated, all analyses were performed against the 783 release version (that is, the second public data release for FlyWire).

80. Mu, S. et al. 3D reconstruction of cell nuclei in a full *Drosophila* brain. Preprint at *bioRxiv* <https://doi.org/10.1101/2021.11.04.467197> (2021).
81. Truman, J. W., Schuppe, H., Shepherd, D. & Williams, D. W. Developmental architecture of adult-specific lineages in the ventral CNS of *Drosophila*. *Development* **131**, 5167–5184 (2004).
82. Pereanu, W. & Hartenstein, V. Neural lineages of the *Drosophila* brain: a three-dimensional digital atlas of the pattern of lineage location and projection at the late larval stage. *J. Neurosci.* **26**, 5534–5553 (2006).
83. Cardona, A. et al. Identifying neuronal lineages of *Drosophila* by sequence analysis of axon tracts. *J. Neurosci.* **30**, 7538–7553 (2010).
84. Kuert, P. A., Hartenstein, V., Bello, B. C., Lovick, J. K. & Reichert, H. Neuroblast lineage identification and lineage-specific Hox gene action during postembryonic development of the subesophageal ganglion in the *Drosophila* central brain. *Dev. Biol.* **390**, 102–115 (2014).
85. Lee, T. & Luo, L. Mosaic analysis with a repressible cell marker (MARCM) for *Drosophila* neural development. *Trends Neurosci.* **24**, 251–254 (2001).
86. Lovick, J. K. et al. Patterns of growth and tract formation during the early development of secondary lineages in the *Drosophila* larval brain. *Dev. Neurobiol.* **76**, 434–451 (2016).
87. Hartenstein, V. et al. Lineage-associated tracts defining the anatomy of the *Drosophila* first instar larval brain. *Dev. Biol.* **406**, 14–39 (2015).
88. Lacin, H. & Truman, J. W. Lineage mapping identifies molecular and architectural similarities between the larval and adult *Drosophila* central nervous system. *eLife* **5**, e133399 (2016).
89. Bello, B. C., Izergina, N., Caussinus, E. & Reichert, H. Amplification of neural stem cell proliferation by intermediate progenitor cells in *Drosophila* brain development. *Neural Dev.* **3**, 5 (2008).
90. Boone, J. Q. & Doe, C. Q. Identification of *Drosophila* type II neuroblast lineages containing transit amplifying ganglion mother cells. *Dev. Neurobiol.* **68**, 1185–1195 (2008).
91. Larsen, C. et al. Patterns of growth, axonal extension and axonal arborization of neuronal lineages in the developing *Drosophila* brain. *Dev. Biol.* **335**, 289–304 (2009).
92. McInnes, L., Healy, J. & Astels, S. hdbscan: hierarchical density based clustering. *J. Open Source Softw.* **2**, 205 (2017).
93. Fischbach, K.-F. & Dittrich, A. P. M. The optic lobe of *Drosophila melanogaster*. I. A Golgi analysis of wild-type structure. *Cell Tissue Res.* **258**, 441–475 (1989).
94. Davis, F. P. et al. A genetic, genomic, and computational resource for exploring neural circuit function. *eLife* <https://doi.org/10.7554/eLife.50901> (2020).
95. Nern, A., Pfeiffer, B. D. & Rubin, G. M. Optimized tools for multicolor stochastic labeling reveal diverse stereotyped cell arrangements in the fly visual system. *Proc. Natl Acad. Sci. USA* **112**, E2967–E2976 (2015).
96. Shinomiya, K., Nern, A., Meinertzhagen, I. A., Plaza, S. M. & Reiser, M. B. Neuronal circuits integrating visual motion information in *Drosophila*. *Curr. Biol.* <https://doi.org/10.1016/j.cub.2022.06.061> (2022).
97. Takemura, S.-Y. et al. A visual motion detection circuit suggested by *Drosophila* connectomics. *Nature* **500**, 175–181 (2013).
98. Takemura, S.-Y., Lu, Z. & Meinertzhagen, I. A. Synaptic circuits of the *Drosophila* optic lobe: the input terminals to the medulla. *J. Comp. Neurol.* **509**, 493–513 (2008).
99. Gao, S. et al. The neural substrate of spectral preference in *Drosophila*. *Neuron* **60**, 328–342 (2008).
100. Garner, D. et al. Connectomic reconstruction predicts visual features used for navigation. *Nature* <https://doi.org/10.1038/s41586-024-07967-z> (2024).
101. Zhao, A. et al. A comprehensive neuroanatomical survey of the lobula plate tangential neurons with predictions for their optic flow sensitivity. *eLife* <https://doi.org/10.7554/eLife.93659.1> (2024).
102. Eichler, K. et al. Somatotopic organization among parallel sensory pathways that promote a grooming sequence in *Drosophila*. *eLife* <https://doi.org/10.7554/eLife.87602.1> (2024).
103. Engert, S., Sterne, G. R., Bock, D. D. & Scott, K. *Drosophila* gustatory projections are segregated by taste modality and connectivity. *eLife* **11**, e78110 (2022).
104. Hampel, S. et al. Distinct subpopulations of mechanosensory chordotonal organ neurons elicit grooming of the fruit fly antennae. *eLife* **9**, e59976 (2020).
105. Kim, H. et al. Wiring patterns from auditory sensory neurons to the escape and song-relay pathways in fruit flies. *J. Comp. Neurol.* **528**, 2068–2098 (2020).
106. Bates, A. S. et al. Complete connectomic reconstruction of olfactory projection neurons in the fly brain. *Curr. Biol.* **30**, 3183–3199 (2020).
107. Namiki, S., Dickinson, M. H., Wong, A. M., Korff, W. & Card, G. M. The functional organization of descending sensory-motor pathways in *Drosophila*. *eLife* **7**, e34272 (2018).
108. Stürmer, T. et al. Comparative connectomics of the descending and ascending neurons of the *Drosophila* nervous system: stereotypy and sexual dimorphism. Preprint at *bioRxiv* <https://doi.org/10.1101/2024.06.04.596633> (2024).
109. Takemura, S.-Y. et al. A connectome of the male *Drosophila* ventral nerve cord. *eLife* **13**, RP97769 (2024).
110. Marin, E. C. et al. Systematic annotation of a complete adult male *Drosophila* nerve cord connectome reveals principles of functional organisation. *eLife* **13**, RP97766 (2024).
111. Court, R. et al. A systematic nomenclature for the *Drosophila* ventral nerve cord. *Neuron* **107**, 1071–1079 (2020).
112. Pascual, A., Huang, K.-L., Neveu, J. & Pr at, T. Neuroanatomy: brain asymmetry and long-term memory. *Nature* **427**, 605–606 (2004).
113. Wolff, T. & Rubin, G. M. Neuroarchitecture of the *Drosophila* central complex: a catalog of nodulus and asymmetrical body neurons and a revision of the protocerebral bridge catalog. *J. Comp. Neurol.* <https://doi.org/10.1002/cne.24512> (2018).
114. Lapraz, F. et al. Asymmetric activity of NetrinB controls laterality of the *Drosophila* brain. *Nat. Commun.* **14**, 1052 (2023).
115. Musso, P.-Y., Junca, P. & Gordon, M. D. A neural circuit linking two sugar sensors regulates satiety-dependent fructose drive in *Drosophila*. *Sci. Adv.* **7**, eabj0186 (2021).
116. Dorkenwald, S. et al. FlyWire: online community for whole-brain connectomics. *Nat. Methods* **19**, 119–128 (2022).
117. Bogovic, J. A. et al. An unbiased template of the *Drosophila* brain and ventral nerve cord. *PLoS ONE* **15**, e0236495 (2020).
118. Barnes, C. L., Bonn ry, D. & Cardona, A. Synaptic counts approximate synaptic contact area in *Drosophila*. *PLoS ONE* **17**, e0266064 (2022).
119. Gerhard, S., Andrade, I., Fetter, R. D., Cardona, A. & Schneider-Mizell, C. M. Conserved neural circuit structure across larval development revealed by comparative connectomics. *eLife* **6**, e29089 (2017).
120. Saalfeld, S., Cardona, A., Hartenstein, V. & Tomancak, P. CATMAID: collaborative annotation toolkit for massive amounts of image data. *Bioinformatics* **25**, 1984–1986 (2009).
121. Takemura, S.-Y. et al. A connectome of a learning and memory center in the adult *Drosophila* brain. *eLife* **6**, e26975 (2017).
122. Litwin-Kumar, A., Harris, K. D., Axel, R., Sompolinsky, H. & Abbott, L. F. Optimal degrees of synaptic connectivity. *Neuron* **93**, 1153–1164 (2017).
123. Virtanen, P. et al. SciPy 1.0: fundamental algorithms for scientific computing in Python. *Nat. Methods* **17**, 261–272 (2020).
124. Cohen, J. *Statistical Power Analysis for the Behavioral Sciences* (Routledge, 2013).
125. Hofmann, H., Wickham, H. & Kafadar, K. Letter-value plots: boxplots for large data. *J. Comput. Graph. Stat.* **26**, 469–477 (2017).
126. Schlegel, P. & Jefferis, G. S. X. E. Supplemental files for Schlegel et al., Nature (2024). [zenodo https://doi.org/10.5281/zenodo.10877326](https://doi.org/10.5281/zenodo.10877326) (2024).
127. FlyWire Consortium. FlyWire whole-brain connectome connectivity data. [Zenodo https://doi.org/10.5281/zenodo.10676866](https://doi.org/10.5281/zenodo.10676866) (2024).
128. Bates, A. S. et al. The natverse, a versatile toolbox for combining and analysing neuroanatomical data. *eLife* **9**, e53350 (2020).
129. Lin, S., Kao, C.-F., Yu, H.-H., Huang, Y. & Lee, T. Lineage analysis of *Drosophila* lateral antennal lobe neurons reveals notch-dependent binary temporal fate decisions. *PLoS Biol.* **10**, e1001425 (2012).
130. Hartenstein, V. et al. Structure and development of the subesophageal zone of the *Drosophila* brain. I. Segmental architecture, compartmentalization and lineage anatomy. *J. Comp. Neurol.* **526**, 6–32 (2018).

Acknowledgements We thank A. Champion and the members of the MRC LMB Scientific Computing group for assistance with compute and web infrastructure; A. McLachlan, R. Court, C. Pilgrim, D. Goutte-Gattat and D. Osumi-Sutherland from the Virtual Fly Brain for helping mapping annotations into their ontology; F. Collman and C. Schneider-Mizell for developing and maintaining the CAVE engine and associated tools; B. Pedigo for discussions as well as help with matching and typing of some FlyWire neurons; we thank the members of R. Wilson’s laboratory (A.S.B. with Q. Vanderbeck, A. Li, I. Haber and P. Gibb), who reconstructed the asymmetric body neurons; P. Kandimalla, S. Noselli and the members of R. Wilson’s laboratory for pointing out the left/right inversion of FAFB; and P. Kandimalla and S. Noselli for sharing their observations that situs inversus is extremely rare in wild-type *Drosophila*; L. Luo and J. Macke for comments on an early version of this manuscript; reviewers for suggestions and criticisms on the submitted version; and I. Tastekin and the members of the Ribeiro laboratory for their input on gustatory sensory neuron typing. A.S.B. thanks R. I. Wilson for her support and interest as he finished this project after having moved to the Wilson laboratory. D.S.H. thanks A. Cardona for support and mentoring while in his group. This work was supported by an NIH BRAIN Initiative grant 1RF1MH120679-01 to D.D.B. with G.S.X.E.J.; a Neuronex2 award to G.S.X.E.J. and D.D.B. (NSF 2014862, MRC MC_EX_MR/TO46279/1); Wellcome Trust Collaborative Awards (203261/Z/16/Z, 220343/Z/20/Z and 221300/Z/20/Z) and core support from the MRC (MC-U105188491) to G.S.X.E.J.; DFG Walter-Benjamin-Fellowship (STU 793/2-1) to T.S.; EMBO fellowship (ALTF 1258-2020) and a Sir Henry Wellcome Postdoctoral Fellowship (222782/Z/21/Z) to A.S.B.

Author contributions P.S., Y.Y., A.S.B., K.E., P.B., M.G., M.d.S., E.J.M., G.B., L.S.C., V.A.S., A.M.C.F., L.K., M.W.P., I.F.M.T., C.R.D., I.S., A.J. and S.F. and the members of the FlyWire consortium contributed proofreading. Y.Y., K.E., P.B., P.S., A.S.B., M.C. and G.S.X.E.J. led the targeted

Article

proofreading effort in Cambridge. S.D., M.M. and H.S.S. led the overall effort. S.D., P.S. and G.S.X.E.J. maintained the proofreading and annotation management platforms. A.R.S., S.-c.Y. and C.E.M. managed the FlyWire community and onboarded new members. P.S., A.S.B., S.D., K.E., P.B., M.G., M.d.S., E.J.M., G.B., L.S.C., V.A.S., A.M.C.F., L.K., M.W.P., M.C., V.H. and G.S.X.E.J. contributed annotations. K.E., P.B. and T.S. provided the cell types for ANs and DNs. A.M. ingested annotations into Codex. D.D.B., E.P. and T.K. developed and hosted CATMAID spaces, the FlyWire supervoxel lookup and FlyWire \rightleftharpoons FAFB transform services. S.R.J. developed pyroglancer. P.S., A.S.B. and G.S.X.E.J. developed the R and Python packages to work with the FlyWire and hemibrain datasets. P.S., Y.Y., D.S.H. and G.S.X.E.J. analysed the data and generated the figures. P.S., Y.Y., D.S.H., A.S.B., L.S.C., G.S.X.E.J. and D.D.B. wrote the manuscript with feedback from all of the authors.

Competing interests H.S.S. declares a financial interest in Zetta AI. The other authors declare no competing interests.

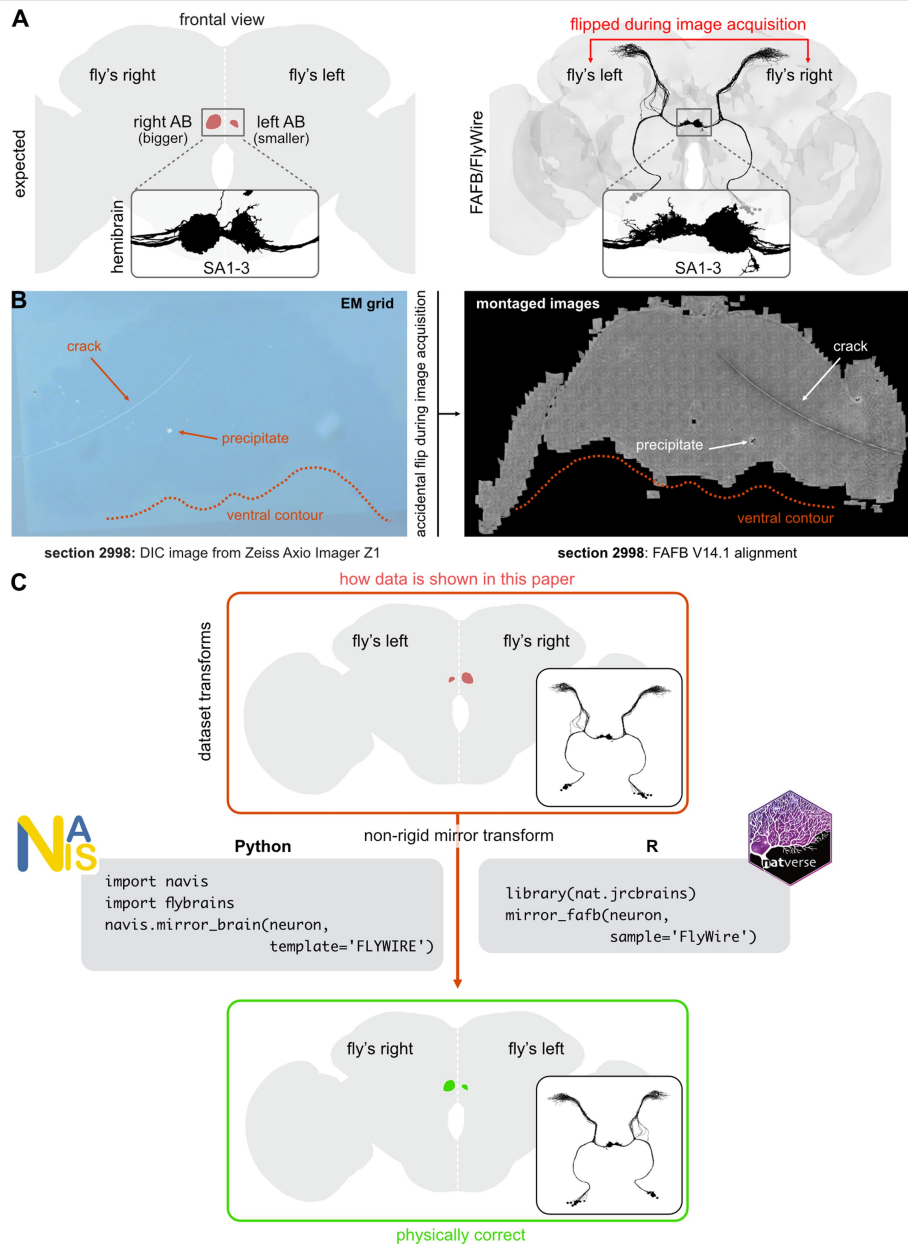
Additional information

Supplementary information The online version contains supplementary material available at <https://doi.org/10.1038/s41586-024-07686-5>.

Correspondence and requests for materials should be addressed to Davi D. Bock or Gregory S. X. E. Jefferis.

Peer review information *Nature* thanks Srinivas Turaga and the other, anonymous, reviewer(s) for their contribution to the peer review of this work. Peer reviewer reports are available.

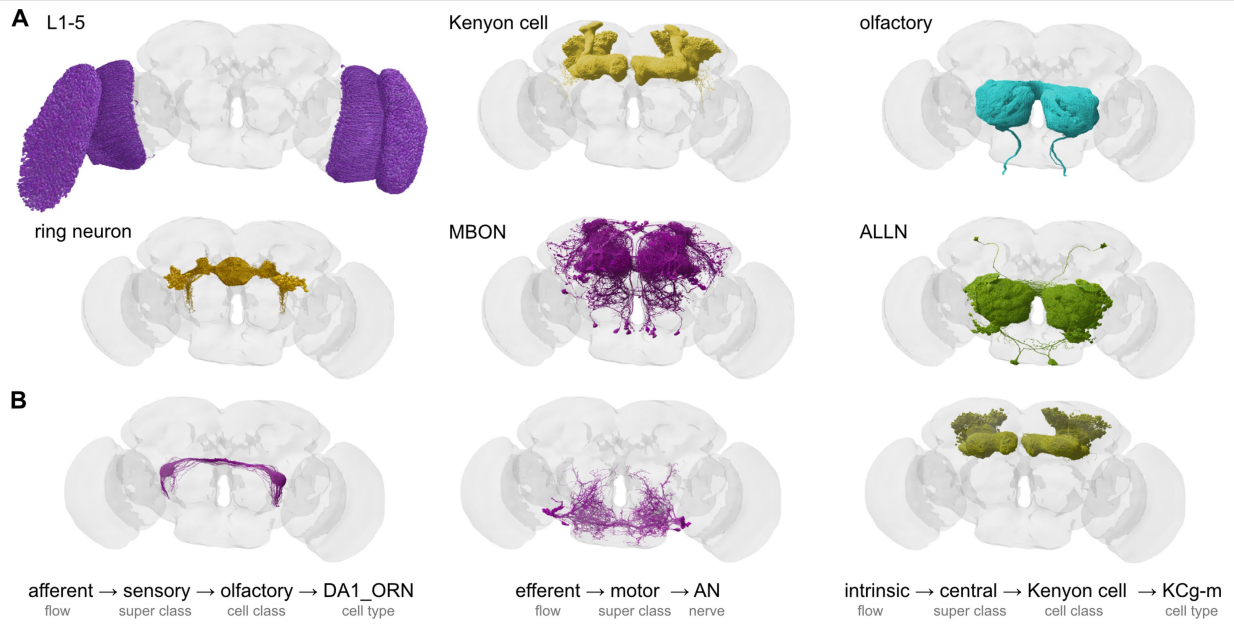
Reprints and permissions information is available at <http://www.nature.com/reprints>.



Extended Data Fig. 1 | Completion of the FlyWire whole-brain connectome and cell typing reveal a left-right inversion of EM image data during acquisition of the underlying FAFB EM dataset. **A** Frontal views of the adult fly brain are by convention shown in 2D projection, placing the fly's right on the left of the page. In this view, the asymmetric body (AB), which is nearly always larger on the fly's right¹¹²⁻¹¹⁴, therefore appears on the left of the page (left panel). During acquisition of the FAFB dataset, image mosaics were acquired and inadvertently stored to disk with the left-right axis inverted. Therefore in frontal view, the right side of the FAFB/FlyWire brain, and the larger AB, appear on the viewer's right (right panel). Insets show axons of SA1-3 neurons, which form the major input to the AB. **B** Direct examination of an original EM-imaged

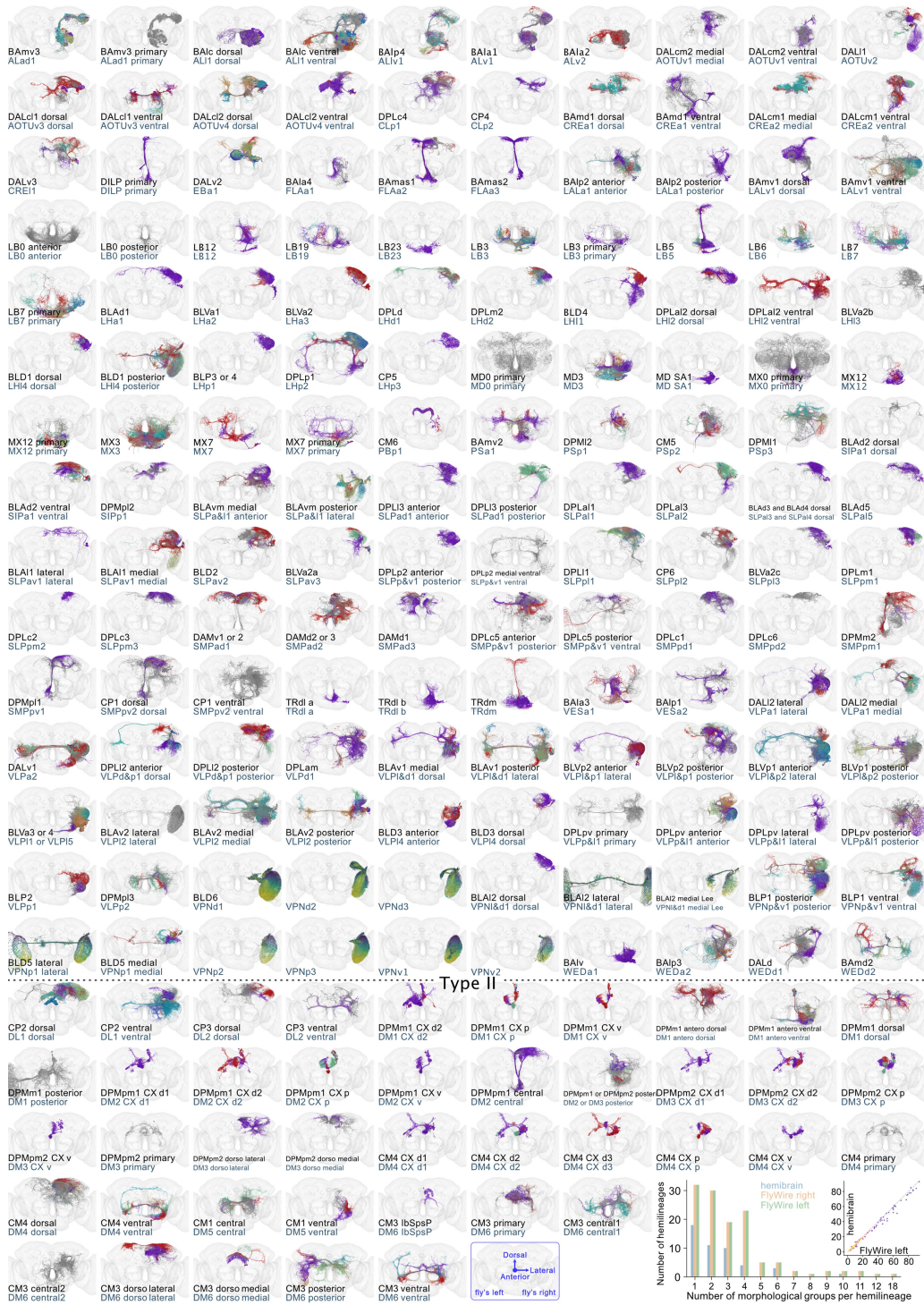
grid using differential interference contrast (DIC) microscopy and an acquired EM mosaic in neuroglancer/catmaid confirms a left-right inversion during image acquisition. A grid with a crack in the support film and staining artefact precipitate was selected in order to provide fiducials easily visible by light microscopy (left panel). These same artefacts can be seen in the EM mosaic (right panel). **C** Showcase of how to programmatically correct the inversion of FAFB/FlyWire data. Due to the large size of the original and derived datasets, it was not technically practical to correct the left-right inversion once it was detected. Therefore this must be corrected post hoc. Code samples show how this can be done for e.g. mesh or skeleton data using Python or R (Methods, "FAFB Laterality").

Article



Extended Data Fig. 2 | Hierarchical annotation examples. A Examples for cell class annotations. **B** Examples for labels derived from the hierarchical annotations. Abbreviations: ALRN, antennal lobe receptor neuron; MBON,

mushroom body output neuron; ALLN, antennal lobe local neuron; ORN, olfactory receptor neuron; AN, antennal nerve.

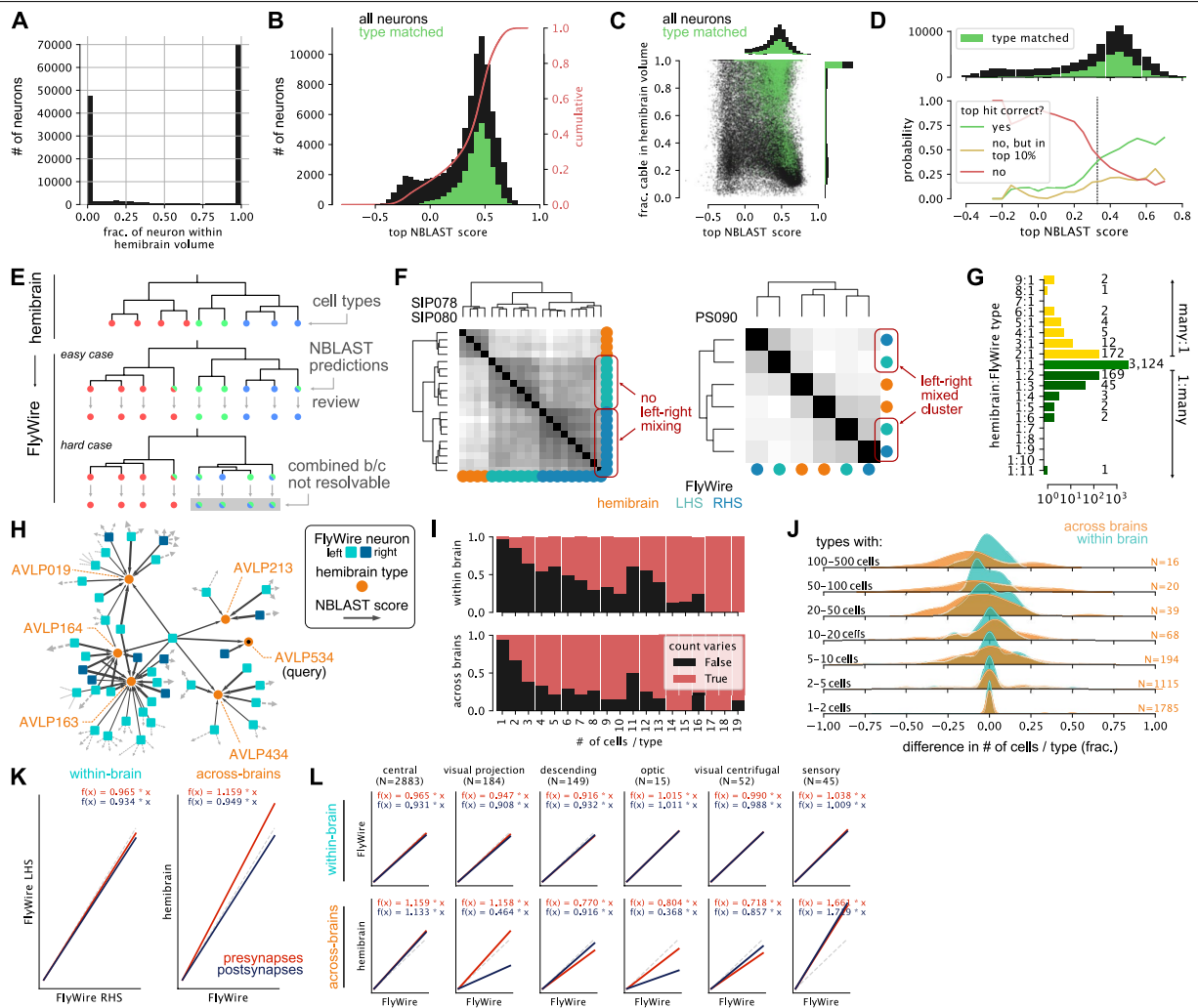


Extended Data Fig. 3 | See next page for caption.

Article

Extended Data Fig. 3 | Hemilineage atlas. Anterior views of neurons within a hemilineage (based on^{37,129}), or neurons whose cell bodies form a cluster in a lineage clone (also referred to as “hemilineages” hereafter), based on the light-level data from^{31-34,130}. The names of the hemilineages are at the bottom of each panel (top: Hartenstein nomenclature; bottom: ItoLee nomenclature). The snapshots only include neurons with cell bodies on the right hemisphere, and the central unpaired lineages. Except for the hemilineages that tile the optic lobe, the neurons are coloured by morphological groups (see Methods, Hemilineage annotations section). The neurons that form cohesive tracts with

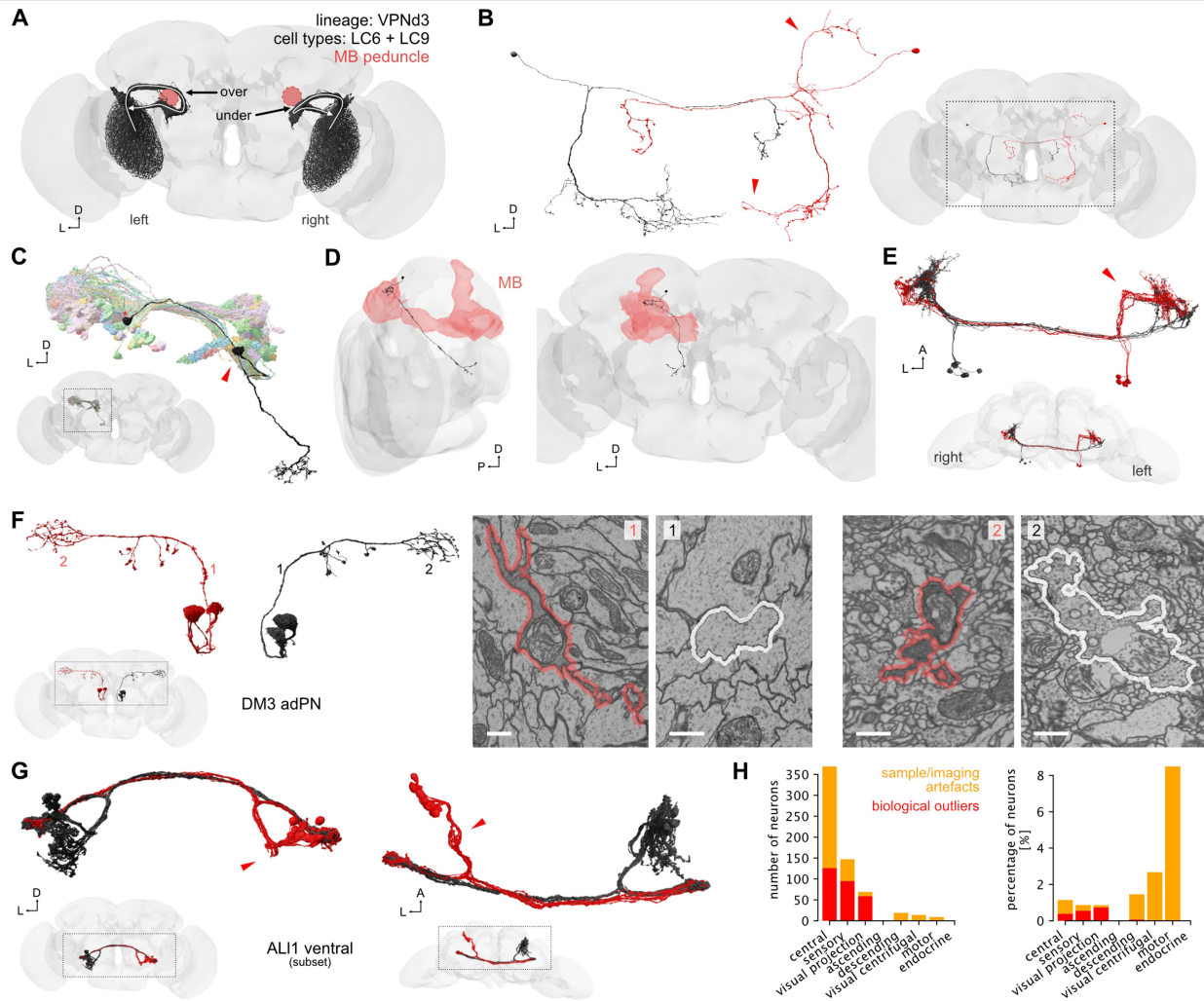
their cell body fibres in the Type II lineages (see Methods) are at the lower part of the panels. The last panel of the “Type II” section is for orientation purposes. The bottom right panel is a histogram of the number of morphological groups per hemilineage (blue: hemibrain; orange: FlyWire right; green: FlyWire left). Inset is the number of neurons per hemisphere in each morphological group, with points coloured by their density (yellow: denser). Corresponding group names, together with FlyWire and neuroglancer links are available in Supplementary Files 2 and 3.



Extended Data Fig. 4 | Across-brain neuron matching. **A** Distribution of the fraction of each FlyWire neuron's cable that is contained within the hemibrain volume: 1 = fully contained; 0 = entirely outside the volume. Note that where necessary FlyWire neurons were transformed onto the opposite side of the brain to better overlap with the hemibrain. **B** Distribution of top FlyWire \rightarrow hemibrain NBLAST scores. **C** Top NBLAST score vs fraction of neuron contained within hemibrain volume. In a fraction of cases, even heavily truncated neurons can produce good scores and be successfully matched. **D** Top: distribution of top NBLAST scores and fraction which was type matched. Bottom: probability that the correct hit was the top NBLAST hit (green) or at least among (yellow) the top 10% as a function of the top NBLAST score. **E** When some FlyWire neurons had good NBLAST matches against multiple hemibrain cell types, we cross-compared within-dataset morphological clustering (dendrograms). We tried to assign hemibrain types to those ambiguous FlyWire neurons to exactly match clusters in the two dendrograms ("easy case"). When this failed because a cluster in the dendrogram contained clear matches to >1 hemibrain types, we merged types ("hard case"). **F** Cross-brain NBLAST co-clustering for example cell types in Fig. 3: SIP078/SIP080 (left) and PS090 (right). All hemibrain neurons are truncated. The FlyWire PS090

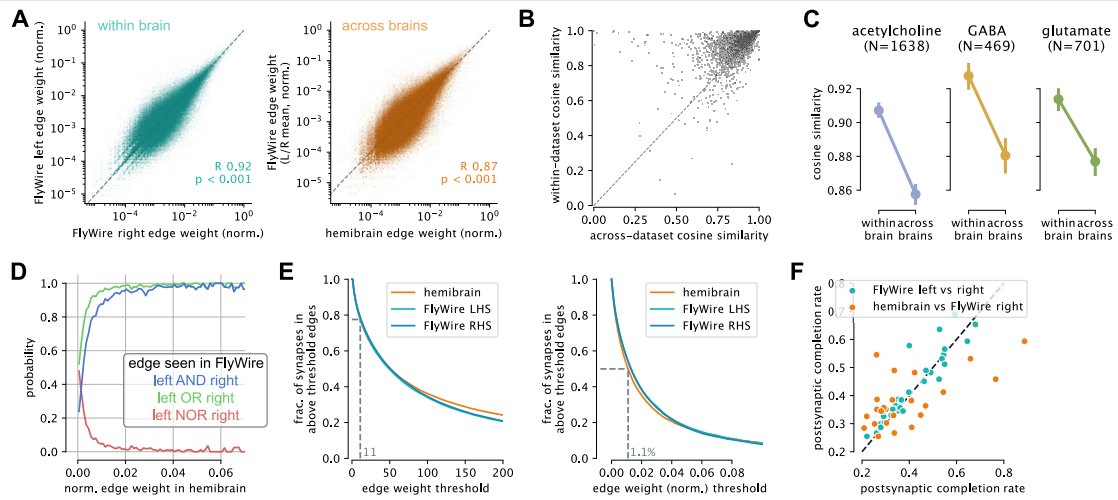
neurons (2 per hemisphere, none truncated) split into two well-separated clusters each containing one left and one right neuron, suggesting that the hemibrain cell type should be split. This is not the case for SIP078/SIP080 where the dendrogram cannot be split into subclusters containing neurons from each hemisphere. **G** Counts for 1:many and many:1 type matches. These also include types derived from previously untyped hemibrain neurons. **H** Extended version of NBLAST hit graph from Fig. 3k. Here, grey dotted arrows indicate matches to types outside of the displayed subgraph. **I** Fraction of cell types showing a difference in cell counts within (left/right, top) and across (bottom) brains. **J** Distribution of cell count differences. **K** Robust linear regression (Huber w/ intercept at 0) for within- and across-dataset pre/postsynapse counts from Fig. 3h. **L** Same data as in K but separated by superclass. Slopes are generally close to 1:1.021 (pre-) and 1.035 (postsynapses, i.e. inputs) between the left and right hemisphere of FlyWire, and 1.176 (presynapses, i.e. outputs) 0.983 (post) between FlyWire and the hemibrain. Note that correlation and slope are noticeably worse for cell types known to be truncated such as visual projection neurons which suggests that we did not fully compensate for the hemibrain's truncation and that the actual across-brain correlation might be even better.

Article



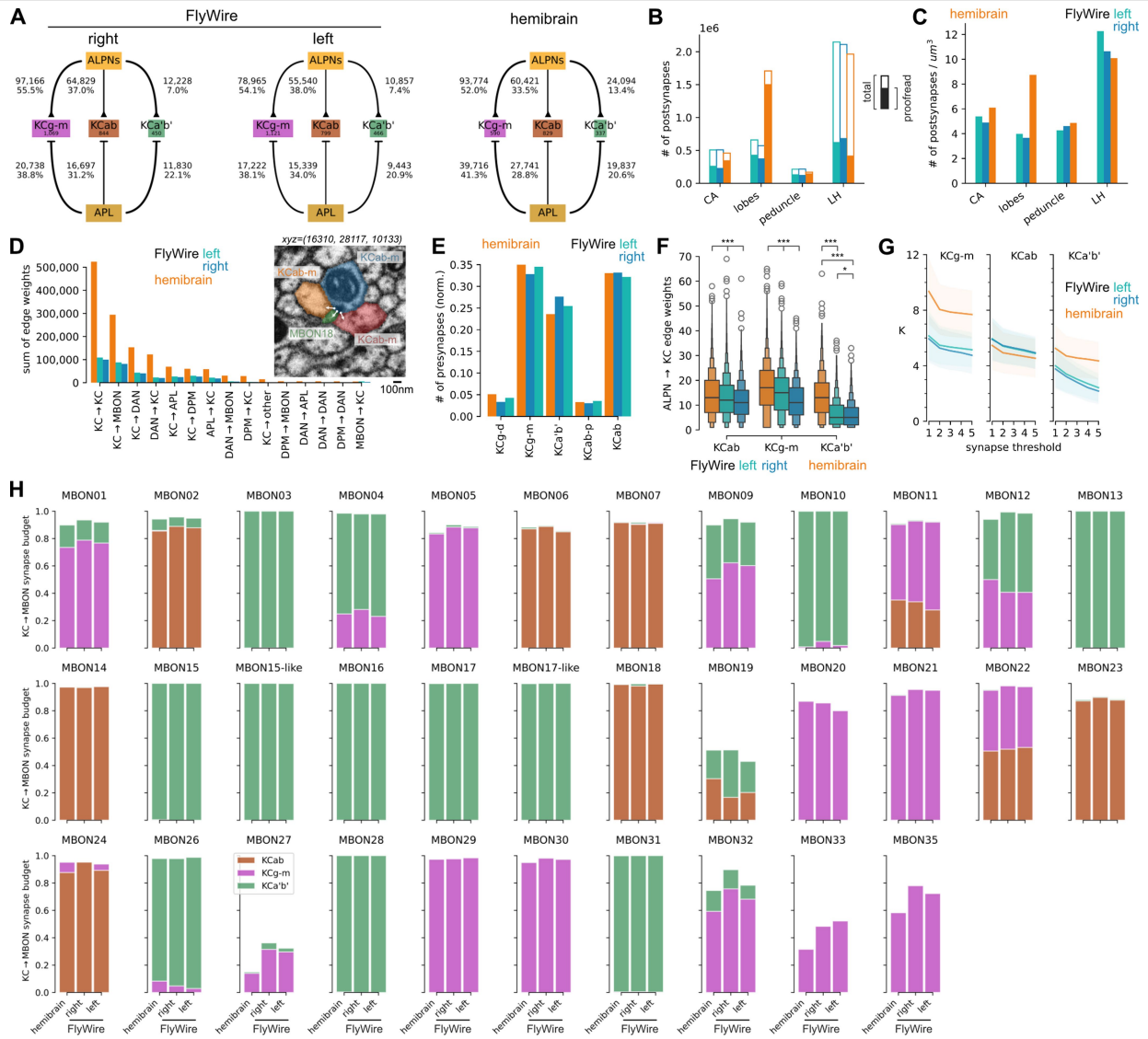
Extended Data Fig. 5 | Examples of biological outliers and sample artefacts. **A** LC6 and LC9 neurons (lineage VPNd3) of the right and left hemispheres take different routes in FlyWire to equivalent destinations (previously reported in⁴³). Mushroom body (MB) peduncle is shown in pink. **B** Example of a left/right neuron pair where one side has extra dorsal and smaller ventral dendrites (red arrowheads). **C** A TuBu neuron (black) with correctly placed axon but misplaced ventral dendrites. Regular TuBu neurons shown in background for reference. **D** A single Kenyon Cell whose axon projects outside of the mushroom body, descending through the medial antennal lobe tract. **E** Cell type (CB1029, DM6 ventral hemilineage) where the left neurons' dendrites

(red) take a different tract. **F** Example of sample artefact: the axon of the left DM3 adPN has very dark cytosol which affects both the neuron segmentation as well as synapse detection. Insets compare two locations along the axons between the left and right neurons. **G** A subset of neurons from the ALI1 ventral hemilineage where the right neurons are missing their entire dendrites (red arrow). The exact reason for this is unknown but it is not due to insufficient proofreading. **H** Quantification of recorded outliers and sampling artefacts broken down by super class. Total number of neurons (left) as well as fraction (right) are shown. The number of biological outlier neurons is -0.4% of the total number of neurons in the brain.



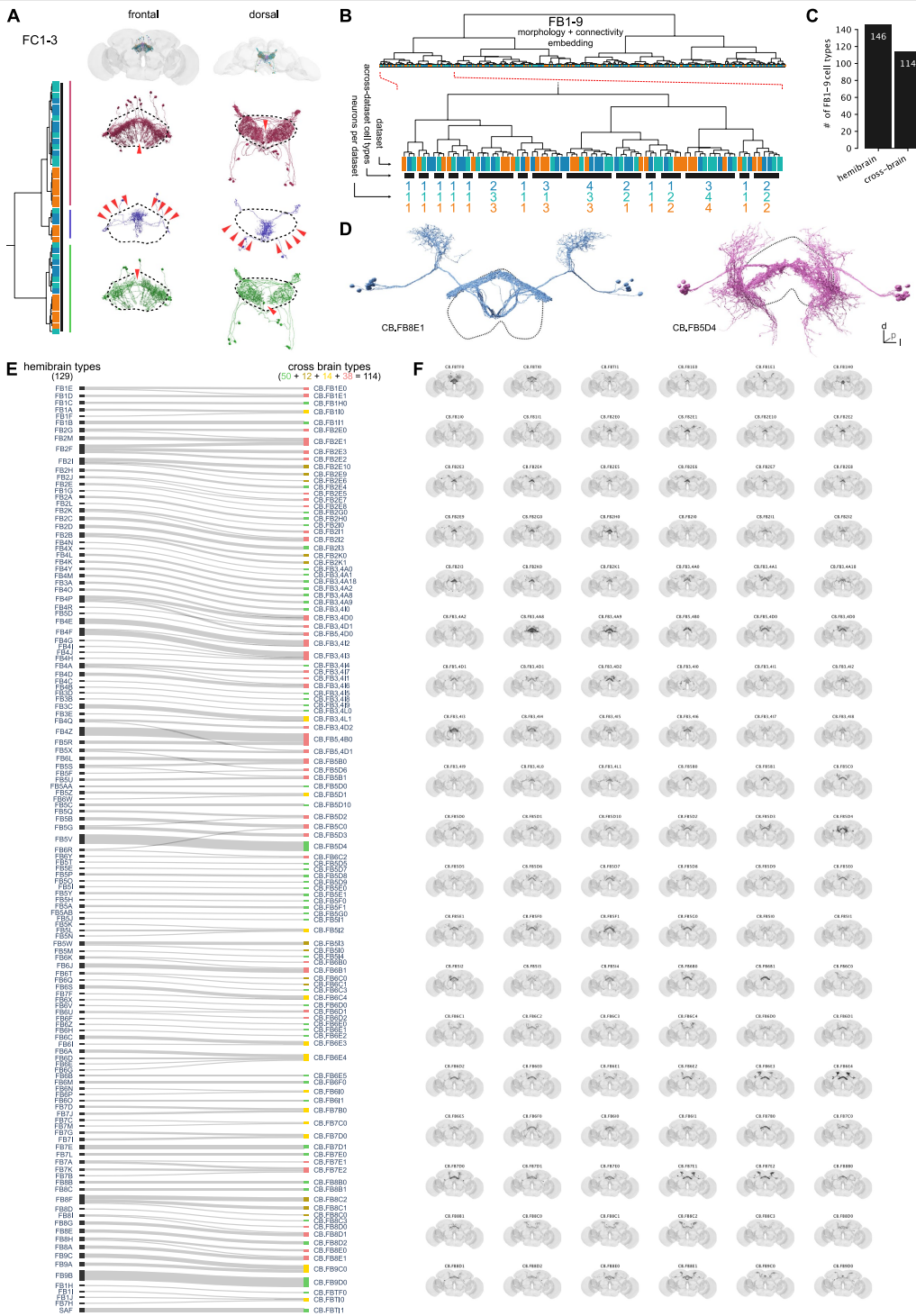
Extended Data Fig. 6 | Across-brain connectivity. **A** Comparison of normalized edge weights within (left) and across (right) brains. **B** Connectivity cosine similarity within and across brains. Each datapoint is a cell type identified across the three hemispheres. Size correlates with the number of cells per type. **C** Connectivity cosine similarity separated by neurotransmitter. Error bars represent the 95% CI. **D** Probability that an edge present in the

hemibrain is found in one, both or neither of the FlyWire hemispheres. **E** Fraction of synapses contained in edges above given absolute (left) and normalized (right) weight. Horizontal lines mark the thresholds for a 90% chance that an edge is found in another hemisphere. **F** Postsynaptic completion rates. Each datapoint is a neuropil.



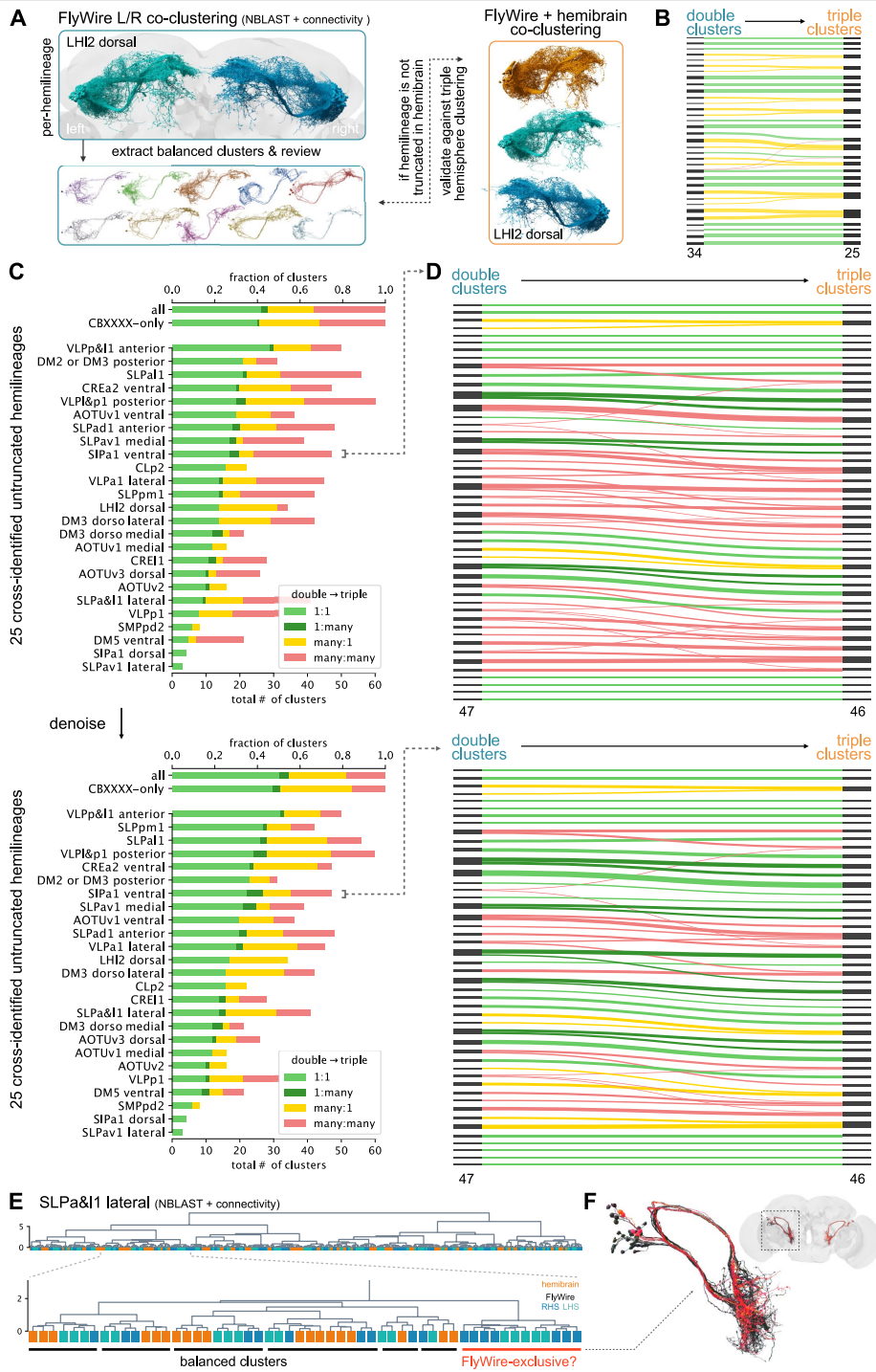
Extended Data Fig. 7 | Across-brain mushroom body comparison. **A** Graph showing ALPN/APL → KC connectivity across the three datasets. Edge labels provide weights both as total synapse counts and normalized to the total output budget of the source. In FlyWire, the mushroom bodies (MB) have 57.2% (left) and 60.7% (right) postsynaptic completion rate while the hemibrain MB has been proofread to 81.3% (see also B). To compensate for this we typically used normalized synapse counts and edge weights. Note that KCab act as an internal control as their numbers are consistent across all hemispheres and we don't expect to see any changes in their connectivity. **B** Total versus proofread postsynapse counts across MB compartments. Lateral horn (LH) shown for

comparison. **C** Postsynapse density across MB compartments. **D** Connectivity between different MB cell classes. Inset shows an example of KC → KC and KC → MBON synapse in the hemibrain. **E** Presynapse counts per KC type normalized to the total number of KC synapses per dataset. **F** ALPN → KC edge weights. See Methods for details on enhanced box plots. **G** # of ALPN types providing input to a single KC under different synapse thresholds. **H** Fraction of MBON input budget coming from individual KCab, KCg-m and KCa'b'. Abbreviations: CA, calyx; DAN, dopaminergic neuron; ALPN, antennal lobe projection neuron; KC, Kenyon Cell; MBON, mushroom body output neurons. Kolmogorov-Smirnov test (F): *, $p < 0.05$; **, $p < 0.01$; ***, $p < 0.001$.



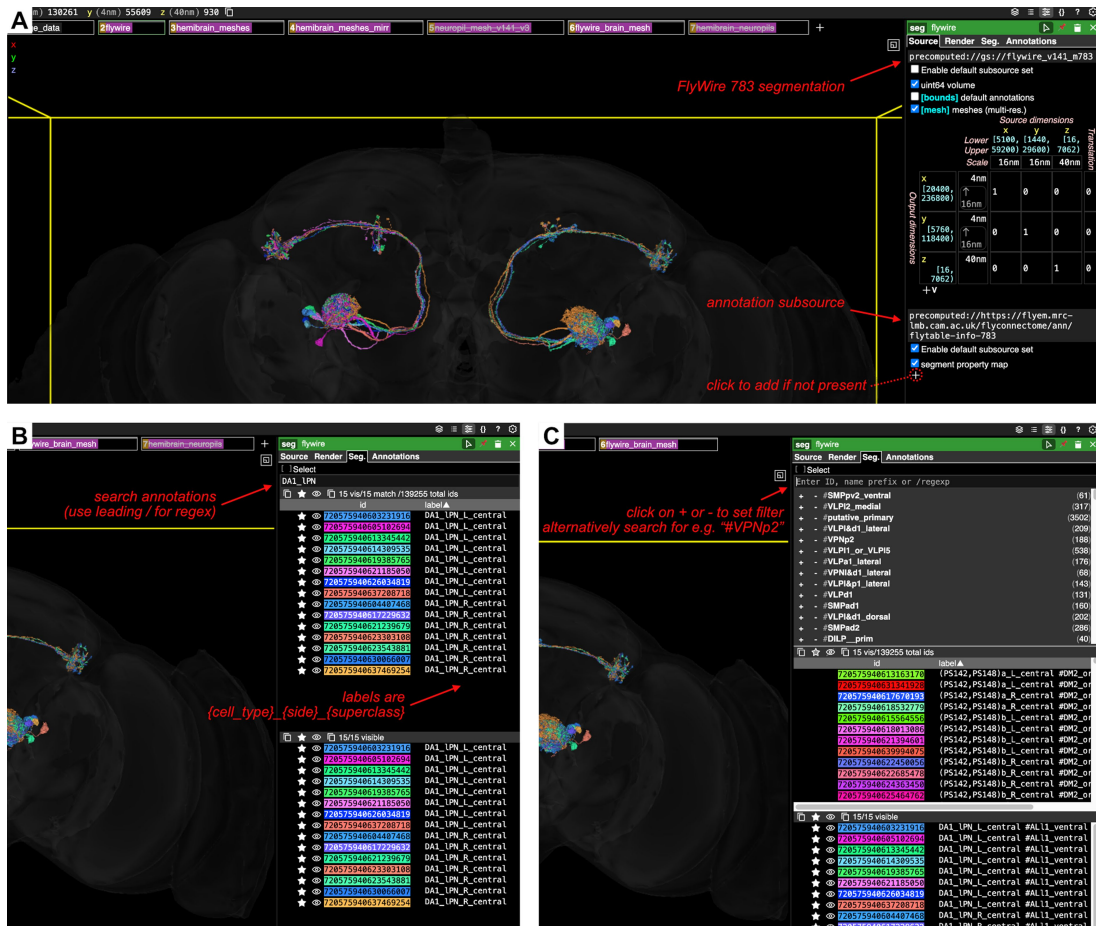
Extended Data Fig. 8 | Across-brain co-clustering. **A** FC1-3 cross-brain cluster from Fig. 6d (asterisk) that was manually adjusted. This group consists of three sub-clusters that technically fulfil our definition of cell type. They were merged, however, because they individually omit columns of the fan-shaped body (arrowheads) and are complementary to each other. **B** Hierarchical clustering from combined morphology + connectivity embedding for FB1-9. Zoom-in shows cross-brain cell type clusters. **C** Number of hemibrain vs

cross-brain FB1-9 cell types. **D** Examples from the FB1-9 cross-brain cell typing. Labels are composed from CB.FB{layer}{hemilineage-id}{subtype-id}; fan-shaped body outlined. **E** Flow chart comparing FB1-9 hemibrain and cross-brain cell types. Colours correspond to 1:1, 1:many, many:1 and many:many mappings between hemibrain and cross-brain cell types. **F** Renderings of all FB1-9 cross-brain cell types.



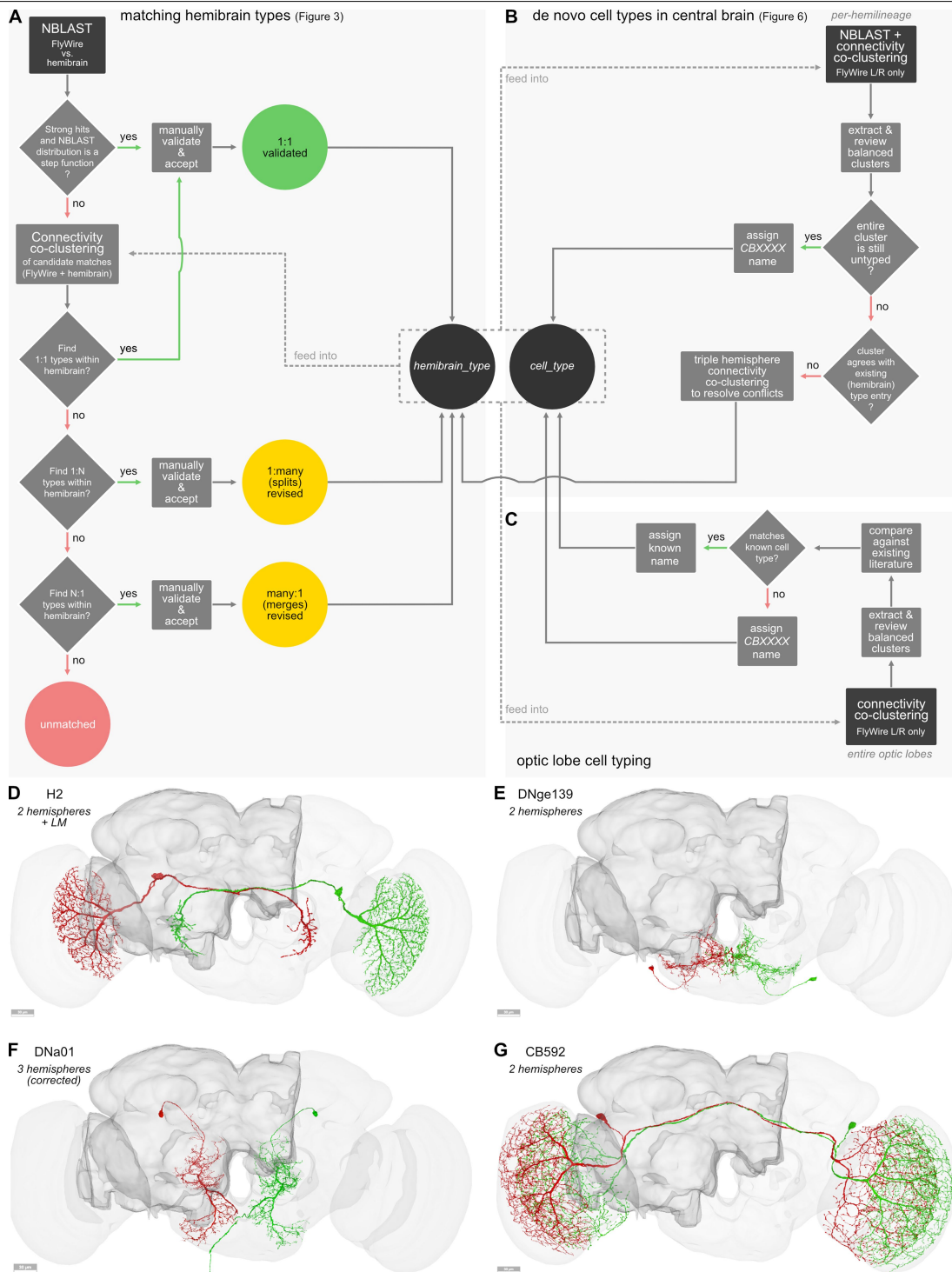
Extended Data Fig. 9 | Double vs triple co-clustering analyses. **A** Pipeline for comparing putative cell types from double (FlyWire left/right) and triple (FlyWire + hemibrain) hemisphere co-clustering. **B** Flow chart for hemilineage LHI2 dorsal illustrating how individual FlyWire neurons move between double and triple clusters. Black bars represent clusters; thickness is proportional to the number of neurons in each cluster. **C** Summary over all 25 hemilineages that were cross-identified and are untruncated in the hemibrain connectome.

Top bar chart shows unfiltered results; bottom chart shows results after denoising (removal of single neurons that cause many:many mapping because they swap clusters). **D** Flow chart for example hemilineage SIPa1 ventral. Unfiltered (top) and denoised (bottom). **E-F** Example of a cluster (red in panel F) from hemilineage SLPa&1 lateral that only seems to exist in FlyWire although similar balanced clusters (black) are present in both datasets.



Extended Data Fig. 11 | Annotations in Neuroglancer. A Screenshot of neuroglancer with FlyWire 783 segmentation layer with “flytable-info-783” annotation layer subsource (scene pre-configured at <http://tinyurl.com/>)

flywire783). **B** Example for querying annotation. **C** Example for subsource “flytable-info-783-all” which includes hemilineage annotations.



Extended Data Fig. 12 | Matching workflow. **A** Workflow for matching hemibrain types to FlyWire neurons. **B** Workflow for generation of *de-novo* cell types used to fill the gaps left from the hemibrain type matching. **C** Workflow for cell typing in the optic lobes. **D-G** Examples of cell types. H2 is based on left

vs right FlyWire clustering plus existing LM data; DNge139 and CB592 are based solely on left vs right FlyWire clustering; DNa01 is based on three hemispheres worth of data but was misidentified as "VES006" in the hemibrain.

Reporting Summary

Nature Portfolio wishes to improve the reproducibility of the work that we publish. This form provides structure for consistency and transparency in reporting. For further information on Nature Portfolio policies, see our [Editorial Policies](#) and the [Editorial Policy Checklist](#).

Statistics

For all statistical analyses, confirm that the following items are present in the figure legend, table legend, main text, or Methods section.

n/a Confirmed

- The exact sample size (n) for each experimental group/condition, given as a discrete number and unit of measurement
- A statement on whether measurements were taken from distinct samples or whether the same sample was measured repeatedly
- The statistical test(s) used AND whether they are one- or two-sided
Only common tests should be described solely by name; describe more complex techniques in the Methods section.
- A description of all covariates tested
- A description of any assumptions or corrections, such as tests of normality and adjustment for multiple comparisons
- A full description of the statistical parameters including central tendency (e.g. means) or other basic estimates (e.g. regression coefficient) AND variation (e.g. standard deviation) or associated estimates of uncertainty (e.g. confidence intervals)
- For null hypothesis testing, the test statistic (e.g. F , t , r) with confidence intervals, effect sizes, degrees of freedom and P value noted
Give P values as exact values whenever suitable.
- For Bayesian analysis, information on the choice of priors and Markov chain Monte Carlo settings
- For hierarchical and complex designs, identification of the appropriate level for tests and full reporting of outcomes
- Estimates of effect sizes (e.g. Cohen's d , Pearson's r), indicating how they were calculated

Our web collection on [statistics for biologists](#) contains articles on many of the points above.

Software and code

Policy information about [availability of computer code](#)

Data collection Data collection is described in our companion paper by Dorkenwald et al. and is cited at appropriate locations throughout our manuscript.

Data analysis For analysis we developed open-source software packages. These tools are detailed in the Methods, which also includes download locations, all of which are on Github. The key software packages are:
- navis: <https://github.com/navis-org/navis> v1.5.0
- fabbseg-py: <https://github.com/navis-org/fabbseg-py> v3.0.5
- flybrains: <https://github.com/navis-org/navis-flybrains> v0.2.9
- skeleton: <https://github.com/navis-org/skeleton> v1.2.3
- fabbseg: <https://github.com/natverse/fabbseg> v0.14.0
- coconatfly: <https://github.com/natverse/coconatfly> v0.1.0

For manuscripts utilizing custom algorithms or software that are central to the research but not yet described in published literature, software must be made available to editors and reviewers. We strongly encourage code deposition in a community repository (e.g. GitHub). See the Nature Portfolio [guidelines for submitting code & software](#) for further information.

Data

Policy information about [availability of data](#)

All manuscripts must include a [data availability statement](#). This statement should provide the following information, where applicable:

- Accession codes, unique identifiers, or web links for publicly available datasets
- A description of any restrictions on data availability
- For clinical datasets or third party data, please ensure that the statement adheres to our [policy](#)

Data artefacts from this paper are available at https://github.com/flyconnectome/flywire_annotiations.

This includes:

- neuron annotations + other metadata
- high quality skeletons for all proofread FlyWire neurons
- NBLAST scores for FlyWire vs. hemibrain
- all-by-all NBLAST scores for FlyWire

The repository may periodically be updated to improve annotations but older versions will always remain available via Github's versioning system.

In addition, neuron annotations + other meta data are also available for download in the supplementary materials; NBLAST scores and skeletons have been deposited in a Zenodo repository: <https://zenodo.org/records/10877326> (doi: 10.5281/zenodo.10877326).

We provide a neuroglancer scene preconfigured for display and query of our annotations alongside the FlyWire neuron meshes and segmentation at <http://tinyurl.com/flywire783>. Users can add the annotations to arbitrary neuroglancer scenes themselves by adding a data subsource (see Extended Data Figure 11). There are two options:

- "precomputed://https://flyem.mrc-lmb.cam.ac.uk/flyconnectome/ann/flytable-info-783" containing super class, cell type and side labels
- "precomputed://https://flyem.mrc-lmb.cam.ac.uk/flyconnectome/ann/flytable-info-783-all" additionally contains hemi-lineage information

We also provide programmatic access to the annotations through our `fabseg` R and Python packages (see Table 1 and the online documentation for examples).

Annotations have also been shared with Codex (<https://codex.flywire.ai/>), the connectome annotation versioning engine (CAVE) which can be queried through e.g. the CAVEclient (<https://github.com/seung-lab/CAVEclient>), and the FAFB-FlyWire CATMAID spaces (<https://fab-flywire.catmaid.org>). At the time of writing access to Codex and CAVE requires signing up using a Google account.

To aid a number of analyses, hemibrain neuron meshes were mapped into FlyWire (FAFB14.1) space. These can be co-visualised with FlyWire neurons within neuroglancer (e.g. <https://tinyurl.com/flywire783>; this scene also includes a second copy of the hemibrain data (layer `hemibrain_meshes_mirr`) which has been non-rigidly mapped onto the opposite side of FAFB).

Research involving human participants, their data, or biological material

Policy information about studies with [human participants or human data](#). See also policy information about [sex, gender \(identity/presentation\), and sexual orientation](#) and [race, ethnicity and racism](#).

Reporting on sex and gender	<input type="text" value="Does not apply."/>
Reporting on race, ethnicity, or other socially relevant groupings	<input type="text" value="Does not apply."/>
Population characteristics	<input type="text" value="Does not apply."/>
Recruitment	<input type="text" value="Does not apply."/>
Ethics oversight	<input type="text" value="Does not apply."/>

Note that full information on the approval of the study protocol must also be provided in the manuscript.

Field-specific reporting

Please select the one below that is the best fit for your research. If you are not sure, read the appropriate sections before making your selection.

- Life sciences Behavioural & social sciences Ecological, evolutionary & environmental sciences

For a reference copy of the document with all sections, see [nature.com/documents/nr-reporting-summary-flat.pdf](https://www.nature.com/documents/nr-reporting-summary-flat.pdf)

Life sciences study design

All studies must disclose on these points even when the disclosure is negative.

Sample size

Data exclusions	No neurons were excluded from overall annotation or analyses. For the analysis of across brain stereotypy we used a subset of the available matches; the specific exclusion criteria and rationale are clearly detailed in the methods.
Replication	Does not apply.
Randomization	Does not apply.
Blinding	Does not apply.

Reporting for specific materials, systems and methods

We require information from authors about some types of materials, experimental systems and methods used in many studies. Here, indicate whether each material, system or method listed is relevant to your study. If you are not sure if a list item applies to your research, read the appropriate section before selecting a response.

Materials & experimental systems

n/a	Involvement in the study
<input checked="" type="checkbox"/>	<input type="checkbox"/> Antibodies
<input checked="" type="checkbox"/>	<input type="checkbox"/> Eukaryotic cell lines
<input checked="" type="checkbox"/>	<input type="checkbox"/> Palaeontology and archaeology
<input checked="" type="checkbox"/>	<input type="checkbox"/> Animals and other organisms
<input checked="" type="checkbox"/>	<input type="checkbox"/> Clinical data
<input checked="" type="checkbox"/>	<input type="checkbox"/> Dual use research of concern
<input checked="" type="checkbox"/>	<input type="checkbox"/> Plants

Methods

n/a	Involvement in the study
<input checked="" type="checkbox"/>	<input type="checkbox"/> ChIP-seq
<input checked="" type="checkbox"/>	<input type="checkbox"/> Flow cytometry
<input checked="" type="checkbox"/>	<input type="checkbox"/> MRI-based neuroimaging

Plants

Seed stocks	Does not apply.
Novel plant genotypes	Does not apply.
Authentication	Does not apply.

4 MANUSCRIPT 4: NEURONAL PARTS LIST AND WIRING DIAGRAM FOR A VISUAL SYSTEM

Summary

A catalogue of neuronal cell types has often been called a ‘parts list’ of the brain¹, and regarded as a prerequisite for understanding brain function. In the optic lobe of *Drosophila*, rules of connectivity between cell types have already proven to be essential for understanding fly vision. Here we analyse the fly connectome to complete the list of cell types intrinsic to the optic lobe, as well as the rules governing their connectivity. Most new cell types contain 10 to 100 cells, and integrate information over medium distances in the visual field. Some existing type families (Tm, Li, and LPi) at least double in number of types. A new serpentine medulla (Sm) interneuron family contains more types than any other. Three families of cross-neuropil types are revealed. The consistency of types is demonstrated by analysing the distances in high-dimensional feature space, and is further validated by algorithms that select small subsets of discriminative features. We use connectivity to hypothesize about the functional roles of cell types in motion, object and colour vision. Connectivity with ‘boundary types’ that straddle the optic lobe and central brain is also quantified. We showcase the advantages of connectomic cell typing: complete and unbiased sampling, a rich array of features based on connectivity and reduction of the connectome to a substantially simpler wiring diagram of cell types, with immediate relevance for brain function and development.

Authors

Arie Matsliah, Szi-chieh Yu, Krzysztof Kruk, Doug Bland, Austin Burke, Jay Gager, James Hebditch, Ben Silverman, Kyle Willie, Ryan Willie, Marissa Sorek, Amy R. Sterling, Emil Kind, Dustin Garner, Gizem Sancer, Mathias F. Wernet, Sung Soo Kim, Mala Murthy, H. Sebastian Seung, the **FlyWire Consortium**

This article is published in *Nature*; [Matsliah et al. \(2024\)](#).

Contributions

D.G., E.K. and G.S. annotated cells under the supervision of S.S.K. and M.F.W. M.S. and A.R.S. recruited, trained and managed citizen scientists with help from E.K. K.K. annotated cells and created computational cell typing tools for use by the community. S.-c.Y. trained and managed D.B., A.T.B., J.G., J.H., B.S., K.P.W. and R.W. to annotate the remaining known cell types and identify and annotate new types. A.M. and H.S.S. created semiautomated cell typing tools. A.M. and H.S.S. carried out the final automated stage of typing. A.M. verified types with predicates. H.S.S. verified types with 2D projections. S.-c.Y., H.S.S. and M.M. devised type family names. A.M. and H.S.S. defined and characterized subsystems.

A.M. drew wiring diagrams. S.S.K., M.F.W., M.M. and H.S.S. identified implications for visual function. A.T.B., J.G., J.H., B.S., K.P.W., R.W., S.-c.Y., A.M. and H.S.S. created figures. K.K., M.S., A.R.S., A.M., S.-c.Y., S.S.K., M.M. and H.S.S. wrote the text. M.M. and H.S.S. supervised the project. Members listed in the **FlyWire consortium** made at least ten annotations in the optic lobe.

FlyWire Consortium

Krzysztof Kruk, Ben Silverman, Jay Gager, Kyle Patrick Willie, Doug Bland, Austin T Burke, James Hebditch, Ryan Willie, Celia David, Gizem Sancer, Jenna Joroff, Dustin Garner, annkri (Anne Kristiansen), Thomas Stocks, **Amalia Braun**, Szi-chieh Yu, Marion Silies, AzureJay (Jaime Skelton), TR77, Maria Ioannidou, Marissa Sorek, Matt Collie, Gerit Linneweber, Sebastian Mauricio Molina Obando, Rey Adrian Candilada, Alexander Borst, Wei-Chung Lee, Philipp Schlegel, Greg Jefferis, Arie Matsliah, Amy R. Sterling, Emil Kind, Mathias Wernet, Sung Soo Kim, Mala Murthy, H. Sebastian Seung

My contribution to this publication in detail

For this publication I contributed with a number of 246 annotations of intrinsic neurons in the right optic lobe.

Neuronal parts list and wiring diagram for a visual system

<https://doi.org/10.1038/s41586-024-07981-1>

Received: 1 December 2023

Accepted: 21 August 2024

Published online: 2 October 2024

Open access

 Check for updates

Arie Matsliah^{1,16}, Szi-chieh Yu^{1,16}, Krzysztof Kruk^{2,3}, Doug Bland¹, Austin T. Burke¹, Jay Gager¹, James Hebditch¹, Ben Silverman¹, Kyle Patrick Willie¹, Ryan Willie¹, Marissa Sorek^{1,3}, Amy R. Sterling^{1,3}, Emil Kind⁴, Dustin Garner⁵, Gizem Sancer⁶, Mathias F. Wernet⁴, Sung Soo Kim⁵, Mala Murthy^{1,16}, H. Sebastian Seung^{1,7,16} & The FlyWire Consortium*

A catalogue of neuronal cell types has often been called a ‘parts list’ of the brain¹, and regarded as a prerequisite for understanding brain function^{2,3}. In the optic lobe of *Drosophila*, rules of connectivity between cell types have already proven to be essential for understanding fly vision^{4,5}. Here we analyse the fly connectome to complete the list of cell types intrinsic to the optic lobe, as well as the rules governing their connectivity. Most new cell types contain 10 to 100 cells, and integrate information over medium distances in the visual field. Some existing type families (Tm, Li, and LPI)^{6–10} at least double in number of types. A new serpentine medulla (Sm) interneuron family contains more types than any other. Three families of cross-neuropil types are revealed. The consistency of types is demonstrated by analysing the distances in high-dimensional feature space, and is further validated by algorithms that select small subsets of discriminative features. We use connectivity to hypothesize about the functional roles of cell types in motion, object and colour vision. Connectivity with ‘boundary types’ that straddle the optic lobe and central brain is also quantified. We showcase the advantages of connectomic cell typing: complete and unbiased sampling, a rich array of features based on connectivity and reduction of the connectome to a substantially simpler wiring diagram of cell types, with immediate relevance for brain function and development.

Some of the greatest scientific discoveries of the twentieth century concern the neural basis of sensory perception. Hubel and Wiesel’s discovery of simple and complex cells in the visual cortex not only entered neuroscience textbooks, but the hypothetical neuronal wiring diagrams in their 1962 paper¹¹ also inspired convolutional nets^{12,13}, which eventually ignited the deep-learning revolution in artificial intelligence¹⁴. It may come as a surprise that directly mapping such wiring diagrams, influential as they may be, has been highly challenging or even impossible in mammalian brains. Progress is being made by visual physiologists^{15–17}, and the reconstruction of a column of visual cortex from electron microscopy images is also becoming feasible^{18,19}. These are tiny slivers of visual systems; scaling up to the full complexity of mammalian vision is still aspirational.

To imagine the future of visual neuroscience, it is helpful to extrapolate from a brain of a more modest size—that of the fly. Especially over the past 15 years, visual neural circuits have been intensively investigated in *Drosophila*⁴ with great progress in understanding the perception of motion^{5,10}, colour²⁰ and objects²¹, as well as the role of vision in complex behaviours like courtship²². The release of a neuronal wiring diagram of a *Drosophila* brain^{23–25} poses an unprecedented opportunity. The first wiring diagram for a whole brain contains as a corollary the

first wiring diagram for an entire visual system, as well as all the wiring connecting the visual system with the rest of the brain.

About 38,500 neurons are intrinsic to the right optic lobe of the reconstructed *Drosophila* brain (Extended Data Fig. 1a). The full wiring diagram for these neurons is too complex to comprehend or even visualize. It is essential to reduce complexity by describing the connectivity between types of cells. For example, the roughly 800 ommatidia in the compound eye send photoreceptor axons to roughly 800 L1 cells in the lamina, which in turn connect with around 800 Mi1 cells. That is a lot of cells and connections, but they can all be described by the simple rules that photoreceptors connect to L1, and L1 connects to Mi1. Some such rules are known^{7,26–30}, but this knowledge is fragmentary and incomplete.

Here we exhaustively enumerate all cell types intrinsic to the optic lobe, and find all rules of connection between them. We effectively collapse 38,500 intrinsic neurons onto just 227 types, a reduction of more than 150×. The wiring diagram is reduced from a 38,500 × 38,500 matrix to a 227 × 227 matrix, an even greater compression. We additionally provide rules of connectivity between intrinsic types and 500 types of boundary neurons (defined below), which have also been annotated²⁵.

In our connectomic approach, a cell type is defined as a set of cells with similar patterns of connectivity⁹, and such cells are expected to

¹Princeton Neuroscience Institute, Princeton University, Princeton, NJ, USA. ²Independent researcher, Kielce, Poland. ³Eyewire, Boston, MA, USA. ⁴Institut für Biologie—Neurobiologie, Freie Universität Berlin, Berlin, Germany. ⁵Molecular, Cellular and Developmental Biology, University of California, Santa Barbara, Santa Barbara, CA, USA. ⁶Department of Neuroscience, Yale University, New Haven, CT, USA. ⁷Computer Science Department, Princeton University, Princeton, NJ, USA. ¹⁶These authors contributed equally: Arie Matsliah, Szi-chieh Yu. *A list of authors and their affiliations appears at the end of the paper. [✉]e-mail: mmurthy@princeton.edu; sseung@princeton.edu

share the same function². By the same logic, cell types with similar patterns of connectivity should have similar functions. This logic will be used to generate hypotheses about the functions of newly discovered cell types, as well as the previously known cell types for which functional information has been lacking.

Class, family and type

Neurons intrinsic to the optic lobe are those with almost all of their synapses inside the optic lobe (Methods), and are the main topic of this study (Extended Data Fig. 1a). Moreover, there are boundary neurons that straddle the optic lobe and the rest of the brain (Extended Data Fig. 1b). Boundary neurons fall into several classes: visual projection neurons (VPNs) project from the optic lobe to the central brain, visual centrifugal neurons (VCNs) do the opposite and heterolateral neurons extend from one optic lobe to the other while making few or no synapses in the central brain. Targets of boundary neurons in the central brain are generally multimodal and/or sensorimotor²⁴, mixing information coming from the eyes and other sense organs, so we regard the optic lobe proper as the fly's visual system.

The brain of a single *Drosophila* adult female was reconstructed by the FlyWire Consortium^{24,31}. We proofread around 38,500 intrinsic neurons in the right optic lobe (counts by type are shown in Extended Data Table 1), as well as 3,900 VPNs, 250 VCNs, 150 heterolateral neurons and 4,700 photoreceptor cells (left optic lobe numbers are shown in the Methods). In total, 77% of the synapses of intrinsic neurons are with other intrinsic neurons, and 23% are with boundary neurons.

We divide optic lobe intrinsic neurons into four broad classes: columnar, local interneuron, cross-neuropil tangential and cross-neuropil amacrine (Fig. 1a–c). Cells of the columnar class (Fig. 1a) have axons oriented parallel to the main axis of the visual columns ('axon' is defined in the Methods). Following a previous study⁶, the arbour of a columnar neuron is allowed to be wider than a single column; what matters is the orientation of the axon, not the aspect ratio of the arbour. Photoreceptor cells are columnar but are not intrinsic to the optic lobe, strictly speaking, because they enter from the retina. Nevertheless, they will sometimes be included with intrinsic types in the following analyses.

The optic lobe (Extended Data Fig. 1a,b) contains four main neuropils (lamina, medulla, lobula and lobula plate) and a smaller fifth neuropil—the accessory medulla (synapse counts by type family in each neuropil are shown in Extended Data Table 2 and the number of cells in each optic lobe is shown in Extended Data Table 3). We further distinguish between distal and proximal medulla, regarding them as two separate neuropils⁶ (Extended Data Fig. 1c). The border between them is layer 7 of the medulla (M7), which is also known as the serpentine layer^{6,32}.

A columnar cell spans multiple neuropils (Fig. 1a). Cells of the local interneuron class (Fig. 1b) are defined as being confined to a single neuropil. We also define two classes that cross multiple neuropils but are not columnar. A cross-neuropil tangential cell (Fig. 1c) has an axon that is oriented perpendicular to the main axis of the visual columns as it runs inside a neuropil. A cross-neuropil amacrine cell (Fig. 1c) lacks an axon. Interneurons are typically amacrine, but sometimes have an axon in the tangential orientation.

Each class is divided into families. A family is defined as a set of cells that share the same neuropils (Fig. 1a–c and Methods). For example, the Tm family projects from the distal medulla to the lobula, while the TmY family projects from the distal medulla to both the lobula and lobula plate (Fig. 1a; Tm and TmY pass through the proximal medulla, and also typically receive inputs there).

Each family is divided into cell types. All 227 intrinsic types as well as photoreceptor types are available for 3D interactive viewing at the FlyWire Codex (<https://codex.flywire.ai>). Supplementary Data 1 includes a list of all intrinsic types and their properties. Supplementary Data 2 contains one 'card' for each type, which includes its discriminative

logical predicate (see below), basic statistics, diagram showing stratification and other single-cell anatomy, and 3D renderings of all the cells in the type.

Most neurons in the optic lobe are columnar (Fig. 1e (right)), and half of the families are columnar (Fig. 1e (left)). Interneurons constitute just 17% of optic lobe intrinsic neurons, but the majority of cell types (Fig. 1e (middle)). A columnar family (Tm) contains more cells than any other family (Fig. 1f (right)). An interneuron family (Sm) contains more types than any other family (Fig. 1f (left)).

The columnar families (Fig. 1a) are well known⁶. The Sm interneuron family is new (Fig. 1b), and its name is inspired by its stratification in the serpentine medulla (M7). Some of the cross-neuropil families are wholly or almost wholly new (Fig. 1c). Over half of the cell types are new, and many of these are interneuron types.

Connectomic approach to cell types

For each cell, we define an output feature vector by the number of output synapses onto neurons of cell type t , which runs from 1 to T . The output feature vector is a row of the cell-to-type connectivity matrix (Methods). For each cell, we similarly define an input feature vector by the number of input synapses received from neurons of cell type t . This is a column of the type-to-cell connectivity matrix (Methods). The input and output feature vectors are concatenated to form a $2T$ -dimensional feature vector (Fig. 2a). The feature dimensions include only intrinsic types, so T is 227.

A cell type is defined as a set of cells with similar feature vectors⁹. Cells of the same type are near each other in feature space, while cells of different types are far away (Fig. 2b). This was quantified using the weighted Jaccard distance (hereafter, Jaccard distance; Methods).

Our definition of feature vectors requires that some cell types should already exist. An initial set of cell types was defined by human analysts using traditional morphological criteria (Methods). These traditional cell types were used to compute feature vectors, and hierarchical clustering was applied. In many cases, this led to further division into cell types that could not be distinguished by traditional criteria. In other cases, it led to grouping of morphological variants into a single type. After splitting or merging types, the feature vectors were recomputed and the process was continued iteratively.

The final cell types were validated in several ways (Methods). We show that our clustering is self-consistent, in the sense that almost all cells end up in the original cluster if we attempt to reassign each cell's feature vector to the nearest cluster. For more interpretable evaluations, we construct compact connectivity-based discriminators that can predict cell type membership (Extended Data Fig. 2 and Supplementary Data 3). We show that membership can be accurately predicted by a logical conjunction of on average five synaptic partner types. For each interneuron type, we also provide selected pairs of features that can be used to discriminate that type from others in the same neuropil (Extended Data Fig. 3 and Supplementary Data 4).

Hierarchical clustering of cell types

We defined a connectomic cell type as a set of cells with similar feature vectors based on connectivity. It follows that cells of the same type should share the same function, according to the maxim "Nothing defines the function of a neuron better than its connections"³³. The same maxim also implies that cell types with similar feature vectors should have similar visual functions. A cell type feature vector can be obtained by summing the feature vectors over all cells in that type, followed by normalization (Methods). Computing the Jaccard distance between all pairs of cell type feature vectors and applying average linkage hierarchical clustering yields a dendrogram of cell types (Methods and Fig. 2c). Thresholding the dendrogram yields a flat clustering (Fig. 2c), which will be interpreted later on.

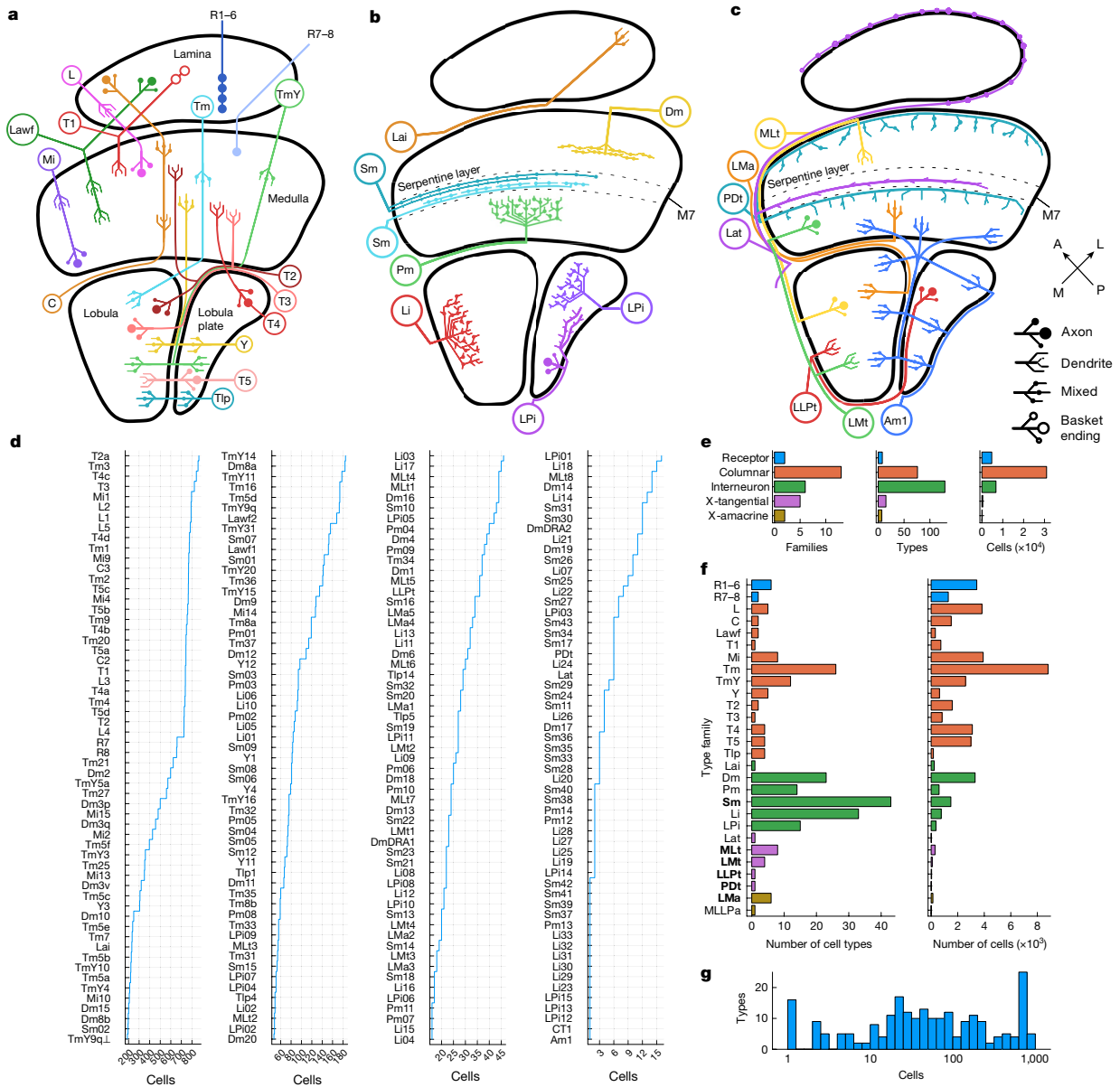


Fig. 1 | Class, family, type and cell. **a**, Families in the columnar class. C, centrifugal; L, lamina monopolar; Lawf, lamina wide-field; Mi, medulla intrinsic; R, receptor; T1–T5, T neuron; Tm, transmedullary; TmY, transmedullary Y; Tlp, translobula plate; Y, Y neuron. **b**, Families in the interneuron class. Serpentine medulla (Sm) is new. Dm, distal medulla; Lai, lamina intrinsic; Li, lobula intrinsic; LPi, lobula plate intrinsic; Pm, proximal medulla. **c**, Families in the cross-neuropil tangential and amacrine classes. For tangential families, axon and dendrite are distinguished graphically. All are new except for Lat and Am1. LLPt, lobula–lobula plate tangential; LMT, lobula–medulla tangential; LMa, lobula medulla amacrine; Lat, lamina tangential; MLt, medulla–lobula tangential; PDt, proximal to distal medulla tangential.

Type-to-type connectivity

We define a type-to-type connection matrix in which the *st* element is the number of synapses from cell type *s* to cell type *t* (Methods). The matrix is visualized in Extended Data Fig. 4, and its numerical values

can be downloaded (see the ‘Data availability’ and ‘Code availability’ sections). The type-to-type connection matrix can also be visualized as a directed graph. As showing all connections is visually overwhelming, it is important to find ways of displaying meaningful subsets of

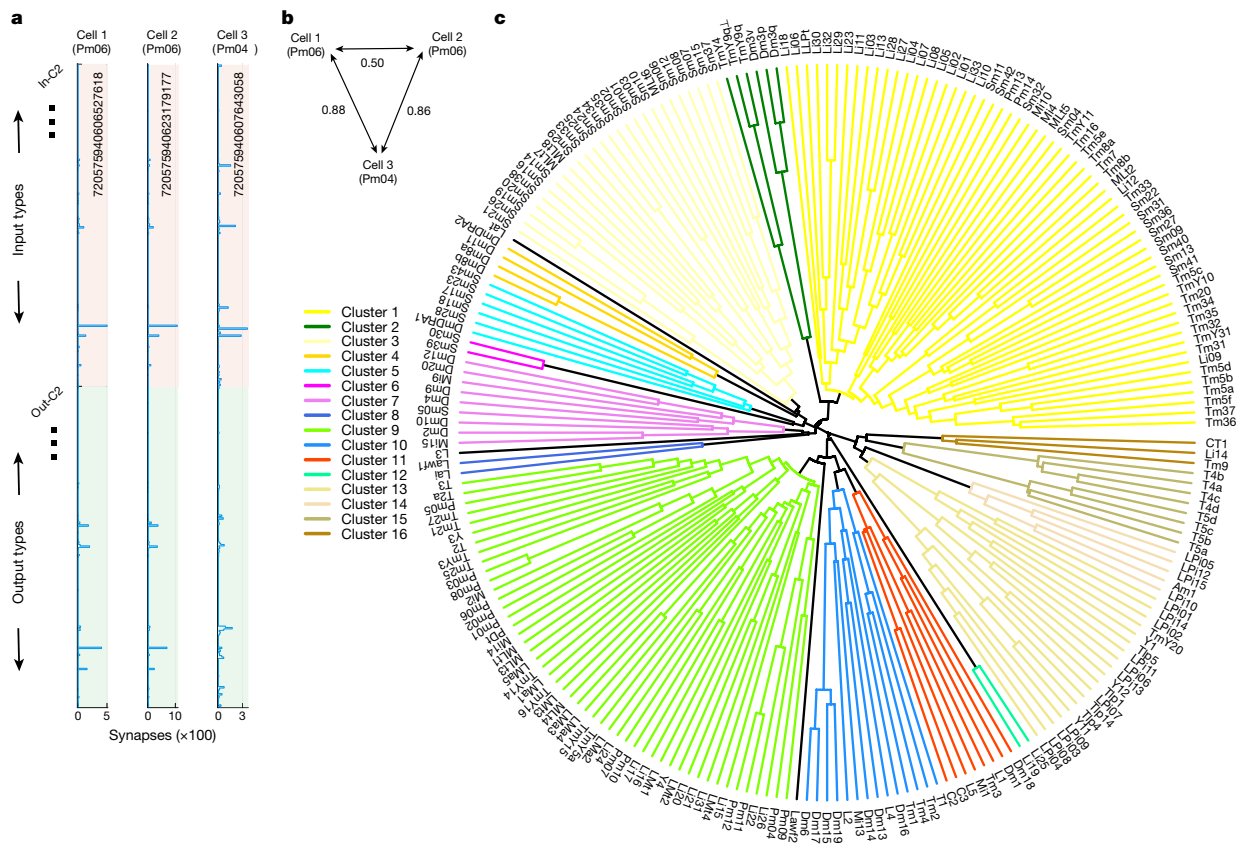


Fig. 2 | Clustering of cells and cell types based on connectivity. **a**, Feature vectors for three example cells. The horizontal axis indicates the synapse numbers that the cell receives from presynaptic types (red region of vertical axis) and sends to postsynaptic types (green region of vertical axis). Cells 1 and 2 (same type) have more similar feature vectors to each other than to cell 3 (different type). The long numbers are the cell IDs in version 783 of the FlyWire connectome. **b**, Cells 1 and 2 (same type) are closer to each other than to cell 3 (a different type), according to the weighted Jaccard distances between the cell feature vectors. Such distances are the main basis for dividing cells into cell types (Methods). **c**, Dendrogram of cell types. Cell types that merge closer

to the circumference are more similar to each other. Flat clustering (16 colours) is created by thresholding at 0.9. A few clusters containing single types (Lat, L3 and Lawf2) are uncoloured. To obtain the dendrogram, feature vectors of cells in each type were summed or averaged to yield a feature vector for that cell type, and then cell type feature vectors were hierarchically clustered using average linkage. Jaccard distances run from 0.4 (circumference) to 1 (centre). Clusters containing more than one cell type (legend with coloured lines) are numbered starting at '3 o'clock' on the dendrogram and proceeding counterclockwise.

connections. One that we have found to be helpful is to display the top input and output connections of each type (Figs. 3–7 and Extended Data Figs. 5 and 6). In such a graph, some nodes can have more than one outgoing and/or more than one incoming connection. A few of these nodes show up as 'hubs' with many visible connections. For example, Mi1 is the top input to a large number of postsynaptic types (Fig. 3 and Extended Data Fig. 5).

The nodes of the graph were positioned in 2D space by a graph layout algorithm that tends to place strongly connected types close together (Methods). It turns out that nearby nodes in the 2D graph layout space tend to belong to the clusters that were extracted from the high-dimensional connectivity-based feature vectors (compare the node colourings of Fig. 3 with clusters of Fig. 2c).

We can also normalize the type-to-type connection matrix to be the fraction of synapses from cell type s to cell type t . Depending on the normalization, this could be the fraction of input to type t or fraction of output from type s (Methods). Input and output fractions are shown in Supplementary Data 5, and are equivalent to the cell type feature vectors defined earlier. The heat maps of Supplementary Data 5 are important because they show a much more complete set of connections than the wiring diagrams, which are highly selective visualizations.

Perplexity as a measure of degree of connectivity

The degree of a cell type can be defined as the number of cell types to which it is connected. Weak connections can be excluded from this definition by thresholding the type-to-type connection matrix before computing degree. For a threshold-independent measure, we instead calculate a 'perplexity'³⁴ for each cell type. The outgoing connection strengths (synapse counts) are normalized as if they were a probability distribution, and out-perplexity is defined as the exponential of the entropy of this distribution. Out-perplexity reduces to out-degree in the special case that the distribution is uniform over the connected partners. In-perplexity is defined analogously.

If intrinsic cell types are ranked by the product of out- and in-perplexity (Extended Data Fig. 7a), then TmY5a is the most connected hub, and various types in the lamina and distal medulla are the least hub-like. Motion-related cell types generally do not have high perplexity. Out-perplexity tends to be greater than in-perplexity (Extended Data Fig. 7a), although they are positively correlated (Extended Data Fig. 7b).

One might expect that 'early' types in visual processing would have divergent connectivity, to distribute photoreceptor signals to many

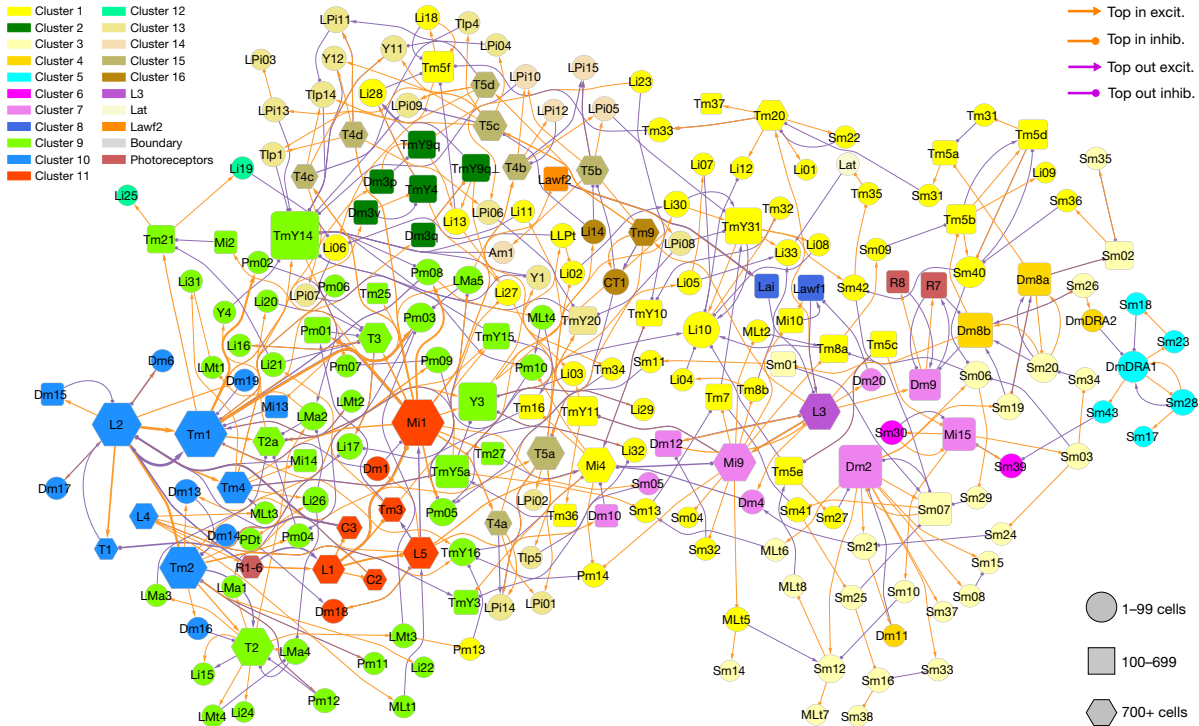


Fig. 3 | Wiring diagram of cell types—top input and output connections. Simplified wiring diagram of all cell types intrinsic to the optic lobe and photoreceptors, showing only the top input and output connections of each type. Colours of types (nodes) indicate membership in flat clusters of Fig. 2c. The node size encodes the number of drawn connections, so that hub types

look larger. The node shape encodes type numerosity (number of cells). The line colour encodes the relationship (top input versus top output) and the line width is proportional to the number of synapses. The line arrowhead shapes encode excitation (excit.) versus inhibition (inhib.). Further explanation is provided in the Methods.

targets, while ‘late’ types would have convergent connectivity, summarizing the final results of optic lobe computations for use by the central brain. This idea can be tested by ranking types according to the ratio of out-perplexity to in-perplexity (Extended Data Fig. 8). Indeed, the top of the list includes early types like the inner photoreceptors R7 and R8, L3 and L5, and many Dm and Pm interneuron types, and many Sm types are near the bottom of the list; they can be interpreted as ‘late’ types given their extensive connectivity with VPNS.

The ‘numerous’ cell types

Photoreceptor axons project retinotopically from the eye to the lamina (R1–6) and distal medulla (R7–8). The medulla is divided into columns, which are presumed to be in one-to-one correspondence with ommatidia of the compound eye. Cell types containing >720 cells in our reconstruction (Fig. 1d), as well as photoreceptor types, will be called ‘numerous’. The top end (800) of this range is probably the true number of columns in this optic lobe. For each numerous type, the cells appear to be distributed one per column (Supplementary Data 2), and the true number of cells is expected to approximate 800. The observed cell numbers are mostly smaller than 800; some cells are missing from columns, presumably due to under-recovery of cells by proofreading (Methods). The connections between numerous types agree well with a previous reconstruction of seven medulla columns²⁷ (Methods and Extended Data Fig. 9).

The 28 numerous types have long been known⁶. At the other extreme, 16 types contain only a single cell. Most types (183) lie between the extremes (Fig. 1g and Extended Data Fig. 1d). It is the less numerous types of which our knowledge has been incomplete, and arguably they are where much of the magic of vision happens. As with the

photoreceptors, neural activity in the numerous cell types like L1 and Mi1 mostly encodes information about the image at or near single points in visual space. But perception requires the integration of information from points that can be quite distant from each other, and this is done by the larger neurons that belong to the less numerous types.

For most of the numerous types, visual responses have been observed previously⁴, and will be used to interpret the dendrogram of Fig. 2c. We will see that the numerous types that belong to a single cluster have similar functions, which enables us to ascribe a function to each cluster as a whole. In other words, we extrapolate from the functions of the numerous types to yield preliminary clues regarding the functions of the less-numerous types.

These extrapolations are speculative, and are merely starting points for hypothesis generation and experimental research, and the clusters are not set in stone. They were obtained by thresholding a hierarchical clustering (Fig. 2c), and adjusting this threshold will change the number of clusters (Extended Data Fig. 10). Rather than use our clusterings, some readers may prefer to directly consult the weighted Jaccard distances between types (Fig. 2, Source Data), from which the clusterings were derived. Other cautionary notes about the clusters are given in the Methods and Discussion. These caveats notwithstanding, we next proceed to functional interpretation of the clusters in Fig. 2c.

ON, OFF and luminance channels

Cluster 10 and cluster 11 (Fig. 2c) both receive strong input from photoreceptors R1–6 (Extended Data Fig. 11), and we propose that they are regarded as OFF and ON channels, respectively, carrying information about light decrements (OFF stimuli) and light increments (ON stimuli). Our concept is similar to the well-known ON and OFF motion

pathways^{35,36}, but differs because our ON and OFF channels are general purpose, feeding into the object and colour subsystems as well as the motion subsystem.

Cluster 10 contains the OFF cells L2, L4, Tm1, Tm2 and Tm4. Cluster 11 contains the ON cells L5, Mi1 and Tm3, and also the OFF cell L1. It makes sense to assign L1 to the ON channel even though it is an OFF cell, because L1 is inhibitory/glutamatergic, so its effects on downstream partners are similar to those of an ON excitatory cell. Note that information about whether synapses are excitatory or inhibitory was not used by our clustering algorithm. Cluster 11 also contains C2 and C3, which are expected to be ON cells because their top inputs are L1 and L5. A companion paper argues that the various Dm interneuron types in cluster 10 and cluster 11 normalize the activities of numerous types in the OFF and ON channels³⁷.

The ON and OFF motion pathways were traditionally defined by working backwards from the T4 and T5 motion detectors, which respectively compute the directions of moving ON and OFF stimuli^{4,5}. The ON motion pathway is directly upstream from T4 and includes Mi1, Mi4, Mi9 and Tm3. The OFF motion pathway is directly upstream from T5 and includes Tm1, Tm2, Tm4 and Tm9. Figure 4 shows that these cell types have other strong targets besides T4/T5, so they do not seem to be solely or chiefly dedicated to motion (see below concerning the lone exception Tm9).

L3 connectivity is sufficiently unique that it stands apart from all of the other cell types as a cluster containing only the single type L3 (Fig. 2c). This is consistent with current thinking that L3 constitutes a separate luminance channel, distinct from ON and OFF channels³⁸. L3 is the only L type with a sustained rather than transient response³⁹, and it encodes luminance rather than contrast⁴⁰.

Cluster 7 includes Dm4, Dm9, Dm12, Dm20 and Mi9, which all have L3 as their strongest input. Mi9 is also the strongest output of L3 and, like L3, exhibits a sustained response⁴¹. We therefore propose that cluster 7 should be lumped with L3 in a hypothetical luminance channel. Mi9 is traditionally grouped in the ON motion pathway, but Mi9 is an input to the object and colour subsystems, not only the motion subsystem. It is less obvious whether the remaining types in cluster 7 (Mi15, Dm2, Dm10 and Sm05) should be grouped in the luminance channel. Indeed, these types break off into a separate cluster when the threshold is adjusted to refine the flat clustering (Extended Data Fig. 10). These types might alternatively be assigned to the colour subsystem as Mi15 and Dm2 are known to receive direct input from inner photoreceptor R8⁴².

Lawf2 is a cluster of its own. By targeting cell types (L5, C2 and C3 in Supplementary Data 5) in cluster 11, Lawf2 provides centrifugal feedback to the ON channel (Extended Data Fig. 11). However, the strongest output of Lawf2 is Lai (Fig. 4), which is thought to mediate lateral inhibition in the lamina⁴³ through pathways such as R1-6→Lai→R1-6 and R1-6→Lai→L3²⁶. Lawf2 may therefore modulate lateral interactions mediated by Lai. The strongest input to Lawf2 is OA-AL2b2, which could be octopaminergic or cholinergic^{44,45}. If it is octopaminergic, this input could be the source of the previously reported octopaminergic gain modulation of Lawf2 neurons⁴⁶. Lawf2 also receives strong input from cluster 9, which is hypothesized to be an object subsystem later on.

Lai and Lawf1, the two types in cluster 8, have similar targets (L3, T1, R1-6 and L2). Cluster 8 provides centrifugal feedback to the OFF channel (through L2) and to R1-6 (Extended Data Fig. 11). Alternatively, cluster 8 could be interpreted as being part of the luminance channel, as cluster 7 is a strong input and L3 a strong output (Extended Data Fig. 11).

Motion

The motion-detecting T4 and T5 families belong to cluster 15 (Fig. 2c). Cluster 16 contains CT1 and Tm9, which are well known to be important for motion computation^{4,5}. It makes sense to regard Tm9 as dedicated to the motion subsystem rather than part of a general-purpose OFF

channel, as 80% of its output synapses are onto CT1 or T5. Cluster 16 also includes Li14, an interneuron type with T5a as the strongest input, and T5a through T5d as the strongest outputs. T4/T5 neurons synapse onto VPNs that exit the optic lobe and enter the central brain (Fig. 5a and Supplementary Data 5).

Cluster 13 and cluster 14 contain the lobula plate interneuron family, LPi1 through LPi15^{6,8}. Over half of these are new (Methods). Some LPi types consist of one or two cells that cover the entire visual field (Fig. 5b). Two LPi types may stratify in the same lobula plate layers, but consist of cells with different sizes (Fig. 5c). Most LPi types are amacrine, but some exhibit axo-dendritic polarization (Fig. 5d). Some types collectively cover only a portion of the visual field (for example, LPi01 and LPi03 are ventral only; Supplementary Data 2).

All LPi types receive input from T4/T5 types, so it is clear that cluster 13 and cluster 14 are related to motion vision. All LPi types receive input from T4/T5 cells with a single preferred direction (Fig. 5a and Supplementary Data 5). The only exception is LPi07, which receives inputs from T4/T5 cells with preferred directions *c* and *d* (Supplementary Data 5). LPi types synapse onto other LPi types and onto VPNs (Fig. 5a and Supplementary Data 5).

Cluster 13 also contains columnar neurons from three Y types and all Tlp types. All of these are predicted to be glutamatergic, and are reciprocally connected with T4/T5 of particular preferred directions. The only exception is Tlp5, which receives input only from T4a/T5a. The Y and Tlp types also connect with LPi and columnar VPN types¹⁰. TmY20 and Am1 also belong to cluster 13, and were previously identified to be motion related¹⁰.

Objects

Cluster 9 includes the numerous types T2 and T3, which have been implicated in the detection of small objects⁴⁷. Their downstream VPN partners LC11⁴⁷ and LC18⁴⁸ (Fig. 6) are also activated by small objects. On the basis of this information, we propose that cluster 9 is part of a hypothetical object subsystem (Fig. 6). Cluster 9 (Fig. 2c) includes many other types from columnar families (Mi, TmY, Y), interneuron families (Li and Pm) and cross-neuropil tangential and amacrine families (LMa, LMt, MLt, Pdt). Downstream targets include LC, LPLC and LT types (Fig. 6).

Mi1 and Tm1 are the most prominent inputs to the subsystem (Fig. 6), and respectively belong to the ON and OFF channels defined above. They are top inputs to T3, explaining why T3 is ON-OFF⁴⁷. T2 is ON-OFF because its top inputs are L5 and Tm2, which respectively belong to the ON and OFF channels. Note that the Tm1 input to T2 and the L5 input to T2 are second from the top, and therefore do not show up in Fig. 6, which is restricted to the top inputs and outputs.

Several types are nearby T2 and T3 in the cell types dendrogram (Fig. 2c). In particular, T2a, Tm21, Tm25, Tm27, TmY3 and Y3 are fairly numerous and excitatory, so we regard them as candidate object detectors. Despite its name, T2a is more similar to T3 in connectivity than to T2 (Fig. 2c). T2a also receives Mi1 and Tm1 input like T3, and is predicted to be ON-OFF. The top output of T2a is LC17, which is known to be activated by small objects⁴⁹ and also receives input from T3.

Cluster 12 contains Li19 and Li25 (Fig. 2c). Cluster 9 is both a strong input to cluster 12 (Extended Data Fig. 11) and a strong output of cluster 12 (Extended Data Fig. 11), largely due to connections between Tm21 and Cluster 12. We therefore include cluster 12 as well as cluster 9 in the object subsystem.

Colour and polarization

The inner photoreceptors R7 and R8 are important for *Drosophila* colour vision because their responses are more narrowly tuned to the wavelength of light than those of the outer photoreceptors R1-6. R7 prefers ultraviolet light, whereas R8 prefers blue or green light²⁰.

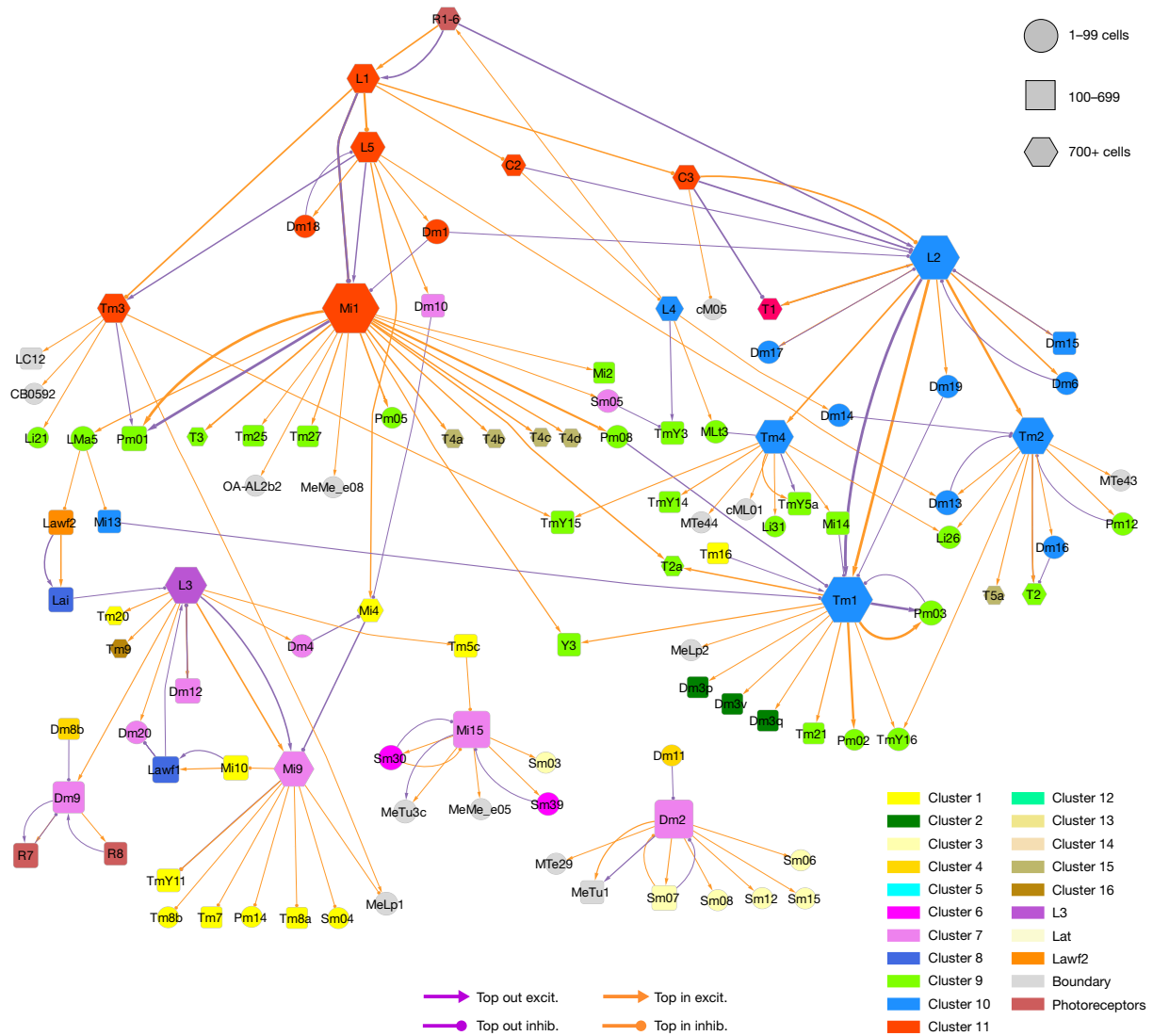


Fig. 4 | ON, OFF and luminance channels—top inputs and outputs only. Simplified wiring diagram of ON (cluster 11, red), OFF (cluster 10, blue) and luminance (cluster 7, violet and L3) channels and their primary connections

with other subsystems and VPNS. For clarity, only the top input and output connections are shown for each type. Further explanation is provided in Fig. 3 and the Methods.

Cluster 4 contains Dm8a, Dm8b, Dm11 and DmDRA2, which are all inner photoreceptor targets⁴². Cluster 1 contains most of the remaining types so far implicated in colour vision. As originally defined by morphology⁶, Tm5 is a potential postsynaptic target of the inner photoreceptors because it stratifies in the distal medulla at the M7 border and also in the M3. These are the medulla layers containing the axon terminals of R7 and R8⁷. We found that Tm5 consists of six cell types (Fig. 7a). Three of our connectomic Tm5 types correspond to canonical Tm5 types that were previously defined by morphology and Ort expression^{7,50}. Tm5a and Tm5b receive R7 input, while Tm5c receives R8 input. Moreover, we found three new types, Tm5d, Tm5e and Tm5f, that receive little or no photoreceptor input, although their stratifications are similar to those of the canonical Tm5 types (Fig. 7a).

The correspondences between connectomic and morphological-molecular Tm5 types were established using morphological criteria (Methods). However, the reader should be cautioned that there is considerable variability within a type, so reliably typing individual cells

based on morphology alone is difficult or impossible. Connectivity is essential for reliable discriminations.

Tm5a and Tm5b receive R7 and Dm8 input, as expected from previous reports^{42,50,51}. Tm5c receives R8 input^{42,50}, and also strong L3 input (Fig. 7c and Supplementary Data 5). While some synapses from Dm8 to Tm5c do exist⁵⁰, this connection seems to be weak.

Tm20 has been implicated in colour vision because it receives R8 input^{27,28,42}. It also receives strong L3 input (Fig. 7c). Thus, Tm20 inputs are similar to Tm5c inputs, consistent with the physiological finding that these two types are more similar to each other in their chromatic responses than they are to Tm5a and Tm5b⁵².

As Tm5a, Tm5b, Tm5c and Tm20 are known to be related to colour vision, we propose that the rest of cluster 1 is also part of a hypothetical colour subsystem (Fig. 7c). The new Tm5 types (Tm5d, Tm5e and Tm5f) receive few or no synapses directly from photoreceptors, but Tm5d receives indirect R7 input from Tm5b and Dm8a, Tm5e receives indirect R8 input from Tm5c (Fig. 7c), and Tm5f receives indirect R8 input from

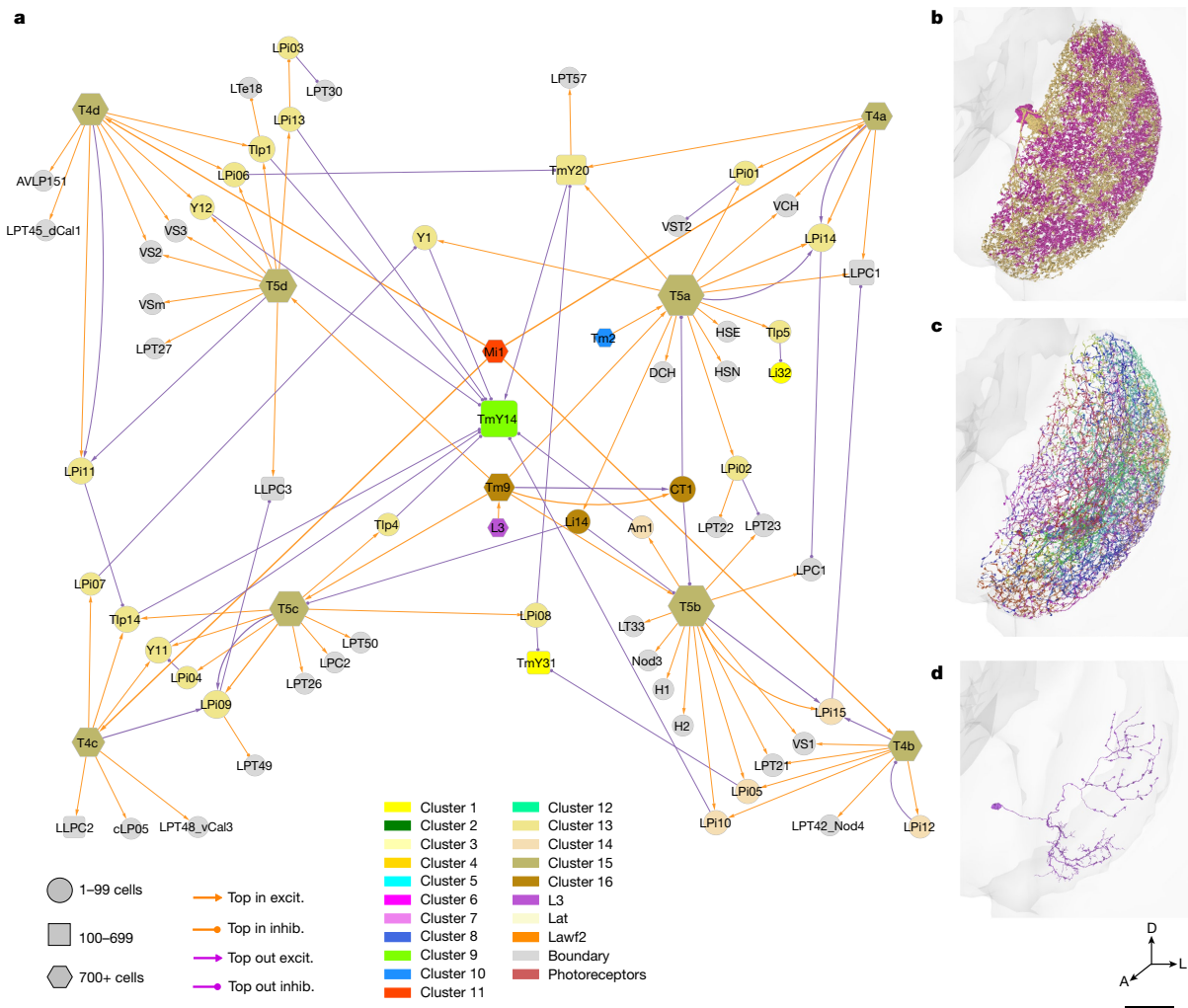


Fig. 5 | Motion subsystem—top inputs and outputs only. **a**, Cell types of the motion subsystem (clusters 13 to 16) and their primary connections with other subsystems and VPNS. The motion-detecting T4 types are located at the corners of the square layout, and often share postsynaptic targets with the corresponding T5 types. TmY14 is the top output of many types. For clarity, only the top input and output connections are shown for each type. Further

explanation is provided in Fig. 3 and the Methods. **b**, LPI14, also called LPI1-2¹⁰, is a jigsaw pair of full-field cells. **c**, LPI02 stratifies in the same lobula plate layers as LPI14, but the cells are smaller. **d**, LPI08 is an example of an interneuron that is not amacrine. It is polarized, with a bouton-bearing axon that is dorsally located relative to the dendrite. D, Dorsal. Scale bar, 30 μ m.

Tm20 (Supplementary Data 5). Tm5d and Tm5e are predicted to be glutamatergic and Tm5f is predicted to be cholinergic.

We have defined Dm8a and Dm8b, which synapse onto Tm5a and Tm5b, respectively (Fig. 7c), and this preference is highly selective (Supplementary Data 5). As with Tm5, splitting Dm8 is straightforward with connectivity but difficult or impossible with morphology. How our two Dm8 types correspond with the two types previously defined by molecular studies (yDm8 and pDm8)^{51,53} remains speculative (Methods).

Cluster 1 also includes Tm7, Tm8a and Tm8b (another novel split), Tm16 and wholly new types Tm31 to Tm37. The latter deviate from the classical definition of the Tm family, which is supposed to project from the distal medulla to the lobula⁶. These types mainly stratify in serpentine medulla and lobula, with little or no presence in distal medulla (Fig. 7b). Nevertheless, we decided to lump them into the Tm family. Tm31 to Tm35 each contain relatively few (<100) cells, and are predicted to not be cholinergic. This departs from the norm for existing Tm types,

which are generally more numerous (>100 cells) and predicted to be cholinergic (exceptions are the three glutamatergic Tm5 types). Tm36 and Tm37 contain more than 100 cells each, and are predicted to be cholinergic.

Cluster 1 includes TmY types, Li, Sm and Pm interneuron types, MLT types and LLPt. Cluster 1 also includes Mi4 and Mi10. Mi4 was traditionally regarded as part of the ON motion pathway, but T4 cells are relatively weak outputs. Mi4 has strong partners in the colour and object subsystems (Fig. 7c (yellow and green)). Its strongest output is Mi9, which we have assigned to the luminance channel and is one of the major inputs to the colour subsystem. This diversity of targets shows that Mi4 is a major hub between multiple subsystems, although it has been assigned by the clustering to a single subsystem. Mi10 mediates a feedback loop L3→Mi9→Mi10→Lawf1→L3, so it might seem to belong to the luminance channel, but the clustering has placed it in cluster 1 because it is similar in connectivity to Mi4.

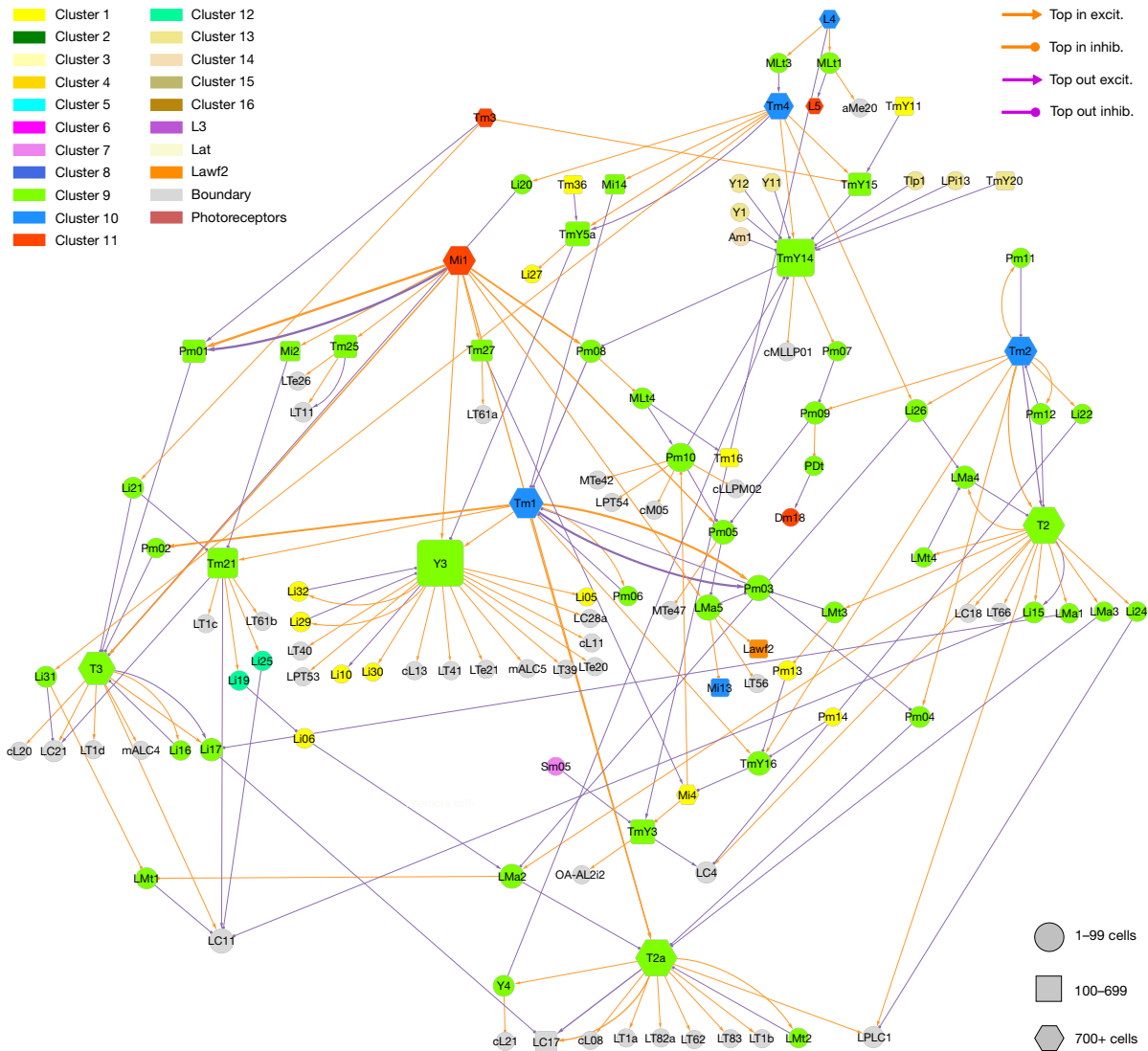


Fig. 6 | Hypothetical object subsystem. Cell types of the object subsystem (clusters 9 and 12) and their primary connections with other subsystems and VPNs. T2 and T3 are known to be activated by small objects⁴⁷. For clarity, only

the top input and output connections are shown for each type. Further explanation is provided in Fig. 3 and the Methods.

Besides L3, Mi9 is another prominent input to the colour subsystem (Fig. 7c). Both L3 and Mi9 belong to the luminance channel defined above. It makes sense that luminance information should be necessary for colour computations³⁸.

Cluster 3 consists mainly of a large number of Sm interneuron types (Fig. 2c). It is well-connected with cluster 1 (Extended Data Fig. 11), so we also include it in the hypothetical colour subsystem (Fig. 7c).

Cluster 5 contains DmDRA1, a cell type at the dorsal rim of the medulla that is known to be important for behaviours that depend on skylight polarization⁵⁴. Cluster 4 is therefore regarded as part of the polarization subsystem. It contains several Sm types, most of which are either situated at the dorsal rim or have some specialization there.

Morphological variation

As mentioned above, connectivity can be essential for distinguishing between types with similar morphologies. Connectivity can also enable

one to ignore morphological variations between cells of the same type. For example, TmY14 was originally identified as a cell type intrinsic to the optic lobe²⁷, but later reclassified as a VPN, because it typically projects to the central brain⁵⁵. In another twist, our optic lobe turns out to contain atypical TmY14 cells that lack the central brain projection (Fig. 8a,b). In cases like this, we double check the proofreading before concluding that this is true biological variation. Even in typical TmY14 cells, the axon has few synapses and minimal impact on connectivity, so TmY14 has reverted to its original status of being intrinsic to the optic lobe (an explanation of the threshold is provided in the Methods). TmY14 ends up as a single type in our connectivity-based clustering, because typical and atypical TmY14 cells have similar connectivity within the optic lobe.

Another interesting example is Tlp4 versus Y11, which have similar connectivity patterns (Fig. 2c and Supplementary Data 5). A major difference is that Tlp4 cells, by definition, have no connectivity in the medulla. However, a few of them do, and look like they do not belong

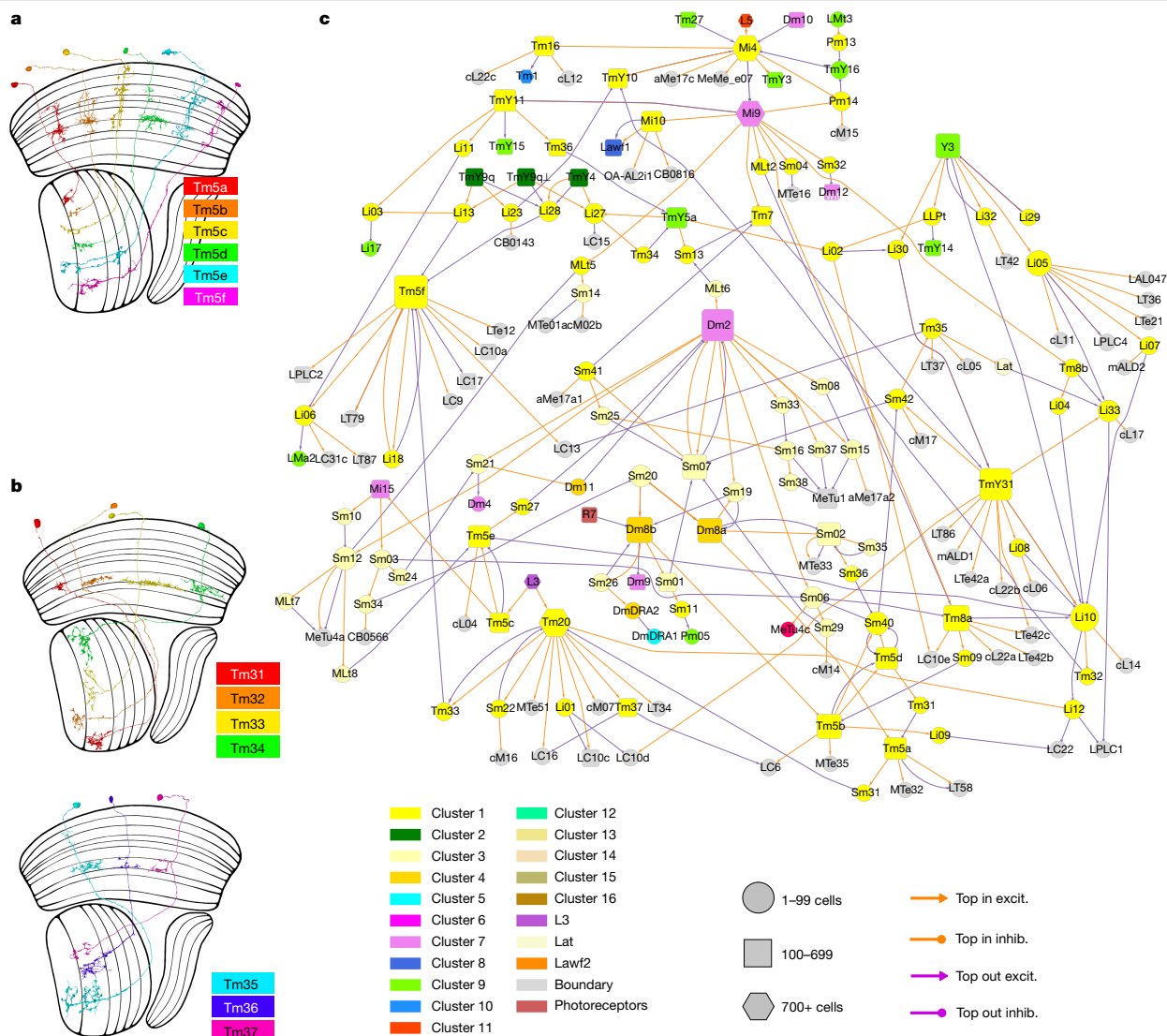


Fig. 7 | Hypothetical colour subsystem. a, Tm5a to Tm5c correspond with types that were previously defined by molecular means. Tm5d to Tm5f have similar morphologies, but different connectivity patterns (Supplementary Data 5). **b**, Tm31 to Tm37 are new members of the Tm family that project from

the serpentine layer (M7) to the lobula. **c**, Cell types in the colour subsystem (clusters 1, 3 and 4) and their top connections with other subsystems and VPNS. For clarity, only the top input and output connections are shown for each type. Further explanation is provided in Fig. 3 and the Methods.

in Tlp4 (Fig. 8c,d). In the first stage of morphology-based classification, these errant cells were assigned to Y11. But such pseudo-Y11 cells were later reassigned to Tlp4 on the basis of connectivity. Their feature vectors match Tlp4 because their medullary projections make few synapses, and their connectivity in the lobula and lobula plate matches Tlp4.

It is worth mentioning an unusual example in which ignoring morphological variation is correct in one sense, but ultimately turns out to be misleading. Three Li11 cells are annotated in the hemibrain reconstruction⁹, and three corresponding cells can be identified in our optic lobe²⁵. We group two of these cells in one type (Fig. 8e). The third cell can be paired with a fourth to form a pseudo-Li11 type with a small axonal projection into the central brain (Fig. 8f). Although the axon is visually striking, it has few synapses and therefore little impact on connectivity. Thus, it might be tempting to ignore the axon as a developmental

‘accident’ and merge Li11 and pseudo-Li11 into a single type. But it turns out that Li11 and pseudo-Li11 are distinct types, owing to their different connectivity in the lobula. For example, Li25 has strong LT61 output, while pseudo-Li11 has strong LT11 input. Pseudo-Li11 also exists in the hemibrain (data not shown), although there it lacks the small projection. So the central brain projection of pseudo-Li11 exhibits variability across individuals, further evidence that it is a developmental accident. We introduce the new names Li25 and Li19 to replace Li11 and pseudo-Li11.

A few cells were dismissed as developmental accidents. This could be done with high confidence when the cells were small and few in number. However, we had difficulty deciding about Li29 because it was a full-field cell in the lobula but it also extended a smaller secondary arbour into the lobula plate (Supplementary Data 2). Originally, we decided that this cell was a developmental accident, and did not include it in our

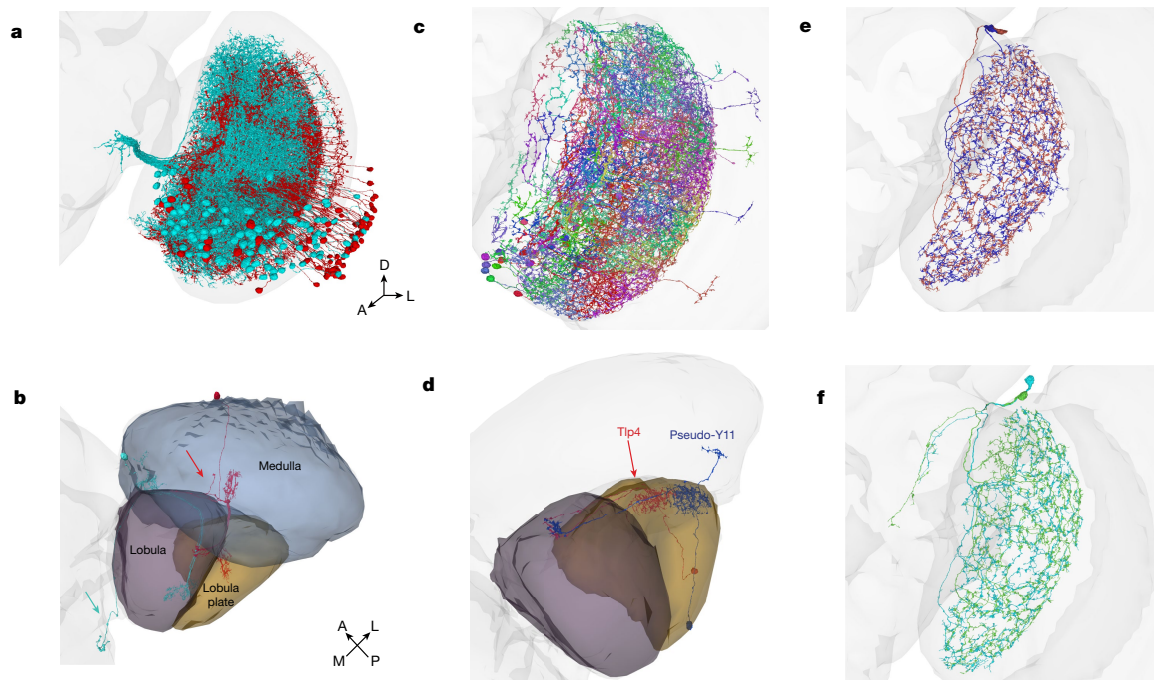


Fig. 8 | Morphological variation. **a**, Typical TmY14 cells (cyan) have axonal projections to the central brain (left). Atypical cells (red) initially project toward the central brain, but their axons turn around and terminate in the medulla. As the axons bear few synapses, typical and atypical cells are approximately the same in connectivity. **b**, Representative typical (cyan) and atypical (red) TmY14 with an axon projecting into the central brain (cyan arrow) and medulla (red arrow), respectively. **c**, Typical Tlp4 cells arborize in the lobula plate and lobula. A few cells (pseudo-Y11) have an additional branch in

the medulla (right), and resemble Y11 cells in morphology but have the same connectivity as Tlp4. **d**, Relative to a typical Tlp4 cell (red), a pseudo-Y11 cell (blue) has an additional branch in the medulla. **e**, LiI1 does not project into the central brain. **f**, Pseudo-LiI1 has an additional arbour projection into the central brain. This arbour makes a few synapses, and might lead to the conclusion that pseudo-LiI1 should be categorized as LiI1. However, the connectivity between LiI1 and pseudo-LiI1 is fundamentally different, making them distinct types. Scale bar, 30 μ m.

list of types. Later on, we found that this odd-looking cell is repeated in the left optic lobe, and promoted it to a type.

Spatial coverage

All cell typing efforts must decide whether to split types more finely or merge types more coarsely. We resolved this lumpers–splitters dilemma by using spatial coverage as a criterion². As a general rule, the cells of a cell type collectively cover all columns of the optic lobe with a density that is fairly uniform across the visual field. This makes sense for implementing translation-invariant computations, a strategy that is commonly used in convolutional networks and other computer vision algorithms. Uniform spatial coverage is sometimes called ‘tiling’, although cell type arbours often overlap so much that the analogy to floor tiles is misleading. Spatial coverage is also a property of many cell types in mammalian retina^{2,56}.

In some types consisting of just one or a few cells, we identified an unconventional jigsaw-style spatial coverage. For example, LPi14, also known as LPi1-2¹⁰, is a pair of full-field cells (Fig. 5b). We refer to them as a jigsaw pair because they jointly cover the visual field in an irregular manner, as if they were cut by a jigsaw. Jigsaw types can also be found in other interneuron families and include Pm14, Li27 and Li28.

Our feature vector (Fig. 2a) includes no explicit information about the spatial coordinates of a cell. Thus, if clustering feature vectors results in cell types with good spatial coverage, that is an independent

validation of the clustering. Coverage also solves the lumpers–splitters dilemma. Suppose that we attempt to split one type into two candidate types, based on hierarchical clustering. If both candidate types exhibit good coverage, then we accept them as valid. If the cells of both candidate types seem randomly scattered, that means our split is invalid, because it is presumably discriminating between cells based on noise. Chromatic types like Tm5 and Dm8 might seem to be an exception to this rule, but their apparently random locations may turn out to depend systematically on pale and yellow columns (Methods).

The above are easy cases, but there are also edge cases. Suppose that splitting results in two candidate types that neatly cover the dorsal field and the ventral field, respectively, without overlap. We then reject the split, preferring to lump the two candidate types in a single type that exhibits dorsoventral spatial variation in connectivity. On the other hand, if one candidate type covers the dorsal field and the other covers the full field, this is an acceptable split.

With these heuristics, some of our cell types end up with only partial coverage of the visual field (Fig. 9). This is especially common for boundary types. Sm is the intrinsic type family containing the most types with partial coverage. This makes sense, given that Sm cells interact closely with many boundary types arborizing in the serpentine layer. Cell types with partial coverage make sense in the later stages of vision. After the early stages of vision, computer vision also often discards translation invariance and may perform different visual computations in different regions of the visual field.

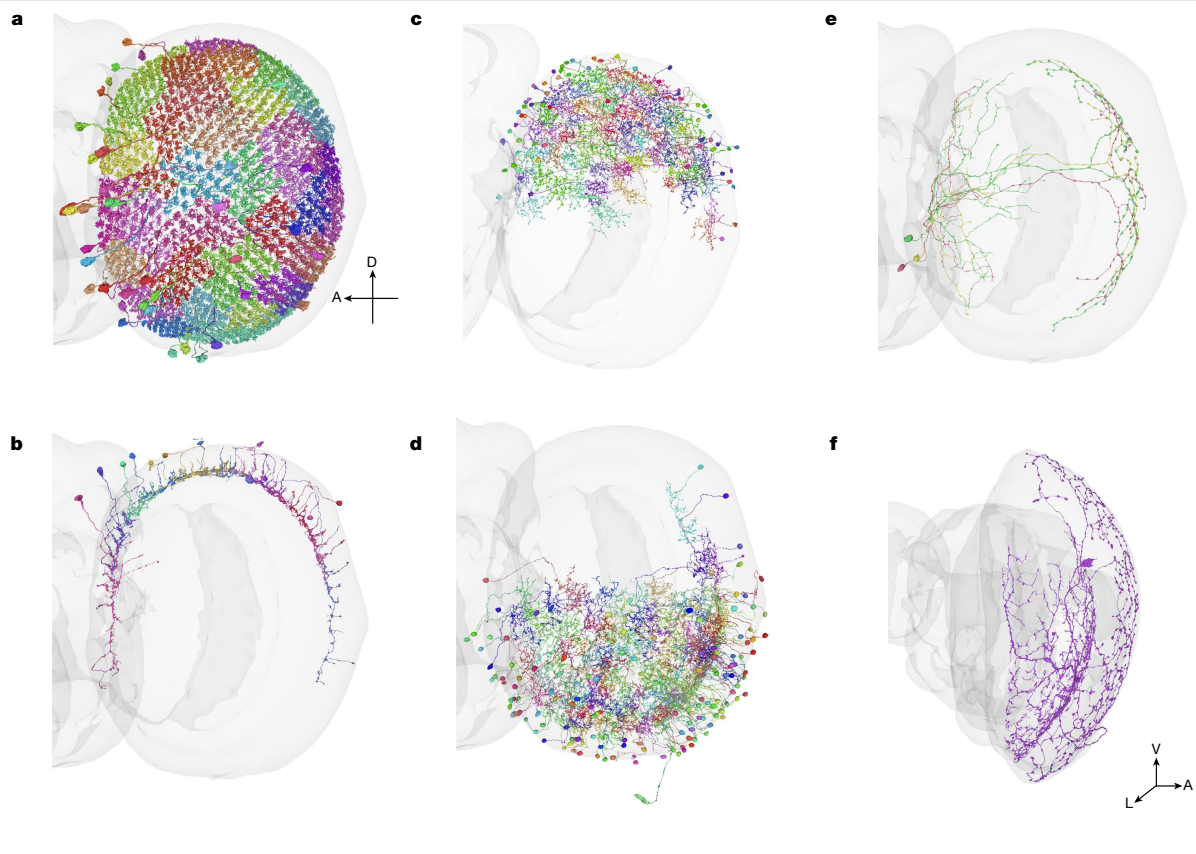


Fig. 9 | Different kinds of spatial coverage. **a**, Dm4 has full spatial coverage, and tiles perfectly with no overlap. **b**, Dm dorsal rim area 2 (DmDRA2) covers the dorsal rim. **c**, Sm05 covers the dorsal hemifield. **d**, Sm01 covers the ventral

hemifield. **e**, Sm33 are H-shaped cells that cover the anterior and posterior rim. **f**, Sm39 is a single cell with mixed coverage: dorsal dendritic arbour in M7 and full-field axonal arbour in M1. V, ventral. Scale bar, 50 μ m.

Discussion

The connectomic approach to cell typing has three powers. First, it is not subject to the incomplete and biased sampling that can affect other methods. Second, connectivity turns out to provide a rich set of features for distinguishing between cell types. Third, connectomic cell typing not only yields cell types, but also, importantly, tells us how they are wired to each other.

Implications for visual function

We clustered cell types with similar connectivity patterns (Fig. 2c), and proposed tentative interpretations of the clusters in terms of visual functions. These interpretations are speculations, but should be useful for generating hypotheses that suggest interesting experiments. Our hypothetical subsystems are devoted to motion, object and colour vision (Figs. 5–7), and are fed by ON, OFF and luminance channels (Fig. 4).

The motion subsystem (clusters 13–16) contains not only the T4 and T5 families but also many interneuron types. Most interneuron types belong to the LPi family, which has been proposed to mediate opponent interactions between cells that are activated by different directions of motion⁸. Such opponency was demonstrated between LPi09 and LPi11, also known as LPi3-4 and LPi4-3³⁷. It is likely that LPi types can also mediate spatial normalization, as described in a companion paper³⁷.

Of the 51 types in the hypothetical object subsystem (clusters 9 and 12), T2 and T3 have been characterized by physiologists as object detectors⁴⁷. Above we hypothesized that a number of other types (T2a, Tm21, Tm25, Tm27, TmY3 and Y3) are object detectors, and these candidates can be tested by future experiments.

The hypothetical colour subsystem (clusters 1,3 and 4) contains 91 types. One can only speculate about the reason for this numeric preponderance. Some insects are known to have sophisticated colour vision capabilities such as colour constancy⁵⁸. The computations required for colour constancy are quite complex, requiring the integration of image information over long ranges⁵⁹. This could potentially be implemented by the large number of Sm and Li interneuron types in the hypothetical colour subsystem, assuming that *Drosophila* turns out to exhibit colour constancy. Alternatively, it is possible that cluster 1 and cluster 3 have additional functions other than colour vision, and should be subdivided more finely (Extended Data Fig. 10). Future experiments will be needed to test these hypotheses.

A companion paper predicts that the six types in cluster 2 (Fig. 2c) should exhibit orientation selectivity⁶⁰, and hypothesizes that cluster 2 is a subsystem for form vision. Cluster 2 connects to cluster 1 (Extended Data Fig. 11), suggesting an interaction between form and colour computations.

Although we have carved the optic lobe into distinct subsystems, we are aware that it is simplistic to assign every cell type to just one functional subsystem. This is the result of the ‘hard’ clustering algorithm that we have used, which always assigns a cell type to a single cluster.

Article

In reality, a cell type could have more than one function, or a cell type might mediate interactions between more than one subsystem. The wiring diagrams show many connections between cell types in different subsystems (Figs. 3–7 and Supplementary Data 5). Assigning such a cell type to a single subsystem is inherently ambiguous.

Implications for visual development

The detailed wiring diagram for an adult visual system precisely specifies the end goal of visual system development. Single-cell transcriptomics is providing detailed information about the molecules in fly visual neurons^{61–63}. Comparison of transcriptomic and connectomic information is already uncovering molecules that are important for the development of the fly visual system⁶⁴, and this trend is bound to increase in momentum. Such research could be aided by our low-dimensional discriminators of cell types (Supplementary Data 4 and Extended Data Fig. 3).

Complete and unbiased

Early studies^{6,32} relied on Golgi staining to sample neurons from multiple individuals, a technique that is best suited for identifying the most numerous types. Most of our new types are not as numerous (10 to 100 cells), which may be why they were missed. Furthermore, Golgi studies⁶ may have mistaken morphological variants for types, which could explain why many of their types cannot be identified in our optic lobe.

Contemporary light-microscopy anatomy leverages genetic lines, but still does not evade the limitations of incomplete and biased sampling. The story of Tm5 serves as a case in point. A breakthrough in colour vision started by genetically labelling neurons that express the histamine receptor Ort⁷. Researchers reasoned that Ort would be expressed by cells postsynaptic to the chromatic photoreceptors R7 and R8, which are histaminergic. Then, light-microscopy anatomy was used to make fine distinctions between three Tm5 types labelled in the transgenic line⁷. The present connectomic work has revealed six Tm5 types, a finding that was only foreshadowed by previous work on the same EM dataset⁴². The three new Tm5 types were presumably missed by previous studies because they receive little or no direct photoreceptor input (Fig. 7c), and do not express Ort. Nevertheless, they are similar to the old Tm5 types in morphology (Fig. 7a) and connectivity (Fig. 2c), and have been grouped in the hypothetical colour subsystem (Fig. 7c).

The Tm5 example demonstrates that connectomics can find fresh patches in well-trodden ground. More telling is that connectomics can guide us to entirely new landscapes, such as the 43 Sm types in an entirely new type family.

Distinguishing cell types using connectivity

Features based on connectivity (Fig. 2a) enabled us to discriminate between cell types that stratify in very similar neuropil layers. Stratification constrains connectivity, because neurons cannot connect with each other unless they overlap in the same layers¹. However, stratification does not completely determine connectivity, because neurons in the same layer may or may not connect with each other. Classical neuroanatomy, whether based on Golgi or genetic staining, relied on stratification because it could be seen with a light microscope. Now that we have electron microscopy data, we can rely on connectivity for cell typing, rather than settle for stratification as a proxy².

That being said, the present study used only connectivity at the final stage of cell typing, which was seeded by the morphological types identified during the first and second stages (Methods). It was possible to demonstrate self consistency of the final cell types using connectivity-based features only. We expect that it should be possible to eliminate all dependence on morphological typing, and base the approach on connectivity from start to finish. This challenge is left for future work.

Spatial organization of connectivity

According to our wiring diagrams (Figs. 3–7 and Extended Data Figs. 4–6), whether two neurons are connected depends on their cell types. Connectivity also depends on the locations of the neurons in the retinotopic maps of the optic lobe. As a trivial example, it is impossible for cells with small arbours to be connected if they are at distant locations. Less trivial dependences of connectivity on location also exist. We expect them to be important for understanding vision, although they turned out to be unnecessary for classifying cell types. To facilitate spatial analyses of connectivity, the FlyWire Codex maps a number of cell types to locations in the hexagonal lattice of columns and ommatidia. In such analyses, it may be helpful to regard cell types and spatial locations as discrete and continuous latent variables⁶⁵. A companion paper demonstrates how to predict visual function by characterizing how connectivity depends on both cell type and spatial location. The cell types of cluster 2 are predicted to exhibit orientation selectivity and related phenomena reminiscent of the primary visual cortex⁶⁰.

Artificial intelligence

This paper began by recounting the story⁶⁶ of how wiring diagrams for visual cortex drawn in the 1960s inspired convolutional nets, which eventually sparked the deep learning revolution in artificial intelligence. Convolutional nets have now been applied to reconstruct the fly brain from electron microscopy images²⁴, making the current study possible. Coming full circle, the fly optic lobe turns out to be as literal an implementation of a convolutional net as one could ever expect from a biological system. The columns of the optic lobe form a hexagonal lattice, rather than the square lattice used in computer vision, but it is a highly regular lattice nonetheless, and the activities of the neurons in each cell type are analogous to a feature map in a convolutional net⁶⁷. Although the connective architecture of the optic lobe conforms closely to the definition of a convolutional net, the connections do not appear to be learned in the sense of artificial intelligence. No changes in VPN structure⁶⁸ and function⁶⁹, and only subtle changes in visual behaviour⁷⁰ have been detected after rearing flies in darkness, suggesting that visual experience may have little role in *Drosophila* visual development. However, mechanisms based on spontaneous activity in the pupal brain (before visual experience) might have a role⁷¹.

Implications for mammalian cell types

In the central brain of *Drosophila*, cell types usually consist of just a pair of mirror symmetric neurons^{9,25} (Extended Data Fig. 1e), as is also the case for *C. elegans*⁷². By contrast, most optic lobe cell types are represented by many neurons (Fig. 1d and Extended Data Fig. 1d), a situation that is more reminiscent of mammalian brains^{3,73}. Could our connectomic approach generalize to mammalian brain structures such as retina and cortex, which are laminated like the optic lobe?

Single-cell transcriptomics, often hailed as the solution to classifying cortical cell types⁷⁴, has also been applied to the *Drosophila* optic lobe. One study reported 172 transcriptomic cell types, a figure that includes VPNs as well as intrinsic neurons⁶². Our connectomic study has revealed the existence of a much larger set of types (700+ including boundary types). Encouragingly, many connectomic types can be conclusively matched with transcriptomic types⁶². Failures to match are interesting because they illustrate potential pitfalls of the transcriptomic approach. For example, all eight T4/T5 types look like a single transcriptomic type in adult flies⁶², and are only transcriptionally distinct at earlier stages of development. This could be analogous to the fact that adult cortical neurons of the same transcriptomic type can have highly variable morphological properties^{75,76}. It will be important to scale up the connectomic approach, and make it as definitive for the cortex as it is now for the fly visual system. A first attempt has already been made in visual cortex¹⁹.

Online content

Any methods, additional references, Nature Portfolio reporting summaries, source data, extended data, supplementary information, acknowledgements, peer review information; details of author contributions and competing interests; and statements of data and code availability are available at <https://doi.org/10.1038/s41586-024-07981-1>.

- Masland, R. H. Neuronal cell types. *Curr. Biol.* **14**, R497–R500 (2004).
- Seung, H. S. & Sumbul, U. Neuronal cell types and connectivity: lessons from the retina. *Neuron* **83**, 1262–1272 (2014).
- Zeng, H. & Sanes, J. R. Neuronal cell-type classification: challenges, opportunities and the path forward. *Nat. Rev. Neurosci.* **18**, 530–546 (2017).
- Currier, T. A., Pang, M. M. & Clandinin, T. R. Visual processing in the fly, from photoreceptors to behavior. *Genetics* **224**, iyad064 (2023).
- Borst, A. & Groschner, L. N. How flies see motion. *Annu. Rev. Neurosci.* **46**, 17–37 (2023).
- Fischbach, K.-F. & Dittrich, A. P. M. The optic lobe of *Drosophila melanogaster*. I. A Golgi analysis of wild-type structure. *Cell Tissue Res.* **258**, 441–475 (1989).
- Gao, S. et al. The neural substrate of spectral preference in *Drosophila*. *Neuron* **60**, 328–342 (2008).
- Mauss, A. S. et al. Neural circuit to integrate opposing motions in the visual field. *Cell* **162**, 351–362 (2015).
- Scheffer, L. K. et al. A connectome and analysis of the adult *Drosophila* central brain. *eLife* **9**, e57443 (2020).
- Shinomiya, K., Nern, A., Meinertzhagen, I. A., Plaza, S. M. & Reiser, M. B. Neuronal circuits integrating visual motion information in *Drosophila melanogaster*. *Curr. Biol.* **32**, 3529–3544 (2022).
- Hubel, D. H. & Wiesel, T. N. Receptive fields, binocular interaction and functional architecture in the cat's visual cortex. *J. Physiol.* **160**, 106–154 (1962).
- Fukushima, K. Neocognitron: a self organizing neural network model for a mechanism of pattern recognition unaffected by shift in position. *Biol. Cybern.* **36**, 193–202 (1980).
- LeCun, Y. et al. Backpropagation applied to handwritten ZIP code recognition. *Neural Comput.* **1**, 541–551 (1989).
- LeCun, Y., Bengio, Y. & Hinton, G. Deep learning. *Nature* **521**, 436–444 (2015).
- Jia, H., Rochefort, N. L., Chen, X. & Konnerth, A. Dendritic organization of sensory input to cortical neurons in vivo. *Nature* **464**, 1307–1312 (2010).
- Cossell, L. et al. Functional organization of excitatory synaptic strength in primary visual cortex. *Nature* **518**, 399–403 (2015).
- Wilson, D. E., Whitney, D. E., Scholl, B. & Fitzpatrick, D. Orientation selectivity and the functional clustering of synaptic inputs in primary visual cortex. *Nat. Neurosci.* **19**, 1003–1009 (2016).
- The MICrONS Consortium. Functional connectomics spanning multiple areas of mouse visual cortex. Preprint at *bioRxiv* <https://doi.org/10.1101/2021.07.28.454025> (2021).
- Schneider-Mizell, C. M. et al. Cell-type-specific inhibitory circuitry from a connectomic census of mouse visual cortex. Preprint at *bioRxiv* <https://doi.org/10.1101/2023.01.23.525290> (2023).
- Schnaitmann, C., Pagni, M. & Reiff, D. F. Color vision in insects: insights from *Drosophila*. *J. Comp. Physiol. A* **206**, 183–198 (2020).
- Wu, M. et al. Visual projection neurons in the *Drosophila* lobula link feature detection to distinct behavioral programs. *eLife* **5**, e21022 (2016).
- Ribeiro, I. M. A. et al. Visual projection neurons mediating directed courtship in *Drosophila*. *Cell* **174**, 607–621 (2018).
- Zheng, Z. et al. A complete electron microscopy volume of the brain of adult *Drosophila melanogaster*. *Cell* **174**, 730–743 (2018).
- Dorkenwald, S. et al. Neuronal wiring diagram of an adult brain. *Nature* <https://doi.org/10.1038/s41586-024-07558-y> (2024).
- Schlegel, P. et al. Whole-brain annotation and multi-connectome cell typing quantifies circuit stereotypy in *Drosophila*. *Nature* <https://doi.org/10.1038/s41586-024-07686-5> (2024).
- Meinertzhagen, I. A. & O'Neil, S. D. Synaptic organization of columnar elements in the lamina of the wild type in *Drosophila melanogaster*. *J. Comp. Neurol.* **305**, 232–263 (1991).
- Takemura, S.-Y. et al. A visual motion detection circuit suggested by *Drosophila* connectomics. *Nature* **500**, 175–181 (2013).
- Takemura, S.-Y. et al. Synaptic circuits and their variations within different columns in the visual system of *Drosophila*. *Proc. Natl Acad. Sci. USA* **112**, 13711–13716 (2015).
- Takemura, S., Nern, A., Chklovskii, D. B. & Scheffer, L. K. The comprehensive connectome of a neural substrate for 'ON' motion detection in *Drosophila*. *eLife* **6**, e24394 (2017).
- Shinomiya, K. et al. Comparisons between the ON- and OFF-edge motion pathways in the *Drosophila* brain. *eLife* **8**, e40025 (2019).
- Dorkenwald, S. et al. FlyWire: online community for whole-brain connectomics. *Nat. Methods* **19**, 119–128 (2022).
- Strausfeld, N. J. The optic lobes of Diptera. *Philos. Trans. R. Soc. Lond. B* **258**, 135–223 (1970).
- Mesulam, M. in *Fiber Pathways of the Brain* (eds Schmahmann, J. & Pandya, D.) ix–x (Oxford Univ. Press, 2009).
- Jelinek, F., Mercer, R. L., Bahl, L. R. & Baker, J. K. Perplexity—a measure of the difficulty of speech recognition tasks. *J. Acoust. Soc. Am.* **62**, S63 (1977).
- Joesch, M., Schnell, B., Raghu, S. V., Reiff, D. F. & Borst, A. ON and OFF pathways in *Drosophila* motion vision. *Nature* **468**, 300–304 (2010).
- Strother, J. A., Nern, A. & Reiser, M. B. Direct observation of ON and OFF pathways in the *Drosophila* visual system. *Curr. Biol.* **24**, 976–983 (2014).
- Seung, H. S. Interneuron diversity and normalization specificity in a visual system. Preprint at *bioRxiv* <https://doi.org/10.1101/2024.04.03.587837> (2024).
- Ketkar, M. D. et al. First-order visual interneurons distribute distinct contrast and luminance information across ON and OFF pathways to achieve stable behavior. *eLife* **11**, e74937 (2022).
- Drews, M. S. et al. Dynamic signal compression for robust motion vision in flies. *Curr. Biol.* **30**, 209–221 (2020).
- Ketkar, M. D. et al. Luminance information is required for the accurate estimation of contrast in rapidly changing visual contexts. *Curr. Biol.* **30**, 657–669 (2020).
- Arenz, A., Drews, M. S., Richter, F. G., Ammer, G. & Borst, A. The temporal tuning of the *Drosophila* motion detectors is determined by the dynamics of their input elements. *Curr. Biol.* **27**, 929–944 (2017).
- Kind, E. et al. Synaptic targets of photoreceptors specialized to detect color and skylight polarization in *Drosophila*. *eLife* **10**, e71858 (2021).
- Strausfeld, N. J. & Campos-Ortega, J. A. Vision in insects: pathways possibly underlying neural adaptation and lateral inhibition. *Science* **195**, 894–897 (1977).
- Busch, S., Selcho, M., Ito, K. & Tanimoto, H. A map of octopaminergic neurons in the *Drosophila* brain. *J. Comp. Neurol.* **513**, 643–667 (2009).
- Eckstein, N. et al. Neurotransmitter classification from electron microscopy images at synaptic sites in *Drosophila melanogaster*. *Cell* **187**, 2574–2594.e23 (2024).
- Tuthill, J. C., Nern, A., Rubin, G. M. & Reiser, M. B. Wide-field feedback neurons dynamically tune early visual processing. *Neuron* **82**, 887–895 (2014).
- Keleş, M. F., Hardcastle, B. J., Stadele, C., Xiao, Q. & Frye, M. A. Inhibitory interactions and columnar inputs to an object motion detector in *Drosophila*. *Cell Rep.* **30**, 2115–2124 (2020).
- Klapoetke, N. C. et al. A functionally ordered visual feature map in the *Drosophila* brain. *Neuron* **110**, 1700–1711 (2022).
- Turner, M. H., Krieger, A., Pang, M. M. & Clandinin, T. R. Visual and motor signatures of locomotion dynamically shape a population code for feature detection in *Drosophila*. *eLife* **11**, e82587 (2022).
- Karupudurai, T. et al. A hard-wired glutamatergic circuit pools and relays UV signals to mediate spectral preference in *Drosophila*. *Neuron* **81**, 603–615 (2014).
- Menon, K. P., Kulkarni, V., Takemura, S.-Y., Anaya, M. & Zinn, K. Interactions between Dpr11 and DLPv control selection of amacrine neurons in *Drosophila* color vision circuits. *Elife* **8**, e48935 (2019).
- Christenson, M. P., Sanz Diez, A., Heath, S. L. et al. Hue selectivity from recurrent circuitry in *Drosophila*. *Nat. Neurosci.* **27**, 1137–1147 (2024).
- Courgeon, M. & Desplan, C. Coordination between stochastic and deterministic specification in the *Drosophila* visual system. *Science* **366**, eaay6727 (2019).
- Sancer, G. et al. Modality-specific circuits for skylight orientation in the fly visual system. *Curr. Biol.* **29**, 2812–2825 (2019).
- Shinomiya, K. et al. The organization of the second optic chiasm of the *Drosophila* optic lobe. *Front. Neural Circuits* **13**, 65 (2019).
- Bae, J. A. et al. Digital museum of retinal ganglion cells with dense anatomy and physiology. *Cell* **173**, 1293–1306 (2018).
- Ammer, G. et al. Multilevel visual motion opponency in *Drosophila*. *Nat. Neurosci.* **26**, 1894–1905 (2023).
- Song, B.-M. & Lee, C.-H. Toward a mechanistic understanding of color vision in insects. *Front. Neural Circuits* **12**, 16 (2018).
- Land, E. H. & McCann, J. J. Lightness and retinex theory. *J. Opt. Soc. Am.* **61**, 1–11 (1971).
- Seung, H. S. Predicting visual function by interpreting a neuronal wiring diagram. *Nature* <https://doi.org/10.1038/s41586-024-07953-5> (2024).
- Kurmangaliyev, Y. Z., Yoo, J., Valdes-Aleman, J., Sanfilippo, P. & Zipursky, S. L. Transcriptional programs of circuit assembly in the *Drosophila* visual system. *Neuron* **108**, 1045–1057 (2020).
- zel, M. N. et al. Neuronal diversity and convergence in a visual system developmental atlas. *Nature* **589**, 88–95 (2021).
- Konstantinides, N. et al. A complete temporal transcription factor series in the fly visual system. *Nature* **604**, 316–322 (2022).
- Yoo, J. et al. Brain wiring determinants uncovered by integrating connectomes and transcriptomes. *Curr. Biol.* **33**, 3998–4005 (2023).
- Seung, H. S. Reading the book of memory: sparse sampling versus dense mapping of connectomes. *Neuron* **62**, 17–29 (2009).
- Seung, H. S. & Yuste, R. in *Principles of Neural Science* (eds Kandel, E. R. et al.) 5th edn, 1581–1600 (2012).
- Lappalainen, J. K. et al. Connectome-constrained networks predict neural activity across the fly visual system. *Nature* <https://doi.org/10.1038/s41586-024-07939-3> (2024).
- Scott, E. K., Reuter, J. E. & Luo, L. Dendritic development of *Drosophila* high order visual system neurons is independent of sensory experience. *BMC Neurosci.* **4**, 14 (2003).
- Karmeier, K., Tabor, R., Egelhaaf, M. & Krapp, H. G. Early visual experience and the receptive-field organization of optic flow processing interneurons in the fly motion pathway. *Vis. Neurosci.* **18**, 1–8 (2001).
- Hirsch, H. V. et al. Rearing in darkness changes visually-guided choice behavior in *Drosophila*. *Vis. Neurosci.* **5**, 281–289 (1990).
- Bajar, B. T. et al. A discrete neuronal population coordinates brain-wide developmental activity. *Nature* **602**, 639–646 (2022).
- White, J. G., Southgate, E., Thomson, J. N. & Brenner, S. The structure of the nervous system of the nematode *Caenorhabditis elegans*. *Philos. Trans. R. Soc. Lond.* **314**, 1–340 (1986).
- BRAIN Initiative Cell Census Network (BICCN). A multimodal cell census and atlas of the mammalian primary motor cortex. *Nature* **598**, 86–102 (2021).
- Yuste, R. et al. A community-based transcriptomics classification and nomenclature of neocortical cell types. *Nat. Neurosci.* **23**, 1456–1468 (2020).

Article

75. Scala, F. et al. Phenotypic variation of transcriptomic cell types in mouse motor cortex. *Nature* **598**, 144–150 (2020).
76. Gouwens, N. W. et al. Integrated morphoelectric and transcriptomic classification of cortical GABAergic cells. *Cell* **183**, 935–953 (2020).

Publisher's note Springer Nature remains neutral with regard to jurisdictional claims in published maps and institutional affiliations.



Open Access This article is licensed under a Creative Commons Attribution 4.0 International License, which permits use, sharing, adaptation, distribution and reproduction in any medium or format, as long as you give appropriate credit to the original author(s) and the source, provide a link to the Creative Commons licence, and indicate if changes were made. The images or other third party material in this article are included in the article's Creative Commons licence, unless indicated otherwise in a credit line to the material. If material is not included in the article's Creative Commons licence and your intended use is not permitted by statutory regulation or exceeds the permitted use, you will need to obtain permission directly from the copyright holder. To view a copy of this licence, visit <http://creativecommons.org/licenses/by/4.0/>.

© The Author(s) 2024

The FlyWire Consortium

Krzysztof Kruk^{2,3}, Ben Silverman¹, Dustin Garner⁵, Jay Gager¹, Kyle Patrick Willie¹, Doug Bland¹, Austin T. Burke¹, James Hebditch¹, Ryan Willie¹, Celia David^{1,3}, Gizem Sancer⁶, Jenna Joroff⁶, Anne Kristiansen³, Thomas Stocks³, Amalia Braun⁹, Szi-chieh Yu^{1,6}, Emil Kind⁴, Marion Silies¹⁰, Jaime Skelton³, Travis R. Aiken³, Maria Ioannidou¹⁰, Marissa Sorek^{1,3}, Matt Collie¹¹, Gerit A. Linneweber¹², Sebastian Molina-Obando¹⁰, Sven Dorkenwald^{1,7}, Nelsie Panes¹³, Allien Mae Gogo¹³, Dorfam Rastgarmoghaddam¹⁰, Cathy Pilapil¹³, Rey Adrian Candilada¹³, Nikitas Serafetinidis³, Arie Matsliah^{1,6}, Amy R. Sterling^{1,3}, Mathias F. Wernet⁴, Sung Soo Kim⁵, Mala Murthy¹, H. Sebastian Seung^{1,7}, Wei-Chung Lee⁸, Alexander Borst⁹, Rachel I. Wilson⁹, Philipp Schlegel^{14,15} & Gregory S. X. E. Jefferis^{14,15}

¹Harvard Medical School, Boston, MA, USA. ²Department Circuits–Computation–Models, Max Planck Institute for Biological Intelligence, Planegg, Germany. ³Johannes-Gutenberg University Mainz, Mainz, Germany. ⁴Harvard, Boston, MA, USA. ⁵Freie Universität Berlin, Berlin, Germany. ⁶SixEleven, Davao City, Philippines. ⁷Neurobiology Division, MRC Laboratory of Molecular Biology, Cambridge, UK. ⁸Drosophila Connectomics Group, Department of Zoology, University of Cambridge, Cambridge, UK.

Methods

Reconstruction accuracy and completeness

The overall quality of our *Drosophila* brain reconstruction has been evaluated elsewhere^{24,31} (a summary of the current status is shown in Extended Data Table 3). Here we describe a few additional checks that are specific to the optic lobe. A small percentage of cells have eluded proofreading efforts. The worst cases are some types with visible 'bald spots' in the mid posterior side of the right optic lobe (Supplementary Data 2). In this region, we observed a narrowing and discontinuation of neuronal tracks. Many of these tracks appear to terminate within glial cells, suggesting a potential engulfment of neurons by glia. For most types, under-recovery is hardly visible (Supplementary Data 2).

For a quantitative estimate of under-recovery, we can rely on the 'modular' types²⁷, defined as cell types that are in one-to-one correspondence with columns. A previous reconstruction of seven medulla columns identified 20 modular types²⁸. These largely correspond to the cell types that contain from 720 to 800 cells in our reconstruction (Fig. 1d). The top end (800) of this range is probably the true number of columns in this optic lobe. The lower end of this range is 720, suggesting that under-recovery is 10% at most, and typically less than that.

The inner photoreceptors R7 and R8 are about 650 cells each, and the outer photoreceptors R1–6 total about 3,400 in version 783 of the FlyWire connectome. These numbers are not inconsistent with modularity because photoreceptors are especially challenging to proofread in this dataset and under-recovery is higher than typical.

In the left optic lobe, we have proofread around 38,500 intrinsic neurons, as well as 3,700 VPNS, 250 VCNs, 150 heterolateral neurons and 5,000 photoreceptor cells. Tables comparing precise left/right counts by superclass as well as by type are available for download (see the 'Data availability' section).

Tm21 (also known as Tm6), Dm2, TmY5a, Tm27 and Mi15 are substantially less numerous than 800, so we agree with the seven column reconstruction²⁸ that they are not modular. On the other hand, some of our types (T2a, Tm3, T4c and T3) contain more than 800 proofread cells (Fig. 1d), which violates the definition of modularity. This partially agrees with the seven column reconstruction²⁸, which regarded T3 and T2a as modular, and T4 and Tm3 as not modular. T4 is an unusual case, as T4c is above 800 while the other T4 types are below 800. It should be noted that all of the above cell numbers could still creep upward with further proofreading.

A genuine analysis of modularity requires going beyond simple cell counts, and analysing locations to check the idea of one-to-one correspondence. Such an analysis is left for future work. Here we apply the term 'numerous' to those types containing 720 or more cells, as well as photoreceptor types, and do not commit to whether these types are truly modular.

The seven column reconstruction²⁸ provided a matrix of connections between their modular types. This shows good agreement with our data (Methods and Extended Data Fig. 9), providing a check on the accuracy of our reconstruction in the optic lobe. This validation complements the estimates of reconstruction accuracy in the central brain that are provided in the flagship paper²⁴.

The major limitation of our reconstruction in the optic lobe concerns the automatically detected synapses⁷⁷. Although accuracy is high overall, outgoing photoreceptor synapses are markedly underdetected. This may be because dark cytoplasm (characteristic of photoreceptors) is not well represented in the example synapse images that were used to train the automated synapse detector. Example images of photoreceptor synapses have been included in the training set of an improved automated synapse detector, but the results were not ready in time for this publication, and will be made available in a future release. The classification of inner photoreceptors as yellow and pale is postponed until the future release. In the present paper, the connectivity from photoreceptors to other cell types in this paper is only qualitative

and not quantitative. Furthermore, underdetection of photoreceptor synapses could affect the input fractions of other connections due to normalization.

Another cautionary note is that weaker connections in the type–type connectivity matrix (Extended Data Fig. 4) could be artifactual, due to false positives of automated synapse detection. There are some heuristics for guessing whether a connection is artifactual, short of manually inspecting the original EM images. For example, one might distrust weak connections between cells, that is, those with less than some threshold number of synapses. The choice of the threshold value depends on the context⁹. For example, the flagship paper²⁴ discarded connections with less than five synapses, a convention followed by the FlyWire Codex. The predicates of the present work apply a threshold of two synapses rather than five. The different thresholds were chosen because the central brain and optic lobes are very different contexts, as we now explain.

In the central brain, most cell types have cardinality 2 (cell and its mirror twin in the opposite hemisphere; Extended Data Fig. 1e). In the hemibrain, the cardinality is typically reduced to one. Therefore, whether there is a connection between cell type A and cell type B must be decided based on only two or three examples of the ordered pair (A, B) in all the connectomic data that is so far available. Given the small sample size, it makes sense to set the threshold to a relatively high value, if false positives are to be avoided.

On the other hand, in the optic lobe, there are often many examples of the ordered pair (A, B), because so many cell types have high cardinality. Therefore, if a connection is consistently found from type A to type B, one can have reasonable confidence even if the average number of synapses in the connection is not so high. That is why we set the threshold to a relatively low value in the optic lobe predicates. In particular, we have found that certain inhibitory types consistently make connections that involve relatively few synapses, and these connections seem real.

Another heuristic is to look for extreme asymmetry in the matrix. If the number of synapses from A to B is much larger than from B to A, the latter connection might be spurious. The reason is that the strong connection from A to B means the contact area between A and B is large, which means more opportunity for false-positive synapses from B to A. False-positive rates for synapses are estimated in the flagship paper²⁴.

Finally, it may be known from other studies that a connection does not exist. For example, T1 cells lack output synapses^{26,78}. Therefore, in our analyses, we typically regarded the few outgoing T1 synapses in our data as false positives and discarded them.

Morphological cell typing

Our connectomic cell approach to typing is initially seeded with some set of types, to define the feature vectors for cells (Fig. 2a), after which the types are refined by computational methods. For the initial seeding, we relied on the time-honoured approach of morphological cell typing, sometimes assisted by computational tools that analysed connectivity. It is worth noting that 'morphology' is a misnomer, because it refers to shape only, strictly speaking. Orientation and position are actually more fundamental properties because of their influence on stratification in neuropil layers. Thus, 'single-cell anatomy' would be more accurate than morphology, although the latter is the standard term.

Stage 1: crowdsourced annotation of known types. Annotations of optic lobe neurons were initially crowdsourced. The first annotators were volunteers from *Drosophila* laboratories. They were later joined by citizen scientists. At this stage, the annotation effort was mainly devoted to labelling cells of known types, especially the most numerous types.

***Drosophila* lab annotators.** E.K. and D.G. proofread and annotated medulla neurons that were upstream of the anterior visual pathway. These included many of the medulla and lamina neurons discussed in this study. The annotated neurons were primarily Dm2, Mi15, R7,

Article

and R8, but also comprised various L, Dm, Mi, Tm, C and Sm cells. Previously known neuron types were identified primarily by morphology and partially by connectivity. Annotators additionally found all MI1 neurons in both hemispheres to find every medulla column. These MI1 neurons were used to create a map of medulla layers based on MI1 stratification⁶, which later aided citizen scientists to identify medulla cell types.

Citizen scientists. The top 100 players from Eyewire⁷⁹ had been invited to proofread in FlyWire²⁴. After 3 months of proofreading in the right optic lobe, they were encouraged to also label neurons when they felt confident. Most citizen scientists did a mixture of annotation and proofreading. Sometimes they annotated cells after proofreading, and other times searched for cells of a particular type to proofread.

Citizen scientists were provided with a visual guide to optic lobe cells sourced from the literature^{6,80}. FlyWire made available a 3D mesh overlay indicating the four main optic lobe neuropils. Visual identification was primarily based on single-cell anatomy. Initially, labelling of type families (that is, Dm, Tm, Mi and so on) was encouraged, especially for novices. Annotation of specific types (such as Dm3, Tm2) developed over time. The use of canonical names was further enforced by a software tool that enabled easy selection and submission of preformatted type names.

Additional community resources (discussion board/forum, blog, shared Google drive, chat, dedicated email and Twitch livestream) fostered an environment for sharing ideas and information between community members (citizen scientists, community managers and researchers). Community managers answered questions, provided resources such as the visual guide, shared updates, performed troubleshooting and general organization of community activity. Daily stats including number of annotations submitted per individual were shared on the discussion board/forum to provide project progress. Live interaction, demonstrations and communal problem solving occurred during weekly Twitch video livestreams led by a community manager. The environment created by these resources allowed citizen scientists to self-organize in several ways: community driven information sharing, programmatic tools and 'farms'.

Community-driven information sharing. Citizen scientists created a comprehensive guide with text and screenshots that expanded on the visual guide. They also found and studied any publicly available scientific literature or resources regarding the optic lobe. They shared findings at discuss.flywire.ai, which as of 10 October 2023 had over 2,500 posts. Community managers interacted with citizen scientists by sharing findings from the scientific literature, consulting *Drosophila* specialists on FlyWire and providing feedback.

Programmatic Tools. Programmatic tools were created to help with searching for cells of the same type. One important script traced partners-of-partners, that is, source cell → downstream partners → their upstream partners, or source cell → upstream partners → their downstream partners. This was based on the assumption that cells of the same type will probably synapse with the same target cells, which often turned out to be true. The tool could either look for partners-of-all-partners or partners-of-any-partners. The resulting lists of cells could be very long, and were filtered by excluding cells that had already been identified, or excluding segments with small sizes or low ID numbers (which had probably not yet been proofread). Another tool created from lobula plate tangential cells (for example, HS, VS, HI) aided definition of layers in the lobula plate. This facilitated identification of various cell types, especially T4 and T5.

Cell farms. Citizen scientists created farms in FlyWire or Neuroglancer with all the found cells of a given type visible. Farms showed visually where cells still remained to be found. If they found a bald spot, a popular method to find missing cells was to move the 2D plane in that place and add segments to the farm one after another in search of cells of the correct type. Farms also helped with identifying cells near to the edges of neuropils, where neurons are usually deformed. Having a view of all

other cells of the same type made it possible to extrapolate to how a cell at the edge should look.

Stage 2: centralized annotation and discovery of new types. A team of image analysts at Princeton finished the annotation of the remaining cells in known types, and also discovered new types. Community annotations were initially compared with existing literature to confirm accuracy. Once validated, these cells were used to query various Codex search tools that returned previously unannotated cells exhibiting connectivity similar to that of the cell in the query. The hits from the search query were evaluated by morphology and stratification to confirm match with the target cell type. In some cases in which cell type distinctions were uncertain, predicted neurotransmitters⁴⁵ were used for additional guidance. This process enabled us to create a preliminary clustering of all previously known and new types.

Connectomic cell typing

Eventually morphology became insufficient for further progress. Expert annotators, for example, struggled to classify Tm5 cells into the three known types, not knowing that there would turn out to be six Tm5 types. At this point, we were forced to transition to connectomic cell typing. In retrospect, this transition could have been made much earlier. As mentioned above, connectomic cell typing must be seeded with an initial set of types, but the seeding did not have to be as thorough as it ended up. We leave for future work the challenge of extending the connectomic approach so it can be used from start to finish.

Stage 3: connectivity-based splitting and merging of types and auto-correction. We used computational methods to split types that could not be properly split in stage 2. Some candidates for splitting (such as Tm5) were suggested by the image analysts. Some candidates were suspicious because they contained so many cells. Finally, some candidates were scrutinized because their type radii were large. We applied hierarchical clustering with average linkage, and accepted the splits if they did not violate the tiling principle as described in the 'Spatial coverage' section.

We also applied computational methods to merge types that had been improperly split in stage 2. Here the candidates were types with low spatial coverage of the visual field, or types that were suspiciously close in the dendrogram of cell types (Fig. 2c). Merge decisions were made by hierarchical clustering of cells from types that were candidates for merging, and validated if they improved spatial coverage.

Once we arrived at the final list of types, we estimated the 'centre' of each type using the element-wise trimmed mean. Then, for every cell, we computed the nearest type centre by Jaccard distance. For 98% of the cells, the nearest type centre coincided with the assigned type. We sampled some disagreements and reviewed them manually. In the majority of cases, the algorithm was correct, and the human annotators had made errors, usually of inattention. The remaining cases were mostly attributable to proofreading errors. There were also cases in which type centres had been contaminated by human-misassigned cells (see the 'Morphological variation' section), which in turn led to more misassignment by the algorithm. After addressing these issues, we applied the automatic corrections to all but 0.1% of cells, which were rejected using distance thresholds.

Validation

On the basis of the auto-correction procedure, we estimate that our cell type assignments are between 98% and 99.9% accurate. For another measure of the quality of our cell typing, we computed the 'radius' of each type, defined as the average distance from its cells to its centre. Here we computed the centre by approximately minimizing the sum of Jaccard distances from each cell in the type to the centre (see the 'Computational concepts' section). A large type radius can be a sign that the type contains dissimilar cells, and should be split. For our final

types, the radii vary, but almost all lie below 0.6 (Extended Data Fig. 3a). Lat has an exceptionally high type radius, and deserves to be split (see the ‘Cross-neuropil tangential and amacrine’ section). The type radii are essentially the same, whether or not boundary types are included in the feature vector (data not shown).

Discrimination with logical predicates. Because the feature vector is rather high dimensional, it would be helpful to have simpler insights into what makes a type. One approach is to find a set of simple logical predicates based on connectivity that predict type membership with high accuracy. For a given cell, we define the attribute ‘is connected to input type t' ’ as meaning that the cell receives at least one connection from some cell of type t . Similarly, the attribute ‘is connected to output type t' ’ means that the cell makes at least one connection onto some cell of type t .

An optimal predicate is constructed for each type that consists of 2 tuples: input types and output types. Both tuples are limited to size 5 at most, and they are optimal with respect to the F -score of their prediction of the subject type, defined as follows:

- Recall of a predicate for type T is the ratio of true positive predictions (cells matching the predicate) to the total number of true positives (cells of type T). It measures the predicate’s ability to identify all positive instances of a given type.
- Precision is the ratio of true positive predictions (predictions that are indeed of type T) to the total number of positive predictions made by the logical predicate.
- F -score is the harmonic mean of precision and recall—a single metric that combines both precision and recall into one value.

On a high level, the process for computing the predicates is exhaustive—for each type, we look for all possible combinations of input type tuples and output type tuples and compute their precision, recall and F -score. A few optimization techniques are used to speed up this computation, by calculating minimum precision and recall thresholds from the current best candidate predicate and pruning many tuples early.

For example, the logical predicate ‘is connected to input type Tm9 and output type Am1 and output type LPi15’ predicts T5b cells with 99% precision and 99% recall. For all but three of the identified types, we found a logical predicate with 5 or fewer input/output attributes that predicts type membership with an average F -score of 0.93, weighted by the number of cells in type (Extended Data Fig. 4 and Supplementary Data 1). Some of the attributes in a predicate are the top most connected partner types, but this is not necessarily the case. The attributes are distinctive partners, which are not always the most connected partners. The predicate for each type is shown on its card in Supplementary Data 2. For each family, the predicates for all types can be shown together in a single graph containing all of the relevant attributes (Supplementary Data 3).

We experimented with searching for predicates after randomly shuffling a small fraction of types (namely, swapping types for 5% of randomly picked pairs of neurons). We found that precision and recall of the best predicates dropped substantially, suggesting that we are not overfitting. This was expected because the predicates are short.

We also measured the drop in the quality of predicates if excluding boundary types (where the predicates are allowed to contain intrinsic types only). As is the case with the clustering metrics, the impact on predicates is marginal (weighted mean F -score drops from 0.93 to 0.92).

Discrimination with two-dimensional projections. Another approach to interpretability is to look at low-dimensional projections of the 27-dimensional feature vector. For each cell type, we select a small subset of dimensions that suffice to accurately discriminate that type

from other types (Extended Data Fig. 3c). Here we normalize the feature vector so that its elements represent the ‘fraction of input synapses received from type t' ’ or ‘fraction of output synapses sent to type t' ’. In these normalized quantities, the denominator is the total number of all input or output synapses, not just the synapses with other neurons intrinsic to the optic lobe.

For example, we can visualize all cells in the Pm family in the two-dimensional space of C3 input fraction and TmY3 output fraction (Extended Data Fig. 3c). In this space, PmO4 cells are well-separated from other Pm cells, and can be discriminated with 100% accuracy by ‘C3 input fraction greater than 0.01 and TmY3 output fraction greater than 0.01’. This conjunction of two features is a more accurate discriminator than either feature by itself.

More generally, a cell type discriminator is based on thresholding a set of input and output fractions, and taking the conjunction of the result. The search for a discriminator finds a set of dimensions, along with threshold values for the dimensions. To simplify the search, we require that the cell type be discriminated only from other types in the same neuropil family, rather than from all other types. Under these conditions, it almost always suffices to use just two dimensions of the normalized feature vector.

Discriminators for all types in all families containing more than one type are provided in Supplementary Data 4. Many although not all discriminations are highly accurate. Both intrinsic and boundary types are included as discriminative features.

Computational concepts

Connectivity: cell-to-cell, type-to-cell, cell-to-type and type-to-type. Define a (weighted) cell-to-cell connectivity matrix w_{ij} , as the number of synapses from neuron i to neuron j . The weighted out-degree and in-degree of neuron i are:

$$d_i^+ = \sum_j w_{ij} \quad d_i^- = \sum_j w_{ji}$$

The sums are over all neurons in the brain. If neuron i is a cell intrinsic to one optic lobe, the only nonvanishing terms in the sums are due to the intrinsic and boundary neurons for that optic lobe.

Let A_{it} be the 0–1 matrix that assigns neuron i to type t . The column and row sums of the assignment matrix satisfy

$$n_t = \sum_i A_{it} \quad 1 = \sum_t A_{it} \quad (2)$$

where n_t is the number of cells assigned to type t .

The cell-to-type connectivity matrix O_{it} is the number of output synapses from neuron i to neurons of type t ,

$$O_{it} = \sum_j w_{ij} A_{jt} \quad (3)$$

For fixed i , O_{it} is known as the output feature vector of cell i . Similarly, the type-to-cell connectivity matrix I_{ij} is the number of input synapses from neurons of type t onto neuron j ,

$$I_{ij} = \sum_t A_{it} w_{tj} \quad (4)$$

For fixed j , I_{ij} is known as the input feature vector of cell j . The i th row and i th column of these matrices are concatenated to form the full feature vector for cell i (Fig. 2a).

The input and output feature vectors can be normalized by degree to yield input and output fractions of cell i , O_{ii}/d_i^+ and I_{ii}/d_i^- . Elements of these matrices are used for the discriminating 2D projections (Extended Data Fig. 3c).

Article

The type-to-type connectivity matrix is the number of synapses from neurons of type s to neurons of type t ,

$$W_{st} = \sum_j A_{is} w_{ij} A_{jt} \quad (5)$$

The weighted degree of type t is the sum of the weighted degrees of the cells in type t ,

$$D_t^+ = \sum_i A_{it} d_i^+ \quad D_t^- = \sum_i A_{it} d_i^- \quad (6)$$

The sums are over all neurons in the brain, similar to equation (1). Normalizing by degree yields the output fractions of type s , W_{st}/D_s^+ , where t runs from 1 to T . The input fractions of type t are similarly given by W_{st}/D_t^- , where s runs from 1 to T . Selected output and input fractions of types are shown in Supplementary Data 5.

Alternatively, the feature vectors can be based on connection number rather than synapse number, where a connection is defined as two or more synapses from one neuron to another. Then, weighted degree is replaced by unweighted degree in the above definitions. The threshold of two synapses is intended to suppress noise due to false positives in the automated synapse detection. Synapse number and connection number give similar results, and we use both in our analyses.

We found that it was sufficient for feature dimensions to include only intrinsic types ($T = 227$). Alternatively, feature dimensions can be defined as including both intrinsic and boundary types ($T > 700$), and this yields similar results (data not shown).

For the hierarchical clustering of cell types (Fig. 2c), the feature vector for each cell type is obtained by concatenating the vectors of input and output fractions for that cell type.

Similarity and distance measures. The weighted Jaccard similarity between feature vectors \mathbf{x} and \mathbf{y} is defined by

$$J(\mathbf{x}, \mathbf{y}) = \frac{\sum_t \min(x_t, y_t)}{\sum_t \max(x_t, y_t)} \quad (7)$$

and the weighted Jaccard distance $d(\mathbf{x}, \mathbf{y})$ is defined as one minus the weighted Jaccard similarity. These quantities are bounded between zero and one since our feature vectors are nonnegative. In our cell typing efforts, we have found empirically that Jaccard similarity works better than cosine similarity when feature vectors are sparse.

Type centres. Given a set of feature vectors \mathbf{x}^a , the centre \mathbf{c} can be defined as the vector minimizing

$$\sum_a d(\mathbf{x}^a, \mathbf{c}) \quad (8)$$

This cost function is convex, as d is a metric satisfying the triangle inequality. Therefore, the cost function has a unique minimum. We used various approximate methods to minimize the cost function.

For auto-correction of type assignments, we used the element-wise trimmed mean. We found empirically that this gave good robustness to noise from false synapse detections. For the type radii, we used a coordinate descent approach, minimizing the cost function with respect to each c_i in turn. The loop included every i for which some x_i was non-zero. This converged within a few iterations of the loop.

Hierarchical clustering of cell types

The type-to-type connectivity matrix of equation (5) was the starting point for clustering the cell types. For each cell type, the corresponding row and column of the matrix were normalized to become input and output fractions, as described in the text following equation (6), and then concatenated (this is yet another way of computing type centres). Feature vectors included only dimensions corresponding to cell types

intrinsic to the optic lobe. Then, average linkage hierarchical clustering was applied to yield a dendrogram (Fig. 2c). The dendrogram was thresholded to produce a flat clustering (Fig. 2c).

The precise memberships in the clusters warrant cautious interpretation, as the clusters are the outcome of just one clustering algorithm (average linkage), and differ if another clustering algorithm is used. Each cluster contains core groups of types that are highly similar to each other, that is, types that merge early during agglomeration (closer to the circumference of the dendrogram). These are more certain to have similar visual functions, and tend to be grouped together by any clustering algorithm. Types that are merged late (closer to the origin of the dendrogram) are less similar, and their cluster membership is more arbitrary. Some degree of arbitrariness is inevitable when one divides the visual system into separate subsystems, because subsystems interact with each other, and types that mediate such interactions are borderline cases.

Each cluster is generally a mixture of types from multiple neuropil families. Sceptics might regard such mixing as arising from the 'noisiness' in the clustering noted above at the largest distances. Indeed, the nearest types, those that merge in the dendrogram farther from the centre (Fig. 2c), tend to be from the same neuropil family. But plenty of dendrogram merges between types of different families happen at intermediate distances rather than the largest distances. Thus, some of the mixing of types from different neuropil families seems genuinely rooted in biology.

Wiring diagrams

Reduction. To make the wiring diagrams readable, we display only the top type-to-type connections, which are defined as follows. For every cell type, the top input cell type and top output cell type are selected by ranking connected partners by the total number of synapses in the connection. If cell types are nearly tied, any runner up within 5% of the winner is also displayed. Figure 3 shows the top connections between all optic lobe intrinsic types. Figures 4–7 each focus on one or a few subsystems, but also include the top input/output connections they participate in with the rest of the network as well as top output connections to boundary types (for example, in Fig. 4, Dm2 is selected because it belongs to cluster 5, luminance channel, but then also other types outside of ON, OFF, and luminance channels are included because either Dm2 is their top input/output type or the other way around). Extended Data Figs. 5 and 6 show the top input and top output connections separately, for improved readability. For the top output connections we also include boundary types (VPNs).

Colours and shapes. Nodes, representing cell types, are coloured by clusters. Node size encodes the number of drawn connections, so that types that are top input/output of many other types look larger. Node shapes encode type numerosities (number of cells of that type), from most numerous (hexagon) to least (ellipse) (see the figure legends). The lines indicate connections between cell types. The line colour encodes the relationship (top input or top output) and the line width is proportional to the number of synapses connecting the respective types. The line arrowheads encode neurotransmitter predictions (excitatory/cholinergic or inhibitory/GABAergic/glutamatergic).

Layout. We used Cytoscape⁸¹ to draw the wiring diagrams. Organic layout was used for Figs. 3 and 7c, and hierarchical layout was used for the others. The hierarchical layout tries to make arrows point downwards. After Cytoscape automatically generated a diagram, nodes were manually shifted by small displacements to minimize the number of obstructions.

Intrinsic versus boundary

The optic lobes are divided into five regions (neuropils): lamina of the compound eye (LA); medulla (ME); accessory medulla (AME); lobula

(LO); lobula plate (LOP). All non-photoreceptor cells with synapses in these regions are split into two groups: optic lobe intrinsic neurons and boundary neurons.

Optic lobe intrinsic neurons are almost entirely contained in one of the optic lobes (left or right), more precisely, 95% or more of their synapses are assigned to the five optic lobe regions listed above.

Boundary neurons are those with at least 5% (and less than 95%) of synapses in the optic lobe regions, and are either visual projection, visual centrifugal or heterolateral neurons.

Axon versus dendrite

In the main text (in the ‘Class, family and type’ section), we used the term ‘axon’. An axon is defined as some portion of the neuron with a high ratio of presynapses to postsynapses. This ratio might be high in an absolute sense. Or the ratio in the axon might only be high relative to the ratio elsewhere in the neuron (the dendrite). In either case, the axon is typically not a pure output element, but has some postsynapses as well as presynapses. For many types it is obvious whether there is an axon, but for a few types we have made judgement calls. Even without examining synapses, the axon can often be recognized from the presence of varicosities, which are presynaptic boutons. The opposite of an axon is a dendrite, which has a high ratio of postsynapses to presynapses.

An amacrine cell is defined as one for which the axon–dendrite distinction does not hold, and presynapses and postsynapses are intermingled in roughly the same ratio throughout. The branches of an amacrine cell are often called dendrites, but the neutral term ‘neurite’ is perhaps better for avoiding confusion.

Columnar neurons

Fischbach and Dittrich⁶ defined 13 columnar families based on neuropils (Fig. 1a). Families consisting exclusively of ‘numerous’ (~800 cells) types include L (lamina to medulla), C (medulla to lamina), T1 (distal medulla to lamina), T2 (distal and proximal medulla to lobula), T3 (proximal medulla to lobula), T4 (proximal medulla to lobula plate) and T5 (lobula to lobula plate). We follow the convention of grouping the less numerous Lawf1 (distal medulla to lamina) and Lawf2 (proximal and distal medulla to lamina) types in the same family, despite the differences between their neuropils and connectivity. Although T1 shares the same neuropils with Lawf1, T1 lacks output synapses^{26,78}, so it is an outlier and deserves to be a separate family. Distal and proximal medulla are regarded as two separate neuropils⁶.

Mi. Fischbach and Dittrich⁶ defined Mi as projecting from distal to proximal medulla. Mi contains both numerous and less numerous types. We identified five (Mi1, 2, 4, 9, 10) of the dozen Mi types originally defined⁶, and three (Mi13, 14, 15) types uncovered by EM reconstruction²⁷. Mi1, Mi4, and Mi9 are consistent with the classical definition, but Mi13 projects from proximal to distal medulla. Other Mi types are less polarized, and the term “narrow-field amacrine” might be more accurate than “columnar”. Nevertheless we will adhere to the convention that they are columnar. Narrow-field amacrine cells are also found in the Sm family, and exist in the mammalian retina⁸².

Tm transmedullary. As classically defined⁶, Tm cells project from the distal medulla to the lobula. Tm1 through Tm26 and Tm28 were defined⁶, and Tm27/Tm27Y was reported later⁸³. We were able to identify Tm1, 2, 3, 4, 7, 9, 16, 20, 21, 25 and 27. We split Tm5 into six types, and Tm8 into two types. We merged Tm6 and Tm21 into a single type Tm21. We prefer the latter name because the cells more closely match the Tm21 stratification as drawn by Fischbach and Dittrich⁶. Tm1a and Tm4a were defined as morphological variants⁶, but we have found that they do not differ in connectivity and are not common, so we have merged them into Tm1 and Tm4, respectively. We merged Tm27Y into Tm27⁸³. TmY5 was merged into TmY5a^{6,84}, the name that has appeared more often in the literature. These morphological distinctions originally arose

because the projection into the lobula plate, the differentiator between Tm and TmY, can vary across cells in a type. We added new types Tm31 to Tm37, which project from the serpentine medulla to the lobula. We moved Tm23 and Tm24 to the Li family. They were originally classified as Tm because their cell bodies are in the distal rind of the medulla, and they send a neurite along the columnar axis of the medulla to reach the lobula⁶. However, they do not form synapses in the medulla, so we regard them as Li neurons despite their soma locations. Overall, around half of the 26 types in the Tm family are new.

TmY. TmY cells project from the distal medulla to the lobula and lobula plate. The Y refers to the divergence of branches to the lobula and lobula plate. Previous definitions include TmY1 to TmY13⁶; TmY5a^{6,84}; TmY14²⁷; TmY15²⁹; and TmY16, TmY18 and TmY20³⁰. We identified TmY3, TmY4, TmY5a, TmY10, TmY11, TmY14, TmY15, TmY16 and TmY20. We divided TmY9 into two types, as discussed in a companion paper⁶⁰. We added a new type, TmY31.

Y. Y cells project from the proximal medulla to the lobula and lobula plate. They are similar to TmY cells, but the latter traverse both the distal and proximal medulla⁶. Previous definitions were Y1 and Y3 to Y6⁶; and Y11 and Y12¹⁰. We have identified Y1, Y3, Y4, Y11 and Y12 in our reconstruction, and have not found any new Y types. Y1, Y11 and Y12 have the majority of their synapses in the lobula plate, and are assigned to the motion subsystem. Y3 and Y4 have few synapses in the lobula plate, and are assigned to the object subsystem (Fig. 2). Y3 is more numerous (~300 cells) than Y4, and is the only Y type that is predicted cholinergic.

Tlp. A Tlp neuron projects from the lobula plate to the lobula. Tlp1 to Tlp5 were defined first⁶, and Tlp11 to Tlp14 were defined later on¹⁰. We have identified Tlp1, Tlp4, Tlp5 and Tlp14. We propose that the names Tlp11, Tlp12 and Tlp13 should be retired¹⁰, as these types can now be unambiguously identified with Tlp5, Tlp1 and Tlp4, respectively.

Interneurons

A local interneuron is defined as being completely confined to a single neuropil (Fig. 1b). Interneurons make up the majority of types, but a minority of cells (Fig. 1e). Lai is the only lamina interneuron. Dm and Pm interneurons⁶ stratify in the distal or proximal medulla, respectively. We have more than doubled the number of Pm types, and slightly increased the number of Dm types. We introduce the Sm family, which is almost completely new and contains more types than any other family (Fig. 1f). Li and LPi interneurons stratify in the lobula or lobula plate, respectively. Interneurons are usually amacrine and presumed inhibitory (GABA or glutamate), but some are tangential or cholinergic. Interneurons are often wide field but some are narrow field.

Dm. Dm1 to Dm8⁶; Dm9 and 10²⁷; and Dm11 to Dm20⁸⁵ were previously defined. We do not observe Dm5 and Dm7, consistent with a previous study⁸⁵. Most types are predicted to secrete glutamate or GABA, but there are also a few cholinergic types (Supplementary Data 1). To Dm3p and Dm3q^{61,62,85}, we added a third type, Dm3v (Supplementary Data 2). We split Dm8 into Dm8a and Dm8b (see the ‘Correspondences with molecular–morphological types’ section).

DmDRA. The DRA differs from the rest of the retina in its organization of inner photoreceptors. Photoreceptors in non-DRA and DRA differ in their axonal target layers and output cell types^{54,86}. Specifically, DRA-R7 connects with DmDRA1, whereas DRA-R8 connects to DmDRA2^{54,87}. These distinctive connectivity patterns result in DmDRA1 and DmDRA2 types exhibiting an arched coverage primarily in the M6 layer of the dorsal medulla (Fig. 9b). R7-DRA and R8-DRA are incompletely annotated at present, and this will be rectified in a future release. DmDRA1

Article

receives R7 input, but sits squarely in M7. This could be regarded as an Sm type, but we have chosen not to change the name for historical reasons.

Pm. Pm1, 1a and 2⁶ were each split into two types. Pm3 and 4 remain as previously defined⁸⁵. We additionally identified six new Pm types, for a total of 14 Pm types, numbered Pm01 to Pm14 in order of increasing average cell volume. The new names can be distinguished from the old ones by the presence of leading zeros. All are predicted GABAergic. Pm1 was split into Pm06 and Pm04, Pm1a into Pm02 and Pm01, and Pm2 into Pm03 and Pm08.

Sm. Dm and Pm interneurons are defined⁶ to stratify on the distal or proximal side, respectively, of the serpentine layer (M7) of the medulla. Many interneuron types turn out to have significant stratification in the serpentine layer, and these borderline cases constitute a large new Sm family of interneurons, almost all new. They have been named Sm01 to Sm43, mostly in order of increasing average cell volume. The Sm family includes types recently named medulla tangential intrinsic⁴². We avoid using this term indiscriminately because some Sm types are tangential while others are amacrine. Some Sm types spill over from M7 into the distal or proximal medulla, and a few reach from M7 to more distant medulla layers.

Sm stratification in M7 has functional implications. First, Sm types are positioned to communicate with the medulla tangential (Mt) cells and other boundary types that are important conduits of information in and out of the optic lobe (Supplementary Data 5). Second, Sm types are positioned to communicate with the inner photoreceptor terminals, which are in M6 or at the edge of M7. Consequently many Sm types are involved in the processing of chromatic stimuli, and end up being assigned to the colour subsystem.

The Sm family more than doubles the number of medulla interneuron types, relative to the old scheme with only Pm and Dm. The Sm family might be related to the M6-LN class of neuron previously defined⁸⁸. The correspondence is unclear because M6-LN neurons are defined to stratify in M6, while Sm mainly stratifies in M7. But some Sm types stratify at the border between M6 and M7, and therefore could be compatible with the M6-LN description.

Li. After two lobula intrinsic types (Li1 and Li2) were initially defined⁶, 12 more (Li11 to 20 and mALC1 and mALC2) were identified by the hemibrain reconstruction⁹. Of these, we have confirmed Li2, Li12, Li16, mALC1 and mALC2. We identified 21 additional Li types, but have not been able to make conclusive correspondences with previously identified types. As mentioned earlier, we transfer Tm23 and Tm24⁶ from the Tm to the Li family. This amounts to a total of 33 Li types, which have been named Li01 to Li33 in order of increasing average cell volume.

Collisions with Li1 and Li2⁶ are avoided by the presence of leading zeros in our new names. The hemibrain names Li11 to Li20 and mALC1 and mALC2⁹ have been used by few or no publications, so there is little cost associated with name changes. In any case, we were only able to establish conclusive correspondences for a minority of the hemibrain Li11 to Li20 types, which are detailed in Supplementary Data 1. Hemibrain Li12 is now Li27 (jigsaw pair), and hemibrain Li16 is now Li28 (pair of full-field cells). Hemibrain Li11 was split into Li25 and Li19 (see the 'Morphological variation' section). Hemibrain Li18 was split into three types: (1) Li08 covers the whole visual field. (2) Li04 covers a dorsal region except for the dorsal rim. It is tangentially polarized, with the axon more dorsal than the dendrites. Both axon and dendrite point in the posterior direction, perpendicular to the direction of polarization. The dendrites are more thickly stratified than the axon. (3) Li07 has ventral coverage only. The axons are in one layer, and extend over a larger area than the dendrites, which hook around into another layer and are mostly near the ventral rim.

We considered merging Li04 and Li07, but their connectivity is quite different. Furthermore, in a hierarchical agglomerative clustering, Li07 would merge with Li08 before Li04.

LPi. LPi names were originally based on stratification in layers 1 to 4 of the lobula plate, including LPi1-2 and 2-1¹⁰; LPi3-4 and 4-3⁸; and LPi2b and LPi34-12¹⁰ (we are not counting fragments for which correspondences are not easy to establish). We have added nine new types, for a total of 15 LPi types.

Now that LPi types have multiplied, stratification is no longer sufficient for naming. The naming system could be salvaged by adding letters to distinguish between cells of different sizes. For example, LPi15 and LPi05 could be called LPi2-1f and LPi2-1s, where 'f' means full-field and 's' means small. For simplicity and brevity, we instead chose the names LPi01 to LPi15, in order of increasing average cell volume. Correspondences with old stratification-based names are detailed in Codex.

Cross-neuropil tangential and amacrine

Most types that span multiple neuropils are columnar. One tangential type that spans multiple neuropils inside the optic lobe was previously described: Lat has a tangential axon that projects from the medulla to the lamina⁶. There is some heterogeneity in the Lat population, as reflected in the large type radius (Extended Data Fig. 3a). We have decided to leave splitting for future work, as Lat has many dense core vesicles that are presently unannotated.

Here we introduce two new families of cross-neuropil types that are tangential (MLt1-8 and LMt1-4), and one that is amacrine (LMa1-5). Along with two new tangential families (PDT, LLPt) that contain only single types, and the known CT1 and Am1 types, that is a total of 21 cross-neuropil types that are non-columnar (Fig. 1c). Each of the new types (except PDT with 6 cells) contains between 10 and 100 cells.

The tangential types connect neuropils within one optic lobe and do not leave the optic lobe. Our usage of the term 'tangential' focuses on axonal orientation only. It should not be misunderstood to imply a wide-field neuron that projects out of the optic lobe, which is the case for the well-known lobula plate tangential cells or lobula tangential cells. The term 'tangential' presupposes that we can identify an axonal arbour for the cell (see the 'Axon versus dendrite' section).

PDT. We found one tangential type that projects from proximal to distal medulla (Supplementary Data 2).

MLt. ML1 was previously identified⁴² as a tangential neuron projecting from the medulla to lobula. We will refer to this type as MLt1, and have discovered more types of the same family, MLt2 to MLt8. MLt1 and MLt2 dendrites span both distal and proximal medulla, and MLt3 dendrites are in the distal medulla, so MLt1 to MLt3 receive L input (Supplementary Data 2 and 5). MLt4 dendrites are in the proximal medulla (Supplementary Data 2). MLt5 to MLt8 have substantial arbour overlap with the serpentine layer M7 (Supplementary Data 2), and are therefore connected with many Sm types to be discussed later on (Supplementary Data 5). Interaction between MLt types is fairly weak, with the exception of MLt7 to MLt5 (Supplementary Data 5). MLt7 and MLt8 are restricted to the dorsal and dorsal rim areas.

LMt. We identified four tangential types (LMt1 to LMt4) that project from the lobula to medulla. Their axonal arbours are all in the proximal medulla (Supplementary Data 2), thinly stratified near layer M7, so they have many Pm targets (Supplementary Data 5). Only LMt4 exhibits partial coverage.

LLPt. We discovered one tangential type that projected from the lobula to lobula plate, and called it LLPt. This is just a single type, rather than a family.

LMa. We discovered four amacrine types that extend over the lobula and medulla. LMa1 to LMa4 are coupled with T2, T2a and T3, and LMa4 and LMa3 synapse onto T4 and T5 (Supplementary Data 5). The LMa family could be said to include CT1, a known amacrine cell that also extends over both the lobula and medulla. However, the new LMa types consist of smaller cells that each cover a fraction of the visual field, whereas CT1 is a wide-field cell.

MLLPa. Am1 was defined¹⁰ as a wide-field amacrine cell that extends over the medulla, lobula and lobula plate. We found no other amacrine types like Am1 with such an extended reach.

Correspondences with molecular–morphological types

Tm5. Tm5a, Tm5b and Tm5c were originally defined by single-cell anatomy and Ort expression^{7,50}. Tm5a is cholinergic, the majority of the cells extend one dendrite from M6 to M3, and often has a ‘hook’ at the end of its lobula axon. Tm5b is cholinergic, and most (~80%) cells extend several dendrites from M6 to M3. Tm5c is glutamatergic and extends its dendrites up to the surface of the distal medulla. Three of our types are consistent with these morphological descriptions (Fig. 7a), and receive direct input from inner photoreceptors R7 or R8.

Dm8. Molecular studies previously divided Dm8 cells into two types (yDm8 and pDm8), depending on whether or not they express DIPY^{51,53}. Physiological studies demonstrated that yDm8 and pDm8 have differing spectral sensitivities⁸⁹. The main dendrites of yDm8 and pDm8 were found to connect with R7 in yellow and pale columns, respectively. On the basis of its strong coupling with Tm5a, our Dm8a probably has some correspondence with yDm8, which is likewise selectively connected with Tm5a^{51,53}. It is not yet clear whether there is a true one-to-one correspondence of yDm8 and pDm8 with Dm8a and Dm8b. It is the case that Dm8a and Dm8b strongly prefer to synapse onto Tm5a and Tm5b, respectively. However, Tm5a and Tm5b are not in one-to-one correspondence with yellow and pale columns. Rather, the main dendritic branch of Tm5a is specific to yellow columns, while the main dendritic branches of Tm5b are found in both yellow and pale columns⁵⁰. Furthermore, Dm8a and Dm8b cells are roughly equal in number, while the yDm8:pDm8 ratio is expected to be substantially greater than one^{51,53}, like the ratio of yellow to pale columns. Thus, the correspondence of Dm8a and Dm8b with yDm8 and pDm8 is still speculative. The yellow/pale issue should be revisited in the future when accurate photoreceptor synapses become available (see the ‘Reconstruction accuracy and completeness’ section).

Additional validation. HHMI Janelia has released a preprint detailing cell types in the right optic lobe of an adult male *Drosophila* brain⁹⁰. The list of intrinsic cell types is almost identical to ours, apart from naming differences in new types. Since our original submission, we have completed typing of the left optic lobe of our female fly brain reconstruction, and the results match the right optic lobe analysed in the present paper. These replications in another hemisphere of the same brain and in the brain of another individual fly provide additional validation of our findings.

Reporting summary

Further information on research design is available in the Nature Portfolio Reporting Summary linked to this article.

Data availability

The present work is based on version 783 of the FlyWire connectome, which incorporates proofreading up to 30 September 2023 (stats are shown in Extended Data Table 3). A static snapshot of the data used in this work is available in a dedicated repository at GitHub

(<https://github.com/murthylab/visual-system-parts-list>). This repository contains the proofread cell IDs, their types, connectivity (broken up by regions), as well as aggregate information such as type summary table, type connectivity table and raw data used to make the figures, including CSV files for each of the wiring diagrams. Most up to date information can be browsed, searched and downloaded at the FlyWire Codex (<https://codex.flywire.ai>). Codex will also provide access to future releases of the FlyWire connectome, incorporating updated proofreading and annotations. Pre-release annotations can be downloaded directly from the Codex download portal (<https://codex.flywire.ai/api/download>). Pre-release proofread cells are available through CAVEclient^{24,91}.

Code availability

Code for making the figures along with additional data analysis tools are also included/linked in GitHub repositories (<https://github.com/murthylab/visual-system-parts-list> and <https://github.com/hsseung/OpticLobe.jl>). Most up to date information can be browsed, searched and downloaded at the FlyWire Codex (<https://codex.flywire.ai>).

77. Buhmann, J. et al. Automatic detection of synaptic partners in a whole-brain *Drosophila* electron microscopy data set. *Nat. Methods* **18**, 771–774 (2021).
78. Takemura, S.-Y., Lu, Z. & Meinertzhagen, I. A. Synaptic circuits of the *Drosophila* optic lobe: the input terminals to the medulla. *J. Comp. Neurol.* **509**, 493–513 (2008).
79. Kim, J. S. et al. Space-time wiring specificity supports direction selectivity in the retina. *Nature* **509**, 331–336 (2014).
80. Davis, F. P. et al. A genetic, genomic, and computational resource for exploring neural circuit function. *eLife* **9**, e50901 (2020).
81. Kohl, M., Wiese, S. & Warscheid, B. Cytoscape: software for visualization and analysis of biological networks. *Methods Mol. Biol.* **696**, 291–303 (2011).
82. Marc, R. E., Anderson, J. R., Jones, B. W., Sigulinsky, C. L. & Lauritzen, J. S. The All amacrine cell connectome: a dense network hub. *Front. Neural Circuits* **8**, 104 (2014).
83. Hasegawa, E. et al. Concentric zones, cell migration and neuronal circuits in the *Drosophila* visual center. *Development* **138**, 983–993 (2011).
84. Morante, J. & Desplan, C. The color-vision circuit in the medulla of *Drosophila*. *Curr. Biol.* **18**, 553–565 (2008).
85. Nern, A., Pfeiffer, B. D. & Rubin, G. M. Optimized tools for multicolor stochastic labeling reveal diverse stereotyped cell arrangements in the fly visual system. *Proc. Natl Acad. Sci. USA* **112**, E2967–E2976 (2015).
86. von Philipsborn, A. & Labhart, T. A behavioural study of polarization vision in the fly, *Musca domestica*. *J. Comp. Physiol. A* **167**, 737–743 (1990).
87. Hardcastle, B. J. et al. A visual pathway for skylight polarization processing in *Drosophila*. *eLife* **10**, e63225 (2021).
88. Chin, A.-L., Lin, C.-Y., Fu, T.-F., Dickson, B. J. & Chiang, A.-S. Diversity and wiring variability of visual local neurons in the *Drosophila* medulla M6 stratum. *J. Comp. Neurol.* **522**, 3795–3816 (2014).
89. Li, Y. et al. Neural mechanism of spatio-chromatic opponency in the *Drosophila* amacrine neurons. *Curr. Biol.* **31**, 3040–3052 (2021).
90. Nern, A. et al. Connectome-driven neural inventory of a complete visual system. Preprint at *bioRxiv* <https://doi.org/10.1101/2024.04.16.589741> (2024).
91. Dorkenwald, S. et al. CAVE: Connectome Annotation Versioning Engine. *Nat. Methods* <https://doi.org/10.1038/s41592-024-02426-z> (2024).

Acknowledgements We thank all those who proofread optic lobe intrinsic neurons²⁴; A. Nern and M. Reiser for educating and advising the FlyWire community members who engaged in annotation of visual neurons, and for sharing correspondences with optic lobe cell types identified at HHMI Janelia; the members of the FAFB tracing community for supportive and open sharing of methods and data, especially the FAFB optic lobe working group; Y. Kurmangaliyev for his comments on the manuscript; R. Behnia and K. Zinn for advice about colour; R. Behnia and M. Silies for feedback about visual motion detection pathways; J. Wiggins, G. McGrath and D. Barlieb for computer system administration; M. Hussein for project administration; and J. Maitin-Shepard for Neuroglancer. M.M. and H.S.S. acknowledge support from the National Institutes of Health (NIH) BRAIN Initiative RF1 MH117815, RF1 MH129268 and U24 NS126935, from the Princeton Neuroscience Institute, as well as assistance from Google. D.G. and S.S.K. were supported by the National Eye Institute of the NIH (DP2EY032737), Searle Scholars Program, Sloan Research Fellowship and Klingenstein-Simons Fellowship in Neuroscience. E.K., G.S. and M.F.W. were supported by Deutsche Forschungsgemeinschaft (DFG) grant WE 5761/4-1, SPP 2205, FOR 5289 and AFOSR grant FA9550-19-1-7005.

Author contributions D.G., E.K. and G.S. annotated cells under the supervision of S.S.K. and M.F.W. M.S. and A.R.S. recruited, trained and managed citizen scientists with help from E.K., K.K. annotated cells and created computational cell typing tools for use by the community. S.-c.Y. trained and managed D.B., A.T.B., J.G., J.H., B.S., K.P.W. and R.W. to annotate the remaining known cell types and identify and annotate new types. A.M. and H.S.S. created semiautomated cell typing tools. A.M. and H.S.S. carried out the final automated stage of typing. A.M. verified

Article

types with predicates. H.S.S. verified types with 2D projections. S.-c.Y., H.S.S. and M.M. devised type family names. A.M. and H.S.S. defined and characterized subsystems. A.M. drew wiring diagrams. S.S.K., M.F.W., M.M. and H.S.S. identified implications for visual function. A.T.B., J.G., J.H., B.S., K.P.W., R.W., S.-c.Y., A.M. and H.S.S. created figures. K.K., M.S., A.R.S., A.M., S.-c.Y., S.S.K., M.M. and H.S.S. wrote the text. M.M. and H.S.S. supervised the project. Members listed in the FlyWire consortium made at least ten annotations in the optic lobe.

Competing interests H.S.S. declares financial interests in Zetta AI. The other authors declare no competing interests.

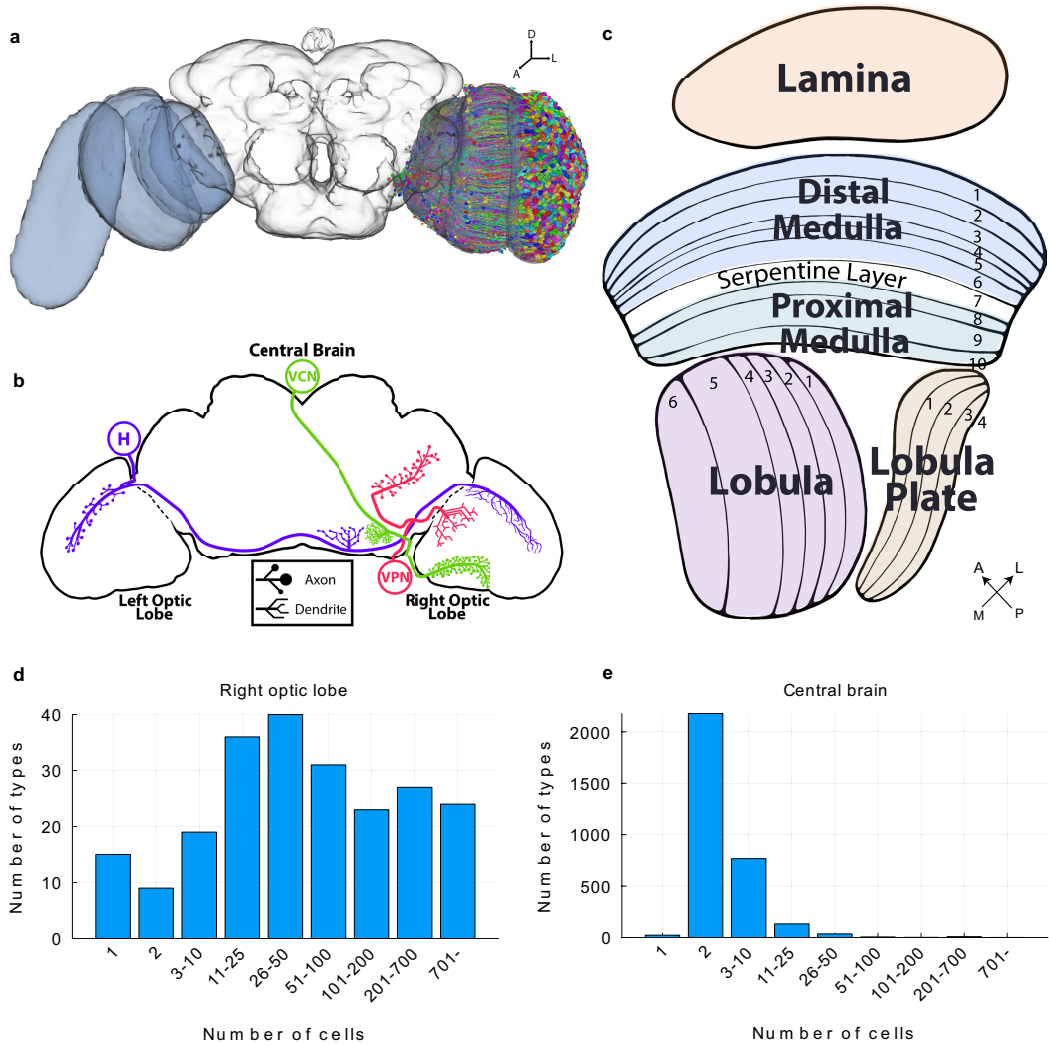
Additional information

Supplementary information The online version contains supplementary material available at <https://doi.org/10.1038/s41586-024-07981-1>.

Correspondence and requests for materials should be addressed to Mala Murthy or H. Sebastian Seung.

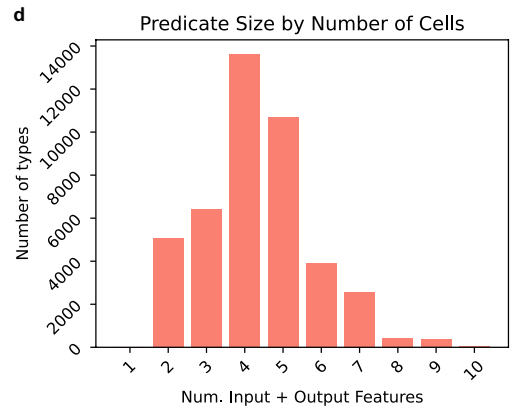
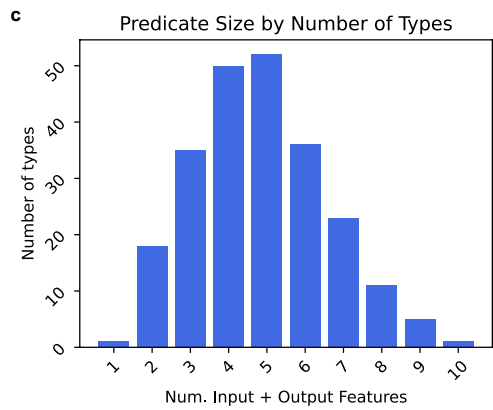
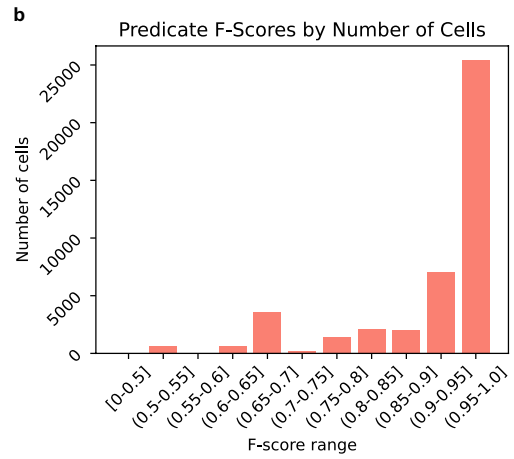
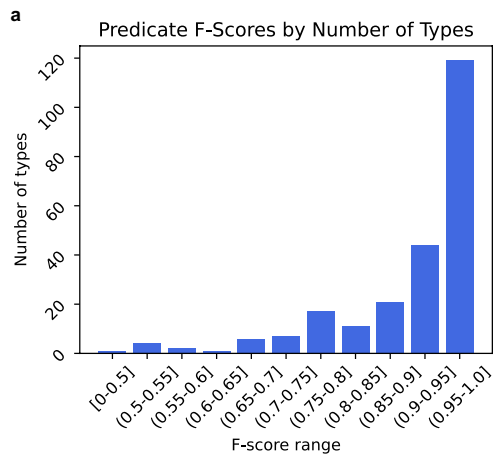
Peer review information Nature thanks Dierk Reiff, Aref Zarin and the other, anonymous, reviewer(s) for their contribution to the peer review of this work. Peer reviewer reports are available.

Reprints and permissions information is available at <http://www.nature.com/reprints>.



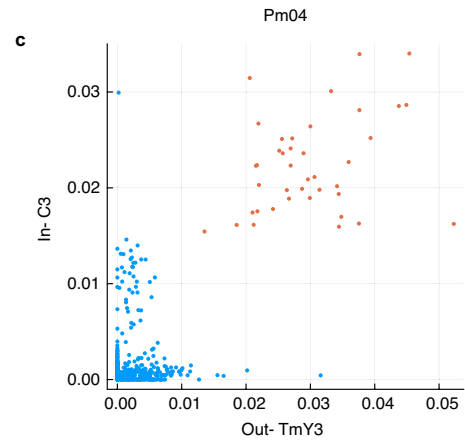
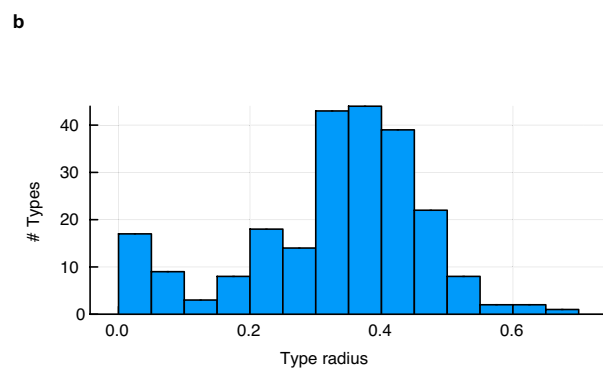
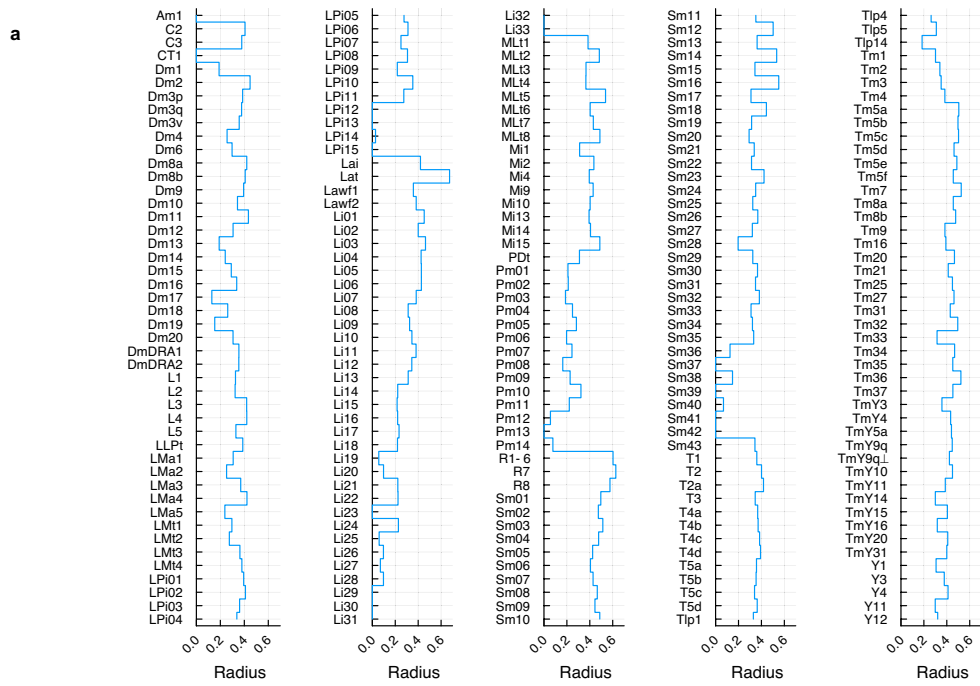
Extended Data Fig. 1 | Cell counts of types in optic lobe versus central brain. **a**, *Drosophila* central brain and flanking optic lobes. Neurons intrinsic to the optic lobes (colours) are the subject of this study. (A: Anterior, L: Lateral, D: Dorsal). **b**, Boundary cells straddle the optic lobe and central brain (H: heterolateral, VCN: visual centrifugal neuron; VPN: visual projection neuron). **c**, Optic lobe main neuropils (brain regions) and their layering (A: Anterior, L: Lateral, M: Medial, P: Posterior). **d**, Distribution of number of **optic lobe**

types by bucketed unilateral cardinality. Each bar represents types whose cardinality (number of cells) is within the specified range. Most types contain 10+ cells, and a significant portion of types contain hundreds of cells. **e**, Distribution of the number of **central brain** types by bucketed bilateral cardinality. In contrast to the optic lobe, here most types have cardinality 2 (cell and its mirror twin in the opposite hemisphere).



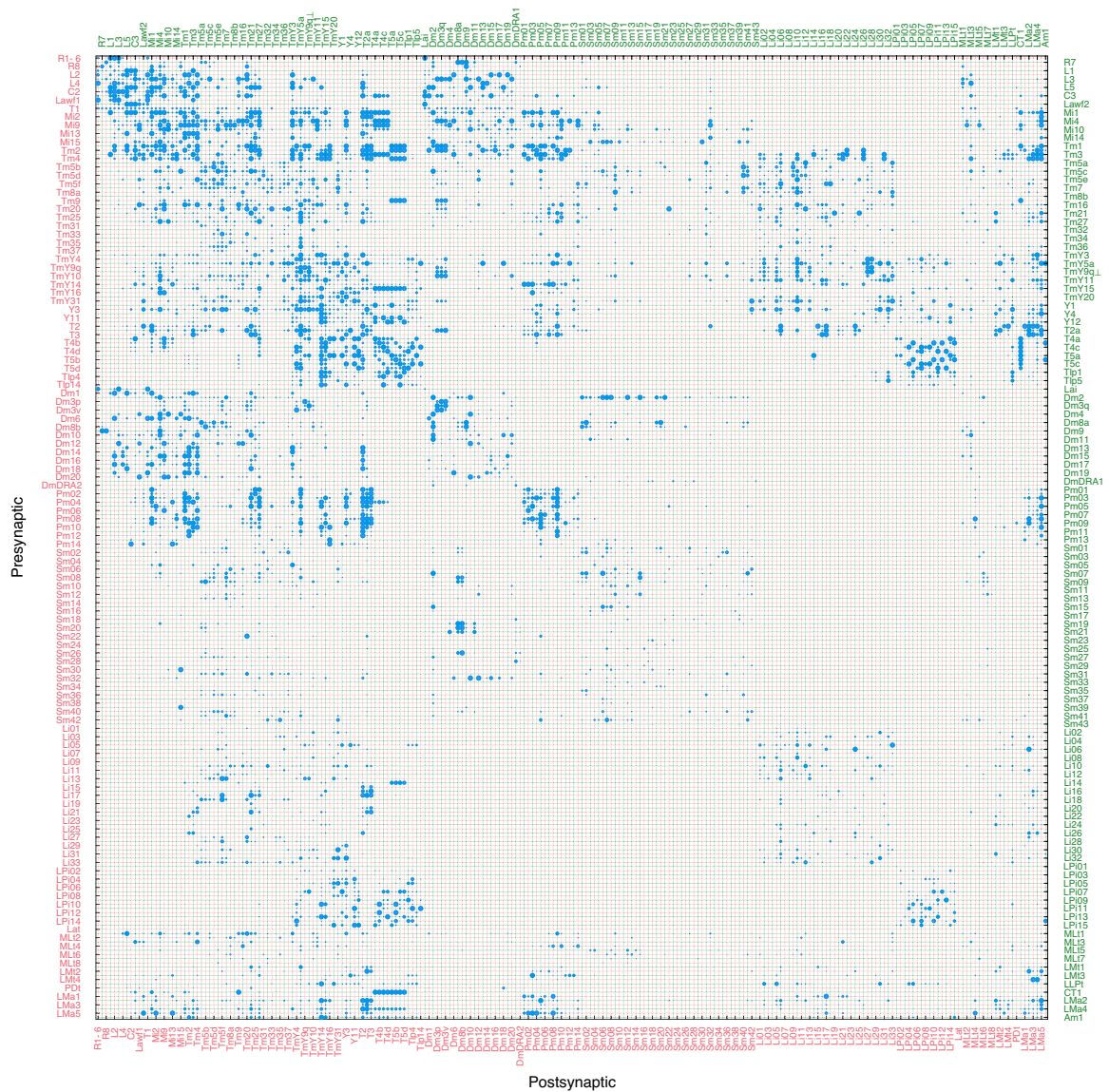
Extended Data Fig. 2 | Logical connectivity predicate statistics. **a**, Number of types by predicate F-score range. **b**, Number of cells by their types' predicate F-score range. **c**, Number of types by predicate size, that is the sum of the

number of input features and output features participating in the binary conjunction. **d**, Number of cells by their types' predicate size.



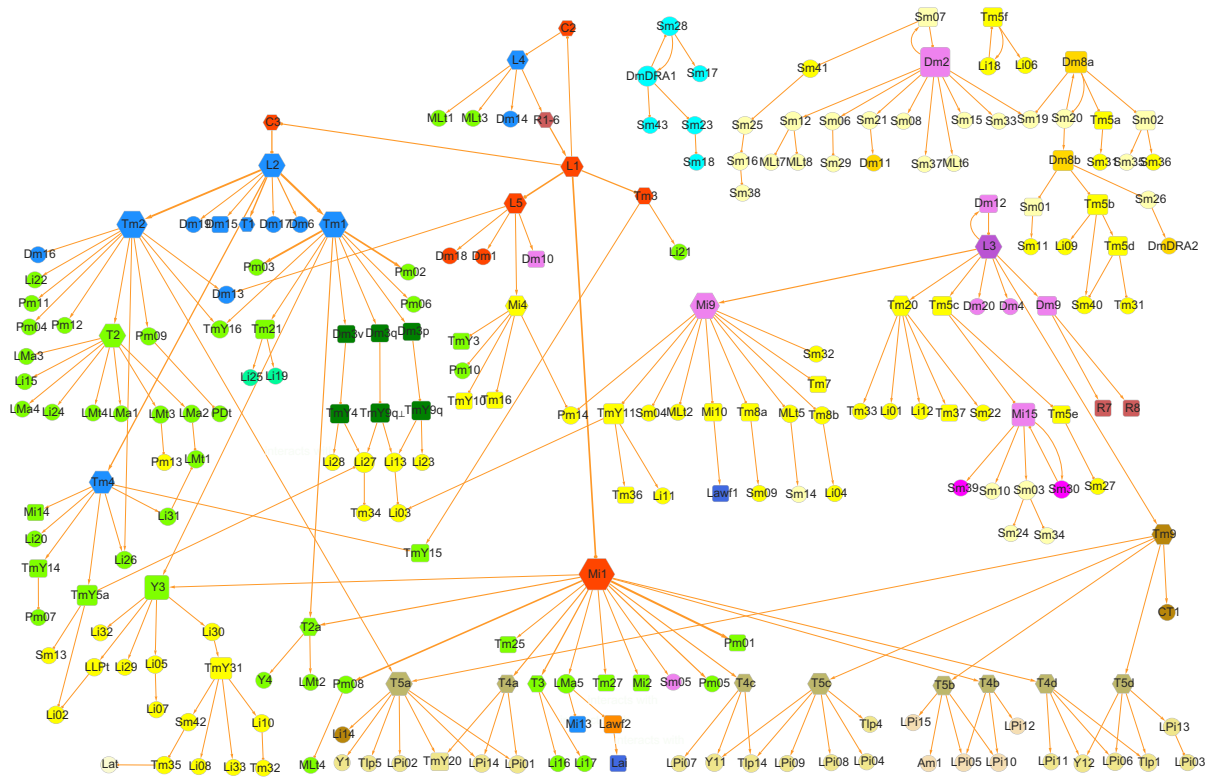
Extended Data Fig. 3 | Discrimination in high and low dimensions. a, Radii of types in high-dimensional feature space. **b,** Histogram of type radii in high-dimensional feature space. **c,** Example 2D discriminator for Pm04 cells (red)

versus other Pm types (blue). On the X and Y axis are the fraction of their inputs/ outputs in C3/ TmY3 respectively.



Extended Data Fig. 4 | Type-to-type connectivity as a matrix. The number of synapses from one cell type to another is indicated by the area of the corresponding dot. Dot area saturates above 3600 synapses, to make weaker

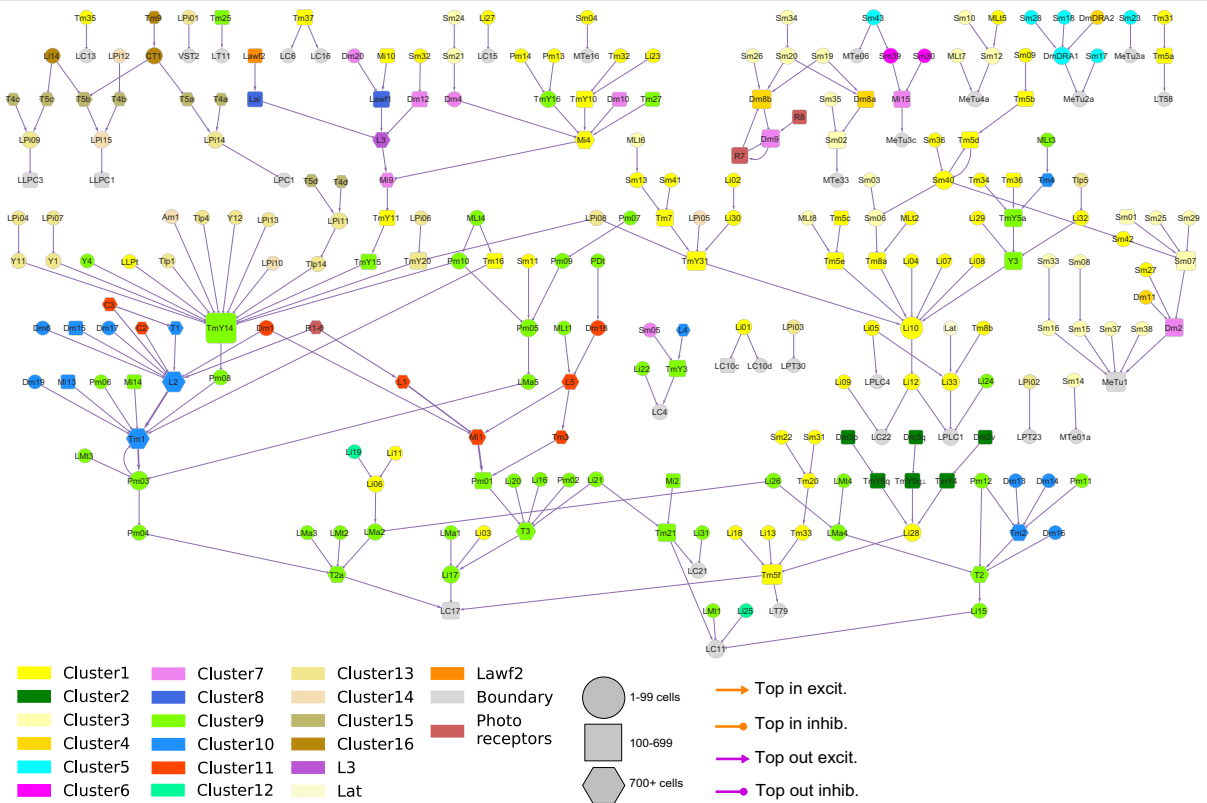
connections visible. For legibility, the type names alternate between left and right edges, and bottom and top edges, and are colour coded to match the lines that are guides to the eye.



- | | | | | | | |
|--|--|--|--|---|--|---|
| Cluster1 | Cluster7 | Cluster13 | Lawf2 | Boundary | 1-99 cells | → Top in excit. |
| Cluster2 | Cluster8 | Cluster14 | Photo receptors | 100-699 | → Top in inhib. | → Top out excit. |
| Cluster3 | Cluster9 | Cluster15 | L3 | 700+ cells | → Top out inhib. | |
| Cluster4 | Cluster10 | Cluster16 | Lat | | | |

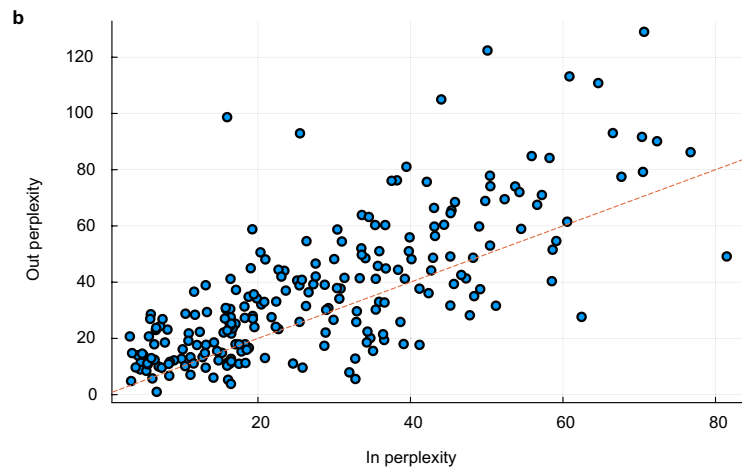
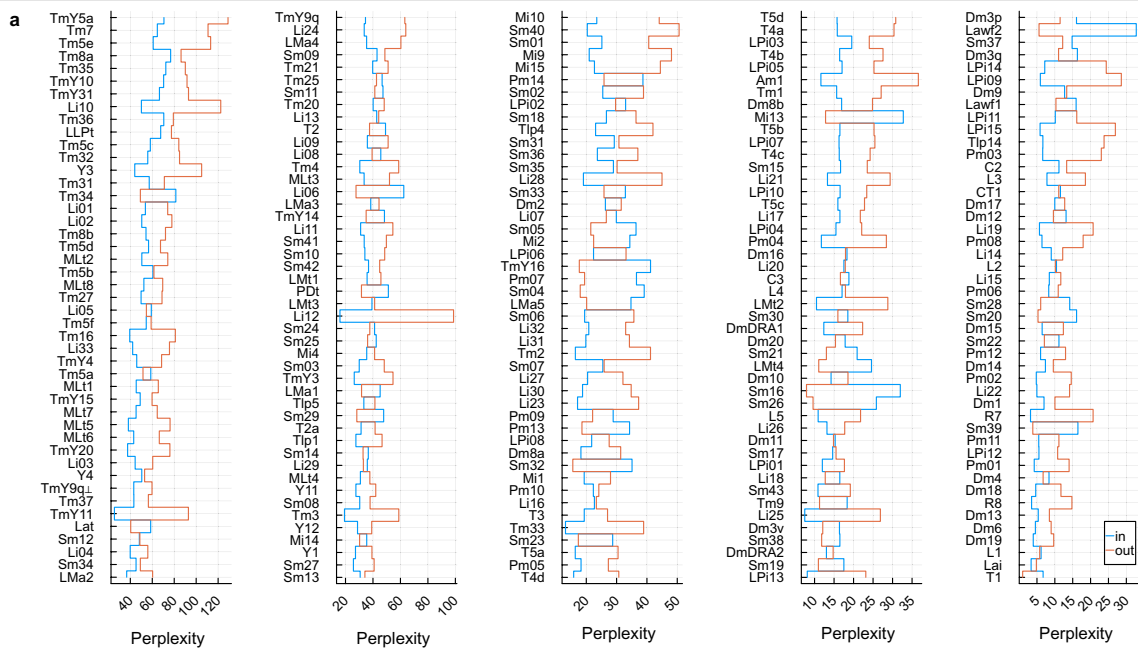
Extended Data Fig. 5 | Wiring diagram of cell types (top input connections). Wiring diagram depicting top inputs for all cell types intrinsic to the optic lobe, as well as photoreceptors. Node size encodes the number of drawn

connections, highlighting "hub" inputs. Node colour indicates membership in the subsystems defined in the text. See legend and additional explanation in Fig. 3 and Methods.



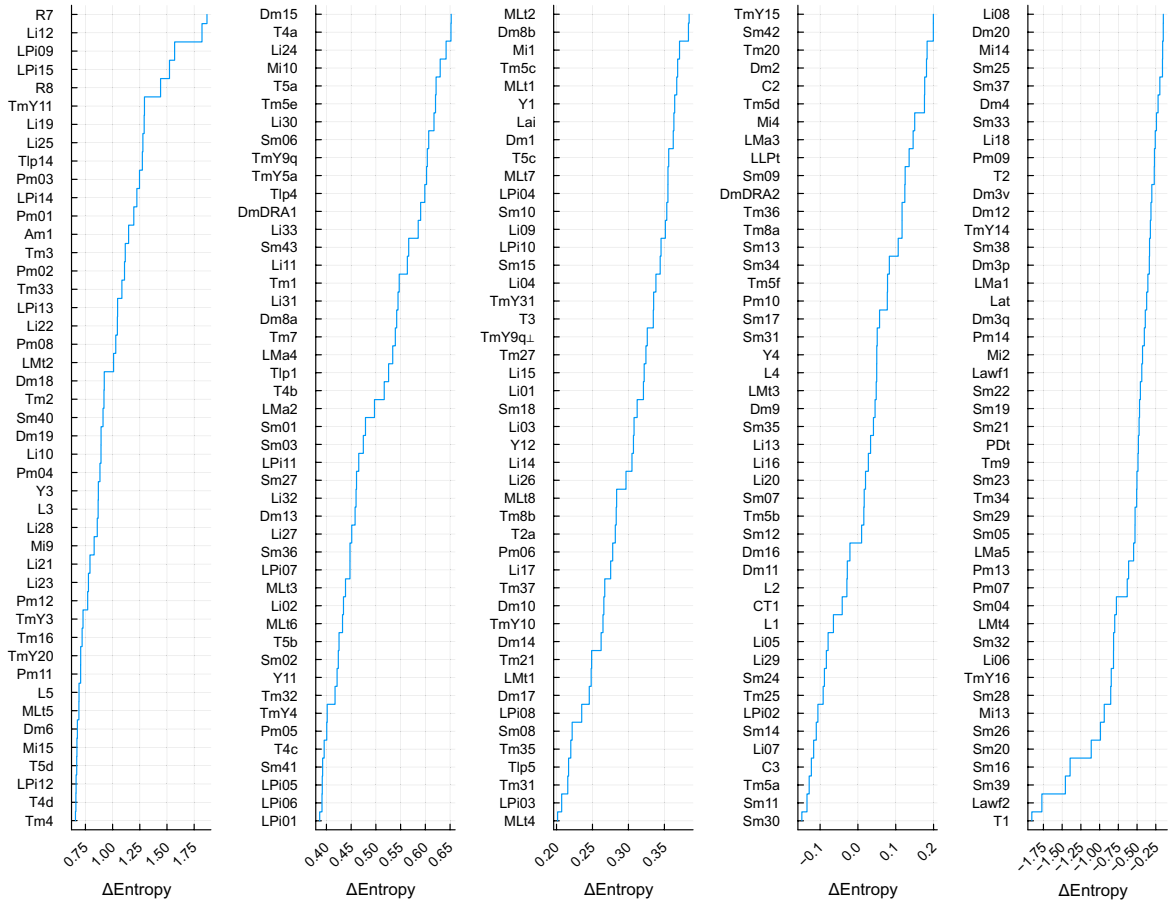
Extended Data Fig. 6 | Wiring diagram of cell types (top output connections). Wiring diagram depicting top outputs for all types intrinsic to the optic lobe. Node size encodes the number of drawn connections, highlighting “hub” outputs.

Node colour indicates membership in the subsystems defined in the text. See legend and additional explanation in Fig. 3 and Methods.



Extended Data Fig. 7 | Input and output perplexity. a, Input (blue) and output (red) perplexities. Types are ordered by the product of input and output perplexities. **b,** Output and input perplexity are correlated. Out-perplexity

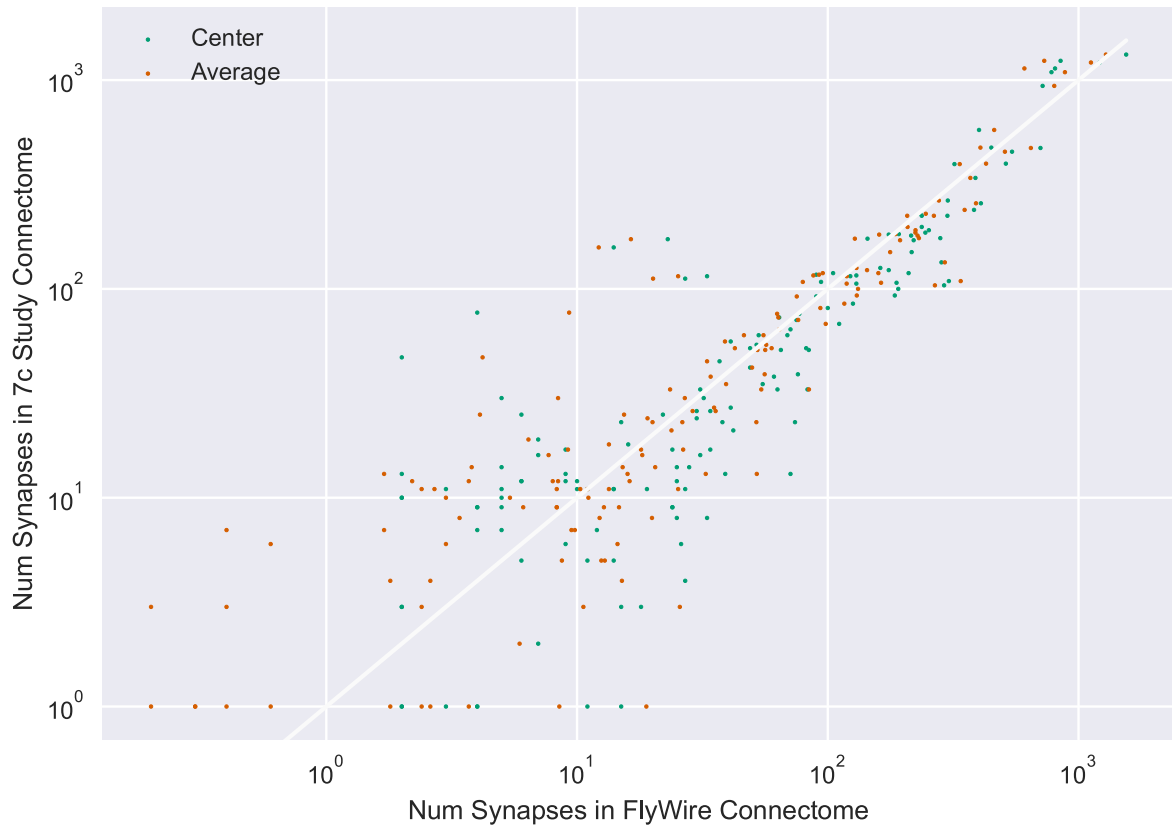
tends to exceed in-perplexity (more points above red line drawn to indicate equality of out and in).



Extended Data Fig. 8 | Difference between output and input entropies. The difference between output and input entropies (units of nats) quantifies the degree of divergence or convergence. This difference is equivalent to the logarithm of the ratio of out- and in-perplexities. The connectivity of the top

types (top left) is more divergent, as the output entropy is greater than the input entropy. The connectivity of the bottom types (bottom right) is more convergent, as the input entropy is greater than the output entropy.

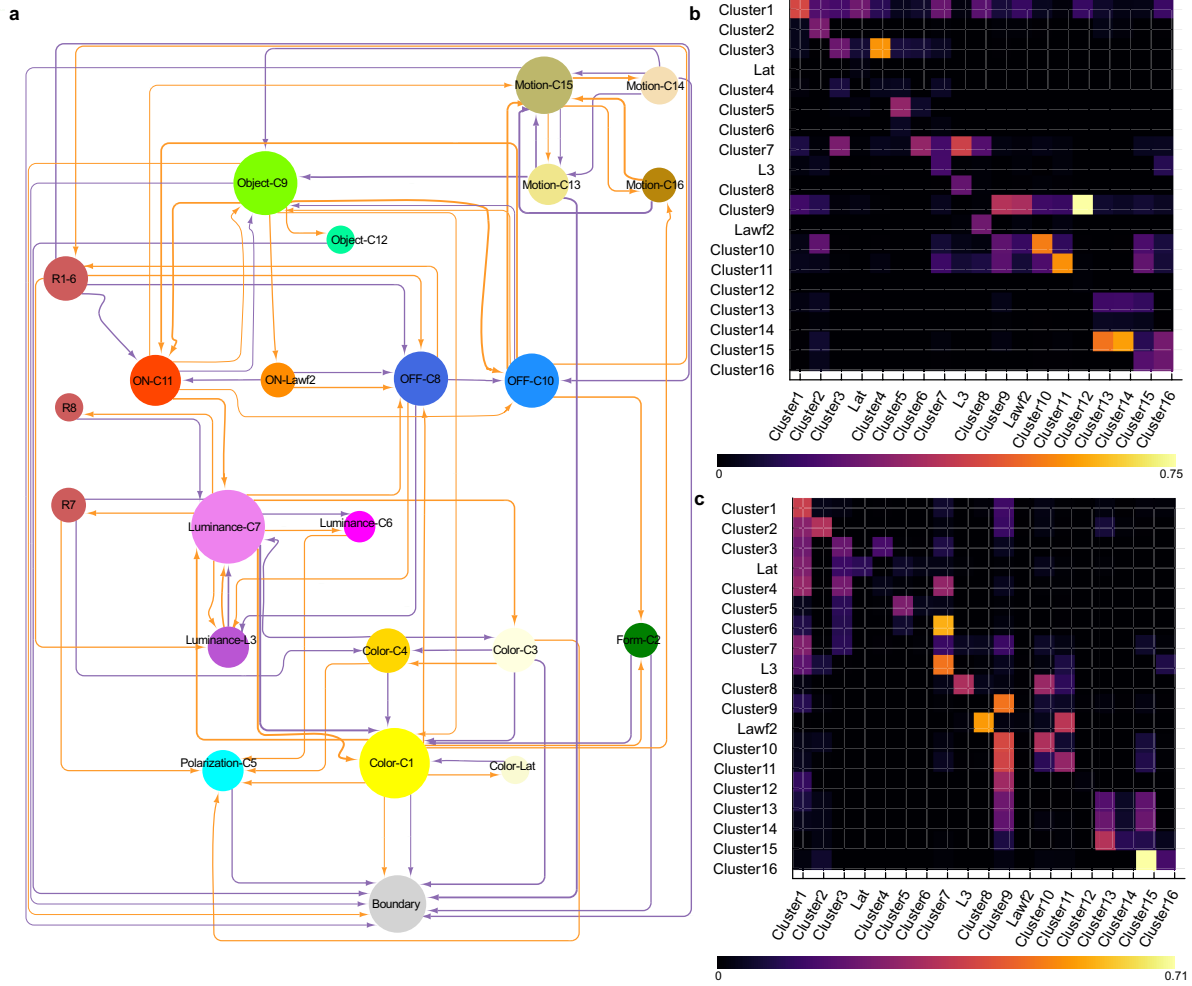
Comparison To 7 Column Study (log scale)



Extended Data Fig. 9 | Comparison with seven-column reconstruction.

We compared the synapse counts between type pairs to the corresponding synapse counts in the seven-column reconstruction²⁸. The types included in the reconstruction are: C2, C3, L1, L2, L3, L4, L5, Mi1, Mi4, Mi9, R7, R8, T1, T2, T2a, T3, Tm1, Tm2, Tm20 and Tm9. For this comparison we used the centre column and its surrounding 6 columns from our dataset (green dots) as well as

the average of 100 columns and their surrounding ones (red dots). Each point represents an ordered pair of types, and the number of synapses between them in the FlyWire connectome (X) and the seven-column reconstruction (Y). Correlation coefficients are 0.952 for the centre + 6 columns and 0.954 for the average.



Extended Data Fig. 11 | Wiring diagram of type clusters (major input and output connections). **a**, Wiring diagram depicting major input and output connections between type clusters of Fig. 2c. Node size encodes the number of drawn connections. For each cluster major inputs are drawn as orange inbound edges, and major outputs as purple outbound edges. Major input/output connection is defined as having at least 50% synapses relative to top input/

output connection respectively, excluding loops. **b**, Heatmap is strength of connectivity (fraction of input synapses to post) from pre- to post-synaptic cluster. Heatmap maximum of 0.75. **c**, Strength of connectivity (fraction of output synapses from pre) from pre- to post-synaptic cluster. Heatmap maximum of 0.71.

Article

Extended Data Table 1 | Type families and their properties

Family	Affinity	Linkage	Types	Cells	Trans	Neuropils
Centrifugal	Cross Neuropil	Axon Bearing / Columnar	2	1511	GABA	ME → ME, LA
Distal Medulla	Neuropil Intrinsic	Non-columnar	21	3284	GLUT	ME → ME
Distal Medulla Dorsal Rim Area	Neuropil Intrinsic	Non-columnar	2	35	GLUT	ME → ME
Lamina Intrinsic	Neuropil Intrinsic	Non-columnar	1	231		LA → LA
Lamina Monopolar	Cross Neuropil	Axon Bearing / Columnar	5	3831	ACH	ME, LA → ME
Lamina Tangential	Neuropil Intrinsic	Axon Bearing / Tangential	1	6		ME, LO, AME, PLP → LO
Lamina Wide Field	Cross Neuropil	Axon Bearing / Columnar	2	320	ACH	ME → LA
Lobula Intrinsic	Neuropil Intrinsic	Non-columnar	33	761	GABA	LO → LO
Lobula Lobula Plate Tangential	Cross Neuropil	Axon Bearing / Tangential	1	36	GABA	LO, LOP → LO, LOP
Lobula Medulla Amacrine	Cross Neuropil	Amacrine	6	134	GABA	ME, LO → ME, LO
Lobula Medulla Tangential	Cross Neuropil	Axon Bearing / Tangential	4	88	GLUT	LO, ME → LO, ME
Lobula Plate Intrinsic	Neuropil Intrinsic	Non-columnar	15	363	GLUT	LOP → LOP
Medulla Intrinsic	Neuropil Intrinsic	Axon Bearing / Columnar	8	3922	ACH	ME → ME
Medulla Lobula Lobula Plate Amacrine	Cross Neuropil	Amacrine	1	1	GABA	LOP, ME, LO → LOP, LO, ME
Medulla Lobula Tangential	Cross Neuropil	Axon Bearing / Tangential	8	295	ACH	ME, LO → ME, LO
Photo Receptors	Neuropil Intrinsic	Axon Bearing / Columnar	3	4751		ME, LA → LA, ME
Proximal Distal Medulla Tangential	Neuropil Intrinsic	Axon Bearing / Tangential	1	6	DA	ME → ME
Proximal Medulla	Neuropil Intrinsic	Non-columnar	14	599	GABA	ME → ME
Serpentine Medulla	Neuropil Intrinsic	Non-columnar	43	1488	GABA	ME → ME
T Neuron	Cross Neuropil	Axon Bearing / Columnar	12	9252	ACH	ME, LO, LOP → LOP, LO, ME
Translobula Plate	Cross Neuropil	Axon Bearing / Columnar	4	172	GLUT	LOP → LOP, LO
Transmedullary	Cross Neuropil	Axon Bearing / Columnar	26	8855	ACH	ME, LO → ME, LO
Transmedullary Y	Cross Neuropil	Axon Bearing / Columnar	12	2598	ACH	ME, LOP, LO → LO, ME, LOP
Y Neuron	Cross Neuropil	Axon Bearing / Columnar	5	631	GLUT	LOP, ME, LO → LO, LOP, ME

Families of optic-lobe intrinsic types. Number of types/cells in each family, predicted neurotransmitter type and primary synapse regions.

Extended Data Table 2 | Distribution of synapses over neuropils for each type family

Family	Affinity	Linkage	Types	Cells	Trans	Neuropils
Centrifugal	Cross Neuropil	Axon Bearing / Columnar	2	1511	GABA	ME → ME, LA
Distal Medulla	Neuropil Intrinsic	Non-columnar	21	3284	GLUT	ME → ME
Distal Medulla Dorsal Rim Area	Neuropil Intrinsic	Non-columnar	2	35	GLUT	ME → ME
Lamina Intrinsic	Neuropil Intrinsic	Non-columnar	1	231		LA → LA
Lamina Monopolar	Cross Neuropil	Axon Bearing / Columnar	5	3831	ACH	ME, LA → ME
Lamina Tangential	Neuropil Intrinsic	Axon Bearing / Tangential	1	6		ME, LO, AME, PLP → LO
Lamina Wide Field	Cross Neuropil	Axon Bearing / Columnar	2	320	ACH	ME → LA
Lobula Intrinsic	Neuropil Intrinsic	Non-columnar	33	761	GABA	LO → LO
Lobula Lobula Plate Tangential	Cross Neuropil	Axon Bearing / Tangential	1	36	GABA	LO, LOP → LO, LOP
Lobula Medulla Amacrine	Cross Neuropil	Amacrine	6	134	GABA	ME, LO → ME, LO
Lobula Medulla Tangential	Cross Neuropil	Axon Bearing / Tangential	4	88	GLUT	LO, ME → LO, ME
Lobula Plate Intrinsic	Neuropil Intrinsic	Non-columnar	15	363	GLUT	LOP → LOP
Medulla Intrinsic	Neuropil Intrinsic	Axon Bearing / Columnar	8	3922	ACH	ME → ME
Medulla Lobula Lobula Plate Amacrine	Cross Neuropil	Amacrine	1	1	GABA	LOP, ME, LO → LOP, LO, ME
Medulla Lobula Tangential	Cross Neuropil	Axon Bearing / Tangential	8	295	ACH	ME, LO → ME, LO
Photo Receptors	Neuropil Intrinsic	Axon Bearing / Columnar	3	4751		ME, LA → LA, ME
Proximal Distal Medulla Tangential	Neuropil Intrinsic	Axon Bearing / Tangential	1	6	DA	ME → ME
Proximal Medulla	Neuropil Intrinsic	Non-columnar	14	599	GABA	ME → ME
Serpentine Medulla	Neuropil Intrinsic	Non-columnar	43	1488	GABA	ME → ME
T1 Neuron	Cross Neuropil	Axon Bearing / Columnar	1	738		ME, LA → ME, LA
T2 Neuron	Cross Neuropil	Axon Bearing / Columnar	2	1591	ACH	ME, LO → LO, ME
T3 Neuron	Cross Neuropil	Axon Bearing / Columnar	1	823	ACH	ME, LO → LO, ME
T4 Neuron	Cross Neuropil	Axon Bearing / Columnar	4	3104	ACH	ME, LOP → LOP, ME
T5 Neuron	Cross Neuropil	Axon Bearing / Columnar	4	2996	ACH	LO, LOP → LOP, LO
Translobula Plate	Cross Neuropil	Axon Bearing / Columnar	4	172	GLUT	LOP → LOP, LO
Transmedullary	Cross Neuropil	Axon Bearing / Columnar	26	8855	ACH	ME, LO → ME, LO
Transmedullary Y	Cross Neuropil	Axon Bearing / Columnar	12	2598	ACH	ME, LOP, LO → LO, ME, LOP
Y Neuron	Cross Neuropil	Axon Bearing / Columnar	5	631	GLUT	LOP, ME, LO → LO, LOP, ME

Families of optic-lobe intrinsic types and the number of their input / output synapses in each of the optic lobe regions.

Article

Extended Data Table 3 | Cells and cell types by super class

Family	Abbrev.	in LA	in ME	in LO	in LOP	out LA	out ME	out LO	out LOP
Centrifugal	C	2361	110557	0	5	25499	192287	0	6
Distal Medulla	Dm	109	493242	29	0	3	461042	66	0
Distal Medulla Dorsal Rim Area	DmDRA	0	5510	0	0	0	6164	0	0
Lamina Intrinsic	Lai	53890	14	0	0	4729	0	0	0
Lamina Monopolar	L	118627	335509	0	0	4644	1018207	0	0
Lamina Tangential	Lat	0	168	138	0	0	0	11	0
Lamina Wide Field	Lawf	212	76784	0	0	39998	583	0	0
Lobula Intrinsic	Li	0	165	465695	242	0	5	311758	25
Lobula Lobula Plate Tangential	LLPt	0	0	18515	1542	0	0	13572	6752
Lobula Medulla Amacrine	LMa	0	222413	118357	2571	0	139822	115942	585
Lobula Medulla Tangential	LMt	0	6226	42542	72	0	22192	26123	25
Lobula Plate Intrinsic	LPI	0	1	3	320696	0	36	13	222563
Medulla Intrinsic	Mi	318	530040	2	0	1	1075969	16	0
Medulla Lobula Lobula Plate Amacrine	Am	0	3201	2183	27387	0	3449	3762	12089
Medulla Lobula Tangential	MLt	0	33346	2088	10	0	28384	10823	1
Photo Receptors	R	1356	21647	0	0	108499	27109	0	0
Proximal Distal Medulla Tangential	PDt	0	2978	0	0	0	1186	0	0
Proximal Medulla	Pm	0	966964	3	350	0	444691	1	265
Serpentine Medulla	Sm	0	240804	10	0	0	239769	25	0
T1 Neuron	T1	6513	100560	0	0	127	2629	0	0
T2 Neuron	T2	0	207836	14421	229	0	46074	176480	85
T3 Neuron	T3	0	117157	7188	18	0	24435	81576	0
T4 Neuron	T4	0	210989	32	28749	0	26568	19	240567
T5 Neuron	T5	0	7	216802	20094	0	0	22862	257408
Translobula Plate	Tlp	0	46	2767	92321	0	176	16095	51725
Transmedullary	Tm	0	939034	92457	920	0	1025728	583491	1679
Transmedullary Y	TmY	0	363265	111320	151107	0	147000	202629	65437
Y Neuron	Y	0	82196	23732	84795	0	55853	78668	56706

Proofread cell and type stats broken up by super class in the FlyWire connectome dataset as of October 2023.

Reporting Summary

Nature Portfolio wishes to improve the reproducibility of the work that we publish. This form provides structure for consistency and transparency in reporting. For further information on Nature Portfolio policies, see our [Editorial Policies](#) and the [Editorial Policy Checklist](#).

Statistics

For all statistical analyses, confirm that the following items are present in the figure legend, table legend, main text, or Methods section.

- n/a Confirmed
- The exact sample size (n) for each experimental group/condition, given as a discrete number and unit of measurement
 - A statement on whether measurements were taken from distinct samples or whether the same sample was measured repeatedly
 - The statistical test(s) used AND whether they are one- or two-sided
Only common tests should be described solely by name; describe more complex techniques in the Methods section.
 - A description of all covariates tested
 - A description of any assumptions or corrections, such as tests of normality and adjustment for multiple comparisons
 - A full description of the statistical parameters including central tendency (e.g. means) or other basic estimates (e.g. regression coefficient) AND variation (e.g. standard deviation) or associated estimates of uncertainty (e.g. confidence intervals)
 - For null hypothesis testing, the test statistic (e.g. F , t , r) with confidence intervals, effect sizes, degrees of freedom and P value noted
Give P values as exact values whenever suitable.
 - For Bayesian analysis, information on the choice of priors and Markov chain Monte Carlo settings
 - For hierarchical and complex designs, identification of the appropriate level for tests and full reporting of outcomes
 - Estimates of effect sizes (e.g. Cohen's d , Pearson's r), indicating how they were calculated

Our web collection on [statistics for biologists](#) contains articles on many of the points above.

Software and code

Policy information about [availability of computer code](#)

Data collection This study is based on the FlyWire fly brain connectome (flywire.ai). List of all data sources used for making this resource is available here: https://codex.flywire.ai/about_flywire (along with publication rules and TOS).

Data analysis Python, Julia programming languages were used for analysis. Some of the tools from FlyWire Codex: <https://github.com/murthylab/codex>

For manuscripts utilizing custom algorithms or software that are central to the research but not yet described in published literature, software must be made available to editors and reviewers. We strongly encourage code deposition in a community repository (e.g. GitHub). See the Nature Portfolio [guidelines for submitting code & software](#) for further information.

Data

Policy information about [availability of data](#)

All manuscripts must include a [data availability statement](#). This statement should provide the following information, where applicable:

- Accession codes, unique identifiers, or web links for publicly available datasets
- A description of any restrictions on data availability
- For clinical datasets or third party data, please ensure that the statement adheres to our [policy](#)

Data produced by this study is available at: <https://github.com/murthylab/flywire-visual-neuron-types>

Research involving human participants, their data, or biological material

Policy information about studies with [human participants or human data](#). See also policy information about [sex, gender \(identity/presentation\), and sexual orientation](#) and [race, ethnicity and racism](#).

Reporting on sex and gender	N/A
Reporting on race, ethnicity, or other socially relevant groupings	N/A
Population characteristics	N/A
Recruitment	N/A
Ethics oversight	N/A

Note that full information on the approval of the study protocol must also be provided in the manuscript.

Field-specific reporting

Please select the one below that is the best fit for your research. If you are not sure, read the appropriate sections before making your selection.

Life sciences Behavioural & social sciences Ecological, evolutionary & environmental sciences

For a reference copy of the document with all sections, see [nature.com/documents/nr-reporting-summary-flat.pdf](https://www.nature.com/documents/nr-reporting-summary-flat.pdf)

Life sciences study design

All studies must disclose on these points even when the disclosure is negative.

Sample size	N/A
Data exclusions	N/A
Replication	N/A
Randomization	N/A
Blinding	N/A

Reporting for specific materials, systems and methods

We require information from authors about some types of materials, experimental systems and methods used in many studies. Here, indicate whether each material, system or method listed is relevant to your study. If you are not sure if a list item applies to your research, read the appropriate section before selecting a response.

Materials & experimental systems

- | n/a | Involvement in the study |
|-------------------------------------|--|
| <input checked="" type="checkbox"/> | <input type="checkbox"/> Antibodies |
| <input checked="" type="checkbox"/> | <input type="checkbox"/> Eukaryotic cell lines |
| <input checked="" type="checkbox"/> | <input type="checkbox"/> Palaeontology and archaeology |
| <input checked="" type="checkbox"/> | <input type="checkbox"/> Animals and other organisms |
| <input checked="" type="checkbox"/> | <input type="checkbox"/> Clinical data |
| <input checked="" type="checkbox"/> | <input type="checkbox"/> Dual use research of concern |
| <input checked="" type="checkbox"/> | <input type="checkbox"/> Plants |

Methods

- | n/a | Involvement in the study |
|-------------------------------------|---|
| <input checked="" type="checkbox"/> | <input type="checkbox"/> ChIP-seq |
| <input checked="" type="checkbox"/> | <input type="checkbox"/> Flow cytometry |
| <input checked="" type="checkbox"/> | <input type="checkbox"/> MRI-based neuroimaging |

Plants

Seed stocks	N/A
Novel plant genotypes	N/A
Authentication	N/A

III

DISCUSSION

An organism's chance of survival is highly dependent on its ability to interact with the environment via a sensory system. Sensory inputs are processed by neural networks, which decode external signals and drive appropriate behavioural action of the organism. Studying the functions of specific neural circuits can provide critical insights into the broader mechanisms of the brain. My research focused on investigating the neural circuit underlying direction selectivity in the visual system of the fruit fly *Drosophila melanogaster*. To understand how the brain extracts meaningful information from the sensory environment, the motion vision circuit of *Drosophila melanogaster* is a powerful model. Building on knowledge gained by many scientists, through a combination of physiological testing and genetic modification of specific neurons, I could achieve deeper insight into the neuronal computation of direction of movement. In [Manuscript 1; Braun et al. \(2023\)](#), I describe how null-direction suppression is realised in the *Drosophila* OFF motion vision pathway. I demonstrated how disynaptic inhibition shapes the tuning of OFF motion detectors in *Drosophila*, directly linked to a columnar microcircuit. Additionally, I pinpointed the CT1 neuron as the specific input neuron crucial for null-direction suppression in T5 neurons.

To study neural circuits, knowledge about the connectivity between neurons is crucial. Therefore, EM based wiring diagrams serve as an invaluable resource in modern circuit neuroscience. As part of a global collaboration, I contributed to complete the connectome of a whole adult fly brain.

1 CONNECTOMES

Several parts of fly brains have been mapped using electron microscopy datasets before my doctoral studies, which provided important insights into neural circuits and their functions ([Shinomiya et al., 2015](#); [Li et al., 2020b](#)). Building on these analyses of smaller brain regions, approximately half of the central brain and a small part of the optic lobe, known as the hemibrain, was subsequently imaged by using focused ion beam scanning electron microscopy (FIB-SEM) with an isotropic resolution of $8 \times 8 \times 8 \text{ nm}^3$ voxels ([Scheffer et al., 2020](#)). With the help of automated neuron segmentation and synapse detection, the authors created a dataset of neuron morphology and connectivity. This dataset was made publicly accessible via a web interface and programming tools ([Scheffer et al., 2020](#); [Plaza et al., 2022](#)), facilitating large-scale analyses of the central brain ([Hulse et al., 2021](#); [Schlegel et al.,](#)

2021). In parallel, a full adult fly brain (FAFB) dataset was acquired using serial section transmission electron microscopy (ssTEM), with a resolution of $4 \times 4 \times 40 \text{ nm}^3$ voxels (Zheng et al., 2018). The analysis of this dataset also employed automated segmentation and synapse detection (Scheffer et al., 2020; Dorkenwald et al., 2021; Heinrich et al., 2018; Buhmann et al., 2021). Additionally, with this dataset the neurotransmitter identity of each neuron was predicted based on ultrastructural differences (Eckstein et al., 2023). Recently, an international collaboration called FlyWire (Dorkenwald et al., 2021) has achieved a significant milestone by completing the first full neuronal wiring diagram of an entire adult fly brain, using the FAFB dataset (Dorkenwald et al., 2024, **Manuscript 2**). A variety of analytical tools were provided and are accessible via a web interface, enabling detailed exploration of wiring diagrams for any neuron or circuit in the fly brain (Schlegel et al., 2024, **Manuscript 3**; Matsliah et al., 2024, **Manuscript 4**).

To gain deeper insight into how the brain controls behaviour, additional efforts have focused on mapping neuronal circuits to the motor neurons. In insects such as flies, the majority of motor neurons are located in the ventral nerve cord (VNC), equivalent to the mammalian spinal cord. A team of researchers generated a connectome of the VNC of a male adult fly (Takemura et al., 2024). More connectomes in the field of *Drosophila* neuroscience are awaited. For example, a full connectome of a complete central nervous system, with the VNC attached to the brain, comprising all intact ascending and descending neurons. The FIB-SEM dataset containing this central nervous system and a full connectome of its right optic lobe has recently been preprinted (Nern et al., 2024), while proofreading of the rest of the central nervous system is ongoing.

It is important to note that current EM methods used in *Drosophila* research are limited in resolving chemical synaptic connections and do not resolve electrical synapses. Considering the significant role of electrical synapses, for example in the ON and OFF motion vision pathways in *Drosophila* (Ammer et al., 2022), in the lobula plate of blowflies (Haag and Borst, 2005), and in the mammalian retina (Bloomfield and Völgyi, 2009), it becomes evident that existing connectomes do not fully capture all potential neuronal connections. Until recently, EM with its nanometer-scale resolution was the only technology capable of dense connectomic analysis. However, a new technology, named light microscopy based connectomics (LICONN; Tavakoli et al., 2024), has been reported to achieve 3D-nanoscale resolution ($\sim 10 \times 10 \times 25 \text{ nm}^3$) using light microscopy instead of EM, but by physically expanding the tissue (~ 16 -fold) with a hydrogel. Using LICONN, researchers can acquire detailed, molecularly informed reconstructions through common immunolabeling techniques. This enables, for example, the detection and precise mapping of the distribution of receptor molecules or gap junction proteins (Tavakoli et al., 2024).

The field of connectomics has revolutionised *Drosophila* circuit neuroscience in recent years. Its impact spans from enabling rapid analysis of neuronal partners and (chemical) synaptic strength to facilitating the discovery of new circuits and predicting their functions within days (Seung, 2024). A computational model based on the entire *Drosophila* connectome, including neural connectivity, synaptic weights, and neurotransmitter predictions

is capable of generating experimentally testable hypotheses (Shiu et al., 2024; Dorkenwald et al., 2024; Buhmann et al., 2021; Eckstein et al., 2023). Supported by results of calcium imaging and behavioural experiments in the circuitry of feeding and grooming, the model accurately describes complete sensorimotor transformations (Shiu et al., 2024). To conclude, connectomes will not replace functional experiments. Both approaches complement each other to decipher the complexity of neural circuits.

2 FROM MOTION INFORMATION TO BEHAVIOUR

Visual motion information is processed in the optic lobe of *Drosophila* and is then relayed by a sophisticated network of neurons directly to the central brain, where it integrates with signals from other modalities for further processing and behavioural output (Reinhard et al., 2022; Currier et al., 2023). T4 and T5 neurons in the optic lobe are the primary motion detectors. These neurons, which terminate in the lobula plate, play a critical role in processing visual information by distinguishing between ON and OFF motion cues that are directionally selective. These two pathways converge again in the lobula plate tangential cells, which are not selective for luminance polarity (Hausen, 1984).

Neurons that extend from the optic lobes to the central brain primarily originate in the medulla, lobula, and lobula plate. From these neuropils, several downstream circuits emerge (Wu et al., 2016; Shinomiya et al., 2022; Kim et al., 2023). Visual projection neurons receive input from T4 and T5 neurons and transmit signals to the central brain. The axon terminals of a given subtype project to distinct brain structures in the central brain known as optic glomeruli. Most optic glomeruli do not show internal retinotopy of their input neurons, as in the optic lobe (Wu et al., 2016). From the optic glomeruli, visual motion information is further processed and forwarded to descending neurons from the central brain to the ventral nerve cord (VNC) and further to motor neurons to perform specific behaviour. The VNC is part of the central nervous system and houses motor areas that are responsible for most types of locomotor behaviour. The male adult nerve cord (MANC) connectome (Takemura et al., 2024) together with the whole brain connectome (Dorkenwald et al., 2024) serve as a useful tool to discover neural circuits from the optic lobe over the central brain to the motor neurons.

2.1 Downstream circuits of T4 and T5 neurons

In recent years, connectome analysis has been conducted to identify downstream partners and circuits of T4 and T5 neurons in the lobula plate (Shinomiya et al., 2022; Tanaka and Clark, 2022). However, a limitation of the available dataset was that it only included a fraction of the lobula plate in connection with the central brain (Scheffer et al., 2020; Plaza et al., 2022). The recent completion of the full connectome of the adult fly brain (Dorkenwald et al., 2024, **Manuscript 2**) now allows for identifying the large diversity of visual projection neurons and circuits downstream of T4 and T5 neurons. The annotation of every single neuron makes it possible to identify neurons within a circuit without knowing their morphology (Schlegel et al., 2024, **Manuscript 3**).

Lobula Plate Tangential Cells (LPTCs) cover a wide area of the visual field and integrate the signals of many hundreds of direction-selective T4 and T5 neurons (Joesch et al., 2008; Schnell et al., 2012; Maisak et al., 2013; Mauss et al., 2015; Barnhart et al., 2018; Shinomiya et al., 2022). LPTCs

depolarize when stimulated by motion along their preferred direction and hyperpolarize during motion along the opposite, null direction. Blocking synaptic transmission from both T4 and T5 cells causes LPTCs to lose their responsiveness to moving gratings (Schnell et al., 2012; Maisak et al., 2013). Different LPTCs provide distinct signals about the comprehensive motion patterns surrounding the fly, and have been associated with head and body movements (Krapp and Hengstenberg, 1996; Haikala et al., 2013; Kim et al., 2017). Among LPTCs, vertical system (VS) and horizontal system (HS) cells have been most thoroughly studied. Blocking the synaptic output of VS and HS cells through expression of an inwardly rectifying potassium channel (Kir2.1) strongly affects the head optomotor response and also, but to a lesser extent, reduces wing steering (Kim et al., 2017). Within the central brain, LPTCs form connections with descending neurons that transfer the signal to motor neurons (Strausfeld et al., 1987; Suver et al., 2016). Notably, certain descending neurons show minimal response to only visual stimuli, yet they are significantly activated when input from multiple sensory modalities are presented simultaneously (Haag et al., 2010; Huston and Krapp, 2009). Moreover, many of the descending neurons receive bilateral visual input, which is believed to improve their ability to detect and react to movement patterns in their surroundings (optic flow fields) (Huston and Krapp, 2008; Wertz et al., 2009).

Across the optic lobe, the dendrites of each Lobula Columnar (LC) and Lobula Plate Lobula Columnar (LPLC) neuron cover several columns in the optic lobe and thus receive input from multiple individual neurons within these columns. The complete set of neurons of each LC and LPLC subtype covers the whole area of the visual field. LC neurons are proposed to detect different visual features, such as the presence of objects and their general location within the visual field (Wu et al., 2016). The functional relevance of LC/LPLC neuron subtypes have only been discovered for some of the subtypes. Specifically the LPLC2 subtype has been found to be very selective to detect local looming stimuli (Klapoetke et al., 2017). Both LC and LPLC neuron subtypes transfer visual information to a variety of neurons in the central brain, mainly to distinct descending neurons (Mu et al., 2012; Panser et al., 2016; Namiki et al., 2018).

A looming stimulus, which occurs when an object rapidly increases in size as it approaches an observer, is characterised by multiple prominent visual features, including the angular velocity at which the object expands and its angular size. An example of this in the real world of flies is a predator moving directly towards it, appearing larger as it gets closer. Both features, angular velocity and angular size, are encoded by two different visual projection neurons. LC4 encodes for expansion velocity and LPLC2 encodes for expansion size (von Reyn et al., 2017; Ache et al., 2019b). LC4 and LPLC2 are the primary input neurons to the giant fibre, a premotor descending neuron. The giant fibre integrates LC4 and LPLC2 input to trigger escape responses to looming threats (von Reyn et al., 2017; Ache et al., 2019b).

Close to the glomeruli in the central brain of LC4 and LPLC2 reside two other visual projection neuron types, LPLC3 and LPLC4 (Namiki et al., 2018). These subtypes show extensive anatomical overlap with the

dendrites of two descending neurons, DNp07 and DNp10 (Ache et al., 2019a). These descending neurons contribute to visually evoked landing responses. Optogenetic activation of DNp07 and DNp10 drives landing responses (Ache et al., 2019a). It is unclear whether LPLC3 and LPLC4 transmit the same type of visual information via two parallel visual pathways. However, connectomic analysis of the recently available full adult fly brain (Dorkenwald et al., 2024) revealed that LPLC4 neurons form a strong synaptic upstream partner of DNp07. There is currently a lack of functional evidence for this connection. Blocking T4 and T5 neurons using TNT effectively abolishes both behavioural landing and avoidance responses (Schilling and Borst, 2015). Additional functional experiments are necessary to further demonstrate the role of T4 and T5 neurons within the circuits mentioned above.

3 COMPARING VERTEBRATE AND INVERTEBRATE VISUAL SYSTEMS

Many animals use vision to navigate through their environments. The eyes of each animal species are highly adapted to collect information from its environment that it needs to survive and reproduce. Adaptations of different species to some visual surroundings can already be observed in the structure and functionality of the retinal circuits. An example of this adaptation is the ratio of rod to cone photoreceptors in mammals, which varies depending on the animal's level of activity during different light conditions (Peichl, 2005). For instance, animals like squirrels, which are active during the day, have a higher proportion of cone photoreceptors for better colour vision and detail recognition in bright light (Kryger et al., 1998), whereas nocturnal animals like owls have a higher proportion of rod photoreceptors, enhancing their ability to see in low light conditions (Braekevelt et al., 1996).

Visual motion detection is a key feature of the visual perception in animals, playing a critical role in their ability to interact and navigate through their environment. In the following section I will briefly compare the neural circuitry of motion vision in vertebrate retina and the optic lobe of invertebrates.

Both visual systems have striking similarities of how motion is computed at this early stage of the visual system (Baden et al., 2020; Lettvin et al., 1959; Mauss et al., 2017b), even though the last common ancestor of insects and mammals lived some 500 million years ago. Intriguingly, early studies on motion detection in beetles and rabbits led to analogous correlation-based algorithmic models, the Hassenstein-Reichardt detector and Barlow-Levick detector (see also section 2.1 and 2.2 in the introduction; Von Hassenstein and Reichardt, 1956; Barlow and Levick, 1965). The underlying mechanism seems to be conserved across different animal species. In particular, flies and mice have been prime subjects for investigating the initial mechanism underlying motion vision due to their genetic accessibility. As in flies, the mammalian retina is layered, retinotopically organised, and contains five primary cell types (Masland, 2001): Photoreceptors, bipolar cells, horizontal cells, amacrine cells, and ganglion cells, each of which has many different subtypes, totalling ~140 cell types (Baden, 2024). In vertebrates, two types of photoreceptors, rods and cones, differ in light sensitivity and transduce light into electrical signals. Rods are highly sensitive to low light and are crucial for night vision, while cones require brighter light and are responsible for day vision. Cones come in different subtypes that differ in spectral sensitivity, enabling colour vision. The sensitivity difference of rods and cones varies among vertebrates (Ingram et al., 2016). Downstream of the photoreceptors are the bipolar and horizontal cells. Horizontal cells provide lateral interactions in the outer plexiform layer. Bipolar cells transfer the light signal onto the dendrites of amacrine and retinal ganglion cells. Retinal ganglion cell axons form the output of the retina, the optic nerve, and transmit the signals to visual brain areas. Downstream of vertebrate photoreceptors, at the level of bipolar cells, the signals become separated into ON and OFF pathways, as is the case in the fly lamina (Joesch et al., 2008;

Wässle, 2004). In vertebrates, excitatory and inhibitory glutamate receptors lead to OFF centre and ON centre bipolar cell responses, respectively (Chau et al., 2024). Further subtypes of bipolar cells express glutamate receptors with different kinetics, thereby filtering different temporal frequencies of visual information (Puthussery et al., 2014; Awatramani and Slaughter, 2000; DeVries, 2000). These bipolar cells initiate a set of parallel visual pathways. The computation of motion direction is independently conducted within each ON and OFF pathway in both flies and mice. In mice a subset of amacrine cells — starburst amacrine cells (SACs) — are the first cells within the retina to be motion sensitive, as T₄ and T₅ cells are in flies. Once the direction of motion is detected, the information from both ON and OFF pathways is integrated at the next synapse. Within the optic lobe of flies, T₄ (ON) and T₅ (OFF) neurons connect to LPTCs, generating a unified motion signal that does not distinguish between brightness increments or decrements. Similarly, in the mouse retina, motion sensitive ON and OFF starburst amacrine cells are essential for ON-OFF direction-selective ganglion cells. Like LPTCs in flies, they do not distinguish between brightness increments or decrements.

Starburst amacrine cells are named for their star-like shape, characterised by a radially symmetric dendritic tree. Each cell features a central soma from which multiple dendritic branches radiate outward. Starburst amacrine cells' exhibits a preference for motion direction that extends from the soma towards the tip of their distinct, radially symmetric arranged dendritic tree (Euler et al., 2002). This unique structure allows starburst amacrine cells to analyse motion in all directions within one cell. Each dendritic branch of the SAC acts as an independent computational unit, processing its own inputs and outputs. This is in contrast to T₄ and T₅ cells in flies, which are limited to detecting motion in just four cardinal directions through their four distinct subtypes, each aligned to a specific direction. Recently, it was found that SAC-like cells are also present in zebrafish (Li et al., 2024). This suggests the ancient origin of these cells, dating back at least 400 million years. Further, it also means that probably all other tetrapods have starburst cells as well (Yoshimatsu and Baden, 2024).

Upstream of amacrine and ganglion cells in vertebrates are the ON and OFF bipolar cells. Bipolar cells show a wide range of response kinetics in the vertebrate retina which is also true for ON and OFF input cells in flies (Baden et al., 2013; Serbe et al., 2016; Arenz et al., 2017; Strother et al., 2017). Reconstructions of starburst amacrine cells and their bipolar input cells revealed that faster bipolar cells prefer to wire with SACs near their dendritic tips, whereas slower bipolar cells prefer to wire with SACs close to the soma (Kim et al., 2014). This suggests a Hassenstein-Reichardt detector-like computation at direction-selective starburst amacrine cells. This arrangement, where synaptic inputs have different temporal properties depending on their location of connection on the dendrite, mirrors the principle of the Hassenstein-Reichardt detector model (Von Hassenstein and Reichardt, 1956; section 2.1 in introduction). Such a spatial-temporal gradient in synaptic inputs to SACs allows these cells to effectively determine the direction of motion by detecting the sequence in which signals arrive across their dendritic span. Reconstructions of multi-columnar T₄ and

T5 neurons in *Drosophila* and their inputs describe a similar phenomenon (see introductory [section 4.2](#); [Takemura et al., 2017](#); [Shinomiya et al., 2019](#)). Parallel circuits for ON and OFF signal processing are observed across a wide range of organisms and sensory systems. Studies have demonstrated this in the olfactory system of *C. elegans* ([Chalasan et al., 2007](#)), thermosensation in fruit flies ([Gallio et al., 2011](#)) and auditory processing in the rat ([Scholl et al., 2010](#)). Across phyla, the detection of visual motion is organised separately into parallel signal processing of brightness increments (ON) and decrements (OFF). It is ranging from flies ([Joesch et al., 2010](#)) over mice ([Euler et al., 2014](#)), salamander ([Hensley et al., 1993](#)), cats ([Wässle, 2004](#)), and primates ([Field and Chichilnisky, 2007](#)) to humans ([Hashimoto et al., 2013](#)). This highlights the universal role of ON and OFF pathways in sensory perception. Although the exact functional benefits of this division between ON and OFF pathways are not fully understood, transmitting information about both increases and decreases in luminance seems to provide an evolutionary fitness benefit. The ON-OFF split might provide an enhanced contrast sensitivity. Earlier studies have proposed that the ON-OFF split developed to enable fast and metabolically efficient signalling of contrasting changes in light intensity, as both increases and decreases in light are common features in natural environments ([Schiller et al., 1986](#); [Schiller, 1992](#); [Westheimer, 2007](#)). Under natural conditions, splitting visual information into ON and OFF pathways enhances the neural coding efficiency ([Gjorgjieva et al., 2014](#)). Models that utilise both ON and OFF pathways are more effective in terms of information transmission per neural spike compared to models with only ON pathways. This division of pathways reduces metabolic demands, thus potentially boosting evolutionary fitness.

4 COMPARING T4 ON NEURONS AND T5 OFF NEURONS IN *DROSOPHILA*

T4 and T5 neurons were first described by Ramon y Cajal & Sanchez in 1915 (Cajal and Sánchez, 1915). Morphologically T4 and T5 neurons differ only in the location of their dendrites within the optic lobe: T4 neuron dendrites are localised in layer 10 of the medulla, while T5 neuron dendrites are localised in layer 1 of the lobula. Both neuron types are subdivided into four subtypes, each selective for one of the four cardinal directions (Figure 9A; Maisak et al., 2013). The axon terminals of each of the four T4/T5 subtypes project to a specific layer in the lobula plate (Figure 8A; Fischbach and Dittrich, 1989). The dendritic morphology varies slightly among the subtypes, with dendrites oriented in one of the four cardinal directions, opposite to their preferred direction. Although T4 and T5 neurons share similarities in response to the orientation and velocity of moving stimuli, they differ in their preferred contrast polarity. T4 neurons respond to brightness increments and T5 neurons respond to brightness decrements. Volumetric electron microscopy data analysis of the *Drosophila* optic lobe revealed all presynaptic partners of T4 and T5 neurons and their spatial retinotopic organisation on T4 and T5 dendrites (Takemura et al., 2017; Shinomiya et al., 2019). T4 and T5 neurons receive input from different neurons. Mi9 inputs are located on the distal side, Mi1 and Tm3 in the centre, and Mi4, C3, and CT1 on the proximal side for T4 dendrites. Unlike T4, T5 receives Tm9 input on the distal side, Tm1, Tm2 and Tm4 input in the centre, and CT1 input (like T4) on the proximal side. Immunohistochemical studies as well as single-cell RNA sequencing data revealed that Mi9 uses glutamate, Mi1 and Tm3 use acetylcholine, and Mi4, C3, and CT1 use γ -aminobutyric acid (GABA) as their neurotransmitter. Contrary to T4 input neurons, all columnar T5 input neurons (Tm9, Tm1, Tm2 and Tm4 neurons) utilise acetylcholine as neurotransmitter, except the columnar CT1 input neuron on the proximal side of T5 which utilises GABA (Pankova and Borst, 2017; Richter et al., 2018; Takemura et al., 2017; Davis et al., 2020). The impact on the postsynaptic cell of these transmitters is determined by the receptors that the postsynaptic neurons express. Conditional tagging of endogenous proteins revealed that T4 dendrites express GluCl α channels on the distal side, nicotinic acetylcholine (D α 5 and D α 7) receptors in the centre, and GABA receptors (Rdl) on the proximal side (Davis et al., 2020; Hörmann et al., 2020; Pankova and Borst, 2016; Fendl et al., 2020; Sanfilippo et al., 2024). This matches the distribution of the different T4 inputs and their neurotransmitter. Consistent with the observation that T5 dendrites do not receive glutamatergic input, the adult T5 dendrite also lacks expression of GluCl α channels. T5 cells express nicotinic acetylcholine receptors at the centre (D α 5 and D α 7), and GABA receptors (Rdl) at the base of the dendrite (Davis et al., 2020; Hörmann et al., 2020; Pankova and Borst, 2016; Fendl et al., 2020; Sanfilippo et al., 2024). In contrast to GluCl α receptors located on the distal part of T4 dendrites, the specific receptor expressed on the distal side of T5 dendrites, meant to interact with the Tm9 input neuron, has not yet been identified. Recent work suggests that heteromeric receptors formed

by nicotinic acetylcholine receptor subunits $D\alpha 1$ and $D\beta 1$ may be present on the distal side of T5 dendrites (Sanfilippo et al., 2024). However, these findings await functional validation and could as well be of T5-T5 neuron connections. Furthermore, analysis of RNA sequencing data (Davis et al., 2020) supports the speculation that muscarinic acetylcholine receptors may be involved in the synapses between Tm9 and the distal side of T5 dendrites (Fendl et al., 2020). Calcium imaging experiments showed that knocking down mAChR-A in T5c neurons using RNA interference (RNAi) did not have any impact on the directional tuning of T5 neurons when compared to the control condition (Figure 10). Tests on mAChR-B and other muscarinic acetylcholine receptors have not been conducted yet. Therefore, additional functional analysis and receptor tagging studies are necessary to identify the specific type of acetylcholine receptor that receives Tm9 input.

This comprehensive set of information is crucial for understanding the mechanisms behind the direction selectivity of T4 and T5 neurons and the biophysical principles that underlie this process. Despite the apparent similarities in their function, the significant differences in the inputs and receptors between T4 and T5 neurons suggest that different biophysical mechanisms are likely responsible for their direction selectivity.

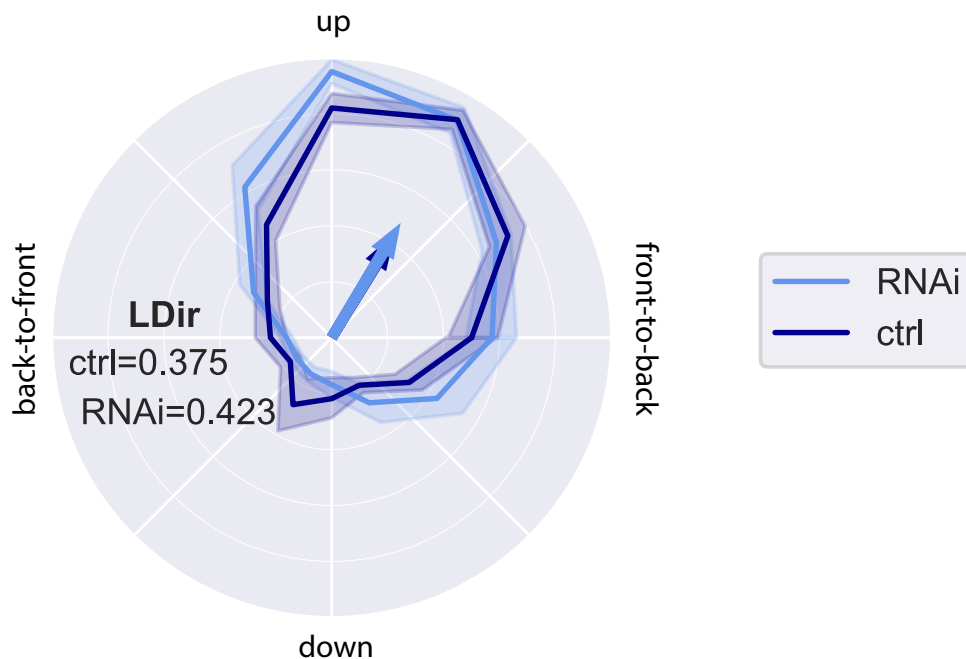


Figure 10: Directional tuning of T5c: Directional tuning curves of T5c calcium responses in T4/T5-Gal4, UAS-mAChRA-RNAi flies to dark edges moving in 11 different directions. Each data point represents the maximum T5c response to either direction of visual motion, normalised to the maximum response per fly. Dark traces represent signals from the control flies; bright traces represent signals from mAChRA-RNAi flies ($n_{ctrl} = 9$, $n_{mAChRA-RNAi} = 5$). Error shades indicate \pm SEM. Width of the directional tuning curves indicated by directional index LDir.

4.1 Multiplicative disinhibition in the preferred direction of T4 neurons

To unravel the biophysical mechanism of the preferred direction of T4 neurons, electrophysiological whole cell patch clamp recordings of T4 neurons and their inputs were carried out. [Groschner et al. \(2022\)](#) demonstrated with whole cell patch clamp recordings of Mi9 neurons that Mi9 is constantly depolarised in darkness while it is more hyperpolarized in brightness. The unusual OFF neuron characteristic of Mi9 within the ON pathway had been shown before by calcium imaging experiments ([Arenz et al., 2017](#)). As mentioned before, Mi9 neurons transmit glutamate, which binds to inhibitory glutamate-gated chloride channels (GluCl α) located on the distal side of T4 dendrites. Therefore, a stimulus moving in a T4 neuron's preferred direction will first affect the Mi9 inputs onto the T4 neuron. If the stimulus is a moving ON edge, Mi9 synaptic output will be suppressed due to the neuron's OFF-cell characteristics. Less glutamate in the synaptic cleft will lead to a closure of GluCl α receptors in T4 neurons. The closure of these GluCl α channels causes a significant increase in the input resistance in T4 neurons by removing the Cl $^-$ -conductance related shunting inhibition ([Groschner et al., 2022](#)). The ON stimulus moving in the preferred direction of T4 next activates the excitatory cholinergic Mi1 and Tm3 inputs in the centre of the T4 dendrite. Since the input resistance is high at this time, the excitatory current will have a large effect on the depolarization of the membrane potential. The Mi1/Tm3 activation is followed by an activation of the inhibitory Mi4 and C3 input neurons on the proximal side of the T4 dendrite, causing GABA receptors to open their Cl $^-$ channels and hyperpolarize T4. Crucially, the inhibitory signals from Mi9 and Mi4 create a 'window of opportunity' for the Mi1/Tm3 signal to depolarize the T4 neuron, resulting in a strong depolarization in the preferred direction of T4 ([Groschner et al., 2022](#)). In contrast, for motion in the null direction, the overlapping inhibitory signals from Mi9 and Mi4 neurons close this window, resulting in the T4 neuron not to depolarize. Importantly the directional tuning of T4 neurons decreases in absence of GluCl α receptors ([Groschner et al., 2022](#)). This biophysical disinhibitory mechanism underlies preferred-direction enhancement in T4 neurons.

4.2 Potential biophysical mechanism for preferred direction-enhancement in T5 neurons

The biophysical mechanism underlying preferred-direction enhancement in T5 neurons is a pressing question. In the ON pathway, the input neuron Mi9 on the preferred side (distal side) of the T4 dendrite, is OFF responsive. For equivalence in the OFF pathway, the corresponding input neuron for T5, namely Tm9, would need to be responsive to ON signals. However, this is not the case. Tm9 is an OFF neuron as well as all other T5 input neurons. Based on receptor field mapping during calcium imaging it has been suggested that Tm9 neurons and other T5 input neurons can also have ON centre receptive fields ([Ramos-Traslosheros and Silies, 2021](#)). But considering the visual stimuli used in that study (narrow flashing

bright or dark bars), their results are more likely to show the effects of the strong ON surround of these neurons (Arenz et al., 2017). Additionally, electrophysiological recordings of T5 inputs did not show ON responses in the centre of their receptive fields for Tm9, Tm2 and CT1 neurons (Kohn et al., 2021). With all the T5 input neurons being characterised with OFF centre receptive fields (Serbe et al., 2016; Meier and Borst, 2019; Kohn et al., 2021), it is clear that a disinhibitory mechanism, similar to that observed in T4 neurons (Groschner et al., 2022), is not likely to occur in T5 neurons.

For the computation on the level of T5 neurons, several studies have been conducted using either two-photon calcium imaging or electrophysiological recordings. Electrophysiological recordings of T5 neurons have not shown evidence for an amplifying nonlinearity (Gruntman et al., 2019), nor have they seen evidence for a preferred-direction enhancement mechanism in T5 neurons, as previously shown with calcium imaging (Haag et al., 2017). How can the different results be explained? One possible explanation is that the summation of sequential inputs behaves linearly in membrane potential, and nonlinearity (enhancement) arises from the transformation of membrane potential into calcium signals (Mishra et al., 2023). Another explanation for the preferred-direction enhancement in T5, observed with calcium signals (Haag et al., 2017), suggests that the summation of sequential inputs is inherently nonlinear for the membrane potential, as in T4 cells (Groschner et al., 2022). Wienecke et al. (2018) propose that the membrane potential of T5 behaves linearly, and that the enhancement in preferred direction, observed only in calcium signals, is due to an adaptive nonlinearity of the calcium channel (Wienecke et al., 2018; Mishra et al., 2023).

Our understanding of the computational processes underlying the capability to perceive visual motion is guided by theoretical models that explain motion vision. Correlation-type motion detectors compute the direction of motion by identifying sequential light signals, followed by nonlinear mathematical computations (Von Hassenstein and Reichardt, 1956; Barlow and Levick, 1965). In T4 neurons, a nonlinear, multiplication-like operation, similar to the Hassenstein-Reichardt detector, was recently explained biophysically (Groschner et al., 2022).

Which mechanism of preferred-direction enhancement is implemented in T5 neurons remains unclear. In the following paragraph I will propose a potential biophysical mechanism for the enhancement in T5 neurons:

It has been shown that acetylcholine, acting through metabotropic receptors, can inhibit eag-potassium channels (Cui and Strowbridge, 2019). RNA sequencing data suggest the expression of G protein-coupled metabotropic acetylcholine receptors (mAChR-B) in the T5 neuron (Hörmann et al., 2020). This receptor could potentially be located on the distal side of the T5 neuron corresponding to input from Tm9 neurons (Figure 9C-D). Muscarinic receptors do not themselves constitute ion channels. The stimulation of muscarinic receptors has to be transduced into a change in activity of endogenous ion channels that regulate neural excitability. Additional RNA

sequencing analysis revealed the expression of the ether-a-go-go (*eag*) gene at the mRNA level (Hörmann et al., 2020). This gene encodes for specific voltage-gated potassium channels called *eag* channels. The presence of the protein for mAChR-B and voltage-gated *eag* channels within the adult T5 neurons remains uncertain, as current data only regard the mRNA level. Assuming that mAChR-B and *eag* are expressed in T5 neurons and that they respond to Tm9, the following mechanism can be speculated. In brightness, Tm9 does not release acetylcholine so the *eag* channels are continuously open and potassium ions can flow through the channels to maintain a steady state. When Tm9 is stimulated by an OFF edge moving in the preferred direction, it releases acetylcholine, which binds to mAChR-B and causes *eag* potassium channels to close. This closure causes an increase in input resistance of T5 neurons. As a result, this mechanism, similar to the T4 mechanism, allows Tm1, Tm2, and Tm4 neurons, which are activated after Tm9, to induce a large depolarization of the T5 neuron in its preferred direction (see [section 5](#)). This hypothetical mechanism underscores the intricate interplay between neurotransmitter receptors and ion channels in shaping neural responses to visual stimuli.

5 OUTLOOK

In the course of my PhD project, as reflected by [Manuscript 1](#) in this thesis, I could contribute new insights into the circuit of the OFF motion vision pathway in T5. We could demonstrate by connectome analysis and functional calcium imaging experiments that disynaptic inhibition within a columnar microcircuit mediates null-direction suppression in T5. Further, we identified the CT1 neuron and the GABA-receptor subunit Rdl as crucial components in this process. The [section 4.2](#) of the thesis highlights the unresolved question of the biophysical mechanism underlying the preferred-direction enhancement observed in T5 neurons. To verify whether the hypothesised biophysical mechanism is indeed responsible for the preferred directionality of T5 neurons, as discussed in [section 4.2](#), a series of electrophysiological experiments can be proposed.

The first experiment involves whole patch clamp recordings of T5 neurons in response to dark and bright moving edges presented in several directions. This approach is expected to reveal the characteristic membrane voltage responses of T5 neurons when exposed to preferred and null directions in relation to ON and OFF signals. It is anticipated that moving OFF edges will induce strong depolarization in the preferred direction, while causing only weak depolarization in the null direction. Conversely, ON edges are expected to elicit weaker depolarization in both preferred and null directions. If a disinhibition mechanism is used by T5 neurons for preferred-direction enhancement like in T4 neurons, one expects to see a similar peak in input resistance immediately prior to the depolarization ([Groschner et al., 2022](#)). This can be tested using current clamp recordings with different holding currents. The neuron's input resistance at different time points can be calculated from the slope of a linear regression of voltages onto the holding currents. An increase in membrane resistance could be indicative of a mechanism enhancing the neuron's sensitivity to specific directional stimuli. If this experiment reveals an increase in input resistance, it would be interesting to next investigate the underlying mechanism, i.e. the membrane channels that are responsible for the change of input resistance. For this, a crucial experiment to test the proposed hypothesis involves assessing the role of the ether-a-go-go (eag) gene in T5 neurons, particularly whether these potassium channels are expressed in adult T5 neurons. To determine whether eag potassium channels play a role in modulating input resistance in T5 neurons, one could knock down the eag gene via RNAi and conduct patch-clamp recordings with different holding currents as described earlier. If the eag channel is indeed part of this mechanism, its knockdown is expected to result in consistently higher input resistance in T5 neurons. This could lead to less direction selective responses to moving OFF stimuli in several directions, due to the lack of characteristic increase in input resistance before depolarization. Similar experiments could be conducted by knocking down the mAChR-B.

Finally, to investigate whether particularly Tm9 (providing distal input; [Figure 9B-C](#)) is causing the change of input resistance in T5, the most straightforward experiment is to optogenetically activate Tm9 neurons by expressing CsChrimson, while performing electrophysiological recordings

from a T5 neuron. Since we can only optogenetically activate all columnar Tm9 neurons, the columnar microcircuit of Tm9 and CT1 (Braun et al., 2023; **Manuscript 1**) would manipulate the proposed experiment. The activation of Tm9 would lead to an unintended activation of the inhibitory CT1 neuron. To exclusively activate Tm9 neurons, the CT1 neuron would need to be genetically ablated. The expected outcome of this experiment is an increased input resistance in T5 neurons without visual stimuli, occurring whenever Tm9 is activated by light.

Through a combination of electrophysiological recordings of T5, optogenetic activation of Tm9, and genetic knockdown of the *eag* gene, the outlined experiments represent a detailed approach to investigate the biophysical mechanism of the preferred direction in T5 neurons.

BIBLIOGRAPHY

- Abdelfattah, A. S., Kawashima, T., Singh, A., Novak, O., Liu, H., Shuai, Y., Huang, Y.-C., Campagnola, L., Seeman, S. C., Yu, J., Zheng, J., Grimm, J. B., Patel, R., Friedrich, J., Mensh, B. D., Paninski, L., Macklin, J. J., Murphy, G. J., Podgorski, K., Lin, B.-J., Chen, T.-W., Turner, G. C., Liu, Z., Koyama, M., Svoboda, K., Ahrens, M. B., Lavis, L. D. and Schreier, E. R. (2019) Bright and photostable chemigenetic indicators for extended in vivo voltage imaging. *Science*, eaav6416.
- Ache, J. M., Namiki, S., Lee, A., Branson, K. and Card, G. M. (2019a) State-dependent decoupling of sensory and motor circuits underlies behavioral flexibility in *Drosophila*. *Nature Neuroscience*, **22**, 1132–1139.
- Ache, J. M., Polsky, J., Alghailani, S., Parekh, R., Breads, P., Peek, M. Y., Bock, D. D., von Reyn, C. R. and Card, G. M. (2019b) Neural Basis for Looming Size and Velocity Encoding in the *Drosophila* Giant Fiber Escape Pathway. *Current Biology*, **29**, 1073–1081.e4.
- Adrian, E. D. and Zotterman, Y. (1926) The impulses produced by sensory nerve endings. *The Journal of Physiology*, **61**, 465–483.
- Ammer, G., Leonhardt, A., Bahl, A., Dickson, B. J. and Borst, A. (2015) Functional Specialization of Neural Input Elements to the *Drosophila* ON Motion Detector. *Current Biology*, **25**, 2247–2253.
- Ammer, G., Serbe-Kamp, E., Mauss, A. S., Richter, F. G., Fendl, S. and Borst, A. (2023) Multilevel visual motion opponency in *Drosophila*. *Nature Neuroscience*, **26**, 1894–1905.
- Ammer, G., Vieira, R. M., Fendl, S. and Borst, A. (2022) Anatomical distribution and functional roles of electrical synapses in *Drosophila*. *Current Biology*, **32**, 2022–2036.e4.
- Arenz, A., Drews, M. S., Richter, F. G., Ammer, G. and Borst, A. (2017) The Temporal Tuning of the *Drosophila* Motion Detectors Is Determined by the Dynamics of Their Input Elements. *Current Biology*, **27**, 929–944.
- Awatramani, G. B. and Slaughter, M. M. (2000) Origin of transient and sustained responses in ganglion cells of the retina. *Journal of Neuroscience*, **20**, 7087–7095.
- Baden, T. (2024) The vertebrate retina: a window into the evolution of computation in the brain. *Current Opinion in Behavioral Sciences*, **57**, 101391.
- Baden, T., Euler, T. and Berens, P. (2020) Understanding the retinal basis of vision across species. *Nature Reviews Neuroscience*, **21**, 5–20.

- Baden, T., Schubert, T., Chang, L., Wei, T., Zaichuk, M., Wissinger, B. and Euler, T. (2013) A tale of two retinal domains: Near-Optimal sampling of achromatic contrasts in natural scenes through asymmetric photoreceptor distribution. *Neuron*, **80**, 1206–1217.
- Bahl, A., Ammer, G., Schilling, T. and Borst, A. (2013) Object tracking in motion-blind flies. *Nature Neuroscience*, **16**, 730–738.
- Baines, R. A., Uhler, J. P., Thompson, A., Sweeney, S. T. and Bate, M. (2001) Altered electrical properties in *Drosophila* neurons developing without synaptic transmission. *Journal of Neuroscience*, **21**, 1523–1531.
- Barlow, H. B. and Levick, W. R. (1965) The mechanism of directionally selective units in rabbit's retina. *The Journal of Physiology*, **178**, 477–504.
- Barnhart, E. L., Wang, I. E., Wei, H., Desplan, C. and Clandinin, T. R. (2018) Sequential Nonlinear Filtering of Local Motion Cues by Global Motion Circuits. *Neuron*, **100**, 229–243.e3.
- Bates, A. S., Schlegel, P., Roberts, R. J., Drummond, N., Tamimi, I. F., Turnbull, R., Zhao, X., Marin, E. C., Popovici, P. D., Dhawan, S., Jamasb, A., Javier, A., Serratos Capdevila, L., Li, F., Rubin, G. M., Waddell, S., Bock, D. D., Costa, M. and Jefferis, G. S. (2020) Complete Connectomic Reconstruction of Olfactory Projection Neurons in the Fly Brain. *Current Biology*, **30**, 3183–3199.e6.
- Behnia, R., Clark, D. A., Carter, A. G., Clandinin, T. R. and Desplan, C. (2014) Processing properties of ON and OFF pathways for *Drosophila* motion detection. *Nature*, **512**, 427–430.
- Bloomfield, S. A. and Völgyi, B. (2009) The diverse functional roles and regulation of neuronal gap junctions in the retina. *Nature Reviews Neuroscience*, **10**, 495–506.
- Borst, A. (2014) Fly visual course control: behaviour, algorithms and circuits. *Nature Reviews Neuroscience* 2014 15:9, **15**, 590–599.
- Borst, A. and Haag, J. (2002) Neural networks in the cockpit of the fly. *Journal of Comparative Physiology A*, **188**, 419–437.
- Boyden, E. S., Zhang, F., Bamberg, E., Nagel, G. and Deisseroth, K. (2005) Millisecond-timescale, genetically targeted optical control of neural activity. *Nature Neuroscience*, **8**, 1263–1268.
- Braekevelt, C. R., Smith, S. A. and Smith, B. J. (1996) Fine structure of the retinal photoreceptors of the barred owl (*Strix varia*). *Histology and Histopathology*, **11**, 79–88.
- Brand, A. H. and Perrimon, N. (1993) Targeted gene expression as a means of altering cell fates and generating dominant phenotypes. *Development*, **118**, 401–415.
- Braun, A., Borst, A. and Meier, M. (2023) Disynaptic inhibition shapes tuning of OFF-motion detectors in *Drosophila*. *Current Biology*, **33**, 2260–2269.e4.

- Briggman, K. L. and Bock, D. D. (2012) Volume electron microscopy for neuronal circuit reconstruction. *Current Opinion in Neurobiology*, **22**, 154–161.
- Briggman, K. L., Helmstaedter, M. and Denk, W. (2011) Wiring specificity in the direction-selectivity circuit of the retina. *Nature*, **471**, 183–190.
- Buck, L. and Axel, R. (1991) A Novel Multigene Family May Encode Odorant Receptors: A Molecular Basis for Odor Recognition. *Cell*, **65**, 175–187.
- Buhmann, J., Sheridan, A., Malin-Mayor, C., Schlegel, P., Gerhard, S., Kazimiers, T., Krause, R., Nguyen, T. M., Heinrich, L., Lee, W. C. A., Wilson, R., Saalfeld, S., Jefferis, G. S., Bock, D. D., Turaga, S. C., Cook, M. and Funke, J. (2021) Automatic detection of synaptic partners in a whole-brain *Drosophila* electron microscopy data set. *Nature Methods*, **18**, 771–774.
- Cajal, S. R. and Sánchez, D. (1915) *Contribución al conocimiento de los centros nerviosos de los insectos*. Madrid: Imprenta de Hijos de Nicolás Moya.
- Chalasanani, S. H., Chronis, N., Tsunozaki, M., Gray, J. M., Ramot, D., Goodman, M. B. and Bargmann, C. I. (2007) Dissecting a circuit for olfactory behaviour in *Caenorhabditis elegans*. *Nature*, **450**, 63–70.
- Chalfie, M., Tu, Y., Euskirchen, G., Ward, W. W. and Prasher, D. C. (1994) Green fluorescent protein as a marker for gene expression. *Science*, **263**, 802–805.
- Chau, R., Chau, M. and Akter, F. (2024) Sensory Pathways. In *Neuroscience for Neurosurgeons* (eds F.Akter, N.Emptage, F.Engert and M. S.Berger), chap. 6, 99–120. Cambridge University Press, 1 edn.
- Chen, T. W., Wardill, T. J., Sun, Y., Pulver, S. R., Renninger, S. L., Baohan, A., Schreiter, E. R., Kerr, R. A., Orger, M. B., Jayaraman, V., Looger, L. L., Svoboda, K. and Kim, D. S. (2013) Ultrasensitive fluorescent proteins for imaging neuronal activity. *Nature*, **499**, 295–300.
- Cole, K. S. and Moore, J. W. (1960) Ionic current measurements in the squid giant axon membrane. *The Journal of general physiology*, **44**, 123–167.
- Cui, E. D. and Strowbridge, B. W. (2019) Selective attenuation of ether-a-go-go related K⁺ currents by endogenous acetylcholine reduces spike-frequency adaptation and network correlation. *eLife*, **8**.
- Cully, D. F., Pareiss, P. S., Liu, K. K., Schaeffer, J. M. and Arena, J. P. (1996) Identification of a *Drosophila melanogaster* glutamate-gated chloride channel sensitive to the antiparasitic agent avermectin. *Journal of Biological Chemistry*, **271**, 20187–20191.
- Currier, T. A., Pang, M. M. and Clandinin, T. R. (2023) Visual processing in the fly, from photoreceptors to behavior. *Genetics*, **224**, 64.
- Dana, H., Sun, Y., Mohar, B., Hulse, B. K., Kerlin, A. M., Hasseman, J. P., Tsegaye, G., Tsang, A., Wong, A., Patel, R., Macklin, J. J., Chen, Y.,

- Konnerth, A., Jayaraman, V., Looger, L. L., Schreier, E. R., Svoboda, K. and Kim, D. S. (2019) High-performance calcium sensors for imaging activity in neuronal populations and microcompartments. *Nature Methods*, **16**, 649–657.
- Davis, F. P., Nern, A., Picard, S., Reiser, M. B., Rubin, G. M., Eddy, S. R. and Henry, G. L. (2020) A genetic, genomic, and computational resource for exploring neural circuit function. *eLife*, **9**.
- Denk, W. and Horstmann, H. (2004) Serial block-face scanning electron microscopy to reconstruct three-dimensional tissue nanostructure. *PLoS Biology*, **2**, e329.
- Denk, W., Strickler, J. H. and Webb, W. W. (1990) Two-Photon Laser Scanning Fluorescence Microscopy. *Science*, **52**, 1778–1779.
- Deutsch, D., Pacheco, D. A., Encarnacion-Rivera, L., Pereira, T., Fathy, R., Clemens, J., Girardin, C., Calhoun, A., Ireland, E. C., Burke, A. T., Dorkenwald, S., McKellar, C., Macrina, T., Lu, R., Lee, K., Kemnitz, N., Ih, D., Castro, M., Halageri, A., Jordan, C., Silversmith, W., Wu, J., Seung, H. S. and Murthy, M. (2020) The neural basis for a persistent internal state in *Drosophila* females. *eLife*, **9**, 1–74.
- DeVries, S. H. (2000) Bipolar cells use kainate and AMPA receptors to filter visual information into separate channels. *Neuron*, **28**, 847–856.
- Dietzl, G., Chen, D., Schnorrer, F., Su, K. C., Barinova, Y., Fellner, M., Gasser, B., Kinsey, K., Oettel, S., Scheiblauer, S., Couto, A., Marra, V., Keleman, K. and Dickson, B. J. (2007) A genome-wide transgenic RNAi library for conditional gene inactivation in *Drosophila*. *Nature*, **448**, 151–156.
- Dorkenwald, S., Matsliah, A., Sterling, A. R., Schlegel, P., Yu, S.-c., McKellar, C. E., Lin, A., Costa, M., Eichler, K., Yin, Y., Silversmith, W., Schneider-Mizell, C., Jordan, C. S., Brittain, D., Halageri, A., Kuehner, K., Ogedengbe, O., Morey, R., Gager, J., Kruk, K., Perlman, E., Yang, R., Deutsch, D., Bland, D., Sorek, M., Lu, R., Macrina, T., Lee, K., Bae, J. A., Mu, S., Nehoran, B., Mitchell, E., Popovych, S., Wu, J., Jia, Z., Castro, M. A., Kemnitz, N., Ih, D., Bates, A. S., Eckstein, N., Funke, J., Collman, F., Bock, D. D., Jefferis, G. S. X. E., Seung, H. S., Murthy, M., Lenizo, Z., Burke, A. T., Willie, K. P., Serafetinidis, N., Hadjerol, N., Willie, R., Silverman, B., Ocho, J. A., Bañez, J., Candilada, R. A., Kristiansen, A., Panes, N., Yadav, A., Tancontian, R., Serona, S., Dolorosa, J. I., Vinson, K. J., Garner, D., Salem, R., Dagohoy, A., Skelton, J., Lopez, M., Capdevila, L. S., Badalamente, G., Stocks, T., Pandey, A., Akiatan, D. J., Hebditch, J., David, C., Sapkal, D., Monungolh, S. M., Sane, V., Pielago, M. L., Albero, M., Laude, J., dos Santos, M., Vohra, Z., Wang, K., Gogo, A. M., Kind, E., Mandahay, A. J., Martinez, C., Asis, J. D., Nair, C., Patel, D., Manaytay, M., Tamimi, I. F. M., Lim, C. A., Ampo, P. L., Pantujan, M. D., Javier, A., Bautista, D., Rana, R., Seguido, J., Parmar, B., Saguimpa, J. C., Moore, M., Plejzner, M. W., Larson, M., Hsu, J., Joshi, I., Kakadiya, D., Braun, A., Pilapil, C., Gkantia, M., Parmar, K., Vanderbeck, Q., Salgarella, I., Dunne, C., Munnely, E., Kang, C. H., Lörsch, L., Lee, J., Kmecova, L., Sancer, G.,

- Baker, C., Joroff, J., Calle, S., Patel, Y., Sato, O., Fang, S., Salocot, J., Salman, F., Molina-Obando, S., Brooks, P., Bui, M., Lichtenberger, M., Tamboboy, E., Molloy, K., Santana-Cruz, A. E., Hernandez, A., Yu, S., Diwan, A., Patel, M., Aiken, T. R., Morejohn, S., Koskela, S., Yang, T., Lehmann, D., Chojetzki, J., Sisodiya, S., Koolman, S., Shiu, P. K., Cho, S., Bast, A., Reicher, B., Blanquart, M., Houghton, L., Choi, H., Ioannidou, M., Collie, M., Eckhardt, J., Gorko, B., Guo, L., Zheng, Z., Poh, A., Lin, M., Taisz, I., Murfin, W., Díez, Á. S., Reinhard, N., Gibb, P., Patel, N., Kumar, S., Yun, M., Wang, M., Jones, D., Encarnacion-Rivera, L., Oswald, A., Jadia, A., Erginkaya, M., Drummond, N., Walter, L., Tastekin, I., Zhong, X., Mabuchi, Y., Figueroa Santiago, F. J., Verma, U., Byrne, N., Kunze, E., Crahan, T., Margossian, R., Kim, H., Georgiev, I., Szorenyi, F., Adachi, A., Barger, B., Stürner, T., Demarest, D., Gür, B., Becker, A. N., Turnbull, R., Morren, A., Sandoval, A., Moreno-Sanchez, A., Pacheco, D. A., Samara, E., Croke, H., Thomson, A., Laughland, C., Dutta, S. B., de Antón, P. G. A., Huang, B., Pujols, P., Haber, I., González-Segarra, A., Choe, D. T., Lukyanova, V., Mancini, N., Liu, Z., Okubo, T., Flynn, M. A., Vitelli, G., Laturney, M., Li, F., Cao, S., Manyari-Diaz, C., Yim, H., Duc Le, A., Maier, K., Yu, S., Nam, Y., Bāba, D., Abusaif, A., Francis, A., Gayk, J., Huntress, S. S., Barajas, R., Kim, M., Cui, X., Sterne, G. R., Li, A., Park, K., Dempsey, G., Mathew, A., Kim, J., Kim, T., Wu, G.-t., Dhawan, S., Brotas, M., Zhang, C.-h., Bailey, S., Del Toro, A., Yang, R., Gerhard, S., Champion, A., Anderson, D. J., Behnia, R., Bidaye, S. S., Borst, A., Chiappe, E., Colodner, K. J., Dacks, A., Dickson, B., Garcia, D., Hampel, S., Hartenstein, V., Hassan, B., Helfrich-Forster, C., Huetteroth, W., Kim, J., Kim, S. S., Kim, Y.-J., Kwon, J. Y., Lee, W.-C., Linneweber, G. A., Maimon, G., Mann, R., Noselli, S., Pankratz, M., Prieto-Godino, L., Read, J., Reiser, M., von Reyn, K., Ribeiro, C., Scott, K., Seeds, A. M., Selcho, M., Silies, M., Simpson, J., Waddell, S., Wernet, M. F., Wilson, R. I., Wolf, F. W., Yao, Z., Yapici, N. and Zandawala, M. (2024) Neuronal wiring diagram of an adult brain. *Nature*, **634**, 124–138.
- Dorkenwald, S., McKellar, C. E., Macrina, T., Kemnitz, N., Lee, K., Lu, R., Wu, J., Popovych, S., Mitchell, E., Nehoran, B., Jia, Z., Bae, J. A., Mu, S., Ih, D., Castro, M., Ogedengbe, O., Halageri, A., Kuehner, K., Sterling, A. R., Ashwood, Z., Zung, J., Brittain, D., Collman, F., Schneider-Mizell, C., Jordan, C., Silversmith, W., Baker, C., Deutsch, D., Encarnacion-Rivera, L., Kumar, S., Burke, A., Bland, D., Gager, J., Hebditch, J., Koolman, S., Moore, M., Morejohn, S., Silverman, B., Willie, K., Willie, R., chieh Yu, S., Murthy, M. and Seung, H. S. (2021) FlyWire: online community for whole-brain connectomics. *Nature Methods*, **19**, 119–128.
- Dowling, J. (1987) *The Retina—An Approachable Part of the Brain*. Cambridge: Harvard University Press.
- Drews, M. S., Leonhardt, A., Pirogova, N., Richter, F. G., Schuetzenberger, A., Braun, L., Serbe, E. and Borst, A. (2020) Dynamic Signal Compression for Robust Motion Vision in Flies. *Current Biology*, **30**, 209–221.e8.
- Eckstein, N., Bates, A. S., Champion, A., Du, M., Yin, Y., Schlegel, P., Lu, A. K.-Y., Rymer, T., Finley-May, S., Paterson, T., Parekh, R., Dorkenwald, S., Matsliah, A., Yu, S.-C., McKellar, C., Sterling, A., Eichler, K., Costa,

- M., Seung, S., Murthy, M., Hartenstein, V., Jefferis, G. S. and Funke, J. (2023) Neurotransmitter Classification from Electron Microscopy Images at Synaptic Sites in *Drosophila Melanogaster*. *bioRxiv*, 2020.06.12.148775.
- Euler, T., Detwiler, P. B. and Denk, W. (2002) Directionally selective calcium signals in dendrites of starburst amacrine cells. *Nature*, **418**, 845–852.
- Euler, T., Haverkamp, S., Schubert, T. and Baden, T. (2014) Retinal bipolar cells: Elementary building blocks of vision. *Nature Reviews Neuroscience*, **15**, 507–519.
- Exner, S. (1894) *Entwurf zu einer physiologischen Erklärung der psychischen Erscheinungen*. Leipzig und Wien: Deuticke Verlag.
- Fechner, G. T. (1860) *Elemente der Psychophysik*. Leipzig: Breitkopf und Haertel.
- Feiler, R., Bjornson, R., Kirschfeld, K., Mismer, D., Rubin, G. M., Smith, D. P., Socolich, M. and Zuker, C. S. (1992) Ectopic expression of ultraviolet-rhodopsins in the blue photoreceptor cells of *Drosophila*: Visual physiology and photochemistry of transgenic animals. *Journal of Neuroscience*, **12**, 3862–3868.
- Fendl, S., Vieira, R. M. and Borst, A. (2020) Conditional protein tagging methods reveal highly specific subcellular distribution of ion channels in motion-sensing neurons. *eLife*, **9**, 1–48.
- Fenk, L. M., Kim, A. J. and Maimon, G. (2021) Suppression of motion vision during course-changing, but not course-stabilizing, navigational turns. *Current Biology*, **31**, 4608–4619.e3.
- Field, G. D. and Chichilnisky, E. J. (2007) Information processing in the primate retina: Circuitry and coding. *Annual Review of Neuroscience*, **30**, 1–30.
- Fischbach, K. F. and Dittrich, A. P. (1989) The optic lobe of *Drosophila melanogaster*. I. A Golgi analysis of wild-type structure. *Cell and Tissue Research*, **258**, 441–475.
- Fisher, Y. E., Silies, M. and Clandinin Correspondence, T. R. (2015) Orientation Selectivity Sharpens Motion Detection in *Drosophila*. *Neuron*, **88**, 390–402.
- Gabbiani, F., Krapp, H. G. and Laurent, G. (1999) Computation of object approach by a wide-field, motion-sensitive neuron. *Journal of Neuroscience*, **19**, 1122–1141.
- Gallio, M., Ofstad, T. A., Macpherson, L. J., Wang, J. W. and Zuker, C. S. (2011) The coding of temperature in the *Drosophila* brain. *Cell*, **144**, 614–624.
- Gjorgjieva, J., Sompolinsky, H. and Meister, M. (2014) Benefits of pathway splitting in sensory coding. *Journal of Neuroscience*, **34**, 12127–12144.
- Goodale, M. A. and Milner, A. D. (1992) Separate visual pathways for perception and action. *Trends in Neurosciences*, **15**, 20–25.

- Götz, K. G. (1964) Optomotorische Untersuchung des visuellen systems einiger Augenmutanten der Fruchtfliege *Drosophila*. *Kybernetik*, **2**, 77–92.
- Govorunova, E. G., Sineshchekov, O. A., Janz, R., Liu, X. and Spudich, J. L. (2015) Natural light-gated anion channels: A family of microbial rhodopsins for advanced optogenetics. *Science*, **349**, 647–650.
- Gradinaru, V., Thompson, K. R. and Deisseroth, K. (2008) eNpHR: A *Natronomonas halorhodopsin* enhanced for optogenetic applications. *Brain Cell Biology*, **36**, 129–139.
- Groschner, L. N., Malis, J. G., Zuidinga, B. and Borst, A. (2022) A biophysical account of multiplication by a single neuron. *Nature*, **603**, 119–123.
- Gruntman, E., Romani, S. and Reiser, M. B. (2018) Simple integration of fast excitation and offset, delayed inhibition computes directional selectivity in *Drosophila*. *Nature Neuroscience*, **21**, 250–257.
- Gruntman, E., Romani, S. and Reiser, M. B. (2019) The computation of directional selectivity in the *Drosophila* OFF motion pathway. *eLife*, **8**.
- Haag, J., Arenz, A., Serbe, E., Gabbiani, F. and Borst, A. (2016) Complementary mechanisms create direction selectivity in the fly. *eLife*, **5**.
- Haag, J. and Borst, A. (2005) Dye-coupling visualizes networks of large-field motion-sensitive neurons in the fly. *Journal of Comparative Physiology*, **191**, 445–454.
- Haag, J., Mishra, A. and Borst, A. (2017) A common directional tuning mechanism of *Drosophila* motion-sensing neurons in the ON and in the OFF pathway. *Elife*, **6**.
- Haag, J., Wertz, A. and Borst, A. (2007) Integration of lobula plate output signals by DNOVS₁, an identified premotor descending neuron. *Journal of Neuroscience*, **27**, 1992–2000.
- Haag, J., Wertz, A. and Borst, A. (2010) Central gating of fly optomotor response. *Proceedings of the National Academy of Sciences of the United States of America*, **107**, 20104–20109.
- Haikala, V., Joesch, M., Borst, A. and Mauss, A. S. (2013) Optogenetic Control of Fly Optomotor Responses. *Journal of Neuroscience*, **33**, 13927–13934.
- Hamada, F. N., Rosenzweig, M., Kang, K., Pulver, S. R., Ghezzi, A., Jegla, T. J. and Garrity, P. A. (2008) An internal thermal sensor controlling temperature preference in *Drosophila*. *Nature*, **454**, 217–220.
- Hardie, R. C. (1989) A histamine-activated chloride channel involved in neurotransmission at a photoreceptor synapse. *Nature*, **339**, 704–706.
- Harris, K. M., Perry, E., Bourne, J., Feinberg, M., Ostroff, L. and Hurlburt, J. (2006) Uniform serial sectioning for transmission electron microscopy. *Journal of Neuroscience*, **26**, 12101–12103.

- Hashimoto, T., Katai, S., Saito, Y., Kobayashi, F. and Goto, T. (2013) ON and OFF channels in human retinal ganglion cells. *Journal of Physiology*, **591**, 327–337.
- Hausen, K. (1984) The Lobula-Complex of the Fly: Structure, Function and Significance in Visual Behaviour. In *Photoreception and Vision in Invertebrates*, 523–559. New York: Springer, Boston, MA.
- Heinrich, L., Funke, J., Pape, C., Nunez-Iglesias, J. and Saalfeld, S. (2018) Synaptic cleft segmentation in non-isotropic volume electron microscopy of the complete *Drosophila* brain. In *Lecture Notes in Computer Science*, vol. 11071 LNCS, 317–325. Springer Verlag.
- Heisenberg, M. and Buchner, E. (1977) The role of retinula cell types in visual behavior of *Drosophila melanogaster*. *Journal of Comparative Physiology*, **117**, 127–162.
- Heng, J. A., Woodford, M. and Polania, R. (2020) Efficient sampling and noisy decisions. *eLife*, **9**, 1–49.
- Hensley, S. H., Yang, X. L. and Wu, S. M. (1993) Relative contribution of rod and cone inputs to bipolar cells and ganglion cells in the tiger salamander retina. *Journal of Neurophysiology*, **69**, 2086–2098.
- Herculano-Houzel, S. (2009) The human brain in numbers: A linearly scaled-up primate brain. *Frontiers in Human Neuroscience*, **3**, 857.
- Heymann, J. A., Hayles, M., Gestmann, I., Giannuzzi, L. A., Lich, B. and Subramaniam, S. (2006) Site-specific 3D imaging of cells and tissues with a dual beam microscope. *Journal of Structural Biology*, **155**, 63–73.
- Hille, B. (1991) *Ionic channels of excitable membranes*. Sunderland: Sinauer associates inc.
- Hodgkin, A. L. and Huxley, A. F. (1952) The components of membrane conductance in the giant axon of *Loligo*. *The Journal of Physiology*, **116**, 473–496.
- Hörmann, N., Schilling, T., Ali, A. H., Serbe, E., Mayer, C., Borst, A. and Pujol-Martí, J. (2020) A combinatorial code of transcription factors specifies subtypes of visual motion-sensing neurons in *Drosophila*. *Development*, **147**.
- Hulse, B. K., Haberkern, H., Franconville, R., Turner-Evans, D. B., Takemura, S. Y., Wolff, T., Noorman, M., Dreher, M., Dan, C., Parekh, R., Hermundstad, A. M., Rubin, G. M. and Jayaraman, V. (2021) A connectome of the *Drosophila* central complex reveals network motifs suitable for flexible navigation and context-dependent action selection. *eLife*, **10**.
- Huston, S. J. and Krapp, H. G. (2008) Visuomotor transformation in the fly gaze stabilization system. *PLoS Biology*, **6**, 1468–1478.

- Huston, S. J. and Krapp, H. G. (2009) Nonlinear integration of visual and haltere inputs in fly neck motor neurons. *Journal of Neuroscience*, **29**, 13097–13105.
- Inagaki, H. K., Jung, Y., Hoopfer, E. D., Wong, A. M., Mishra, N., Lin, J. Y., Tsien, R. Y. and Anderson, D. J. (2014) Optogenetic control of *Drosophila* using a red-shifted channelrhodopsin reveals experience-dependent influences on courtship. *Nature Methods*, **11**, 325–332.
- Ingram, N. T., Sampath, A. P. and Fain, G. L. (2016) Why are rods more sensitive than cones? *Journal of Physiology*, **594**, 5415–5426.
- Joesch, M., Plett, J., Borst, A. and Reiff, D. F. (2008) Response Properties of Motion-Sensitive Visual Interneurons in the Lobula Plate of *Drosophila melanogaster*. *Current Biology*, **18**, 368–374.
- Joesch, M., Schnell, B., Raghu, S. V., Reiff, D. F. and Borst, A. (2010) ON and OFF pathways in *Drosophila* motion vision. *Nature*, **468**, 300–304.
- Juusola, M., Dau, A., Zheng, L. and Rien, D. (2016) Electrophysiological method for recording intracellular voltage responses of *Drosophila* photoreceptors and interneurons to light stimuli in vivo. *Journal of Visualized Experiments*, **2016**, e54142.
- Kim, A. J., Fenk, L. M., Lyu, C. and Maimon, G. (2017) Quantitative Predictions Orchestrate Visual Signaling in *Drosophila*. *Cell*, **168**, 280–294.e12.
- Kim, H., Park, H., Lee, J. and Kim, A. J. (2023) A visuomotor circuit for evasive flight turns in *Drosophila*. *Current Biology*, **33**, 321–335.e6.
- Kim, J. S., Greene, M. J., Zlateski, A., Lee, K., Richardson, M., Turaga, S. C., Purcaro, M., Balkam, M., Robinson, A., Behabadi, B. F., Campos, M., Denk, W. and Seung, H. S. (2014) Space-time wiring specificity supports direction selectivity in the retina. *Nature*, **509**, 331–336.
- Kitamoto, T. (2001) Conditional modification of behavior in drosophila by targeted expression of a temperature-sensitive *shibire* allele in defined neurons. *Journal of Neurobiology*, **47**, 81–92.
- Klapoetke, N. C., Murata, Y., Kim, S. S., Pulver, S. R., Birdsey-Benson, A., Cho, Y. K., Morimoto, T. K., Chuong, A. S., Carpenter, E. J., Tian, Z., Wang, J., Xie, Y., Yan, Z., Zhang, Y., Chow, B. Y., Surek, B., Melkonian, M., Jayaraman, V., Constantine-Paton, M., Wong, G. K. S. and Boyden, E. S. (2014) Independent optical excitation of distinct neural populations. *Nature Methods*, **11**, 338–346.
- Klapoetke, N. C., Nern, A., Peek, M. Y., Rogers, E. M., Breads, P., Rubin, G. M., Reiser, M. B. and Card, G. M. (2017) Ultra-selective looming detection from radial motion opponency. *Nature*, **551**, 237–241.
- Knoll, M. and Ruska, E. (1932) Das Elektronenmikroskop. *Zeitschrift für Physik*, **78**, 318–339.

- Knöpfel, T. and Song, C. (2019) Optical voltage imaging in neurons: moving from technology development to practical tool. *Nature Reviews Neuroscience*, **20**, 719–727.
- Knott, G., Marchman, H., Wall, D. and Lich, B. (2008) Serial section scanning electron microscopy of adult brain tissue using focused ion beam milling. *Journal of Neuroscience*, **28**, 2959–2964.
- Kohn, J. R., Portes, J. P., Christenson, M. P., Abbott, L. F. and Behnia, R. (2021) Flexible filtering by neural inputs supports motion computation across states and stimuli. *Current Biology*, **31**, 5249–5260.e5.
- Krapp, H. G. and Hengstenberg, R. (1996) Estimation of self-motion by optic flow processing in single visual interneurons. *Nature*, **384**, 463–466.
- Kryger, Z., Galli-Resta, L., Jacobs, G. H. and Reese, B. E. (1998) The topography of rod and cone photoreceptors in the retina of the ground squirrel. *Visual Neuroscience*, **15**, 685–691.
- Lai, S. L. and Lee, T. (2006) Genetic mosaic with dual binary transcriptional systems in *Drosophila*. *Nature Neuroscience*, **9**, 703–709.
- Laughlin, S. (1981) A simple coding procedure enhances a neuron's information capacity. *Zeitschrift für Naturforschung - Section C Journal of Biosciences*, **36**, 910–912.
- Leong, J. C. S., Esch, J. J., Poole, B., Ganguli, S. and Clandinin, T. R. (2016) Direction Selectivity in *Drosophila* Emerges from Preferred-Direction Enhancement and Null-Direction Suppression. *Journal of Neuroscience*, **36**, 8078–8092.
- Lettvin, J. Y., Maturana, H. R., Maturana, H. R., McCulloch, W. S. and Pitts, W. H. (1959) What the Frog's Eye Tells the Frog's Brain. *Proceedings of the IRE*, **47**, 1940–1951.
- Li, B., Chavarha, M., Kobayashi, Y., Yoshinaga, S., Nakajima, K., Lin, M. Z. and Inoue, T. (2020a) Two-Photon Voltage Imaging of Spontaneous Activity from Multiple Neurons Reveals Network Activity in Brain Tissue. *iScience*, **23**, 101363.
- Li, F., Lindsey, J., Marin, E. C., Otto, N., Dreher, M., Dempsey, G., Stark, I., Bates, A. S., Pleijzier, M. W., Schlegel, P., Nern, A., Takemura, S., Eckstein, N., Yang, T., Francis, A., Braun, A., Parekh, R., Costa, M., Scheffer, L., Aso, Y., Jefferis, G. S., Abbott, L. F., Litwin-Kumar, A., Waddell, S. and Rubin, G. M. (2020b) The connectome of the adult *Drosophila* mushroom body provides insights into function. *eLife*, **9**, 1–217.
- Li, Y., Yu, S., Jia, X., Qiu, X. and He, J. (2024) Defining morphologically and genetically distinct GABAergic/cholinergic amacrine cell subtypes in the vertebrate retina. *PLoS Biology*, **22**, e3002506.
- Lima, S. Q. and Miesenböck, G. (2005) Remote control of behavior through genetically targeted photostimulation of neurons. *Cell*, **121**, 141–152.

- Lin, J. Y., Knutsen, P. M., Muller, A., Kleinfeld, D. and Tsien, R. Y. (2013) ReaChR: A red-shifted variant of channelrhodopsin enables deep transcranial optogenetic excitation. *Nature Neuroscience*, **16**, 1499–1508.
- Lin, M. Z. and Schnitzer, M. J. (2016) Genetically encoded indicators of neuronal activity. *Nature Neuroscience*, **19**, 1142–1153.
- Liu, W. W. and Wilson, R. I. (2013) Glutamate is an inhibitory neurotransmitter in the *Drosophila* olfactory system. *Proceedings of the National Academy of Sciences of the United States of America*, **110**, 10294–10299.
- Longden, K. D., Rogers, E. M., Nern, A., Dionne, H. and Reiser, M. B. (2023) Different spectral sensitivities of ON- and OFF-motion pathways enhance the detection of approaching color objects in *Drosophila*. *Nature Communications*, **14**, 1–22.
- Luan, H., Peabody, N. C., Vinson, C. R. R. and White, B. H. (2006) Refined Spatial Manipulation of Neuronal Function by Combinatorial Restriction of Transgene Expression. *Neuron*, **52**, 425–436.
- Maisak, M. S., Haag, J., Ammer, G., Serbe, E., Meier, M., Leonhardt, A., Schilling, T., Bahl, A., Rubin, G. M., Nern, A., Dickson, B. J., Reiff, D. F., Hopp, E. and Borst, A. (2013) A directional tuning map of *Drosophila* elementary motion detectors. *Nature*, **500**, 212–218.
- Malnic, B., Hirono, J., Sato, T. and Buck, L. B. (1999) Combinatorial receptor codes for odors. *Cell*, **96**, 713–723.
- Masland, R. H. (2001) The fundamental plan of the retina. *Nature Neuroscience*, **4**, 877–886.
- Masseck, O. A., Förster, S. and Hoffmann, K. P. (2010) Sensitivity of the goldfish motion detection system revealed by incoherent random dot stimuli: Comparison of behavioural and neuronal data. *PLoS ONE*, **5**.
- Matsliah, A., Yu, S.-c., Kruk, K., Bland, D., Burke, A. T., Gager, J., Hebditch, J., Silverman, B., Willie, K. P., Willie, R., Sorek, M., Sterling, A. R., Kind, E., Garner, D., Sancer, G., Wernet, M. F., Kim, S. S., Murthy, M., Seung, H. S., David, C., Joroff, J., Kristiansen, A., Stocks, T., Braun, A., Silies, M., Skelton, J., Aiken, T. R., Ioannidou, M., Collie, M., Linneweber, G. A., Molina-Obando, S., Dorckenwald, S., Panes, N., Gogo, A. M., Rastgarmoghaddam, D., Pilapil, C., Candilada, R. A., Serafetinidis, N., Lee, W.-C., Borst, A., Wilson, R. I., Schlegel, P. and Jefferis, G. S. X. E. (2024) Neuronal parts list and wiring diagram for a visual system. *Nature*, **634**, 166–180.
- Mauss, A. S. and Borst, A. (2016) Electrophysiological Recordings from Lobula Plate Tangential Cells in *Drosophila*. *Methods Mol Biol*, **1478**, 321–332.
- Mauss, A. S., Busch, C. and Borst, A. (2017a) Optogenetic Neuronal Silencing in *Drosophila* during Visual Processing. *Scientific Reports*, **7**, 1–12.

- Mauss, A. S., Meier, M., Serbe, E. and Borst, A. (2014) Optogenetic and Pharmacologic Dissection of Feedforward Inhibition in *Drosophila* Motion Vision. *Journal of Neuroscience*, **34**, 2254–2263.
- Mauss, A. S., Pankova, K., Arenz, A., Nern, A., Rubin, G. M. and Borst, A. (2015) Neural Circuit to Integrate Opposing Motions in the Visual Field. *Cell*, **162**, 351–362.
- Mauss, A. S., Vlasits, A., Borst, A. and Feller, M. (2017b) Visual Circuits for Direction Selectivity. *Annu Rev Neurosci*, **40**, 211–230.
- Meier, M. and Borst, A. (2019) Extreme Compartmentalization in a *Drosophila* Amacrine Cell. *Current Biology*, **29**, 1545–1550.e2.
- Meier, M., Serbe, E., Maisak, M. S., Haag, J., Dickson, B. J. and Borst, A. (2014) Neural circuit components of the *Drosophila* OFF motion vision pathway. *Current Biology*.
- Meinertzhagen, I. A. and O’Neil, S. D. (1991) Synaptic organization of columnar elements in the lamina of the wild type in *Drosophila melanogaster*. *Journal of Comparative Neurology*, **305**, 232–263.
- Mirzoyan, Z., Sollazzo, M., Allocca, M., Valenza, A. M., Grifoni, D. and Bellosta, P. (2019) *Drosophila melanogaster*: A model organism to study cancer. *Frontiers in Genetics*, **10**, 425859.
- Mishra, A., Serbe-Kamp, E., Borst, A. and Haag, J. (2023) Voltage to Calcium Transformation Enhances Direction Selectivity in *Drosophila* T4 Neurons. *Journal of Neuroscience*, **43**, 2497–2514.
- Morgan, T. H. (1910) Sex limited inheritance in *Drosophila*. *Science*, **32**, 120–122.
- Mu, L., Ito, K., Bacon, J. P. and Strausfeld, N. J. (2012) Optic glomeruli and their inputs in *Drosophila* share an organizational ground pattern with the antennal lobes. *Journal of Neuroscience*, **32**, 6061–6071.
- Murthy, M., Fiete, I. and Laurent, G. (2008) Testing Odor Response Stereotypy in the *Drosophila* Mushroom Body. *Neuron*, **59**, 1009–1023.
- Nagel, G., Szellas, T., Huhn, W., Kateriya, S., Adeishvili, N., Berthold, P., Ollig, D., Hegemann, P. and Bamberg, E. (2003) Channelrhodopsin-2, a directly light-gated cation-selective membrane channel. *Proceedings of the National Academy of Sciences of the United States of America*, **100**, 13940–13945.
- Nakai, J., Ohkura, M. and Imoto, K. (2001) A high signal-to-noise Ca²⁺ probe composed of a single green fluorescent protein. *Nature Biotechnology*, **19**, 137–141.
- Namiki, S., Dickinson, M. H., Wong, A. M., Korff, W. and Card, G. M. (2018) The functional organization of descending sensory-motor pathways in *Drosophila*. *eLife*, **7**.

- Neher, E. and Sakmann, B. (1976) Single-channel currents recorded from membrane of denervated frog muscle fibres. *Nature*, **260**, 799–802.
- Nern, A., Lösche, F., Takemura, S.-y., Burnett, L. E., Dreher, M., Gruntman, E., Hoeller, J., Huang, G. B., Januszewski, M., Klapoetke, N. C., Koskela, S., Longden, K. D., Lu, Z., Preibisch, S., Qiu, W., Rogers, E. M., Seenivasan, P., Zhao, A., Bogovic, J., Canino, B. S., Clements, J., Cook, M., Finley-May, S., Flynn, M. A., Hameed, I., Hayworth, K. J., Hopkins, G. P., Hubbard, P. M., Katz, W. T., Kovalyak, J., Lauchie, S. A., Leonard, M., Lohff, A., Maldonado, C. A., Mooney, C., Okeoma, N., Olbris, D. J., Ordish, C., Paterson, T., Phillips, E. M., Pietzsch, T., Salinas, J. R., Rivlin, P. K., Scott, A. L., Scuderi, L. A., Takemura, S., Talebi, I., Thomson, A., Trautman, E. T., Umayam, L., Walsh, C., Walsh, J. J., Xu, C. S., Yakal, E. A., Yang, T., Zhao, T., Funke, J., George, R., Hess, H. F., Jefferis, G. S., Knecht, C., Korff, W., Plaza, S. M., Romani, S., Saalfeld, S., Scheffer, L. K., Berg, S., Rubin, G. M. and Reiser, M. B. (2024) Connectome-driven neural inventory of a complete visual system. *bioRxiv*, 2024.04.16.589741.
- Oteiza, P., Odstrcil, I., Lauder, G., Portugues, R. and Engert, F. (2017) A novel mechanism for mechanosensory-based rheotaxis in larval zebrafish. *Nature*, **547**, 445–448.
- Pankova, K. and Borst, A. (2016) RNA-Seq Transcriptome Analysis of Direction-Selective T₄/T₅ Neurons in *Drosophila*. *PLoS One*, **11**, e0163986.
- Pankova, K. and Borst, A. (2017) Transgenic line for the identification of cholinergic release sites in *Drosophila melanogaster*. *Journal of Experimental Biology*, **220**, 1405–1410.
- Panser, K., Tirian, L., Schulze, F., Villalba, S., Jefferis, G. S., Bühler, K. and Straw, A. D. (2016) Automatic Segmentation of *Drosophila* Neural Compartments Using GAL4 Expression Data Reveals Novel Visual Pathways. *Current Biology*, **26**, 1943–1954.
- Peichl, L. (2005) Diversity of mammalian photoreceptor properties: Adaptations to habitat and lifestyle? *The Anatomical Record*, **287**, 1001–1012.
- Peng, H., Chung, P., Long, F., Qu, L., Jenett, A., Seeds, A. M., Myers, E. W. and Simpson, J. H. (2011) BrainAligner: 3D registration atlases of *Drosophila* brains. *Nature Methods*, **8**, 493–498.
- Perkins, L. A., Holderbaum, L., Tao, R., Hu, Y., Sopko, R., McCall, K., Yang-Zhou, D., Flockhart, I., Binari, R., Shim, H. S., Miller, A., Housden, A., Foos, M., Randkelv, S., Kelley, C., Namgyal, P., Villalta, C., Liu, L. P., Jiang, X., Huan-Huan, Q., Wang, X., Fujiyama, A., Toyoda, A., Ayers, K., Blum, A., Czech, B., Neumuller, R., Yan, D., Cavallaro, A., Hibbard, K., Hall, D., Cooley, L., Hannon, G. J., Lehmann, R., Parks, A., Mohr, S. E., Ueda, R., Kondo, S., Ni, J. Q. and Perrimon, N. (2015) The transgenic RNAi project at Harvard medical school: Resources and validation. *Genetics*, **201**, 843–852.

- Pfeiffer, B. D., Ngo, T.-T. T., Hibbard, K. L., Murphy, C., Jenett, A., Truman, J. W. and Rubin, G. M. (2010) Refinement of tools for targeted gene expression in *Drosophila*. *Genetics*, **186**, 735–755.
- Plaza, S. M., Clements, J., Dolafi, T., Umayam, L., Neubarth, N. N., Scheffer, L. K. and Berg, S. (2022) neuPrint: An open access tool for EM connectomics. *Frontiers in Neuroinformatics*, **16**, 896292.
- Potter, C. J., Tasic, B., Russler, E. V., Liang, L. and Luo, L. (2010) The Q System: A Repressible Binary System for Transgene Expression, Lineage Tracing, and Mosaic Analysis. *Cell*, **141**, 536–548.
- Puthusser, T., Percival, K. A., Venkataramani, S., Gayet-Primo, J., Grünert, U. and Rowland Taylor, W. (2014) Kainate receptors mediate synaptic input to transient and sustained OFF visual pathways in primate retina. *Journal of Neuroscience*, **34**, 7611–7621.
- Raji, J. I. and Potter, C. J. (2021) The number of neurons in *Drosophila* and mosquito brains. *PLoS ONE*, **16**.
- Ramos-Traslosheros, G. and Silies, M. (2021) The physiological basis for contrast opponency in motion computation in *Drosophila*. *Nature Communications*, **12**, 1–16.
- Reardon, S. (2017) 3D map of mouse neurons reveals complex connections. *Nature*.
- Reichardt, W. (1961) Autocorrelation, a principle for evaluation of sensory information by the central nervous system. 303–317.
- Reinhard, N., Schubert, F. K., Bertolini, E., Hagedorn, N., Manoli, G., Sekiguchi, M., Yoshii, T., Rieger, D. and Helfrich-Förster, C. (2022) The Neuronal Circuit of the Dorsal Circadian Clock Neurons in *Drosophila melanogaster*. *Frontiers in Physiology*, **13**, 886432.
- von Reyn, C. R., Nern, A., Williamson, W. R., Breads, P., Wu, M., Namiki, S. and Card, G. M. (2017) Feature Integration Drives Probabilistic Behavior in the *Drosophila* Escape Response. *Neuron*, **94**, 1190–1204.e6.
- Richter, F. G., Fendl, S., Haag, J., Drews, M. S. and Borst, A. (2018) Glutamate Signaling in the Fly Visual System. *iScience*, **7**, 85–95.
- Rister, J., Pauls, D., Schnell, B., Ting, C. Y., Lee, C. H., Sinakevitch, I., Morante, J., Strausfeld, N. J., Ito, K. and Heisenberg, M. (2007) Dissection of the Peripheral Motion Channel in the Visual System of *Drosophila melanogaster*. *Neuron*, **56**, 155–170.
- Rosenzweig, M., Brennan, K. M., Tayler, T. D., Phelps, P. O., Patapoutian, A. and Garrity, P. A. (2005) The *Drosophila* ortholog of vertebrate TRPA1 regulates thermotaxis. *Genes and Development*, **19**, 419–424.
- Salcedo, E., Huber, A., Henrich, S., Chadwell, L. V., Chou, W. H., Paulsen, R. and Britt, S. G. (1999) Blue- and green-absorbing visual pigments of *Drosophila*: Ectopic expression and physiological characterization of

- the R8 photoreceptor cell- specific Rh5 and Rh6 rhodopsins. *Journal of Neuroscience*, **19**, 10716–10726.
- Sanfilippo, P., Kim, A. J., Bhukel, A., Yoo, J., Mirshahidi, P. S., Pandey, V., Bevir, H., Yuen, A., Mirshahidi, P. S., Guo, P., Li, H. S., Wohlschlegel, J. A., Aso, Y. and Zipursky, S. L. (2024) Mapping of multiple neurotransmitter receptor subtypes and distinct protein complexes to the connectome. *Neuron*, **112**, 942–958.e13.
- Scheffer, L. K., Xu, C. S., Januszewski, M., Lu, Z., Takemura, S. Y., Hayworth, K. J., Huang, G. B., Shinomiya, K., Maitin-Shepard, J., Berg, S., Clements, J., Hubbard, P. M., Katz, W. T., Umayam, L., Zhao, T., Ackerman, D., Blakely, T., Bogovic, J., Dolafi, T., Kainmueller, D., Kawase, T., Khairy, K. A., Leavitt, L., Li, P. H., Lindsey, L., Neubarth, N., Olbris, D. J., Otsuna, H., Trautman, E. T., Ito, M., Bates, A. S., Goldammer, J., Wolff, T., Svirskas, R., Schlegel, P., Neace, E. R., Knecht, C. J., Alvarado, C. X., Bailey, D. A., Ballinger, S., Borycz, J. A., Canino, B. S., Cheatham, N., Cook, M., Dreher, M., Duclos, O., Eubanks, B., Fairbanks, K., Finley, S., Forknall, N., Francis, A., Hopkins, G. P., Joyce, E. M., Kim, S., Kirk, N. A., Kovalyak, J., Lauchie, S. A., Lohff, A., Maldonado, C., Manley, E. A., McLin, S., Mooney, C., Ndama, M., Ogundeyi, O., Okeoma, N., Ordish, C., Padilla, N., Patrick, C., Paterson, T., Phillips, E. E., Phillips, E. M., Rampally, N., Ribeiro, C., Robertson, M. K., Rymer, J. T., Ryan, S. M., Sammons, M., Scott, A. K., Scott, A. L., Shinomiya, A., Smith, C., Smith, K., Smith, N. L., Sobeski, M. A., Suleiman, A., Swift, J., Takemura, S., Talebi, I., Tarnogorska, D., Tenshaw, E., Tokhi, T., Walsh, J. J., Yang, T., Horne, J. A., Li, F., Parekh, R., Rivlin, P. K., Jayaraman, V., Costa, M., Jefferis, G. S., Ito, K., Saalfeld, S., George, R., Meinertzhagen, I. A., Rubin, G. M., Hess, H. F., Jain, V. and Plaza, S. M. (2020) A connectome and analysis of the adult *Drosophila* central brain. *eLife*, **9**, 1–74.
- Schiller, P. H. (1992) The ON and OFF channels of the visual system. *Trends in Neurosciences*, **15**, 86–92.
- Schiller, P. H., Sandell, J. H. and Maunsell, J. H. (1986) Functions of the ON and OFF channels of the visual system. *Nature*, **322**, 824–825.
- Schilling, T. and Borst, A. (2015) Local motion detectors are required for the computation of expansion Flow-Fields. *Biology Open*, **4**, 1105–1108.
- Schlegel, P., Bates, A. S., Stürner, T., Jagannathan, S. R., Drummond, N., Hsu, J., Capdevila, L. S., Javier, A., Marin, E. C., Barth-Maron, A., Tamimi, I. F., Li, F., Rubin, G. M., Plaza, S. M., Costa, M. and Jefferis, G. S. (2021) Information flow, cell types and stereotypy in a full olfactory connectome. *eLife*, **10**.
- Schlegel, P., Yin, Y., Bates, A. S., Dorkenwald, S., Eichler, K., Brooks, P., Han, D. S., Gkantia, M., dos Santos, M., Munnely, E. J., Badalamente, G., Serratos Capdevila, L., Sane, V. A., C Fragniere, A. M., Kiassat, L., Pleijzier, M. W., Stürner, T., M Tamimi, I. F., Dunne, C. R., Salgarella, I., Javier, A., Fang, S., Perlman, E., Kazimiers, T., Jagannathan, S. R., Matsliah, A., Sterling, A. R., Yu, S.-c., McKellar, C. E., Consortium, F., Costa, M.,

- Sebastian Seung, H., Murthy, M., Hartenstein, V., Bock, D. D. and X E Jefferis, G. S. (2024) Whole-brain annotation and multi-connectome cell typing of *Drosophila*. *Nature*, **634**, 139–152.
- Schnell, B., Raghu, S. V., Nern, A. and Borst, A. (2012) Columnar cells necessary for motion responses of wide-field visual interneurons in *Drosophila*. *Journal of Comparative Physiology*, **198**, 389–395.
- Scholl, B., Gao, X. and Wehr, M. (2010) Nonoverlapping Sets of Synapses Drive On Responses and OFF Responses in Auditory Cortex. *Neuron*, **65**, 412–421.
- Schretter, C. E., Aso, Y., Robie, A. A., Dreher, M., Dolan, M. J., Chen, N., Ito, M., Yang, T., Parekh, R., Branson, K. and Rubin, G. M. (2020) Cell types and neuronal circuitry underlying female aggression in *Drosophila*. *eLife*, **9**, 1–82.
- Serbe, E., Meier, M., Leonhardt, A. and Borst, A. (2016) Comprehensive Characterization of the Major Presynaptic Elements to the *Drosophila* OFF Motion Detector. *Neuron*, **89**, 829–841.
- Seung, H. S. (2024) Predicting visual function by interpreting a neuronal wiring diagram. *Nature*, **634**, 113–123.
- Sharkey, C. R., Blanco, J., Leibowitz, M. M., Pinto-Benito, D. and Wardill, T. J. (2020) The spectral sensitivity of *Drosophila* photoreceptors. *Scientific Reports*, **10**, 1–13.
- Shinomiya, K., Huang, G., Lu, Z., Parag, T., Xu, C. S., Aniceto, R., Ansari, N., Cheatham, N., Lauchie, S., Neace, E., Ogundeyi, O., Ordish, C., Peel, D., Shinomiya, A., Smith, C., Takemura, S., Talebi, I., Rivlin, P. K., Nern, A., Scheffer, L. K., Plaza, S. M. and Meinertzhagen, I. A. (2019) Comparisons between the ON- and OFF-edge motion pathways in the *Drosophila* brain. *eLife*, **8**.
- Shinomiya, K., Karuppururai, T., Lin, T. Y., Lu, Z., Lee, C. H. and Meinertzhagen, I. A. (2014) Candidate neural substrates for off-edge motion detection in *Drosophila*. *Current Biology*, **24**, 1062–1070.
- Shinomiya, K., Nern, A., Meinertzhagen, I. A., Plaza, S. M. and Reiser, M. B. (2022) Neuronal circuits integrating visual motion information in *Drosophila melanogaster*. *Current Biology*, **32**, 3529–3544.e2.
- Shinomiya, K., Takemura, S. Y., Rivlin, P. K., Plaza, S. M., Scheffer, L. K. and Meinertzhagen, I. A. (2015) A common evolutionary origin for the ON- and OFF-edge motion detection pathways of the *Drosophila* visual system. *Frontiers in Neural Circuits*, **9**, 152337.
- Shiu, P. K., Sterne, G. R., Spiller, N., Franconville, R., Sandoval, A., Zhou, J., Simha, N., Kang, C. H., Yu, S., Kim, J. S., Dorkenwald, S., Matsliah, A., Schlegel, P., Yu, S. C., McKellar, C. E., Sterling, A., Costa, M., Eichler, K., Bates, A. S., Eckstein, N., Funke, J., Jefferis, G. S., Murthy, M., Bidaye, S. S., Hampel, S., Seeds, A. M. and Scott, K. (2024) A *Drosophila* computational brain model reveals sensorimotor processing. *Nature*, **634**, 210–219.

- Silies, M., Gohl, D. M., Fisher, Y. E., Freifeld, L., Clark, D. A. and Clandinin, T. R. (2013) Modular Use of Peripheral Input Channels Tunes Motion-Detecting Circuitry. *Neuron*, **79**, 111–127.
- Strausfeld, N. J. (1976) *Atlas of an Insect Brain*. Springer Berlin Heidelberg.
- Strausfeld, N. J., Seyan, H. S. and Milde, J. J. (1987) The neck motor system of the fly *Calliphora erythrocephala*. *Journal of Comparative Physiology A*, **160**, 205–224.
- Strother, J. A., Nern, A. and Reiser, M. B. (2014) Direct Observation of ON and OFF Pathways in the *Drosophila* Visual System. *Current Biology*, **24**, 976–983.
- Strother, J. A., Wu, S. T., Rogers, E. M., Eliason, J. L., Wong, A. M., Nern, A. and Reiser, M. B. (2018) Behavioral state modulates the on visual motion pathway of *Drosophila*. *Proceedings of the National Academy of Sciences of the United States of America*, **115**, E102–E111.
- Strother, J. A., Wu, S. T., Wong, A. M., Nern, A., Rogers, E. M., Le, J. Q., Rubin, G. M. and Reiser, M. B. (2017) The Emergence of Directional Selectivity in the Visual Motion Pathway of *Drosophila*. *Neuron*, **94**, 168–182.e10.
- Suver, M. P., Huda, A., Iwasaki, N., Safarik, S. and Dickinson, M. H. (2016) An array of descending visual interneurons encoding self-motion in *Drosophila*. *Journal of Neuroscience*, **36**, 11768–11780.
- Sweeney, S. T., Broadie, K., Keane, J., Niemann, H. and O’Kane, C. J. (1995) Targeted expression of tetanus toxin light chain in *Drosophila* specifically eliminates synaptic transmission and causes behavioral defects. *Neuron*, **14**, 341–351.
- Taisz, I., Donà, E., Münch, D., Bailey, S. N., Morris, B. J., Meechan, K. I., Stevens, K. M., Varela-Martínez, I., Gkantia, M., Schlegel, P., Ribeiro, C., Jefferis, G. S. and Galili, D. S. (2023) Generating parallel representations of position and identity in the olfactory system. *Cell*, **186**, 2556–2573.e22.
- Takemura, S. Y., Bharioke, A., Lu, Z., Nern, A., Vitaladevuni, S., Rivlin, P. K., Katz, W. T., Olbris, D. J., Plaza, S. M., Winston, P., Zhao, T., Horne, J. A., Fetter, R. D., Takemura, S., Blazek, K., Chang, L. A., Ogundeyi, O., Saunders, M. A., Shapiro, V., Sigmund, C., Rubin, G. M., Scheffer, L. K., Meinertzhagen, I. A. and Chklovskii, D. B. (2013) A visual motion detection circuit suggested by *Drosophila* connectomics. *Nature*, **500**, 175–181.
- Takemura, S.-y., Hayworth, K. J., Huang, G. B., Januszewski, M., Lu, Z., Marin, E. C., Preibisch, S., Xu, C. S., Bogovic, J., Champion, A. S., Cheong, H. S., Costa, M., Eichler, K., Katz, W., Knecht, C., Li, F., Morris, B. J., Ordish, C., Rivlin, P. K., Schlegel, P., Shinomiya, K., Stürner, T., Zhao, T., Badalamente, G., Bailey, D., Brooks, P., Canino, B. S., Clements, J., Cook, M., Duclos, O., Dunne, C. R., Fairbanks, K., Fang, S., Finley-May, S., Francis, A., George, R., Gkantia, M., Harrington, K., Hopkins, G. P.,

- Hsu, J., Hubbard, P. M., Javier, A., Kainmueller, D., Korff, W., Kovalyak, J., Krzemiński, D., Lauchie, S. A., Lohff, A., Maldonado, C., Manley, E. A., Mooney, C., Neace, E., Nichols, M., Ogundeyi, O., Okeoma, N., Paterson, T., Phillips, E., Phillips, E. M., Ribeiro, C., Ryan, S. M., Rymer, J. T., Scott, A. K., Scott, A. L., Shepherd, D., Shinomiya, A., Smith, C., Smith, N., Suleiman, A., Takemura, S., Talebi, I., Tamimi, I. F., Trautman, E. T., Umayam, L., Walsh, J. J., Yang, T., Rubin, G. M., Scheffer, L. K., Funke, J., Saalfeld, S., Hess, H. F., Plaza, S. M., Card, G. M., Jefferis, G. S. and Berg, S. (2024) A Connectome of the Male *Drosophila* Ventral Nerve Cord. *eLife*, **13**.
- Takemura, S. Y., Karuppudurai, T., Ting, C. Y., Lu, Z., Lee, C. H. and Meinertzhagen, I. A. (2011) Cholinergic circuits integrate neighboring visual signals in a *Drosophila* motion detection pathway. *Current Biology*, **21**, 2077–2084.
- Takemura, S.-y., Nern, A., Chklovskii, D. B., Scheffer, L. K., Rubin, G. M. and Meinertzhagen, I. A. (2017) The comprehensive connectome of a neural substrate for ‘ON’ motion detection in *Drosophila*. *eLife*, **6**.
- Tanaka, R. and Clark, D. A. (2022) Neural mechanisms to exploit positional geometry for collision avoidance. *Current Biology*, **32**, 2357–2374.e6.
- Tavakoli, M. R., Lyudchik, J., Januszewski, M., Vistunou, V., Agudelo, N., Vorlaufer, J., Sommer, C., Kreuzinger, C., Oliveira, B., Cenameri, A., Novarino, G., Jain, V. and Danzl, J. G. (2024) Light-microscopy based dense connectomic reconstruction of mammalian brain tissue. *bioRxiv*.
- Tuthill, J. C., Nern, A., Holtz, S. L., Rubin, G. M. and Reiser, M. B. (2013) Contributions of the 12 Neuron Classes in the Fly Lamina to Motion Vision. *Neuron*, **79**, 128–140.
- Ugur, B., Chen, K. and Bellen, H. J. (2016) *Drosophila* tools and assays for the study of human diseases. *Disease Models and Mechanisms*, **9**, 235–244.
- Venken, K. J., Simpson, J. H. and Bellen, H. J. (2011) Genetic Manipulation of Genes and Cells in the Nervous System of the Fruit Fly. *Neuron*, **72**, 202–230.
- Von Hassenstein, B. and Reichardt, W. (1956) Systemtheoretische Analyse der Zeit-, Reihenfolgen- und Vorzeichenauswertung bei der Bewegungsperzeption des Rüsselkäfers *Chlorophanus*. *Zeitschrift für Naturforschung - Section B Journal of Chemical Sciences*, **11**, 513–524.
- Wardill, T. J., List, O., Li, X., Dongre, S., McCulloch, M., Ting, C. Y., O’Kane, C. J., Tang, S., Lee, C. H., Hardie, R. C. and Juusola, M. (2012) Multiple spectral inputs improve motion discrimination in the *Drosophila* visual system. *Science*, **336**, 925–931.
- Wässle, H. (2004) Parallel processing in the mammalian retina. *Nature Reviews Neuroscience*, **5**, 747–757.

- Wertz, A., Borst, A. and Haag, J. (2008) Nonlinear integration of binocular optic flow by DNOVS₂, a descending neuron of the fly. *Journal of Neuroscience*, **28**, 3131–3140.
- Wertz, A., Haag, J. and Borst, A. (2009) Local and global motion preferences in descending neurons of the fly. *Journal of Comparative Physiology A*, **195**, 1107–1120.
- Wertz, A., Haag, J. and Borst, A. (2012) Integration of binocular optic flow in cervical neck motor neurons of the fly. *Journal of Comparative Physiology A*, **198**, 655–668.
- Westheimer, G. (2007) The ON–OFF dichotomy in visual processing: From receptors to perception. *Progress in Retinal and Eye Research*, **26**, 636–648.
- White, J. G., Southgate, E., Thomson, J. and Brenner, S. (1986) The structure of the nervous system of the nematode *Caenorhabditis elegans*. *Philosophical Transactions of the Royal Society of London. B, Biological Sciences*, **314**, 1–340.
- White, K., Grether, M. E., Abrams, J. M., Young, L., Farrell, K. and Steller, H. (1994) Genetic control of programmed cell death in *Drosophila*. *Science*, **264**, 677–683.
- Wienecke, C. F., Leong, J. C. and Clandinin, T. R. (2018) Linear Summation Underlies Direction Selectivity in *Drosophila*. *Neuron*, **99**, 680–688.e4.
- Wilson, R. I., Turner, G. C. and Laurent, G. (2004) Transformation of Olfactory Representations in the *Drosophila* Antennal Lobe. *Science*, **303**, 366–370.
- Wu, M., Nern, A., Ryan Williamson, W., Morimoto, M. M., Reiser, M. B., Card, G. M. and Rubin, G. M. (2016) Visual projection neurons in the *Drosophila* lobula link feature detection to distinct behavioral programs. *eLife*, **5**.
- Xu, Y., Zou, P. and Cohen, A. E. (2017) Voltage imaging with genetically encoded indicators. *Current Opinion in Chemical Biology*, **39**, 1–10.
- Yamaguchi, S., Desplan, C. and Heisenberg, M. (2010) Contribution of photoreceptor subtypes to spectral wavelength preference in *Drosophila*. *Proceedings of the National Academy of Sciences of the United States of America*, **107**, 5634–5639.
- Yamaguchi, S., Wolf, R., Desplan, C. and Heisenberg, M. (2008) Motion vision is independent of color in *Drosophila*. *Proceedings of the National Academy of Sciences of the United States of America*, **105**, 4910–4915.
- Yang, H. H. H., St-Pierre, F., Sun, X., Ding, X., Lin, M. Z. Z. and Clandinin, T. R. R. (2016) Subcellular Imaging of Voltage and Calcium Signals Reveals Neural Processing In Vivo. *Cell*, **166**, 245–257.
- Yoshimatsu, T. and Baden, T. (2024) New twists in the evolution of retinal direction selectivity. *PLoS Biology*, **22**, e3002538.

- Zhang, F., Wang, L. P., Brauner, M., Liewald, J. F., Kay, K., Watzke, N., Wood, P. G., Bamberg, E., Nagel, G., Gottschalk, A. and Deisseroth, K. (2007) Multimodal fast optical interrogation of neural circuitry. *Nature*, **446**, 633–639.
- Zhang, Y., Rózsa, M., Liang, Y., Bushey, D., Wei, Z., Zheng, J., Reep, D., Broussard, G. J., Tsang, A., Tsegaye, G., Narayan, S., Obara, C. J., Lim, J. X., Patel, R., Zhang, R., Ahrens, M. B., Turner, G. C., Wang, S. S., Korff, W. L., Schreiter, E. R., Svoboda, K., Hasseman, J. P., Kolb, I. and Looger, L. L. (2023) Fast and sensitive GCaMP calcium indicators for imaging neural populations. *Nature*, **615**, 884–891.
- Zheng, Z., Lauritzen, J. S., Perlman, E., Robinson, C. G., Nichols, M., Milkie, D., Torrens, O., Price, J., Fisher, C. B., Sharifi, N., Calle-Schuler, S. A., Kmecova, L., Ali, I. J., Karsh, B., Trautman, E. T., Bogovic, J. A., Hanslovsky, P., Jefferis, G. S., Kazhdan, M., Khairy, K., Saalfeld, S., Fetter, R. D. and Bock, D. D. (2018) A Complete Electron Microscopy Volume of the Brain of Adult *Drosophila melanogaster*. *Cell*, **174**, 730–743.e22.
- Zhou, L., Schnitzler, A., Agapite, J., Schwartz, L. M., Steller, H. and Nambu, J. R. (1997) Cooperative functions of the reaper and head involution defective genes in the programmed cell death of *Drosophila* central nervous system midline cells. *Proceedings of the National Academy of Sciences of the United States of America*, **94**, 5131–5136.